NUREG/CR–6184
SAND92–1720

Separate Effects Testing and Analyses to Investigate Liner Tearing of the 1:6-Scale Reinforced Concrete Containment Building

Prepared by
B. L. Spletzer, L. D. Lambert, V. L. Bergman, J. R. Weatherby

Sandia National Laboratories
Operated by
Sandia Corporation

Prepared for
U.S. Nuclear Regulatory Commission

AVAILABILITY NOTICE

Availability of Reference Materials Cited in NRC Publications

Most documents cited in NRC publications will be available from one of the following sources:

1. The NRC Public Document Room, 2120 L Street, NW., Lower Level, Washington, DC 20555-0001

2. The Superintendent of Documents, U.S. Government Printing Office, P. O. Box 37082, Washington, DC 20402-9328

3. The National Technical Information Service, Springfield, VA 22161-0002

Although the listing that follows represents the majority of documents cited in NRC publications, it is not intended to be exhaustive.

Referenced documents available for inspection and copying for a fee from the NRC Public Document Room include NRC correspondence and internal NRC memoranda; NRC bulletins, circulars, information notices, inspection and investigation notices; licensee event reports; vendor reports and correspondence; Commission papers; and applicant and licensee documents and correspondence.

The following documents in the NUREG series are available for purchase from the Government Printing Office: formal NRC staff and contractor reports, NRC-sponsored conference proceedings, international agreement reports, grantee reports, and NRC booklets and brochures. Also available are regulatory guides, NRC regulations in the *Code of Federal Regulations,* and *Nuclear Regulatory Commission Issuances.*

Documents available from the National Technical Information Service include NUREG-series reports and technical reports prepared by other Federal agencies and reports prepared by the Atomic Energy Commission, forerunner agency to the Nuclear Regulatory Commission.

Documents available from public and special technical libraries include all open literature items, such as books, journal articles, and transactions. *Federal Register* notices, Federal and State legislation, and congressional reports can usually be obtained from these libraries.

Documents such as theses, dissertations, foreign reports and translations, and non-NRC conference proceedings are available for purchase from the organization sponsoring the publication cited.

Single copies of NRC draft reports are available free, to the extent of supply, upon written request to the Office of Administration, Distribution and Mail Services Section, U.S. Nuclear Regulatory Commission, Washington, DC 20555-0001.

Copies of industry codes and standards used in a substantive manner in the NRC regulatory process are maintained at the NRC Library, Two White Flint North, 11545 Rockville Pike, Rockville, MD 20852-2738, for use by the public. Codes and standards are usually copyrighted and may be purchased from the originating organization or, if they are American National Standards, from the American National Standards Institute, 1430 Broadway, New York, NY 10018-3308.

DISCLAIMER NOTICE

NUREG/CR–6184
SAND92–1720

Separate Effects Testing and Analyses to Investigate Liner Tearing of the 1:6-Scale Reinforced Concrete Containment Building

Manuscript Completed: May 1995
Date Published: June 1995

Prepared by
B. L. Spletzer, L. D. Lambert, V. L. Bergman, J. R. Weatherby

Sandia National Laboratories
Albuquerque, NM 87185

Prepared for
Division of Engineering Technology
Office of Nuclear Regulatory Research
U.S. Nuclear Regulatory Commission
Washington, DC 20555–0001
NRC Job Code A1817

Abstract

The overpressurization of a 1:6-scale reinforced concrete containment building demonstrated that liner tearing is a plausible failure mode in such structures under severe accident conditions. A combined experimental and analytical program was developed to determine the important parameters which affect liner tearing and to develop reasonably simple analytical methods for predicting when tearing will occur. Three sets of test specimens were designed to allow individual control over and investigation of the mechanisms believed to be important in causing failure of the liner plate. The series of tests investigated the effect on liner tearing produced by the anchorage system, the loading conditions, and the transition in thickness from the liner to the insert plate. Before testing, the specimens were analyzed using two- and three-dimensional finite element models. Based on the analysis, the failure mode and corresponding load conditions were predicted for each specimen. Test data and post-test examination of test specimens show mixed agreement with the analytical predictions with regard to failure mode and specimen response for most tests. Many similarities were also observed between the response of the liner in the 1:6-scale reinforced concrete containment model and the response of the test specimens. This work illustrates the fact that the failure mechanism of a reinforced concrete containment building can be greatly influenced by details of liner and anchorage system design. Further, it significantly increases the understanding of containment building response under severe conditions.

Contents

Section		Page
1	Introduction	1
	1.1 Background	1
	1.2 Program Scope	1
2	Basis and Design of Test Specimens	5
	2.1 Weld-Transition Specimen Design	6
	2.2 Separately-Controlled-Loading Specimen Design	8
	2.3 Full-Simulation Specimen Design	8
	2.4 Specimen Material Specifications	12
3	Test Specimen Instrumentation	14
4	Data Acquisition and Test Equipment	20
5	Conduct of Tests	22
6	Test Results	24
	6.1 Weld-Transition Specimen Test Results	24
	6.2 Separately-Controlled-Loading Specimen Test Results	36
	6.3 Full-Simulation Specimen Test Results	50
	6.4 Test Result Conclusions	59
7	Finite Element Models of Test Specimens	64
	7.1 Weld-Transition/Full-Simulation Models	64
	7.2 Separately-Controlled-Loading Model	68
8	Comparison of Finite Element and Experimental Results	71
	8.1 Results for Weld-Transition Model	71
	8.2 Results for Separately-Controlled-Loading Model	71
	8.3 Results for Full-Simulation Model	76
9	Conclusions	81
10	References	82
Appendix A: Detail Drawings of Test Specimens		A-1
Appendix B: Strain Gage Data Plots for the Separate Effects Tests		B-1
Appendix C: Summary of Reduced Photoelastic Data		C-1

Figures

Figure		Page
1.1	Cross-section of 1:6-scale reinforced concrete model	2
1.2	Major tear in 1:6-scale reinforced concrete model	3
1.3	Stretchout of 1:6-scale model showing major tears	4
2.1	Postulated failure mechanism for the 1:6-scale model	6
2.2	Weld-transistion specimens	7
2.3	Separately-controlled loading specimen	9
2.4	Loading sequence for separately-controlled loading	10
2.5	Full-simulation specimen	11
2.6	Stress-strain response of A414, Grade D and A516, Grades 60 and 70 steels	13
3.1	Gage locations for the Weld-transistion specimens	16
3.2	Gage locations for separately-controlled-loading specimen	17
3.3	Gage locations for full-simulation specimens	18
3.4	Typical photoelastic response of a full-simulation specimen	19
4.1	Test configuraation of a separately-controlled-loading specimen	21
5.1	Specimen with external pressure apparatus	23
6.1	Overall response of the weld-transition specimens	25
6.2	Cross-section of specimen weld	26
6.3	Liner edge strip gage response, specimen 2A4	27
6.4	Centerline strip gage response, specimen 2A4	28
6.5	Front edge strip gage, specimen 2A4	29
6.6	Front centerline strip gage, specimen 2A4	30
6.7	Centerline bending strain, specimen 2A4	32
6.8	Failure locations in weld-transistion specimens	33
6.9	Raw photoelastic data from a weld-tranistion specimen	34
6.10	Maximum shearing strain in specimen 2A5	35
6.11	Overall separately-controlled-loading response	37
6.12	Outboard axial strip gage displacement response, 65 ksi specimen	39
6.13	Outboard axial strip gage response, 65 ksi response	40
6.14	Inboard transverse strip gage response, 65 ksi specimen	41
6.15	Poisson strip gage response, 65 ksi specimen	43
6.16	Poisson strip gage displacement response, 63 ksi specimen	44
6.17	Upper single-element gage displacement response, 65 ksi specimen	45
6.18	Lower single-element gage displacement response, 65 ksi specimen	46
6.19	Upper single-element gage displacement response, 63 ksi specimen	47
6.20	Lower single-element gage displacement response, 63 ksi specimen	48

Figures
(cont.)

Figure — Page

6.21 Maximum shearing strain in 60 ksi specimem 49
6.22 Maximum shearing strain in 65 ksi specimen 51
6.23 Overall response of full-simulation specimens 52
6.24 Typical response of reinforcing steel, full -simulation specimens 54
6.25 Full-simulation specimen liner plate single-gage response 55
6.26 Full-simulation specimen liner single-element poisson gage response 56
6.27 Full-simulation specimen lower outboard strip gage response 57
6.28 Full-simulation specimen typical edge strip gage response 58
6.29 Full-simulation specimen typical transverse strip gage response 61
6.30 Full-simulation specimen maximum shearing strain 62
6.31 Posttest conditions of studs near the liner/insert plate junction 63
7.1 Finite element model for the full-simulation and weld-transition specimens 65
7.2 Mises stress vs. equivalent plastic strain in weld-transition and full-simulation specimens 66
7.3 Functions defining the force-displacement relationship for the studs 67
7.4 Finite element model and loading of the separately-controlled-loading specimen 69
7.5 Mises stress vs. equivalent plastic strain for the separately-controlled-loading specimen 70
8.1 Experimental and analytical force-displacement response for the weld-transition specimens 72
8.2 Maximum in-plane shear strain in a wel-transition specimen at 1.5 percent elongation 73
8.3 Maximum in-plane shear strain in the 65 ksi preloaded separately-controlled-loading specimen 75
8.4 Overall force-elongation curve from the finite element analysis of the full-simulation specimen 77
8.5 Experimental and analytical force-elongation relationships for the full-simulation specimens 78
8.6 Maximum in-plane shear strain in a full-simulation specimen at 1.5 percent elongation 79
8.7 Finite element results showing maximum shear strain in full-simulation model without anchorage 80

Tables

Table — Page

8.1 Predicted and observed failure modes for separately-controlled-loading specimens 74
8.2 Measured, Predicted, and net section stress failue load for separately-controlled-loading specimens 74

Executive Summary

This test series was designed to investigate the causes of liner tear failure of the 1:6-scale reinforced concrete containment building. The postulated mechanism to cause liner tearing is that a relatively small load applied to the stud anchors can induce a tear in a highly strained liner. This load is thought to be produced by differential movement between the reinforcing steel and the liner plate. A combined experimental and analytical approach was used to determine the important parameters which affect liner tearing and to develop analytical methods for predicting tearing. The tests investigated the effect on liner tearing produced by the anchorage system, the loading conditions, and the transition in thickness from the liner to the insert plate. Before testing, the specimens were analyzed using two- and three-dimensional finite element models. Based on the analysis, the failure mode and corresponding load conditions were predicted for each specimen.

The test specimens were instrumented with strain gages and photoelastic material. While the tests lend some support to stud loading as a means of initiating a liner tear, not all tests support this. Early tests and analysis showed that the thickness and weld transition between the liner and insert plate did not produce a strain concentration. In addition they show significant edge effects that are an important departure from the actual strain state of the 1:6-scale model.

The tests and analysis to investigate liner tears initiated by stud loading are in good agreement and demonstrate that tearing can be induced in a highly strained liner material with relatively weak anchorage, which transfers the load to the liner. The analytical models provide a reasonable method for predicting the transition between liner tearing and stud failure. The testing also shows that the transition between the failure modes is strongly dependent on material and mechanical properties.

The final tests and analyses were designed to provide conditions very similar to those of the 1:6-scale model. The tests were intended to investigate whether the postulated load transfer could occur and whether the transfer could result in liner tearing. The tests give mixed indications of significant load transfer but are not conclusive. Possible reasons for the discrepancy have been formulated but have not been fully investigated.

Acknowledgments

This project was sponsored by the U.S. Nuclear Regulatory Commission (NRC). Special thanks are due to James Costello of the NRC for his guidance throughout the program.

The specimens were tested in Sandia's Geomechanics Department, where materials testing machines and operators were provided by Wolfgang Wawersik, manager of that department. Thanks to Wolfgang, Robert Hardy and Lawerence Carlson for their assistance and expertise.

Thanks are also due to Robert Eyers[1], Robin Sharpe[1] and David Tanner[1] for instrumentation and setup work on the test specimens.

[1]Ktech Corporation

1. Introduction

The U.S. Nuclear Regulatory Commission (NRC) is investigating the performance of light water reactor (LWR) containments subject to severe accidents. This work is being performed by the International Nuclear Safety Department at Sandia National Laboratories (SNL). In 1987, a 1:6-scale reinforced concrete containment model (RCC) was tested by pressurization to failure (Horschel, 1992). The failure mode was a liner tear. As a result of this test, a separate effects test program has been conducted to investigate a number of parameters which could affect liner tearing. Finite element analyses were also used to investigate analytical modeling techniques for simulation of liner failure. This report discusses the design and instrumentation of a number of test specimens as well as the results of the testing. These results were compared with the results of finite element simulations for each of the specimen types.

The objective of this separate effects test series is to develop an understanding of liner tearing in the 1:6-scale RCC and increase understanding of potential failure modes of LWR containments.

1.1 Background

Figure 1.1 shows a cross section of the 1:6-scale RCC model. This model was tested in July 1987 to a pressure of 145 psig (1.0 MPa), at which time the model began to leak. The mode of failure was a 22 inch (560 mm) tear in the liner adjacent to a penetration insert plate. Figure 1.2 is a photograph of this tear. Upon closer examination, a large number of small tears and distressed areas were found in the liner. In general, the direction of the tears was vertical and the tears occurred at the corners of penetrations near the mid-height of the model cylinder. Figure 1.3 is a stretchout showing the location of tears and distressed areas in the liner.

This post-test examination of the model revealed several important facts. First, the large tear was not an isolated instance caused by some imperfection. This is evidenced by the fact that numerous other tears in similar locations were developing at the same time. All tears occurred near the insert-to-liner weld and thickness transition, which is also the region of closest stud anchorage spacing. Also, all the tears were propagating in a vertical direction, which appeared to be in response to the liner hoop strain. Finally, the tears tended to occur near the mid-height of the cylinder, where the liner strain was the greatest.

These multiple tears in the liner point to a failure mechanism which could possibly involve the weld, the liner/insert thickness transition, the liner anchorage, and the material properties of the liner plate. In order to investigate the interactions of these various items and to develop a fuller understanding of the failure mechanism of the 1:6-scale RCC model, the separate effects test series was initiated.

1.2 Program Scope

The program scope included the development of both experimental and analytical models for investigation of liner tearing.

A number of different test specimens were required and three specific types of test specimens were designed to simulate some features of the 1:6-scale RCC. The specimens were heavily instrumented with strain gages and photoelastic materials. Nine different test sequences were devised to investigate a wide variety of model parameters. The amount of data gathered during this test series was quite large. For a comparison, the 1:6-scale RCC had about 1200 instrumentation channels. In total, the separate effects test series had about 800 instrumentation channels. In addition, the photoelastic techniques used provided very large amounts of data by yielding whole-field indications of strain. These whole-field strain data provided a convenient means of comparing the experimental results with results from finite element simulations.

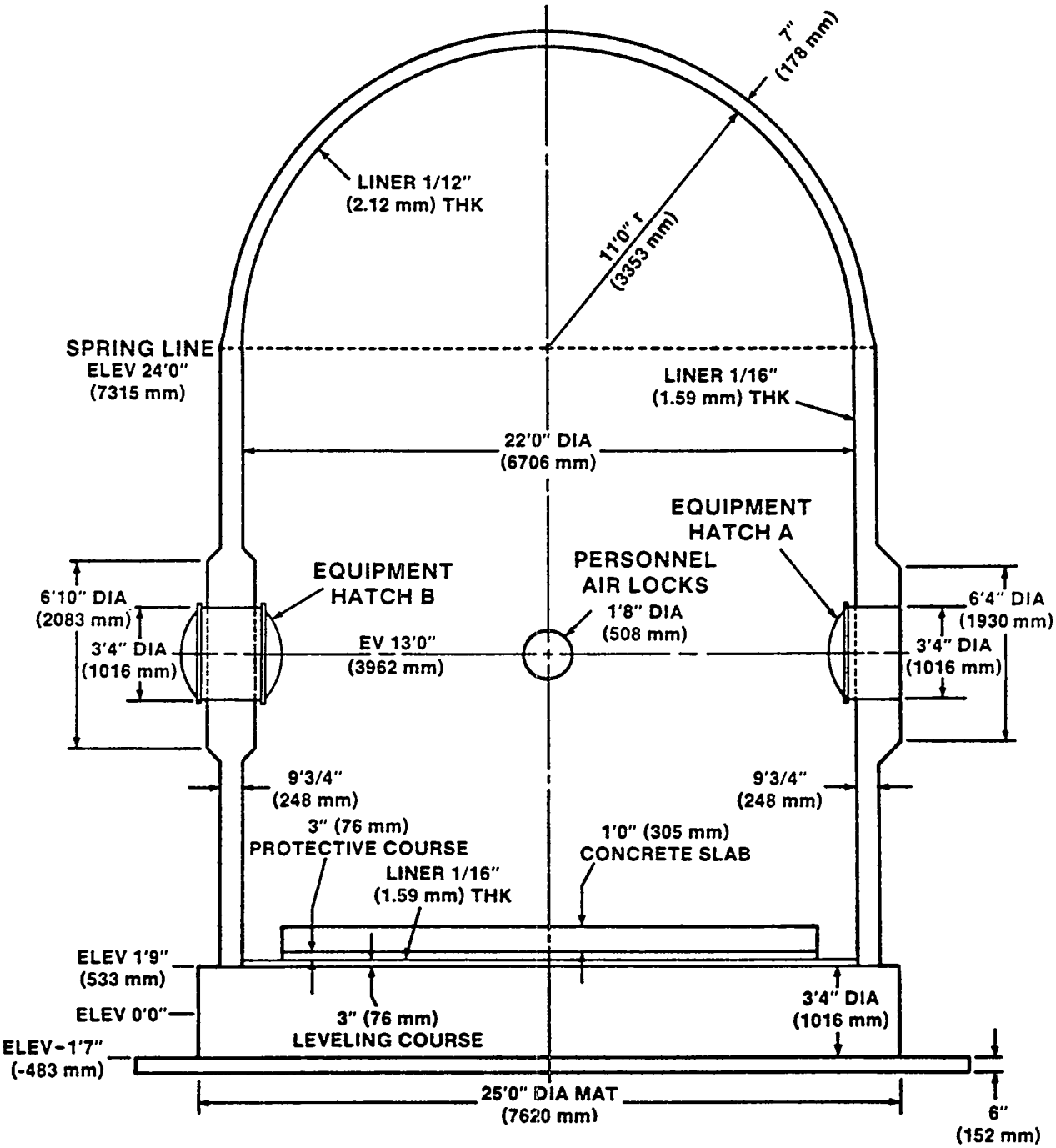

Figure 1.1: Cross-Section of 1:6-scale reinforced concrete model

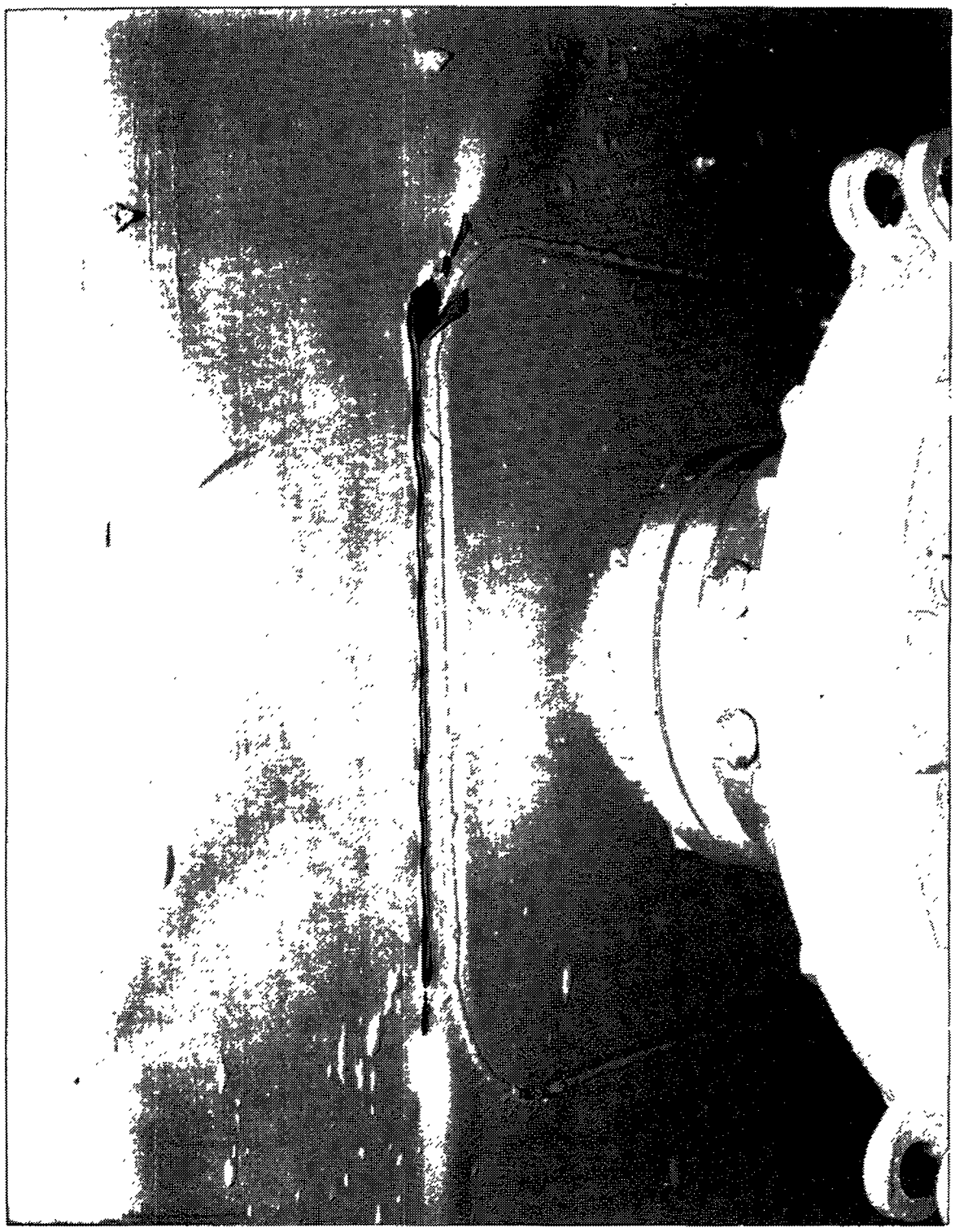

Figure 1.2: Major tear in 1:6-scale reinforced concrete model

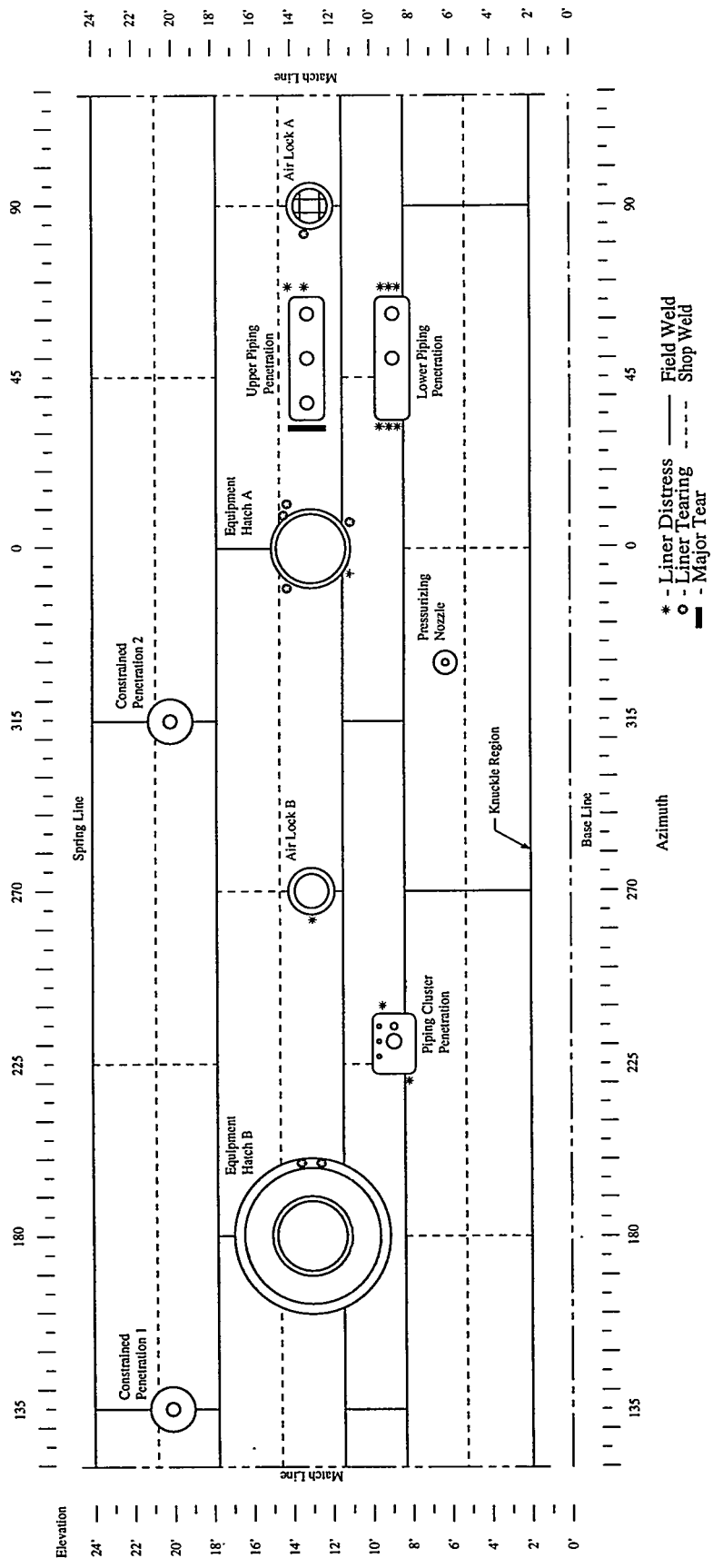

Figure 1.3: Stretchout of 1:6-scale model showing major tears

2. Basis and Design of Test Specimens

Following testing of the 1:6-scale model, a theory was developed to explain the mechanism of liner failure near the insert plate weld. This mechanism is illustrated in Figure 2.1. The upper half of the figure shows a schematic cross section of the 1:6-scale model in the region near the weld and thickness transition. This section is designed to represent a portion of the model wall section in the hoop direction. The lower part of the figure shows this same schematic after a uniform 3 percent strain has been applied to the section. It is assumed that, in regions far from the liner-plate-to-insert-plate weld, there is uniform displacement throughout the wall thickness. Several highlighted regions in the lower part of the figure explain the mechanism leading to liner tearing.

Since the reinforcing steel carries the bulk of the tensile load during the test, it tends to dominate the strain response and strains uniformly throughout its length. This uniform strain causes the concrete to crack regularly along the length of the steel. This regularly fractured concrete is still attached to the relatively closely spaced studs. The liner and insert plate to which the studs are attached do not undergo the same uniform strain. Again, far from the liner-to-insert plate weld, the overall elongation of the liner-insert plate combination is the same as that of the reinforcing steel. However, the insert plate is three times the thickness of the liner plate; therefore, as tension is applied to the combination, the insert plate remains elastic while the liner plate undergoes plastic strain. In the schematic shown in the figure, the active portion of the liner and insert plate are approximately equal and, therefore, since the liner plate must absorb most of the elongation of the combination, the liner plate strain is about twice that of the uniformly strained rebar or 6 percent.

This potential difference in displacement of the liner plate, insert plate, and reinforcing steel creates a potential for shear load transfer. As mentioned previously, the heads of the studs are embedded in the concrete, which is moving with the uniformly strained reinforcing steel. However, the bases of the studs are welded to the liner and insert plate and thus experience the same deflection as the liner and insert plate. This mismatch in deflection cannot be tolerated by the studs and results in a shear load being transferred from the reinforcing steel to the liner and insert plate. In the figure, both the reinforcing steel and liner/insert plate have been strained to the configuration which they would assume if the studs were not present. This difference in deflection causes the studs to bend. The angle at which a stud bends is a measure of the shear load, which could be transmitted from the reinforcing steel into the liner/insert plate region.

Notice in the figure that the studs with the largest angle are those nearest the weld and thickness transition. This leads to the conclusion that, once the liner has undergone plastic strain, the load transferred adds additional stress to the liner. In addition, the maximum stress in the liner should be immediately adjacent to the last row of studs next to the insert-to-liner transition. Finally, notice that the angle of the studs in the first row on the insert plate is the same as the first row in the liner plate. However, since the insert plate is three times thicker than the liner plate, the additional stress induced by this shear transfer is only one-third as great in the insert as in the liner. Recently, this postulated mechanism has been further supported by destructive examination of the 1:6-scale model (Lambert, 1992).

2.1 Design of Weld Transition Specimen

The need to investigate this postulated failure mechanism led to the design and development of a number of specimens to test separate effects. The first specimen developed addressed the fact that the tear occurred very close to the liner-to-insert transition. The mechanism discussed above is capable of producing a tear regardless of the properties near the weld. However, since the actual tear locations are close to a weld, the weld properties, the thickness transition, and their effect on the liner behavior had to be investigated. The first specimen provided a means of testing the effect of the weld and transition on the liner and insert plate and is called the weld transition specimen. Figure 2.2 is a perspective drawing of the specimen as configured and a two-view assembly drawing of the specimen with the major dimensions included. Detailed construction drawings of the specimen are included in Appendix A of this report.

The specimen consisted of a 10 inch (250 mm) wide segment of liner plate 18 inches (450 mm) long. Both ends of the liner plate are attached to insert plate sections using the weld specification and design of the 1:6-scale model. The insert plates are in turn attached to a pull fixture to allow the specimen to be placed in uniaxial tension. As shown in the figure, the pull fixture incorporates a very large number of attachment bolts. Only a very small number of these bolts are necessary to develop sufficient load to fail the specimen. However, to reduce the moment loading in the specimen that could be generated by contact with bolts carrying the shear load, enough bolts are used to ensure that the specimen pull is developed entirely by friction. Since the development of friction force begins in the as-assembled position of the specimen, slight errors in hole placement and diameter do not affect the overall response.

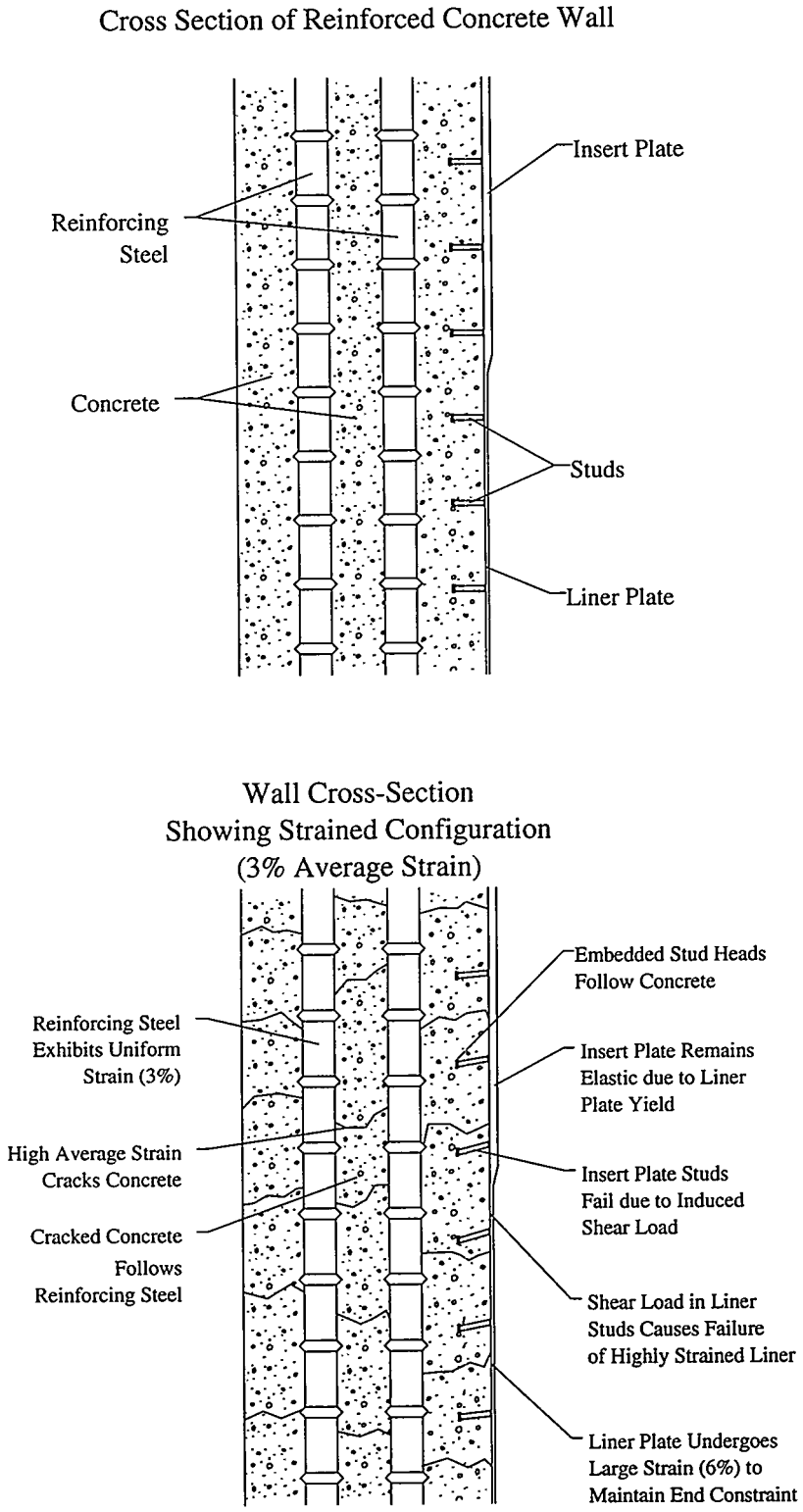

Figure 2.1: Postulated failure mechanism for the 1:6-scale model

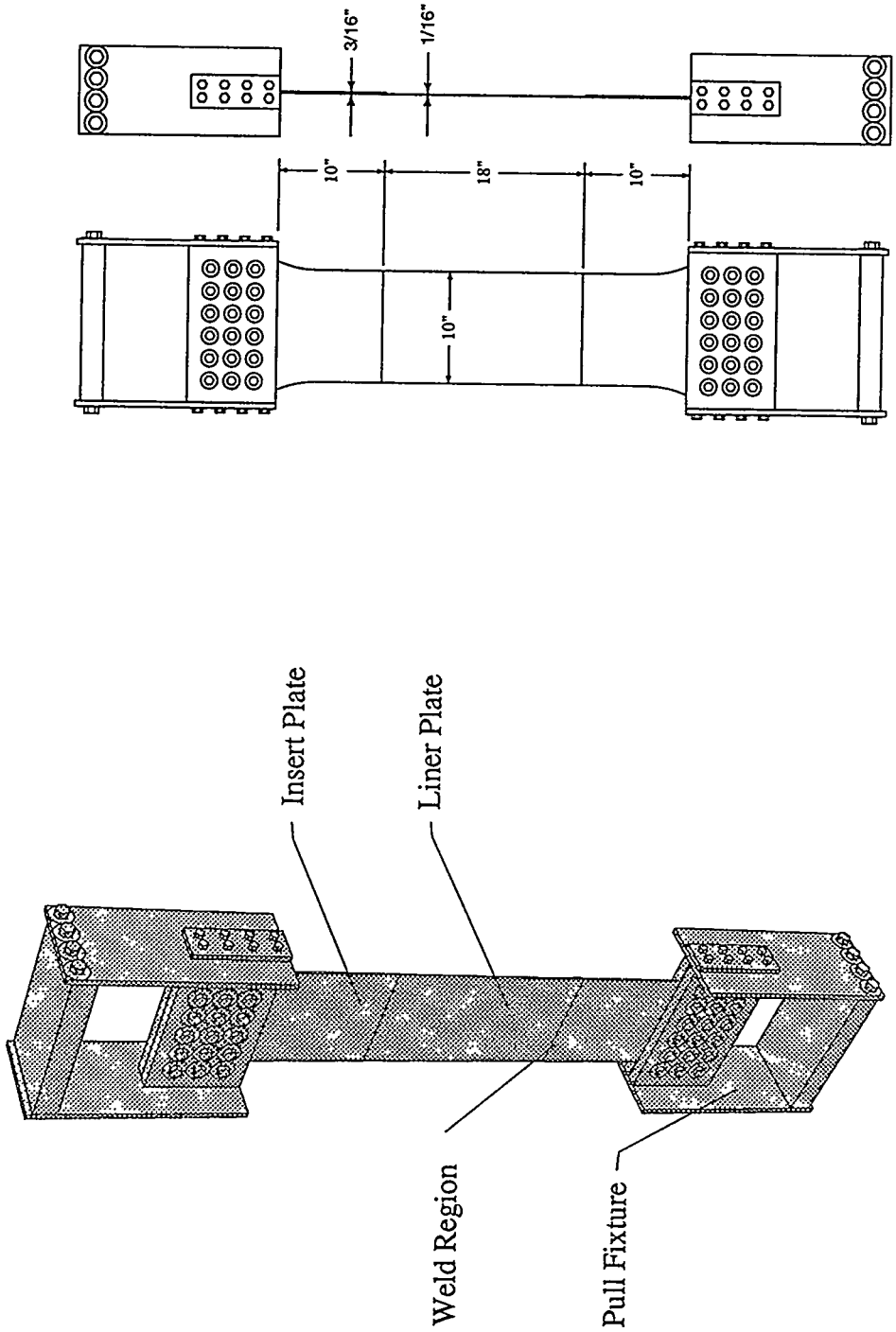

Figure 2.2: Weld transition specimen

2.2 Separately-Controlled-Loading Specimen Design

The next specimen was designed to allow the effects of liner prestress and stud shear to be investigated separately. As discussed above, it appears that stud shear load and hoop strain in the liner combine to produce a liner tear when neither mechanism separately would tear the liner. A simplified model of this mechanism can be envisioned using the idea of stress in the liner. If the liner is preloaded to a stress that is beyond the yield stress of the material, plastic deformation occurs. Since the material has not reached its ultimate strength, liner tearing does not occur. However, at this point, a small increase in the stress could induce liner tearing. This small change could be provided by the stud shear load. The net section stress increase caused by the studs is the total stud load divided by the total liner cross-section. This increase, if large enough, could cause liner failure. This specimen was used to investigate the detailed effects and interactions between liner preload and stud shear.

Figure 2.3 shows a perspective drawing and a two-view assembly drawing of this separately controlled loading specimen, and Appendix A contains detailed drawings of the specimen. This specimen consists of two large dog bone-shaped pieces of liner material with four anchorage studs attached across the neck of each dog bone. One dog bone is mounted on each side of the specimen so that the total specimen is symmetric. A block of concrete is cast around the studs in the central region of the specimen and is attached to the specimen only by the studs. This attachment allows stud shear to be applied separately from axial tension in the specimen. Again, as with the previous specimen, a relatively large number of bolts are used at both ends of the specimen to ensure that the friction developed will be adequate to fail the specimen. The ends of the specimen are significantly wider than the center, unlike the previous specimen, in order to ensure sufficient frictional capability and to guarantee that, when the specimen is loaded beyond yield, the initial yielding takes place in the stud region. The radius of the dog bone is very large to keep the strain concentration as low as possible. Analysis shows the strain concentration for this configuration to be about 4 percent.

During testing, two separately controlled systems were used to apply the load. The loading took place in the three steps illustrated in Figure 2.4. First, the upper end of the specimen was rigidly fixed. Next, the first loading system applied direct tension to the liner by pulling on the lower block. This load was increased to a predetermined net section stress at the narrowest part of the specimen. Once this load was achieved, it was maintained through a load-control device. Finally, the second loading system applied downward load to the concrete block to produce shear loading to the studs. This second system operates under displacement control and slowly displaces the concrete block while measuring the force required to cause the displacement and allowing the load-controlled portion of the experiment to maintain the load in the liner throughout the experiment.

By varying the initial liner preload and then displacing the concrete block until failure occurs, the interaction between liner preload and stud shear can be studied. This specimen allows the liner preload parameter to be varied to investigate the sensitivity of the failure mechanism. From the postulated failure mechanism of the 1:6-scale model, it would be predicted that, at low liner preloads, the motion of the concrete block will simply shear the studs from the liner while, at higher preloads, the motion of the block will initiate a tear in the liner.

2.3 Full-Simulation Specimen Design

The final specimen developed for investigation of the separate effects comes closest to a full simulation of the actual wall section of the 1:6-scale reinforced concrete containment. A perspective drawing of this full-simulation specimen is shown in Figure 2.5 along with a two-view assembly drawing with limited dimensions. Again, details of this specimen are included in Appendix A.

This specimen is sized to closely model the 1:6-scale containment. However, to ensure that the tensile load could be balanced on the specimen, it represents a dual, back-to-back section of the 1:6-scale model. That is, the liner and insert plate region is applied to both the front and back of the specimen. Ten #6 reinforcing steel rods are installed axially in each specimen. The specimen is 10 inches (250 mm) wide and the depth, that is, the distance from the front liner plate to the back liner plate, is 15 inches (375 mm). The reinforcing steel used here is somewhat larger than that used in the 1:6-scale model. However, the fraction of the steel area and the ratio of liner steel to reinforcing steel is the same as in the model. This specimen is designed to directly investigate the failure mechanism discussed earlier. The end blocks on the specimen ensure that the overall elongation of the liner insert plate combination and the reinforcing steel are identical. According to the postulated failure mechanism, this will develop shear through load transfer between the reinforcing steel and the nonuniformally strained liner/insert plate region.

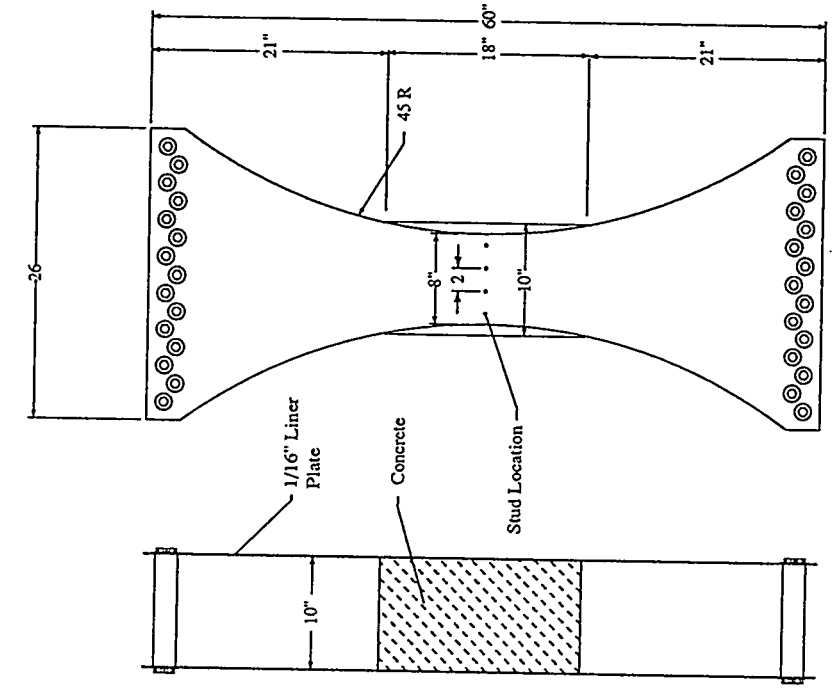

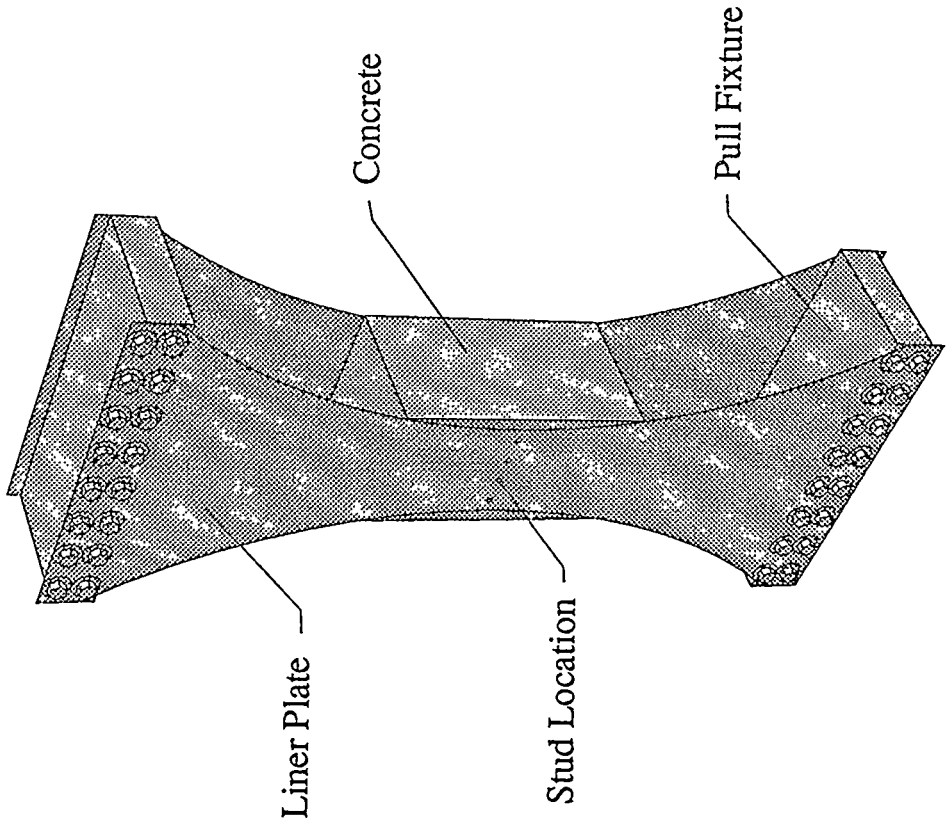

Figure 2.3: Separately-controlled-loading specimen

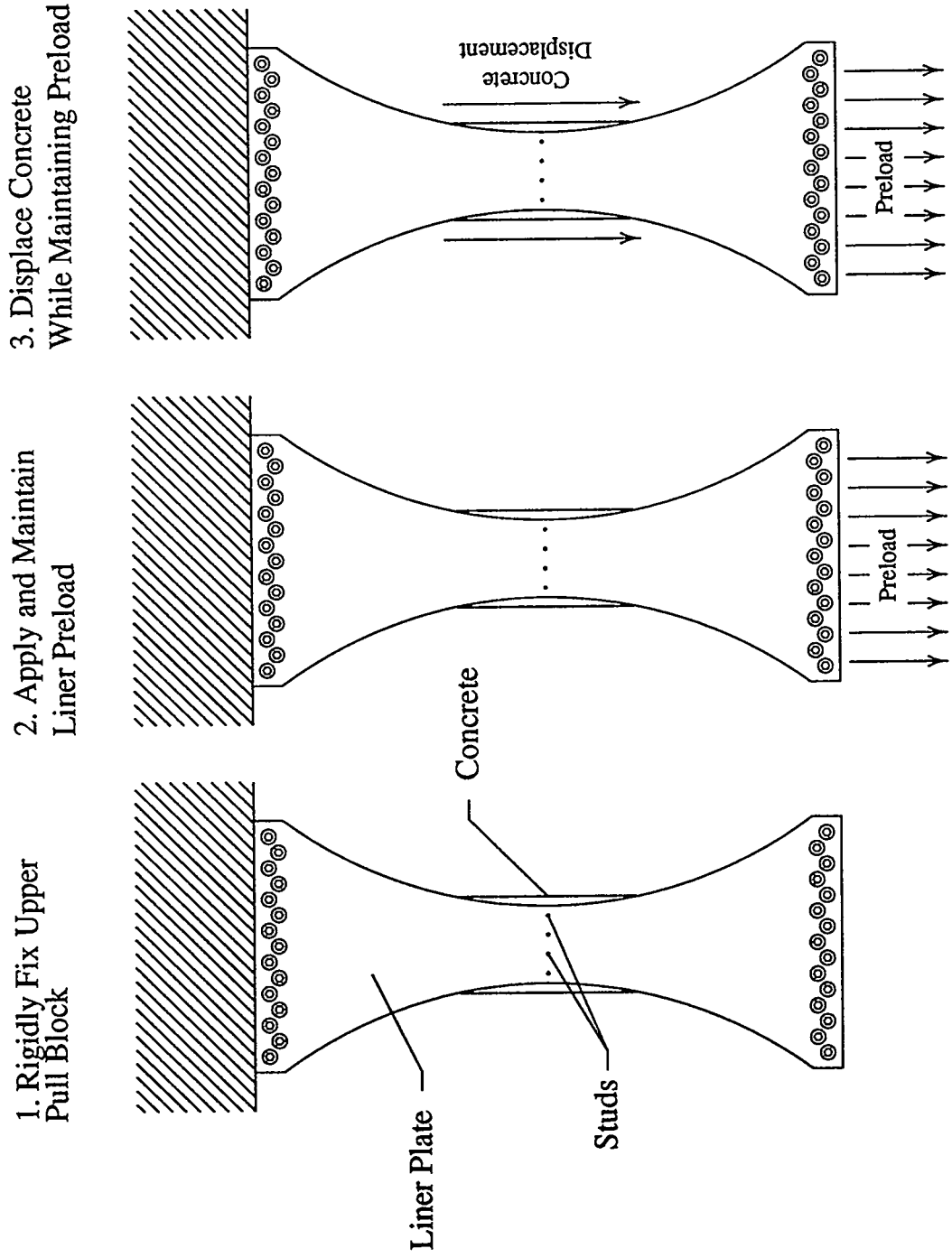

Figure 2.4: Loading sequence for separately controlled loading

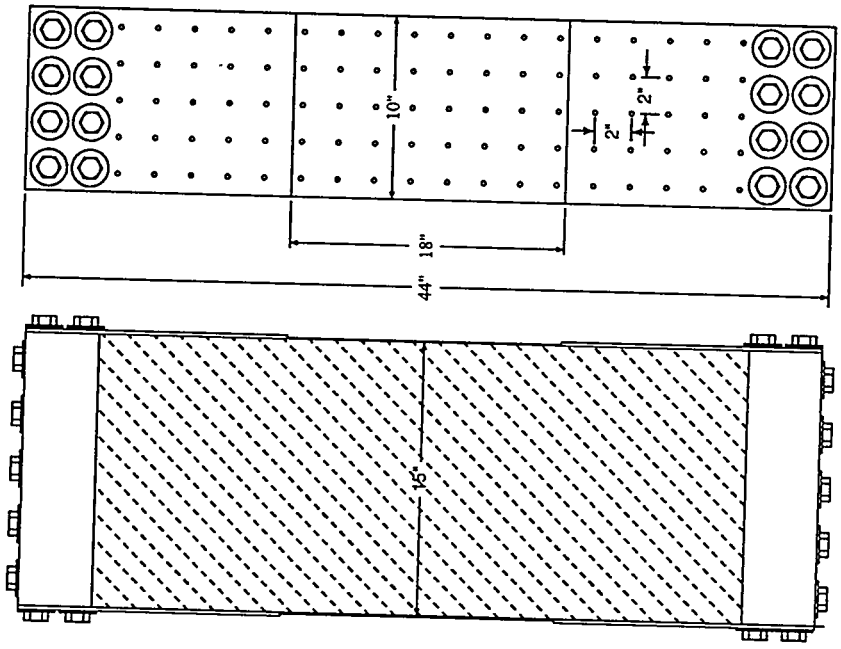

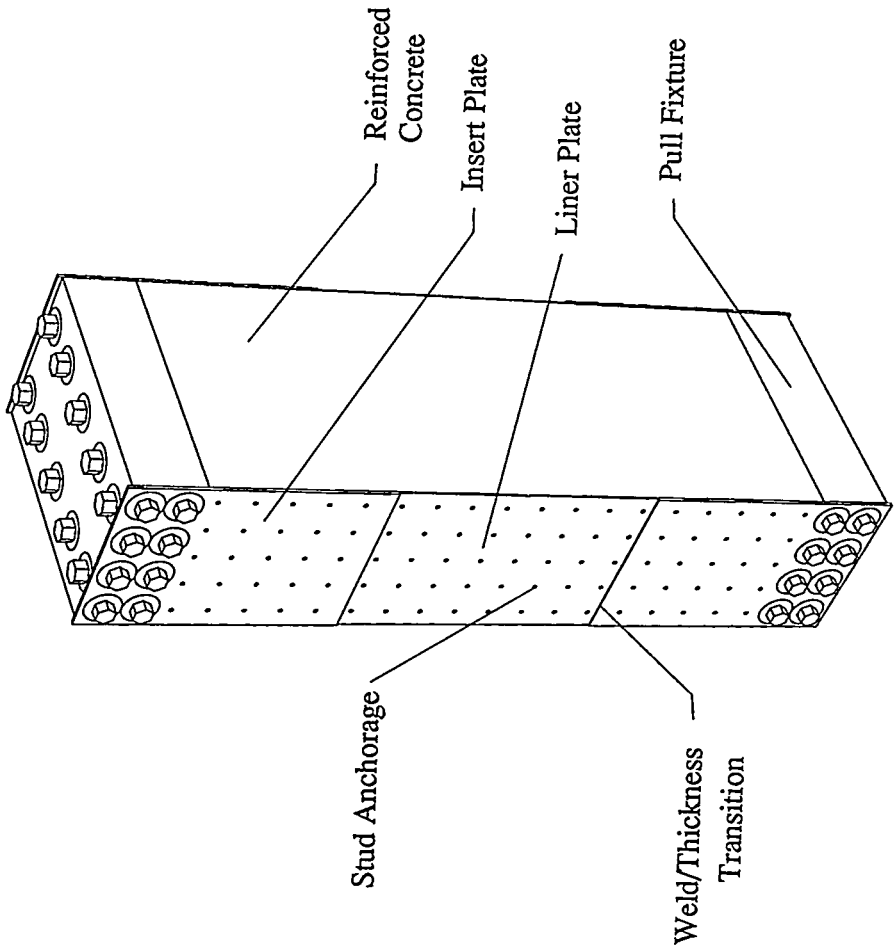

Figure 2.5: Full-simulation specimen

2.4 Specimen Material Specifications

In all the specimens, the specifications and procedures for construction were identical to those used in the 1:6-scale model. However, in some cases, the material used in the model could not be exactly matched. In the case of the reinforcing steel and the anchorage studs, there were no problems in duplicating the material type and fabrication techniques. The reinforcing steel is connected to the pull box by a swage connector. The connector was manufactured and applied by Dayton Bar Splice, who was the supplier for the 1:6-scale model.

However, considerable difficulty was encountered in obtaining insert plate and liner plate material that matched the specifications of the 1:6-scale containment model. In the model, the liner plate of A414, Grade D steel closely matched the characteristics of A516, Grade 60, which is used in the construction of actual containments. The A414 is available in 1/16 inch (1.6 mm) thickness, unlike the A516, which is not available thinner than 3/16 inch (4.8 mm). When the 1:6-scale model was built, an excess amount of A414 steel was purchased. The original plan was to use this steel for fabrication of the test specimens. However, the steel was stored outdoors and exposed to the elements for several years. The resulting corrosion was considered severe enough to affect the outcome of the test, so a search for another suitable material was initiated.

After discussions with several possible sources, it became clear that locating more A414 steel was very unlikely. The only way to obtain A414 steel was to initiate another mill run of the material, which would require 5 months and provide no guarantee of a close match between the material properties of the new mill run and that used in the original liner. This possible mismatch is caused by the extremely wide tolerance in the A414 material specification.

Following the inability to obtain A414, Grade D steel, a search for another type of sheet steel with similar thickness and similar mechanical properties was conducted. Efforts to locate a reasonable substitute proved to be unfruitful. A414 is a medium carbon steel with intermediate strength properties. Such a steel is rarely specified. Also, the liner thickness of 1/16 inch (1.6 mm) seems to be at the transition between thicknesses that are available hot rolled and cold rolled. The original material was hot rolled; however, most steel companies are not capable of providing hot-rolled steel in thicknesses of less than 0.075 inch (1.9 mm). The thickness of most cold-rolled sheet is less than 1/16 inch (1.6 mm). Therefore, there are very few steels of any strength produced in this thickness.

Since locating a steel with the proper thickness and the needed properties did not seem possible, it was decided to use the A516 steel that is typically used in containment construction and is a reasonable match to the A414, Grade D steel. The primary difficulty with this material is that it is not readily available in thicknesses less than 3/16 inch (5 mm). Therefore 3/16 inch (5 mm) material was reduced by surface grinding to a thickness of 1/16 inch (1.6 mm). After consultation with metallurgists at Sandia, it was determined that this grinding would not have an appreciable effect on the mechanical properties of the steel. Further, the grinding operation was much less expensive and could be accomplished much more rapidly than obtaining a dedicated run of steel.

Owing to the wide range in specified properties of both the A516 and the A414, Grade D steel, a lengthy search was required before a small amount of steel that closely matched the desired properties of the A414 could be located. This material was A516, Grade 60, and was used to fabricate the liner for the full simulation specimens, since the liner properties for these specimens were considered the most critical. The amount of A516, Grade 60 located was not sufficient to fabricate the other specimens. An additional search located a heat of A516, Grade 70, with material properties that were fairly close to the A414, Grade D, but not as good a match as the Grade 60. This material was used to fabricate the remainder of the liner plates as well as all insert plates used in the specimens. The material properties of the insert plate are not generally considered important since the plate always behaves elastically.

Finally, to verify the material properties of the steels, samples of both heats were subjected to tensile tests before and after grinding to the 1/16 inch (1.6 mm) thickness. In summary, the search for appropriate liner material was difficult and exhaustive, but the results are that a steel of suitable material properties was located and was used in the specimens. Figure 2.6 is a typical stress-strain plot of the A414, Grade D material and the A516, Grades 60 and 70 materials used in these specimens. The two materials have very similar yield and ultimate strengths. However, the A414 Grade D has significantly less ultimate strain (30 percent) than the A516 material (45 percent) and the effect of this difference has not been assessed.

The final material required for construction of specimens was the concrete. The concrete mix was obtained from the same supplier used during the construction of the 1:6-scale model, and the specifications for the concrete mix were the same as those used in the model. Twenty-four concrete specimens were poured at the same time the concrete was placed for the separate effects test specimens, and the concrete specimens were tested periodically to obtain time-dependent material properties.

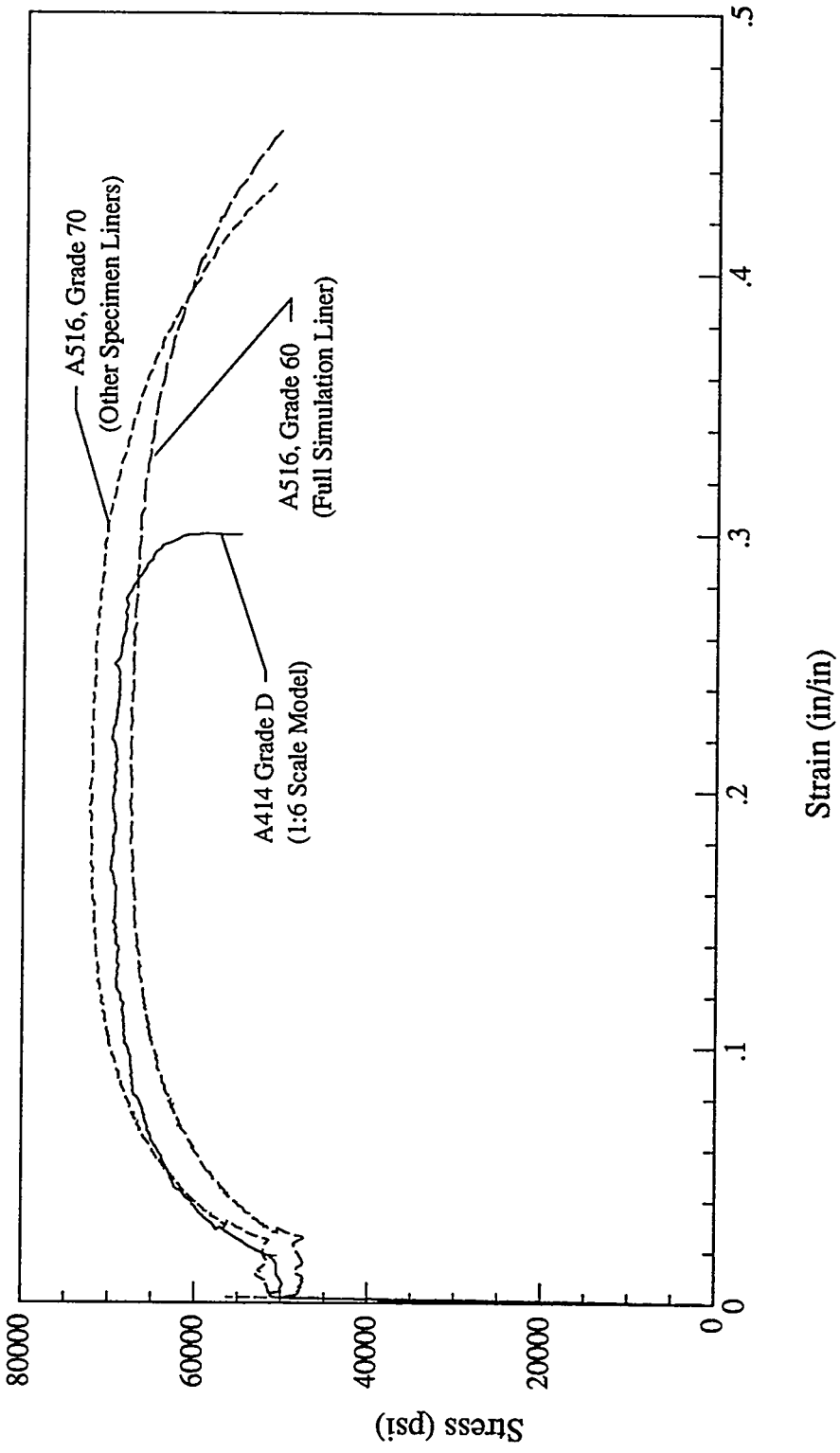

Figure 2.6: Stress-strain response of A414, grade D and A516, grades 60 and 70

3. Test Specimen Instrumentation

Three types of instrumentation were used in these experiments. These were resistance strain gages, load cells and displacement transducers, and photoelastic coatings. This section contains a detailed discussion of each of these three instrumentation classes.

Resistance strain gages were used extensively. The various gage types were single-element gages; 45° three-element rosette gages; axial strip gages, which consist of up to ten single elements over a 1 inch (25 mm) gage length and have their sensitive axis along the axis of the gage; transverse strip gages, which are configured like axial strip gages except the sensitive axis is across the overall gage axis; and weldable gages, which consist of a single wire element welded to the reinforcing steel.

Figure 3.1 shows the front and back gage locations for the weld transition specimens. The figure is drawn to scale and is self-explanatory. One note of clarification here is that the strip gages used were configured so that only six of the gage elements were active. In general, the strip gages were connected so that the first three elements, those being the elements closest to the area of interest, were connected and after that only every other element was connected.

Figure 3.2 shows the gage locations for the separately controlled loading specimens. Only one side of the specimen is shown since only one side had gages applied to it. The opposite side of the specimen was used for photoelastic measurements only. For this specimen, all gage elements were connected on the strip gages, giving a total of 56 strain gages per specimen. All specimens were instrumented identically, with the exception of the outboard transverse strip gage, which is located at the right edge of the figure. An axial gage was used in this location on four of the six specimens to measure Poisson strains, and a transverse strain was used on two of the specimens to measure the axial strains. Since the gage is laid across the axis of the specimen, the axial gage configuration measures Poisson strain and the transverse gage configuration measures axial strains.

Figure 3.3 shows the front and back of the strain gage layout for the full-simulation specimens. Here the strip gages are concentrated near the weld region and primarily down the center line of the specimen to avoid the edge effects induced by the transverse restraint of the insert plate and the lack of restraint in the central region of the specimen. As with the weld transition specimens, one half of one side of the specimen does not have strain gages attached. This is to allow the attachment of photoelastic material. In addition to the externally applied resistance strain gages, each of these specimens has six weldable strain gages applied to the reinforcing steel. These gages are applied to the outermost and central pairs of reinforcing rods at the center section. In one additional test of the full-simulation specimens, external pressure was applied to the liner to simulate the pressure loading of the 1:6-scale model test. For this specimen, surface strain gages and the photoelastic material were not used. Only the six weldable gages were installed.

In addition to the strain gage information, other discrete values were gathered that indicated the load and deflection of the specimens. In the case of the weld transition specimens, the total load applied by the testing machine and the total deflection of the hydraulic ram were measured. These monitor the load-deflection response of the specimen. In the case of the separately controlled loading specimens, the tensile load was applied by hydraulic rams placed between the end pull blocks. Both the total load developed by the rams and the total elongation of the rams were monitored. In addition, the concrete load and ram displacement were monitored. Finally, in the case of the full-simulation specimens, the total load and specimen deflection were recorded. For the single specimen on which external pressure was applied, external pressure was recorded.

On all but one of the specimens, a sheet of photoelastic material was applied to the surface of the specimen to obtain a whole-field strain indication. The photoelastic material exhibits birefringment properties that develop characteristic fringe patterns in which dark or light fringe lines correspond to lines of constant difference in principal stress in the polymer material. The fringe count observed by this method is directly proportional to the difference in principal stresses. Since the material was intimately bonded to the steel plate by an epoxy, the strains in this polymer are identical to the strain field in the steel. Also, since the polymer is behaving elastically, even at very high strain levels, the polymer stress levels are proportional to the strain levels. Therefore, the polymer stress levels and the resulting fringes are a direct measure of the difference in principal strains in the steel material. This difference applies only to the in-plane principal strains; through-thickness strains are not measured by this method. The value of the strain is determined by the wavelength of light used for observation, the thickness of plastic, and the stress optic coefficient of the material. Typically, for the purpose of this experiment, one complete fringe order--that is, from a dark fringe to the next dark fringe--corresponds to about a 0.6 percent difference in principal strains. As used here, where the ultimate response of the materials is of interest, the difference of principal strains, which corresponds to maximum shearing strain, is very useful in determining the areas of highest probability of failure. Figure 3.4 shows a typical photoelastic photograph for a full

simulation specimen under load. The large number of data channels and the use of photoelastic materials allow the response of the various specimens to be monitored with a detail not available during the 1:6-scale model test. This in turn leads to much greater insights into material behavior and, more generally, into the behavior of an anchored system under severe accident loadings.

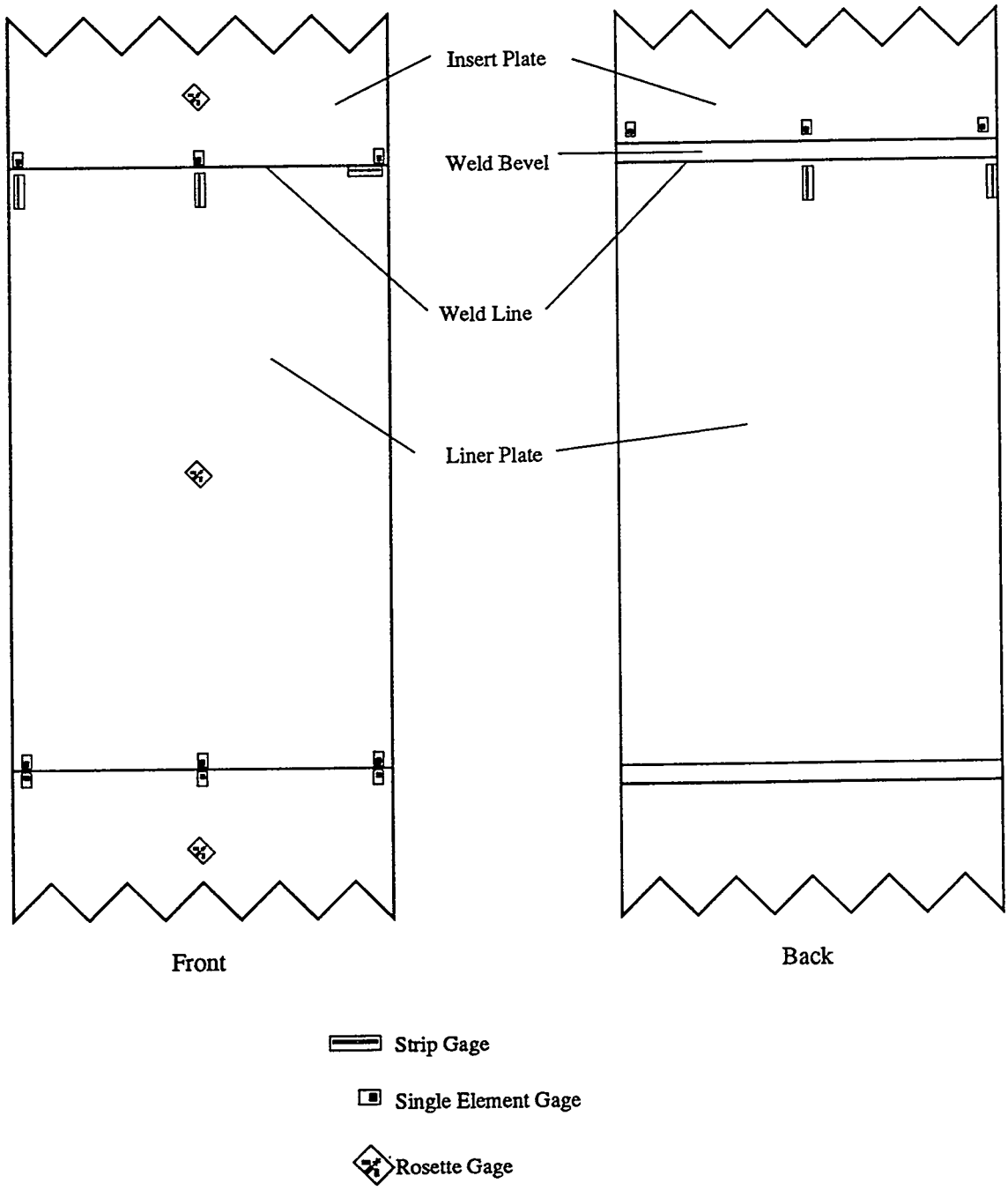

Figure 3.1: Gage locations for the weld-transition specimens

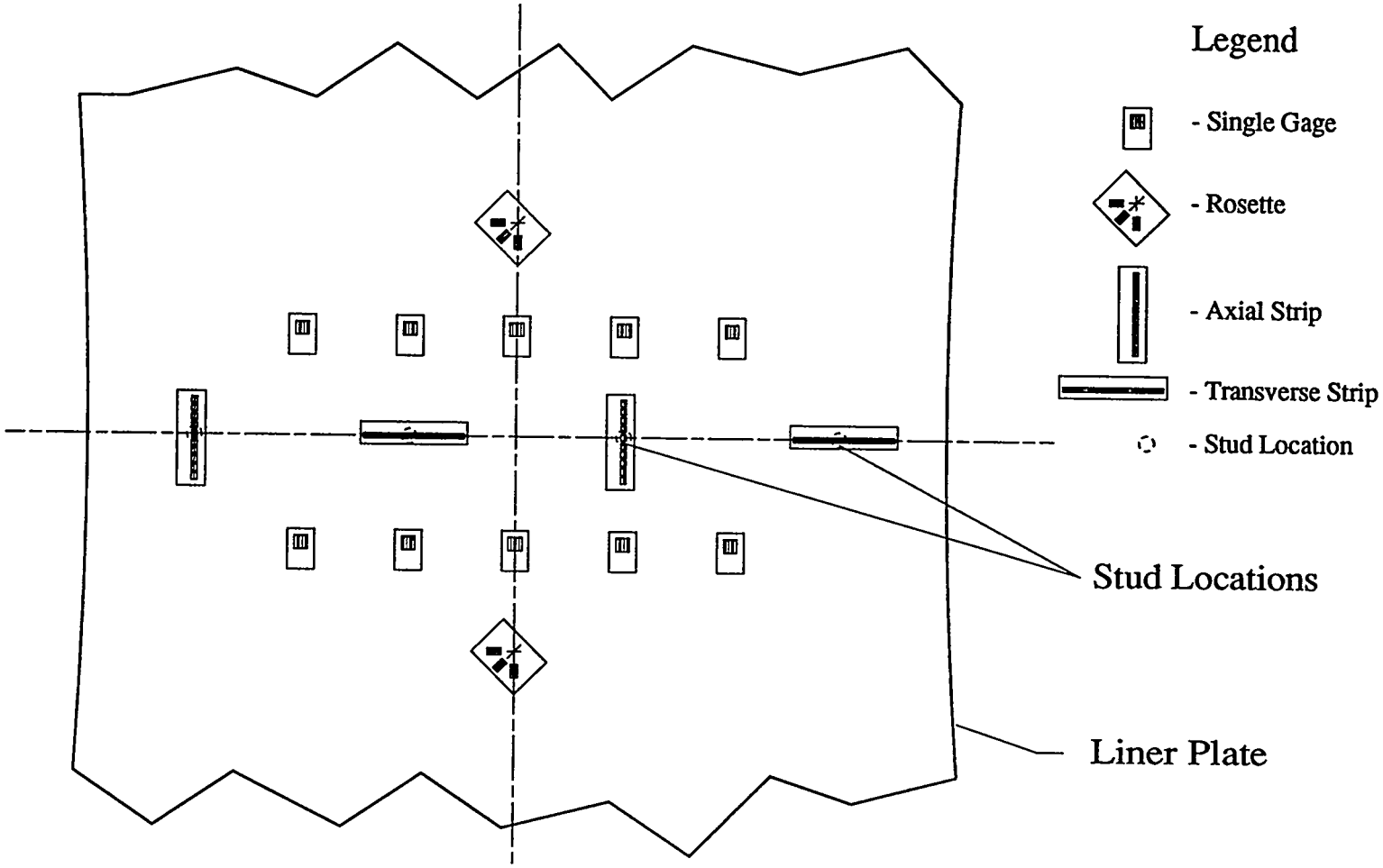

Figure 3.2 Gage locations for separately-controlled-loading specimens

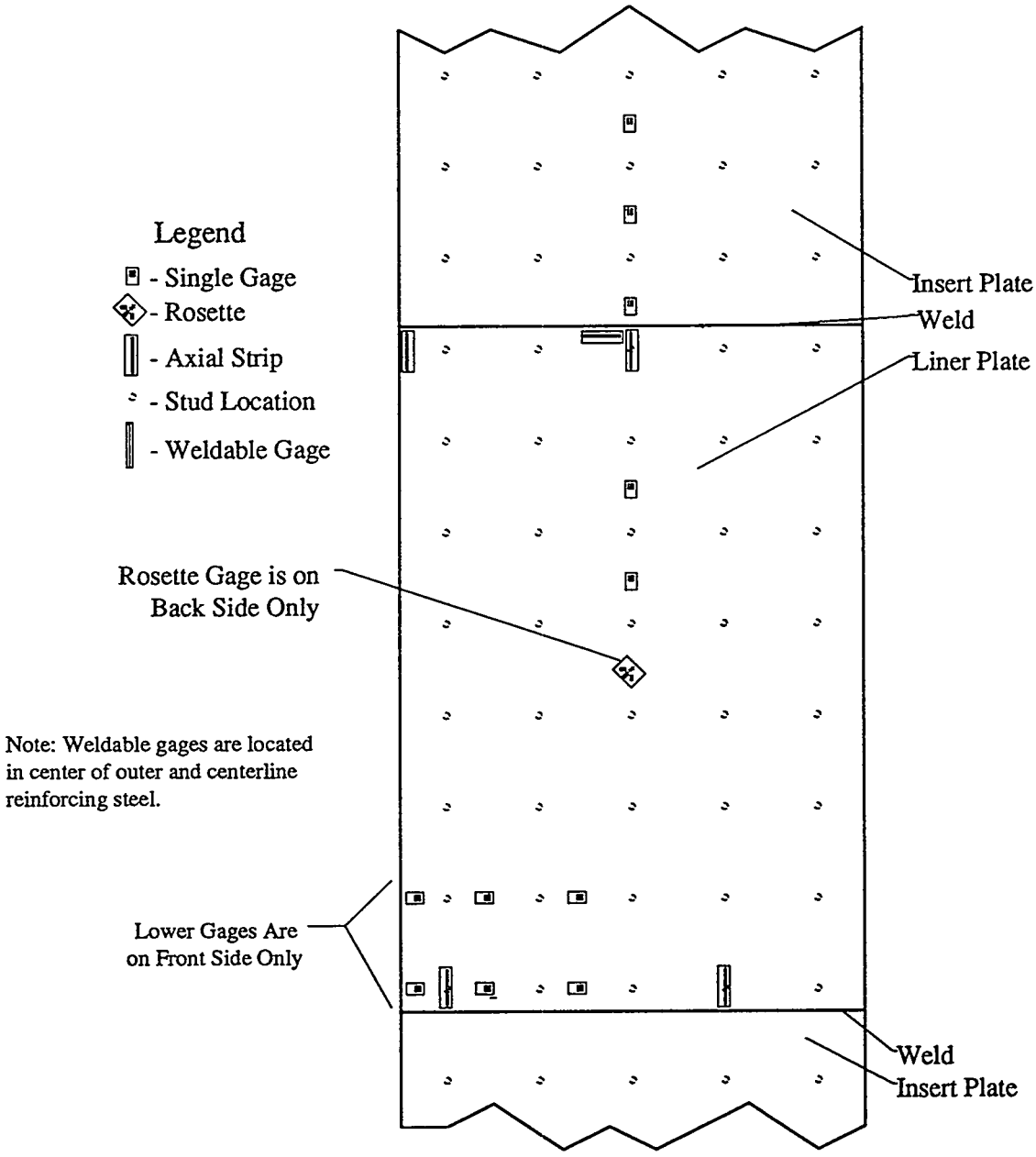

Figure 3.3: Gage locations for full-simulation specimens

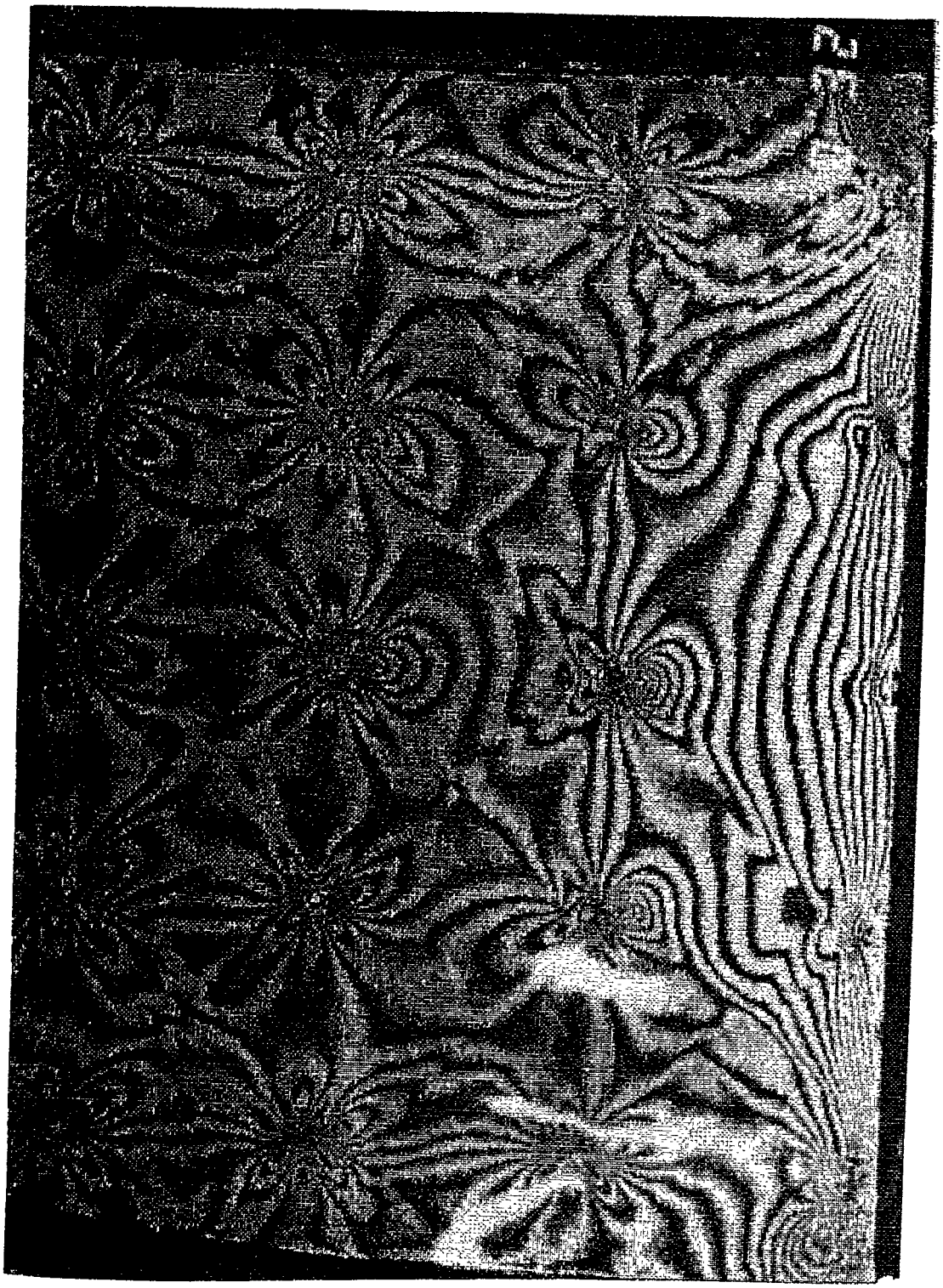

Figure 3.4: Typical photoelastic response of a full-simulation specimen

4. Data Acquisition and Test Equipment

All tests were performed in an MTS load frame operated by the Sandia Geomechanics Department. Depending on the nature of the test, either a 220,000-lb (1 MN) load frame or a 1,000,000-lb (4.4 MN) load frame was used. The 1,000,000-lb load frame was used for the weld transition experiments because of its greater available stroke and for the full-simulation experiments because of its load capacity. The 220,000 lb. load frame was used in the separately-controlled-loading tests since the frame's load mechanism was used to develop the stud shearing load. In this case, the higher resolution of the lower rated frame was important.

The specimen loading was controlled using MTS controllers, which were normally run in the displacement control mode. This allows a very low rate and well-controlled ramp to be applied to the specimen displacement. The only case where displacement control was not used was in the separately controlled loading tests where the liner preload requirements dictated that a controlled load be applied. In this case, external hydraulic rams were used to develop the load, and an MTS controller connected to load cells that sensed the ram load was used to maintain the load at the constant desired value.

All data acquisition was performed using a Hewlett-Packard 3497A Data Acquisition Unit, which was capable of recording the strain gage outputs, the voltage outputs of the load and displacement transducers, and remotely operating the still camera for photoelastic and overall response photographs.

Figure 4.1 shows a typical test setup for the separately controlled loading experiments with a specimen in the load frame. The control console for the testing machine is to the left, and the polariscope for use in recording the photoelastic fringes is directly in front of the specimen.

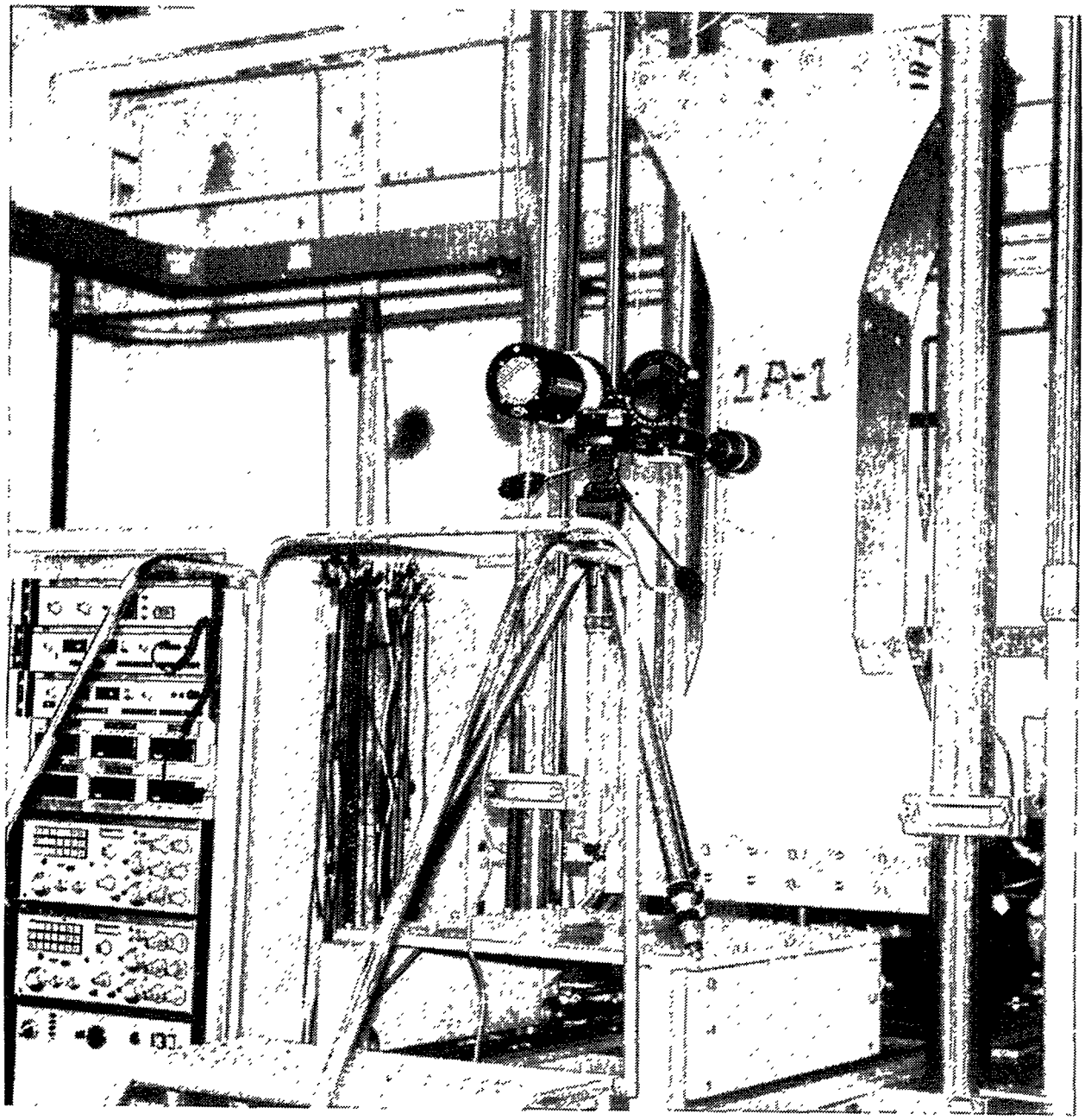

Figure 4.1: Test configuration of a separately-controlled-loading specimen

5. Conduct of Tests

Three of the weld transition specimens were tested to failure in the 1,000,000-lb machine. The test was straightforward since the logging of increasing uniaxial specimen deformation with load and scanning of all available strain gages was all that was required. In addition to this, a sheet of photoelastic polymer was placed in the lower half of one side of the specimen. Since the specimens are virtually identical from one to the next, variations in sensitivity of the photoelastic material could be used. For the first test, the photoelastic material had a sensitivity of approximately one full fringe per 0.1 percent strain. Because of the relatively brittle nature of this polymer, this test was done only to study the early inelastic region of the specimen. On the remaining two tests, a polymer with a much higher ductility was used, so data could be gathered until the time of fracture of the specimen. As will be discussed later, the load deflection curve was essentially identical for all specimens.

The six separately controlled loading specimens presented the greatest challenge with regard to testing. The variation in specimen preloading was the primary parameter investigated. Preloads are expressed as the stress (with 1 ksi equal to 1000 psi) in the liner at the narrowest portion. Liner preloads for the six specimens tested were: no-liner preload; 60 ksi (415 MPa) , 63 ksi (435 MPa), 65 ksi (450 MPa), and 70 ksi (485 MPa); and a specimen which was tested to failure using liner loading only. The unusual spacing of the liner preloading value [the 63 ksi test between the 60 ksi (415 MPa) and 65 ksi (450 MPa) tests] was not determined prior to testing. This test was included to investigate the very sharp transition observed between stud shear and liner tearing modes of failure.

In the four tests where a liner preload was specified, the load was gradually increased under load control until the desired value was reached. During the increase, the attached strain gages were periodically scanned to monitor the early behavior of the specimen. Also, if fringes appeared on the photoelastic material, photographs were taken. During the liner loading, the overall elongation of the specimen was monitored with a linear potentiometer.

Once the desired liner preload was reached, a controlled displacement was applied to the concrete block, causing stud shear loads to develop. Generally, as the stud shear load was applied, the constant liner preload caused the overall specimen to elongate further. As with the response previous to reaching the desired preload, the overall specimen elongation was monitored along with the response of the various strain gages. Specimens were tested in this way until a failure occurred, with the failure being either the shearing of the studs from the liner or tearing of the liner. Since the liner preload portion of the testing was load controlled, it was very difficult to maintain studs intact following tearing of the liner. This is because liner failure would be expected to occur just above the studs where the combined liner preload and stud shear produces the greatest net section stress. Once failure occurs here, the load on the preloading system is significantly reduced. Since this system is load-controlled, once the liner tears, the system extends rapidly to recover the lost load. This produces a large shear load in the studs, which in turn causes the studs to shear very shortly after the liner tears. On some of the later tests, methods of limiting the load control were investigated so that the studs remained intact even though the liner failed.

The full-simulation specimen tests were straightforward. They were conducted under displacement control with an initial displacement rate of approximately 0.002 inch (0.05 mm) per minute. This extremely low displacement rate was used to allow data to be gathered during the elastic range of the test. As specimen testing increased, the ram rate was doubled repeatedly to maintain a reasonable displacement rate. The available strain gages were scanned at periodic intervals based primarily on load during the early portion of the test and on specimen elongation during the latter parts of the test after general yielding had occurred. Three specimens were tested using this method.

One additional specimen of the same type as the full-simulation specimens was also tested. This specimen was configured to allow external pressure to be applied to the liner plate by means of a bladder box bolted around the specimen and pressurized with dry air. Figure 5.1 illustrates this specimen with the bladder box attached. During testing, the pressure in the box was controlled and set to be proportional to the total load to be applied to the specimen. This was to simulate the pressure effects in the 1:6-scale model that are directly proportional to the hoop stresses. The elongation rate of displacement control was constant during the test and the pressure loading was automatically controlled through a system which allowed the load signal to be fed directly into the pressure control system. This test has fewer recorded data than any other test since surface strain gages could not be used because of the presence of the bladder box, and photoelastic methods could not be used since the surface could not be viewed. The data for this test consist of the load and deflection and the response of the six reinforcing steel gages.

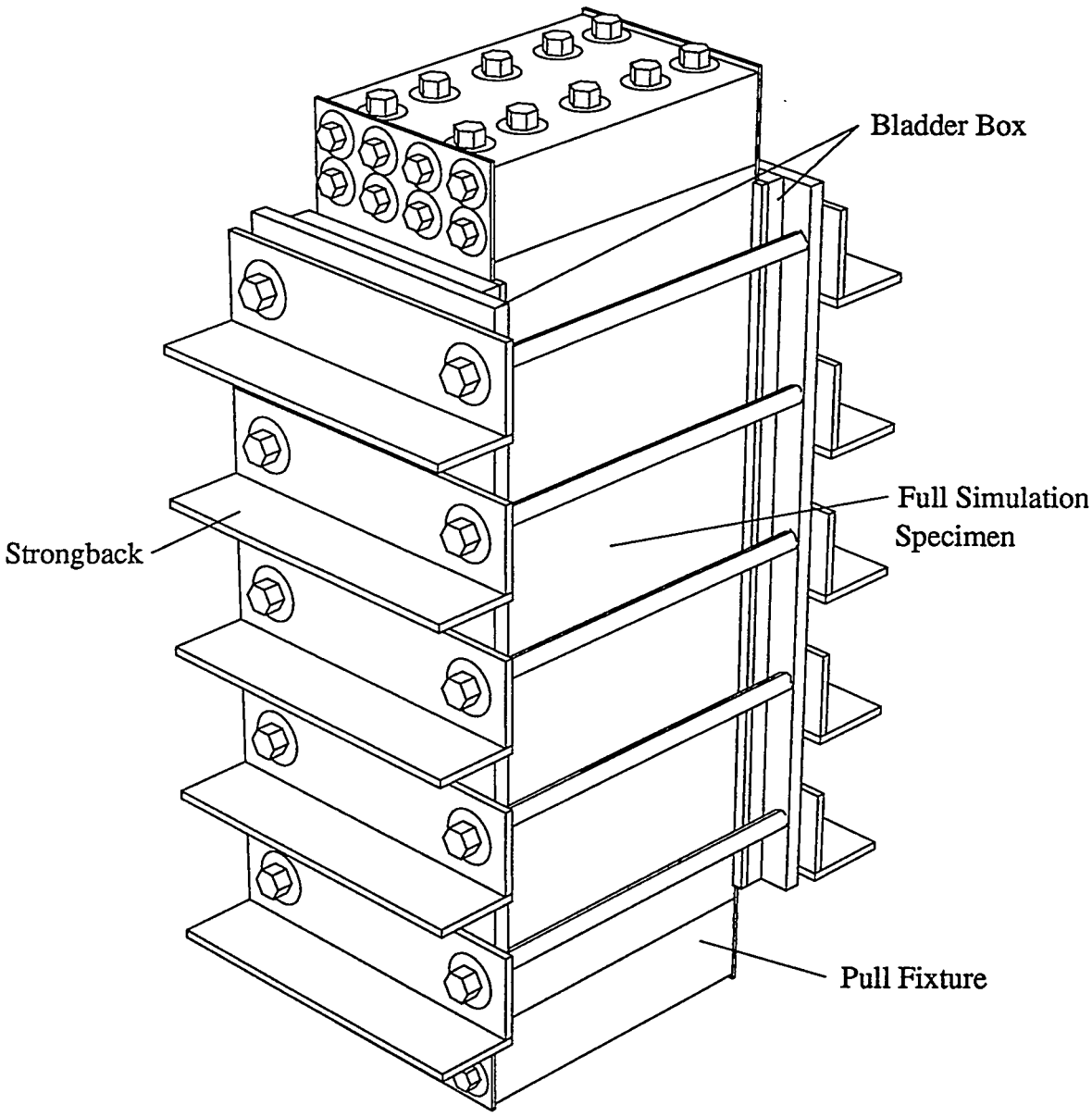

Figure 5.1: Specimen with external pressure apparatus

6. Test Results

The results of the tests of the three types of specimens are presented separately in this section. Owing to the very large amount of data gathered during these tests, only selected plots which illustrate specific behavior are included. Appendix B contains a complete set of plots of all load deflection and strain gage data. Appendix C contains selected photoelastic data, both in raw photographic form and in digitized and reduced maximum shearing strain plots. These appendices are designed to be used independently of this report and contain sufficient information to allow for interpretation of the data.

6.1 Weld Transition Specimen Test Results

Three weld transition specimens were tested during this series. The weld transition specimen was termed a Phase 2A specimen and the specimen numbers tested in this series are 2A3, 2A4, and 2A5. The three tests are differentiated only by serial numbers since in all other respects they are identical.

Figure 6.1 shows that the overall load deflection response of the three weld transition specimens is virtually identical. This can also be seen from examination of the strain gage data contained in Appendix B. The strain gage results of these three specimens are extremely similar from one specimen to the next. The primary purpose of using this specimen type was to investigate the potential strain concentration caused by the existence of the weld and thickness transition at the transition between the insert plate and the liner plate. Figure 6.2 shows a cross-section in detail of this weld. This figure also shows the positioning of the various strain gages in this region. Of particular interest is the fact that the insert plate single-element gages on the backside of the specimen were considerably further back from the weld and placed on a thicker material than were the gages on the front side of the specimen. This effect is caused by the relatively long bevel in the thickness transition between the insert plate and the liner plate. This gage positioning explains the apparent discrepancy in the response between the front and back-side single-element gages on the insert plate. Specifically, the front-side insert plate gages tend to exhibit a much higher strain than the back-side gages. This is caused by a combination of the thicker material for the back-side gages and an offset loading which induces a bending that increases the tensile strain for the front-side gages. Figure 6.2 shows how the offset loading is generated during the uniaxial tension test. The moment generated by this loading would serve to increase the strain on the front-side gages and decrease it on the back-side gages. This bending effect is less pronounced on the thinner liner plate since most gages are positioned more than a few plate thicknesses from the weld.

The most interesting strain gage response for these weld transition specimens is seen in the liner strip gage response. Figure 6.3 shows the edge strip gage response for specimen 2A4, and Figure 6.4 shows the center line strip gage response for the same specimen. Notice that for any given average liner strain, the edge strip gage response is significantly larger than the centerline strip gage response. For example, at about 10 percent average liner strain, the minimum strain in any of the gages along the edge is about 100,000 microstrain. In contrast, the maximum strain exhibited by any of the centerline strip gages is about 54,000 microstrain. The maximum strain on the edge is about five times the maximum strain in the center. Referring to Figure 6.3, the gages that exhibit the highest strain along the edge are located in the center of both the front and back-side edge strip gages. This points to the fact that there is a strain concentration occurring at some distance from the thickness transition. In contrast, the centerline strip gages represented in Figure 6.4 tend to exhibit an increase in strain with increasing distance from the weld.

In general, the overall behavior of the strip gages can be better visualized through the use of a three-dimensional contour plot. A number of these plots are presented. On all contour plots the independent variables are the distance from the detail of interest and the free-field strain. The value plotted on these contours is the strain concentration, which is defined as the local strain at the gage location divided by the free-field strain. In the case of the weld transition specimens, the free-field strain is defined as the axial strain measured on the central rosette located in the liner plate. Figure 6.5 shows the front edge strip gage for specimen 2A4. Here the strain concentration that appears approximately 0.4 inch (10 mm) from the transition is obvious. The very high level of strain concentration shown for small values of free-field strain results from the fact that this region undergoes plastic strain before the free-field values become plastic, thereby giving a large strain concentration. Figure 6.6 shows the response of the front centerline strip gage of specimen 2A4. In this figure the increase in strain concentration with increasing distance from the weld is obvious. Notice that for the later portion of the test when all strains are plastic, the strain concentration factor approaches one with a large distance from the weld, but, in general, is always less than one. This means that the axial strain in this region is less than the free-field strain on the liner.

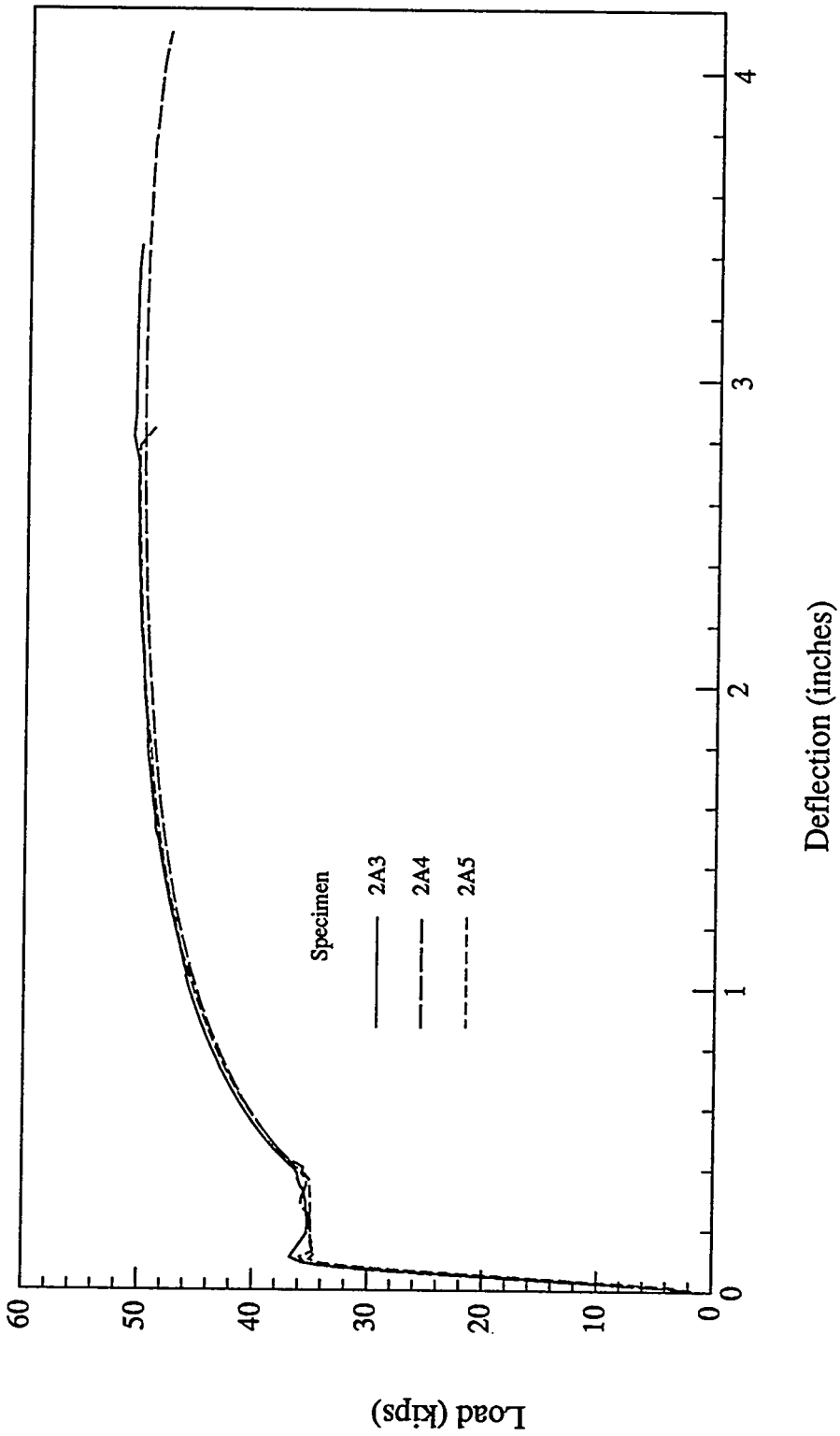

Figure 6.1: Overall response of the weld-transition specimens

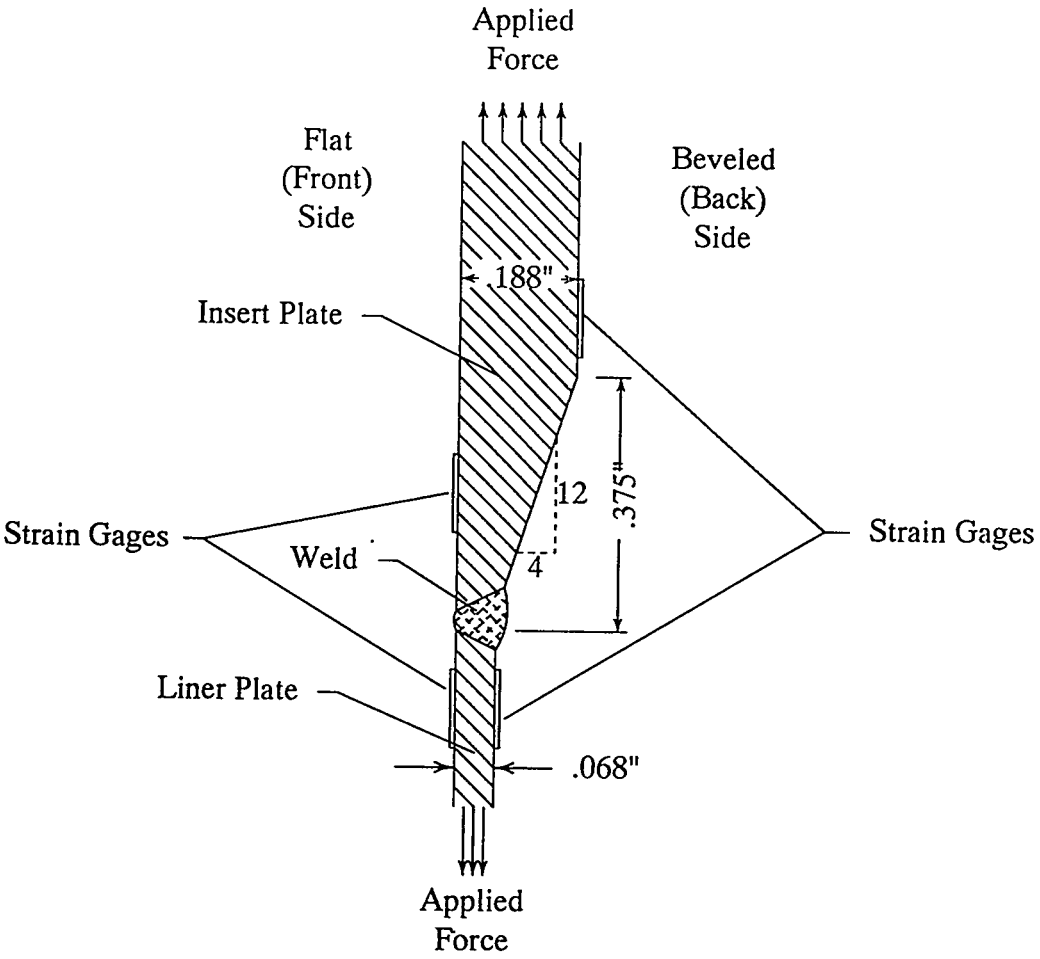

Figure 6.2: Cross-section of specimen weld

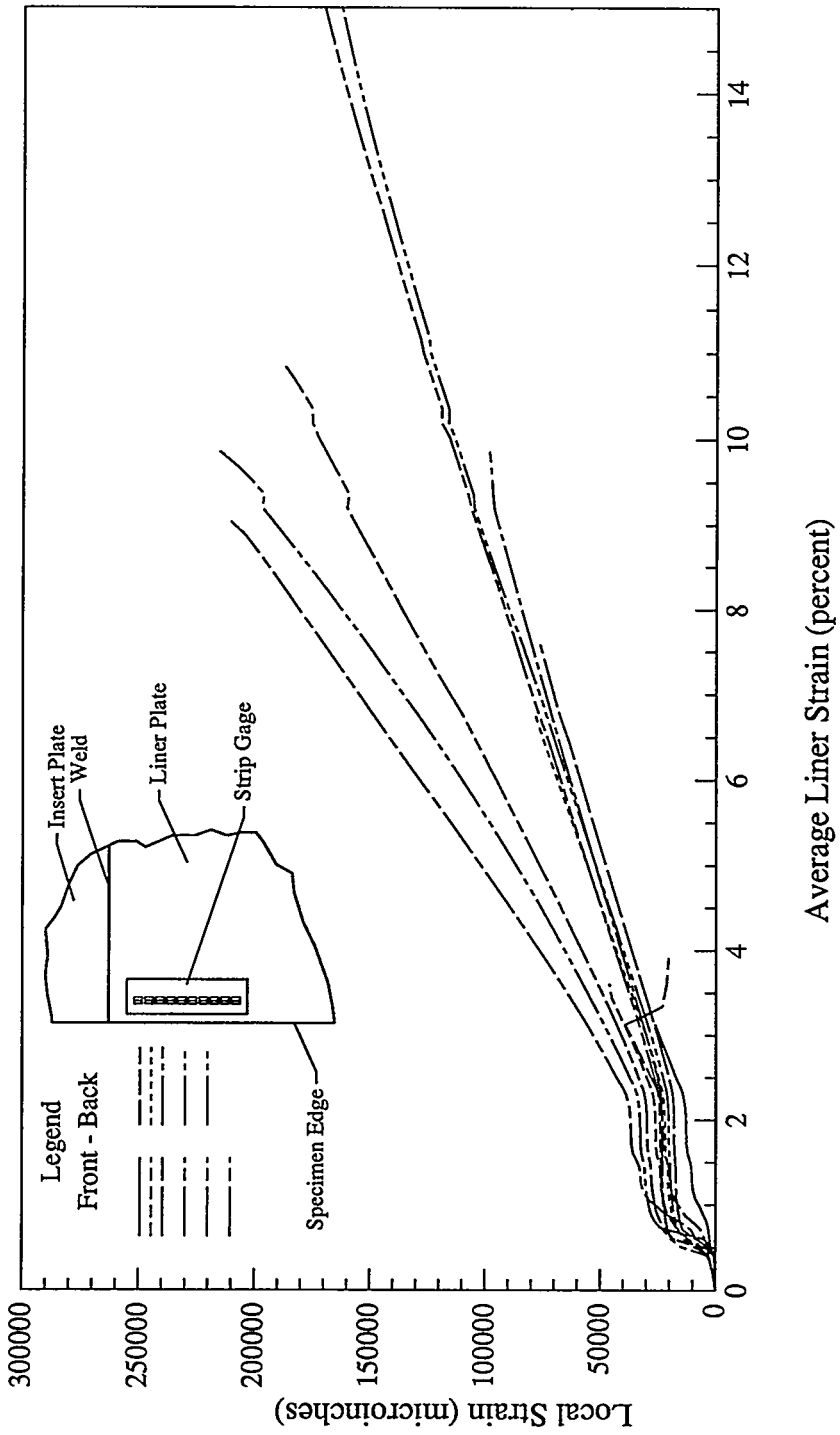

Figure 6.3: Liner edge strip gage response, specimen 2A4

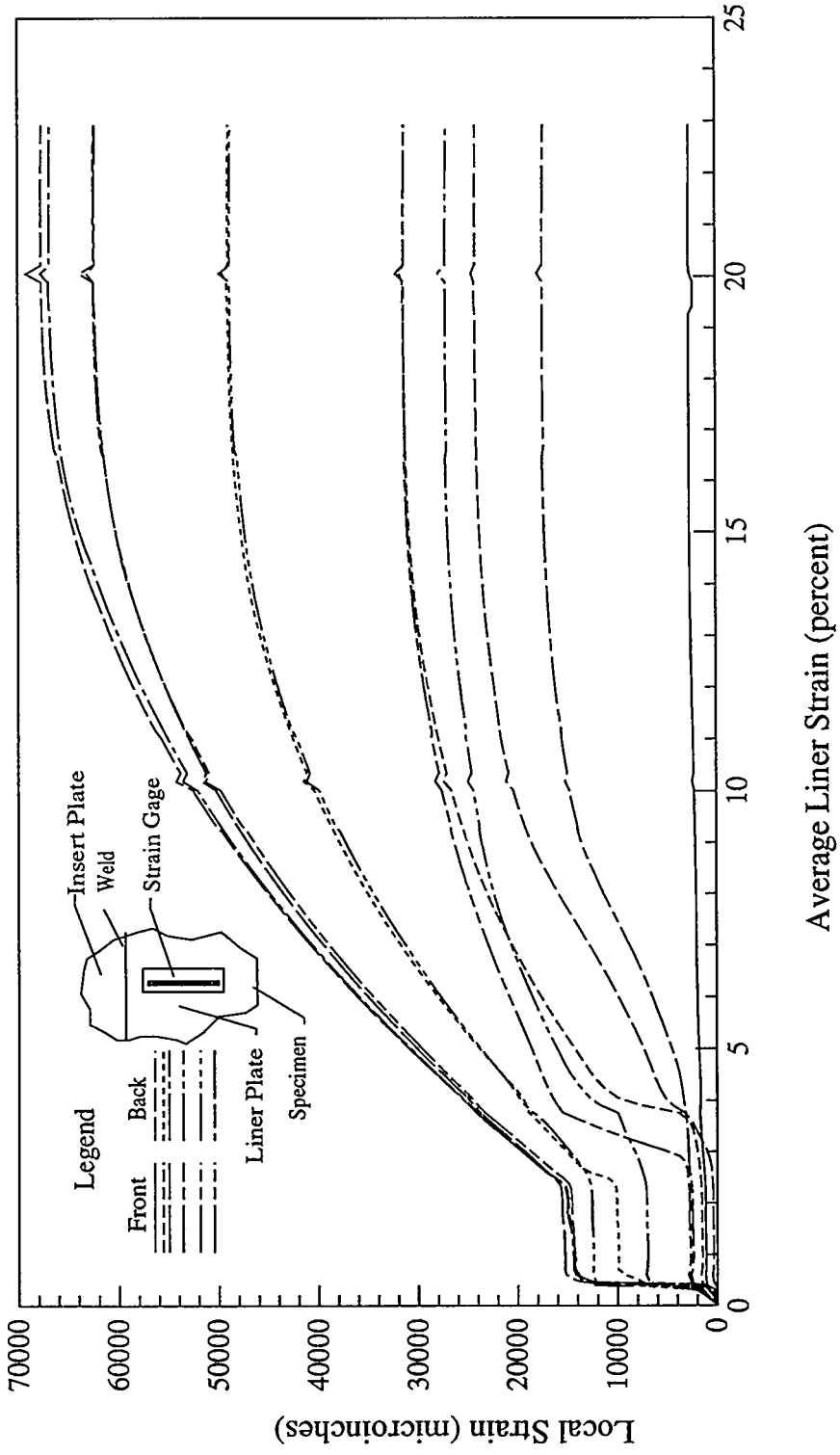

Figure 6.4: Centerline strip gage response, specimen 2A4

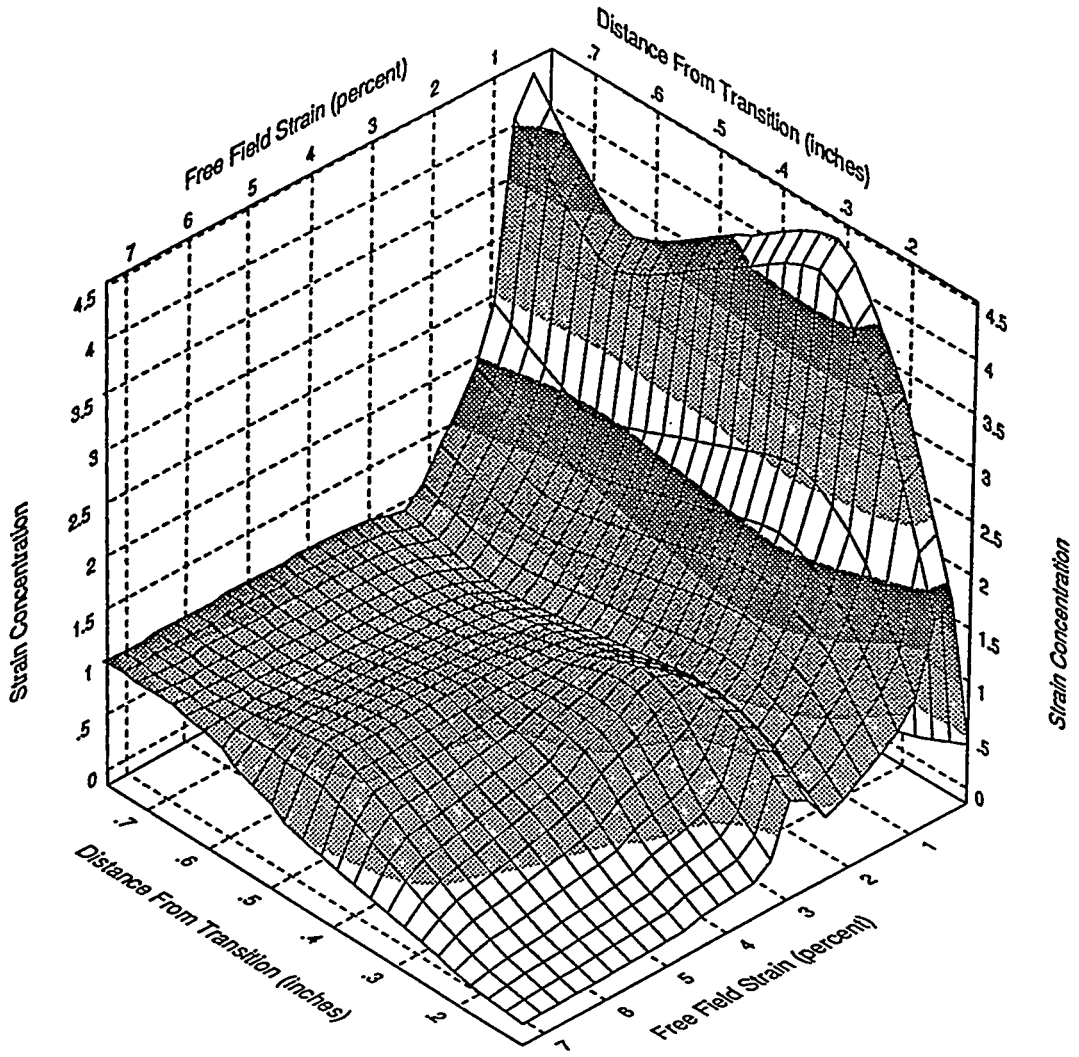

Figure 6.5: Front edge strip gage, Specimen 2A4

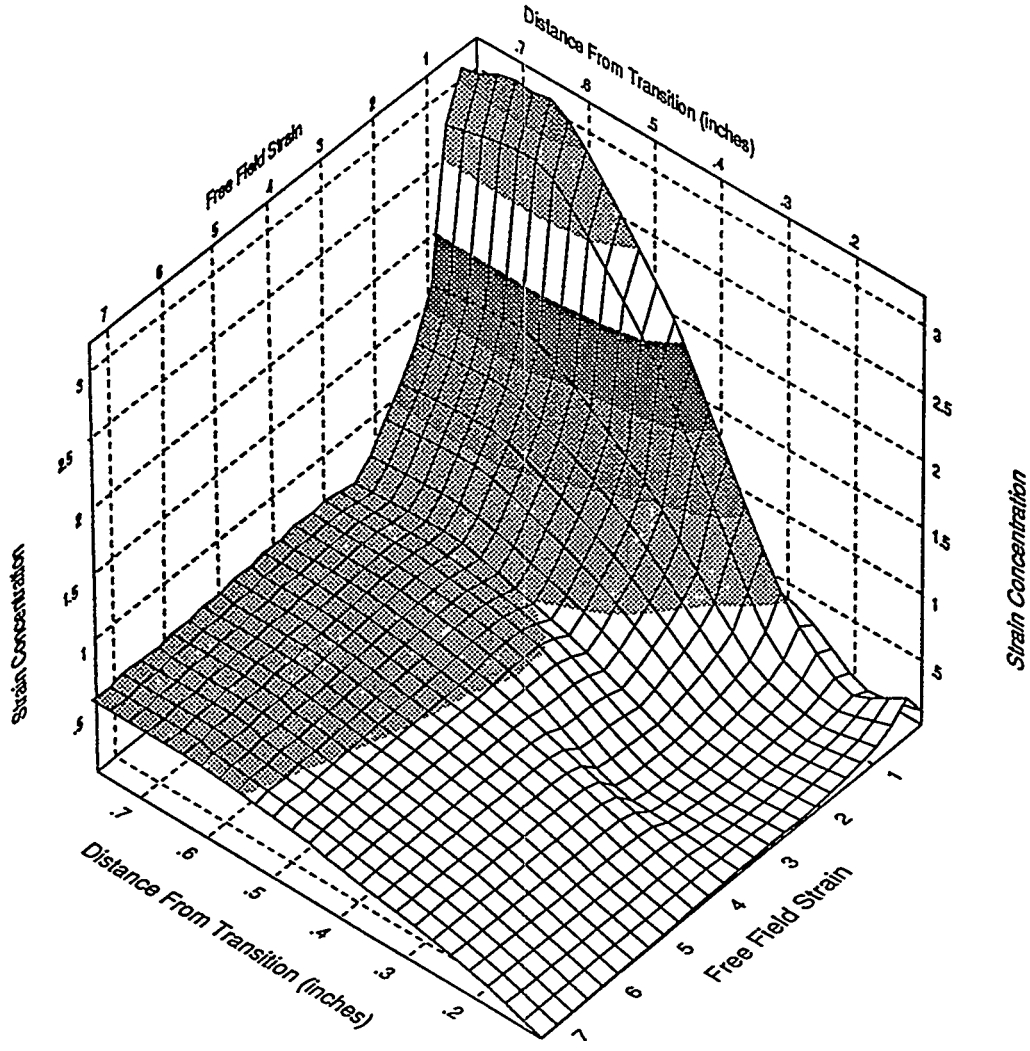

Figure 6.6: Front centerline strip gage, specimen 2A4

As mentioned before, there is some difference in the gage response between the front and the back side of the specimen. This is especially true near the thickness transition region, where the offset nature of the welded joint produces a bending moment in both the liner plate and the insert plate. Figure 6.7 illustrates the bending strain along the central line of specimen 2A4. The bending strain ratio plotted in this figure is derived by taking the front-side strain subtracted from the back-side strain and dividing the result by the average axial strain. Using the difference in front and back strains gives an indication of bending strain, and dividing by the average axial strain normalizes the value. These plots show that relatively large bending strains exist close to the transition, but for all values of free-field strain, these bending strains die away before a distance of 0.7 inch (17 mm) from the transition is reached. In addition, notice that the bending strain effect is largest for small free-field strain values. This is expected since the increase in average strain with large free-field strain values is expected while an increase in bending strain is not expected.

From this examination of the strain gage response of the weld and thickness transition specimens, it is apparent that the weld does not cause a strain increase. Further demonstration of this fact comes from the failure mode of the specimens. In total, four specimens were tested to failure. Owing to a machine malfunction, detailed data exist only for the three that have been reported. Of the four that were tested to failure, two of the specimens failed through tearing of the liner in the central region very far from the weld, and two specimens failed through a tear near the weld and a tear running across the width of the specimen. While this tear started near the weld, it was influenced by the strain concentration along the edge of the liner plate. The cause and meaning of this strain concentration is discussed in detail in the next paragraphs. Figure 6.8 shows three of the weld and thickness transition specimen failures. No photo is available for specimen 2A5, which failed near the weld, like 2A3.

In addition to the strain gage data presented here, each weld transition specimen was also instrumented using a photoelastic polymer. The birefringent properties of the polymer allow photographic data to be taken, which directly measure the difference in principal stresses in the polymer and therefore are also a direct measure of the difference in principal strains in the specimen. The principal strain difference measured here corresponds to the maximum in-plane shearing strain.

The resulting photographic data consist of a series of light and dark bands or fringes, with each fringe representing the same increment in maximum shearing strains. For most of the data presented here, one whole fringe, that is, the transition from a dark fringe through a light fringe to the next dark fringe, corresponds to a maximum shearing strain difference of about 0.6 percent. Figure 6.9 shows the raw photoelastic data of specimen 2A5 in photographic form just prior to failure. Figure 6.10 is a plot of the data reduced from this photograph. In both of these figures the weld between the insert plate and the liner plate is along the bottom edge and the specimen is loaded vertically with the liner plate extending upward from the weld and the thickened insert plate extending downward. The gray-scale plot provides for rapid interpretation of the data. Several items are immediately apparent from an examination of this plot. First, the strain gage data discussed earlier are borne out by the photoelastic data. Specifically, the monotonically increasing strain along the center line with increasing distance from the weld is apparent. Second, the strain concentration along the edge of the plate slightly above the weld is apparent. This figure graphically illustrates that the weld and thickness transition in itself does not produce a strain concentration. In fact, for this particular configuration and specimen, the transition seems to reduce the local strain in the region. This strain reduction, however, is only with reference to the strain response of the central or free-field region of the plate. The primary reason for this reduction in strain near the transition is Poisson stiffening by the thicker insert plate. This stiffening, which is caused by the horizontal restraint of the liner plate, causes the region of the liner plate near the weld to behave in a much stronger manner.

If restraints could be provided along the edges of the liner plate, then the uniform Poisson stiffening along the length of the specimen would significantly reduce or possibly eliminate the reduction in axial strain near the transition. However, for the specimen tested, the Poisson contraction occurs as a result of the lack of edge support and Poisson stiffening along the liner plate weld. This causes a large strain to develop in the transition from the Poisson-stiffened region to the free edge region. This large shear manifests itself as the very high shearing strain regions that exist within 1 inch (25 mm) of the weld along either edge of the specimen. This specimen is designed to simulate the transition in the 1:6-scale model. However, in the case of the model, the liner plate and insert plate were entirely free of edge conditions owing to the cylindrical geometry. This means that the region of the specimen that most closely approaches the actual response of the 1:6-scale containment would be the central area farthest from the specimen edge. The other areas of the specimen may not be representative of the 1:6-scale model. After examining the central region of the specimen, it is apparent that no significant strain concentration exists. In fact, any weld-induced concentration would be expected to occur within about ten plate thicknesses (0.7 inch or 18 mm) from the weld. The strain here shows no concentration in this area.

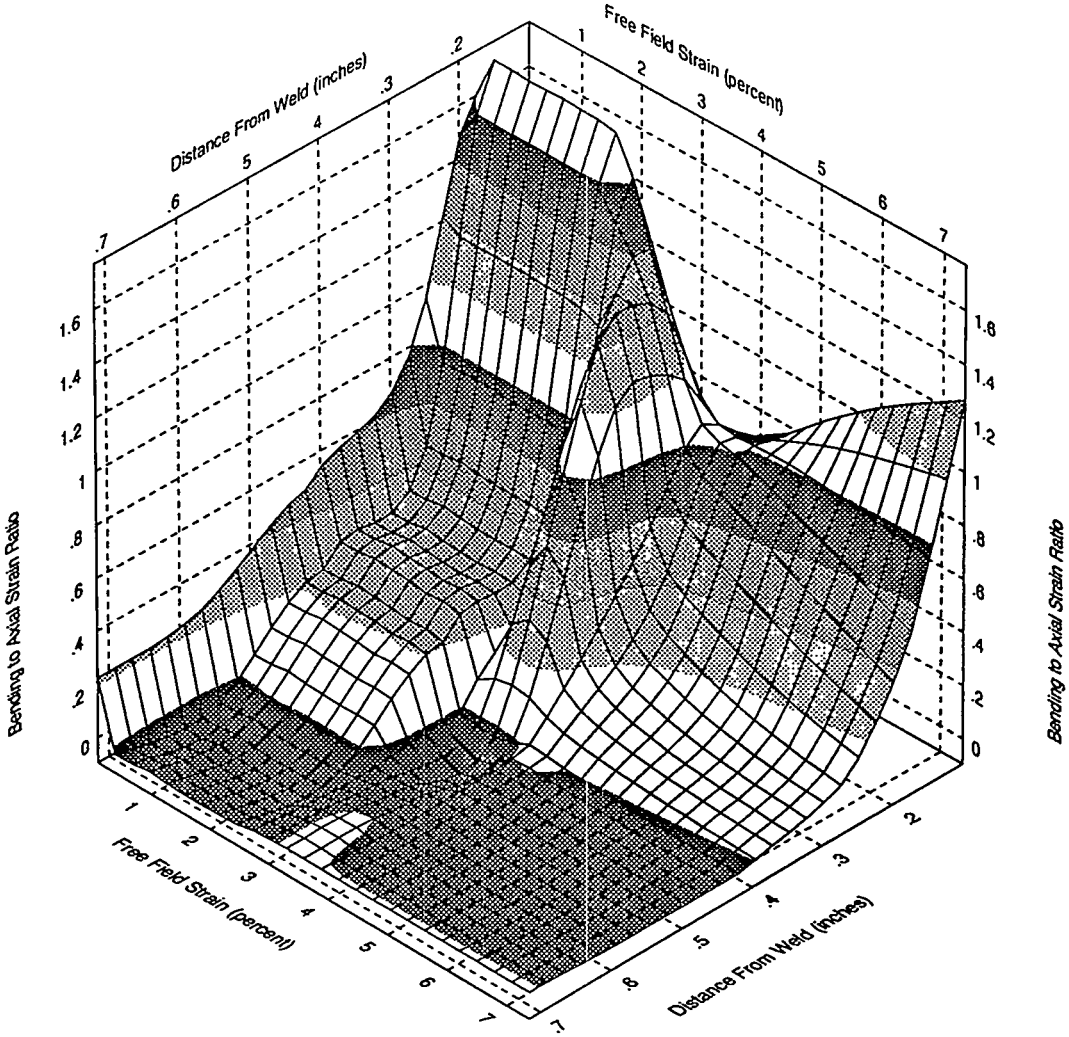

Figure 6.7: Centerline bending strain, 2A4 specimen

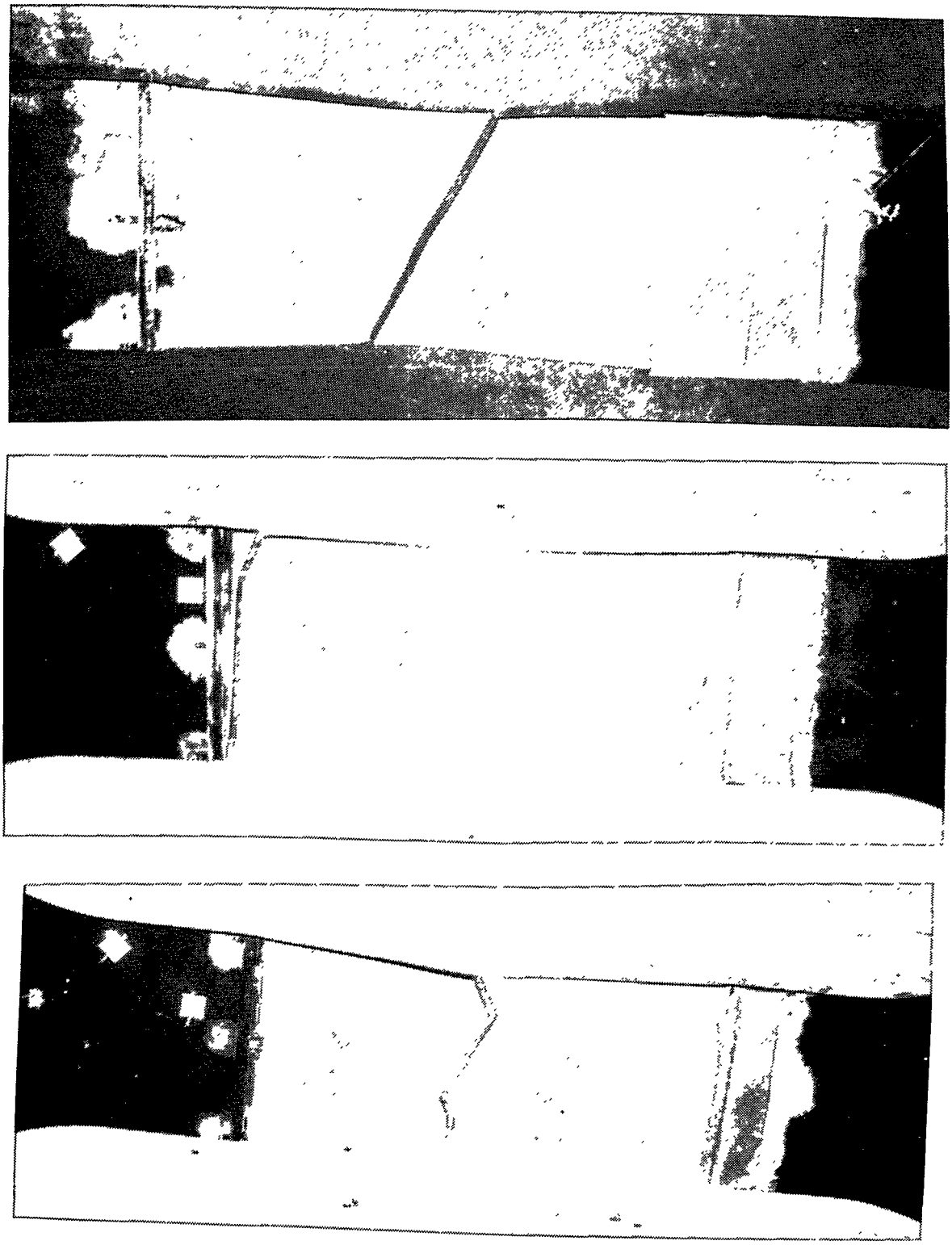

Figure 6.8: Failure locations in weld-transistion specimens

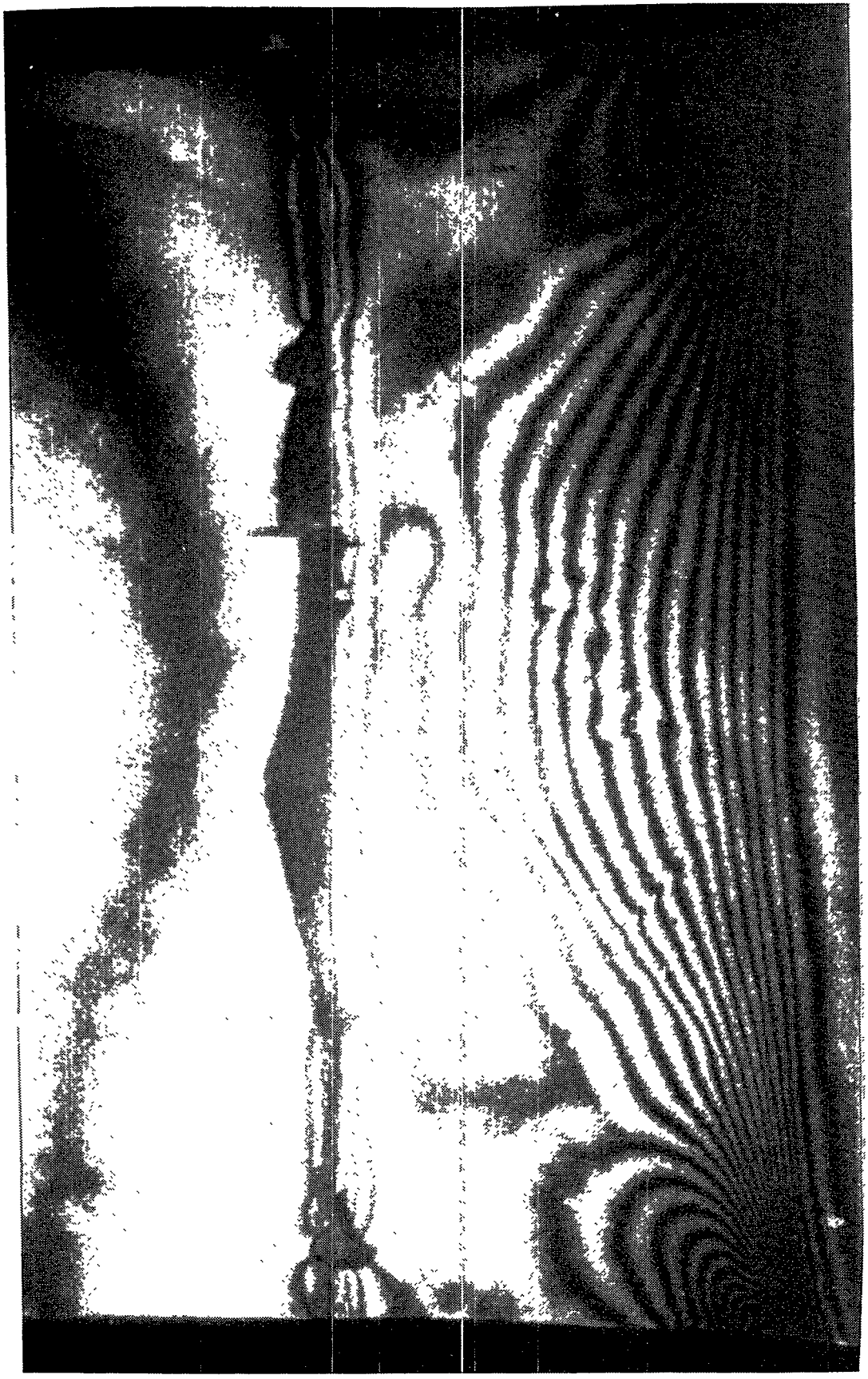

Figure 6.9: Raw photoelastic data from a weld-transition specimen

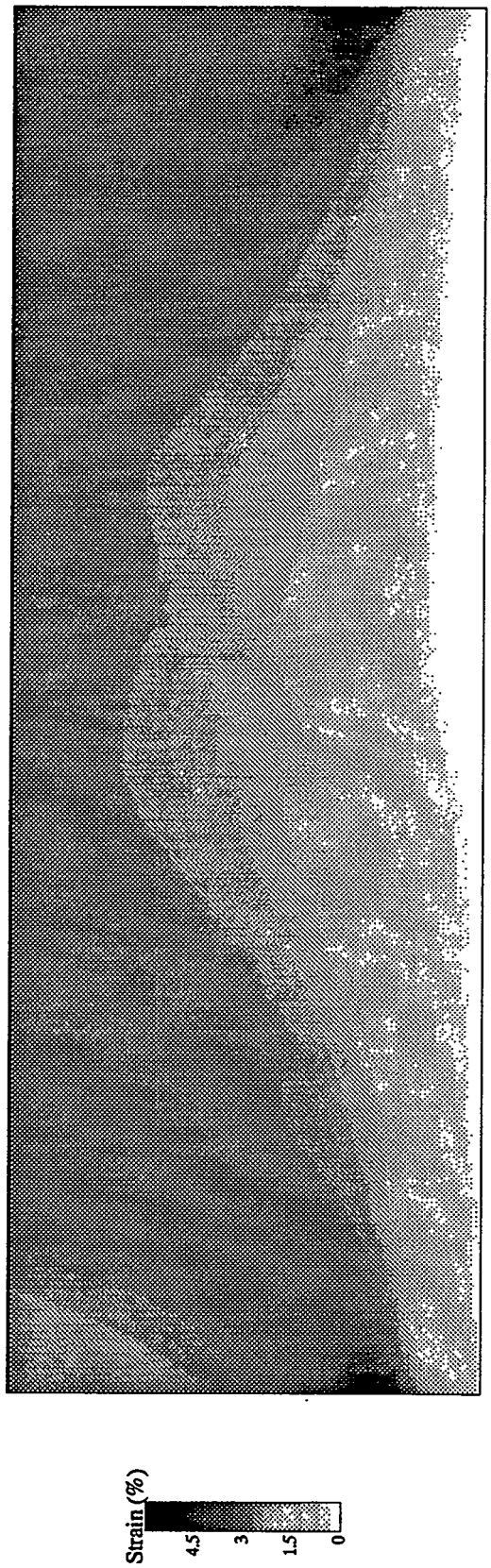

Figure 6.10: Maximum shearing strain in specimen 2A5

In summary, while the bulk of the area of the weld transition specimen is dominated by edge effects which do not exist in the 1:6-scale model, the specimen does provide very strong indication that a strain concentration caused by the transition between the insert plate and the liner plate does not exist. One additional insight is that the potential for bending strains does exist in this region. This was demonstrated by observation of the front and backside strip gages along the specimen center line. Unfortunately, photoelastic data for both sides of the specimen is not available so the strain gage data is the only technique for measurement of this bending strain. As mentioned before, this strain results from the off-center loading due to the non-symmetric thickness transition. It is difficult to say whether this strain would also exist in the 1:6-scale model since the insert and liner plates were both in intimate contact with the concrete on one side which could possibly restrict bending deflections. In any event, the total strain difference from the front side to the backside of the liner produced by this bending moment is relatively small compared to the total strains when the ultimate response and capacity of the material is being considered.

6.2 Separately-Controlled-Loading Specimen Test Results

The most interesting and useful tests of this series are the tests of the separately-controlled-loading specimens. The primary purpose of using these specimens was to investigate the interaction between liner loading and anchorage shear on the failure mechanisms of the liner and anchorage systems. As mentioned before, the specimens consisted of a section of liner plate which could be loaded so that a uniform uniaxial stress could be developed in the liner plate at the row of studs.. A separate loading system was available to allow the shear load to the studs to be varied. As explained before, post-test examination of the 1:6-scale model indicated that a combination of liner preload and stud shear may have led to the liner tear which was experienced when neither loading mechanism alone was capable of producing such a tear.

Six separately-controlled-loading specimens were tested, with each test using a different liner preload. The typical test consisted of applying a predetermined preload to the liner and then, while the preload was held constant, increasing the deflection of the stud shearing mechanism until failure occurred. Two types of failure mechanisms were expected and monitored. These were failure of the liner plate by tearing and failure of the studs by shearing free from the liner plate. The following tests were conducted: on one specimen only liner preload was applied until the specimen failed (stud shearing loads were never applied); on one specimen no liner preload was applied and only stud shear was used to produce failure; other specimens received preloads of 60 ksi (415 MPa), 63 ksi (435 MPa), 65 ksi (450 MPa), and 70 ksi (485 MPa). The specimens with no preload and the 60 ksi (415 MPa) and 63 ksi (435 MPa) preload failed through the studs shearing from the liner plate. The 65 ksi (450 MPa) preload, 70 ksi (485 MPa) preload, and preload-only specimens failed through tearing of the liner plate immediately adjacent to the row of studs. This failure transition between 63 ksi (435 MPa) and 65 ksi (450 MPa) shows a very strong sensitivity of failure mode to liner preload. This sensitivity was predicted and is also thought to be a very strong function of the ultimate strength of the liner material and the ultimate shearing strength of the studs.

A simplistic view of the specimen failure modes can be developed in terms of net section stress in the liner material. When the liner material is loaded to a specified preload, the amount of stud shear necessary to cause failure of the liner material can be roughly determined by calculating the amount of additional load needed to reach the ultimate strength of the material. This additional required load divided by the total number of studs available to carry the load determines the maximum shearing load per stud which will be required for the liner to fail. If the average stud strength is less than this value, then the studs can be expected to shear from the plate before the liner tears. On the other hand, if the studs are strong enough to carry the load required to reach the ultimate strength of the material, then liner tearing will occur before stud failure.

Figure 6.11 shows the overall stress deflection response of the separately controlled loading specimens. The plot shown here is the overall specimen elongation plotted against the net section stress. The dog-bone shape of these specimens precludes easy determination of the average liner strain, so instead, a plot of the overall displacement of one end of the specimen relative to the other was used. The net section stress plotted here is the combination of the stress caused by the preload and the stress induced by the shear load applied to the studs. Only five of the six specimens are plotted here because for the sixth specimen a stud shear only was applied without liner preload. In this case, the liner material response was completely elastic and data for this response are not available.

All five specimens plotted on this graph show very similar behavior in terms of the net section stress at yield and the ultimate strength in terms of net section stress.

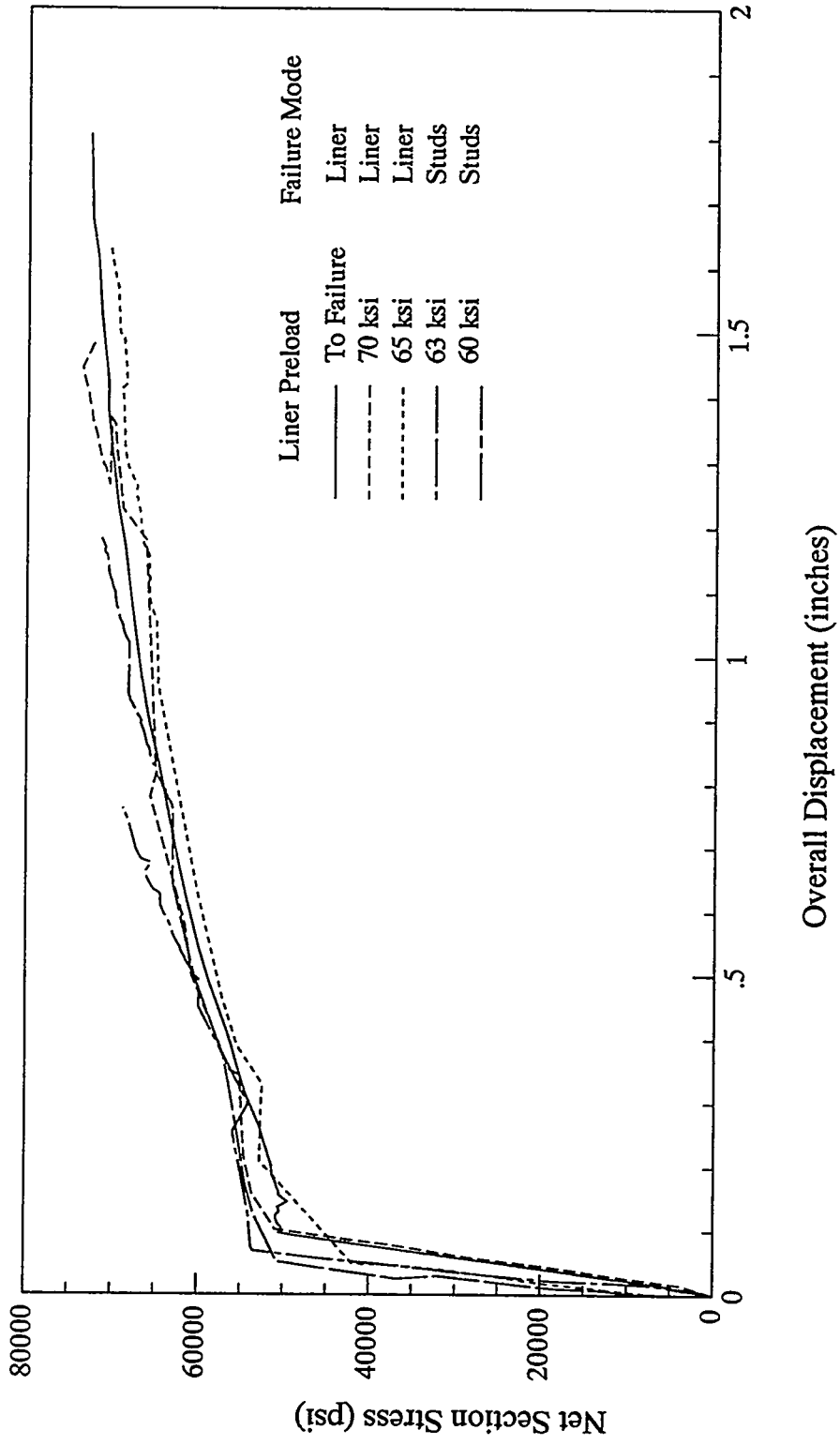

Figure 6.11: Overall separately-controlled-loading response

The region of the plot immediately surrounding initial yielding of the specimen is typically quite sparse in data points because the liner preload must be maintained in a load-controlled configuration so that at the onset of yield the overall displacement increases rapidly until strain hardening begins to take effect. The one specimen on which liner preload was increased to failure and stud shear was never applied is an exception to this. In this case, load could be applied in a displacement-controlled manner, thereby permitting much more frequent data scans to be made during the initial yield. On the plot, this one specimen stands out as having a much more closely defined early yield behavior. The maximum overall displacement of the specimen to failure appears to be a relatively strong function of the liner preload. However, the three specimens for which liner tearing is the mode of failure tend to have an overall specimen displacement at failure which is approximately equal within ±13 percent. On the other hand, the two specimens which exhibited stud shear failure have overall displacements which are significantly less and are a function of liner preload. It should be expected that the specimens which exhibited liner failure showed somewhat similar overall displacements since this represents the overall strain in the liner up until failure. The two specimens which exhibited stud failure represent an incomplete stress-strain curve for the material. Since these specimens never reached ultimate stress, as evidenced by the failure mechanism, the overall specimen displacement should be somewhat less than in those specimens in which liner failure occurred. This is the case, as shown by the figure.

Figure 6.12 shows the response of an axial strip gage on the 65 ksi (450 MPa) preload specimen. The outboard axial strip gage is oriented vertically and centered over one of the outboard studs. The figure plots the strain at the gage locations against the overall specimen elongation. If there were no strain concentration, this plot would consist of straight lines lying on top of one another. While the strain as a function of overall elongation can be easily determined for any specific gage location, the overall response of the gage is very difficult to visualize here. Figure 6.13 is a contour plot of the response of the same strip gage. This plot shows the strain as a function of distance from the stud location and as a function of free-field strain. Free-field strain is defined as the average strain of the 10 single element gages located 1 inch (25 mm) above and 1 inch (25 mm) below the stud line. Rather than plotting strain on the vertical axis, the strain concentration, that is, the actual strain divided by the free-field strain, is plotted.

Several features are notable about the response of this strip gage. The first feature is that the overall response in terms of strain concentration is relatively independent of the free-field strain. This relatively constant behavior with strain indicates that the strip gage strains were constantly increasing at a rate proportional to the free-field strain. The overall response of the strip gage is divided into three major regions. The region a positive distance from the stud corresponding to the area immediately below the studs (the stud shear load is downward) has a strain concentration factor of approximately 1.0. The region within 0.1 inch (2.5 mm) either way of the stud location has a strain concentration factor of about 0.5. This means that the presence of the stud reinforces the liner locally so that the liner plate strain is actually lower than it would be if the stud was not there. The third and final region is the area above the stud where the liner preload and stud shear load combine to produce a larger net section stress than in any other region. Here the strain concentration is highest. For this particular plot, the strain concentration factor peaks at about 1.5.

This large increase in strain is very significant compared with the magnitude of the stud load which produces the strain. For this series of specimens, the stud load is typically in the range of 10 to 15 percent of the liner preload and never exceeds 20 percent of the preload. For this strip gage, the anchorage is capable of producing no more than 20 percent of the ultimate load of the liner, but when this load is used in conjunction with a preexisting liner load, this relatively small load increment is capable of producing a 50 percent increment in overall strain. The behavior illustrated in Figure 6.13 is typical of the axial strip gage behavior for all of the preloaded specimens. Contour plots for all axial strip gages are included in Appendix B.

The second type of strip gage used on the separately-controlled-loading specimens was the transverse strip gage. These gages were oriented horizontally and centered over a stud location. However, like the axial strip gages, the sensitive direction of the gage was still vertical or aligned with the specimen loading. Figure 6.14 is a contour plot of the strain data gathered from the inboard transverse strip gage. This contour plot is quite typical of the response of these gages and both contour plots and strain versus displacement plots for all transverse strip gages are included in Appendix B. As would be expected, Figure 6.14 shows the strain response to be nearly symmetric about the stud location. As with the axial strip gages, the stud appears to provide considerable reinforcement so that the strain response immediately around the stud is about one-half of the free-field strain. Moving away from the stud in either direction, the strain increases rapidly. At about 0.25 inch (6 mm) from the stud location, the strain level peaks at a concentration of 0.9-1.1, which corresponds roughly to the free-field strain. From this position to the edge of the plot, the concentration factor is relatively constant.

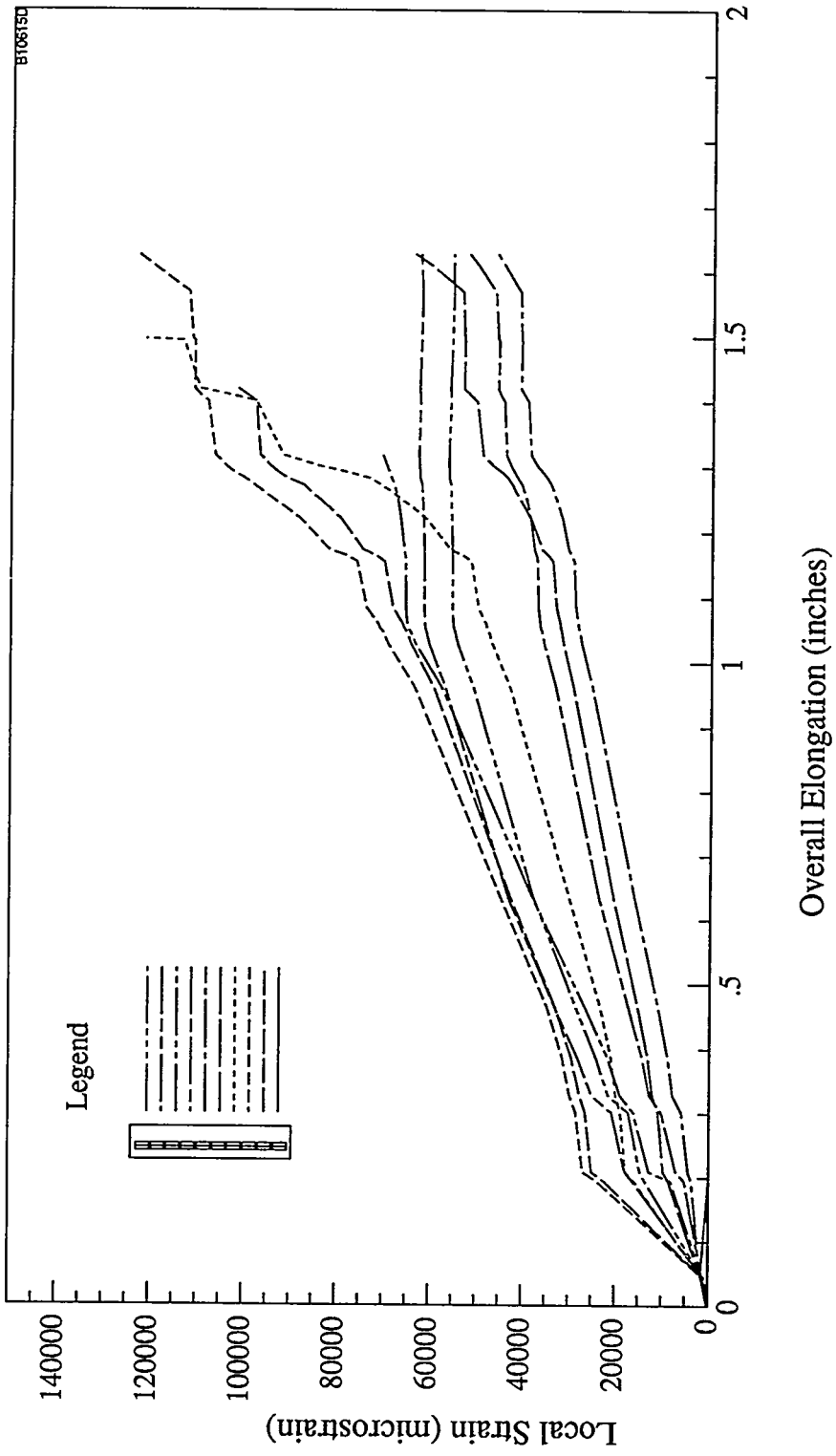

Figure 6.12: Outboard axial strip gage displacement response, 65 ksi specimen

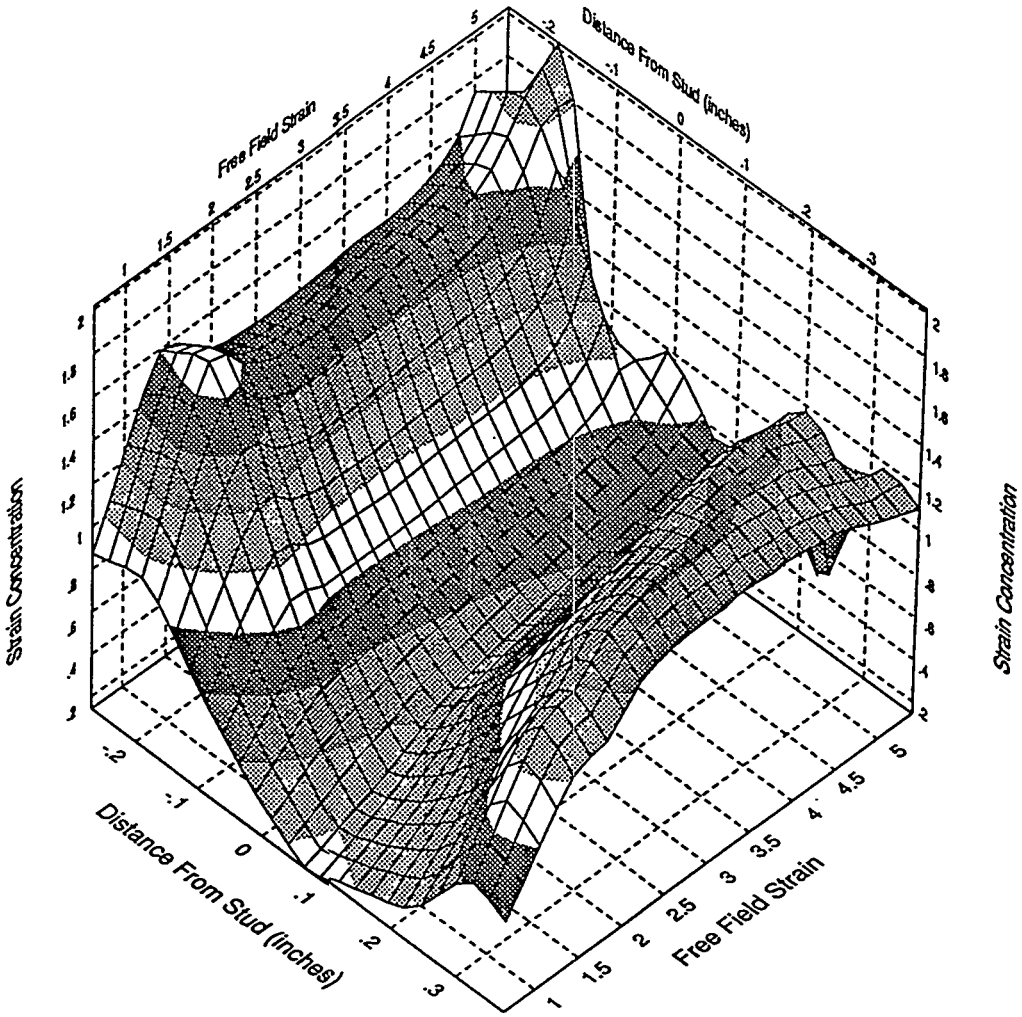

Figure 6.13: Outboard axial strip gage response, 65 ksi specimen

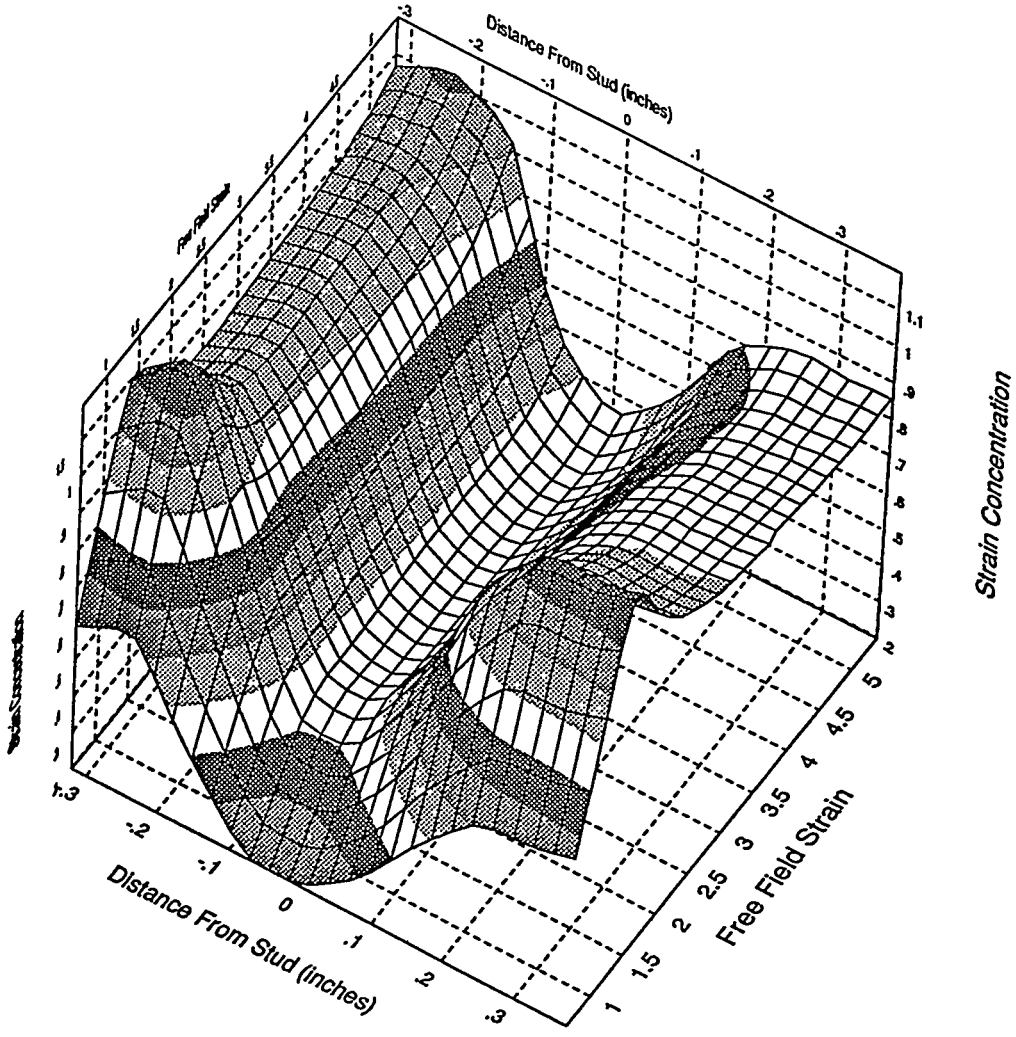

Figure 6.14: Inboard transverse strip gage response, 65 ksi specimen

In addition to the transverse strip gages some specimens were instrumented with Poisson strip gages. These strips were oriented horizontally like the transverse gage, but the gage elements sensed horizontal or Poisson strain. Not all specimens used this type of gage. The Poisson strip gage was located over an outboard stud. The reason for using such a gage was that the lack of edge constraint on the liner plate allowed the specimen to contract in a horizontal direction when the axial load was applied. On the other hand, the studs embedded in a concrete block were not allowed to contract horizontally. This difference in horizontal restraint between the liner plate and the stud is capable of developing a shear load on the stud, which could cause a significant strain in the liner.

A contour plot of the Poisson strip gage for the 63 ksi (435 MPa) preload specimen is shown in Figure 6.15, which is fairly typical of the Poisson strip gage response. Unlike the axial strip gages, the strain concentration factor of the Poisson strip gages does change with free-field strain. In general, the absolute value of strain concentration increases with increasing free-field strain. The strain concentration begins at an average value of about -0.3 and increases to an average value of around -0.5. This behavior should be expected since Poisson's ratio can be expected to change from about 0.3 in the elastic region to about 0.5 in the plastic region of the test. The primary reason for the inclusion of these Poisson gages in the tests was to investigate the effect of the Poisson restraint of the studs on the strain field of the liner plate. As can be seen in Figure 6.15, there is some increase in the compressive strain across the stud. The outboard side of the stud would be expected to experience a larger compressive strain as a result of the outward force of the stud on the contracting liner plate.

The size of this effect is best determined by looking at a plot of the Poisson strip gage strains versus the specimen displacement. This plot is included in Figure 6.16. Here the strain concentration ratio can be more accurately estimated. For example, at an overall specimen elongation of 1 inch (25 mm), the maximum strain of the outer region is about 34,000 microstrain, while the maximum strain of the inner region is about 26,000 microstrain. This indicates that the strain concentration increases by about 30 percent due to the Poisson restraint of the studs. While this amount of concentration is significant, it does not affect the overall failure mechanisms and conclusions for this specimen. The overall mechanism is based on the shear strength of the stud, and regardless of whether the stud load is developed through Poisson effects or direct loading, the stud is still very limited in its capability to increase the stress in the liner because of its relatively low shear strength.

One final set of strain gage responses is presented for the separately-controlled-loading specimens. These are the single-element gages which were located 1 inch (25 mm) above and below the stud row at 1-inch (25 mm) intervals. In total, ten such gages were applied to each specimen. The response of these gages as a function of displacement is shown in Figures 6.17 and 6.18. The specimen chosen here is the specimen with a 65 ksi (450 MPa) preload. Comparison of these two plots shows uniform strain across the width of the specimen for both positions. Furthermore, up to an elongation of 1.2 inches (30 mm), the response of the two specimens is virtually identical, reaching a strain of about 50,000. However, beyond the 1.2 inches (30 mm), the response of the lower single-element gages becomes relatively flat while the upper gages begin to increase more rapidly. At this point it is believed that the stud shear load applied is sufficient to cause a highly preferential strain above the stud row. Of course, if all plastic strain occurs above the stud row, then the response of the lower single-element gages will be constant. Such a response is typical of the specimens in which liner tearing was the mechanism of failure. In contrast, Figures 6.19 and 6.20 illustrate the typical single-element gage response of the 63 ksi (435 MPa) specimen which failed by stud shear. In this case, the average strain exhibited by the single-element gages is about 40,000 microstrain at an elongation of 1 inch (25 mm) for both the upper and lower gages. However, there is more scatter in the data for the upper single-element gages. Here the upper single-element gages do not exhibit rapid change in slope and a large change in strain with increasing displacement immediately before failure. Also, as would be expected from this failure mode, the maximum elongation at failure is significantly less than in the 65 ksi (450 MPa) preload case.

In addition to the strain gage data, photoelastic data are also available for all the separately controlled loading specimens. The figures presented here are from specimens representing both stud failure and liner failure. The 60 ksi (415 MPa) preload specimen failed through shearing of the studs while the 65 ksi (450 MPa) specimen failed through liner tearing. As with the weld transition specimens, the photographic data have been reduced to produce contour plots which give a direct reading of the maximum shearing strain over the specimen of the surface just prior to failure of the specimen.

Figure 6.21 is a maximum shearing strain plot for the 60-ksi (415 MPa) specimen. The locations of the four anchored studs are readily apparent in this plot. Outboard and above the outer studs is a relatively high strain region.

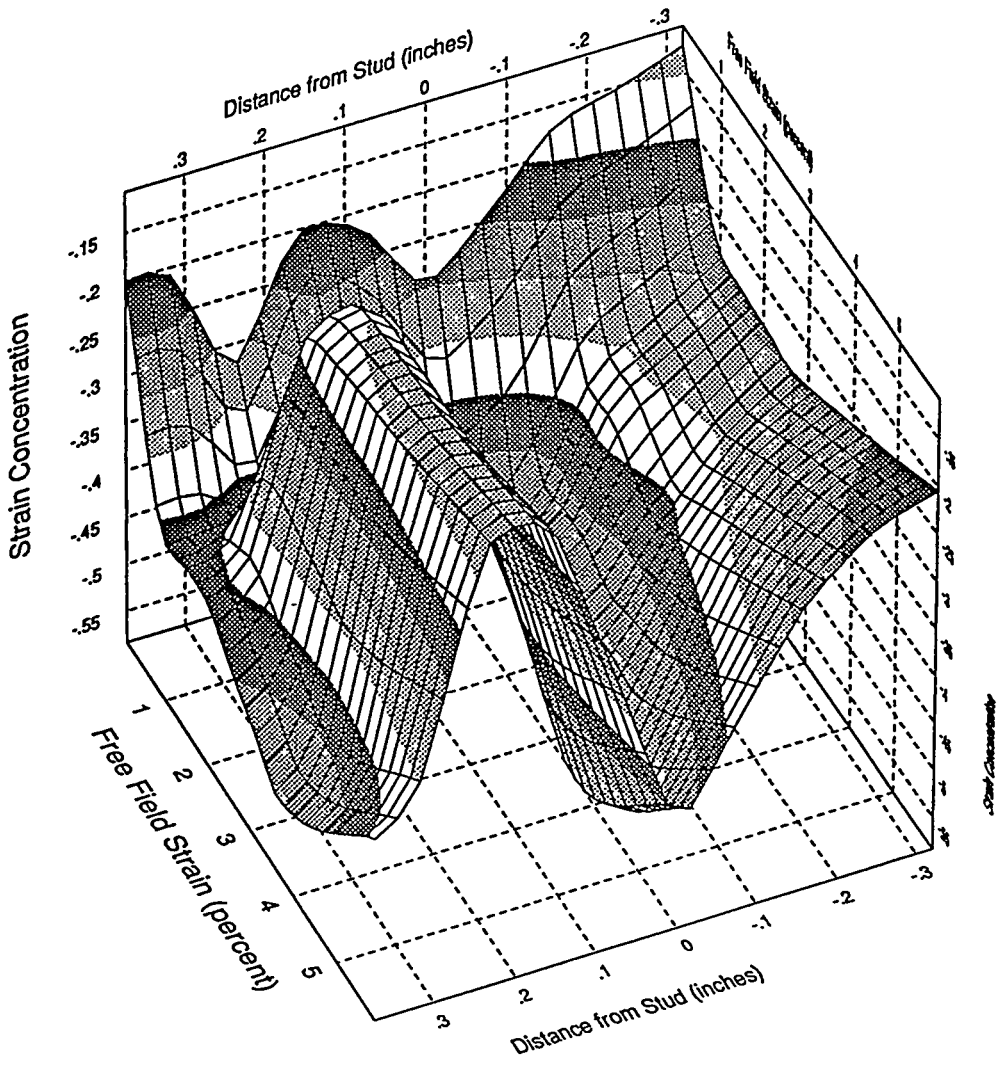

Figure 6.15: Poisson strip gage response, 63 ksi specimen

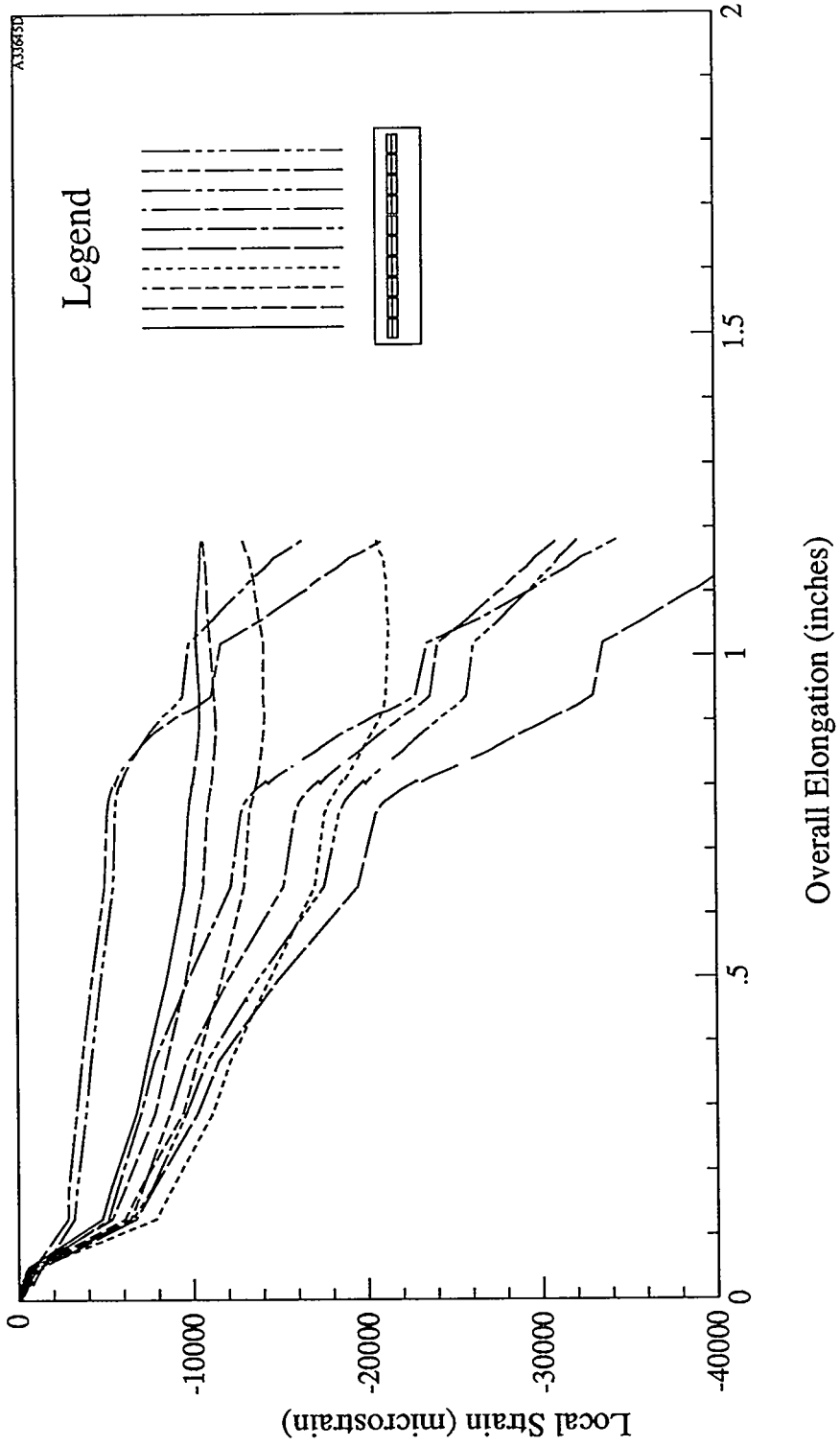

Figure 6.16: Poisson strip gage displacement response, 63 ksi specimen

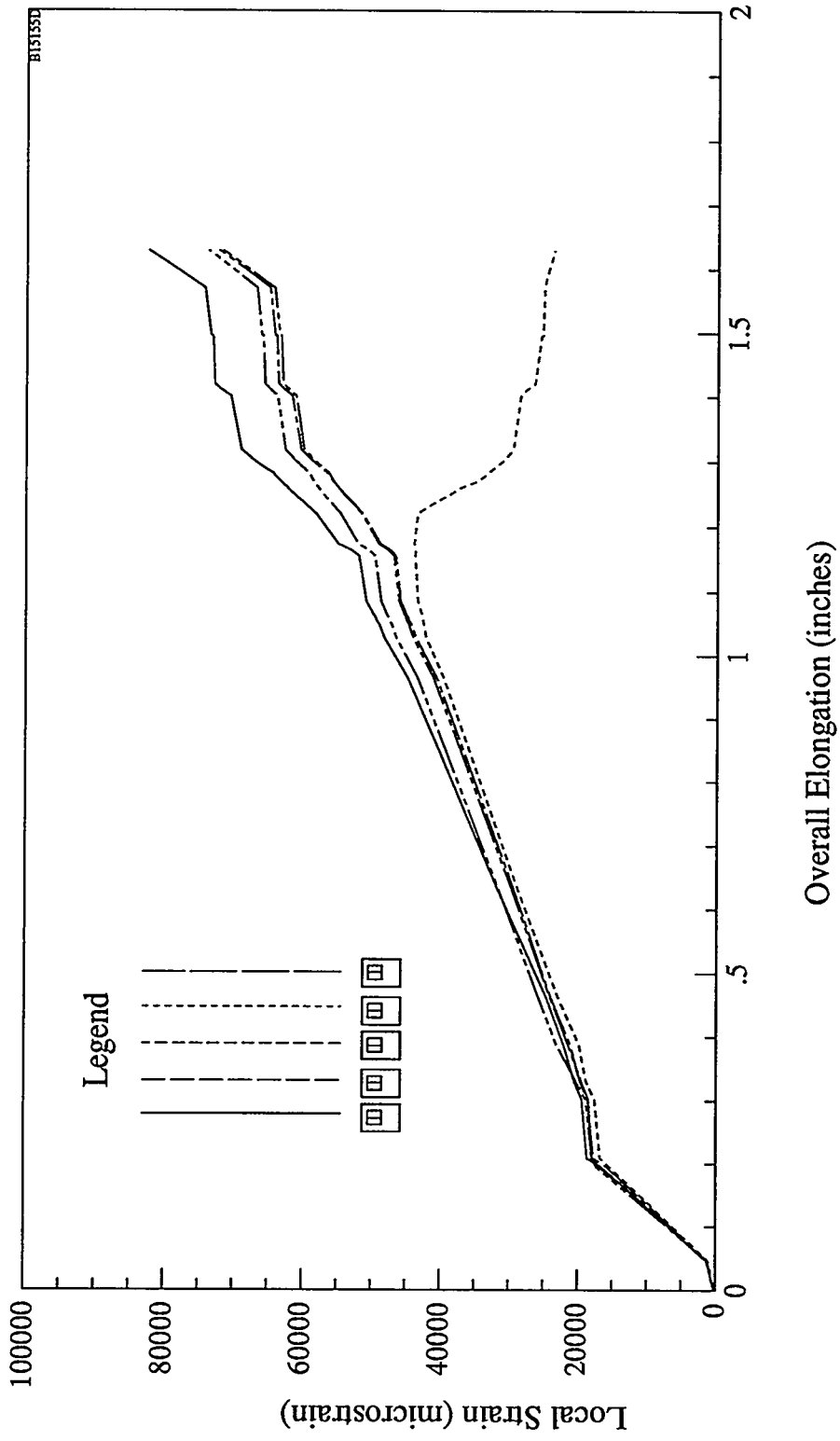

Figure 6.17: Upper single element gage displacement response, 65 ksi specimen

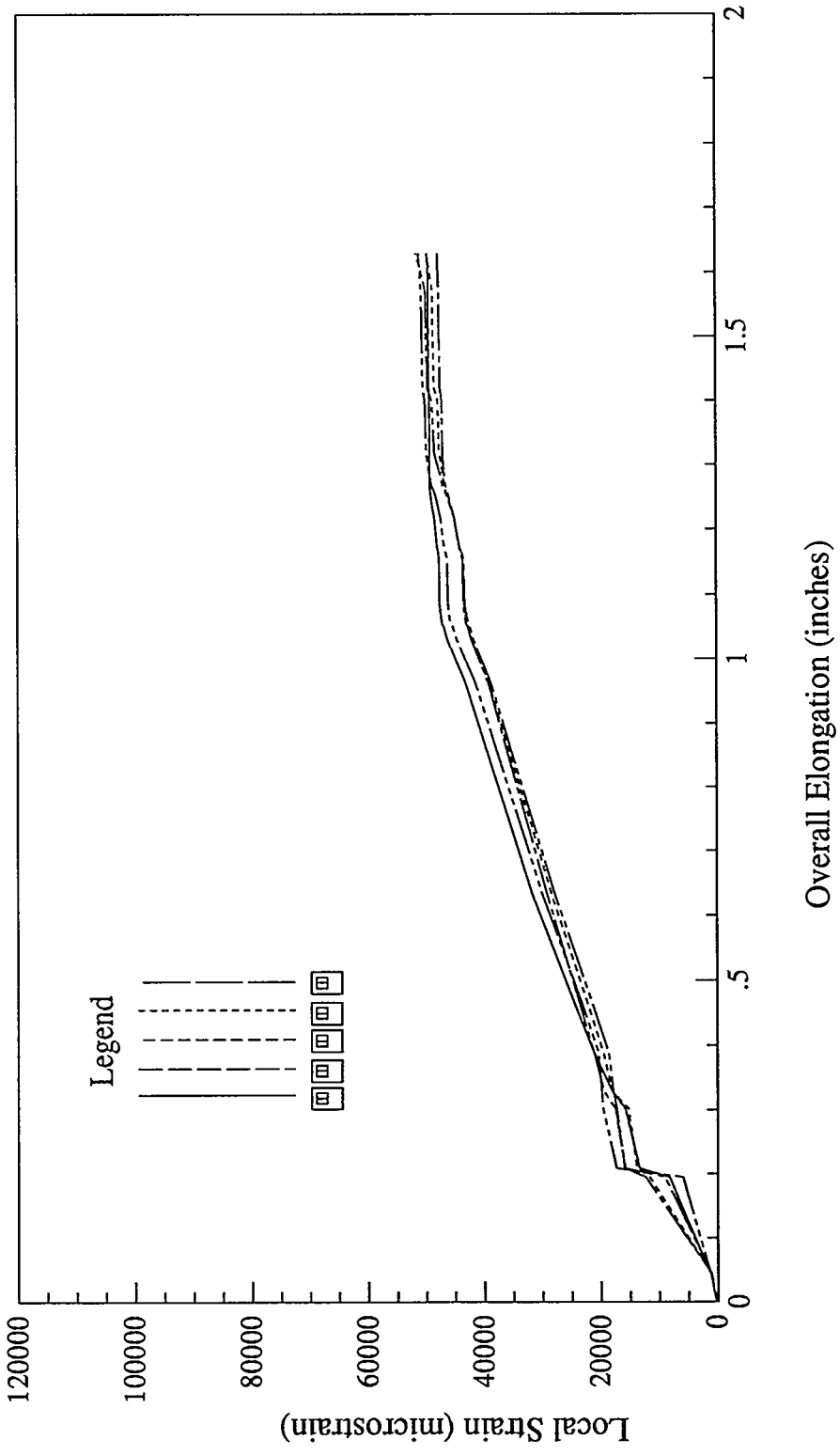

Figure 6.18: Lower single element gage displacement response, 65 ksi specimen

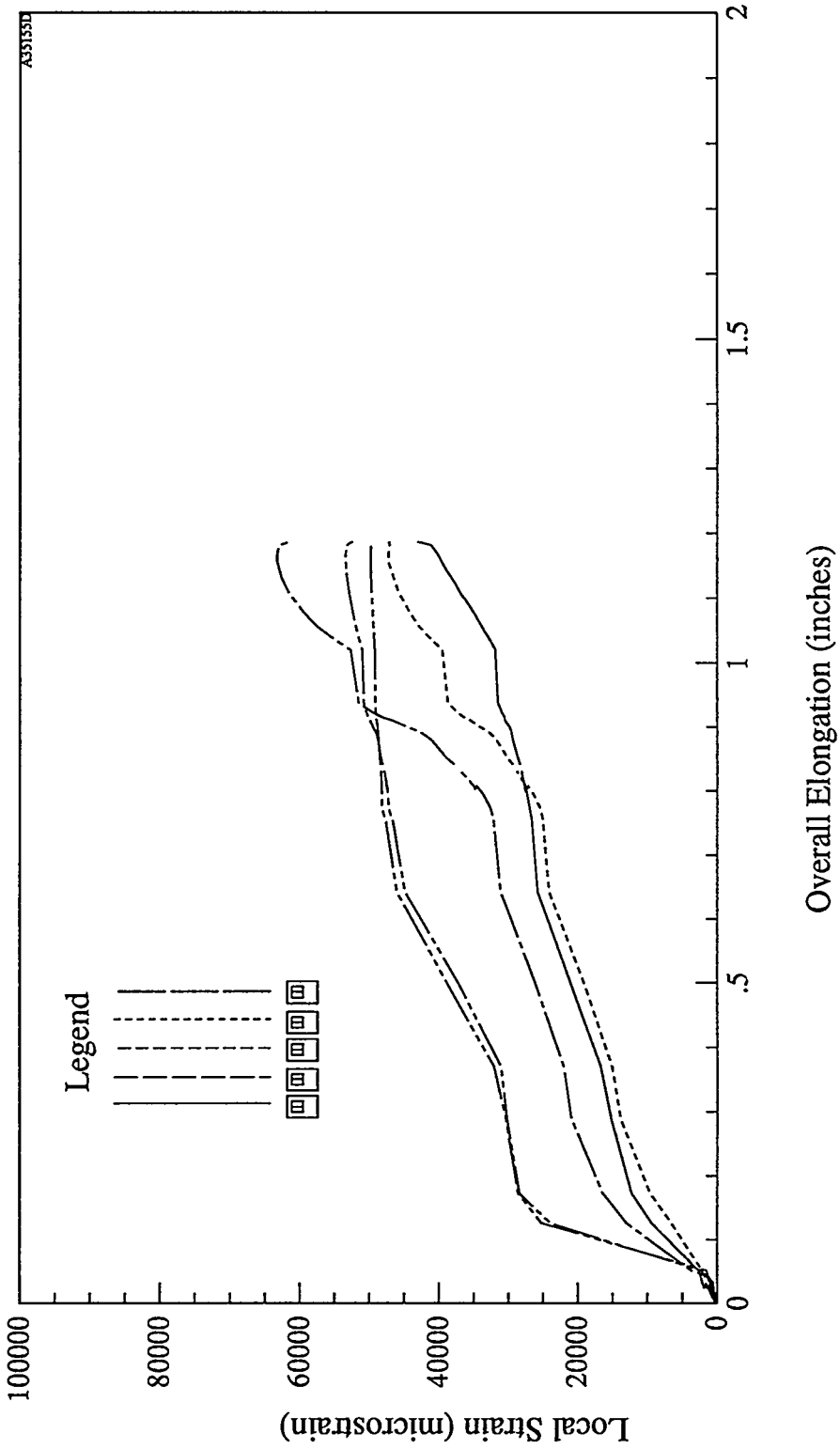

Figure 6.19: Upper single element gage displacement response, 63 ksi specimen

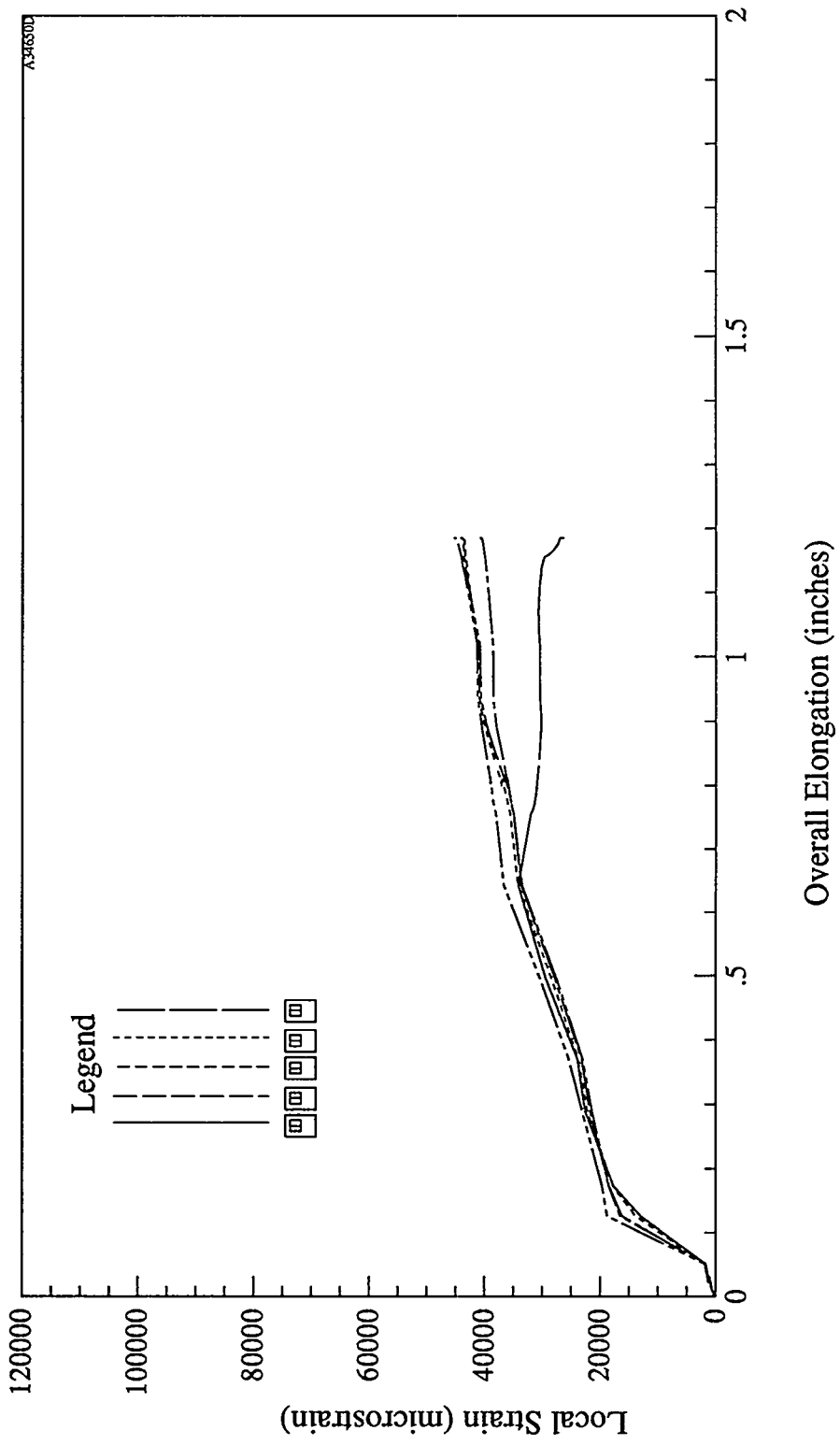

Figure 6.20: Lower single element gage displacement response, 63 ksi specimen

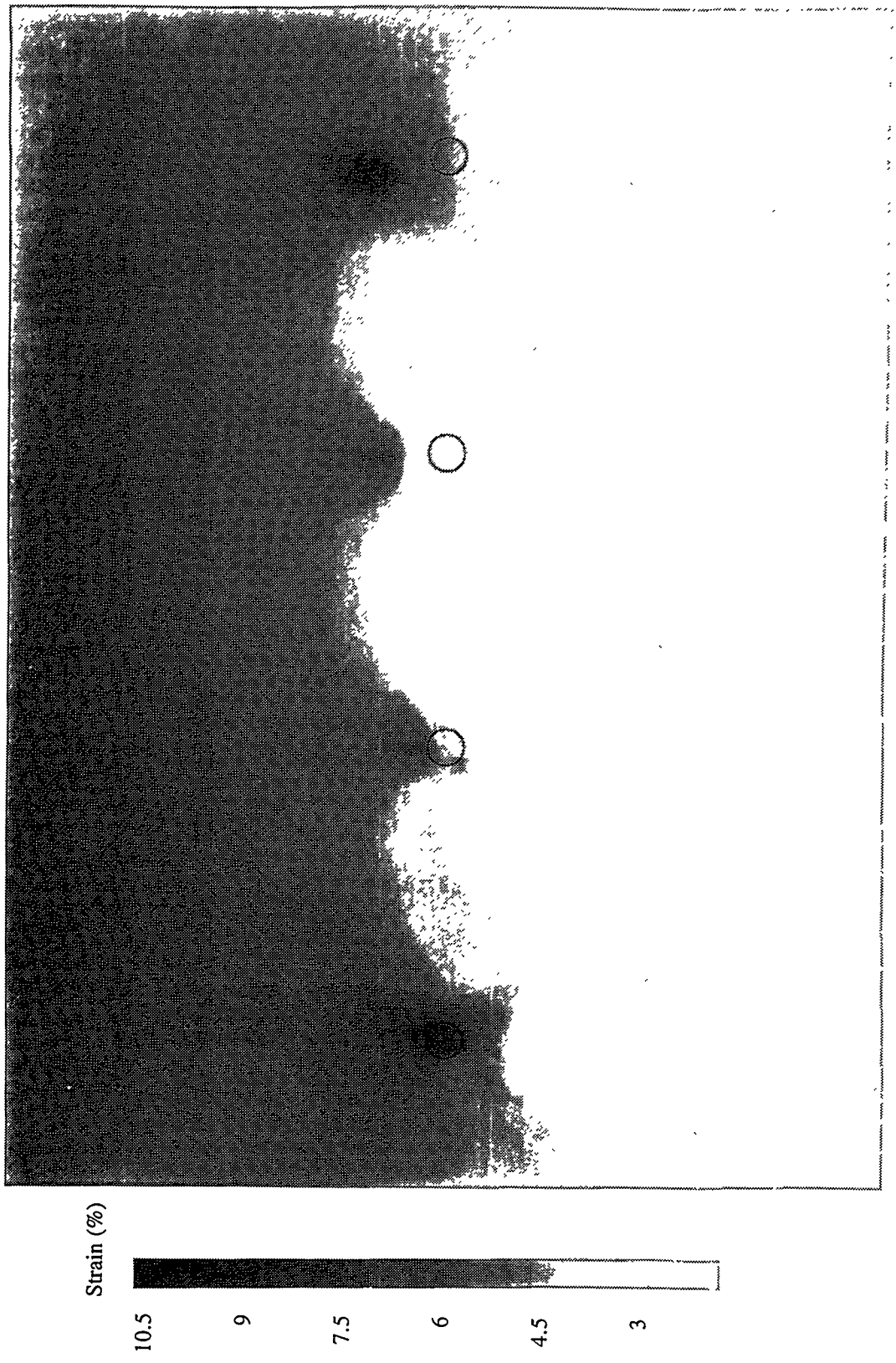

Figure 6.21: Maximum shearing strain in 60 ksi specimen

This region results from the combination of the liner preload, the stud shear load, and the Poisson restraint of the studs. Without the effects of the Poisson restraint, these studs would be very similar to the two inboard studs in terms of strain concentration. Notice here that the free-field strain increases from about 4 percent to about 6 percent going from the region immediately below the stud row to the region immediately above. While this increase is significant, it is apparently not sufficient to induce liner tearing before the maximum stud shearing capability is reached.

Figure 6.22 shows the maximum shearing strain in the 65 ksi (450 MPa) specimen immediately prior to failure. The general features of this figure are very similar to the 60 ksi (415 MPa) specimen, with the primary difference being the increase in strain across the stud row. Here the strain level increases from about 3 percent free-field strain to about 9 percent free-field strain above the stud row. The maximum available shear load the stud can carry is the same for this specimen as in the previous one. However, the more highly strained free-field state of the specimen causes this increase in net section stress to induce a much larger maximum strain in the area immediately above the studs. This specimen failed through liner tearing across the top of the studs. The resulting tear went essentially straight across the top of the four studs and, outboard of each of the outer studs, the tear turned down to about a 30-degree angle, continuing to run perpendicular to the maximum strain shown in the plot.

From the results of the separately-controlled-loading specimens, a very important conclusion can be drawn. Very small changes in the parameters of the liner and anchoring system can have a great effect on the failure mode of the liner. As is shown here, an increase in initial preloading of only 3 percent was sufficient to produce a transition from a stud shearing failure to a full liner tear. Using the concept of net section stress compared with ultimate strength of the material, it can be theorized that similarly small changes in material ultimate strength and stud shearing strength would also produce a sharp shift in the point of transition between liner failure modes. It was stated earlier that post test examination of the 1:6-scale model points to a liner failure mode in which a combination of liner preload and stud shearing load generated by differential strains led to the liner tear experienced in the model. The results of these separately-controlled-loading tests support this as a likely mechanism for producing the observed failure. Furthermore, these tests point to the fact that relatively small changes in liner and anchorage geometry and material properties could change the failure mode of the entire containment model.

6.3 Full-Simulation Specimen Test Results

The full-simulation specimens provided a method by which a full-scale simulated mockup of a section of the wall of the 1:6-scale reinforced concrete model could be tested in the laboratory. Unlike the separately-controlled-loading specimens, the tests for these specimens consisted of increasing the specimen elongation while monitoring the required load and the response of the various strain gages. The stud shear load, which was applied separately in the separately-controlled-loading specimens, was developed by differential strain between the reinforcing steel and the liner and insert plates. Internally, the response of the specimen was expected to be very similar to that described in the schematic cross-sectional drawing of the 1:6-scale model in Figure 2.1.

Four full-simulation specimens were tested. The first three of these were highly instrumented with strain gages and photoelastic material. In addition to the surface strain gages used on the other specimens, six weldable strain gages were applied to the central portion of six of the ten reinforcing rods to allow the reinforcing steel strain to be measured. Tests on the fourth full-simulation specimen went one step further in simulating the conditions of the 1:6-scale reinforced concrete model. On this specimen, in addition to axial load being applied to the reinforcing steel on the liner, pressure was applied to the liner to simulate the internal pressure of the model. This pressure was maintained proportional to the applied load and was such that the load per unit width of the specimen divided by the applied pressure matched that which was used in the 1:6-scale model. This ratio is equal to the radius of the model. On this last specimen, surface strain gages and photoelastic material could not be used. For this specimen, the only data available data are the load versus deflection of the entire specimen and that from the six weldable gages attached to the selected reinforcing rods.

Figure 6.23 shows the overall load deflection response of the full-simulation specimens. During the tests, the specimens without external pressure were termed Phase 2B, and the single specimen on which external pressure was applied was Phase 2C. Notice from the figure that the specimen on which external pressure was applied exhibits a very slightly higher load for a given deflection. This increase in load corresponds to about 3 percent of the total applied load. If this increase in load is attributed to simple dry friction between the pressure system in the specimen, it can be shown that the expected value of this increase is the product of the specimen length and the coefficient of friction divided by the radius of the 1:6-scale model. For the 44-inch long (1120 mm) specimens and the observed load increase of three percent this corresponds to a specimen coefficient of friction of 0.09.

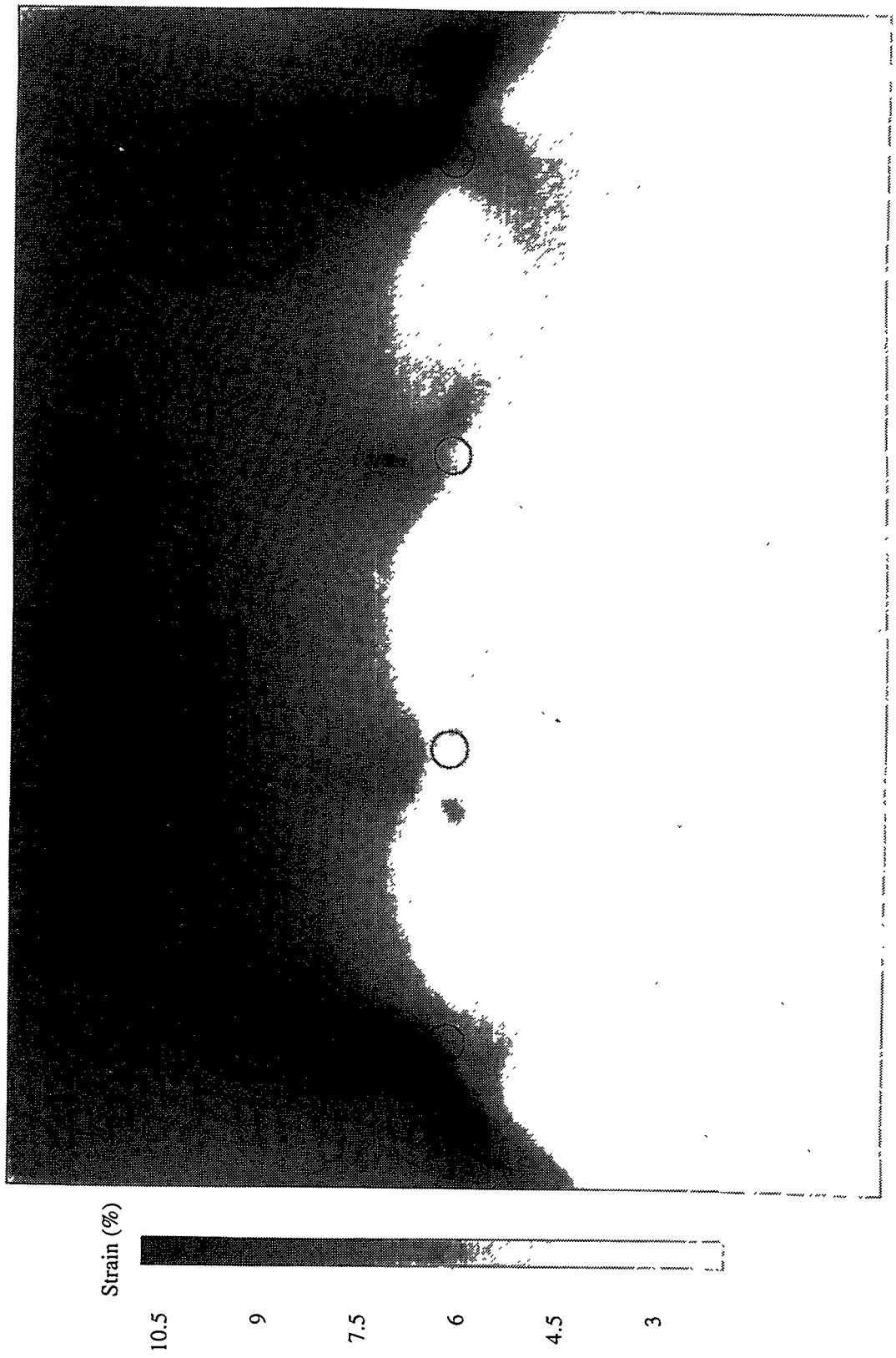

Figure 6.22: Maximum shearing strain in 65 ksi specimen

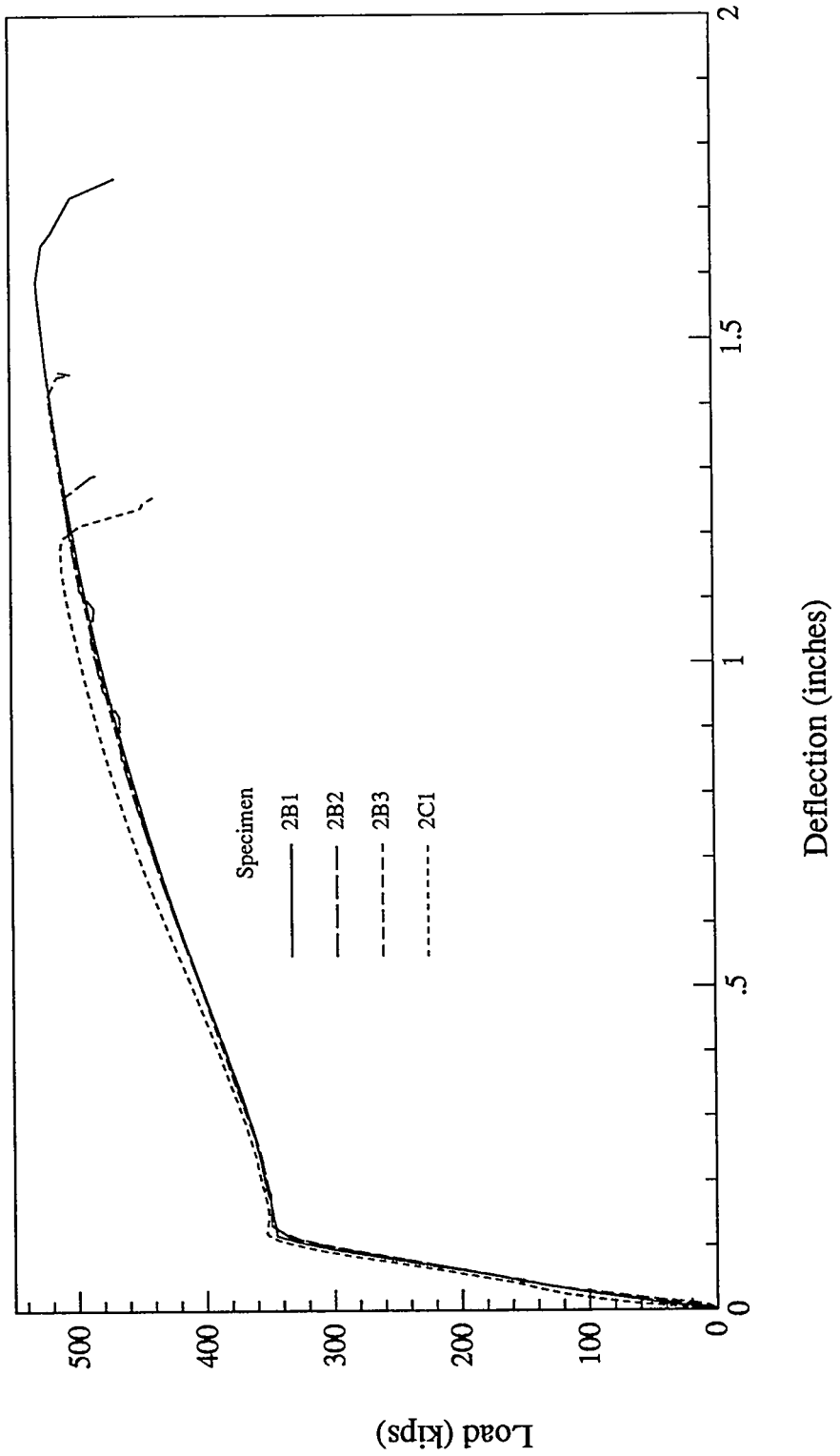

Figure 6.23: Overall response of full-simulation specimens

The bladder used to apply pressure to the specimen was isolated from the specimen by a 0.030-inch (0.75-mm) thick sheet of Teflon. It is not unreasonable to assume that the coefficient of friction between the Teflon and the steel specimen would be on the order of 0.09, thereby causing the increase in load.

The difference in response from one full-simulation specimen to the next is very small. This is true for the recorded strain gage values as well as the overall load deflection response. In general, only representative data are presented and discussed in this section. As with the other specimens, complete plots of all strain gage data are included in Appendix B, and photoelastic data is included in Appendix C.

The full-simulation specimens, in addition to surface strain gages, had six weldable gages attached to six of the ten reinforcing steel bars. A typical response of the reinforcing steel is shown in Figure 6.24. Since the reinforcing steel provides most of the strength of the specimen, the specimen deflection would be expected to be directly related to the reinforcing steel strain. In general, Figure 6.24 shows this to be true. Further, for the fully plastic behavior of the specimen, the average strain, as determined by specimen deflection, should correspond well with the reinforcing steel strain. Referring to Figure 6.24, at an overall specimen deflection of 1 inch (25 mm), which corresponds to 22,000 microstrain, the average strain of the reinforcing steel is about 24,000 microstrain. One aspect of the reinforcing steel response which is somewhat unusual is the large increase in strain for a very small increase in deflection at a deflection value of 0.14 inch (3.5 mm). This step corresponds to initial yielding of the reinforcing steel in the region of the gages and represents a sudden change in local strain during initial yield. The initial tensile fracture of the concrete is not noticeable on the plots. The concrete used has a tensile strength of about 500 psi, which corresponds to fracture at a load of 75,000 lb. From Figure 6.23, this load occurs at a deflection of 0.02 inch (0.5 mm). On the plots, it is not possible to detect the postulated decrease in stiffness that should occur at this deflection.

The first surface strain gages to be discussed are the liner plate single-element gages. These gages are located along the center line of the liner plate and positioned halfway between stud rows. After yielding of the liner plate, it is expected that the load transfer mechanism discussed earlier will cause the strain to be larger in the gage nearer to the thickness transition. Figure 6.25 is a plot of the liner plate single-gage response for specimen 2B1. From these plots it is apparent that, after the early plastic response up to 4 percent strain, no significant strain difference can be seen among the gages. The strain levels shown in Figure 6.24 correspond very well with the average liner plate strain as determined by the rosette placed in the center of the specimen.

Figure 6.26 shows the response of the single-element Poisson gages for specimen 2B1. These gages are placed in a 2 x 3 array, allowing the Poisson strain gradients to be observed in both the axial and transverse direction. Notice from the plot that the Poisson strain is by far the largest in the corner near the weld and thickness transition. The gage located along the specimen edge, but 2 inches (50 mm) farther from the weld shows somewhat less strain, but still exhibits a relatively high strain level. The gages with the lowest strain reading are the two gages positioned along the weld and thickness transition, but away from the specimen edge. Finally, intermediate strain results are seen in the remaining two gages. This observation of six different points corresponds very well with the data seen in the weld and thickness transition specimens. Again, it was expected that the load transfer mechanism of the stud would contribute to the strain levels in this area. This shows that this is not the case. The Poisson gages indicate that there is a significant overall drop in strain levels near the weld and thickness transition.

This indication is borne out in Figure 6.27, which shows the response of the lower outboard strip gage of specimen 2B1. The abscissa of this plot is the average liner plate strain, which is calculated by dividing the specimen elongation by the length of the liner plate. This assumes that all deflection occurs in the thinner liner plate. The gage shown measures axial strain levels in the region of the stud located in the lower left corner of the specimen. This gage exhibits a significant reduction in strain close to the transition. At the region farthest from the weld, the gages show values approximately equal to the average liner strain. Again, this shows very little evidence for load transfer since the predicted value without load transfer (strain concentration of 1.0) and the observed value are the same.

The strain levels drop significantly close to the weld and thickness transition. Once more, this is due primarily to the Poisson restraint, as seen in the weld transition specimens. This general behavior of decreasing strain near the weld and thickness transition is repeated in all appropriate strip gages. (See the plots in Appendix B for examples of these.)

Figure 6.28 shows a typical response of an edge strip gage, in this case the front edge strip gage for specimen 2B1. This response is quite different from that of the interior strip gages. Specifically, the large range in strain concentration does not exist. At high average strain levels, the strain concentration is somewhat uniform and rather than ranging from very low values up to about 1.0, it tends to range from about 1.0 to 2.

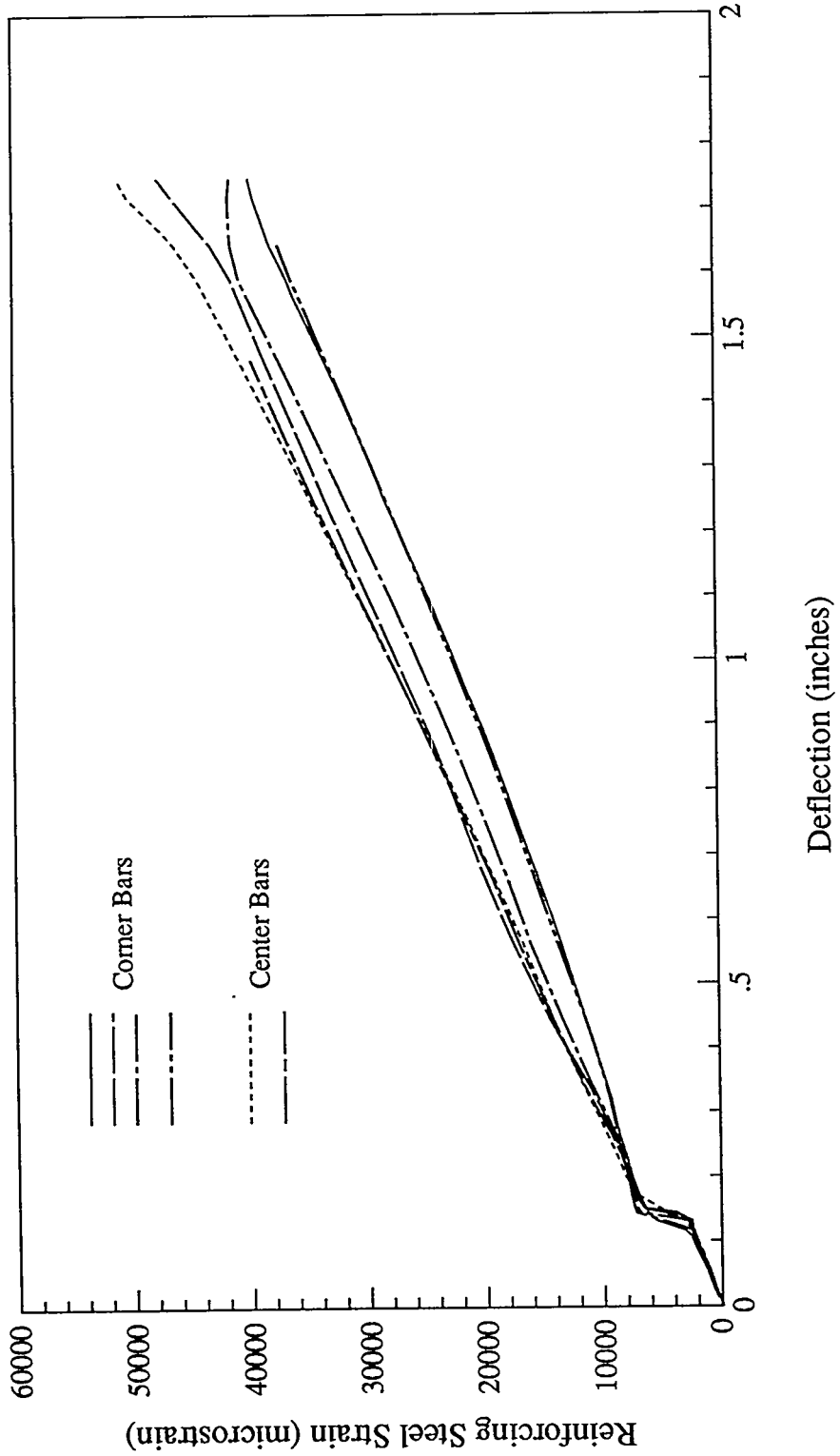

Figure 6.24: Typical response of reinforcing steel, full-simulation specimens

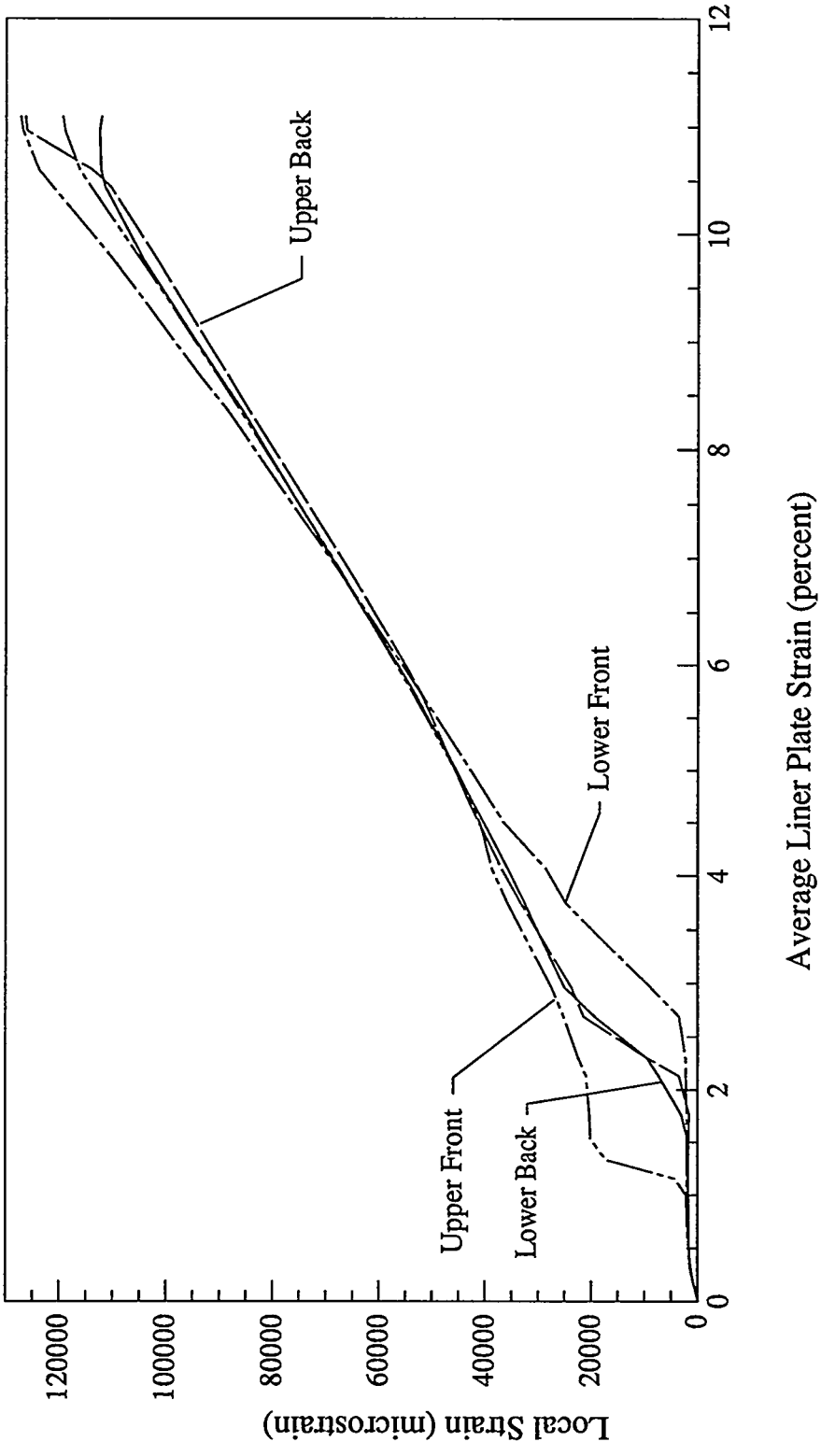

Figure 6.25: Full-simulation specimen liner plate single gage response

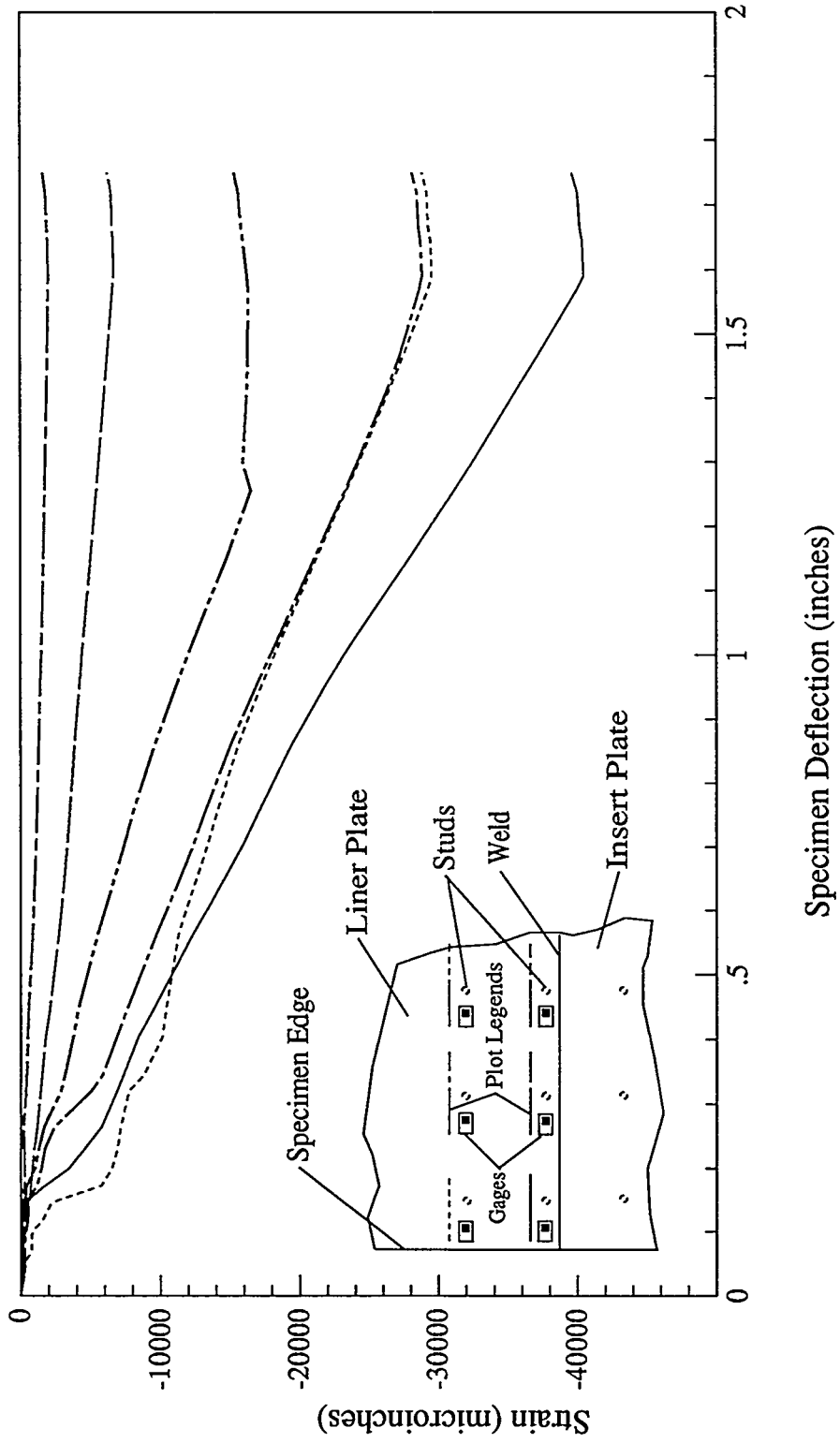

Figure 6.26: Full-simulation specimen liner single element poisson gage response

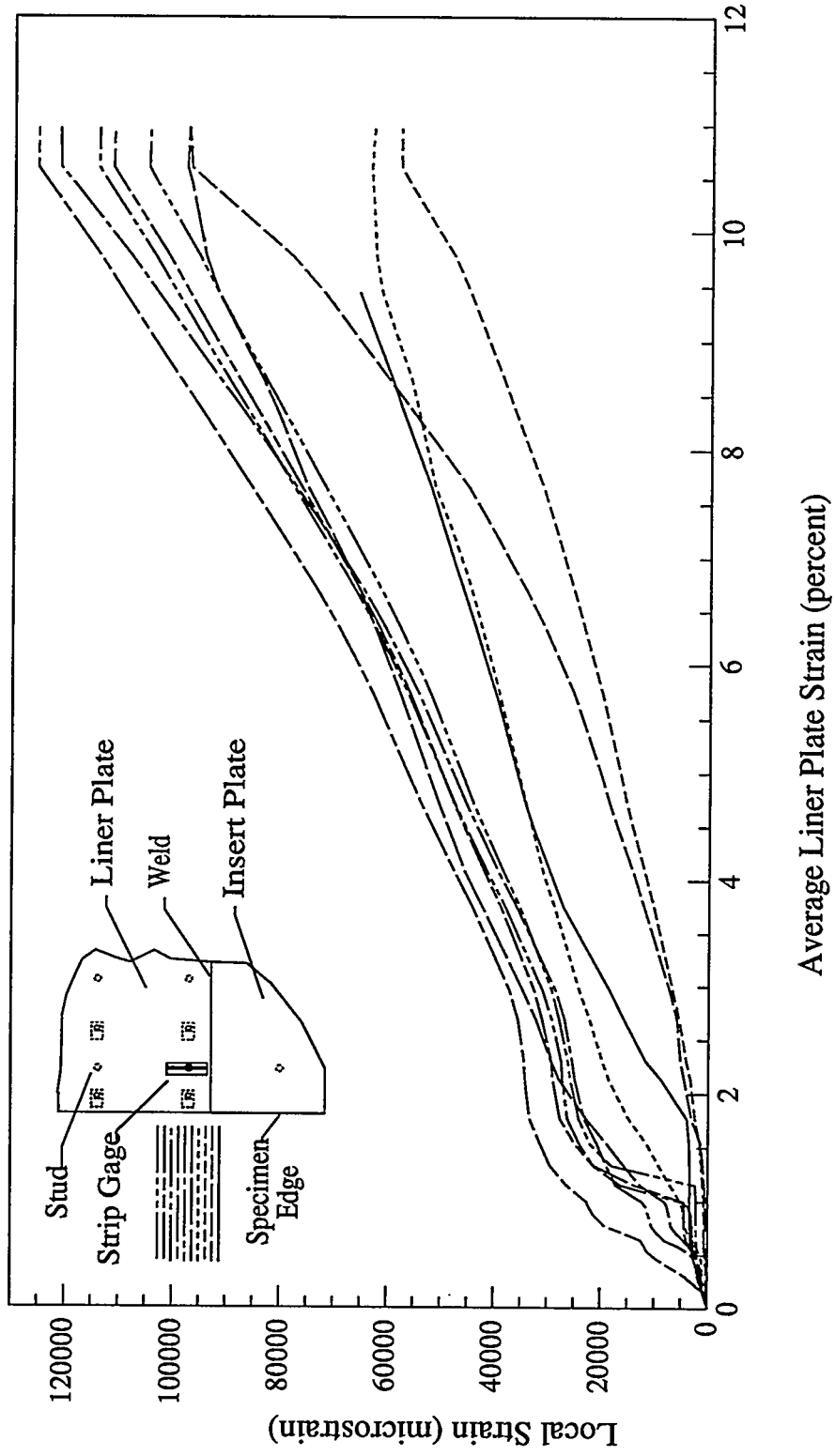

Figure 6.27: Lower outboard strip gage response, full-simulation specimen

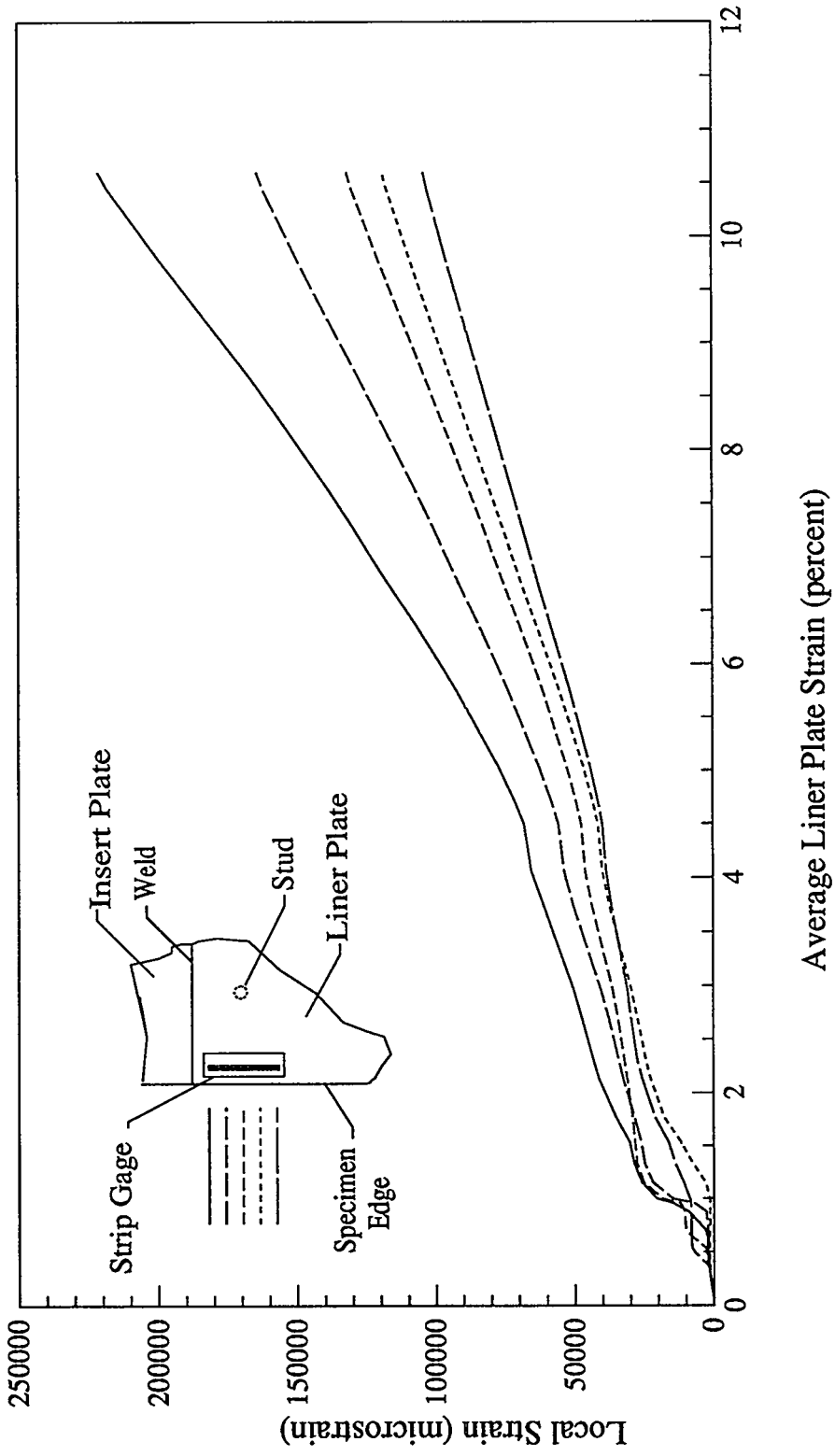

Figure 6.28: Typical edge strip gage response, full-simulation specimen

Also, the strain level increases with decreasing distance to the weld and thickness transition. The strain concentration seen here is due primarily to the very large shear induced by the Poisson stiffening at the weld and thickness transition, and the proximity of a free edge, which allows Poisson contraction a short distance from the transition. Again, this response is very similar to what would be expected from the results of the weld-transition specimens.

One final strip gage type which was used on these full-simulation specimens is the transverse strip gage. These gages were located near the centerline of the specimen and positioned with the strip axis parallel and close to the weld and thickness transition. However, the sensing axis of each element in the gage was vertical. Figure 6.29 shows a typical contour plot response of these gages. In general the gages show a strain concentration factor that is always less than one, indicating that the Poisson stiffing effect is a major factor in this region. This strip gage also shows the most uniform behavior of any gage and has very little variation with distance from stud. The distance from stud here is the distance from the vertical row of studs on the centerline of the specimen. This strip gage had a rapidly increasing strain concentration very early in the test, followed by a decrease with strain concentration levels dipping as low as 0.2. This decrease was very likely caused by the bending moment generated in the liner plate due to the offset nature of the transition from the thickness of the liner plate to insert plate. The bending induces a differential compressive strain, causing the overall strain in the gage to decrease. As the average strain in the specimen is increased, this relatively small bending effect becomes overwhelmed by the overall strain of the plate and the strain concentration factor begins to increase again. This factor reaches a level of about 0.7 to 0.8 and remains there for the remainder of the test.

As with the other specimens tested, the photoelastic data from the full-simulation specimens provide the most easily interpreted and useful information from these tests. The strain gages have shown that the postulated large increase in strain caused by load transfer from the studs does not occur. The photoelastic data support this conclusion. Figure 6.30 is a gray-scale contour plot of the maximum shearing strains in a full-simulation specimen just prior to liner failure (additional plots are included in the appendices.) The figure shows a strong similarity between the full-simulation specimen and the weld-transition specimen. The very low strain levels along the transition and the high strains induced in the corners by the Poisson restraint are obvious. One additional feature of the full-simulation specimens is the appearance of relatively high strain concentrations at some of the studs. However, the very high strain concentration that would be expected along the first row of studs near the thickness transition is almost entirely absent. Some load transfer is apparent, as evidenced by the strain concentration around the second and third row of studs. In all cases, the full simulation specimens failed through liner tearing with the tear starting in one of the high-strain regions in the corners near the weld and propagating horizontally across the specimen. The tear always occurred immediately adjacent to the final stud row and always on the side of the stud nearest the thickness transition, as predicted.

Post-test examination of the condition of the studs points to the fact that large load transfers may be occurring in these specimens. Figure 6.31 is a photograph of the studs in a full-simulation specimen following testing. The studs are bent to an angle very similar to that shown in Figure 2.1. In fact, the row of studs nearest the thickness transition exhibits the largest deflection, with the amount of deflection decreasing with increasing distance from the weld. This is predicted by the postulated failure mechanism. From these post-test data, it seems that a significant load transfer occurred, especially in the row of studs closest to the thickness transition, even though the strain gage data and the photoelastic data show no evidence of a large load transfer.

The photoelastic data and the post test examination do not seem to agree. A possible explanation for this has been developed but has not been thoroughly investigated. As discussed in the weld-transition specimens, the edge effects and Poisson effects are not representative of the response of the 1:6-scale model. These effects produce a strain gradient that causes the strain near the weld to be significantly lower than in the free-field. This is true for both the weld-transition and full-simulation specimens. Lower strain levels correspond to a larger slope of the stress-strain curve so that the small increase in net section stress achievable by load transfer from the studs causes only a very small increase in the strain. However, if the free-field strain levels were significantly larger, as would be the case if edge effects were not present, the level of strain concentration caused by the same load transfer from the studs could be much larger. This mechanism may possibly account for the low strain concentration seen in the photoelastic data and the evidence of significant load transfer observed in the post-test examination.

6.4 Test Result Conclusions

A number of general conclusions can be drawn by observing the results of tests on the three types of specimens. The first of these, based primarily on the data obtained from separately controlled loading specimens, is that the mechanism of liner tearing produced by a combination of liner load and stud shearing is plausible.

In addition, it appears that a reasonable prediction of liner tearing can be based primarily on the net section stress in the liner when liner preload and the stress induced by stud shear are combined.

However, the postulated failure of the 1:6-scale containment model includes both the failure caused by liner preload and stud shearing, and a mechanism to generate this stud shear load, which is based on differential strains between the reinforcing steel and the liner and insert plate combination. The tests conducted here are not conclusive in this second area. The weld transition specimen showed that edge effects may well have a dominant role in the strain behavior of the specimens. In the full-simulation specimens, it is possible that these edge effects completely mask the strain concentrations that would have otherwise been caused by the stud load transfer. The strongest evidence of significant load transfer by studs was found at the post-test examination of the full-simulation specimens, which showed bending of the studs consistent with the postulated mechanism of load transfer.

Although the results are not conclusive, the combination of the separately-controlled-loading specimens tests and the post-test examination of the full-simulation specimens demonstrates the existence of significant load transfer and lends support to the postulated failure mechanism for the 1:6-scale containment model.

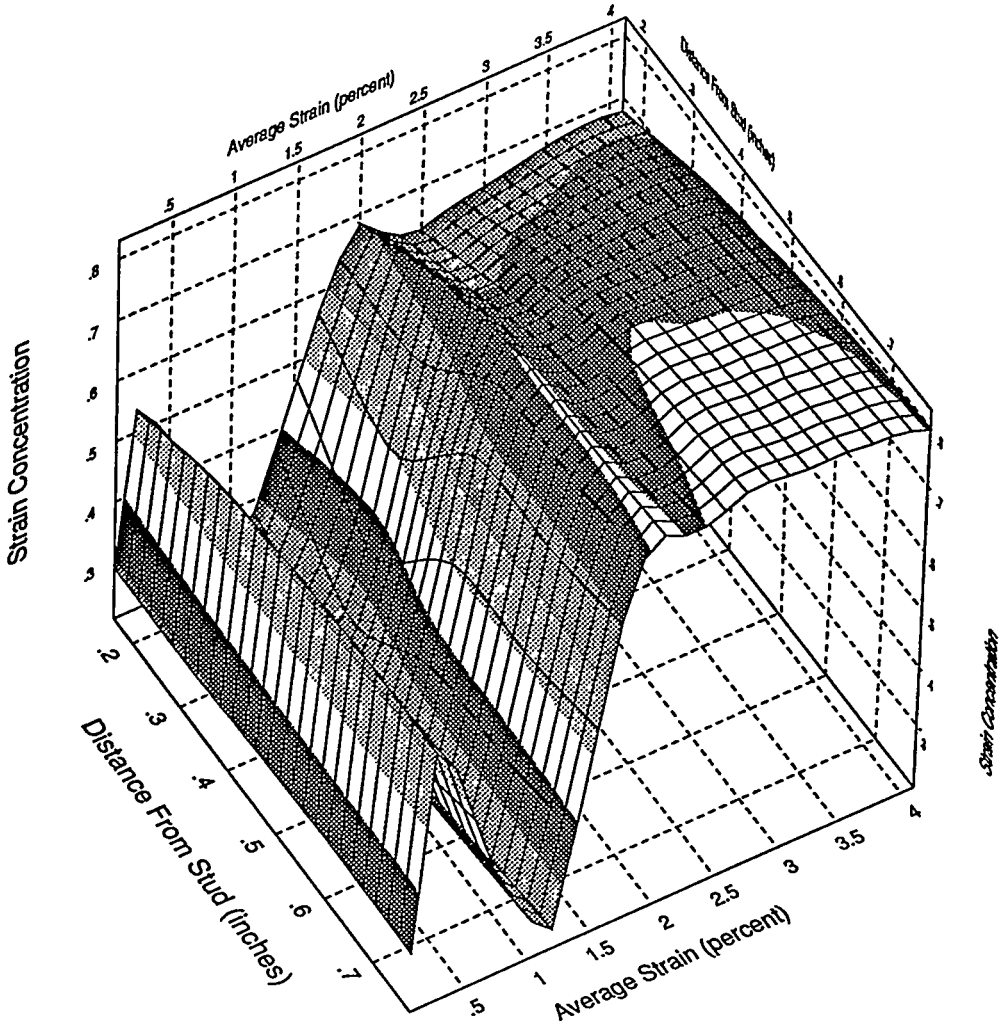

Figure 6.29: Typical transverse strip gage response, full-simulation specimen

Figure 6.30: Maximum shearing strain in a full-simulation specimen

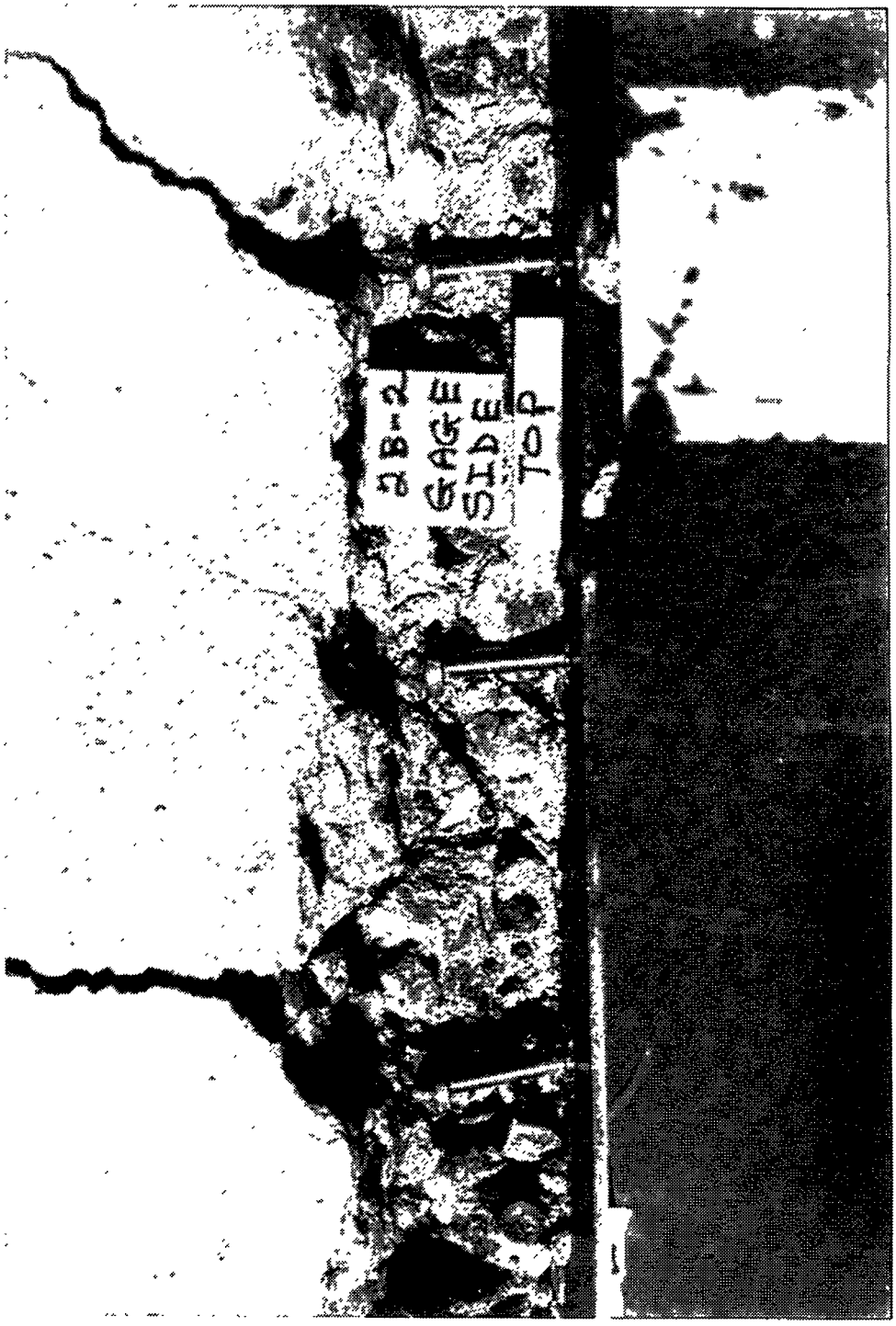

Figure 6.31: Post-test conditions of studs near the liner/insert plate junction

7. Finite Element Models of Test Specimens

The primary purpose of the finite element modeling effort was to identify a set of modeling techniques, assumptions, and failure criteria that could be used to accurately predict failure of the liner and liner anchorage system of the test specimens. Two general finite element models were developed for the three types of test specimens. The weld-transition specimen is identical to the liner/insert plate region of the full-simulation specimen without the studs. Therefore, the finite element model developed for analysis of the full-simulation specimens was also used to simulate the weld-transition specimen with only a few modifications. A separate finite element model was developed for analysis of the separately-controlled-loading specimens. All finite element analyses were run using ABAQUS, a commercially available, general purpose finite element code (Hibbitt, Karlson & Sorensin, 1989).

7.1 Weld-Transition/Full-Simulation Models

The two-dimensional finite element model used to simulate the weld-transition and full-simulation experiments is shown in Figure 7.1. Owing to symmetry conditions, only one-eighth of the specimen was modeled (one-fourth of one side). As shown in the middle drawing in Figure 7.1, symmetry conditions were applied on the left and bottom edges of the finite element model. Load was induced in the liner and rebars by imposing horizontal displacements on the right end. The liner plate was modeled with plane stress elements (ABAQUS element type CPS4), the stud anchors with nonlinear spring elements (SPRINGA), and the steel reinforcement with three rows of truss elements (CID2). The cross-sectional area of the truss elements was selected to provide the correct amount of total steel reinforcement. One end of each spring element was attached to the liner plate, while the opposite end was attached to a rebar element. The two nodes defining each spring element were initially coincident, but separated as the specimen deformed under load. The springs thus provided a path for load transfer between the liner and the reinforcement.

The constitutive response of the liner plate and reinforcement steel was represented by a standard metal plasticity model with a Mises yield surface, associated plastic flow, and isotropic hardening. The relationships between the Mises stress and the equivalent plastic strain shown in Figure 7.2 were obtained from uniaxial tension tests. The curves for the liner plate materials represent the relationship between true stress and true strain. Stress and strain values beyond the point of necking were determined by measuring the thickness of the uniaxial test specimen in the necked-down region. The tensile elongation at failure for the liner plate material in the weld-transition specimen was 60 percent. For the full-simulation specimen, the elongation at failure for the liner plate material was 44 percent.

The load-displacement relationship for the stud anchors was determined from the stud shear experiments described by Horschel (1988) and Weatherby (1990). The specimens used in these experiments were fabricated by welding studs onto strips of 1/16-inch (1.6-mm) plate. Concrete was then placed around the studs. The studs were loaded in shear by applying loads at the end of the metal strips, and the deflection at the head of each stud was measured as a function of the applied load. Considerable scatter was observed in the load-displacement data. The ultimate strengths of the studs ranged from 800 lb (3.6 kNt) to 1600 lb (7.2 kNt), and the shear displacement required to fracture the stud ranged from 0.01 inch (0.25 mm) to 0.07 inch(1.8 mm). Three different functions describing the shear load-displacement relationship were developed and are plotted in Figure 7.3. The middle curve in Figure 7.3, corresponding to a stud strength of 1450 lb. (6.5 kNt), defines the load-displacement relationship for the stud anchors used in the finite element analyses of the full-simulation specimen.

The finite element mesh used for analysis of the weld-transition specimen was the same as that used for the full-simulation specimen. The only differences were in the liner plate material and the definition of the stud strength. The relationship between the Mises stress and the equivalent plastic strain for the steel used as the liner plate material in the weld-transition specimen is shown in Figure 7.2. In the experiments, the weld-transition specimen did not include any studs. Therefore, to simulate this test with the same finite element model as the full-simulation specimens, the studs were assumed to be weak enough that they transferred negligible load into the liner material.

To predict the mode of failure and the loading conditions necessary to cause failure, it is necessary to adopt appropriate failure criteria for the finite element simulations. A stud anchor is assumed to fail when the elongation of the corresponding spring in the finite element model exceeds a specified value. The elongation at fracture is marked in the plots shown in Figure 7.3. Although there is no generally accepted failure criterion applicable to the liner plate, here we have adopted an empirical criterion of failure proposed by Manjoine (1982). The variables which appear in this criterion are the mean stress, the equivalent plastic strain, and the elongation at failure in uniaxial tension.

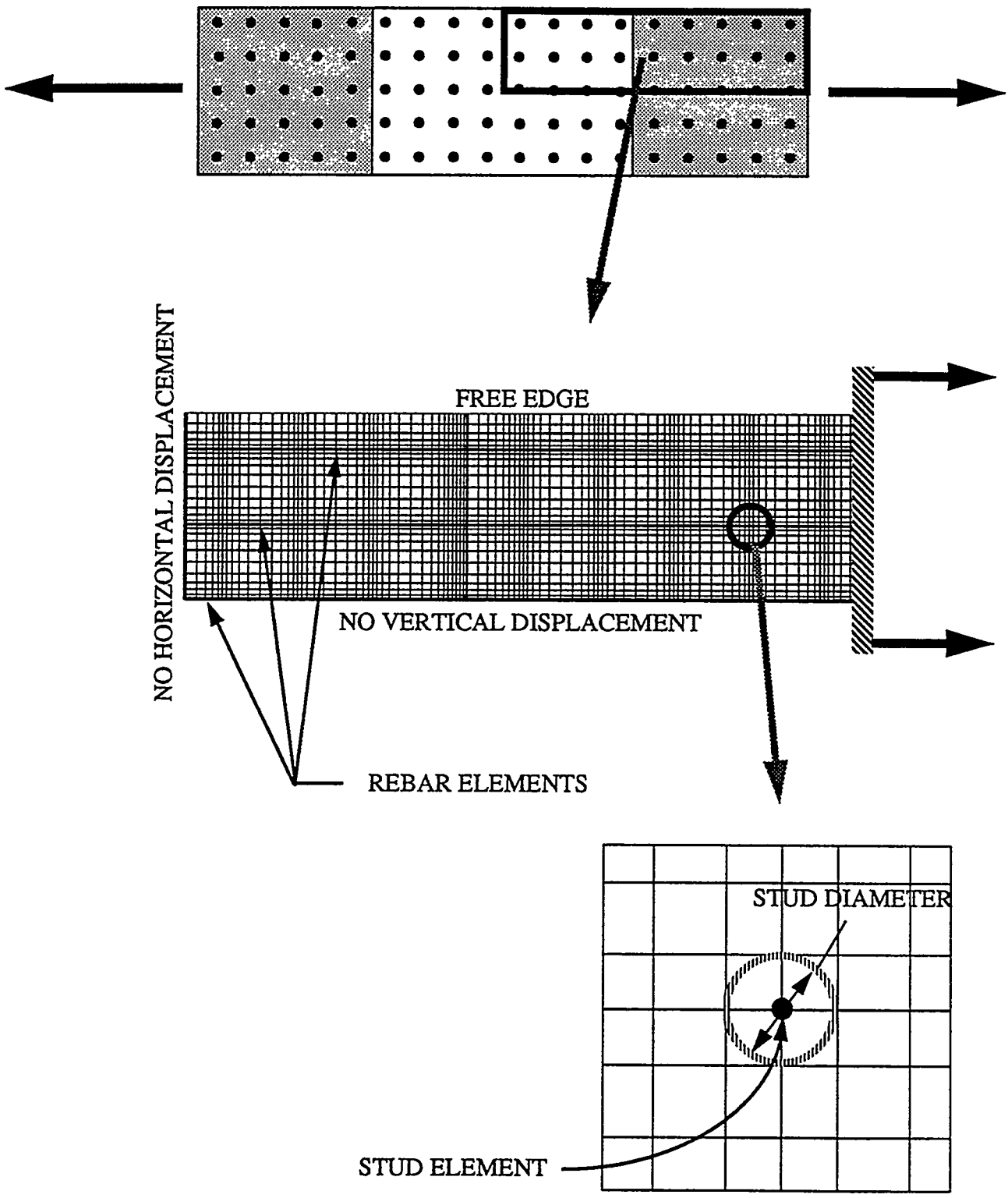

Figure 7.1: Finite element model for the full-simulation and weld-transition specimens

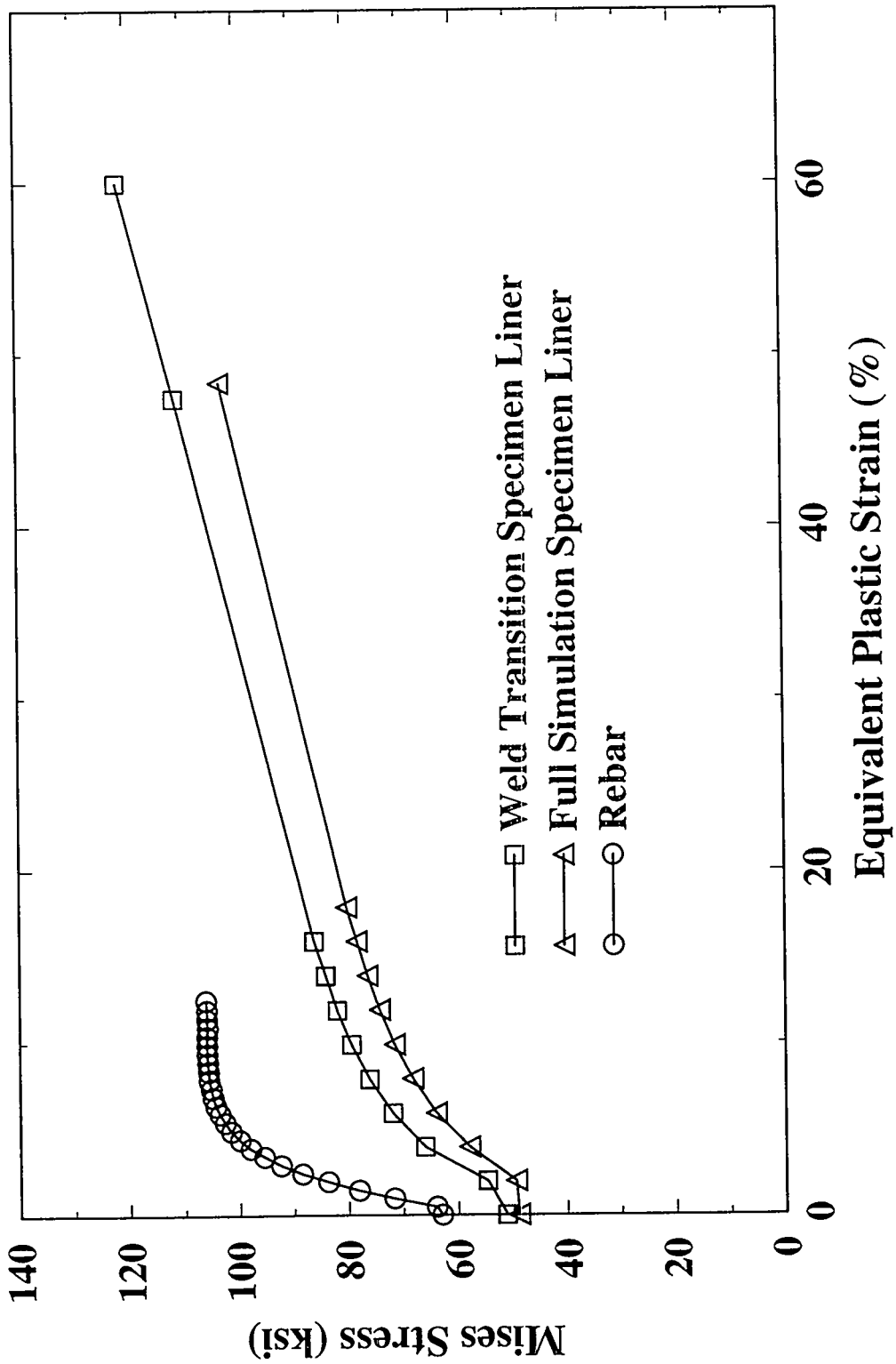

Figure 7.2: Mises stress vs. equivalent plastic strain in weld-transition and full-simulation specimens

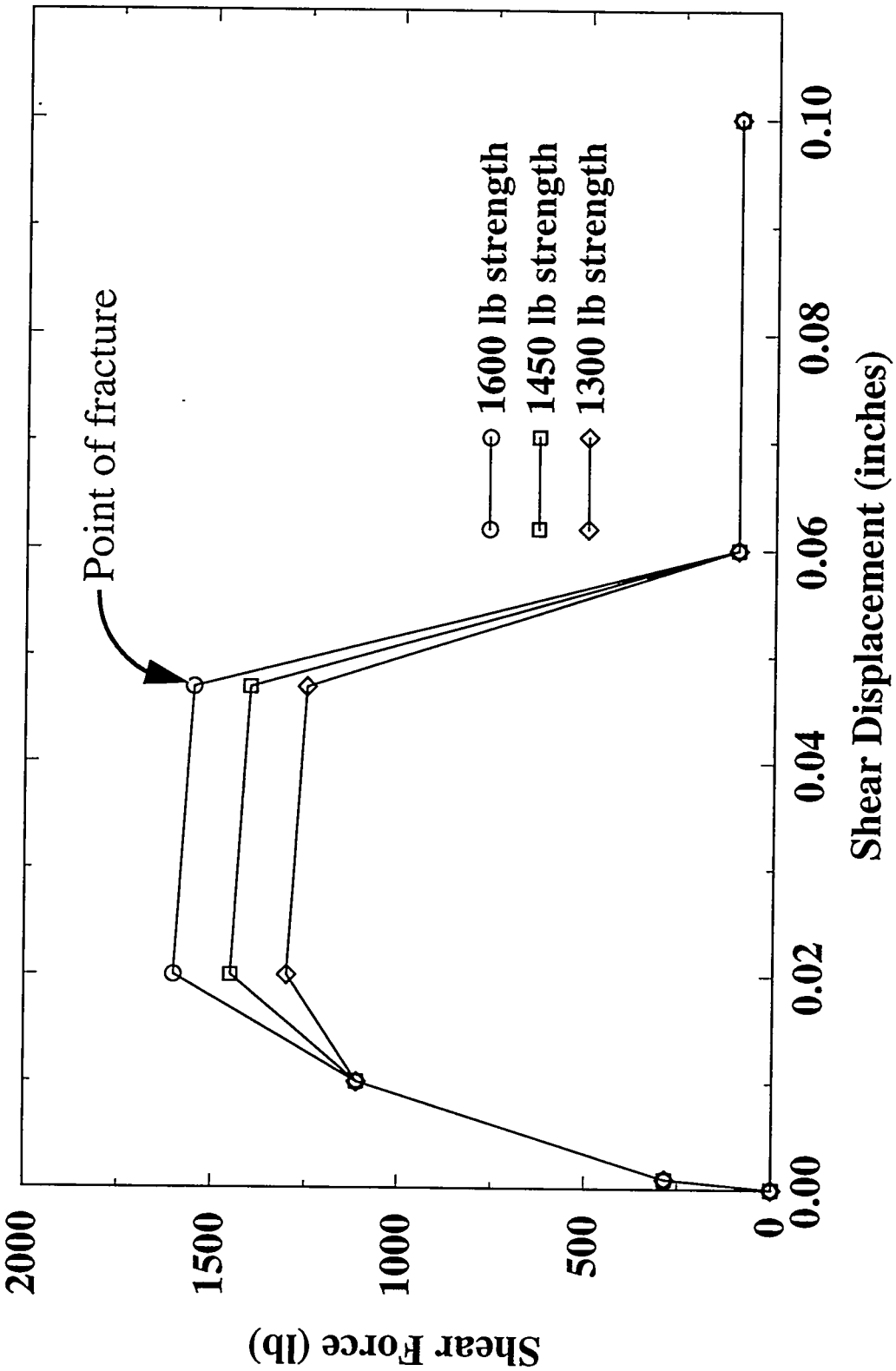

Figure 7.3: Functions defining the force/displacement relationship for the studs

Further details on how Manjoine's criterion is applied can be found in his paper.

In addition to the uncertainty in the failure criterion for the liner plate, the stresses and strains computed in the liner elements that are attached to the studs are strongly dependent on the size of the elements. The extreme mesh sensitivity results from the transfer of load from the spring to the liner through a single point. To account for the fact that the load is actually transferred over a finite area, the continuum elements which are connected to the studs were given a square shape with the length of each side equal to the radius of the stud. Numerical experiments (Weatherby, 1990) indicate that, with this choice of element size, the stress and strain invariants computed in the liner elements adjacent to the stud anchor in a two-dimensional simulation are in reasonable agreement with the invariants computed in a three-dimensional simulation at a point which is located at the mid-thickness of the liner plate directly above the stud.

7.2 Separately-Controlled-Loading Model

A two-dimensional finite element model of the separately-controlled-loading specimen is shown in Figure 7.4. As in the full-simulation specimen models, the liner plate is represented with plane stress continuum elements, and the studs are represented with nonlinear spring elements. One end of the spring is fixed, and the other end is attached to the liner. Initially, the two nodes which define each spring element are coincident, but as the specimen deforms under load, these two nodes separate, and a force develops in the spring.

In the numerical simulations of the separately-controlled-loading experiments, loads were applied to the upper and lower edges of the model as shown in Figure 7.4. Several different simulations were run to determine the response of the specimen under different load histories. The loads on the upper and lower edges of the specimen were initially increased at the same rate. This is referred to as the "preloading" phase. During the preloading phase, lateral forces developed in the studs due to the Poisson contraction of the specimen. Following the preloading phase, the load on the upper edge was increased while the load on the lower edge was held constant. During this loading phase, the forces in the studs increased as they balanced the difference between the loads applied to the upper and lower edges of the specimen.

As in the other models, the liner plate in the simulation of the separately-controlled-loading specimens was assumed to be elastic-plastic with a Mises yield surface. The relationship between the Mises stress and the equivalent plastic strain obtained from a uniaxial tensile test is shown in Figure 7.5. Stress and strain values beyond the point of necking were determined by measuring the thickness of the specimen in the necked-down region, so that this curve represents true stress and true strain.

The load-displacement relationships obtained from experimental data were described in Section 7.1. To investigate the effect of the stud strength on the predicted failure mode of the specimens, the three different functions describing the shear load-displacement relationship plotted in Figure 7.3 were used in simulations of the separately-controlled-loading specimens.

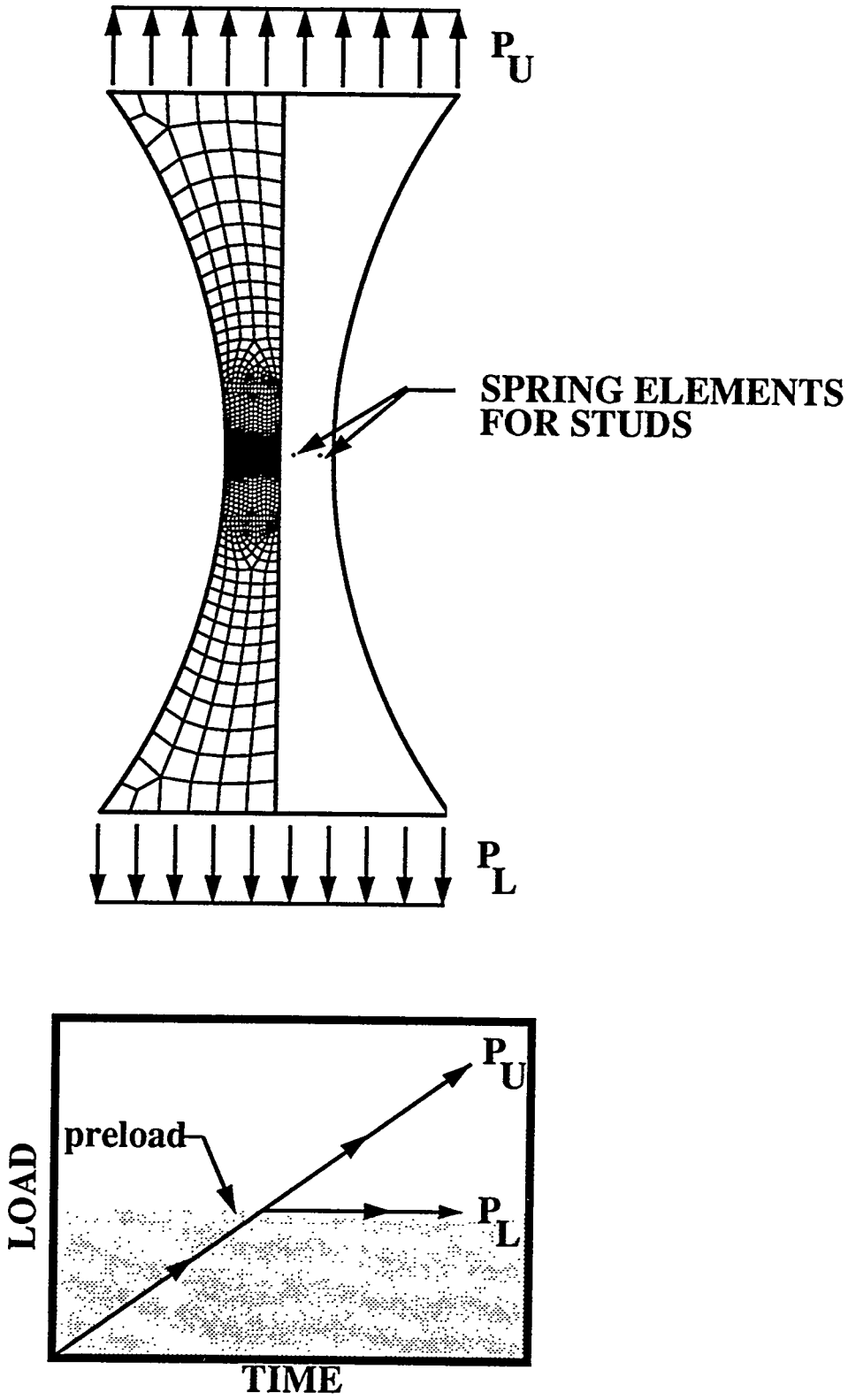

Figure 7.4: Finite element model and loading of the separately-controlled-loading specimens

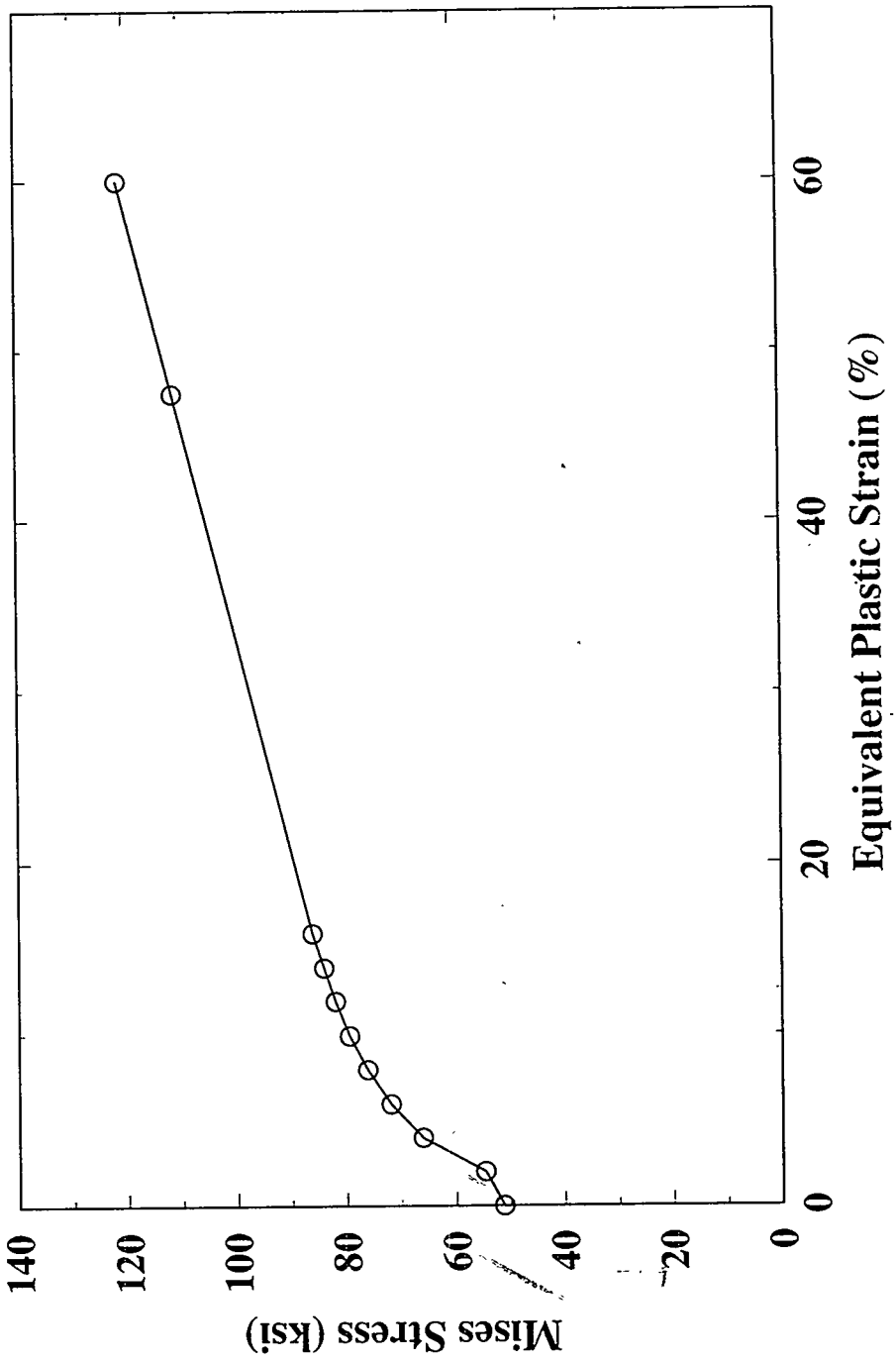

Figure 7.5: Mises stress vs. equivalent plastic strain for the separately-controlled-loading specimens

8. Comparison of Finite Element and Experimental Results

In this section, we provide results of the finite element simulations of each of the three types of test specimens. A comparison of experimental and computational results is used to evaluate the analytical modeling techniques and assumptions. Such comparisons also provide insight as to how the mechanisms present in the separate effects tests compare with the behavior of the 1:6-scale containment model.

The most meaningful comparisons between finite element and experimental results are for the load-deflection behavior and the distribution of maximum shearing strain on the surface of the liner. The load-deflection data indicate the overall specimen response. Because concrete exhibits highly localized damage, a direct comparison of strain gage data with strains at the same location in the finite element mesh is not meaningful. Rather, whole-field strain information available from the photoelastic data provides a global distribution of the maximum shear strain in the experiments, and these data can be directly compared with the maximum shear strain distribution computed by the finite element simulations.

8.1 Results for Weld-Transition Model

The load-deflection response computed by the finite element simulation of the weld-transition specimen is plotted in Figure 8.1 along with the experimental results. As described previously in Section 7.1, the finite element model of the weld-transition specimen included studs and rebar, although the actual specimen did not include either. Therefore, to apply this finite element model to the weld-transition specimen, the studs were assumed to be very weak so that they transferred negligible load into the liner during the simulation. In addition, since the actual specimen did not include rebar, the loads plotted for the finite element results are the total applied load minus the load carried by the rebar. As shown in Figure 8.1, the finite element results for the load-elongation response of the weld-transition specimen compare very well with the results of all of the specimens for which complete load-deflection data is available. Specimens A1 and A2 are not included here since only insufficient load-deflection data is available.

Photoelastic data recorded during the test of the weld-transition specimen provided images of the maximum shear strain field in the plane of the liner plate. These data provide a meaningful comparison between experimental and finite element results. Figure 8.2 contains contour plots of the maximum shear strain from the photoelastic data and the finite element simulation at an overall liner elongation of 1.5 percent. The top line of the plots is the weld line and the edges are the edges of the specimen. In both cases the maximum shear strain is about 12 percent. Furthermore, the strain distribution is very similar in the experimental and computational results. The difference in the location of the stress concentrations along the edge is probably due to the finite thickness of the actual liner plate, which produces a three-dimensional stress state that the plane stress finite element model cannot simulate.

8.2 Results for Separately-Controlled-Loading Model

A total of 15 finite element simulations were conducted for the separately-controlled-loading specimen. Five different loading conditions were considered for each of the three anchorage load-displacement functions shown in Figure 7.3. Table 8.1 shows the predicted failure mode of the specimen for each load case along with the response observed in the experiment. As expected, the predicted failure mode of the specimen depends on both the assumed strength of the stud anchor and the applied prestress. The observed failure modes are most consistent with a stud strength between 1450 lb (6.5 kNt) and 1600 lb (7.2 kNt). For lower values of prestress, the predicted failure mode was fracture of the studs, while for higher values of prestress the predicted mode of failure was liner tearing. Table 8.2 provides a comparison of the measured and predicted failure loads for each set of loading conditions. In this table, the Prestress column is the applied preload divided by the cross-sectional area at the center of the specimen. "Measured" is the experimental average stud load, determined by dividing the maximum total stud force by the number of studs. "Predicted" is the stud load at failure predicted by the finite element model. "Net Stress" is the predicted stud load at failure based on the combined preload and stud load producing a stress equal to the ultimate strength of the material.

Contour plots of computational and photoelastic results for the maximum shear strain are shown in Figure 8.3 for a specimen with a liner prestress of 65 ksi (450 MPa). The photoelastic results show the strain state immediately before the specimen failed through liner tearing. The analytical results correspond to a slightly higher level of stud force than was present when the photoelastic measurements were recorded. In general, the agreement between the photoelastic results and the finite element results is good both quantitatively and qualitatively. There is, however, a large discrepancy between the peak value of the maximum principal shear strain at the edge of the outer stud anchors.

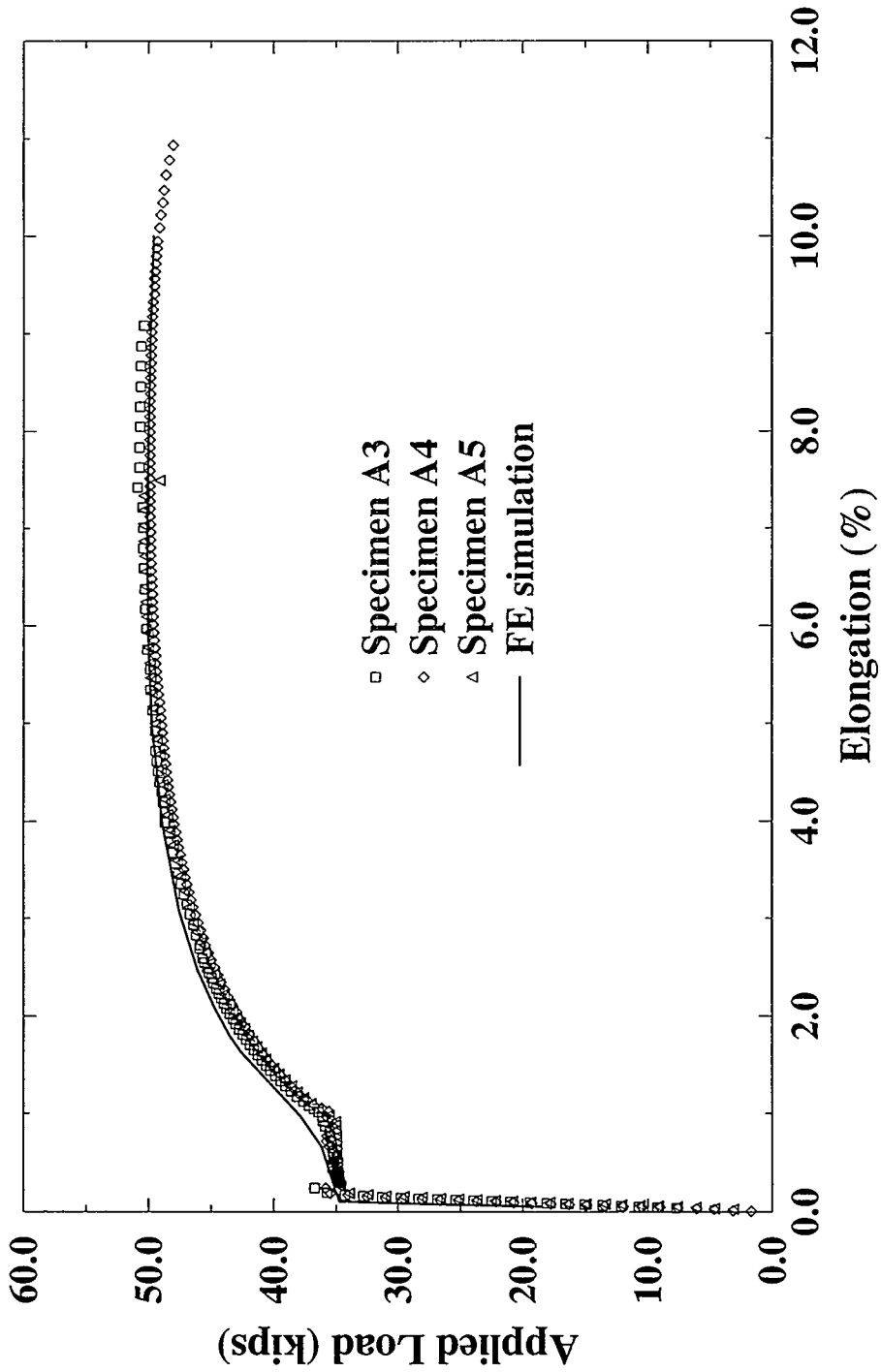

Figure 8.1: Experimental and analytical force-displacement response for the weld-transition specimens

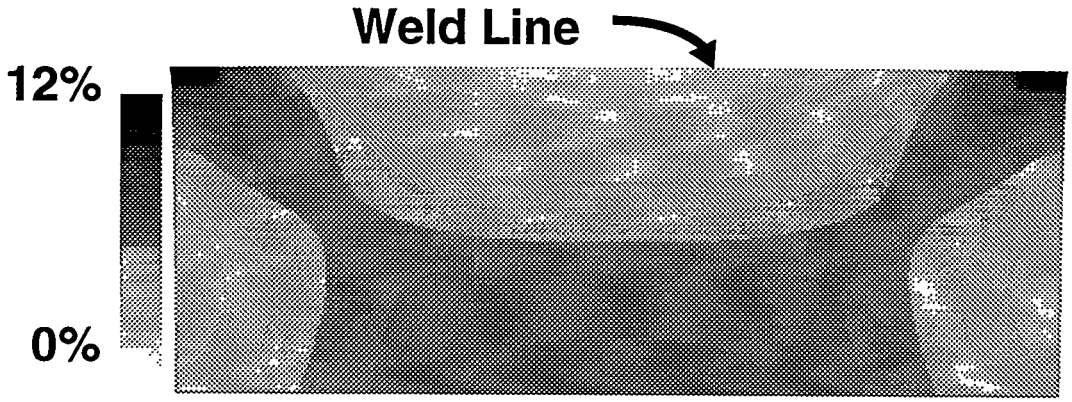

Finite Element Results

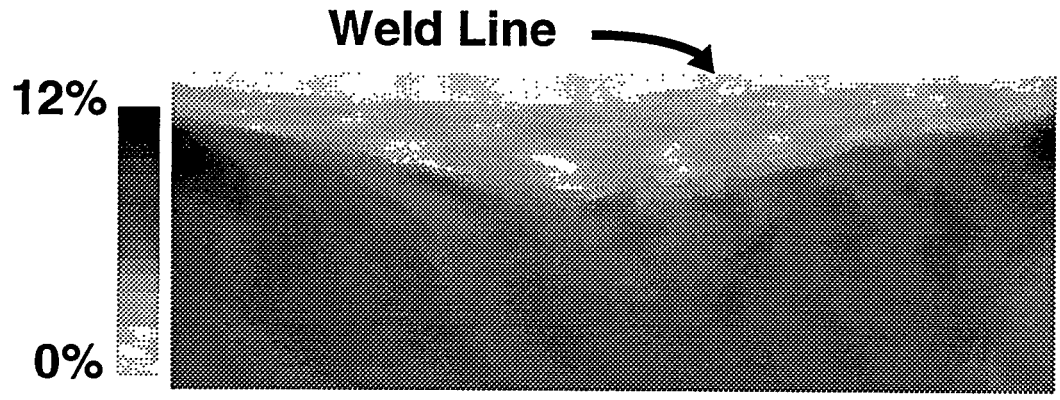

Experimental Results

Figure 8.2: Maximum in-plane shear strain in a weld-transition specimen at 1.5 percent elongation

Table 8.1
Predicted and observed failure modes for separately-controlled-loading specimens

		Liner Preload (ksi)				
	Assumed Stud Strength (lb)	None	60	63	65	70
Predicted Failure	1300	Stud	Stud	---	Stud	Stud
	1450	Stud	Stud	---	Stud	Liner
	1600	Stud	Stud	---	Liner	Liner
Observed Failure	---	Stud	Stud	Stud	Liner	Liner

Table 8.2
Measured, predicted, and net section stress failure load for separately-controlled-loading specimens

Prestress (ksi)	Measured (lb/stud)	Predicted (lb/stud)	Net Stress (lb/stud)
50	---	1392	N.A.*
60	1208	1313	N.A.
63	1171	---	1250
65	780	1173	1000
70	510	107	375

* N.A.=Not Applicable

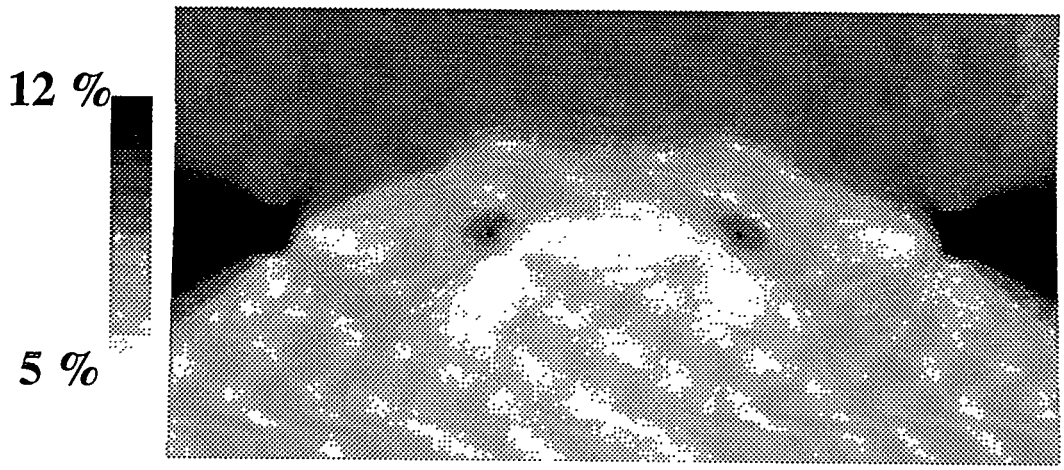

Finite Element Results With Stud Force = 850 lb/stud

Experimental Results With Stud Force = 780 lb/stud

Figure 8.3: Maximum in-plane shear strain in the 65 ksi preload separately-controlled-loading specimen

The analytical results show a maximum shear strain of 30 percent in one of the four elements connected to the outer stud anchors, while the largest shear strain seen in the photoelastic data is approximately 15 percent. There are a number of possible explanations for this discrepancy. At best, the strain in this element represents the strain averaged through the thickness of the liner at this point. Bending of the liner could significantly reduce the surface strains below the average value. Another possible explanation is that the strains in the element next to the stud anchor are simply a poor indicator of the average strains in the liner at this location.

8.3 Results for Full-Simulation Model

Important events in the finite element simulation of the full-simulation experiment are marked in the load-elongation curve shown in Figure 8.4. The first important event in the simulation is the failure of the first row of studs on the 3/16 inch (4.5 mm) insert plate at an elongation of approximately 1 percent. The computed stress and strain state combined with Manjoine's failure criterion indicate that the liner plate would begin to tear at a specimen elongation of 1.2 percent. Liner tearing would start next to the studs located closest to the weld (row 1 in Figure 8.4). If the liner does not tear, the finite element analysis indicates that several more rows of studs would fail before 2 percent elongation.

The overall force-elongation curves for four full-simulation experiments are compared with the finite element results in Figure 8.5. Specimens denoted B1 to B3 are the full-simulation specimens as described previously in Section 2.3. The specimen denoted C1 has the same geometry but was subjected to pressure on the face of the liner plate as well as axial elongation. This surface load was used to simulate the internal pressure on the liner plate in the 1:6-RCC model. The dashed curve in Figure 8.5 represents the calculated response when the anchorage is assumed to have negligible stiffness. The finite element results for the model of the full-simulation specimen match the experimental results very well up to the predicted failure point of 1.2 percent elongation. In addition, the computational results from the finite element simulation with anchorage lie closer to the experimental data than do the results from the simulation without anchorage. This suggests that the anchorage transfers load between the liner and reinforcement as has been assumed in the analysis.

The elongations required to fail the specimens fell between 3 percent and 4.5 percent, considerably more than the 1.2 percent elongation at failure predicted by the analysis. Also contrary to the analytical predictions, no stud failures were observed in any of the full-simulation specimen experiments.

The photoelastic data from the full-simulation specimen experiments provide a valuable source of information for understanding where the finite element results differ from reality. Figure 8.6 contains a contour plot of the maximum shear strain in the liner plate as calculated from the finite element simulation with anchorage at an overall elongation of 1.5 percent. The location of the studs is clearly marked by high strain levels in the liner plate. Strain levels on average are much higher between the weld line and the first row of studs on the thinner liner plate. This is to be expected since load is transferred out of the liner plate and into the reinforcement with each subsequent row of studs on the thinner liner plate. Figure 8.6 also contains a contour plot of the maximum shear strain as determined from the photoelastic technique at an overall elongation of 1.5 percent. The trends are quite different from those seen in the finite element results. Here, the strains on average tend to be lower near the weld than they are toward the center of the specimen. This suggests that the stud anchors near the weld line transmit far less load in the actual experiment than in the finite element simulation.

To investigate the strain field in the absence of load transfer through the anchorage, the specimen was reanalyzed using a very small value for the anchorage strength. Under these conditions, the resulting strain field should look more like that seen in the weld-transition specimen. A contour plot of the maximum principal strain field from the finite element analysis with the reduced anchorage strength is shown in Figure 8.7. As in previous contour plots, the overall elongation is 1.5 percent. The similarity between the computed strain field shown in Figure 8.7 and the photoelastic results shown in Figure 8.6, together with those shown in Figure 8.2 for the weld-transition specimen, reinforce the idea that the stud anchors are less effective in transferring load than was initially assumed. This seems to contradict the previous observations made with regard to the analytical and experimental load-elongation relationships.

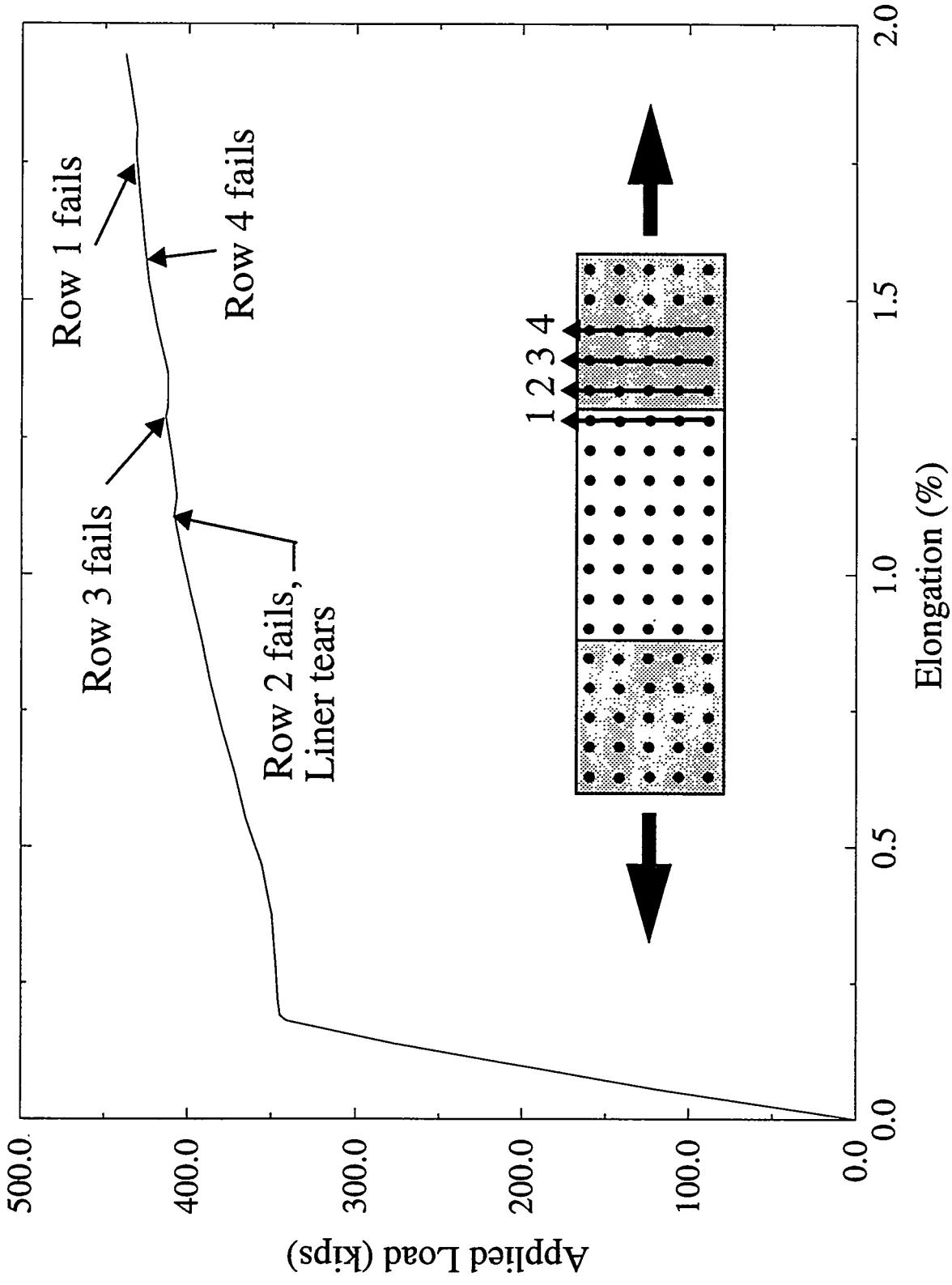

Figure 8.4 Overall force-elongation curve from the finite element analysis of the full-simulation specimen

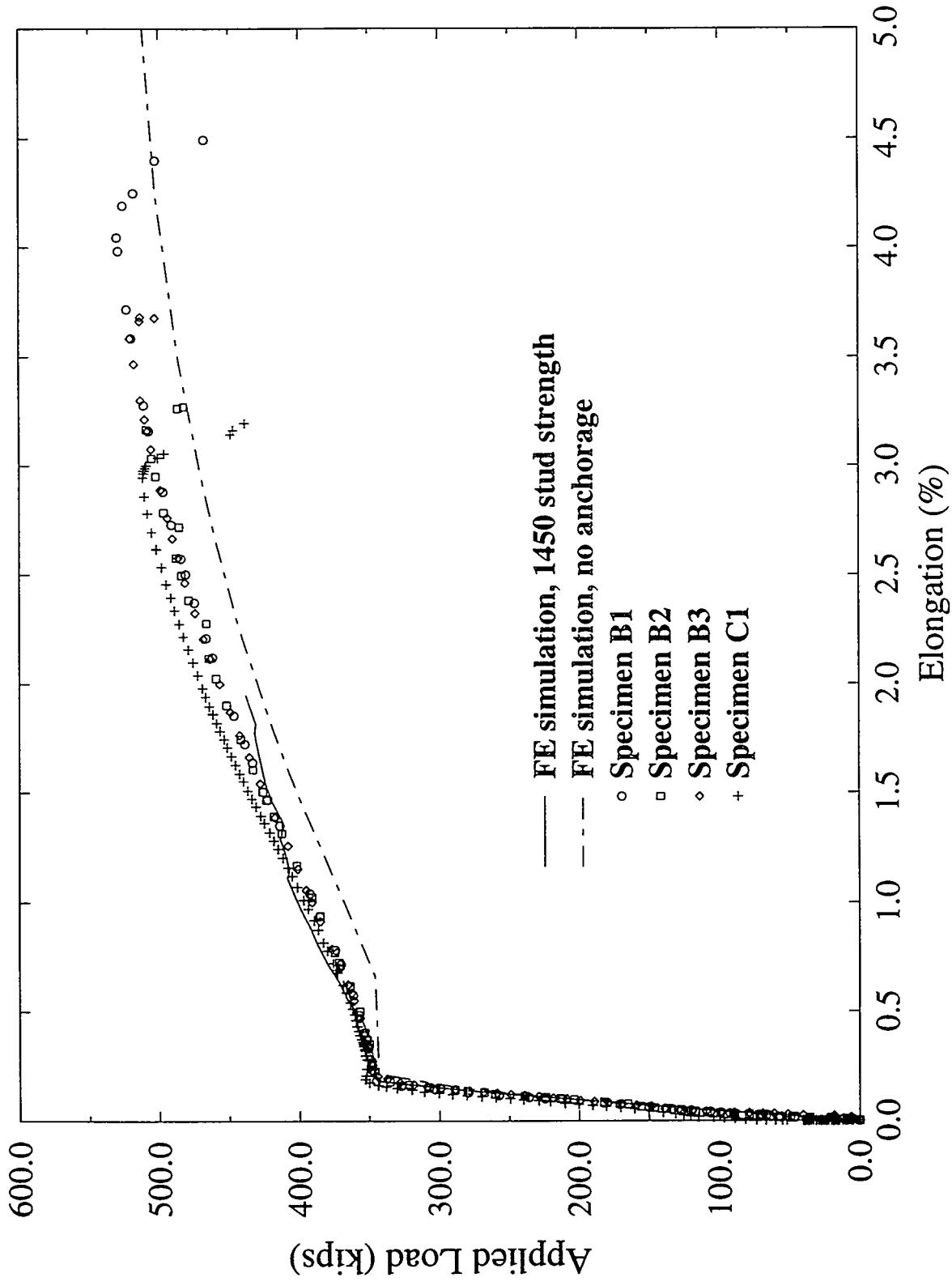

Figure 8.5: Experimental and analytical force-elongation relationships for the full-simulation specimens

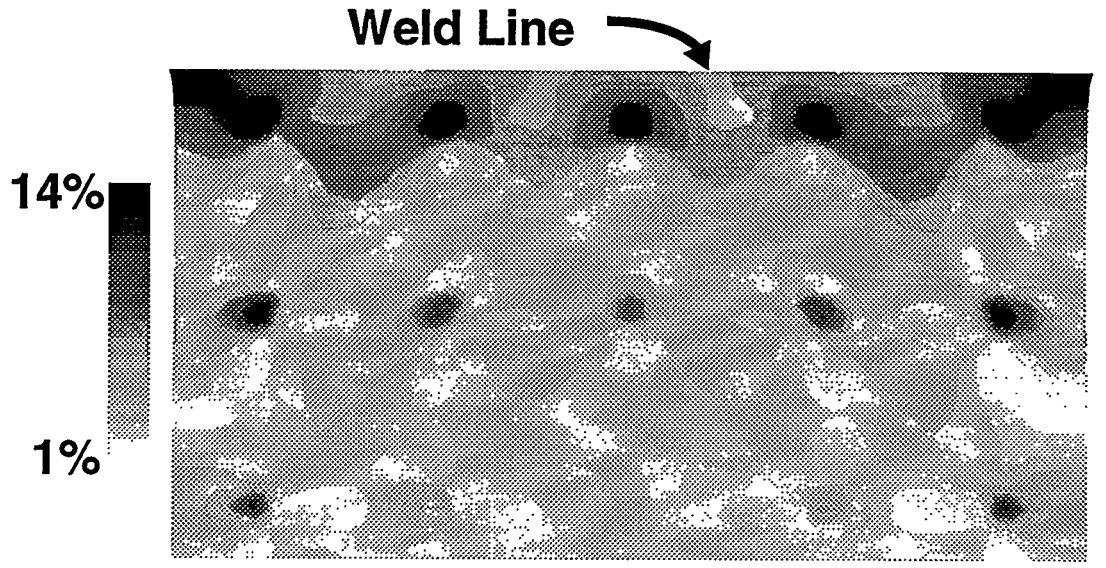

Finite Element Results

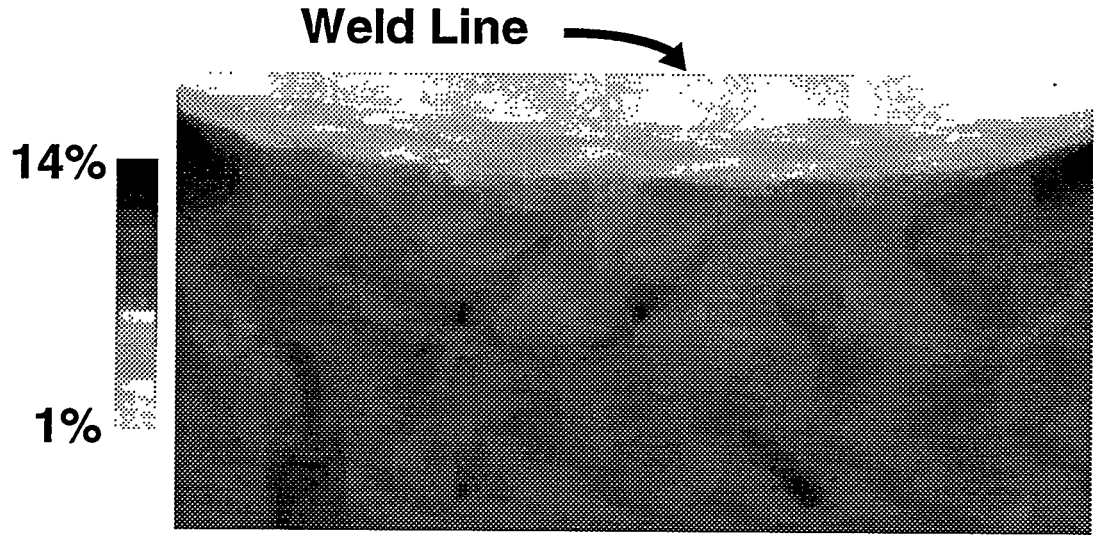

Experimental Results

Figure 8.6: Maximum in-plane shear strain in a full-simulation specimen at 1.5 percent elongation

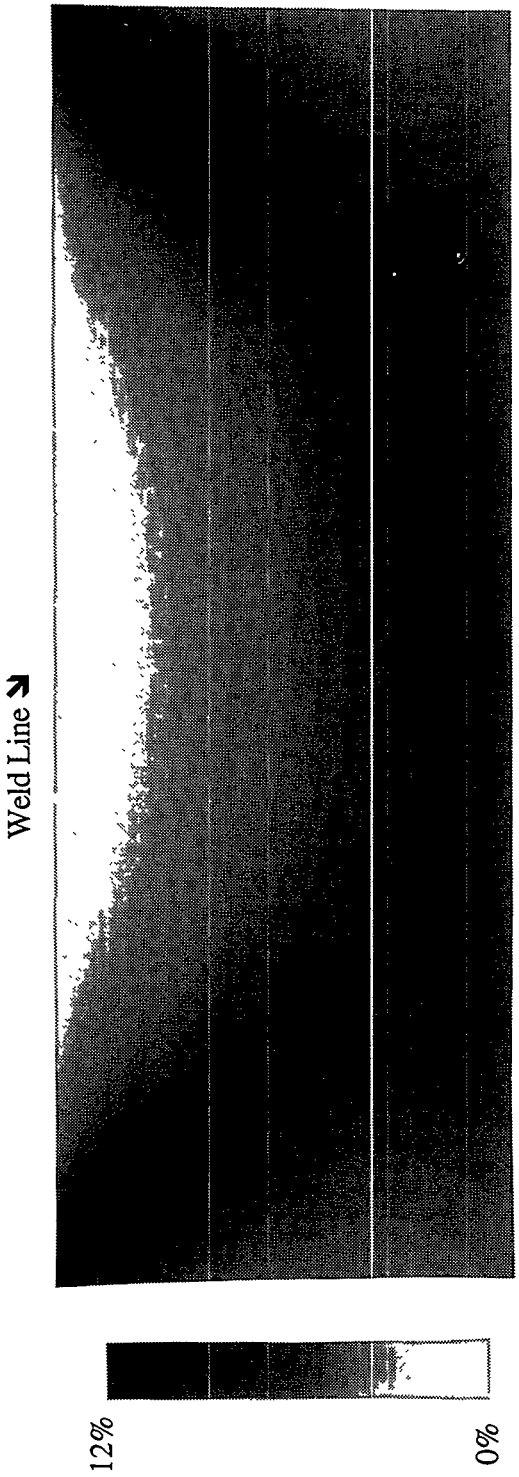

Figure 8.7: Finite element results showing maximum shear strain in full-simulation model without anchorage

9. Conclusions

The analysis and testing of the weld-transition specimens are in good agreement and demonstrate a lack of strain concentration at the weld. In addition they show the significance of edge effects on this and the full-simulation specimens. These edge effects are an important departure from the actual strain state of the 1:6-scale model.

The separately-controlled-loading analysis and testing are in good agreement and demonstrate that liner tearing can be induced in a highly strained liner material with relatively weak anchorage, which transfers the load to the liner. The finite element model as well as the net section stress approach provide a reasonable method for predicting the transition between liner tearing and stud failure. However, it was shown that the transition between the two failure modes is very sharp and strongly dependent on material properties, stud strength, liner strain, and amount of load transfer. The models may be limited in their ability to predict the failure mode by uncertainties in the input parameters required to make the prediction. This is not a weakness of the models but rather an indication of the sensitivity of the transition between the two failure modes.

The full-simulation specimens were designed to provide conditions very similar to those of the 1:6 scale model. As a continuation of the previous two sets of tests, these specimens were used to investigate whether the postulated load transfer could occur and whether the transfer could result in liner tearing. The analysis and post-test examination indicated significant load transfer. However, the photoelastic and strain gage data gave only limited indications of increased strain resulting from the transfer. This disagreement has not been fully resolved. Possible reasons for the discrepancy are the significant edge effects and the fact that the actual load transfer mechanism may not be as strong as postulated for the analysis.

10. References

1. Hibbitt, Karlsson & Sorensin, Inc., 1989, ABAQUS Users' Manual, Version 4.8.

2. Horschel, D. S., 1988, "Design, Construction, and Instrumentation of a 1/6-Scale Reinforced Concrete Containment Building," NUREG/CR-5083, SAND88-0030, Sandia National Laboratories, Albuquerque, NM.

3. Horschel, D. S., 1992, "Experimental Results from Pressure Testing A 1:6-Scale Nuclear Power Plant Containment," NUREG/CR-5121, SAND88-0906, Sandia National Laboratories, Albuquerque, NM.

4. Lambert, L. D., 1992, "Posttest Destructive Examination of the Steel Liner in a 1:6 Scale ReactorContainment Model," SAND92-1721, Sandia National Laboratories, Albuquerque, NM.

5. Manjoine, M. J., 1982, "Creep-Rupture Behavior of Weldments," Welding Journal Vol. 61, No. 2 p. 50.

6. Weatherby, J. R., 1990, "Post test Analysis of a 1:6-Scale Reinforced Concrete Reactor Containment Building," NUREG/CR-5476, SAND89-2603, Sandia National Laboratories, Albuquerque, NM.

Appendix A
Detailed Drawings of Specimens

GENERAL SPECIFICATIONS FOR STRUCTURAL METALS

PART OR DRAWING NUMBER	REVISIONS					
	REV	SHEET (S)	PREPARED BY DESCRIPTION	DATE	CHKR	APVD
3A0511-000	1		KELLOGG, 2853/LAMBERT, 6523 ADDED SOME TOLERANCES AND NOTE AFTER FAB			DL

1.0 QUALITY ASSURANCE STANDARDS AND REQUIREMENTS

FOR STEEL CONSTRUCTION

A. WELDING AND WELDER CERTIFICATION:
APPLICABLE PROVISIONS OF THE AMERICAN WELDING SOCIETY (AWS) STRUCTURAL WELDING CODE, AWS D1.1 AND SANDIA NATIONAL LABORATORIES SPECIFICATION 9012110 (CLASS II, UNLESS OTHERWISE NOTED).

FOR ALUMINUM CONSTRUCTION

A. WELDING AND WELDER CERTIFICATION:
APPLICABLE PROVISIONS OF THE AMERICAN WELDING SOCIETY (AWS) STANDARD SPECIFICATION FOR STRUCTURAL WELDING CODE - ALUMINUM, AWS D1.2-83, OCT. 1983, AND SANDIA NATIONAL LABORATORIES SPECIFICATION 9012114.

2.0 MATERIALS

UNLESS OTHERWISE SPECIFIED ON THE DRAWINGS, THE FOLLOWING MINIMUM MATERIAL STANDARDS SHALL APPLY:

FOR STEEL CONSTRUCTION:

A. STEEL SHAPES AND BARS: AS NOTED ON DWG'S

B. STEEL PLATE: AS NOTED ON DWG'S

C. STEEL PIPE AND TUBE: AS NOTED ON DWG'S

D. THREADED FASTENERS: AS NOTED ON DWG'S

FOR ALUMINUM CONSTRUCTION:

A. STRUCTURAL SHAPES: AS NOTED ON DWG'S

B. TUBING: AS NOTED ON DWG'S

C. PIPE: AS NOTED ON DWG'S

D. SHEET & PLATE: AS NOTED ON DWG'S

3.0 WELDING REQUIREMENTS AND TESTING

A. STRUCTURAL WELDS: WHERE STRUCTURAL JOINTS ARE MADE BY WELDING, THE DETAILS OF ALL JOINTS, THE TECHNIQUES OF WELDING EMPLOYED, THE APPEARANCE AND QUALITY OF WELDS MADE AND THE METHODS USED IN CORRECTING DEFECTIVE WORK SHALL CONFORM TO THE REQUIREMENTS OF THE "SPECIFICATIONS FOR THE DESIGN, FABRICATION AND ERECTION OF STRUCTURAL STEEL FOR BUILDINGS", OF THE AMERICAN INSTITUTE OF STEEL CONSTRUCTION AND THE "STRUCTURAL WELDING CODE", OF THE AMERICAN WELDING SOCIETY.

AGENCY APPROVALS		
ORG	DATE	APPROVALS

NEXT ASSY USED ON: APPLICATION

PART CODE

SHEET 1 2 3 4 5 6

ISSUE 1 1 1 1

PART CLASSIFICATION: UNCLASSIFIED

DRAWING CLASSIFICATION: UNCLASSIFIED

TITLE (U) TITLE CLASSIFICATION: TEST SPECIMEN PHASE I TEST SERIES IA

SIZE D | DRAWING NUMBER 3A0511

CAGE 14213 | SCALE NONE | SHEET 1 OF 4

STATUS LOCAL STORAGE-3-21-9 | ORIGIN SC-AN5-V1 2

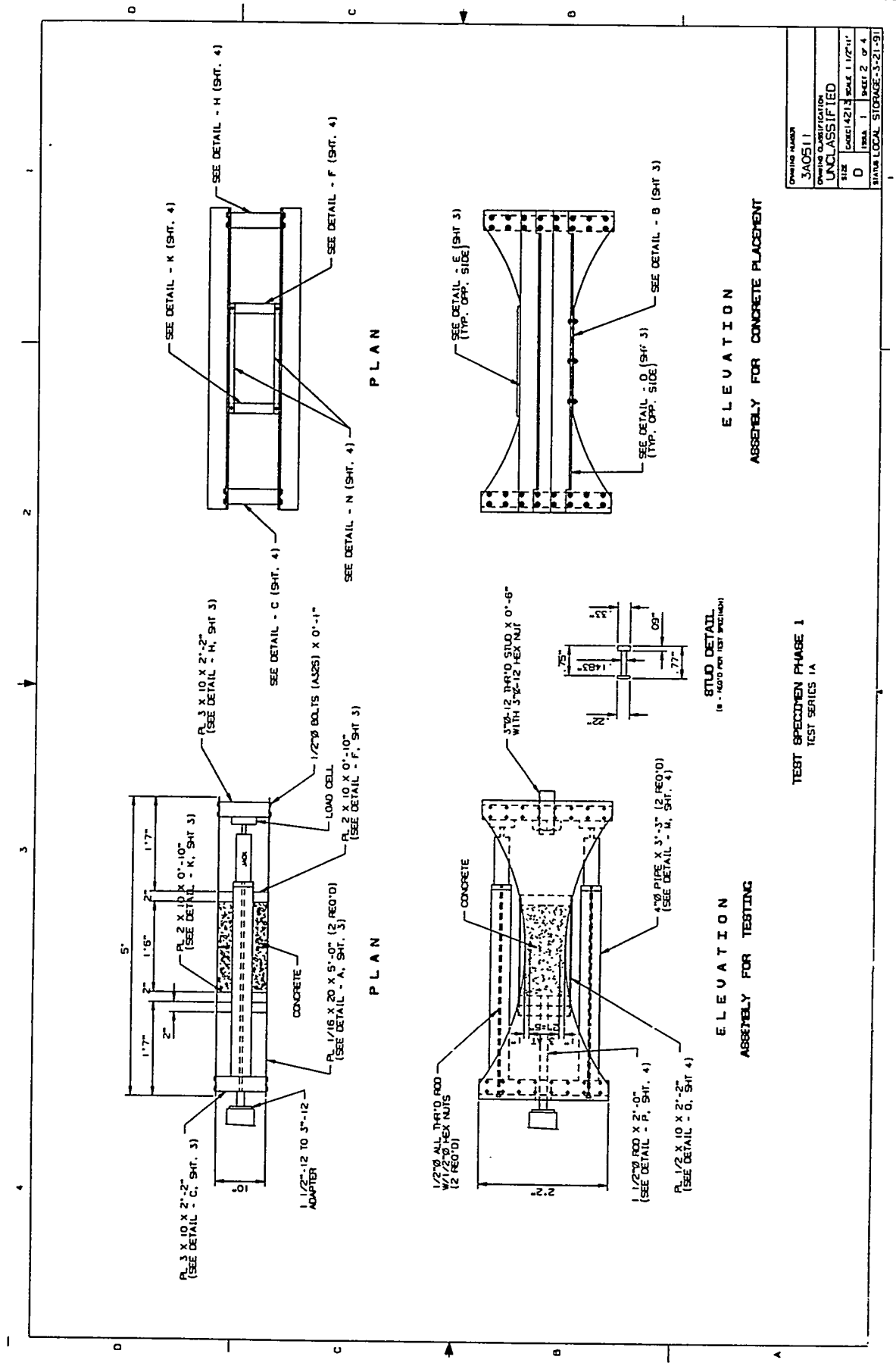
SEE DETAIL - K (SHT. 4)
SEE DETAIL - H (SHT. 4)
SEE DETAIL - F (SHT. 4)
SEE DETAIL - C (SHT. 4)
SEE DETAIL - N (SHT. 4)
PLAN
SEE DETAIL - E (SHT 3)
(TYP. OPP. SIDE)
SEE DETAIL - B (SHT 3)
SEE DETAIL - D (SHT 3)
(TYP. OPP. SIDE)
ELEVATION
ASSEMBLY FOR CONCRETE PLACEMENT
PL 3 X 10 X 2'-2"
(SEE DETAIL - H, SHT 3)
SEE DETAIL - C (SHT. 4)
1/2"Ø BOLTS (A325) X 0'-1"
LOAD CELL
PL 2 X 10 X 0'-10"
(SEE DETAIL - F, SHT 3)
PL 2 X 10 X 0'-10"
(SEE DETAIL - K, SHT 3)
PL 2 X 10 X 5'-0" (2 REQ'D)
(SEE DETAIL - A, SHT. 3)
CONCRETE
PL 1/16 X 20 X 5'-0"
(SEE DETAIL - A, SHT. 3)
PL 3 X 10 X 2'-2"
(SEE DETAIL - C, SHT. 3)
1 1/2"-12 TO 3"-12
ADAPTER
PLAN
3/4"Ø-12 THR'D STUD X 0'-6"
WITH 3"-12 HEX NUT
CONCRETE
4"Ø PIPE X 3'-3" (2 REQ'D)
(SEE DETAIL - M, SHT. 4)
1/2"Ø ALL THR'D ROD
W/1/2"Ø HEX NUTS
(2 REQ'D)
1 1/2"Ø ROD X 2'-0"
(SEE DETAIL - P, SHT. 4)
PL 1/2 X 10 X 2'-2"
(SEE DETAIL - O, SHT 4)
ELEVATION
ASSEMBLY FOR TESTING
STUD DETAIL
TEST SPECIMEN PHASE 1
TEST SERIES 1A
DRAWING NUMBER
3A0511
DRAWING CLASSIFICATION
UNCLASSIFIED
SIZE
D
SCALE 1 1/2"=1'
SHEET 2 OF 4
STATUS LOCAL STORAGE-3-21-91

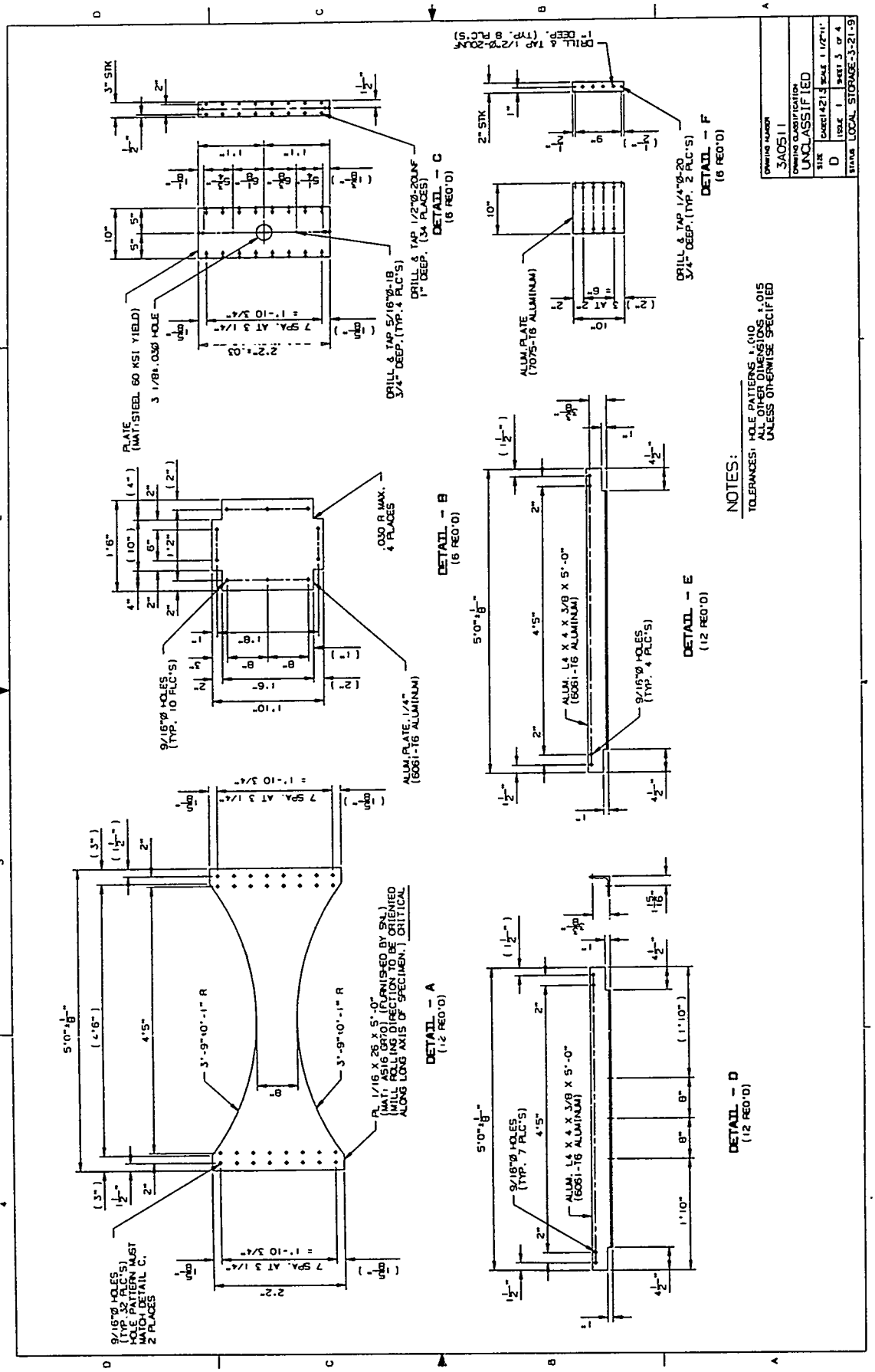
NOTES:
TOLERANCES: HOLE PATTERNS ±.010
ALL OTHER DIMENSIONS ±.015
UNLESS OTHERWISE SPECIFIED
DRAWING NUMBER
3A0511
DRAWING CLASSIFICATION
UNCLASSIFIED
SIZE
D
SCALE 1:12
SHEET 3 OF 4
ISSUE 1
STATUS LOCAL STORAGE-3-21-9
DETAIL - A
(12 REQ'D)
DETAIL - B
(6 REQ'D)
DETAIL - C
(6 REQ'D)
DETAIL - D
(12 REQ'D)
DETAIL - E
(12 REQ'D)
DETAIL - F
(6 REQ'D)
PL 1/16 X 26 X 5'-0"
(MATL 4516 OR 5052) (TURNISHED BY SNL)
(MILL ROLLING DIRECTION TO BE ORIENTED
ALONG LONG AXIS OF SPECIMEN.) CRITICAL
9/16"Ø HOLES
(TYP. 32 PLC'S)
HOLE PATTERN MUST
MATCH DETAIL C.
2 PLACES
PLATE
(MATISIEEL 60 KSI YIELD)
3 1/8t. 030 HOLE
9/16"Ø HOLES
(TYP. 10 PLC'S)
.030 R MAX.
4 PLACES
ALUM. PLATE 1/4"
(6061-T6 ALUMINUM)
9/16"Ø HOLES
(TYP. 7 PLC'S)
ALUM. L4 X 4 X 3/8 X 5'-0"
(6061-T6 ALUMINUM)
9/16"Ø HOLES
(TYP. 4 PLC'S)
ALUM. L4 X 4 X 3/8 X 5'-0"
(6061-T6 ALUMINUM)
ALUM. PLATE
(7075-T6 ALUMINUM)
DRILL & TAP 5/16"Ø-18
3/4" DEEP. (TYP. 4 PLC'S)
DRILL & TAP 1/2"Ø-20UNF
1" DEEP. (34 PLACES)
DRILL & TAP 1/2"Ø-20UNF
1" DEEP. (TYP. 8 PLC'S)
DRILL & TAP 1/4"Ø-20
3/4" DEEP. (TYP. 2 PLC'S)

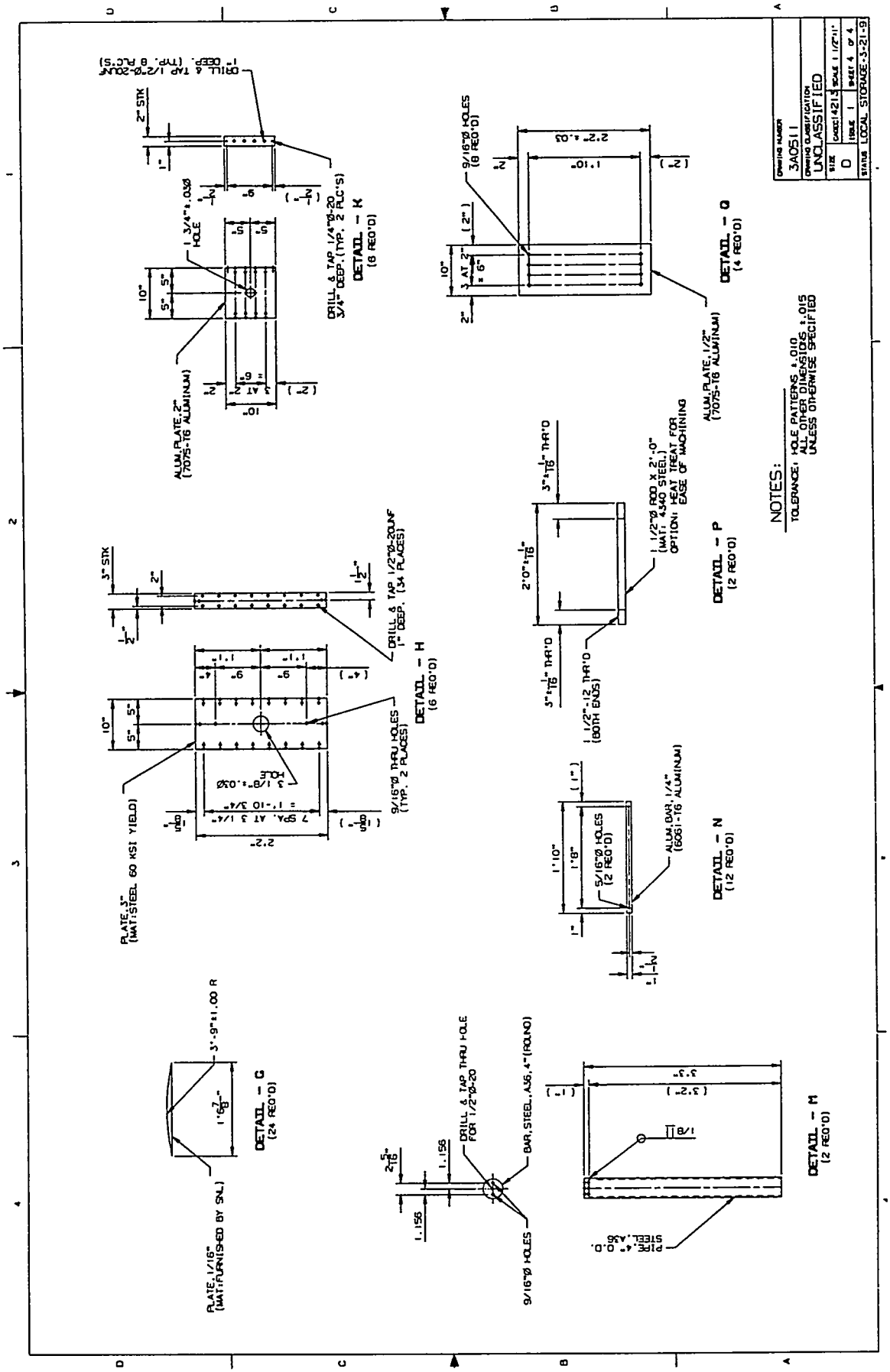
NOTES:
TOLERANCE: HOLE PATTERNS ±.010
ALL OTHER DIMENSIONS ±.015
UNLESS OTHERWISE SPECIFIED
DRAWING NUMBER
3A0511
DRAWING CLASSIFICATION
UNCLASSIFIED
SIZE D
CAGE# 421J3
SCALE 1 1/2"=1"
ISSUE 1
SHEET 4 OF 4
STATUS LOCAL STORAGE-3-21-9
DETAIL - K
(6 REQ'D)
DETAIL - Q
(4 REQ'D)
DETAIL - H
(6 REQ'D)
DETAIL - P
(2 REQ'D)
DETAIL - N
(12 REQ'D)
DETAIL - G
(24 REQ'D)
DETAIL - M
(2 REQ'D)
ALUM. PLATE, 2"
(7075-T6 ALUMINUM)
ALUM. PLATE, 1/2"
(7075-T6 ALUMINUM)
PLATE, 3"
(MAT: STEEL 60 KSI YIELD)
PLATE, 1/16"
(MAT: FURNISHED BY SNL)
ALUM. BAR, 1/4"
(6061-T6 ALUMINUM)
BAR, STEEL, A36, 4" (ROUND)
PIPE, 4" O.D.
STEEL, A36
9/16"Ø HOLES
(8 REQ'D)
9/16"Ø THRU HOLES
(TYP. 2 PLACES)
5/16"Ø HOLES
(2 REQ'D)

GENERAL SPECIFICATIONS FOR STRUCTURAL METALS

PART OR ASSEMBLY NUMBER	REVISIONS					
	ISS	SHEET ZONE	PREPARED BY DESCRIPTION	DATE	CHKR	APVD
3A0512-000	1		KELLOGG, 2853/LAMBERT, 6473 ADDED NOTES AND CHANGED TOLERANCES PER FABRICATOR			DL

1.0 QUALITY ASSURANCE STANDARDS AND REQUIREMENTS

FOR STEEL CONSTRUCTION

A. WELDING AND WELDER CERTIFICATION:
APPLICABLE PROVISIONS OF THE AMERICAN WELDING SOCIETY (AWS) STRUCTURAL WELDING CODE, AWS01 1 AND SANDIA NATIONAL LABORATORIES SPECIFICATION 9012119 (CLASS 1), UNLESS OTHERWISE NOTED).

FOR ALUMINUM CONSTRUCTION

A. WELDING AND WELDER CERTIFICATION:
APPLICABLE PROVISIONS OF THE AMERICAN WELDING SOCIETY (AWS) STANDARD SPECIFICATION FOR STRUCTURAL WELDING CODE - ALUMINUM, AWS 01 2-83, OCT 1905, AND SANDIA NATIONAL LABORATORIES SPECIFICATION 9012114.

2.0 MATERIALS

UNLESS OTHERWISE SPECIFIED ON THE DRAWINGS, THE FOLLOWING MINIMUM MATERIAL STANDARDS SHALL APPLY:

FOR STEEL CONSTRUCTION:

A. STEEL SHAPES AND BARS: AS NOTED ON DRWG'S

B. STEEL PLATE: AS NOTED ON DRWG'S

C. STEEL PIPE AND TUBE: AS NOTED ON DRWG'S

D. THREADED FASTENERS: AS NOTED ON DRWG'S

FOR ALUMINUM CONSTRUCTION:

A. STRUCTURAL SHAPES: AS NOTED ON DRWG'S

B. TUBING: AS NOTED ON DRWG'S

C. PIPE: AS NOTED ON DRWG'S

D. SHEET & PLATE: AS NOTED ON DRWG'S

3.0 WELDING REQUIREMENTS AND TESTING

A. STRUCTURAL WELDS: WHERE STRUCTURAL JOINTS ARE MADE BY WELDING, THE DETAILS OF ALL JOINTS, THE TECHNIQUES OF WELDING EMPLOYED, THE APPEARANCE AND QUALITY OF WELDS MADE AND THE METHODS USED IN CORRECTING DEFECTIVE WORK SHALL CONFORM TO THE REQUIREMENTS OF THE "SPECIFICATIONS FOR THE DESIGN, FABRICATION AND ERECTION OF STRUCTURAL STEEL FOR BUILDINGS", OF THE AMERICAN INSTITUTE OF STEEL CONSTRUCTION AND THE "STRUCTURAL WELDING CODE", OF THE AMERICAN WELDING SOCIETY.

AGENCY APPROVALS			
	ORG	DATE	APPROVALS

NEXT ASSY: APPLICATION

USED ON

PART CODE

SHEET 1 2 3 4 5 6

ISSUE 1 1

TITLE (U) TITLE CLASSIFICATION
TEST SPECIMEN PHASE 1
TEST SERIES 2A

PART CLASSIFICATION: UNCLASSIFIED

DRAWING CLASSIFICATION: UNCLASSIFIED

SIZE D | DRAWING NUMBER 3A0512

CAGEC 14213 | SCALE | SHEET 1 OF 2

STATUS LOCAL STORAGE-3-21-9 | ORIGIN SC-ANS-V1 2

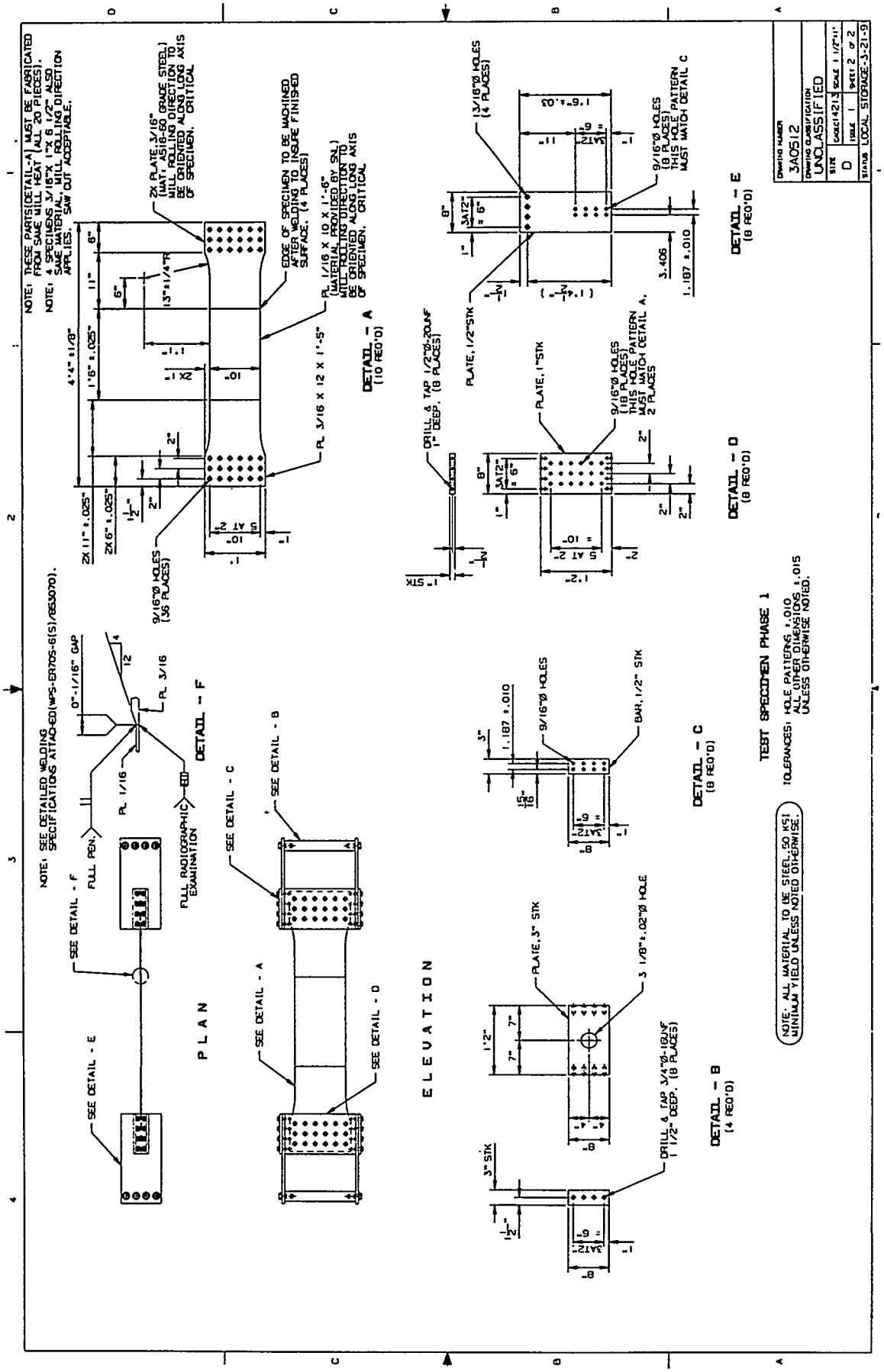
NOTE: THESE PARTS(DETAIL-A) MUST BE FABRICATED FROM SAME MILL HEAT (ALL 20 PIECES).
NOTE: 4 SPECIMENS 3/16"X 1'X 6 1/2" ALSO SAME MATERIAL, MILL ROLLING DIRECTION APPLIES. SAW CUT ACCEPTABLE.
2X PLATE,3/16" (MAT'L AS16-60 GRADE STEEL) MILL ROLLING DIRECTION TO BE ORIENTED ALONG LONG AXIS OF SPECIMEN. CRITICAL
EDGE OF SPECIMEN TO BE MACHINED AFTER WELDING TO INSURE FINISHED SURFACE. (4 PLACES)
PL 1/16 X 10 X 1'-6" (MATERIAL PROVIDED BY SNL) MILL ROLLING DIRECTION TO BE ORIENTED ALONG LONG AXIS OF SPECIMEN. CRITICAL
PL 3/16 X 12 X 1'-5"
9/16"Ø HOLES (36 PLACES)
DETAIL - A (10 REQ'D)
13/16"Ø HOLES (4 PLACES)
9/16"Ø HOLES (18 PLACES) THIS HOLE PATTERN MUST MATCH DETAIL C
DETAIL - E (8 REQ'D)
DRILL & TAP 1/2"Ø-20UNF 1" DEEP. (8 PLACES)
PLATE, 1/2"STK
PLATE, 1"STK
9/16"Ø HOLES (18 PLACES) THIS HOLE PATTERN MUST MATCH DETAIL A. 2 PLACES
DETAIL - D (8 REQ'D)
NOTE: SEE DETAILED WELDING SPECIFICATIONS ATTAQ-ED1(WPS-ER70S-6(S)/B53070).
0"-1/16" GAP
PL 3/16
PL 1/16
FULL PEN.
FULL RADIOGRAPHIC EXAMINATION
SEE DETAIL - F
SEE DETAIL - E
DETAIL - F
PLAN
SEE DETAIL - C
SEE DETAIL - B
SEE DETAIL - A
SEE DETAIL - D
ELEVATION
1.187 ±.010
9/16"Ø HOLES
BAR, 1/2" STK
DETAIL - C (8 REQ'D)
PLATE,3" STK
3 1/8"±.02"Ø HOLE
3" STK
DRILL & TAP 3/4"Ø-16UNF 1 1/2" DEEP. (8 PLACES)
DETAIL - B (4 REQ'D)
TEST SPECIMEN PHASE 1
TOLERANCES: HOLE PATTERNS ±.010
ALL OTHER DIMENSIONS ±.015
UNLESS OTHERWISE NOTED.
NOTE: ALL MATERIAL TO BE STEEL, 50 KSI MINIMUM YIELD UNLESS NOTED OTHERWISE.
DRAWING NUMBER
3A0512
DRAWING CLASSIFICATION
UNCLASSIFIED
SIZE
D
CAGE 14213
SCALE 1 1/2"=1'
ISSUE 1
SHEET 2 OF 2
STATUS: LOCAL STORAGE-3-21-9

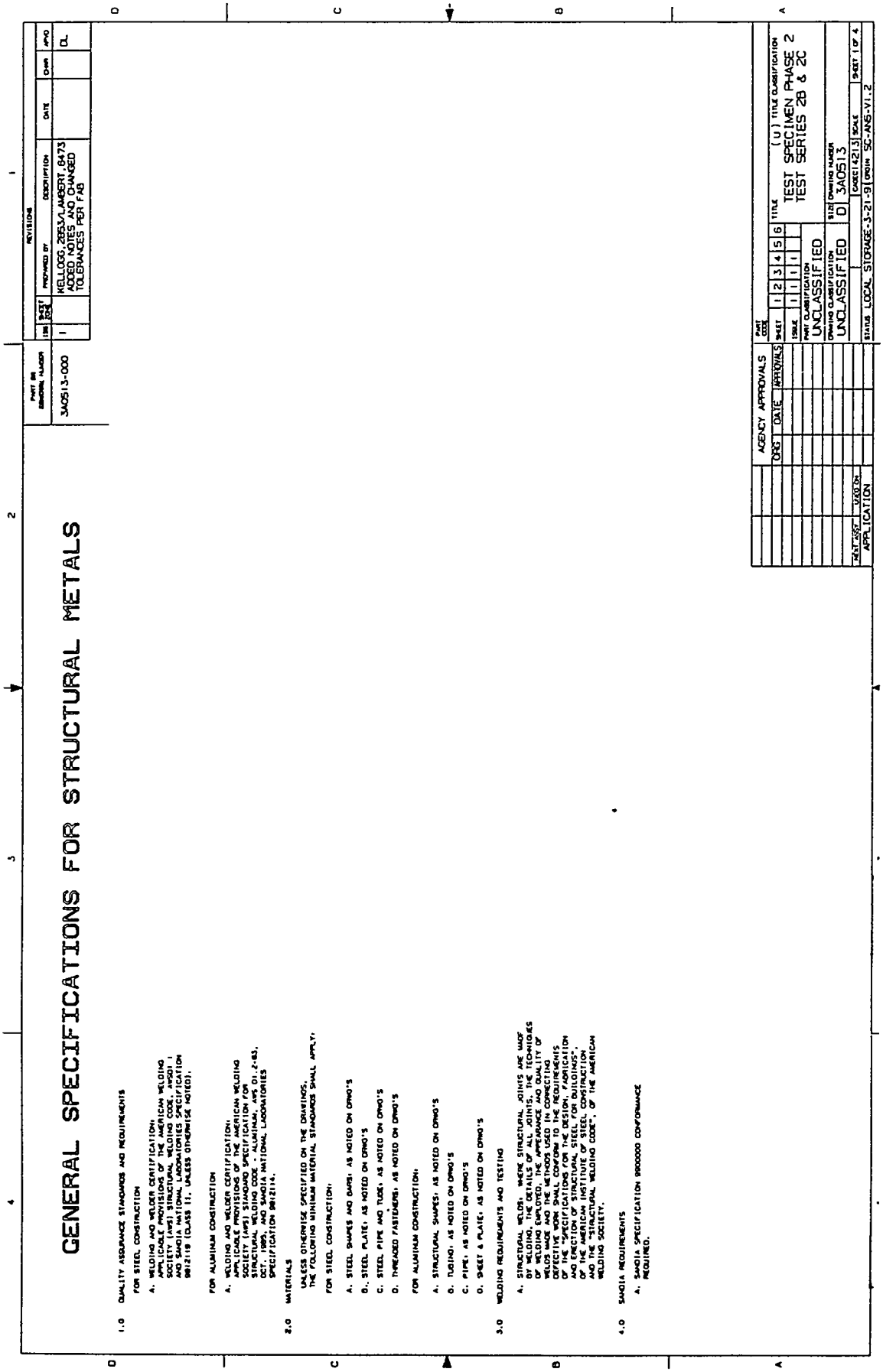

GENERAL SPECIFICATIONS FOR STRUCTURAL METALS

1.0 QUALITY ASSURANCE STANDARDS AND REQUIREMENTS

FOR STEEL CONSTRUCTION

A. WELDING AND WELDER CERTIFICATION:
APPLICABLE PROVISIONS OF THE AMERICAN WELDING SOCIETY (AWS) STRUCTURAL WELDING CODE, AWS D1.1 AND SANDIA NATIONAL LABORATORIES SPECIFICATION SM12118 (CLASS 11, UNLESS OTHERWISE NOTED).

FOR ALUMINUM CONSTRUCTION

A. WELDING AND WELDER CERTIFICATION:
APPLICABLE PROVISIONS OF THE AMERICAN WELDING SOCIETY (AWS) STANDARD SPECIFICATION FOR STRUCTURAL WELDING CODE - ALUMINUM, AWS D1.2-83, OCT. 1985, AND SANDIA NATIONAL LABORATORIES SPECIFICATION SM12114.

2.0 MATERIALS

UNLESS OTHERWISE SPECIFIED ON THE DRAWINGS, THE FOLLOWING MINIMUM MATERIAL STANDARDS SHALL APPLY:

FOR STEEL CONSTRUCTION:

A. STEEL SHAPES AND BARS: AS NOTED ON DRWG'S

B. STEEL PLATE: AS NOTED ON DRWG'S

C. STEEL PIPE AND TUBE: AS NOTED ON DRWG'S

D. THREADED FASTENERS: AS NOTED ON DRWG'S

FOR ALUMINUM CONSTRUCTION:

A. STRUCTURAL SHAPES: AS NOTED ON DRWG'S

B. TUBING: AS NOTED ON DRWG'S

C. PIPE: AS NOTED ON DRWG'S

D. SHEET & PLATE: AS NOTED ON DRWG'S

3.0 WELDING REQUIREMENTS AND TESTING

A. STRUCTURAL WELDS, WHERE STRUCTURAL JOINTS ARE MADE BY WELDING THE DETAILS OF ALL JOINTS, THE TECHNIQUES OF WELDING EMPLOYED, THE APPEARANCE AND QUALITY OF WELDS MADE AND THE METHODS USED IN CORRECTING DEFECTIVE WORK SHALL CONFORM TO THE REQUIREMENTS OF THE "SPECIFICATIONS FOR THE DESIGN, FABRICATION AND ERECTION OF STRUCTURAL STEEL FOR BUILDINGS", OF THE AMERICAN INSTITUTE OF STEEL CONSTRUCTION AND THE STRUCTURAL WELDING CODE", OF THE AMERICAN WELDING SOCIETY.

4.0 SANDIA REQUIREMENTS

A. SANDIA SPECIFICATION 8500000 CONFORMANCE REQUIRED.

REVISIONS					
ITR	SHEET (S)	PREPARED BY	DESCRIPTION	DATE	CHKR	APVD
	1	KELLOGG, 2853/LAMBERT, 8473	ADDED NOTES AND CHANGED TOLERANCES PER FAB			DL

PART OR SEMICONTROL NUMBER
340513-000

AGENCY APPROVALS			PART CODE
ORG	DATE	APPROVALS	SHEET
			ISSUE
			PART CLASSIFICATION
			UNCLASSIFIED
			DRAWING CLASSIFICATION
			UNCLASSIFIED
NEXT ASSY	USED ON		
APPLICATION			

SHEET	1	2	3	4	5	6
ISSUE						

TITLE (U) TITLE CLASSIFICATION
TEST SPECIMEN PHASE 2
TEST SERIES 2B & 2C

SIZE DRAWING NUMBER
D 340513

CODE 14213 SCALE SHEET 1 OF 4

STATUS LOCAL STORAGE-3-21-91 ORIGIN SC-ANS-VI.2

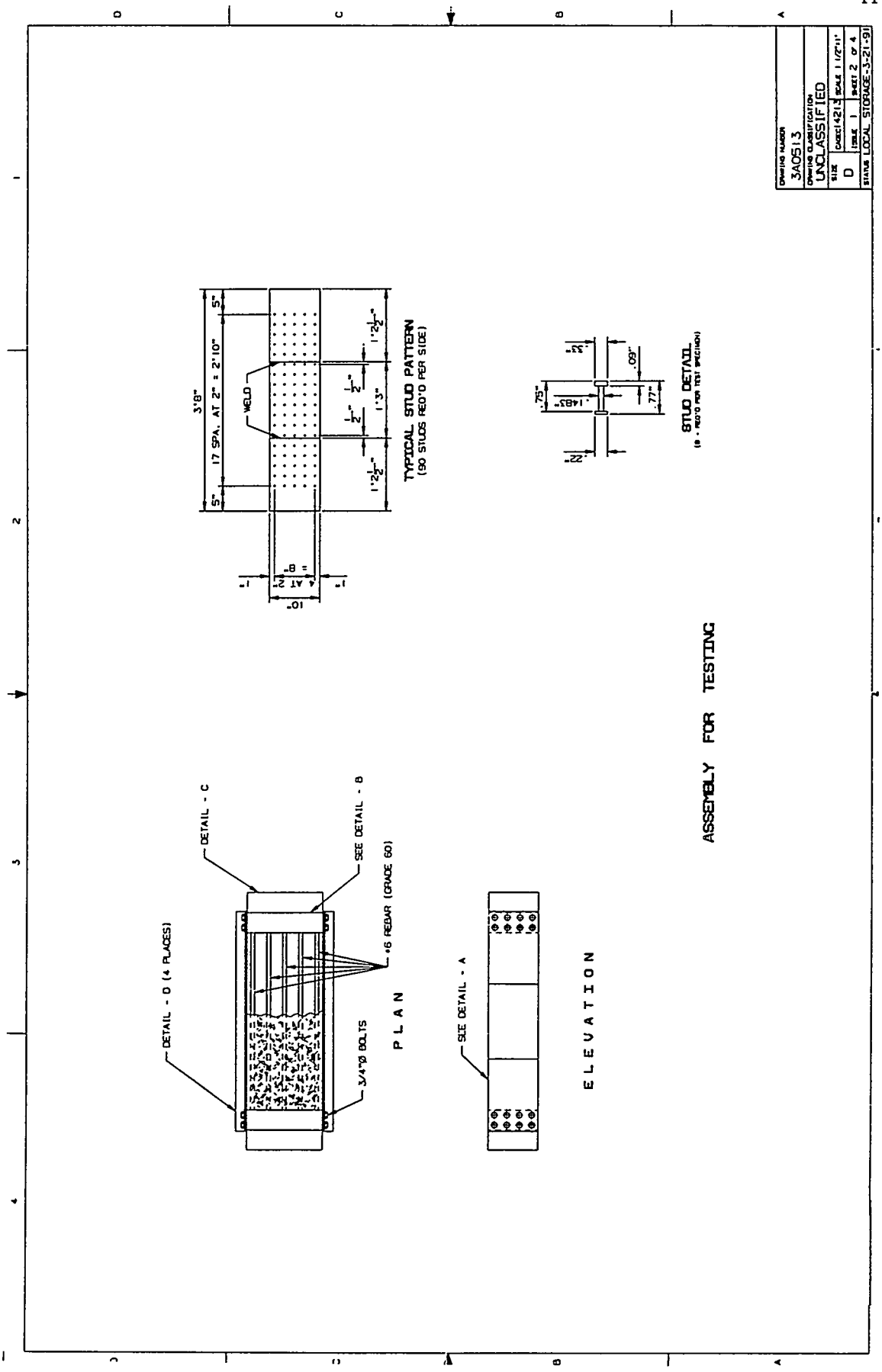
DRAWING NUMBER
3A0513
DRAWING CLASSIFICATION
UNCLASSIFIED
SIZE
D
SCALE 1 1/2"=1"
SHEET 2 OF 4
STATUS LOCAL STORAGE-3-21-91
TYPICAL STUD PATTERN
(90 STUDS REQ'D PER SIDE)
3'8"
17 SPA. AT 2" = 2'10"
5"
WELD
1'2½"
1½"
1'3"
STUD DETAIL
.75"
.09"
.77"
DETAIL - C
SEE DETAIL - B
#6 REBAR (GRADE 60)
DETAIL - D (4 PLACES)
3/4"Ø BOLTS
PLAN
SEE DETAIL - A
ELEVATION
ASSEMBLY FOR TESTING

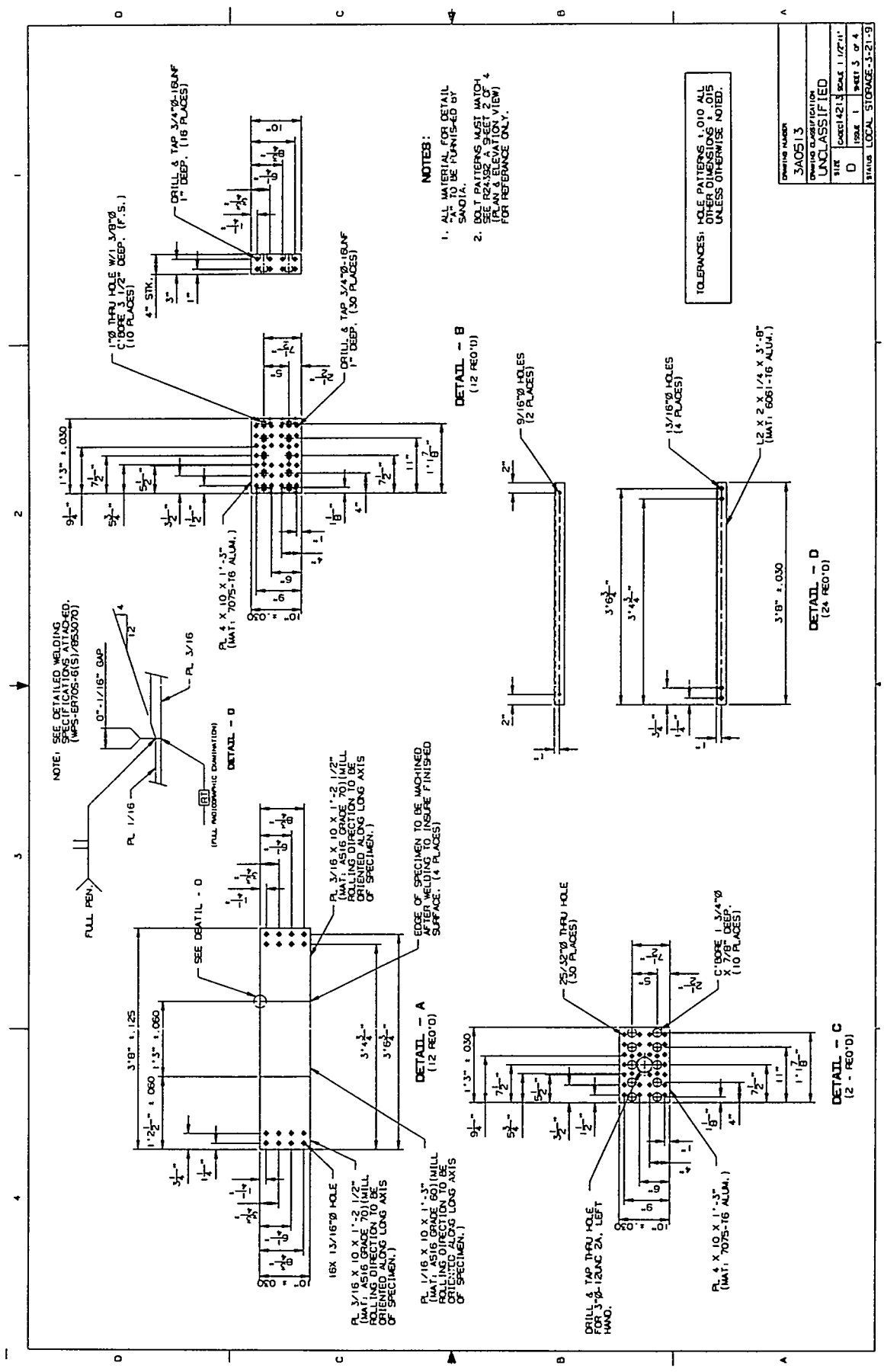
NOTES:
1. ALL MATERIAL FOR DETAIL "A" TO BE FURNISHED BY SANDIA.
2. BOLT PATTERNS MUST MATCH SEE R24.592 A SHEET 2 OF 4 (PLAN & ELEVATION VIEW) FOR REFERENCE ONLY.
TOLERANCES: HOLE PATTERNS ±.010 ALL OTHER DIMENSIONS ±.015 UNLESS OTHERWISE NOTED.
DRAWING NUMBER 3A0513
DRAWING CLASSIFICATION UNCLASSIFIED
SIZE D
CAGE 14213
SCALE 1 1/2"=1'
ISSUE 1
SHEET 3 OF 4
STATUS LOCAL STORAGE-3-21-9
DETAIL - A (12 REQ'D)
DETAIL - B (12 REQ'D)
DETAIL - C (2 - REQ'D)
DETAIL - D (24 REQ'D)
DETAIL - D
NOTE: SEE DETAILED WELDING SPECIFICATIONS ATTACHED. (MPS-ER705-6(S)/8530705)
FULL PEN
PL 1/16
PL 3/16
0"-1/16" GAP
12°
(M) (FULL RADIOGRAPHIC EXAMINATION)
PL 4 X 10 X 1'-3" (MAT; 7075-T6 ALUM.)
1"Ø THRU HOLE W/1 3/8"Ø C'BORE 3 1/2" DEEP. (F.S.) (10 PLACES)
DRILL & TAP 3/4"Ø-16UNF 1" DEEP. (16 PLACES)
DRILL & TAP 3/4"Ø-16UNF 1" DEEP. (30 PLACES)
4" STK.
3"
1"
9/16"Ø HOLES (2 PLACES)
13/16"Ø HOLES (4 PLACES)
L2 X 2 X 1/4 X 3'-8" (MAT; 6061-T6 ALUM.)
3'-8" ±.030
2"
PL 3/16 X 10 X 1'-2 1/2" (MAT; A516 GRADE 70) (MILL ROLLING DIRECTION TO BE ORIENTED ALONG LONG AXIS OF SPECIMEN.)
EDGE OF SPECIMEN TO BE MACHINED AFTER WELDING TO INSURE FINISHED SURFACE. (4 PLACES)
SEE DEATIL - D
3'-8" ±.125
1'-2 1/2" ±.060
1'-3" ±.060
3'-4 1/2"
3'-6 1/2"
16X 13/16"Ø HOLE
PL 1/16 X 10 X 1'-3" (MAT; A516 GRADE 60) (MILL ROLLING DIRECTION TO BE ORIENTED ALONG LONG AXIS OF SPECIMEN.)
25/32"Ø THRU HOLE (30 PLACES)
C'BORE 1 3/4"Ø X 7/8" DEEP. (10 PLACES)
1'-3" ±.030
DRILL & TAP THRU HOLE FOR 3"Ø-12UNC 2A, LEFT HAND.
PL 4 X 10 X 1'-3" (MAT; 7075-T6 ALUM.)

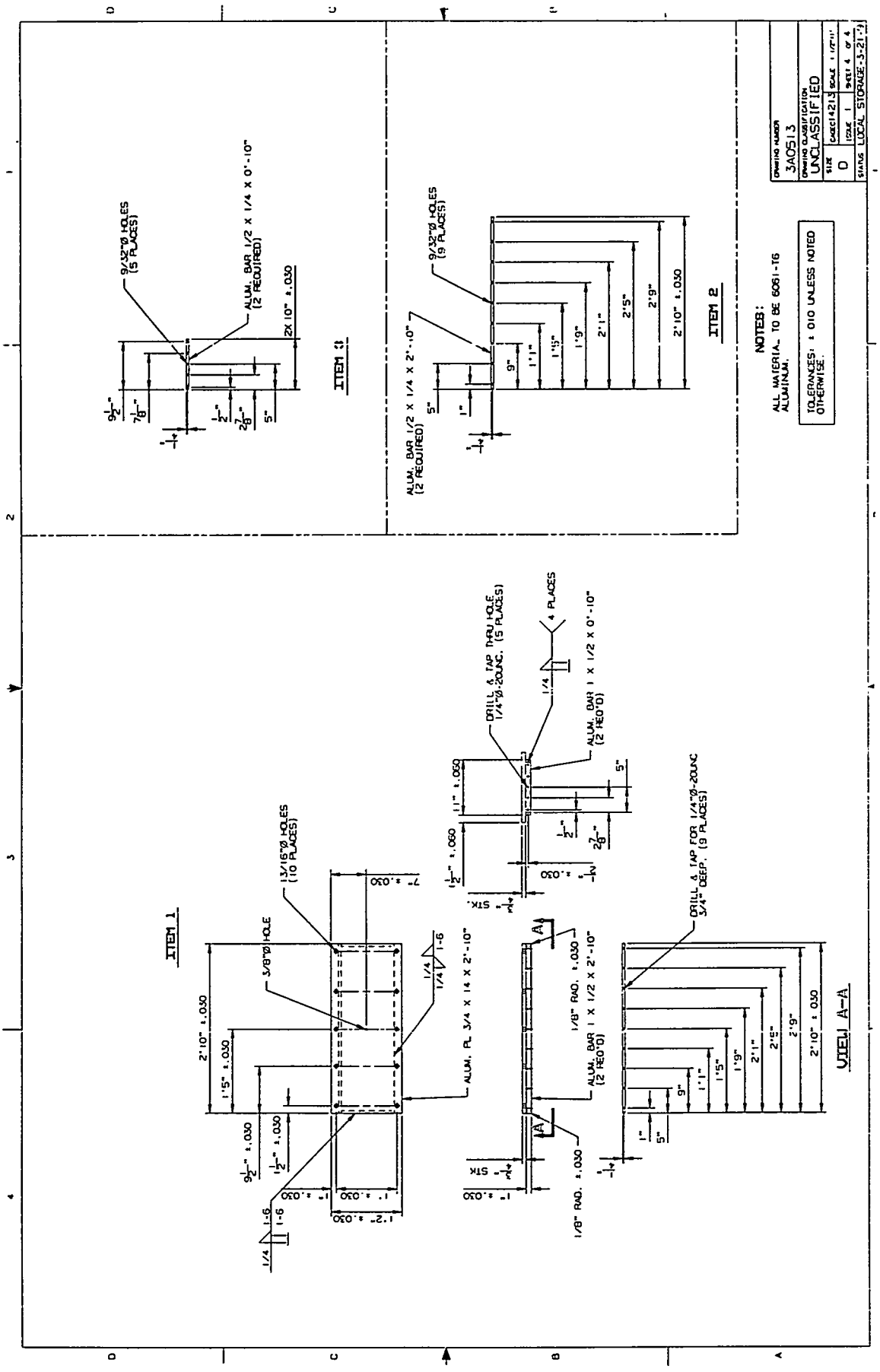
ITEM 1
ITEM 2
ITEM 3
ITEM 4
ITEM A-A
NOTES:
ALL MATERIAL TO BE 6061-T6
ALUMINUM.
TOLERANCES: ± .010 UNLESS NOTED OTHERWISE.
DRAWING NUMBER
3A0513
DRAWING CLASSIFICATION
UNCLASSIFIED
SIZE D
SCALE 1/2
SHEET 4 OF 4
STATUS LOCAL STORAGE 3-21-2
ALUM. BAR 1/2 X 1/4 X 0'-10" (2 REQUIRED)
9/32"Ø HOLES (5 PLACES)
2X 10" ± .030
ALUM. BAR 1/2 X 1/4 X 2'-10" (2 REQUIRED)
9/32"Ø HOLES (9 PLACES)
2'10" ± .030
13/16"Ø HOLES (10 PLACES)
3/8"Ø HOLE
ALUM. PL 3/4 X 14 X 2'-10"
DRILL & TAP THRU HOLE 1/4"Ø-20UNC. (5 PLACES)
4 PLACES
ALUM. BAR 1 X 1/2 X 0'-10" (2 REQ'D)
1/8" RAD. ± .030
ALUM. BAR 1 X 1/2 X 2'-10" (2 REQ'D)
DRILL & TAP FOR 1/4"Ø-20UNC 3/4" DEEP. (9 PLACES)

Appendix B: Strain Gage Data Plots for the Separate Effects Tests

Separately Controlled Loading
Specimen (Phase 1) Strain Gage Plots

Specimen Designation	Liner Preload
1A1	Stud Load Only
1A3	63 ksi
1B1	65 ksi
1B2	70 ksi
1B3	60 ksi
1C1	Liner Load Only

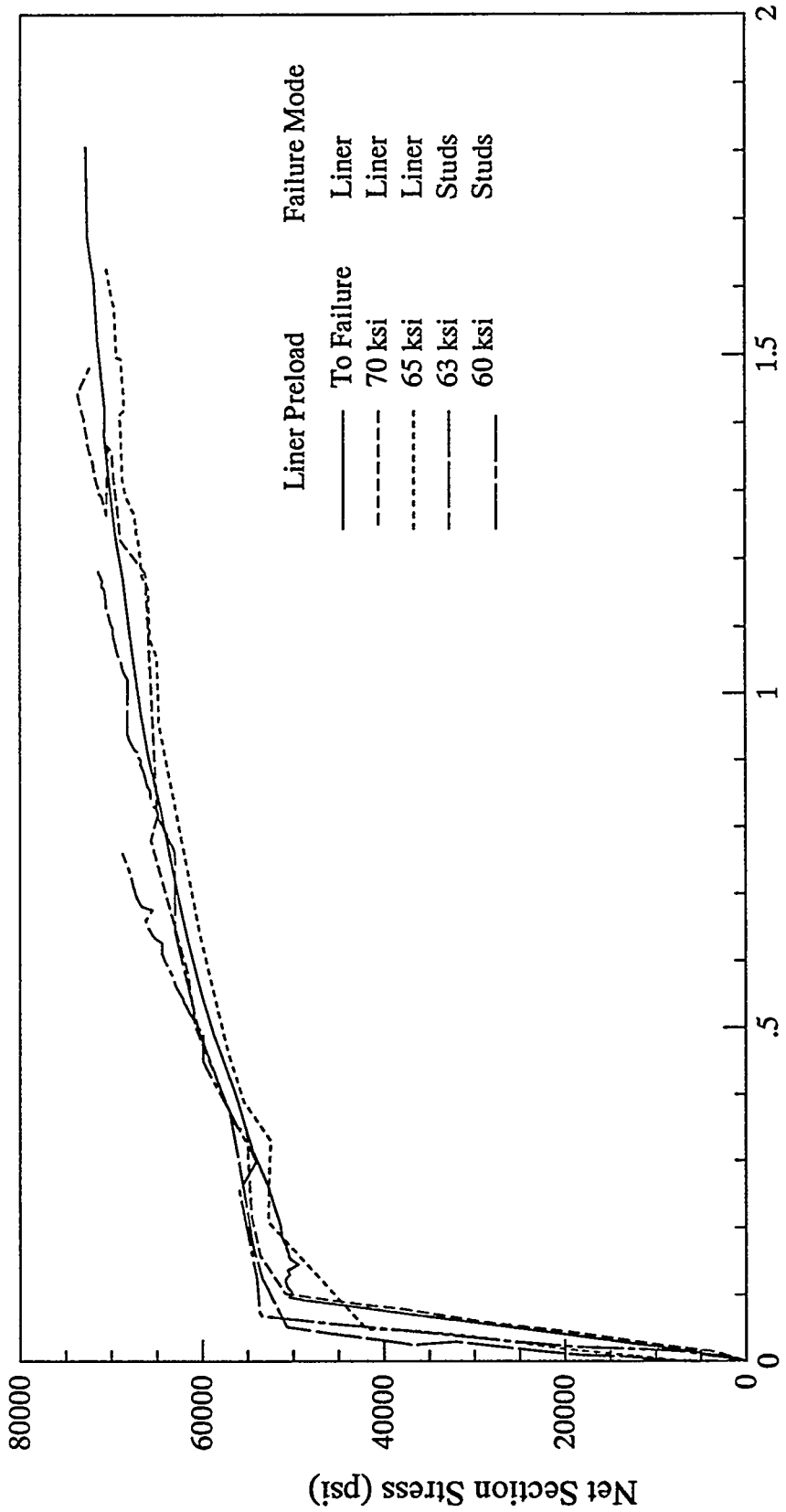

Overall Phase 1 Specimen Response

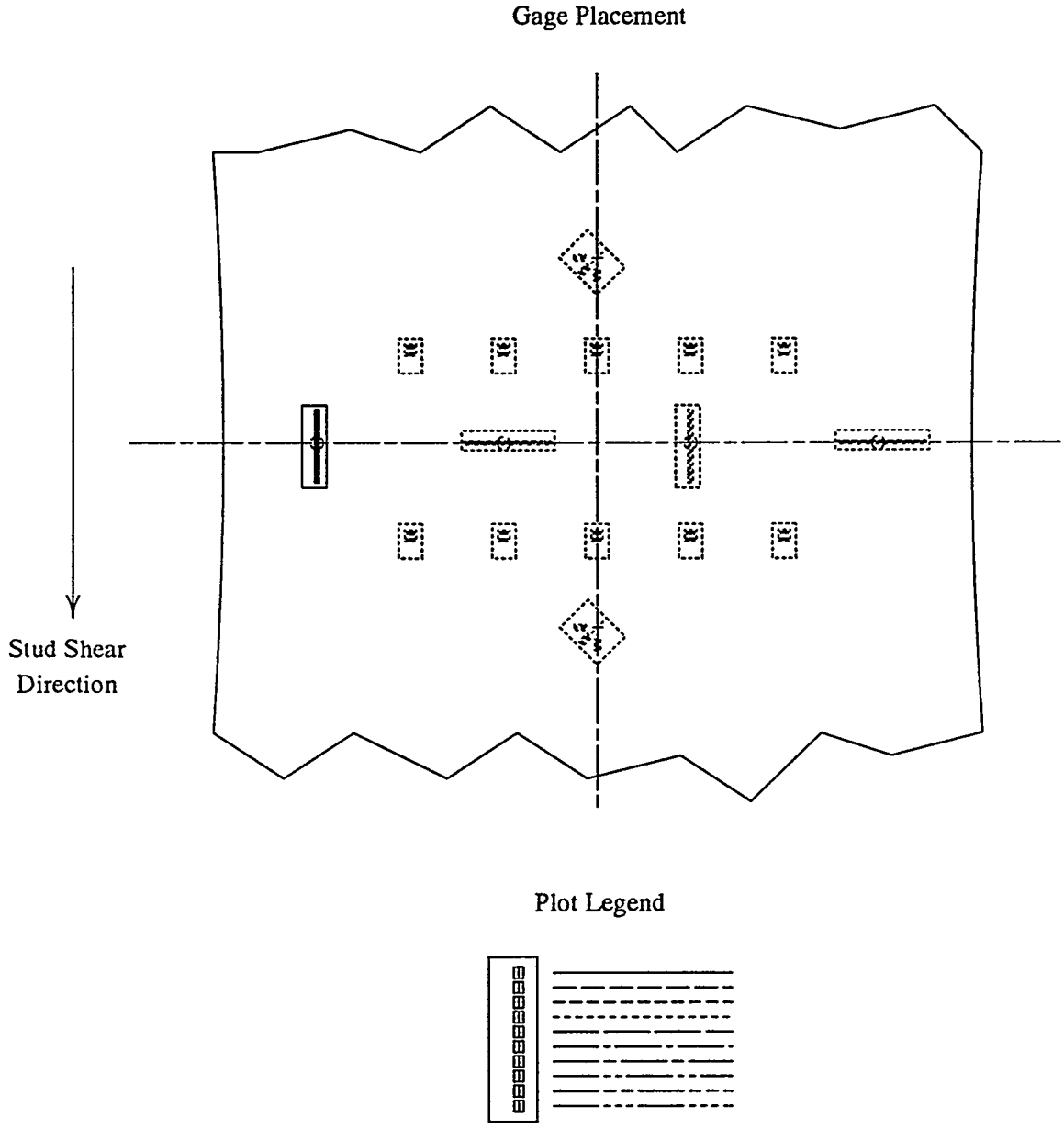

Outboard Axial Strip Gage (all specimens)

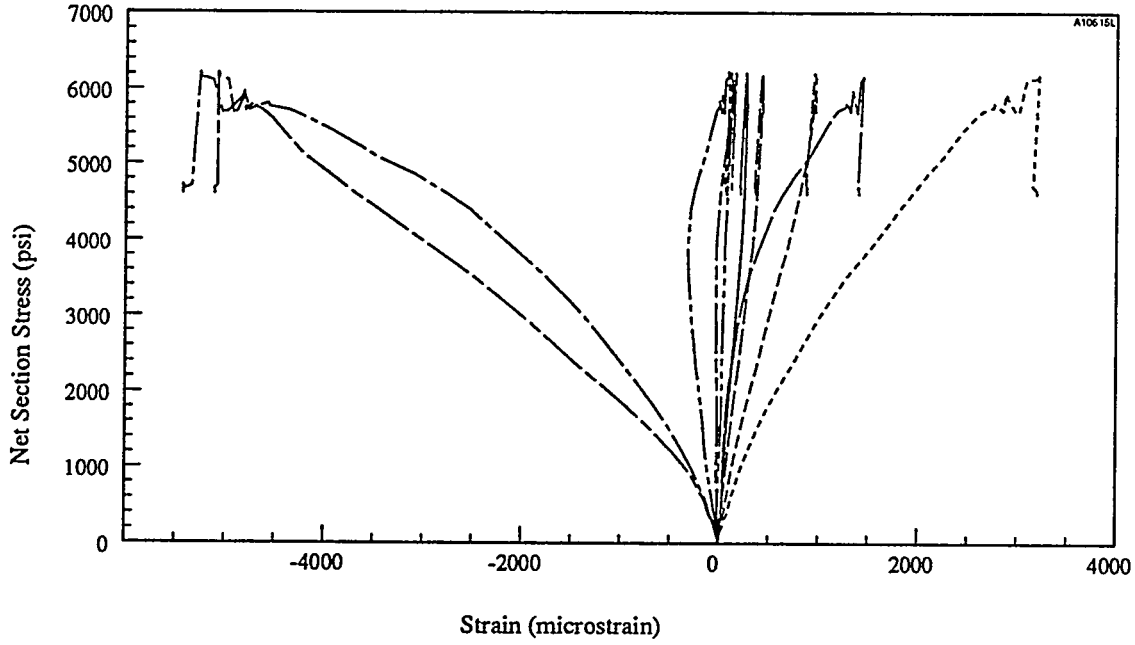

No Initial Liner Stress

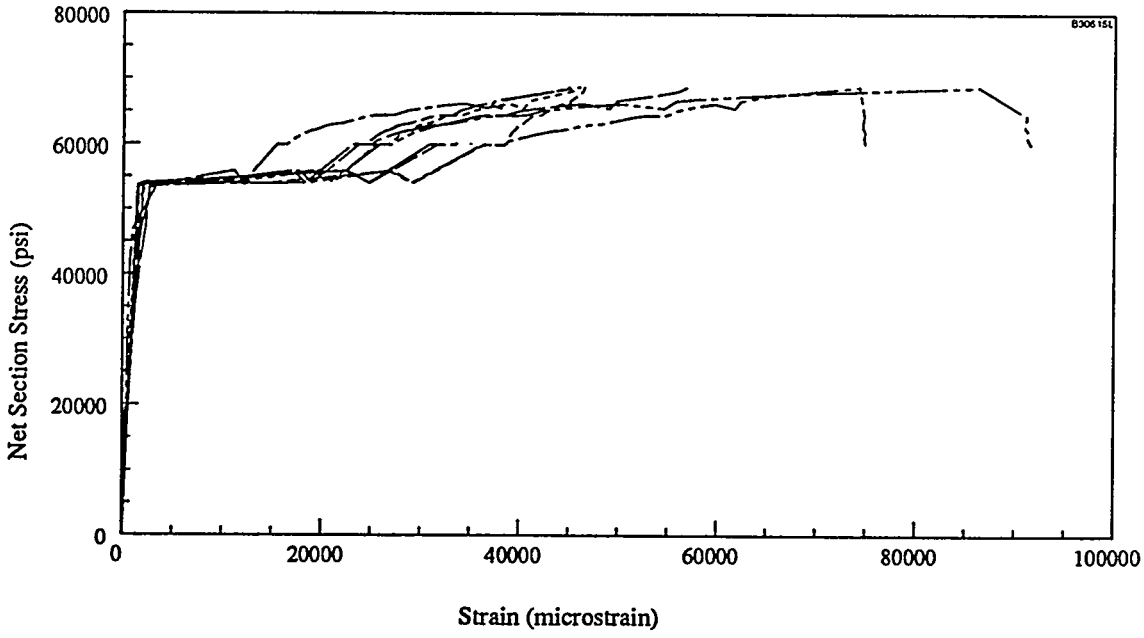

60 ksi Liner Stress

Outboard Axial Strain vs.Load Response

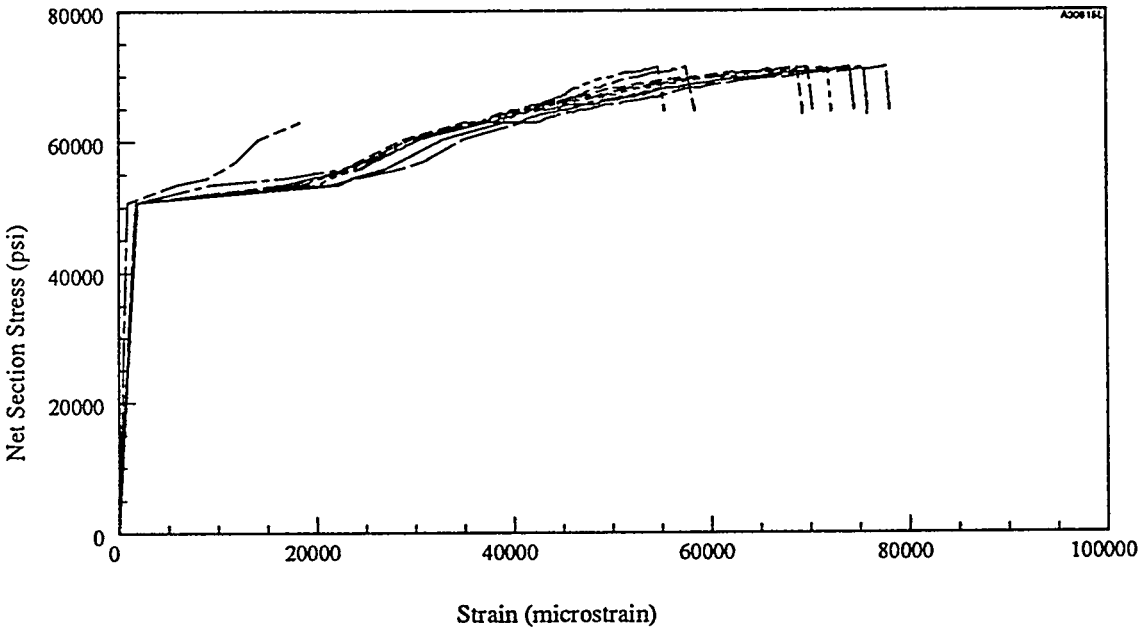

63 ksi Liner Stress

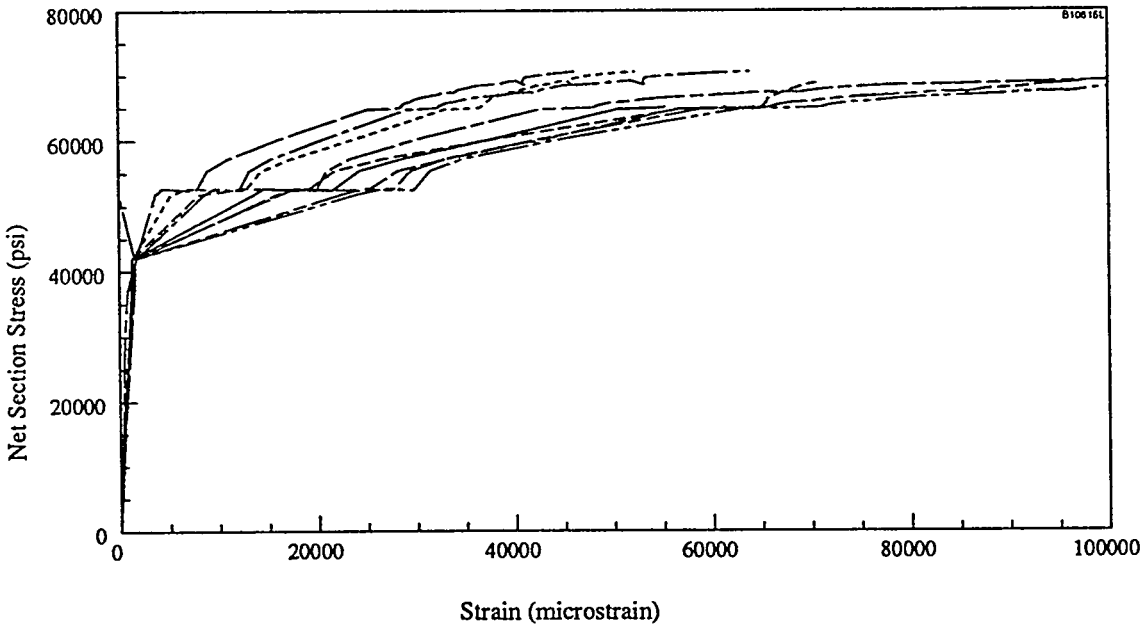

65 ksi Liner Stress

Outboard Axial Strain vs.Load Response (cont.)

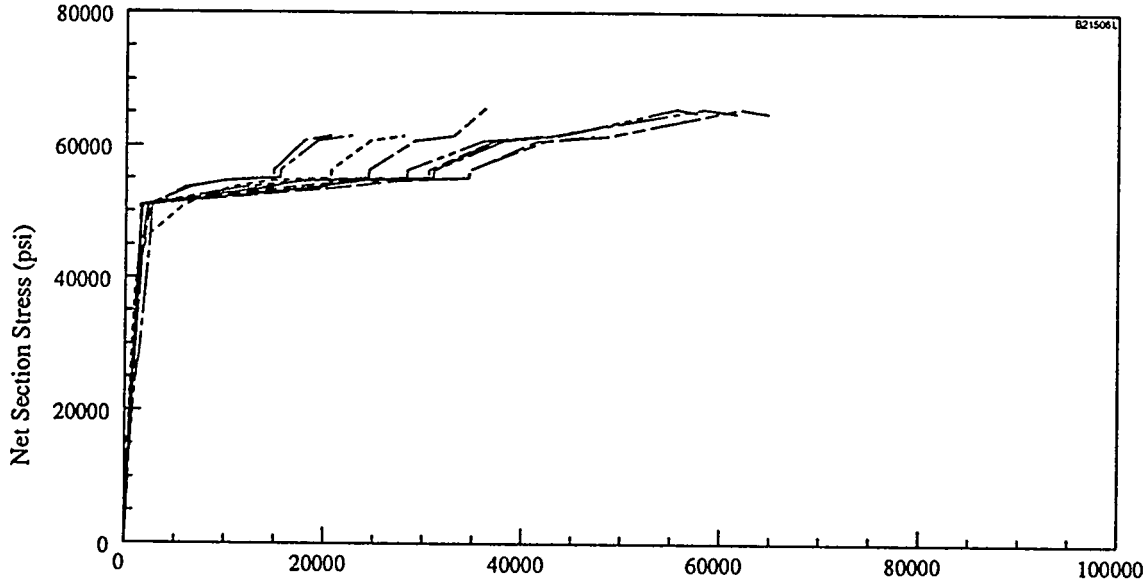

70 ksi Liner Stress

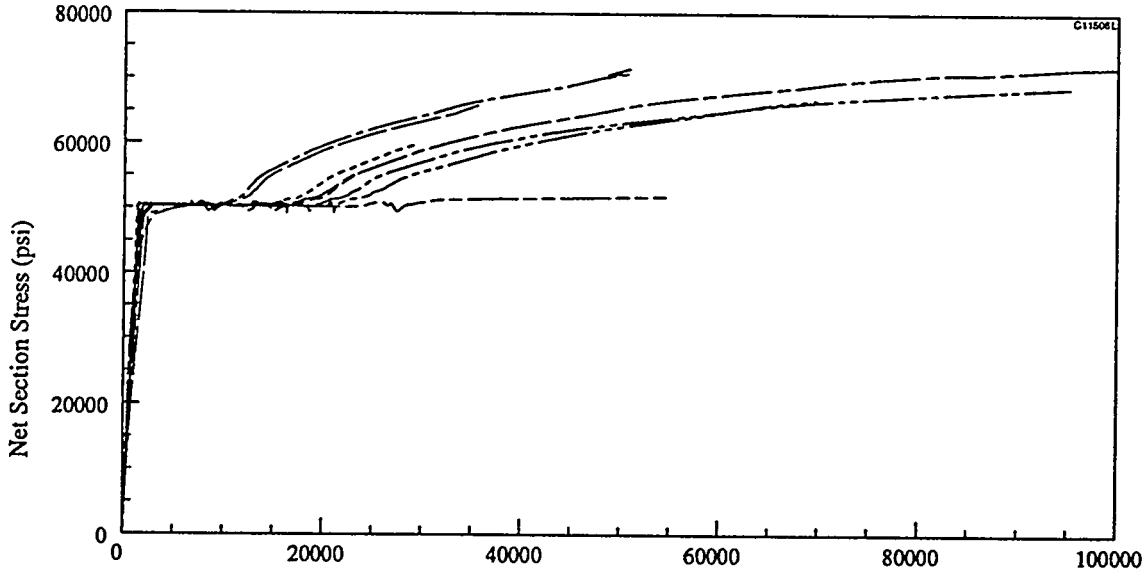

No Stud Load

Outboard Axial Strain vs. Load Response (cont.)

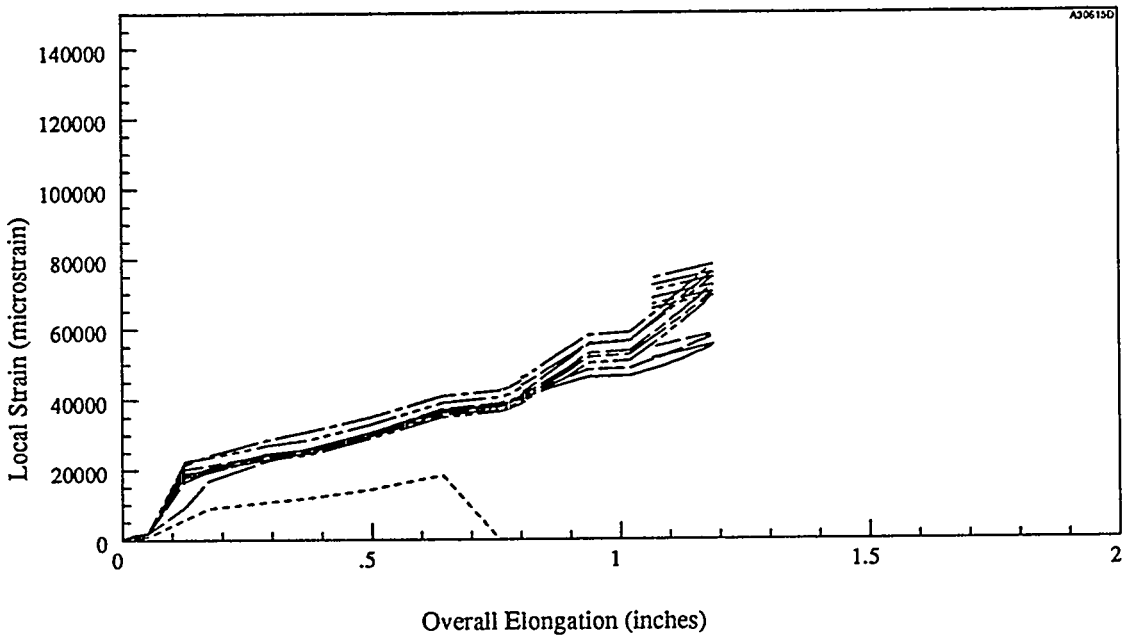

63 ksi Liner Stress

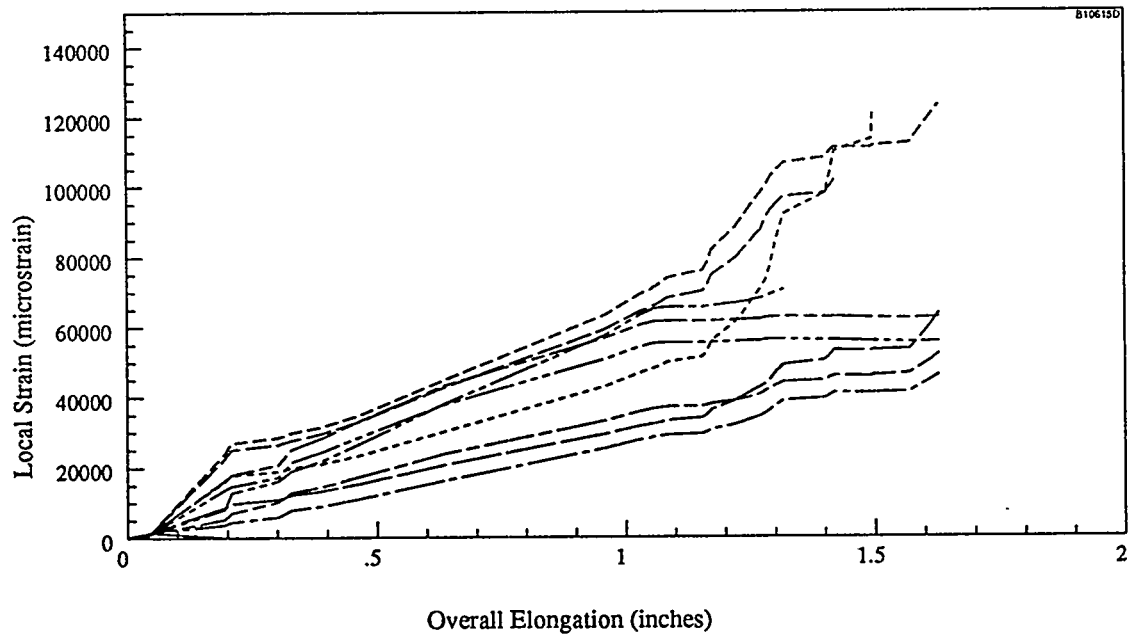

65 ksi Liner Stress

Outboard Axial Strain vs.Displacement Response (cont.)

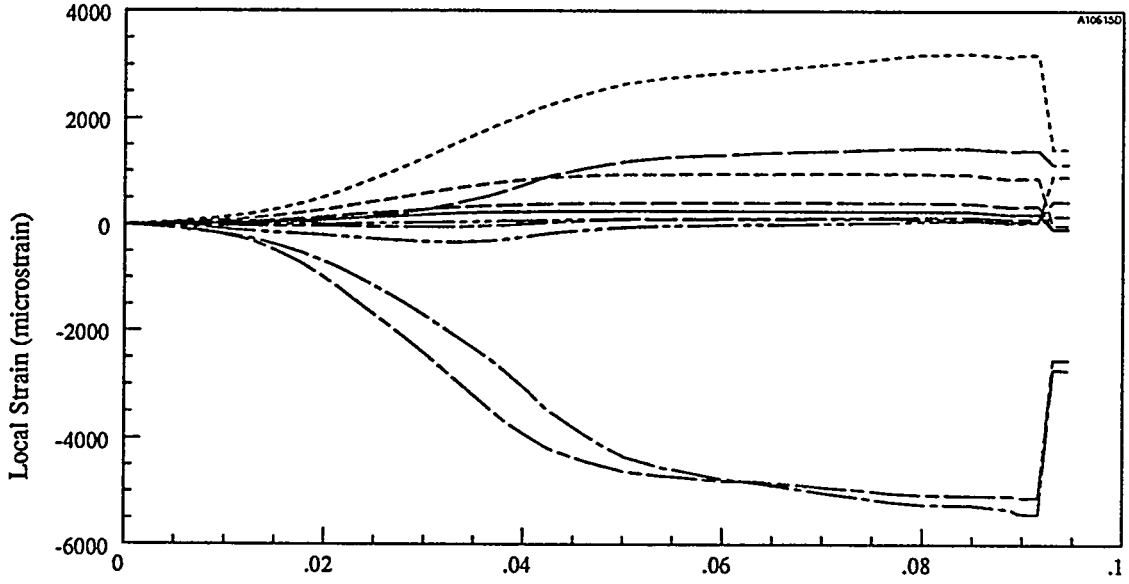

No Initial Liner Stress

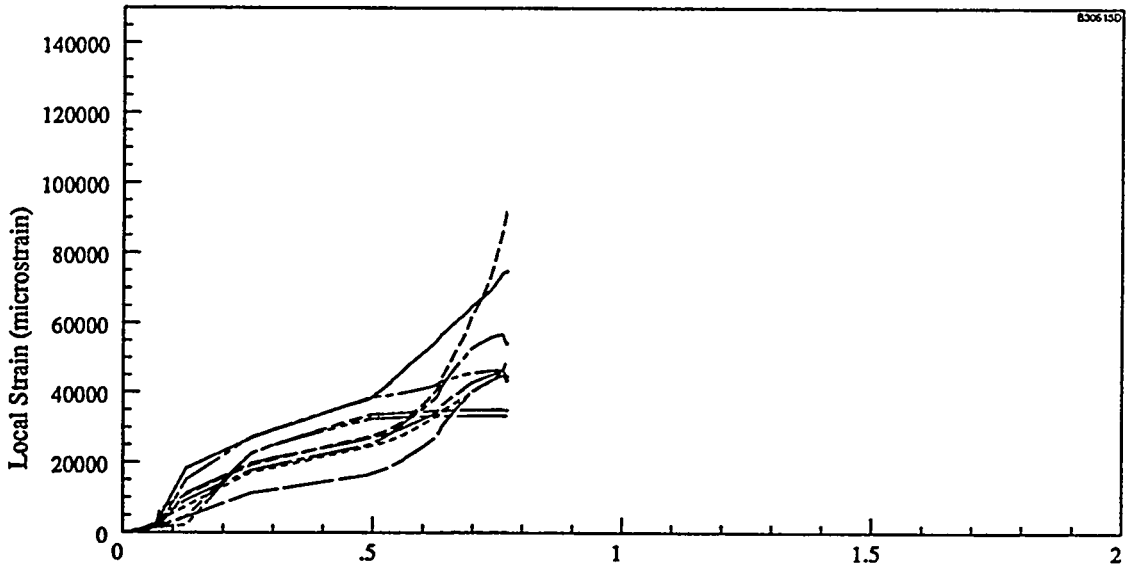

· 60 ksi Liner Stress

Outboard Axial Strain vs. Displacement Response

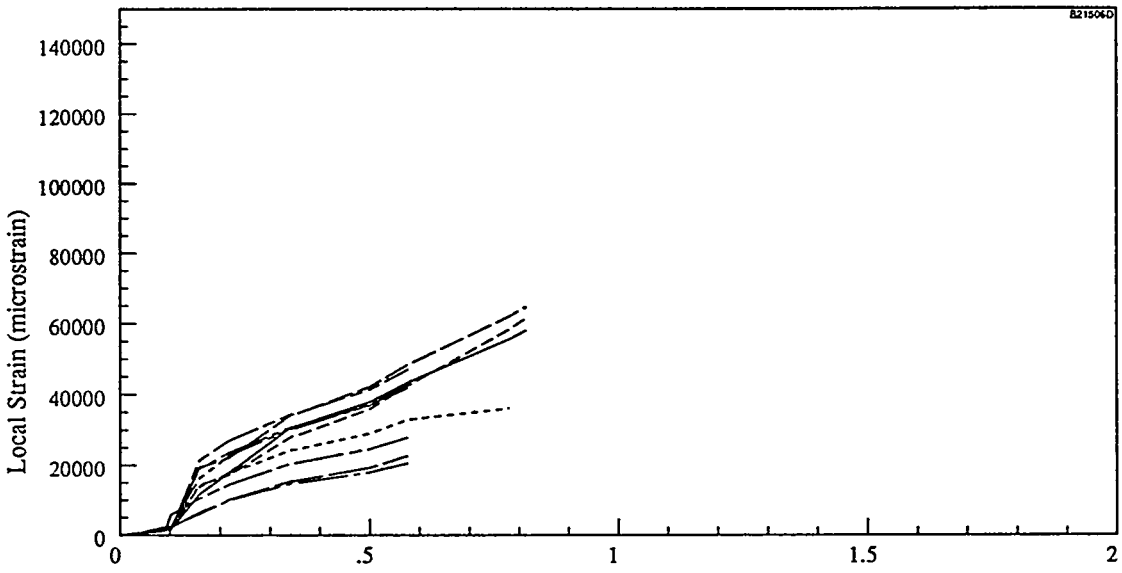

70 ksi Liner Stress

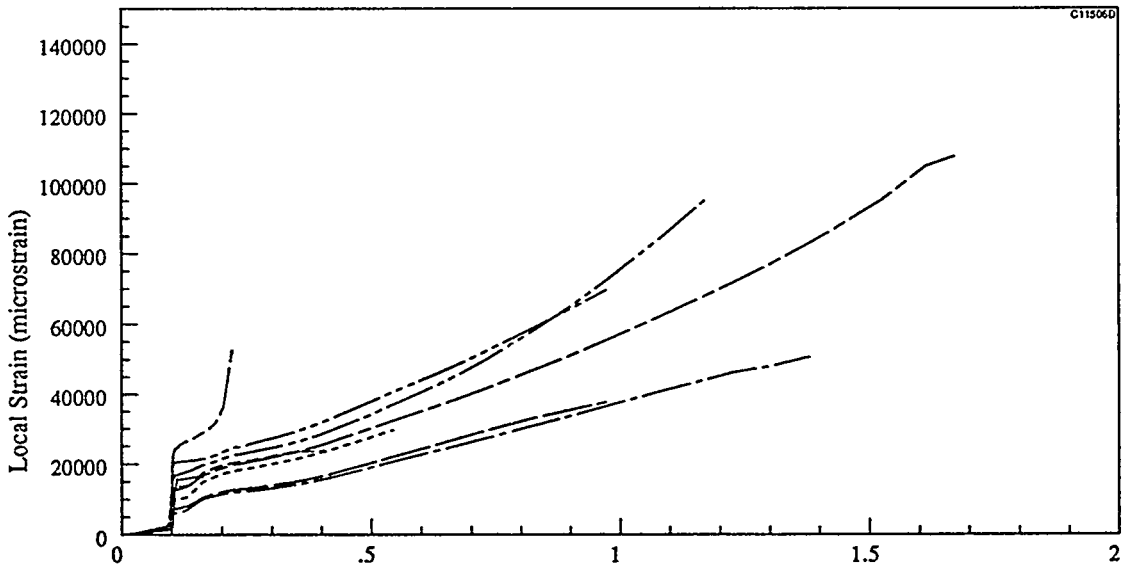

No Stud Load

Outboard Axial Strain vs. Displacement Response (cont.)

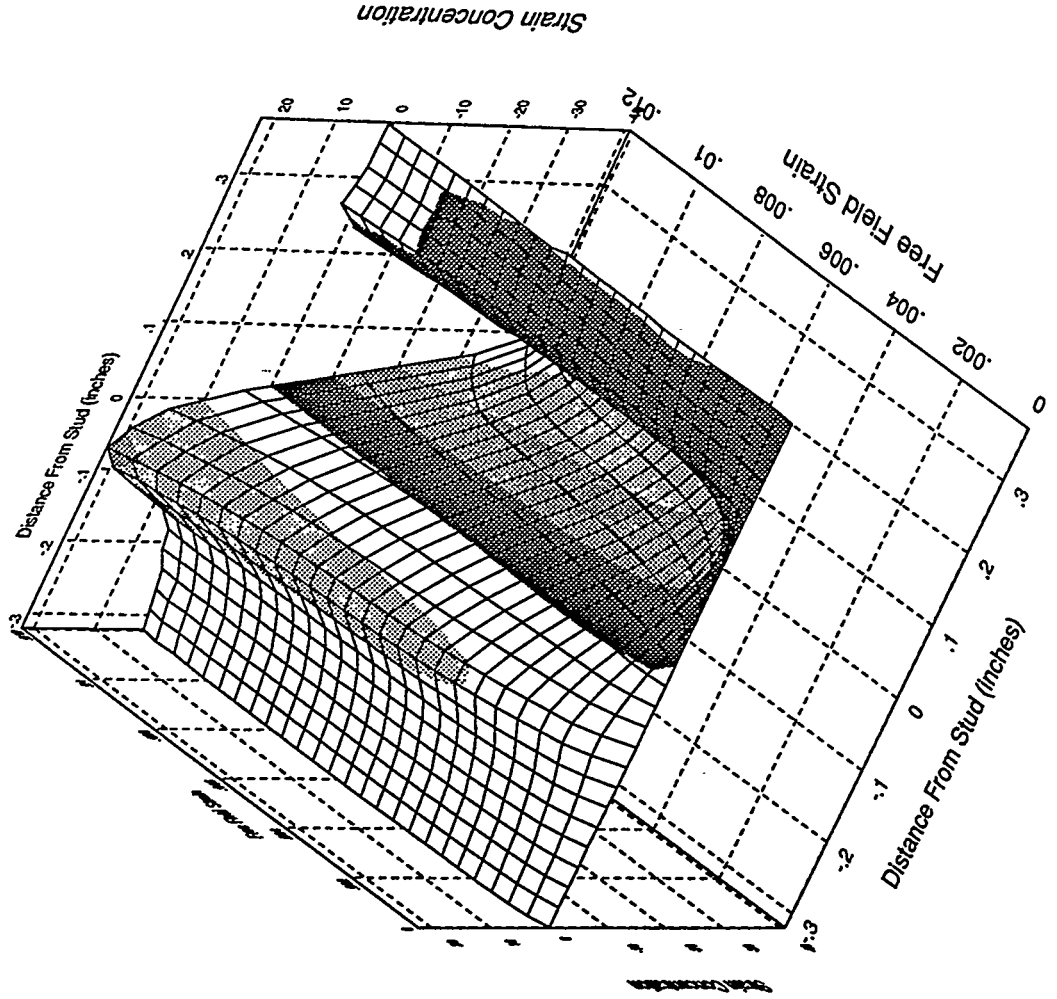

Outboard Axial Strip Gage,No Liner Stress Specimen

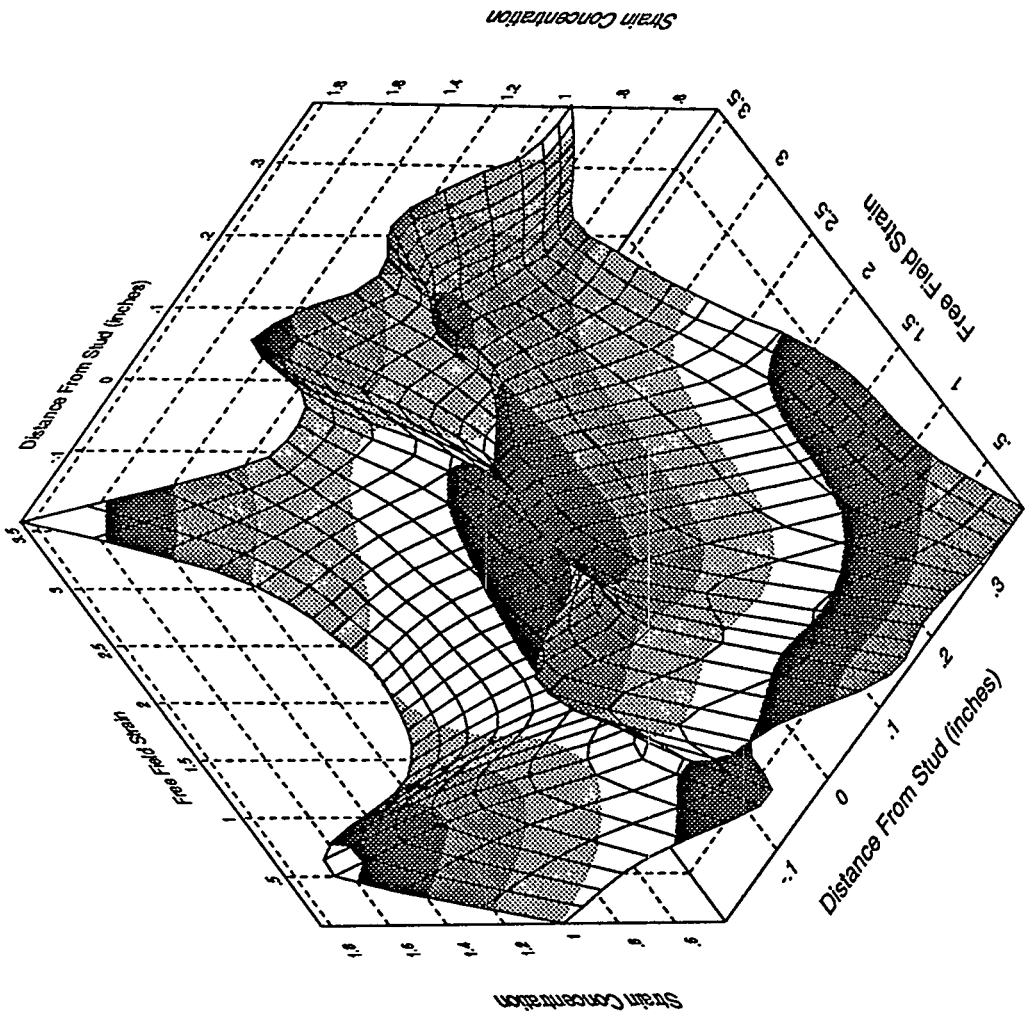

Outboard Axial Strip Gage,60 KSI Specimen

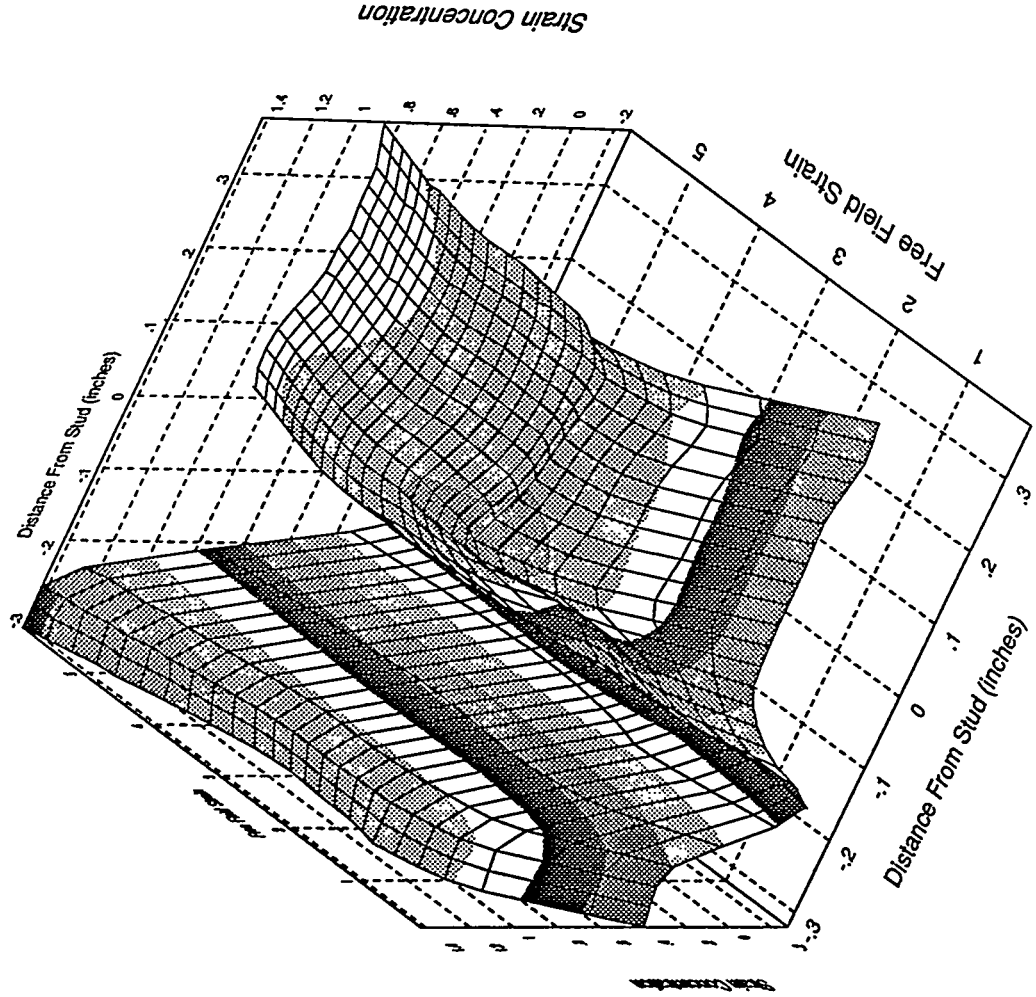

Outboard Axial Strip Gage,63 KSI Specimen

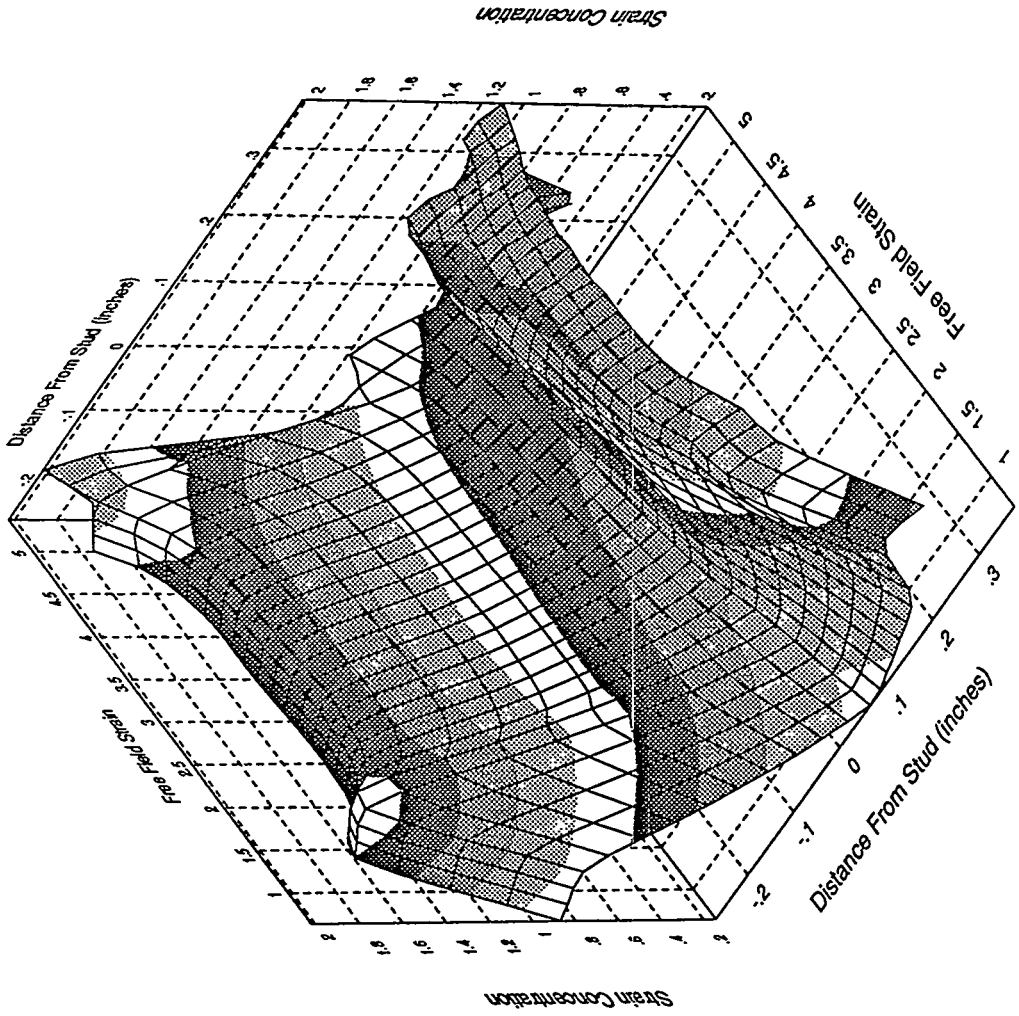

Outboard Axial Strip Gage,65 KSI Specimen

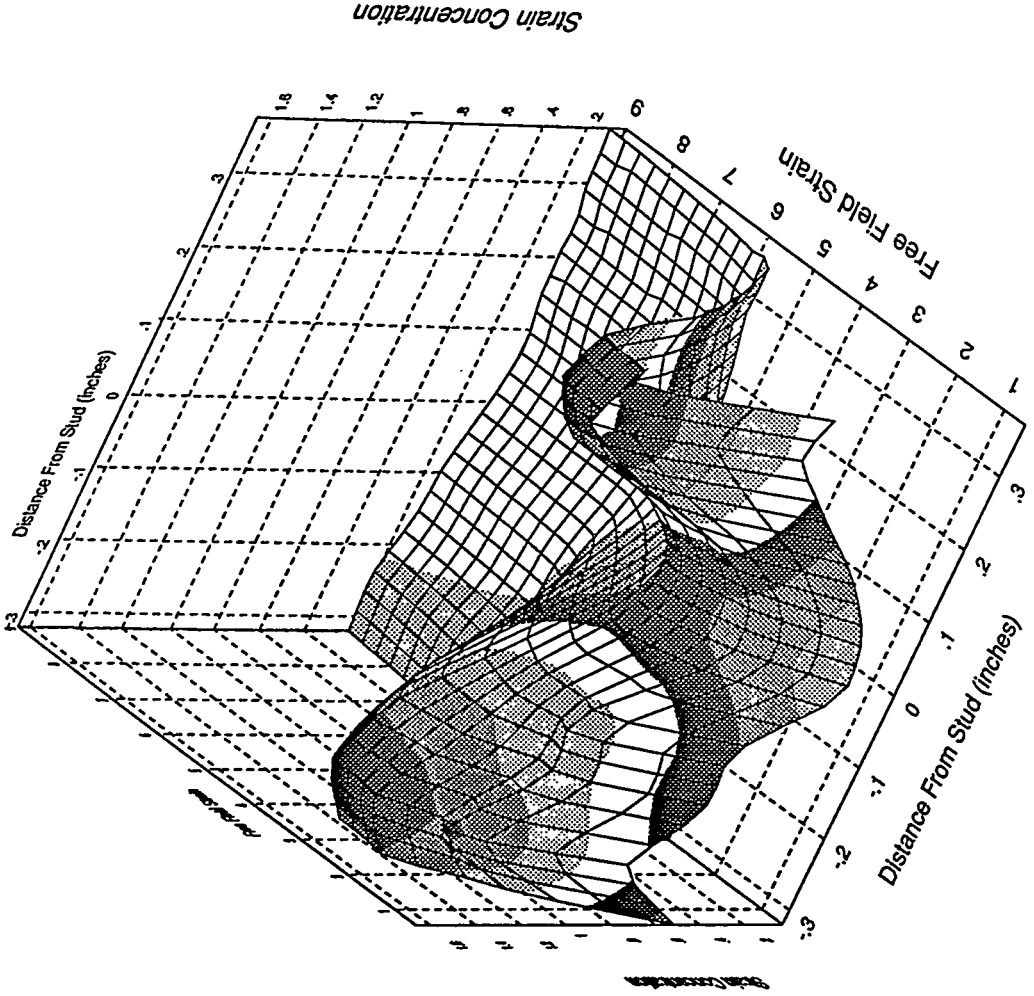

Outboard Axial Strip Gage,70 ksi Specimen

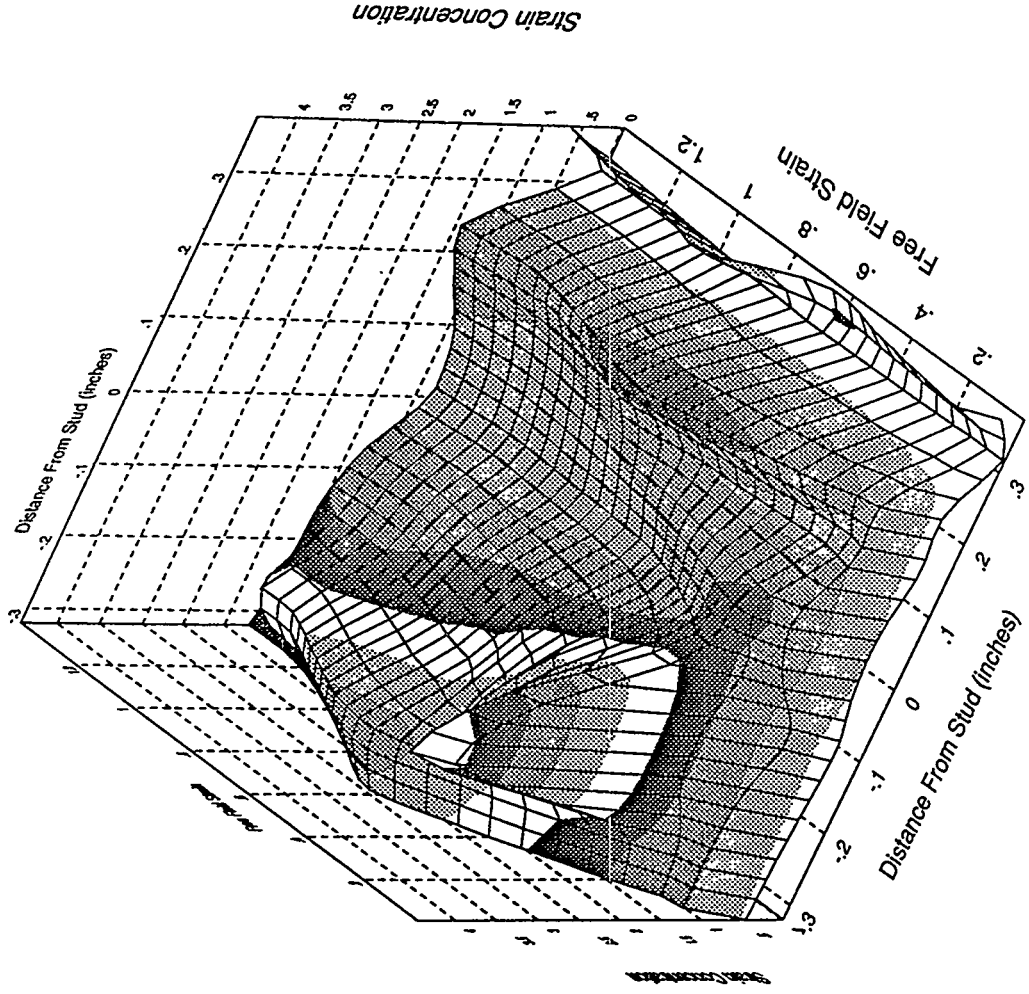

Outboard Axial Strip Gage,No Stud Load Specimen

Gage Placement

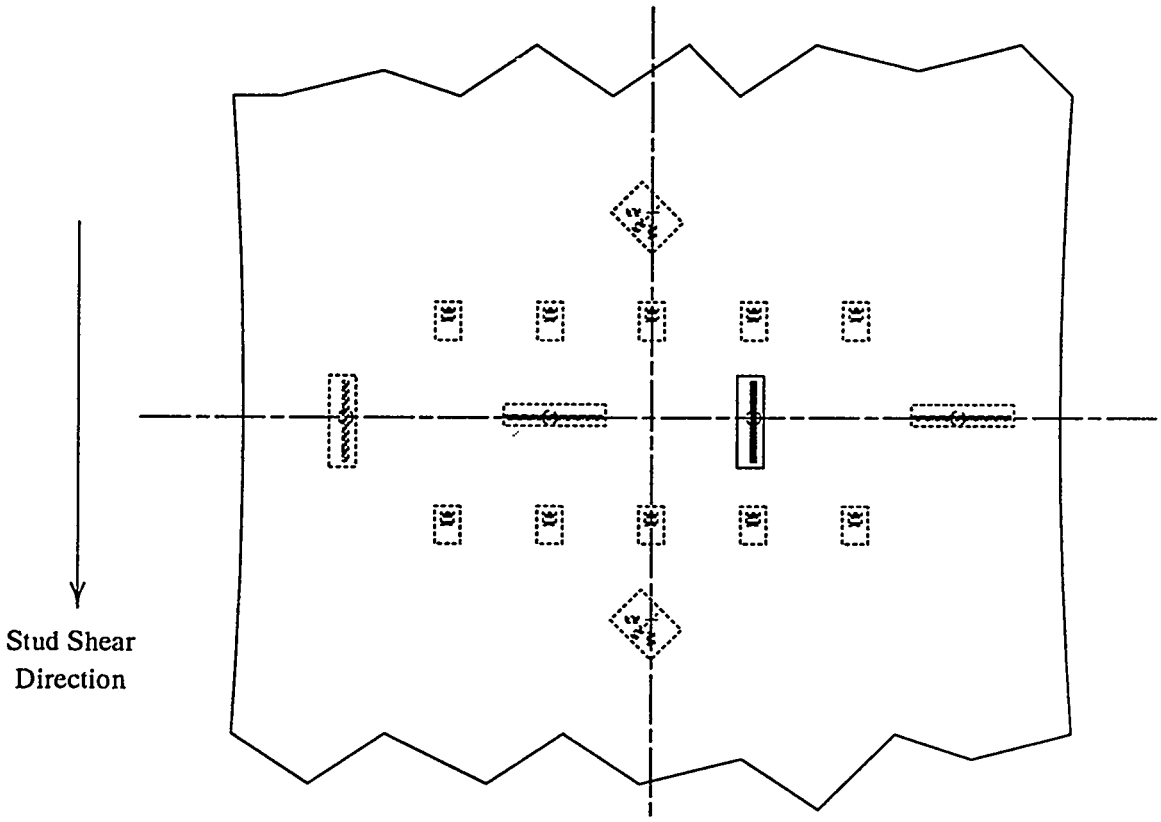

Plot Legend

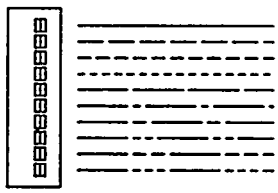

Inboard Axial Strip Gage (all specimens)

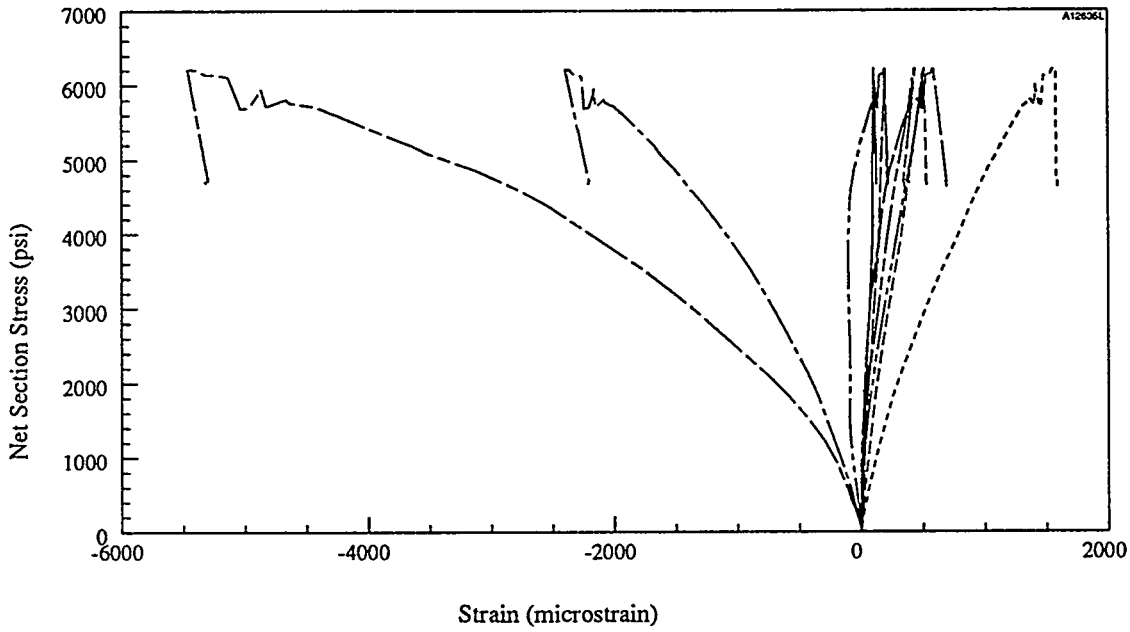

No Initial Liner Stress

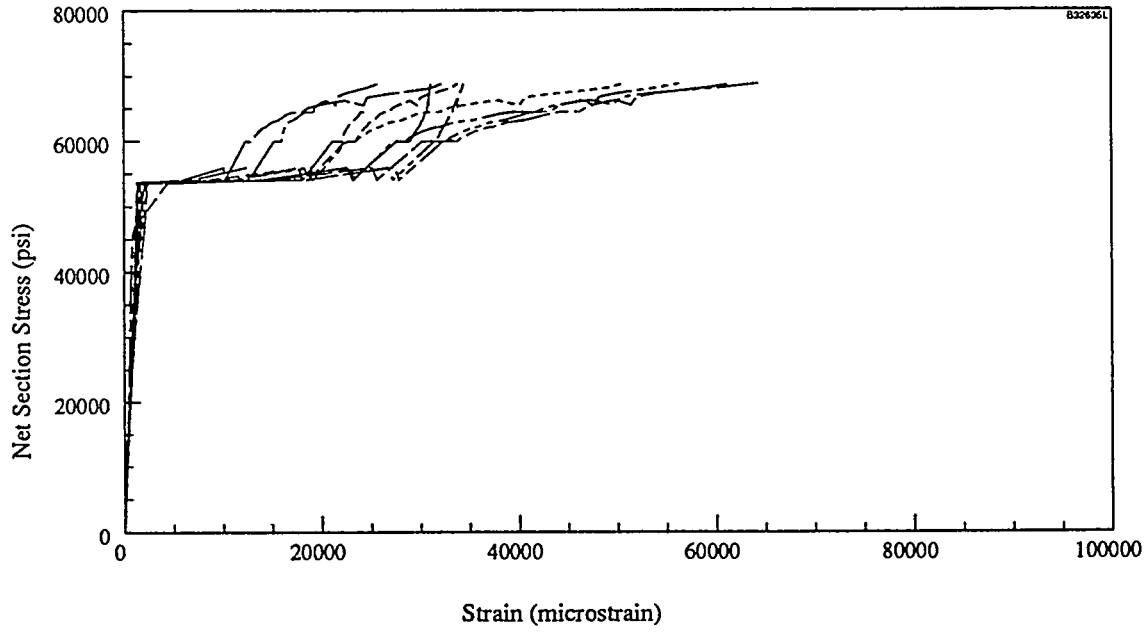

60 ksi Liner Stress

Inboard Axial Strain vs. Load Response

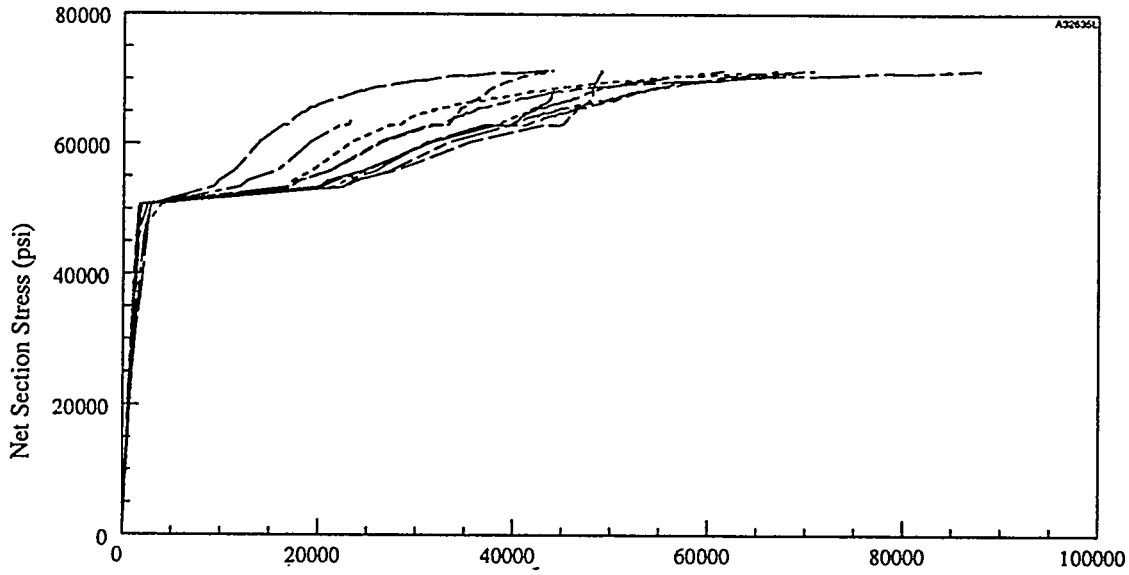

63 ksi Liner Stress

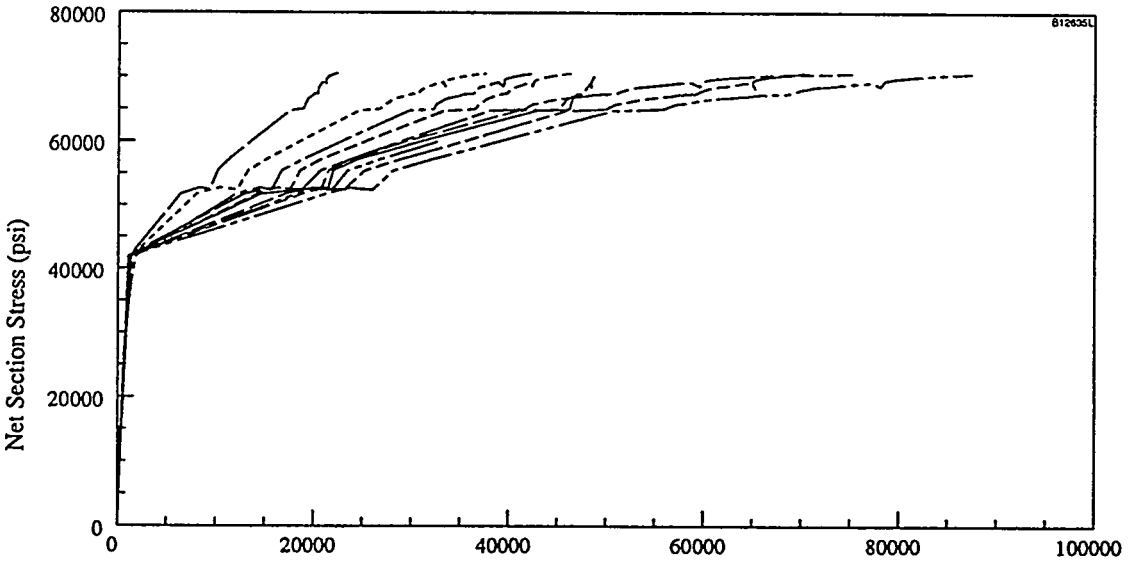

65 ksi Liner Stress

Inboard Axial Strain vs. Load Response (cont.)

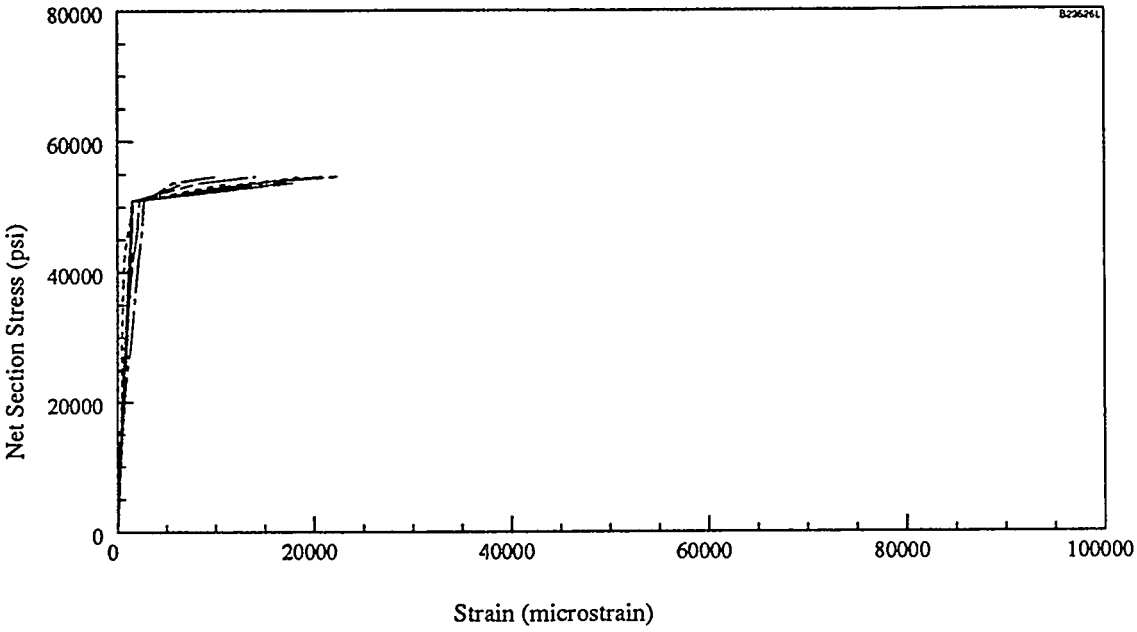

70 ksi Liner Stress

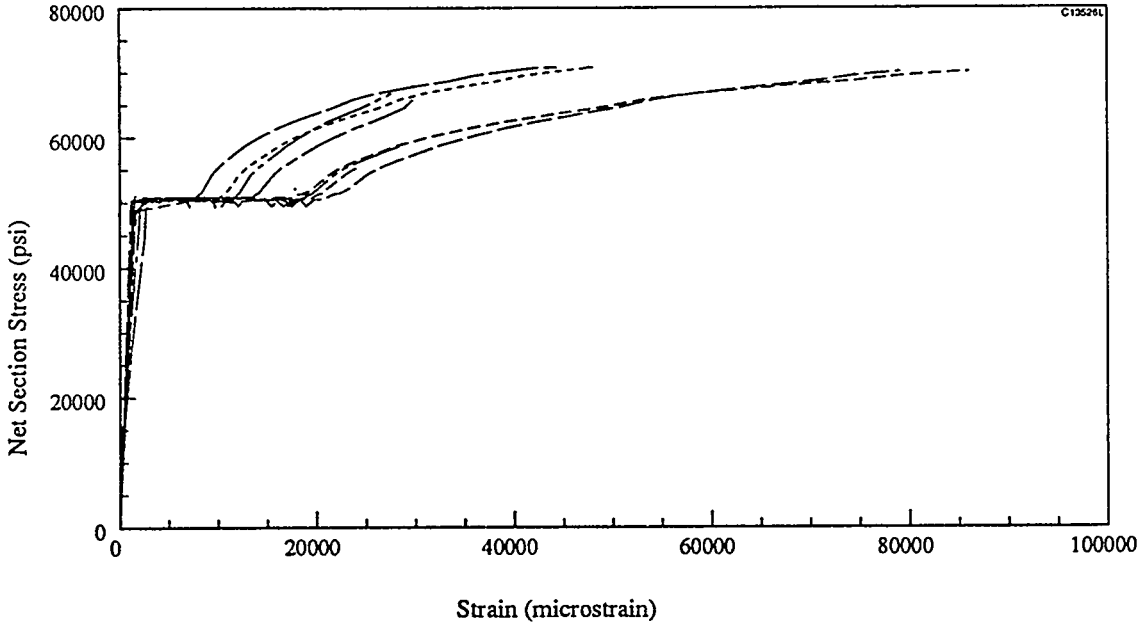

No Stud Load

Inboard Axial Strain vs. Load Response (cont.)

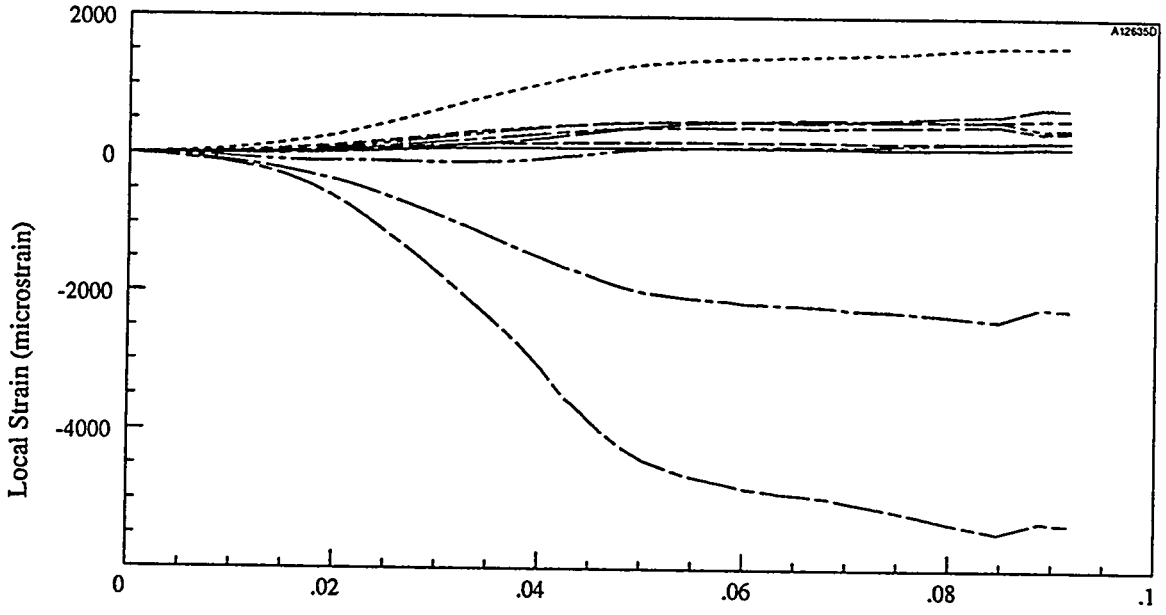

No Initial Liner Stress

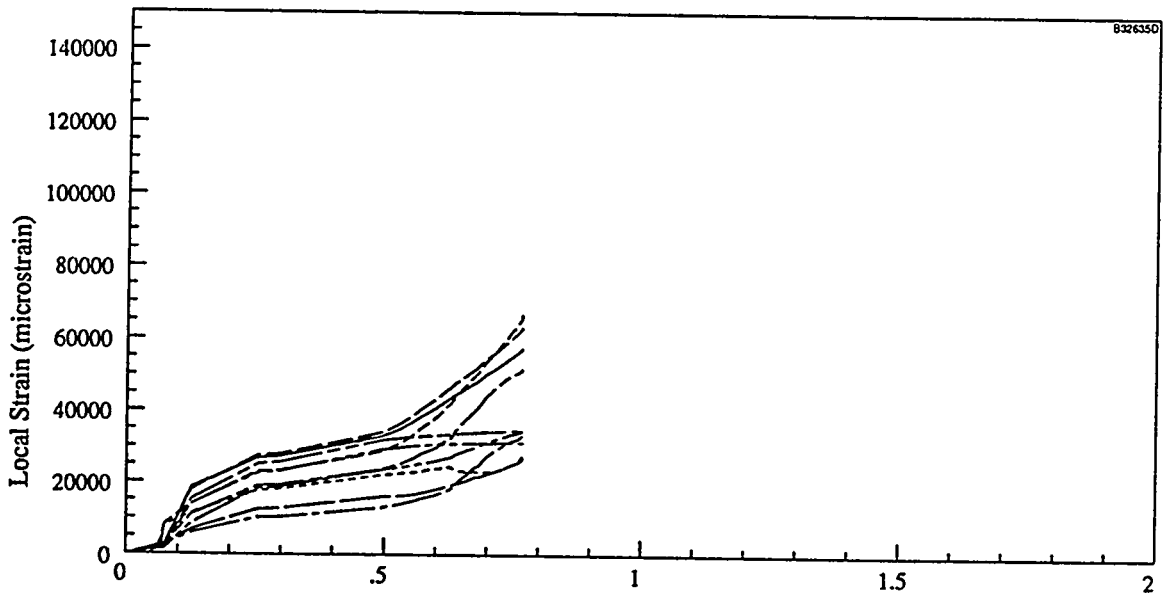

60 ksi Liner Stress

Inboard Axial Strain vs. Displacement Response

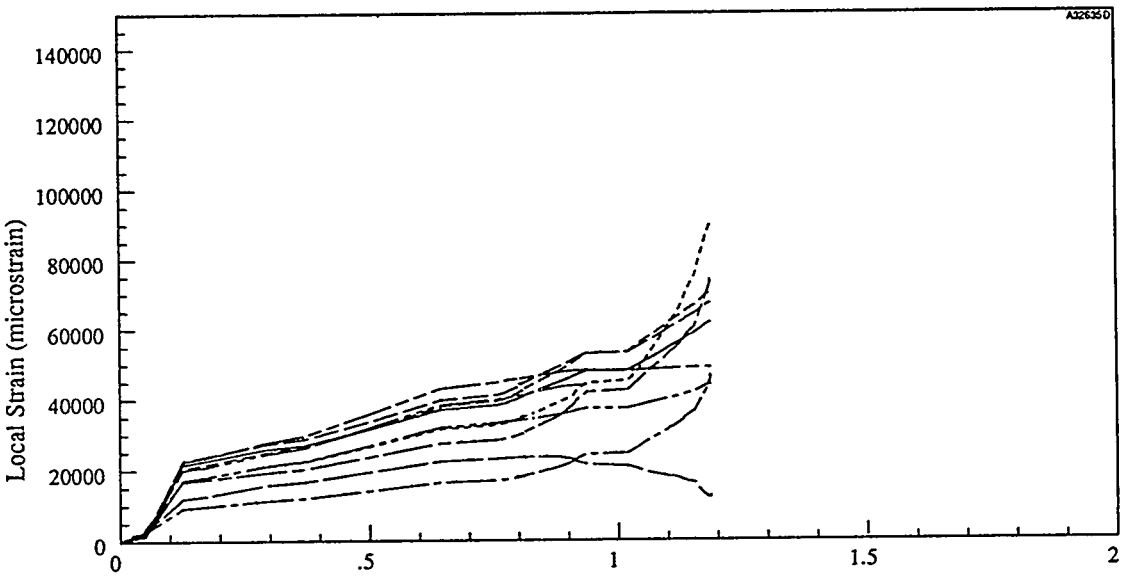

63 ksi Liner Stress

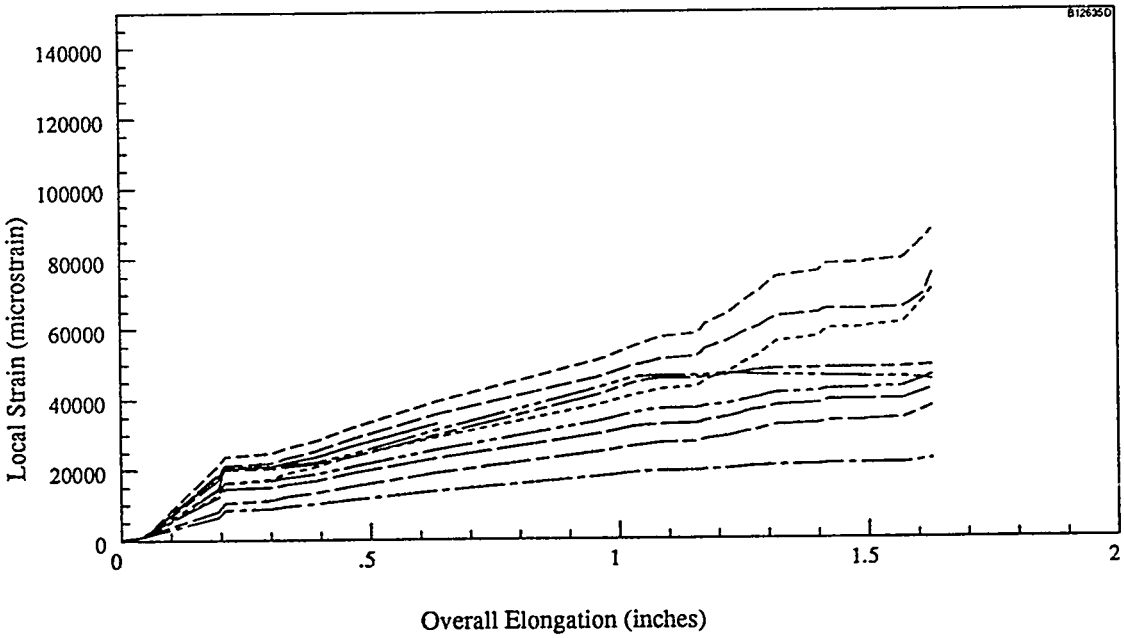

65 ksi Liner Stress

Inboard Axial Strain vs. Displacement Response (cont.)

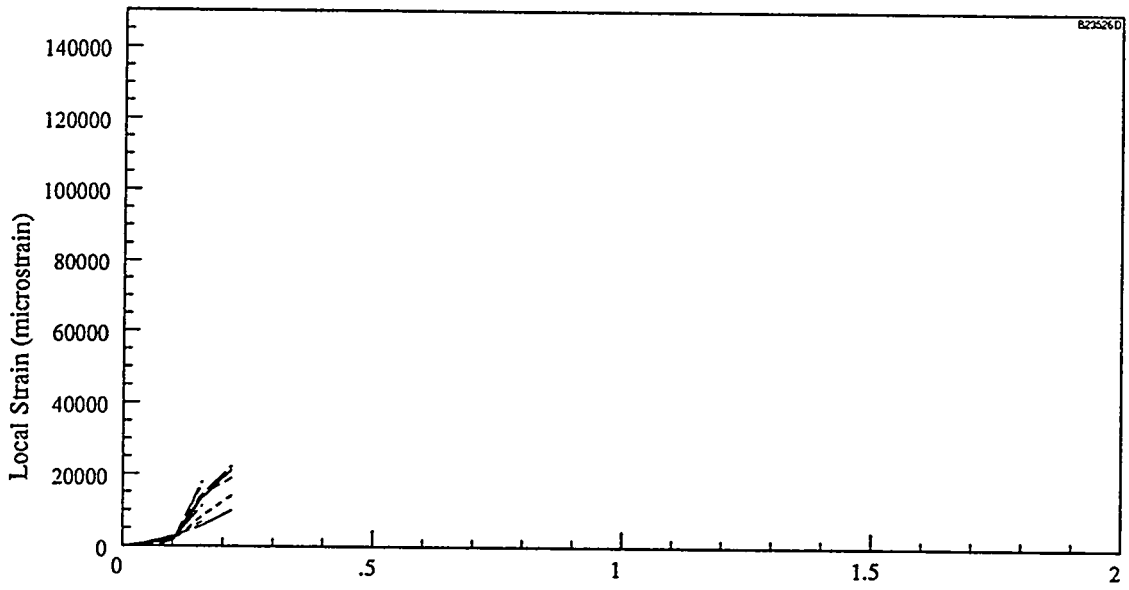

70 ksi Liner Stress

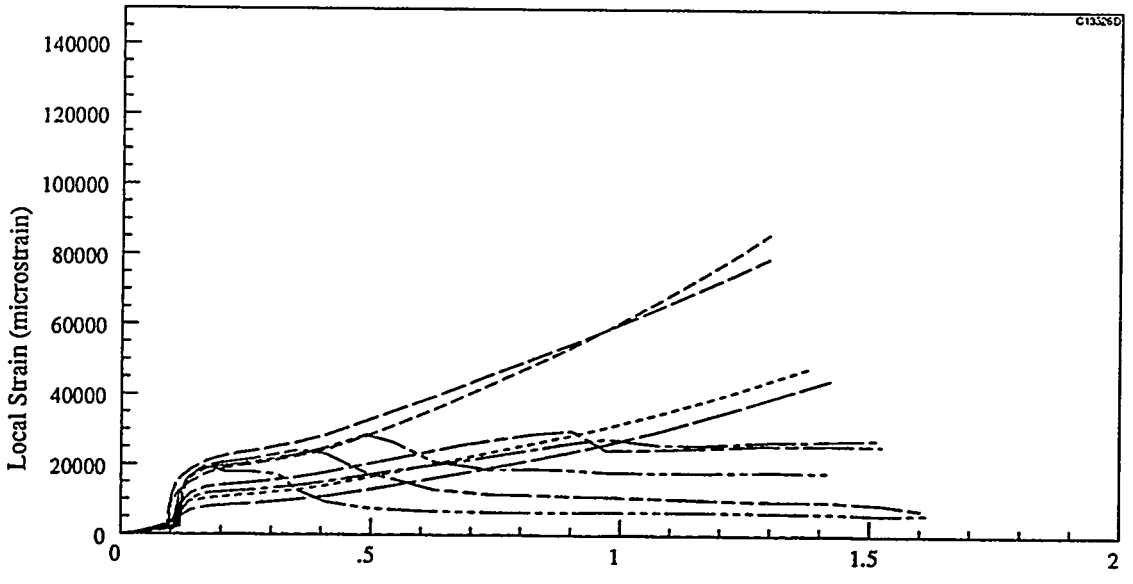

No Stud Load

Inboard Axial Strain vs. Displacement Response (cont.)

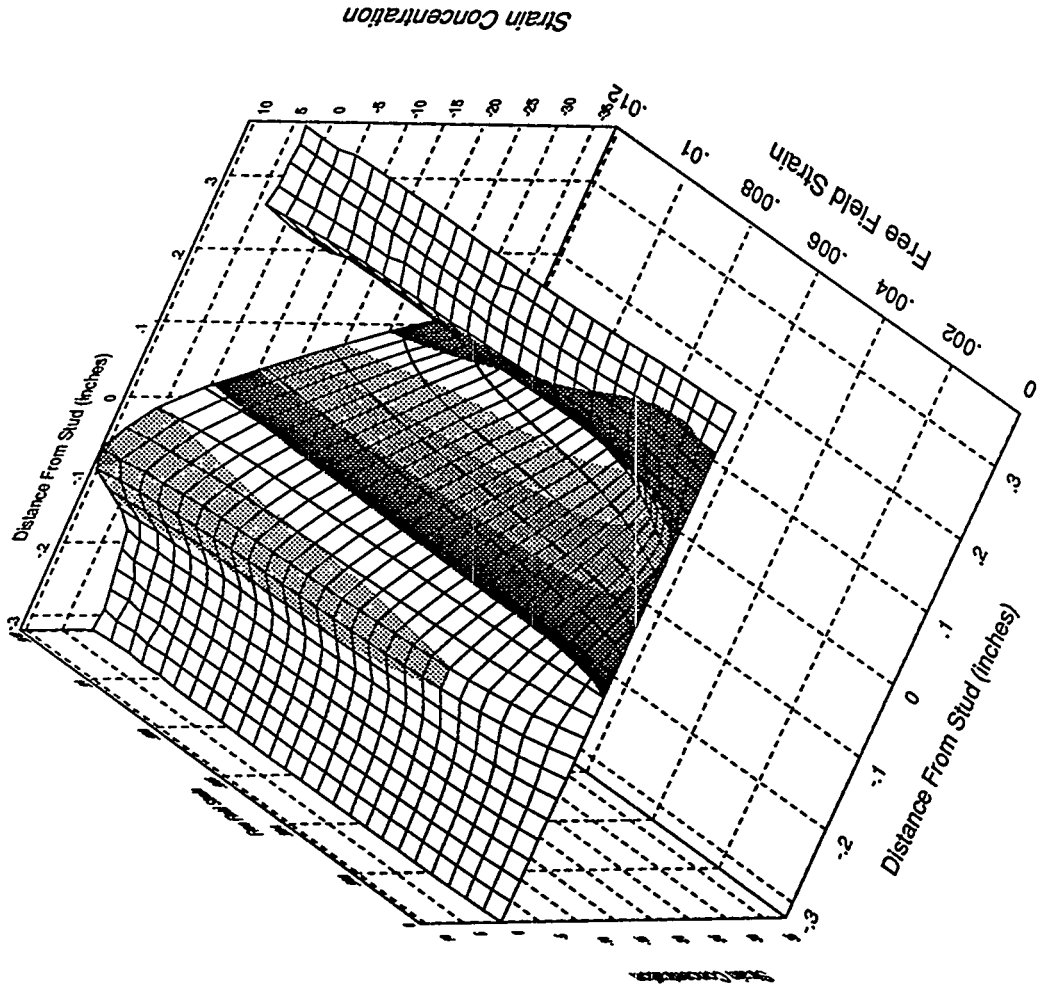

Inboard Axial Strip Gage,No Liner Prestress Specimen

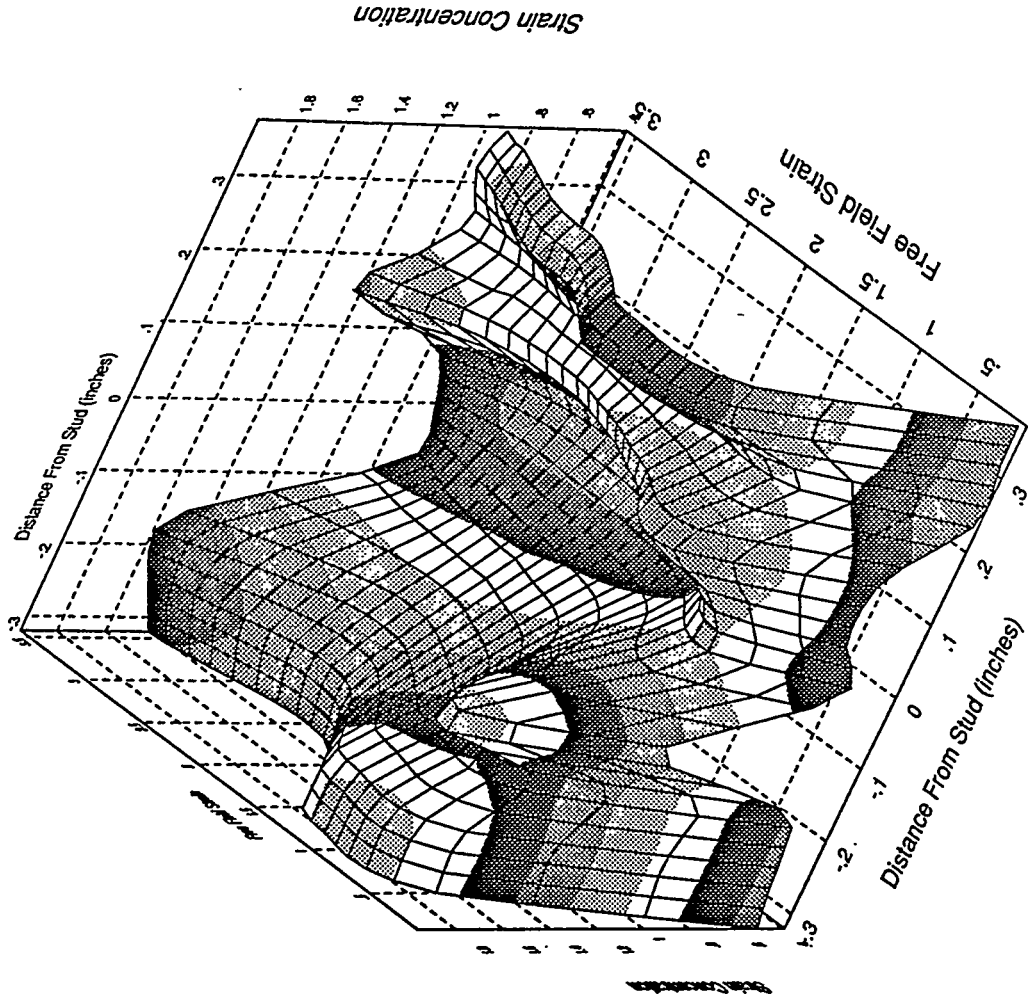

Inboard Axial Strip Gage,60 ksi Specimen

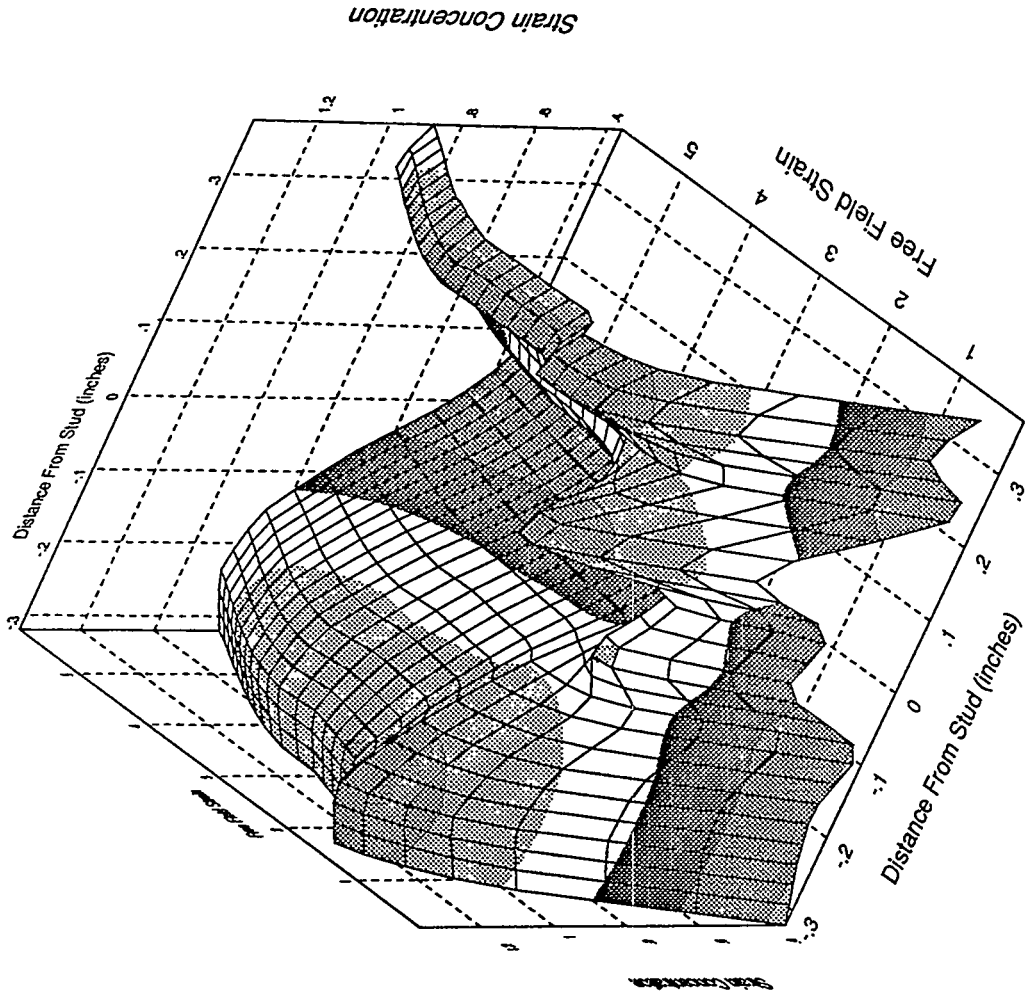

Inboard Axial Strip Gage,63 ksi Specimen

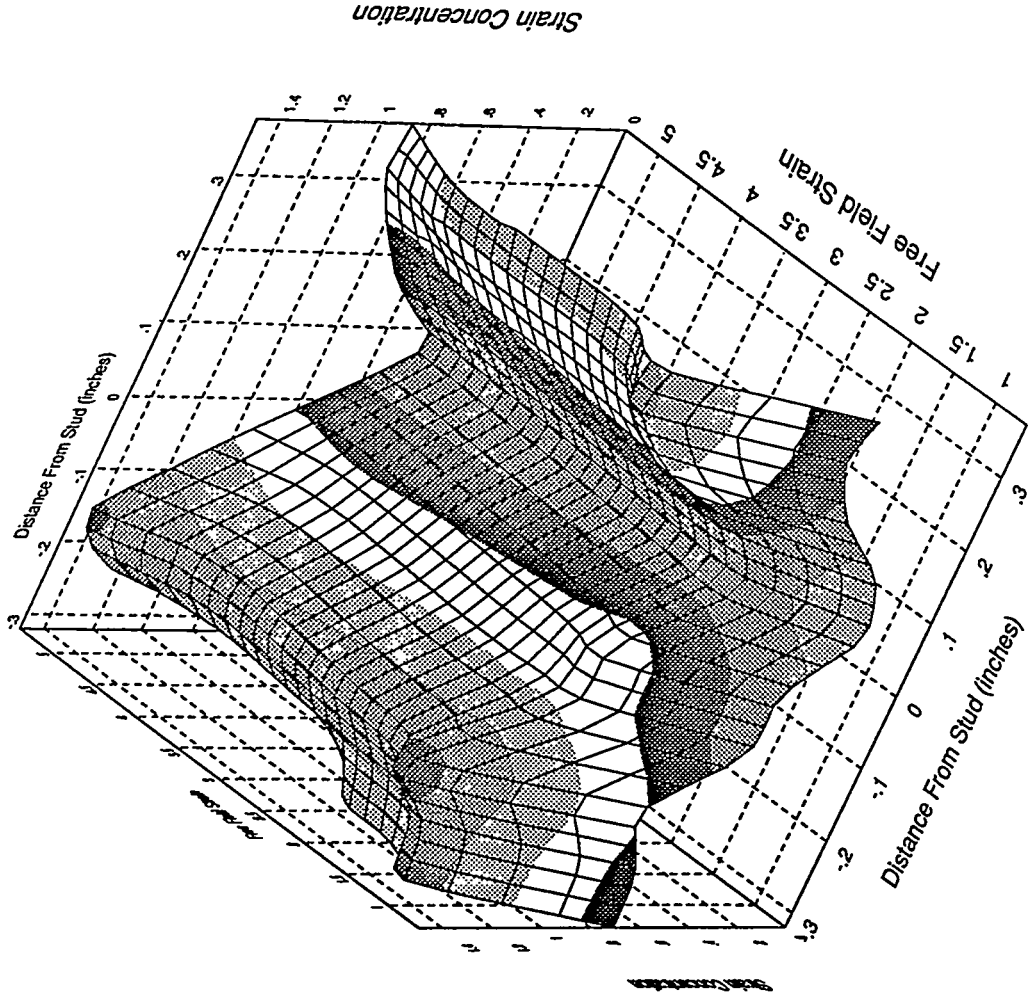

Inboard Axial Strip Gage,65 ksi Specimen

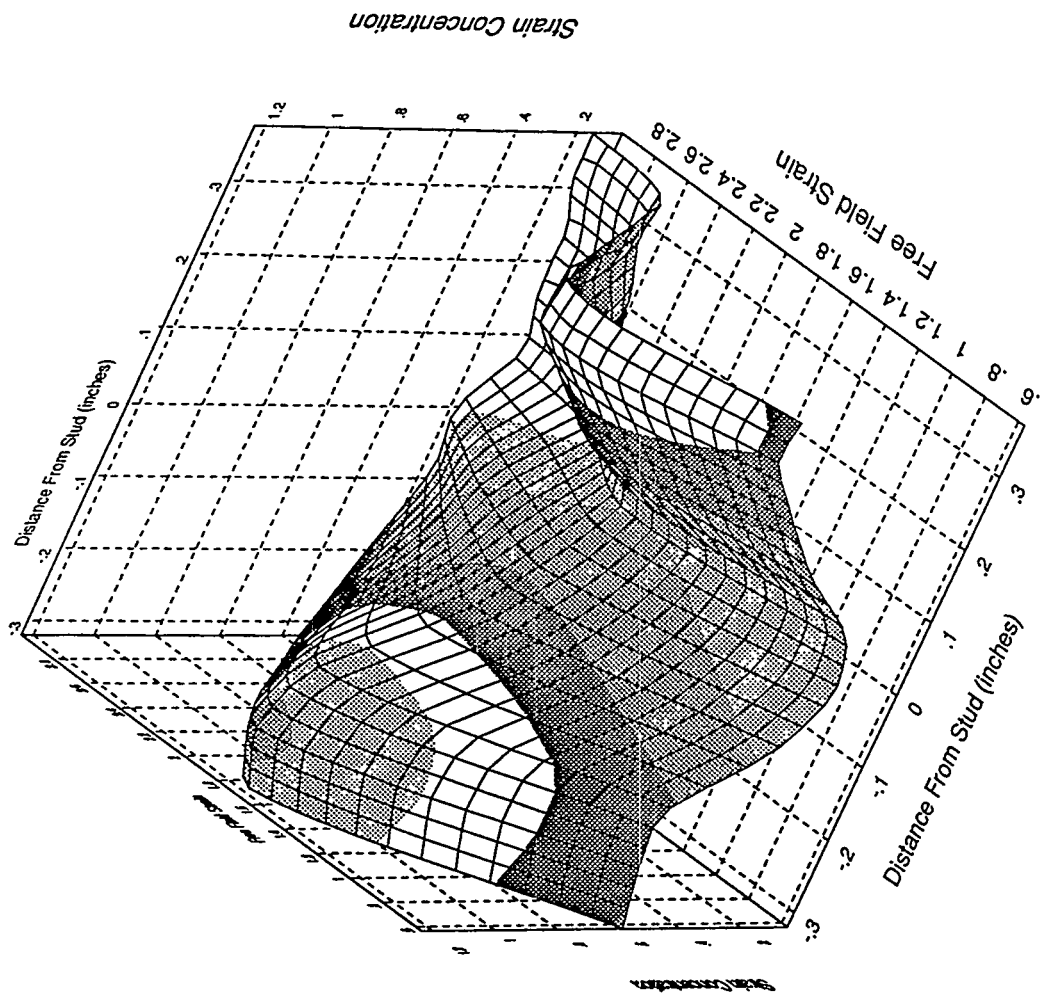

Inboard Axial Strip Gage,70 ksi Specimen

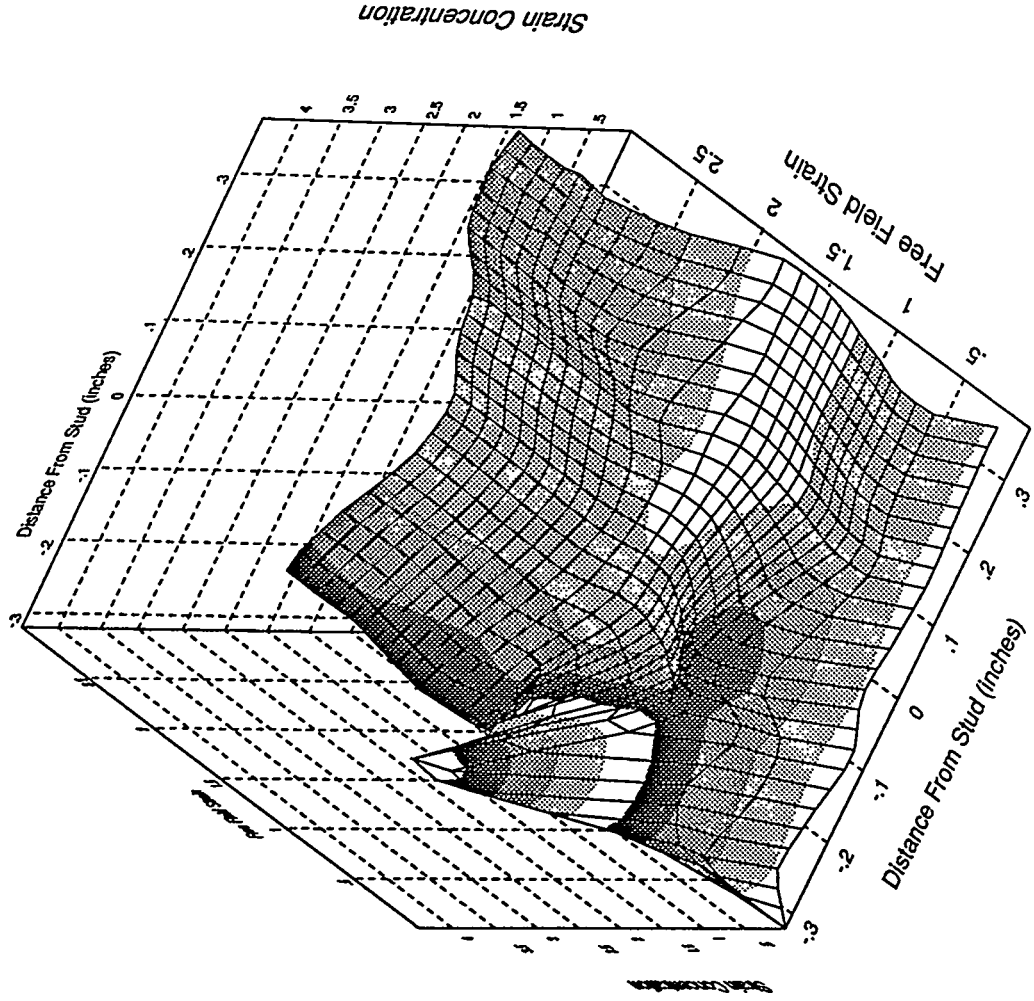

Inboard Axial Strip Gage,No Stud Load Specimen

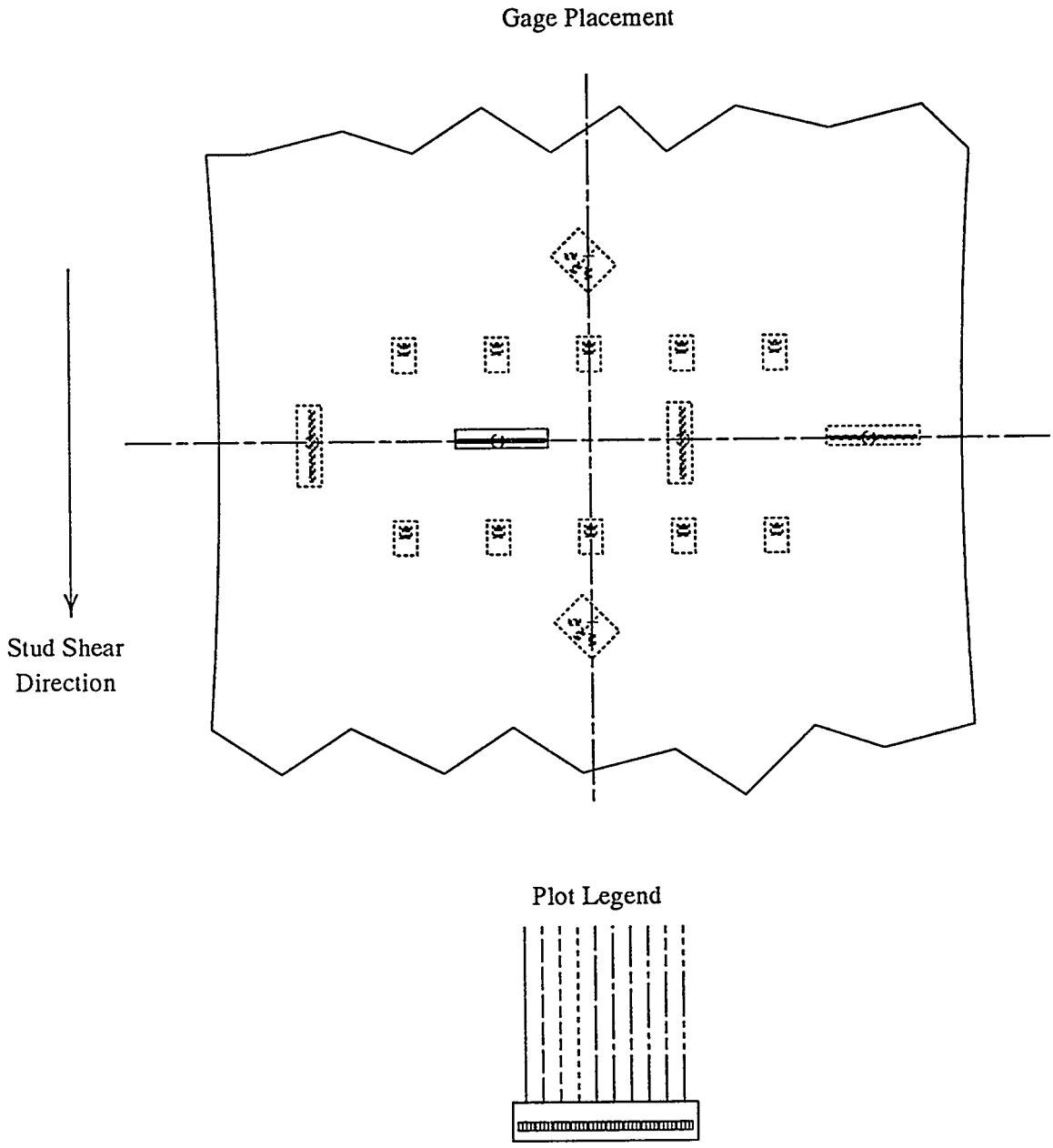

Inboard Transverse Strip Gage (All Specimens)

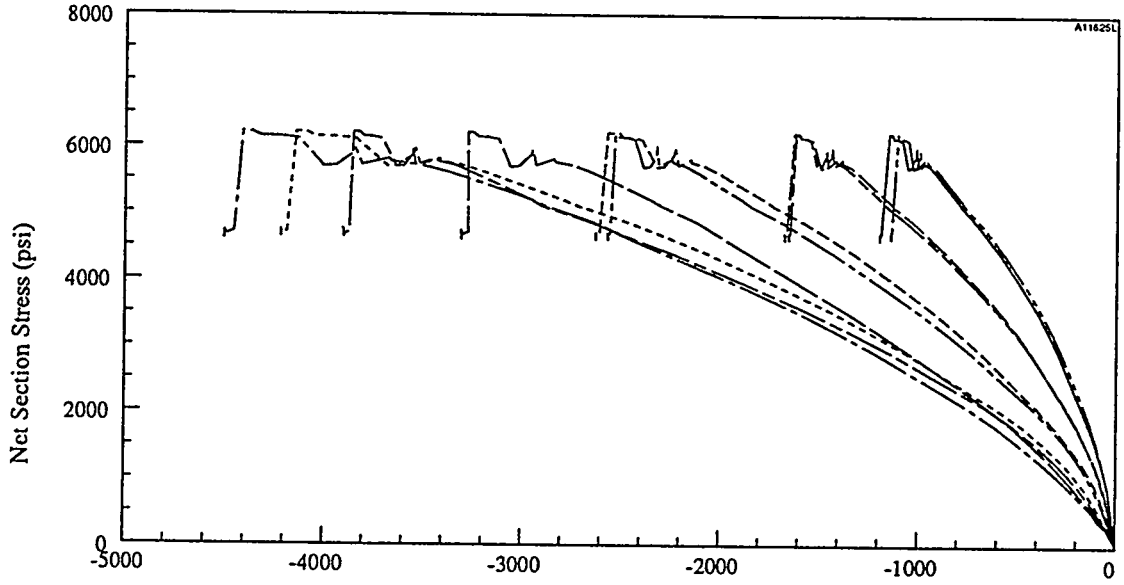

No Initial Liner Stress

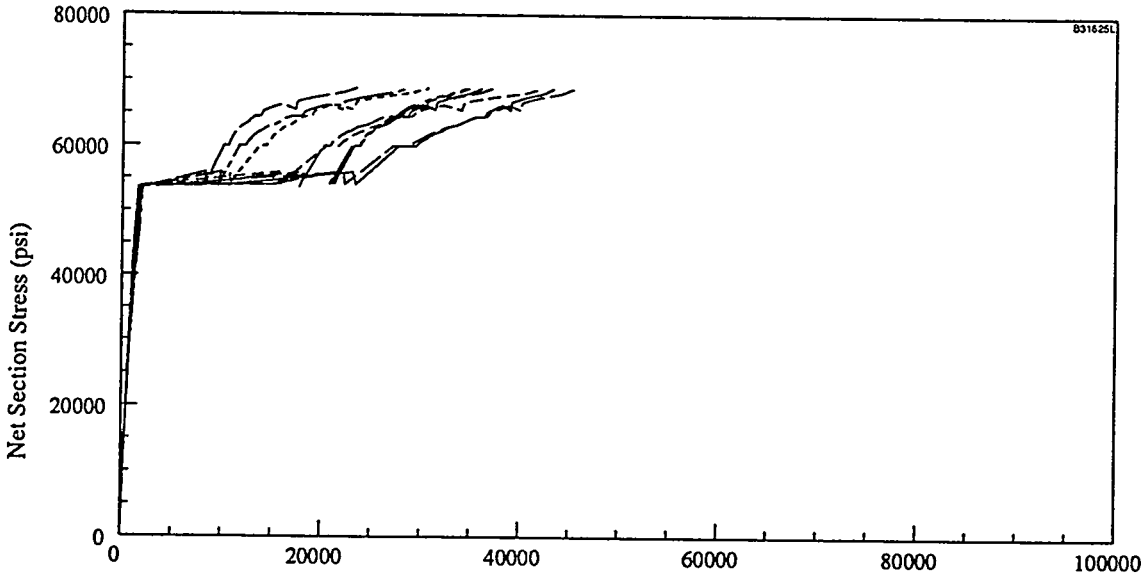

60 ksi Liner Stress

Inboard Strain Traverse vs. Load

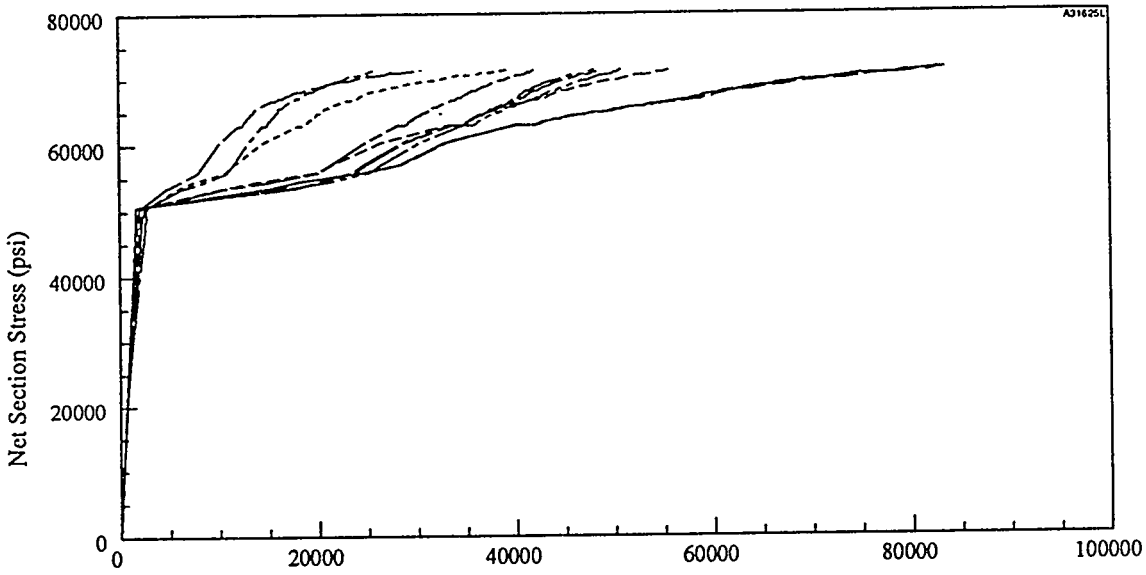

63 ksi Liner Stress

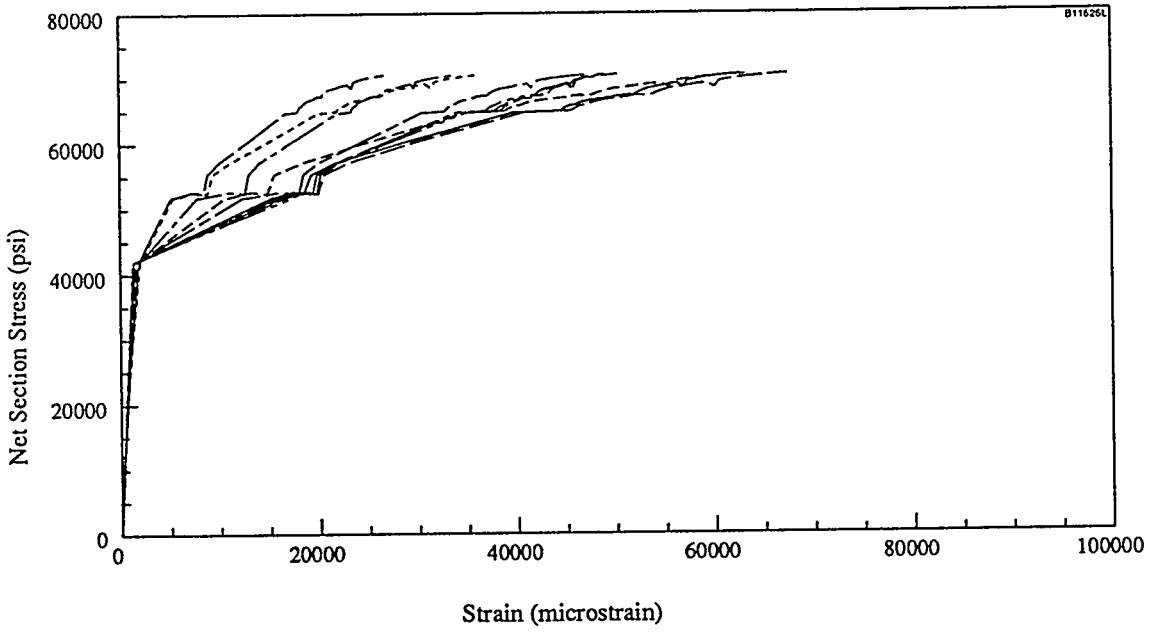

65 ksi Liner Stress

Inboard Strain Traverse vs.Load (cont.)

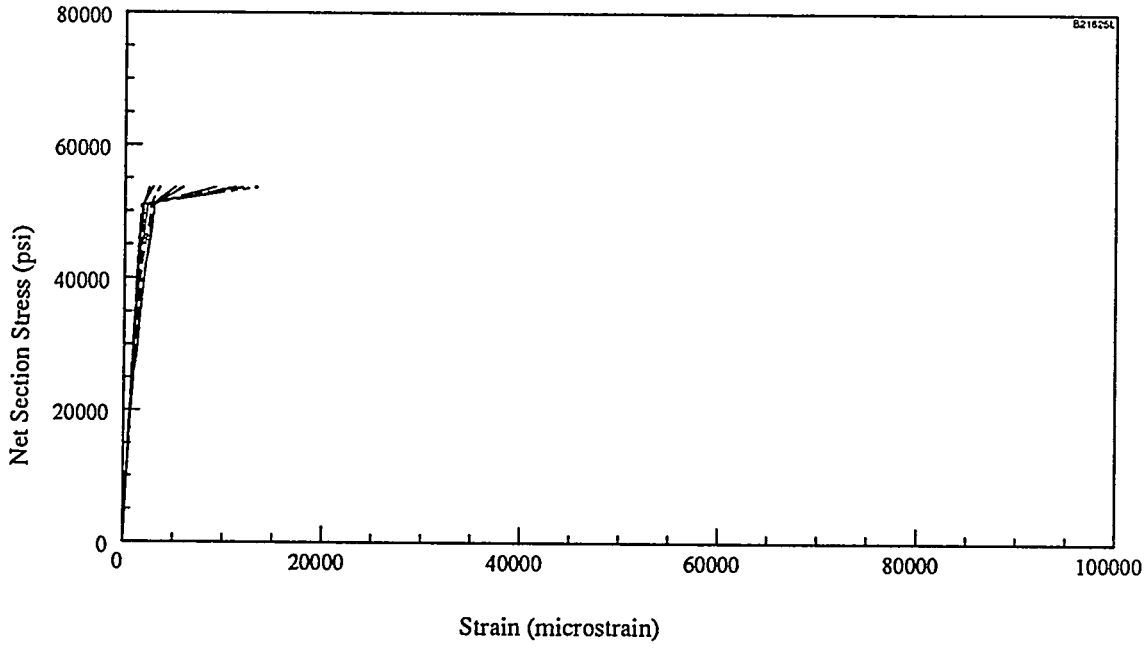

70 ksi Liner Stress

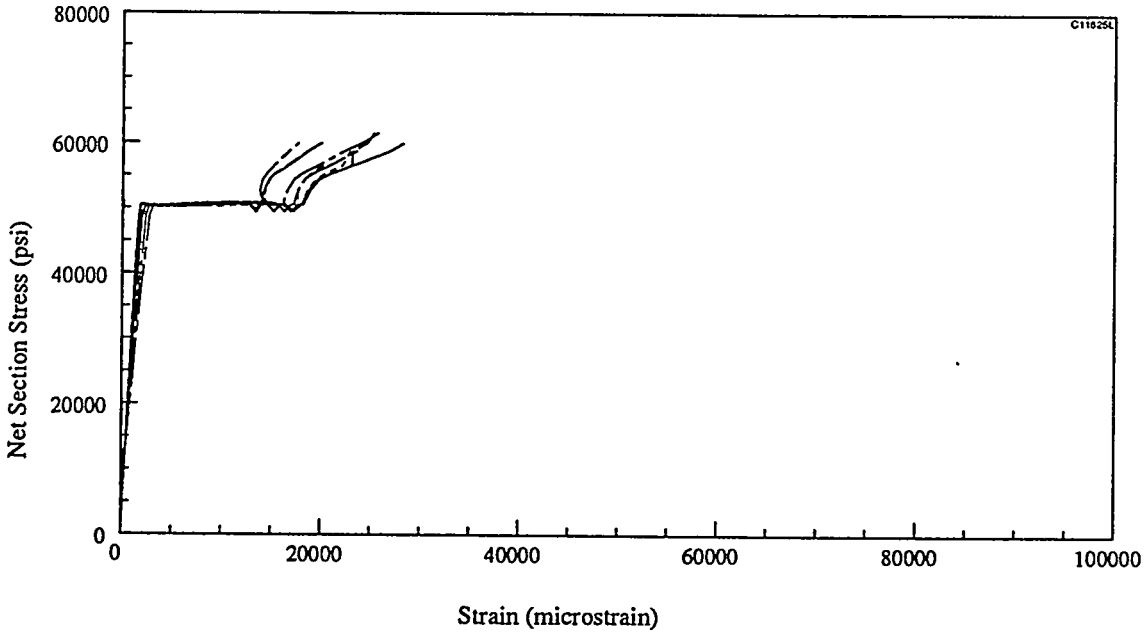

No Stud Load

Inboard Strain Traverse vs. Load (cont.)

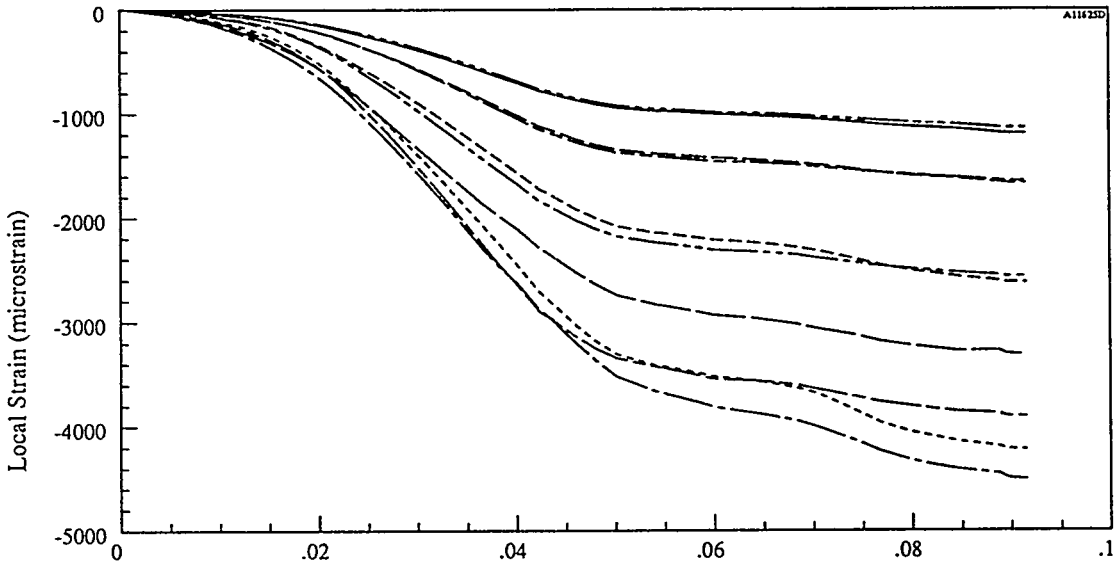

No Initial Liner Stress

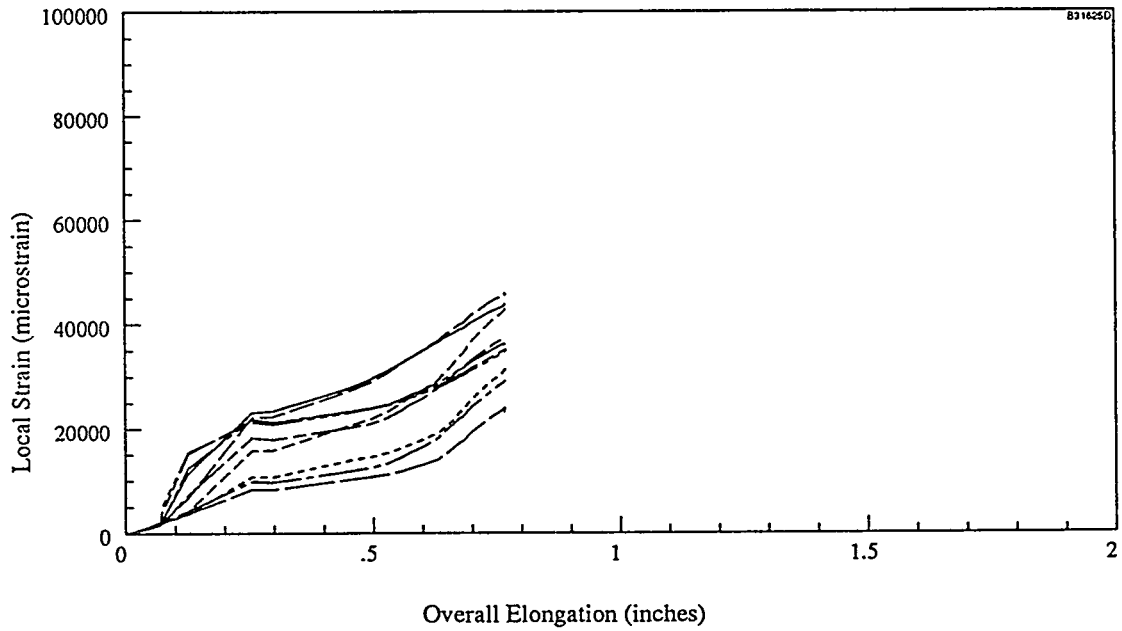

60 ksi Liner Stress

Inboard Strain Traverse vs. Displacement

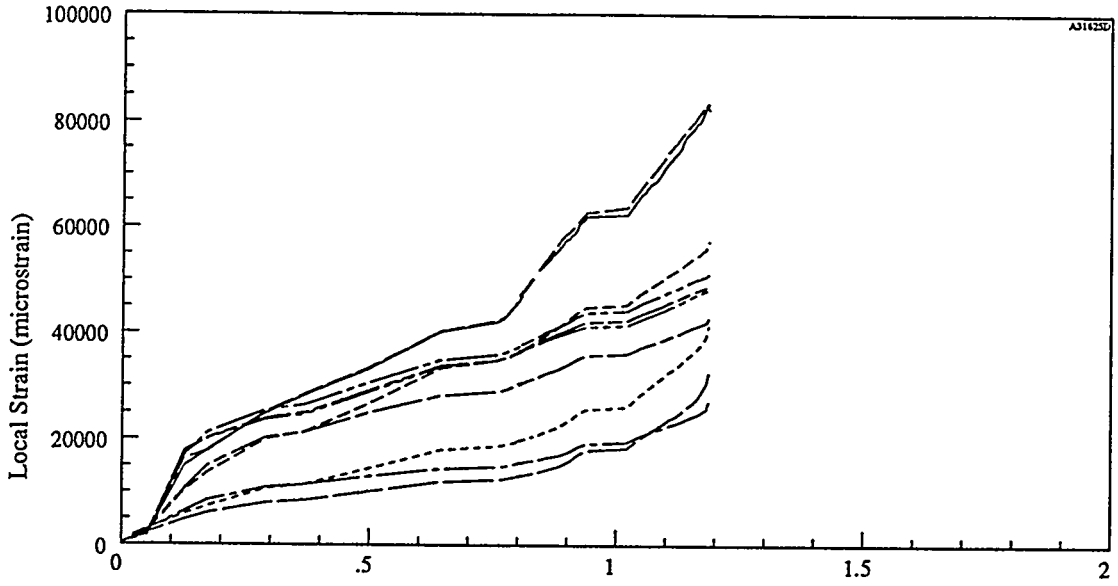

63 ksi Liner Stress

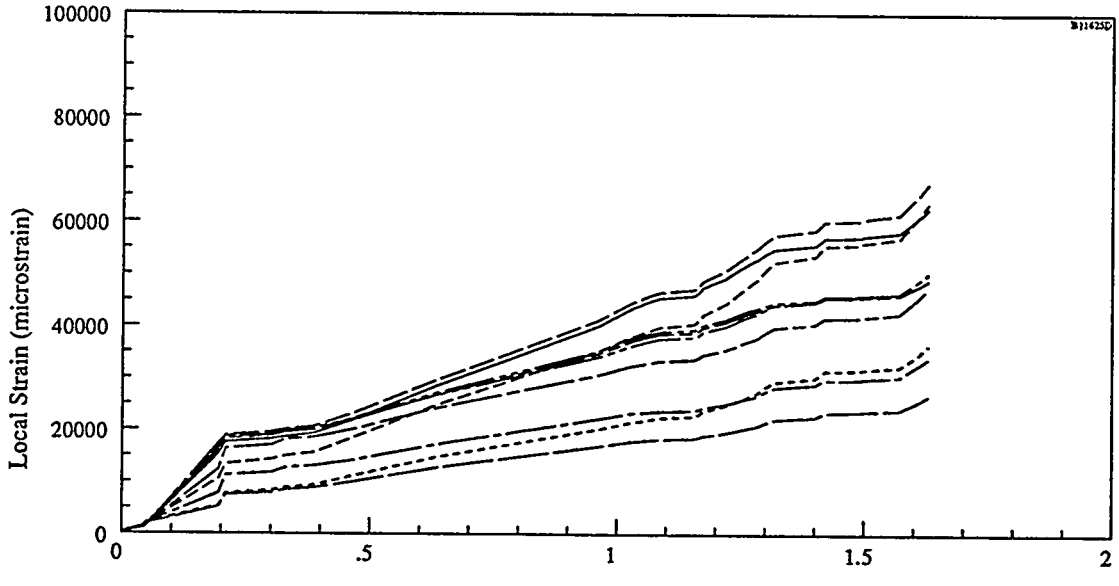

65 ksi Liner Stress

Inboard Strain Traverse vs.Displacement (cont.)

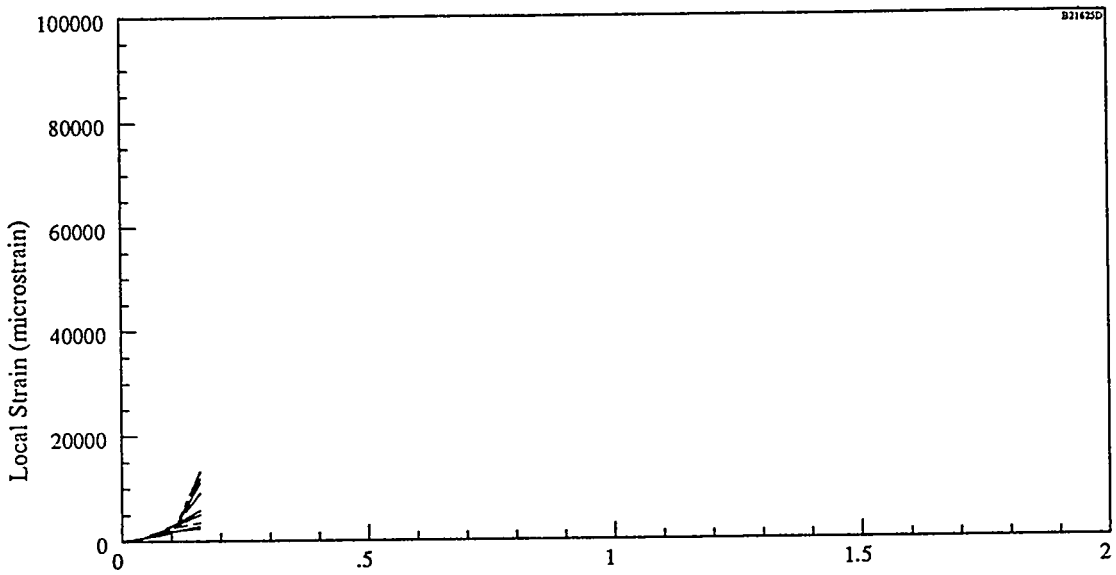

70 ksi Liner Stress

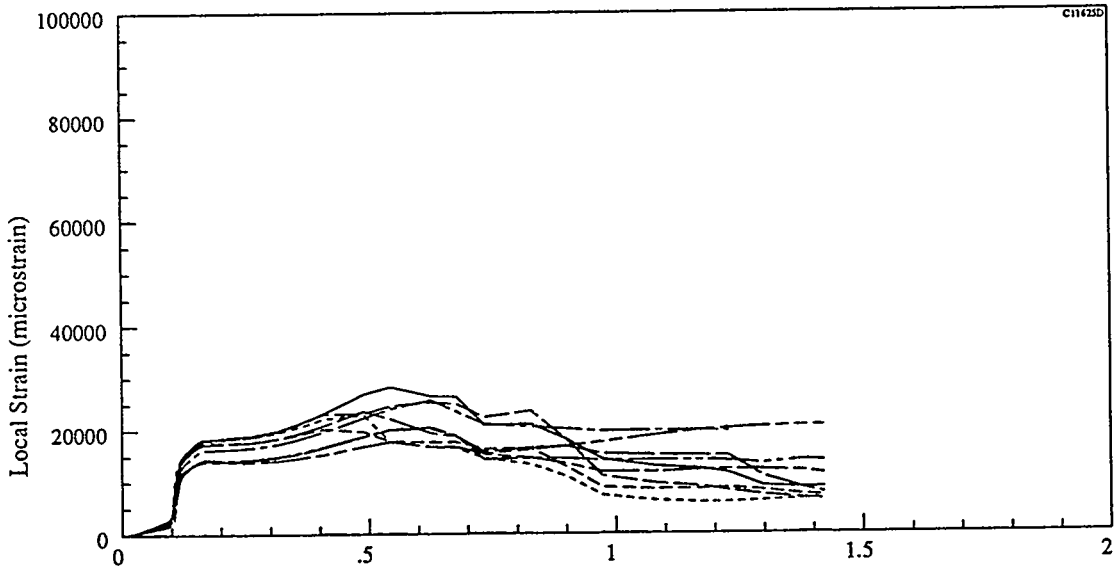

No Stud Load

Inboard Strain Traverse vs. Displacement (cont.)

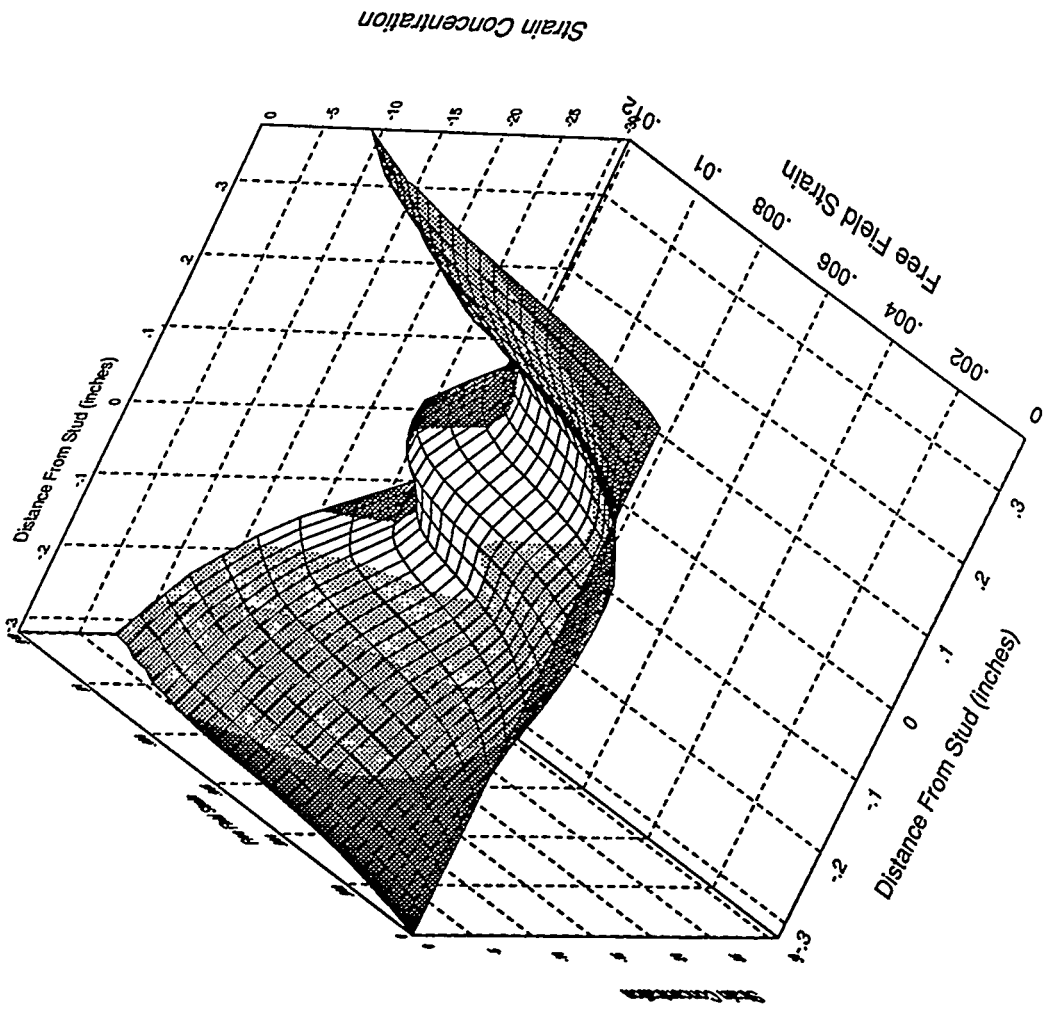

Inboard Transverse Strip Gage,No Liner Prestress Specimen

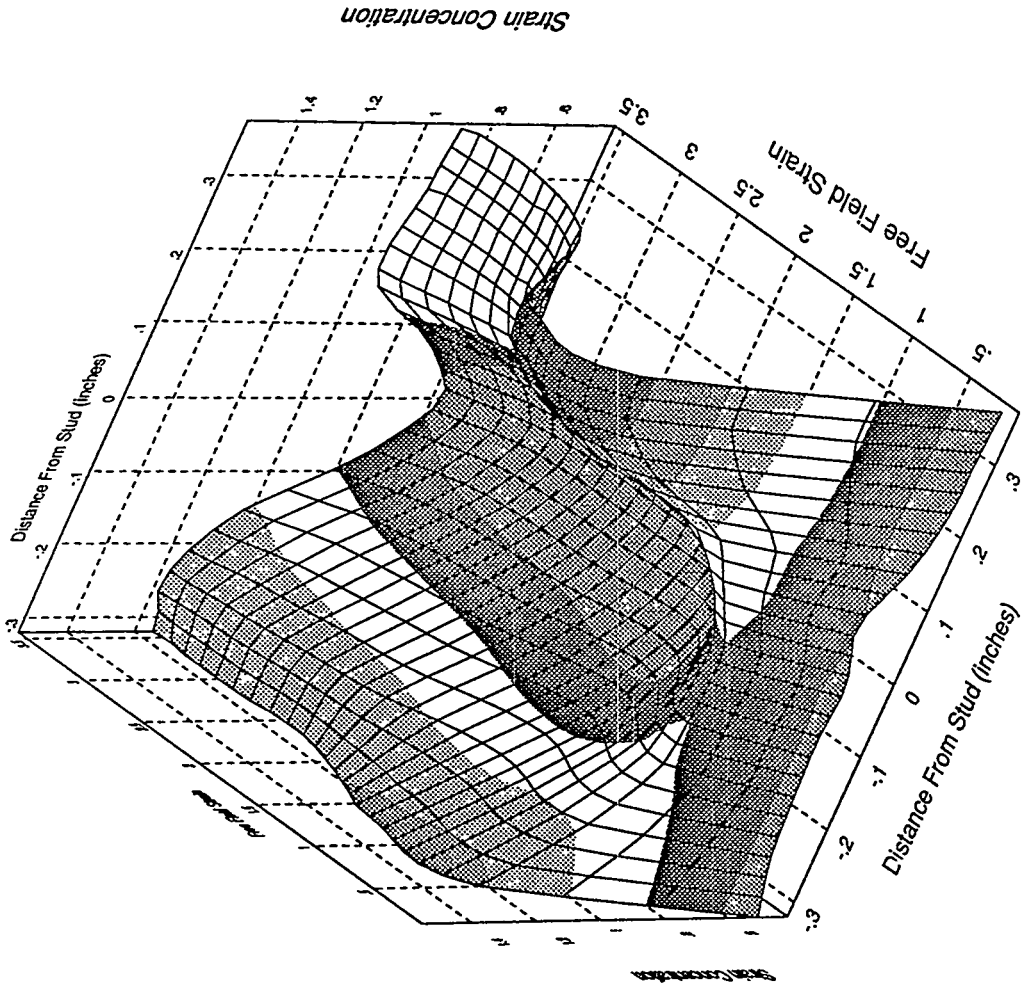

Inboard Transverse Strip Gage,60 ksi Specimen

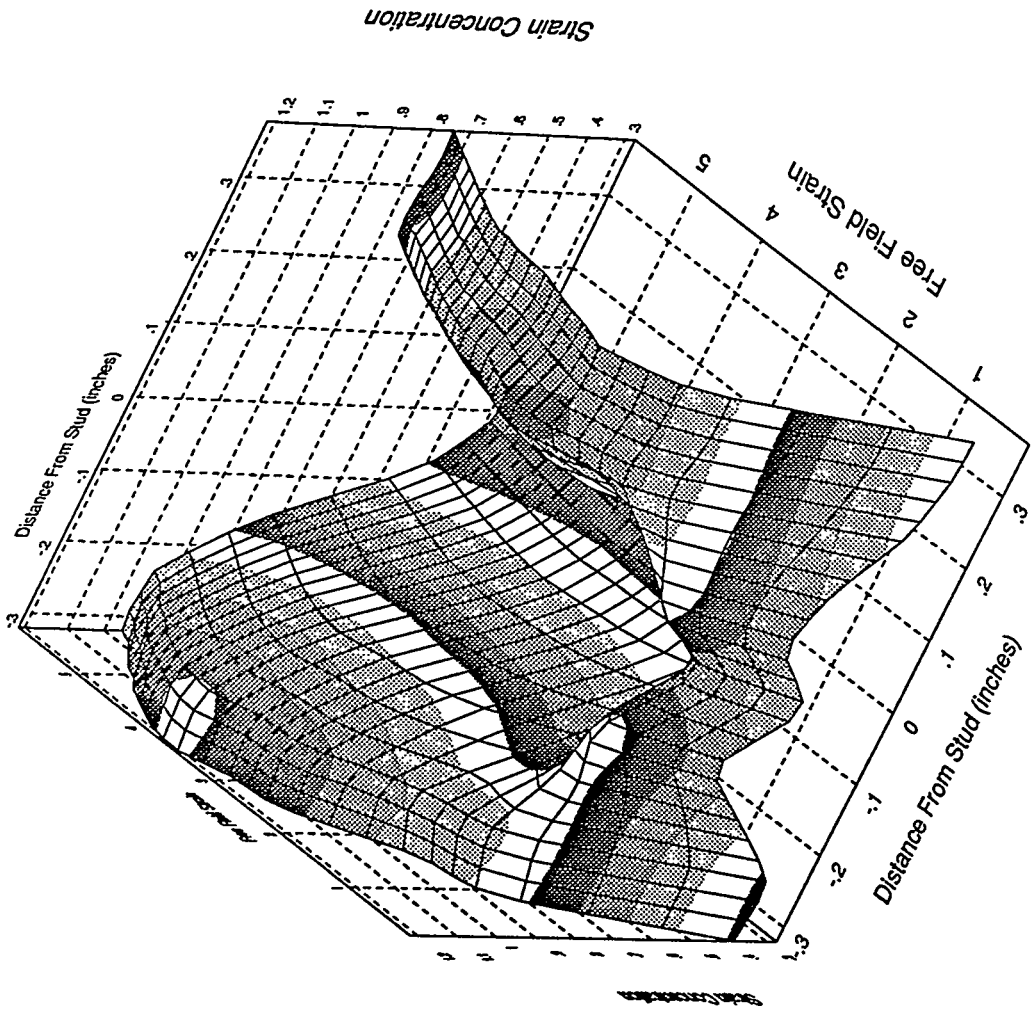

Inboard Transverse Strip Gage,63 ksi Specimen

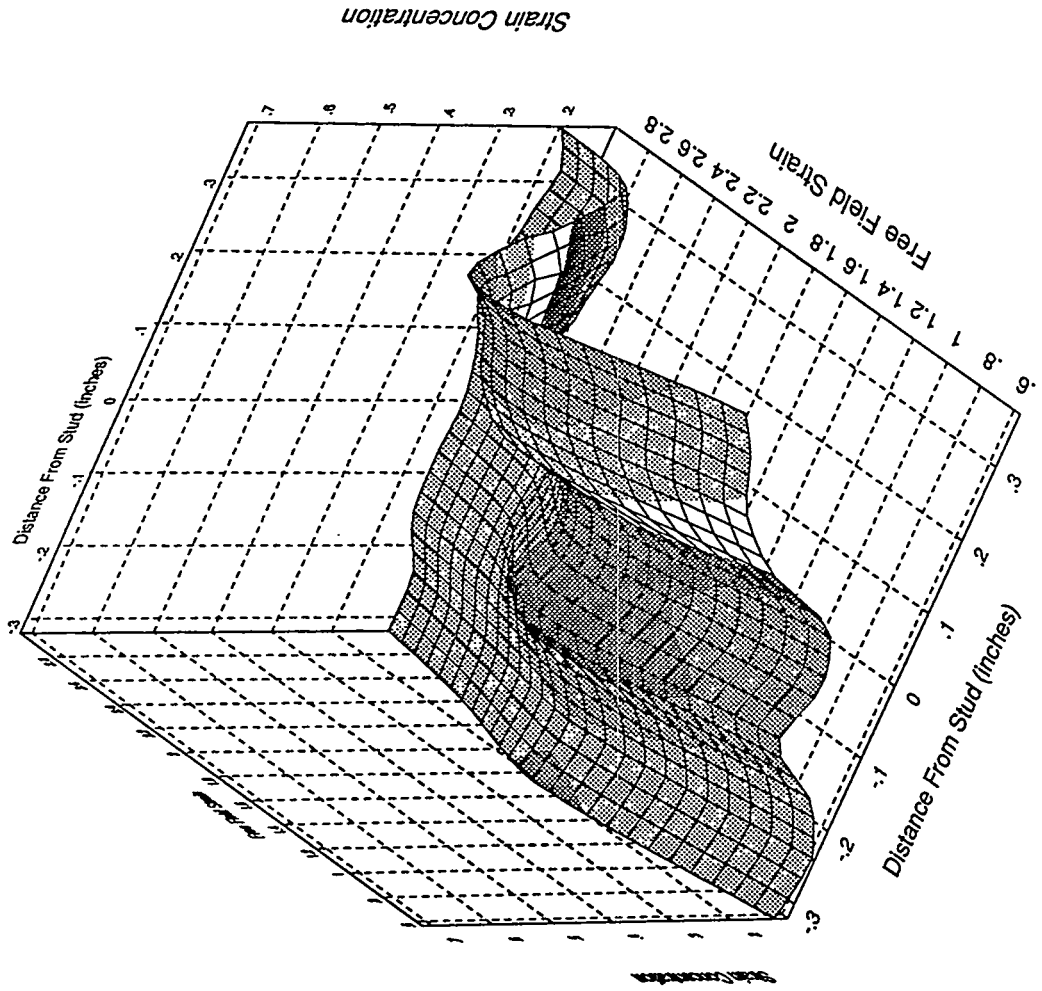

Inboard Transverse Strip Gage,70 ksi Specimen

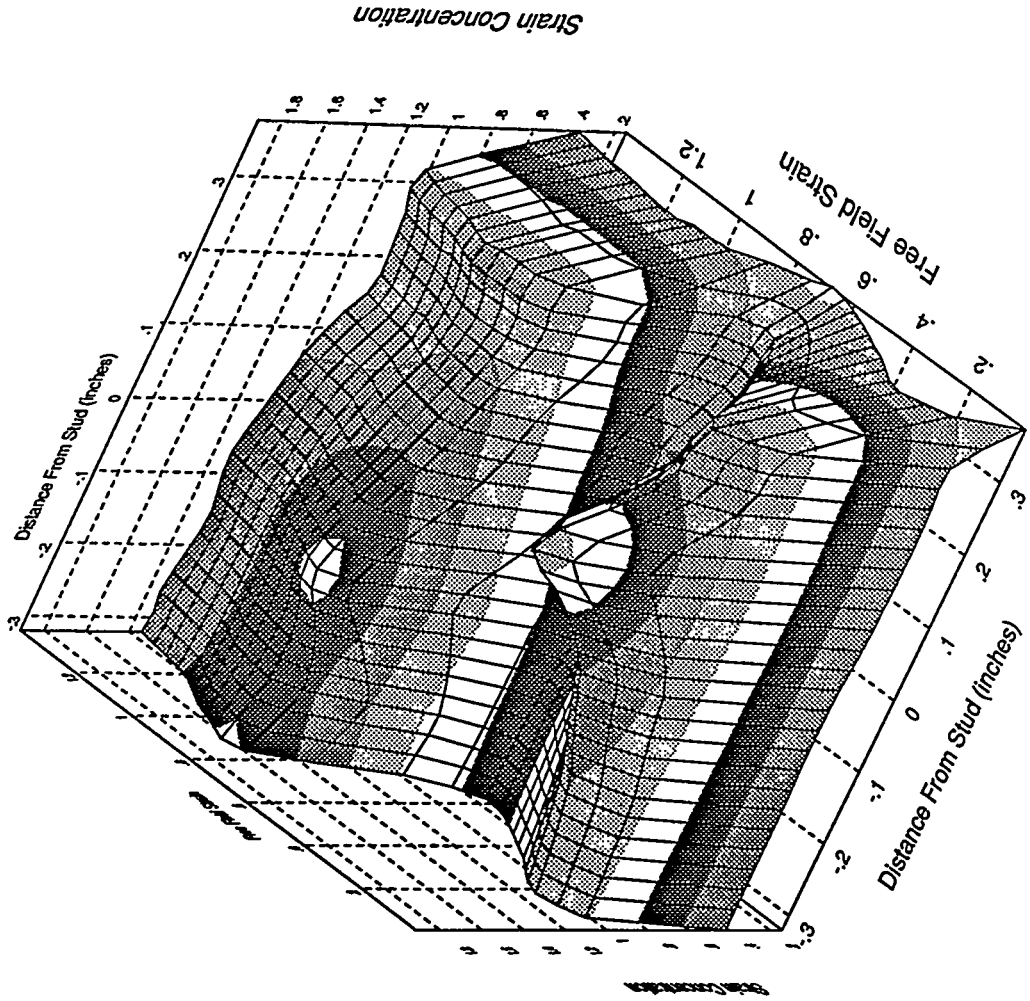

Inboard Transverse Strip Gage,No Stud Load Specimen

Gage Placement

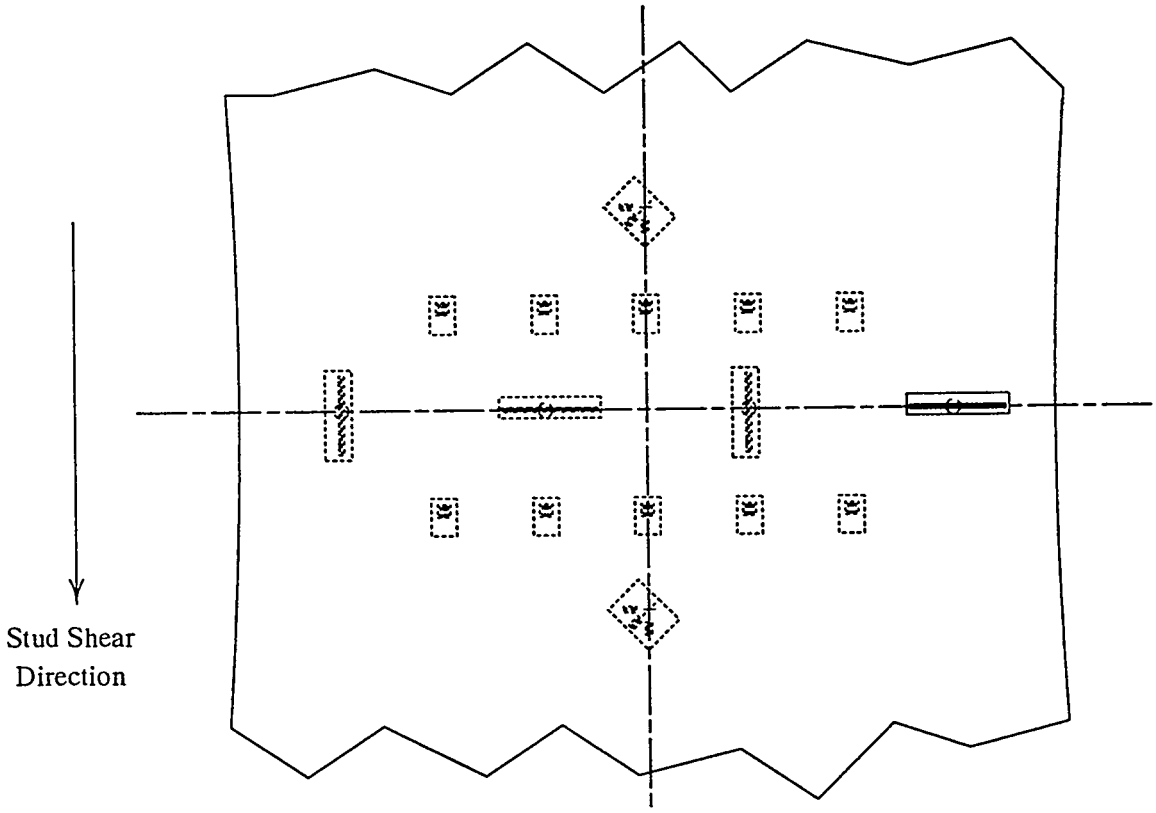

Plot Legend

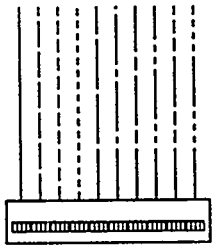

Outboard Transverse Strip Gage
(Liner Only, and Stud Load Only specimens)

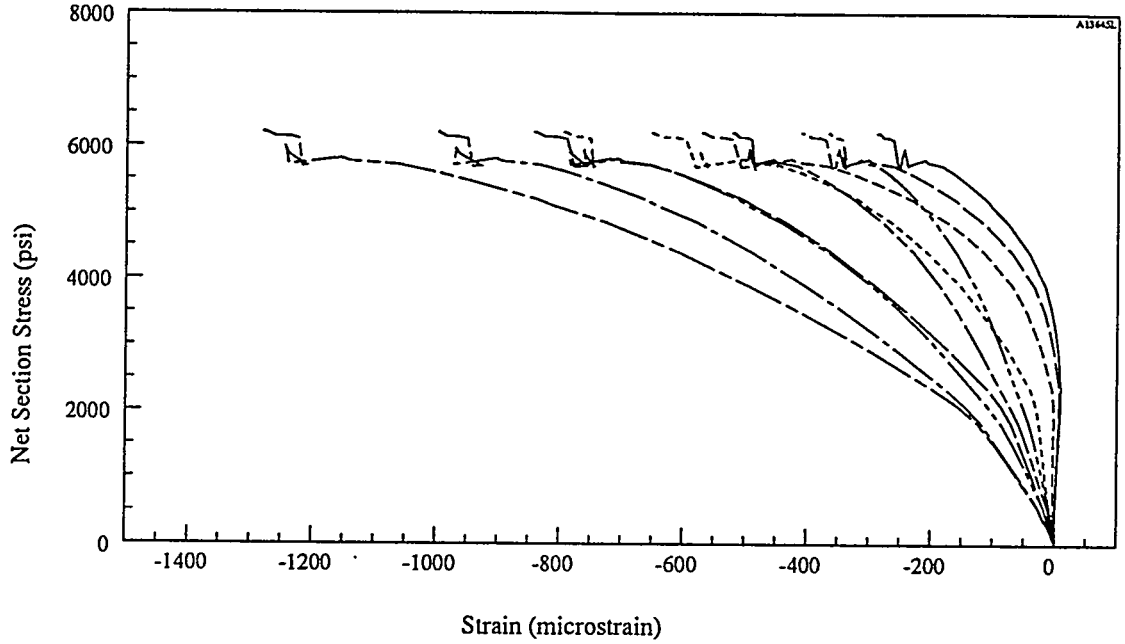

No Initial Liner Stress

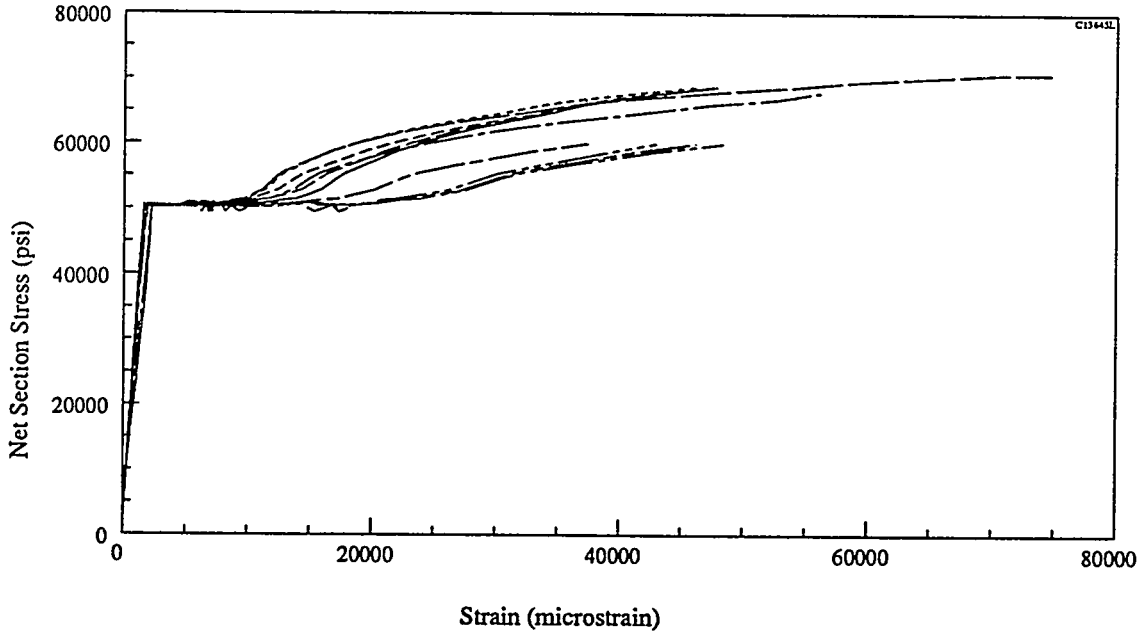

No Stud Load

Outboard Strain Traverse vs. Load

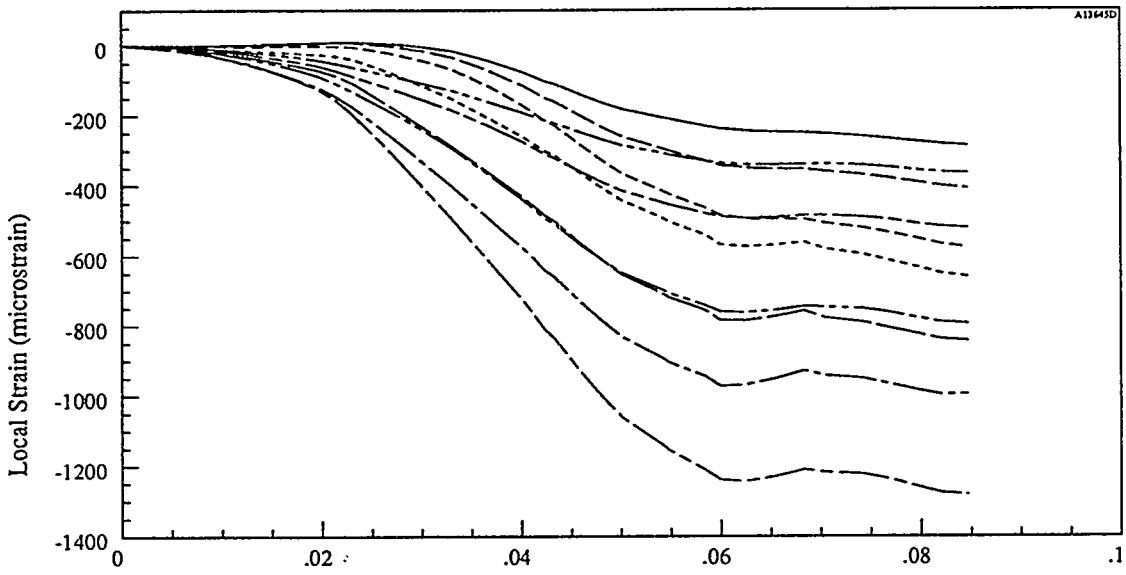

No Initial Liner Stress

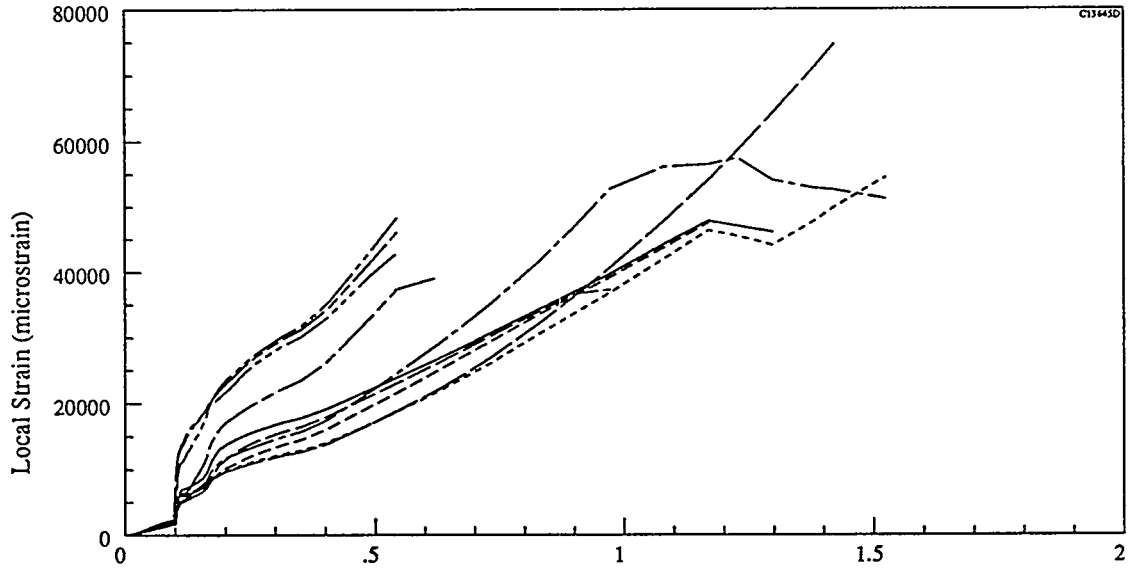

No Stud Load

Outboard Strain Traverse vs. Displacement

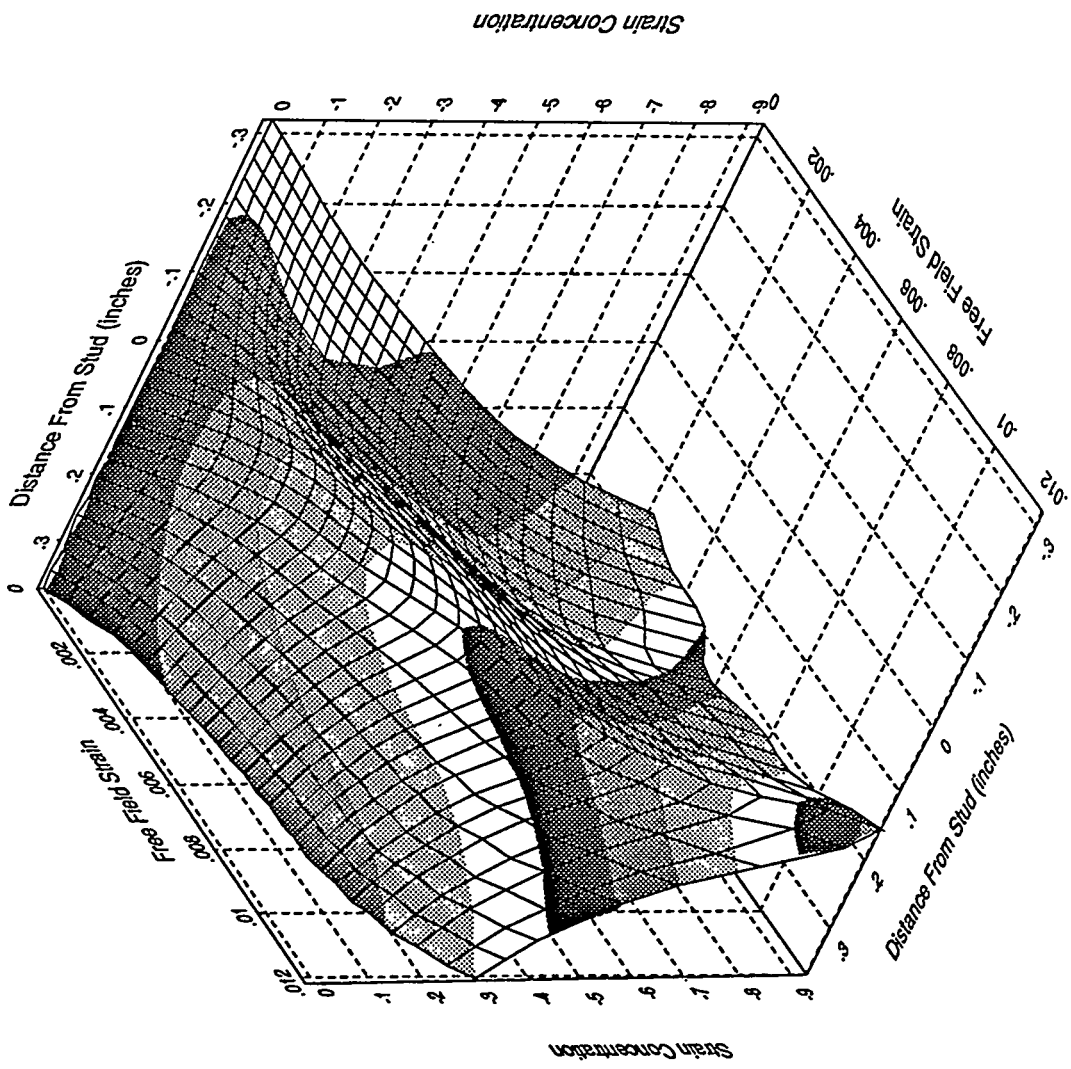

Outboard Transverse Strip Gage,No Liner Prestress Specimen

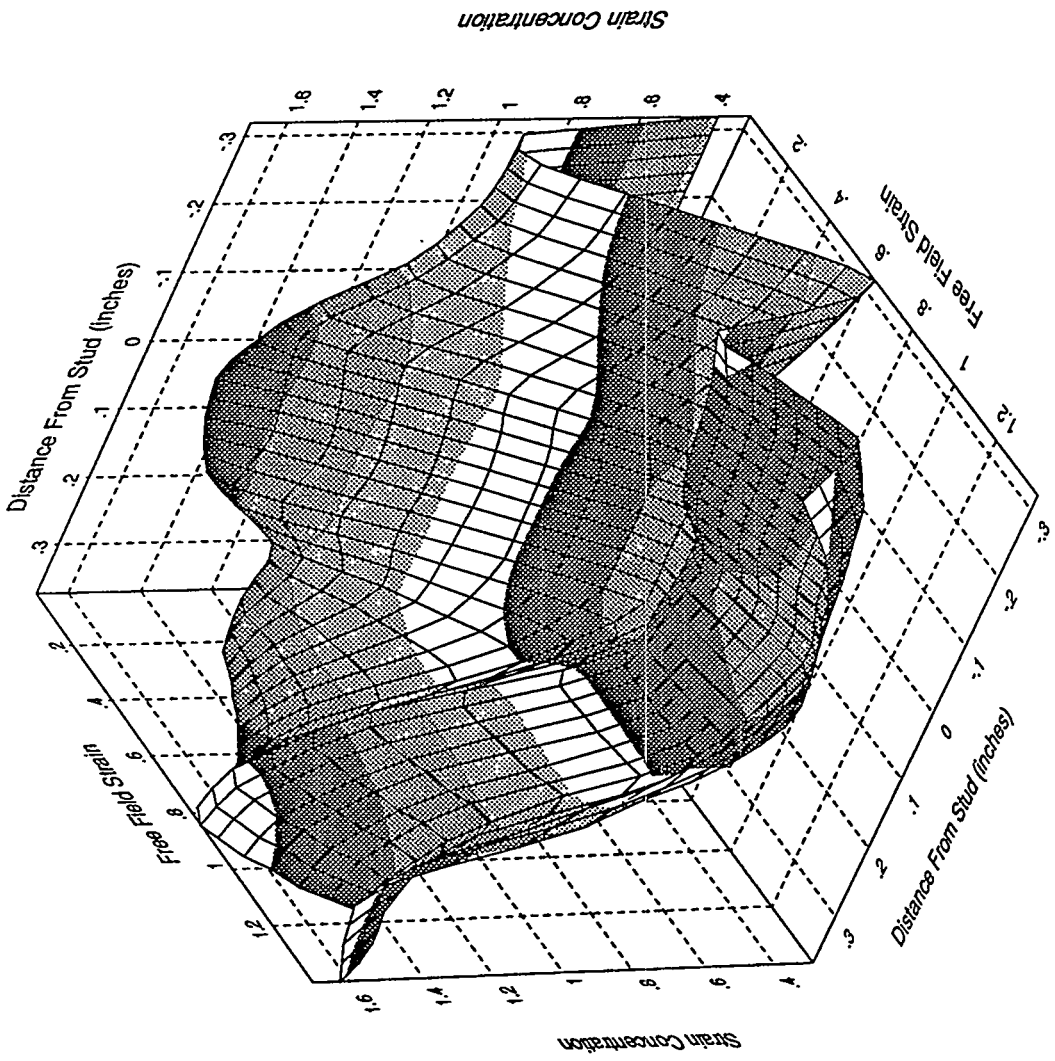

Outboard Transverse Strip Gage,No Stud Load Specimen

Gage Placement

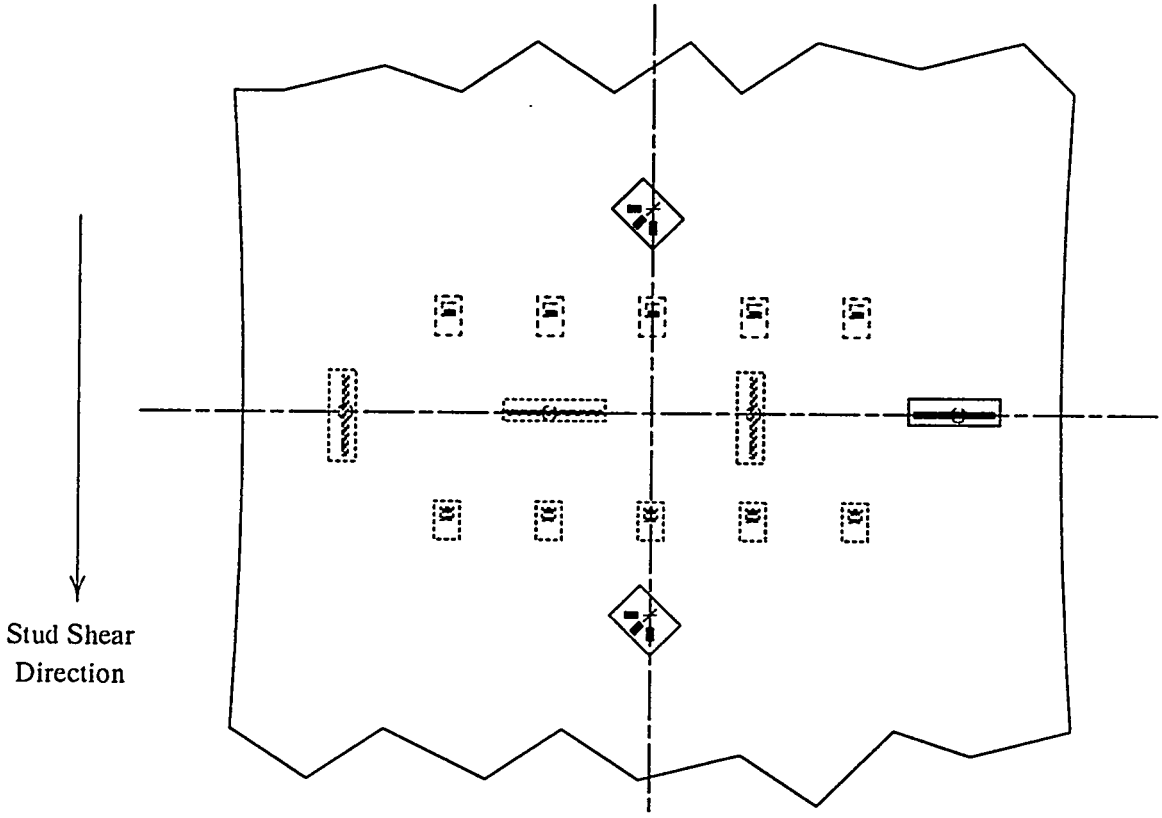

Plot Legend

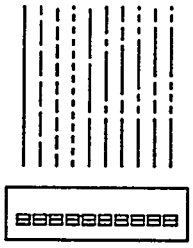

Poisson Strip Gage
(60 ksi, 63 ksi, 65 ksi and 70 ksi specimens)

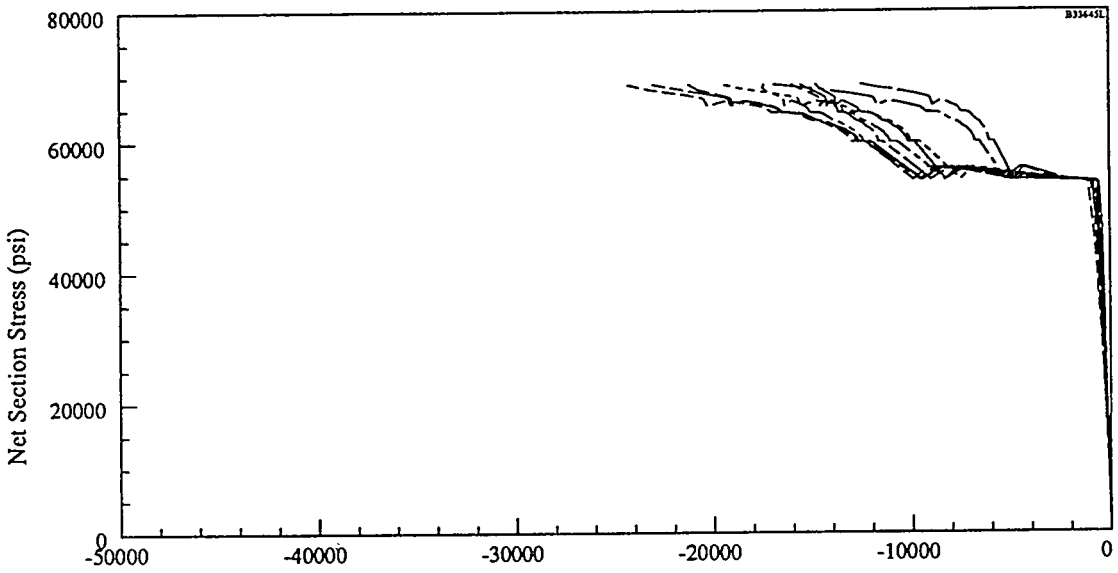

60 ksi Liner Stress

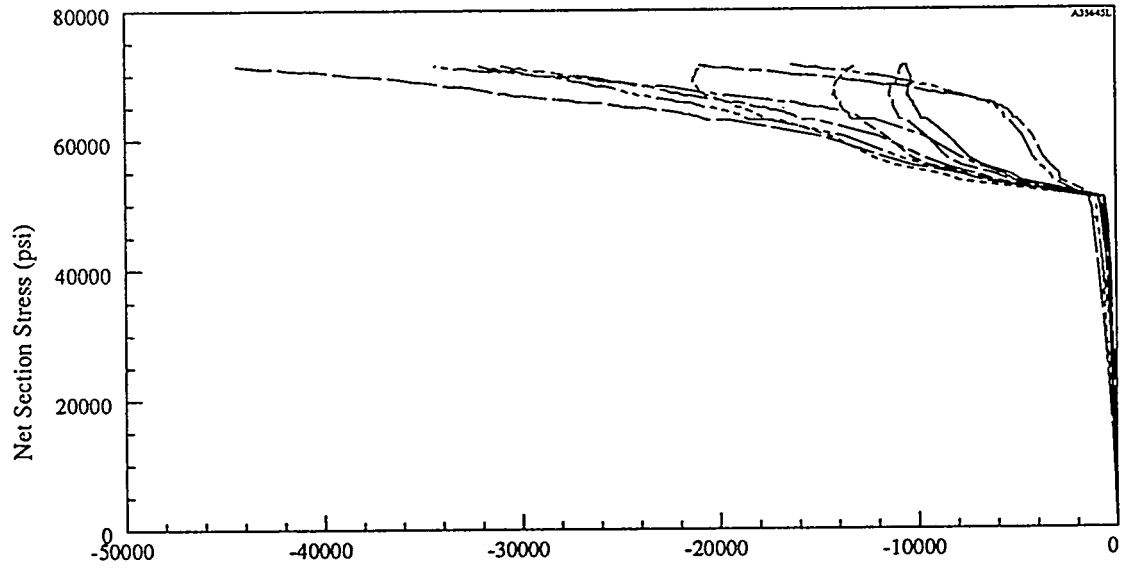

63 ksi Liner Stress

Outboard Poisson Traverse vs. Load

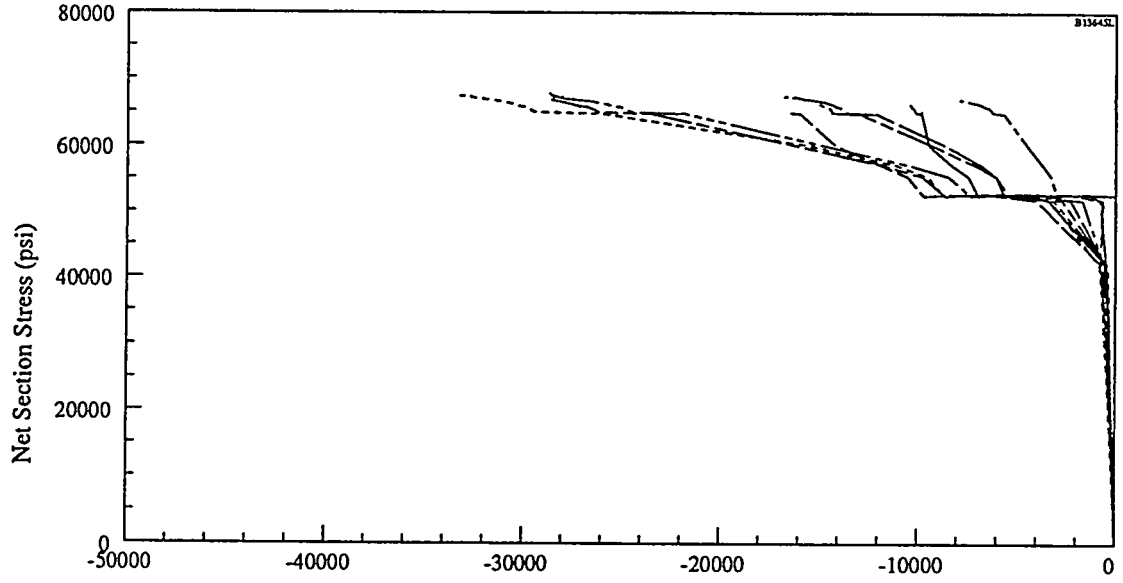

65 ksi Liner Stress

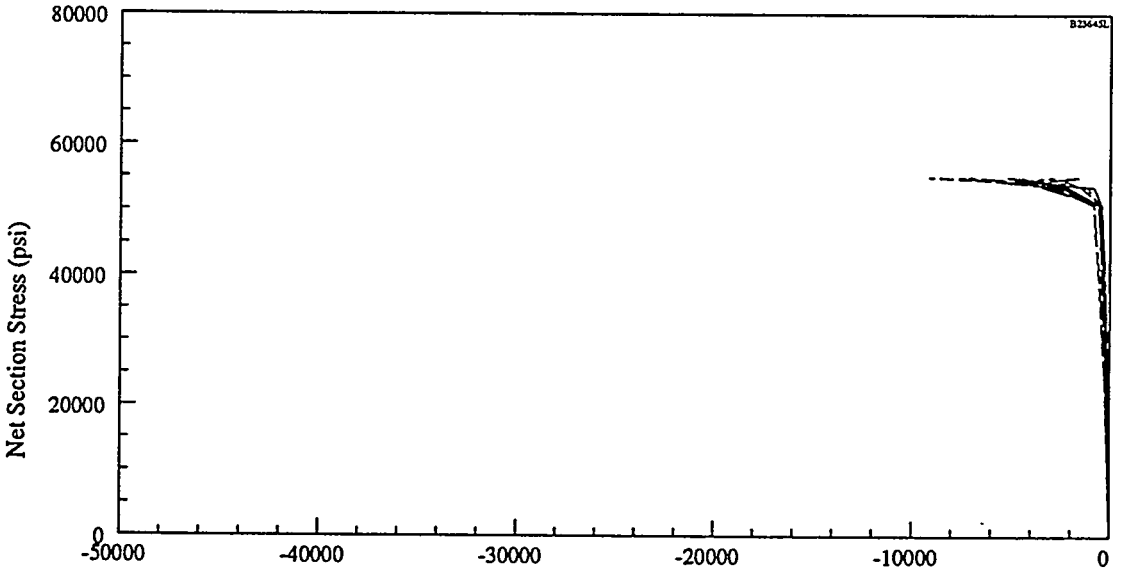

70 ksi Liner Stress

Outboard Poisson Traverse vs.Load (cont.)

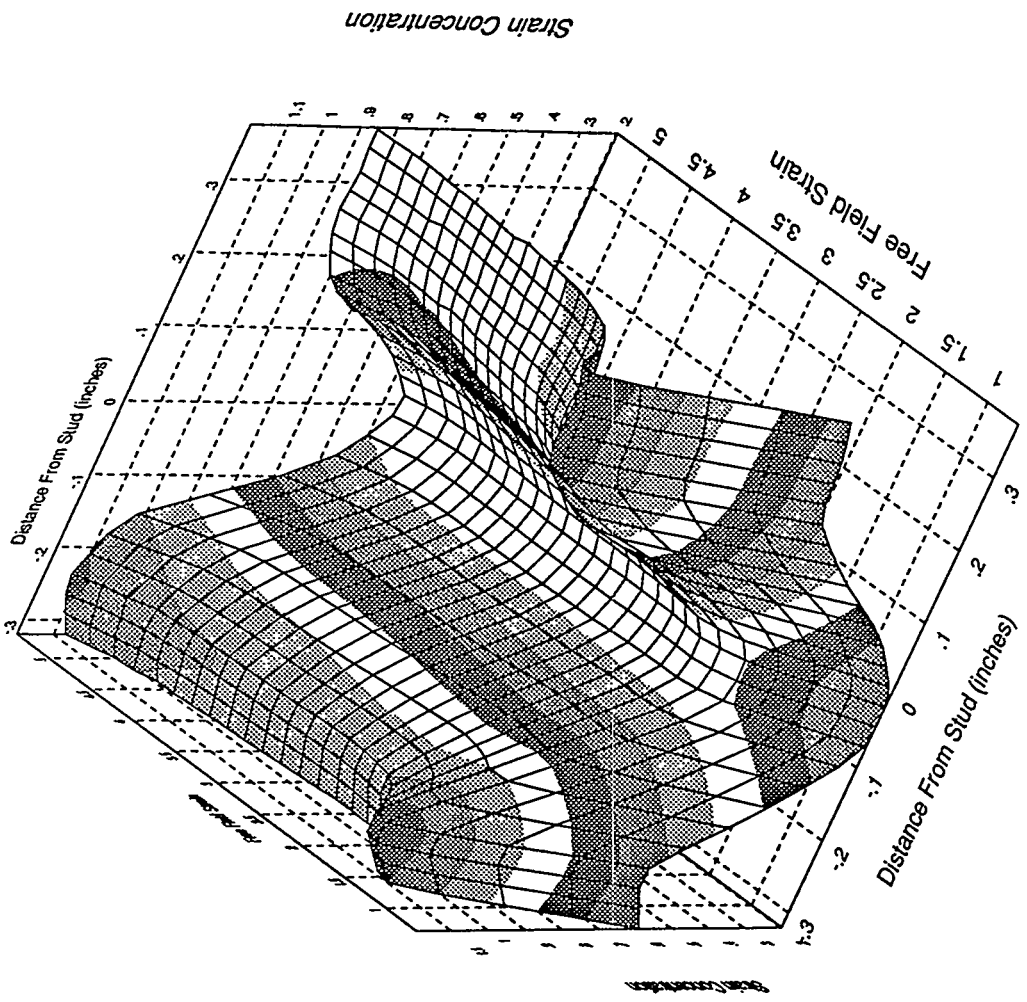

Inboard Transverse Strip Gage,65 ksi Specimen

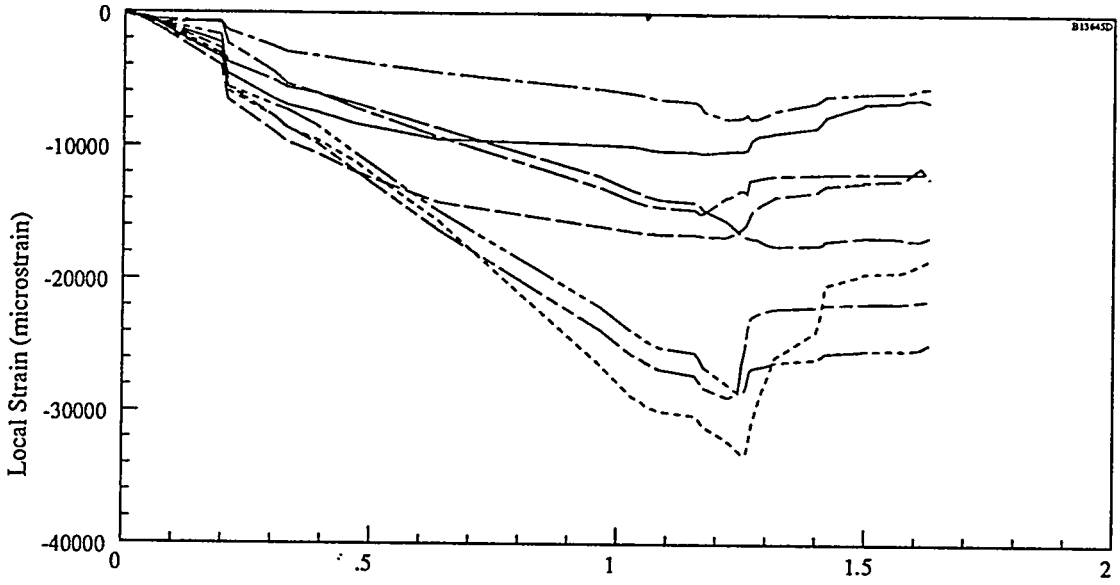

65 ksi Liner Stress

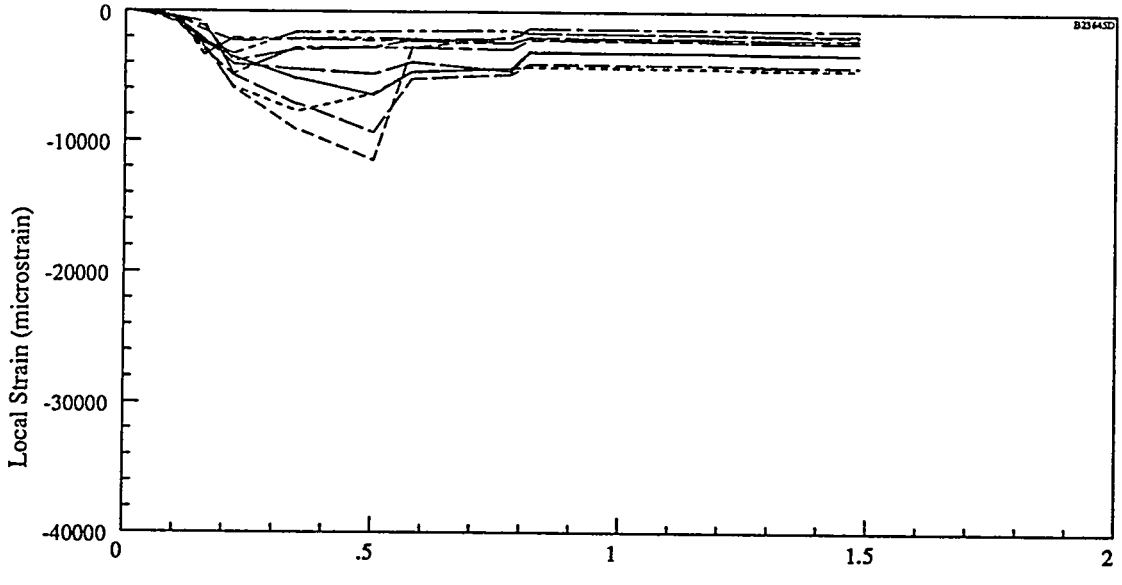

70 ksi Liner Stress

Outboard Poisson Traverse vs. Displacement (cont.)

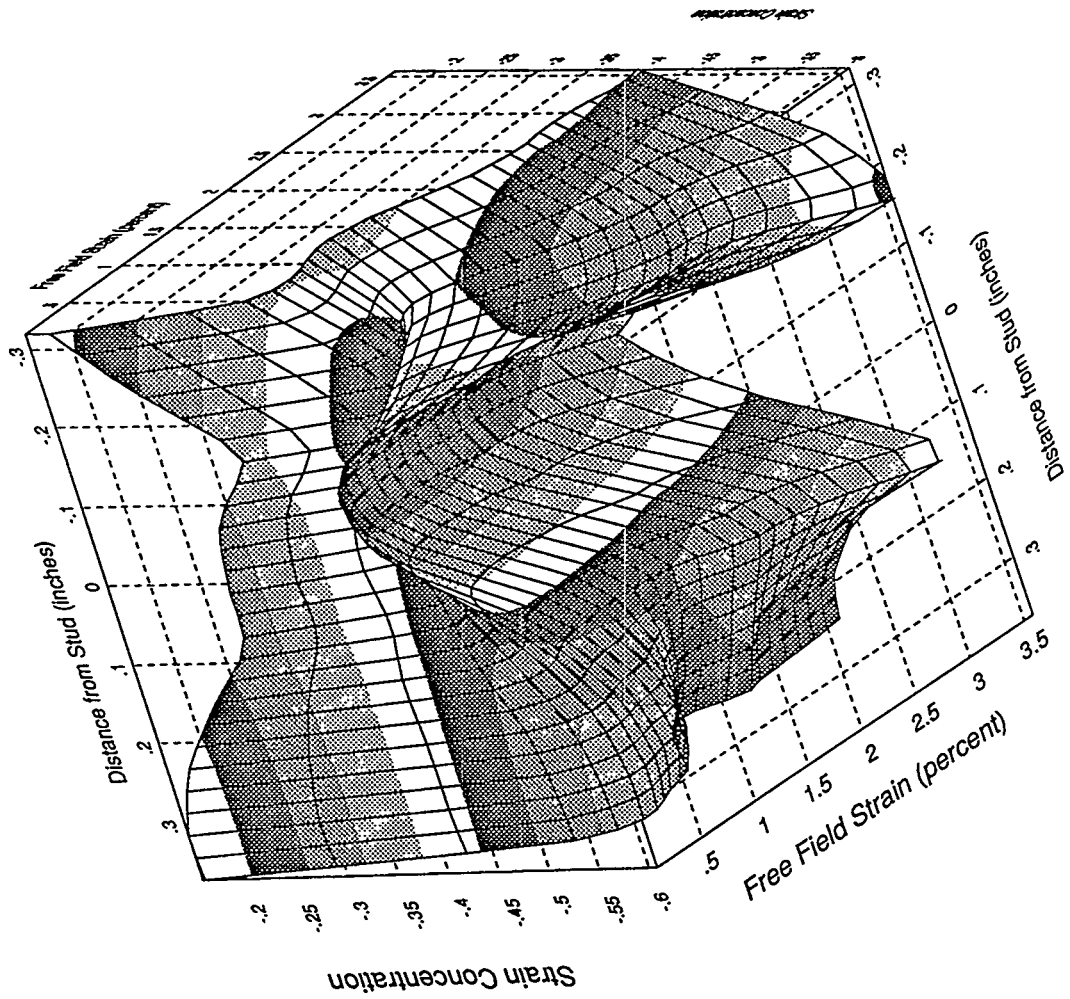

Poisson Strip Gage,60 ksi Specimen

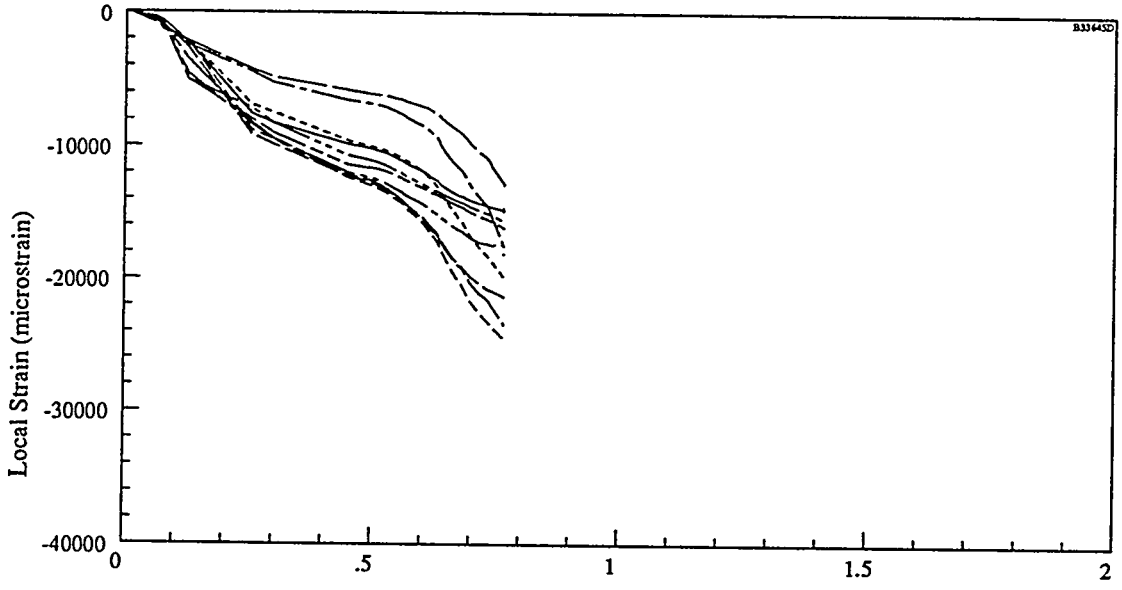

60 ksi Liner Stress

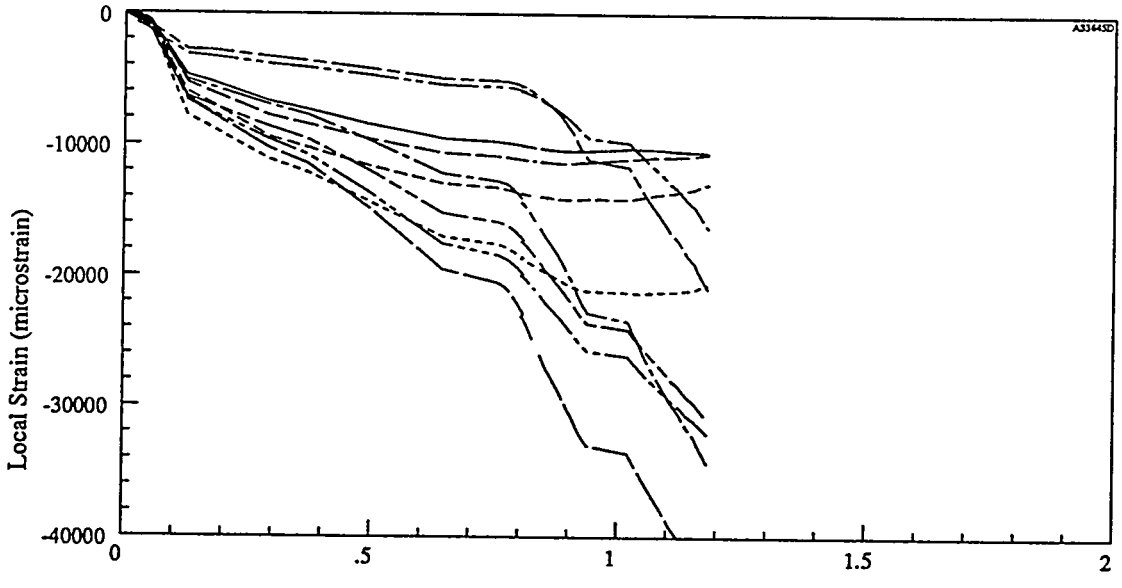

63 ksi Liner Stress

Outboard Poisson Traverse vs. Displacement

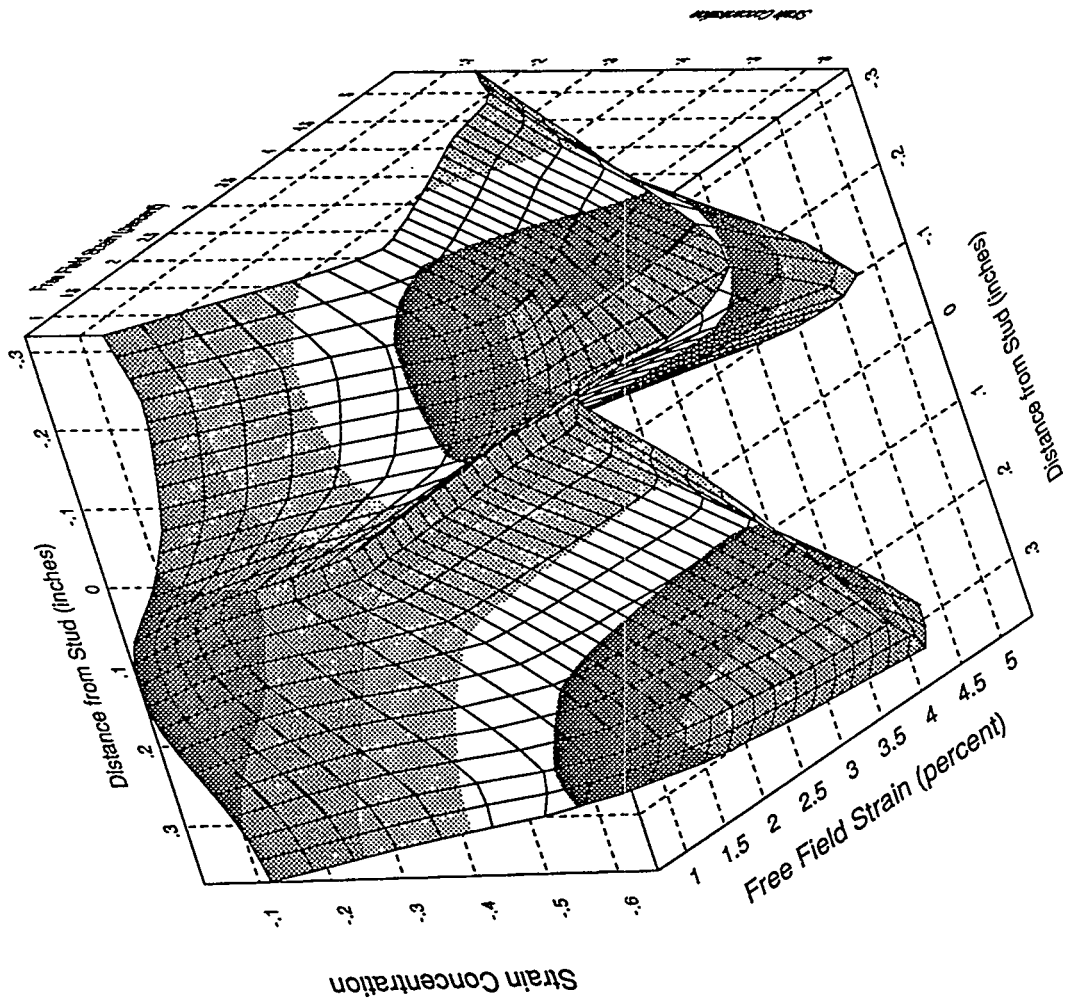

Poisson Strip Gage,65 ksi Specimen

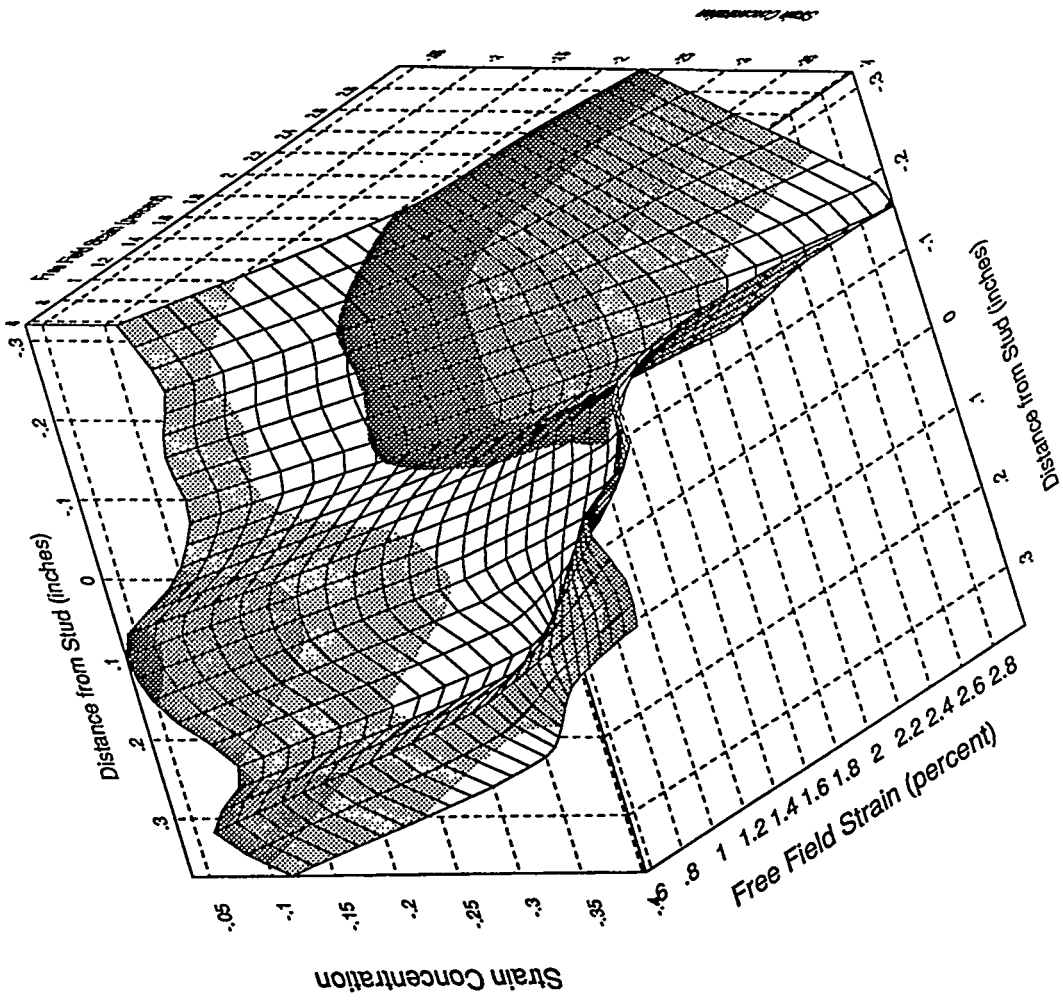

Poisson Strip Gage,70 ksi Specimen

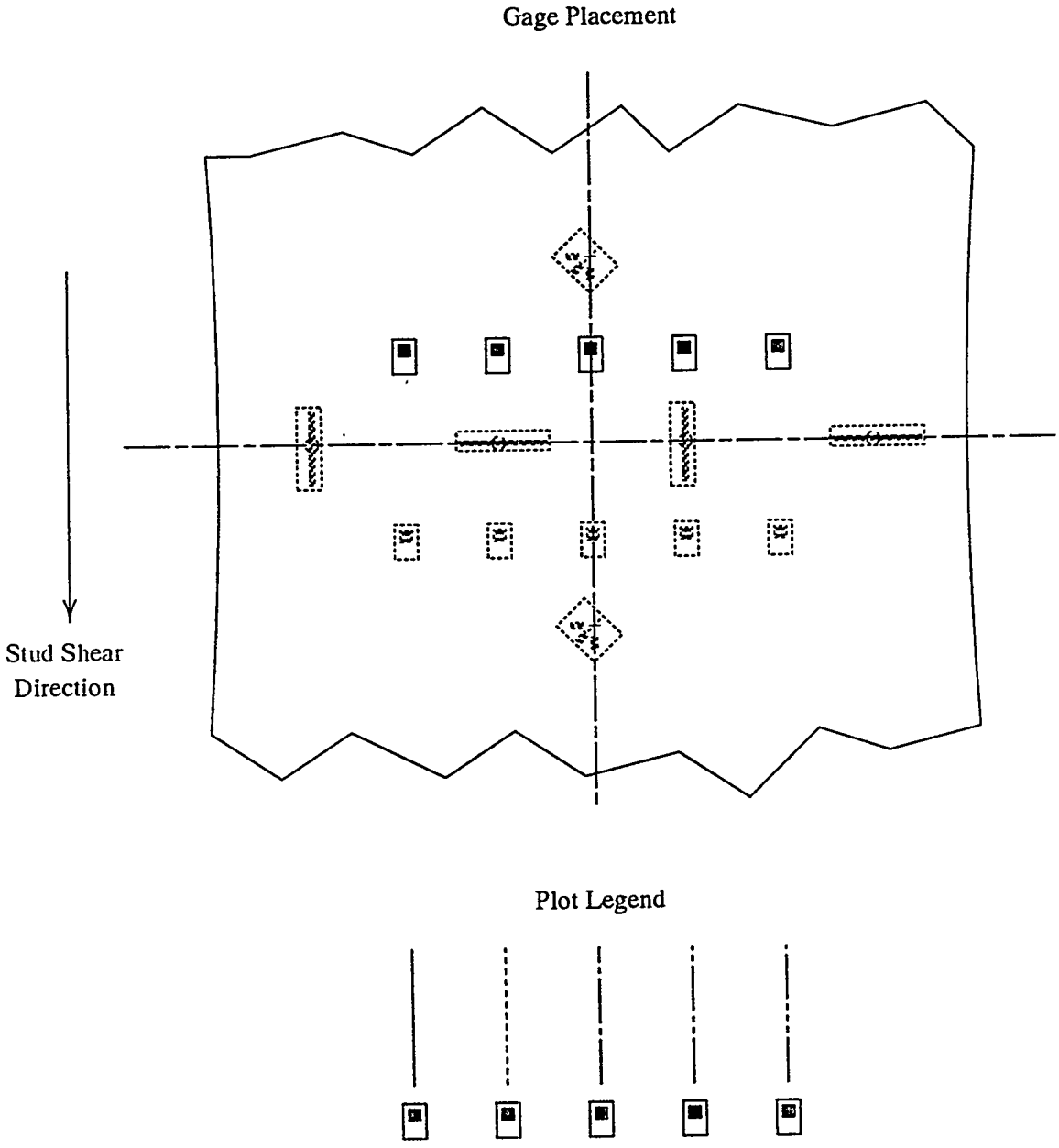

Upper Single-Element Gages (all specimens)

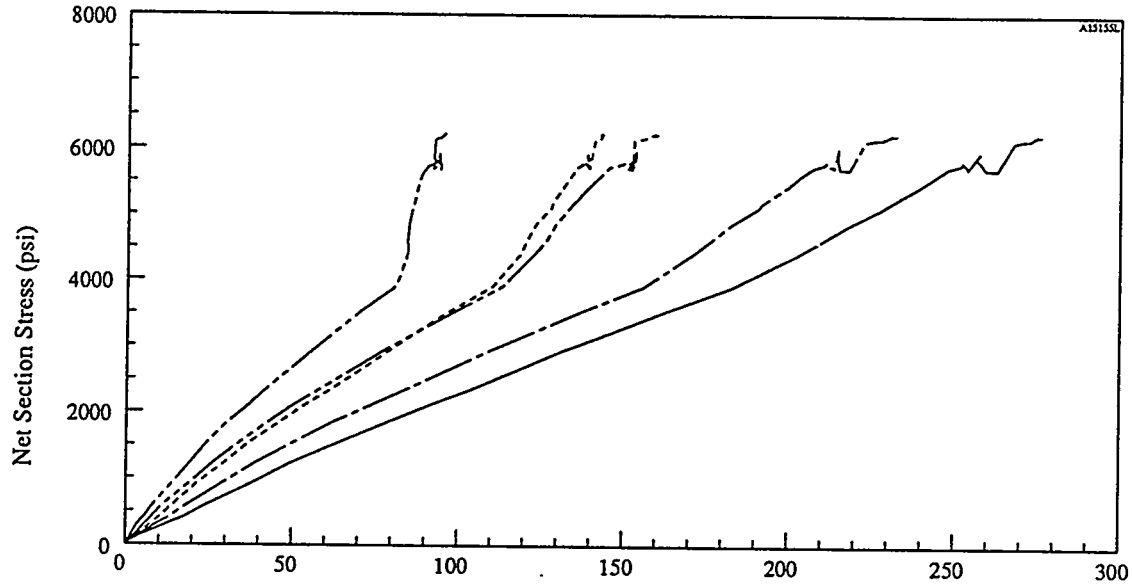

No Initial Liner Stress

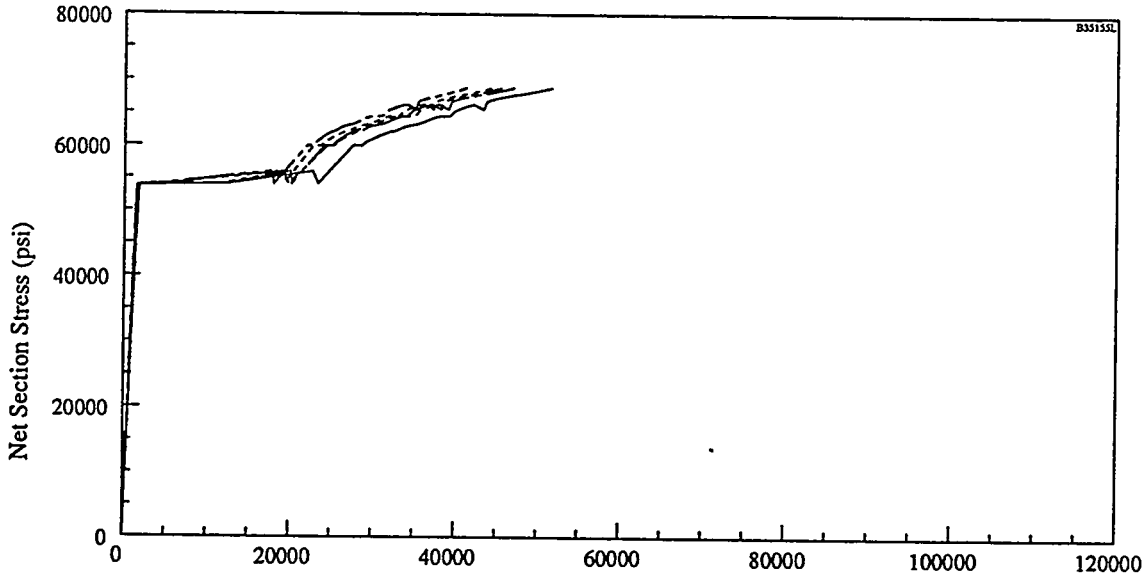

60 ksi Liner Stress

Upper Single-Element Strains vs Load

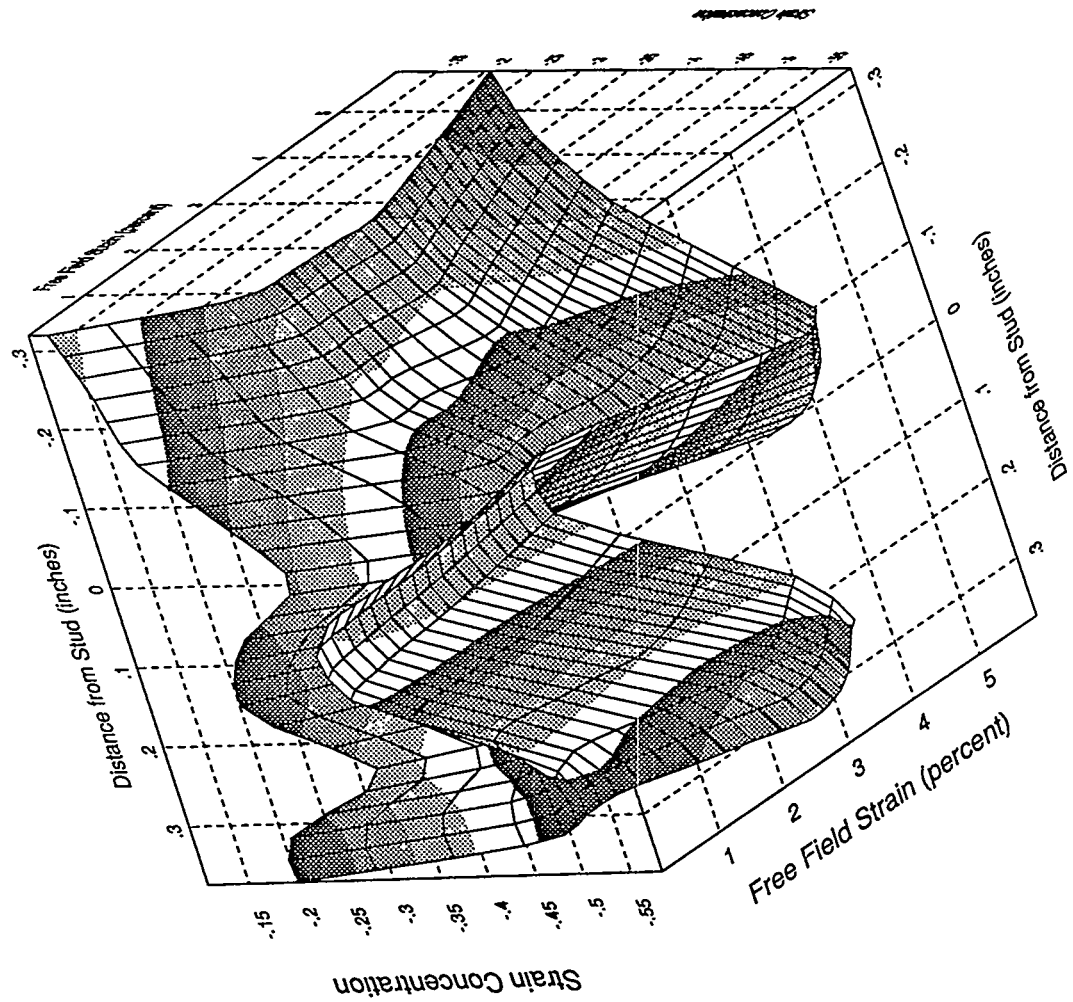

Poisson Strip Gage, 63 ksi Specimen

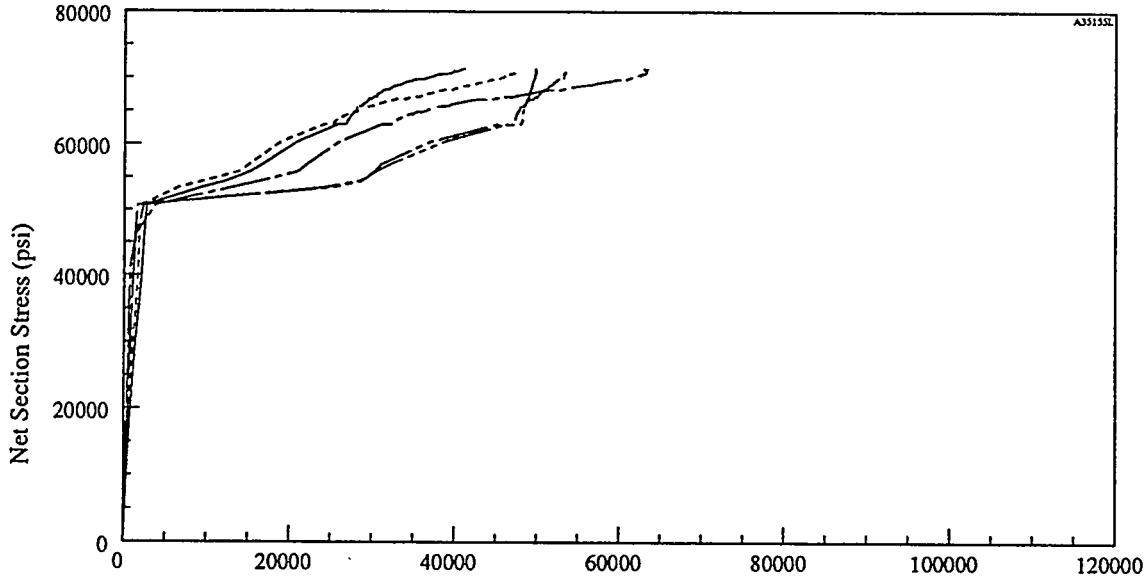

63 ksi Liner Stress

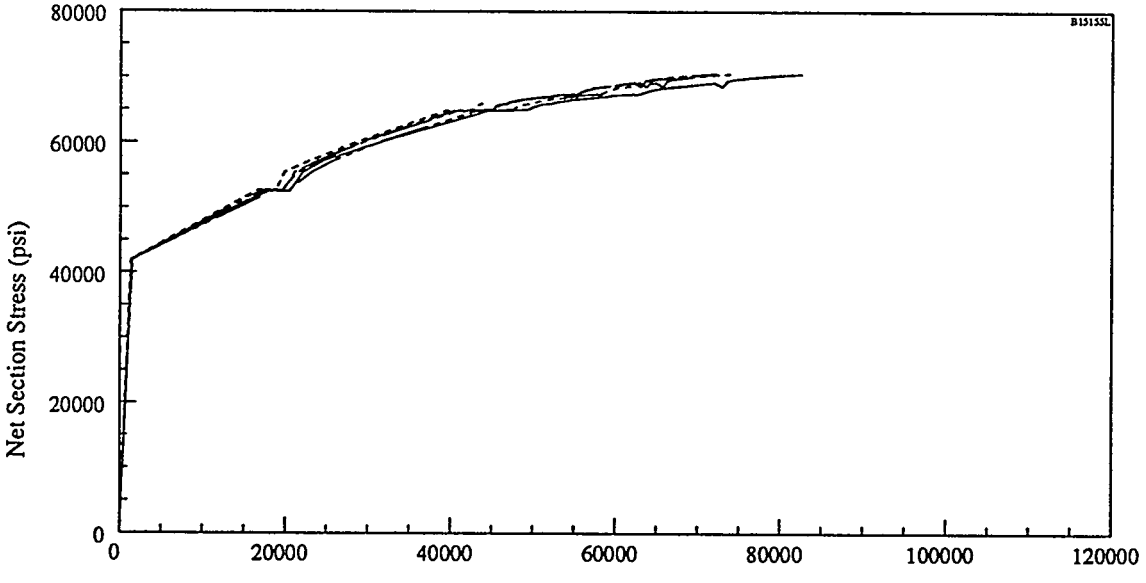

65 ksi Liner Stress

Upper Single-Element Strains vs. Load (cont.)

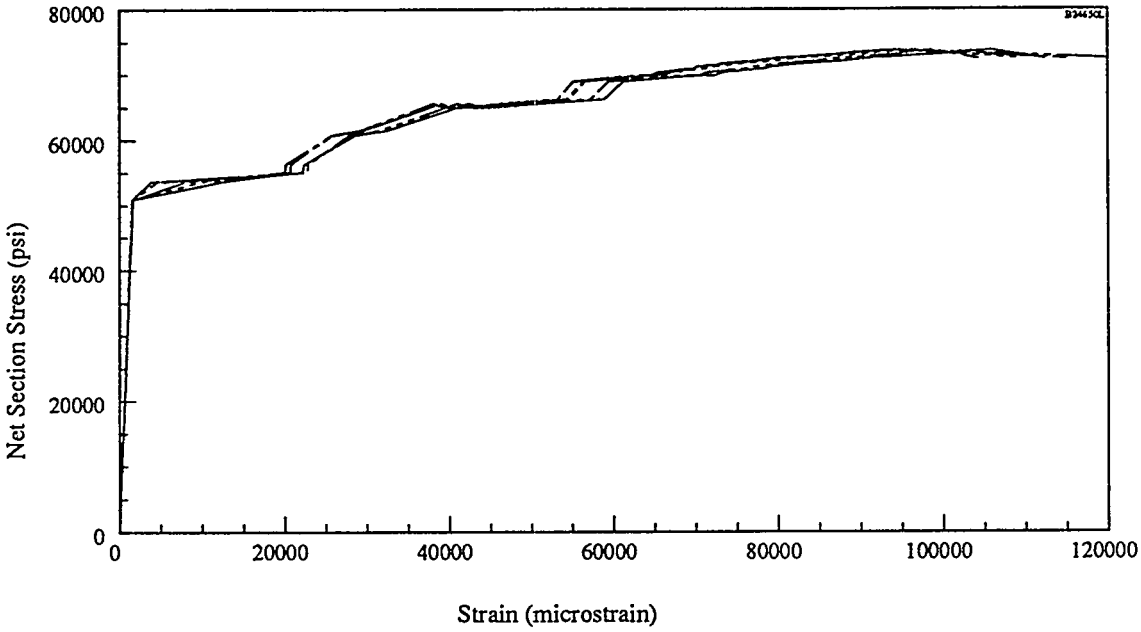

70 ksi Liner Stress

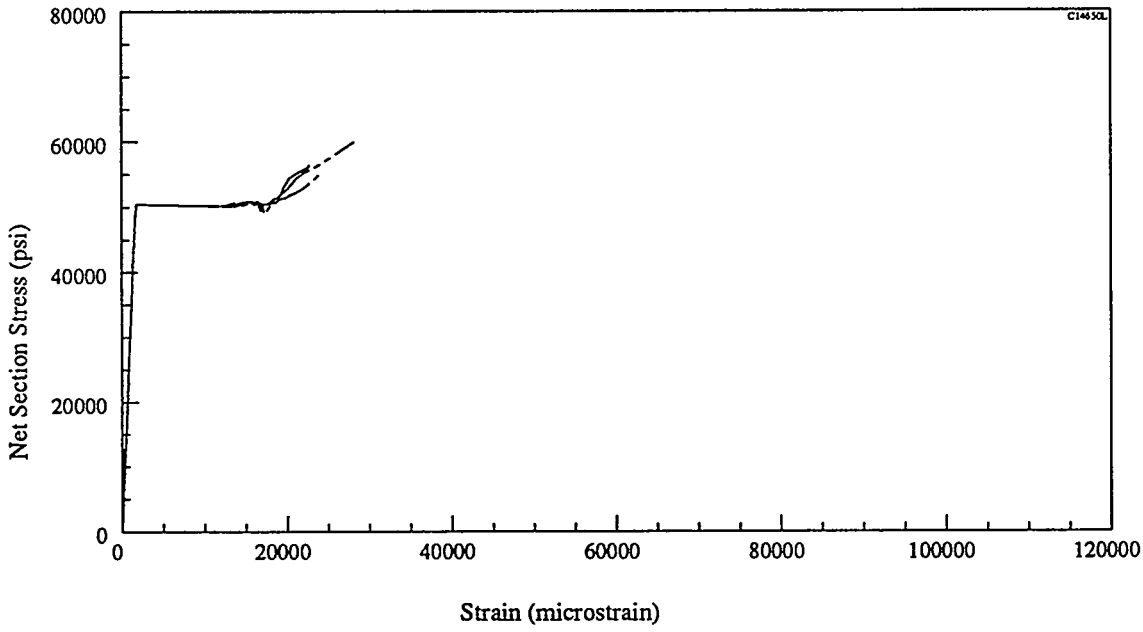

No Stud Load

Upper Single Element Strains vs Load (cont.)

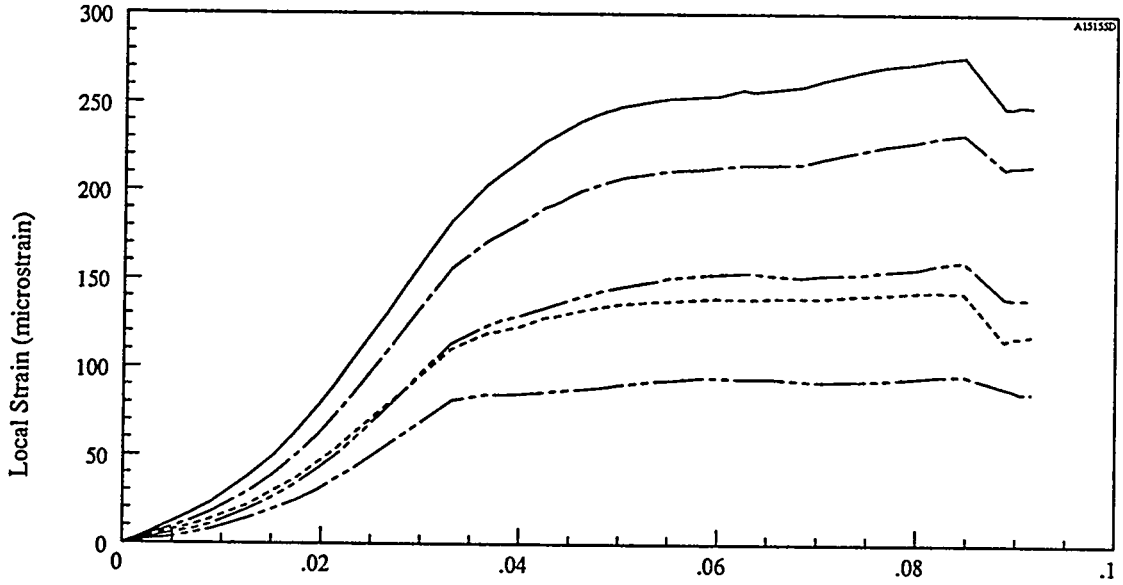

No Initial Liner Stress

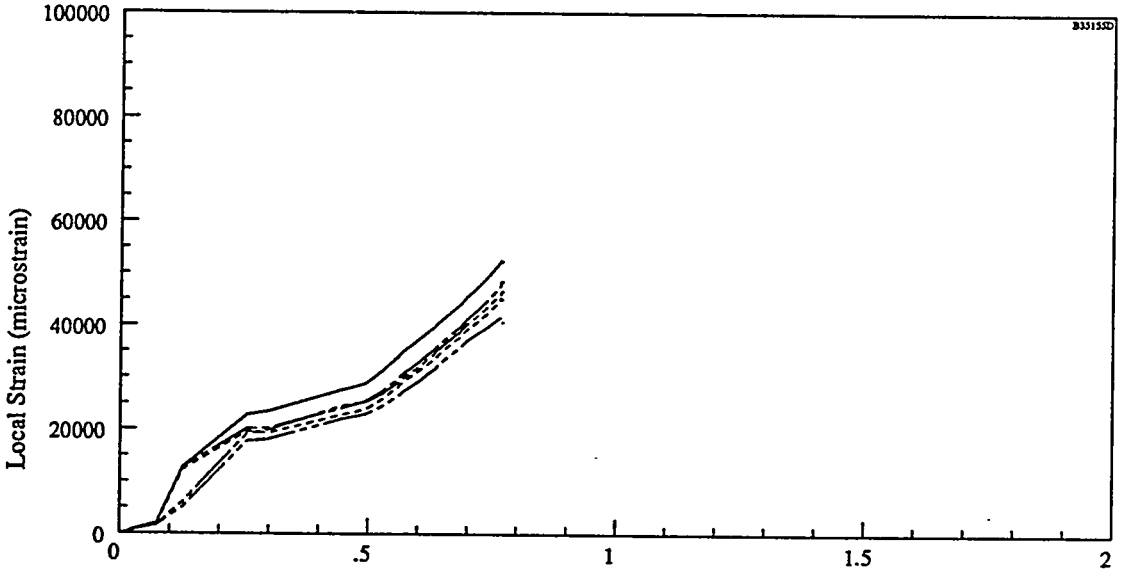

60 ksi Liner Stress

Upper Single Element Strains vs Displacement

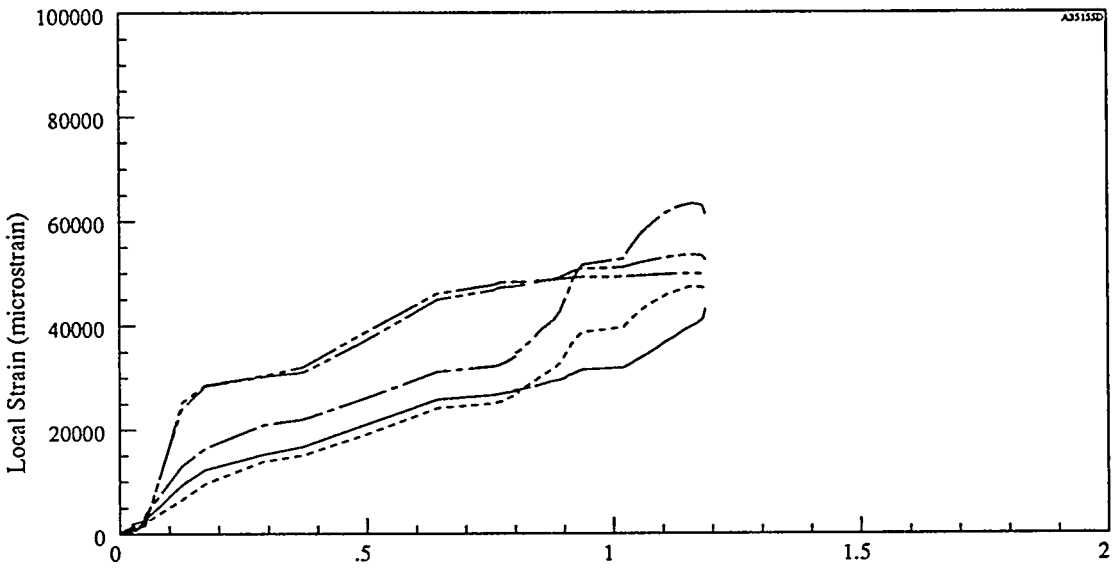

63 ksi Liner Stress

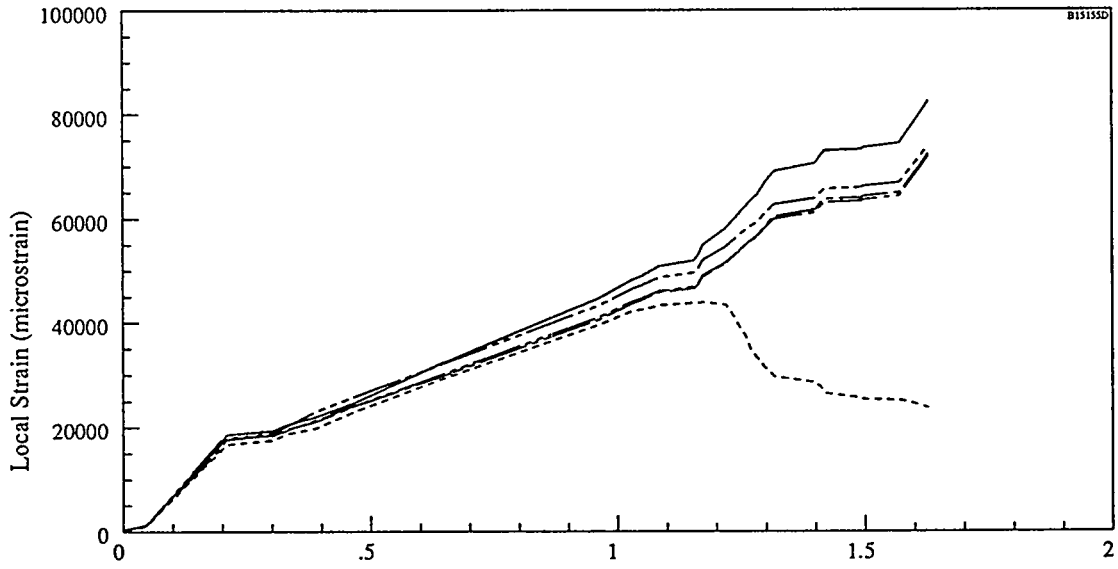

65 ksi Liner Stress

Upper Single Element Strains vs Displacement (cont.)

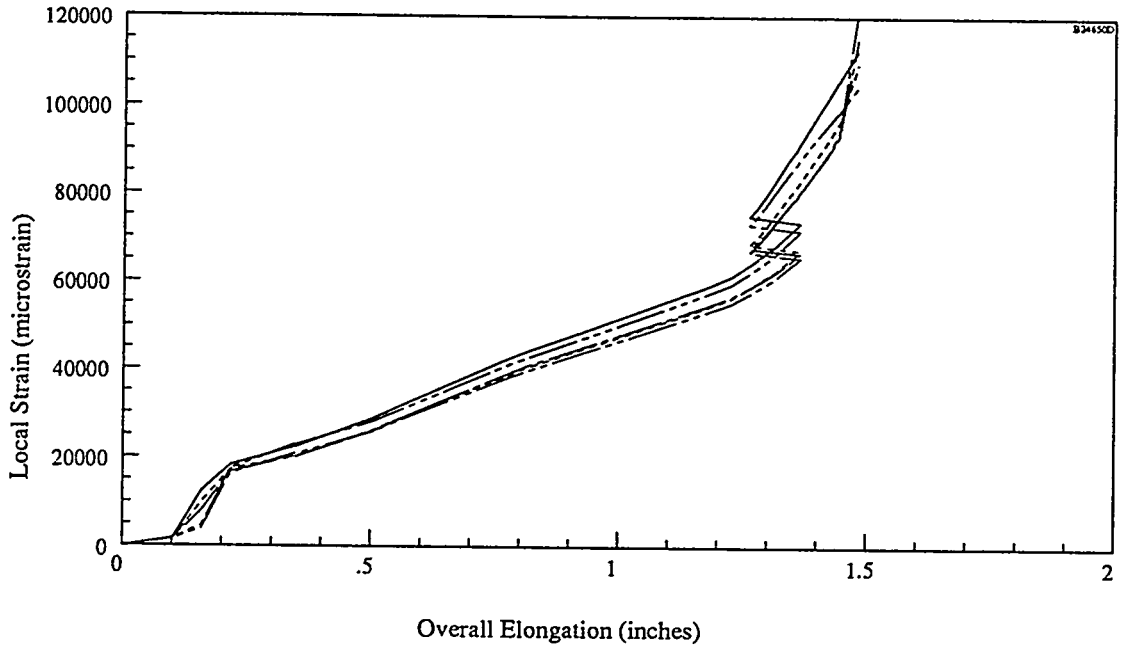

70 ksi Liner Stress

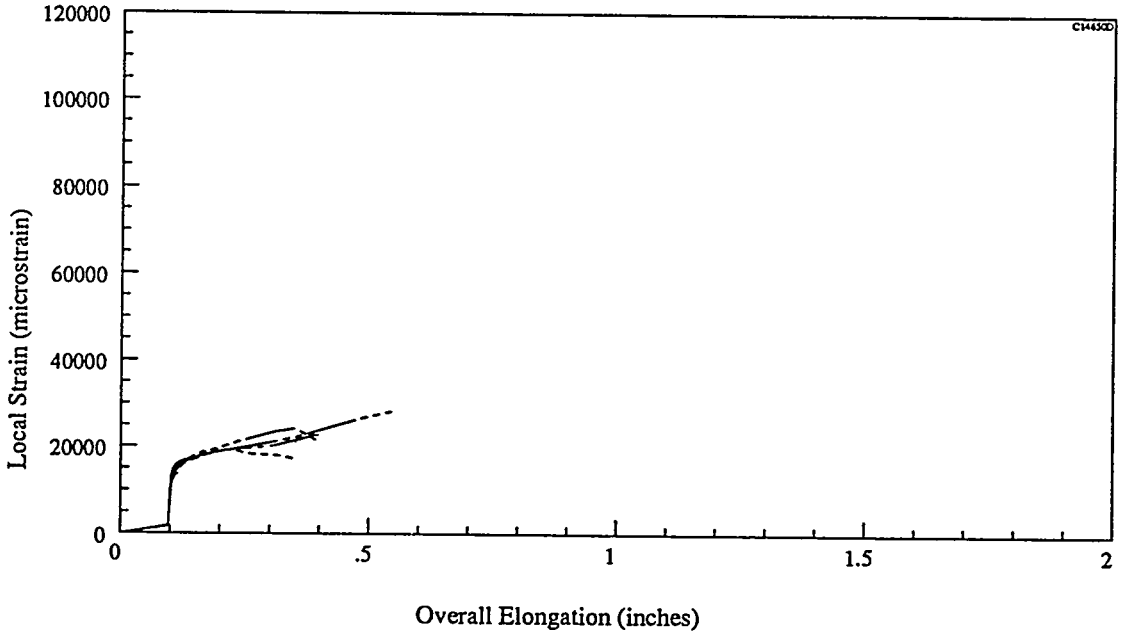

No Stud Load

Upper Single Element Strains vs Displacement (cont.)

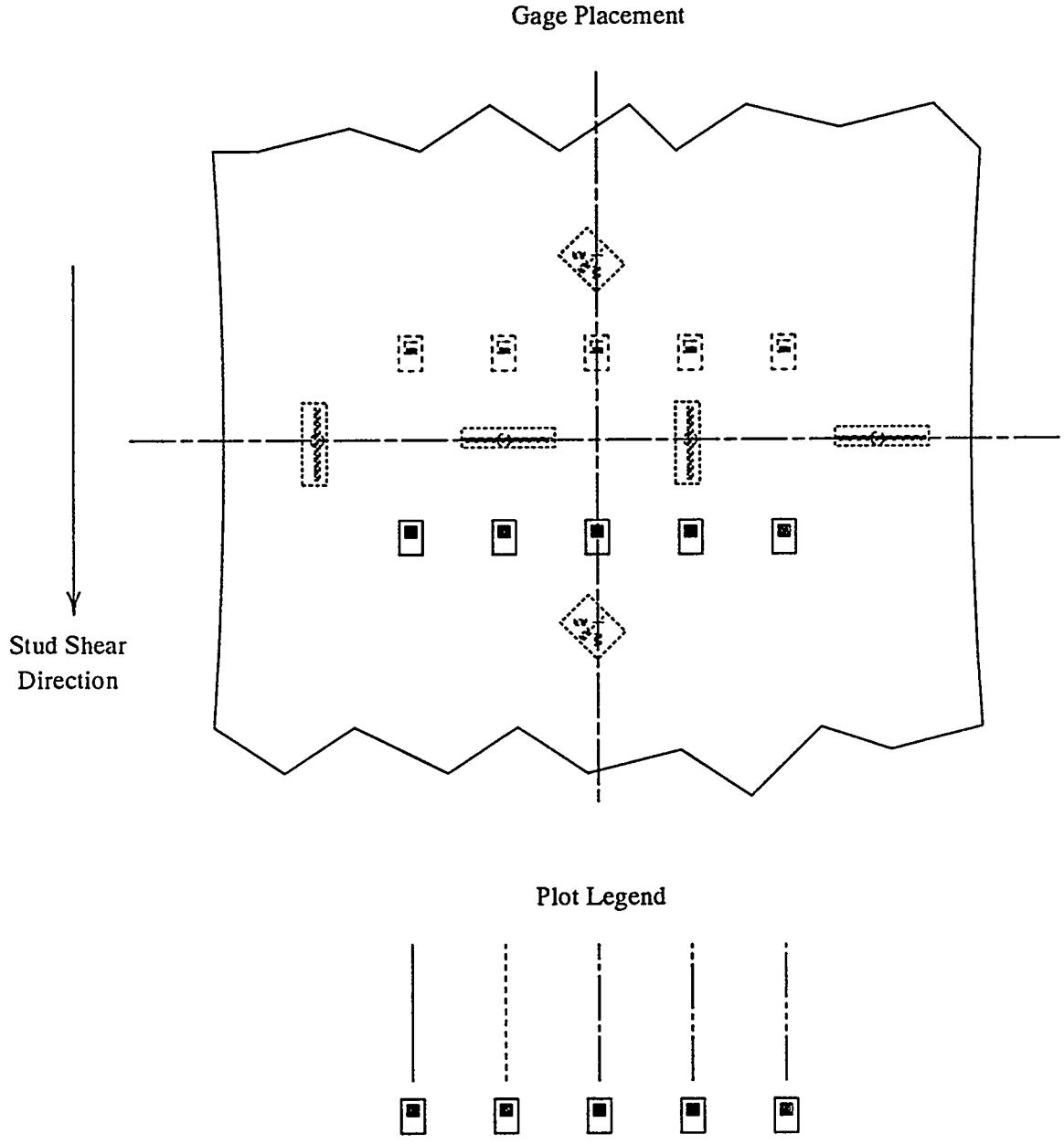

Lower Single-Element Gages (all specimens)

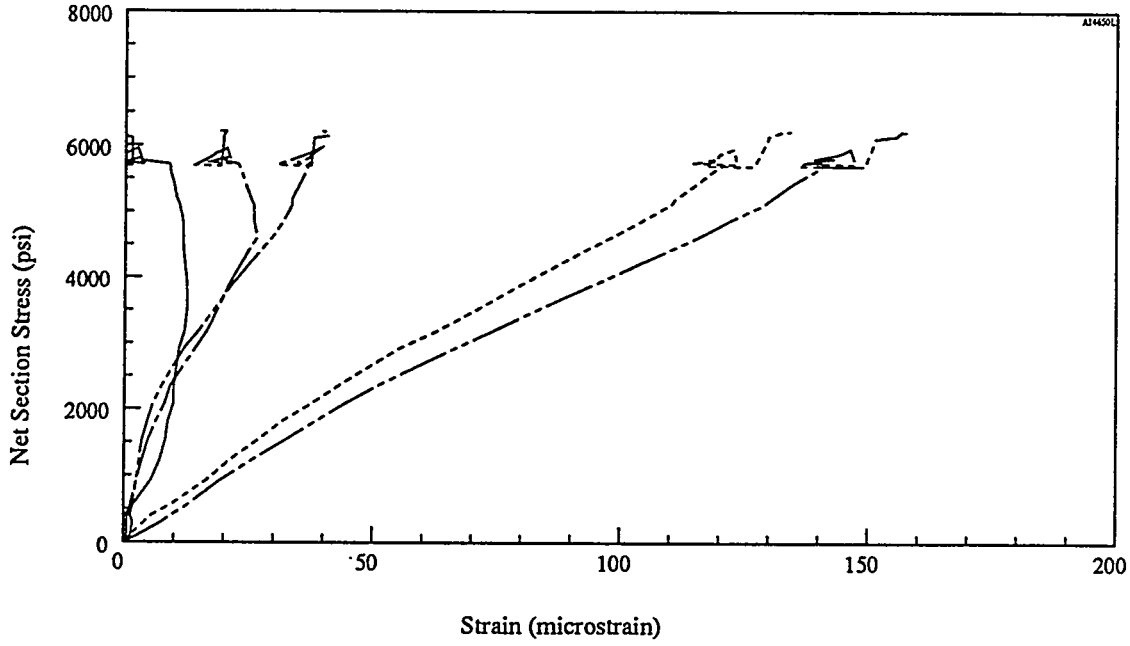

No Initial Liner Stress

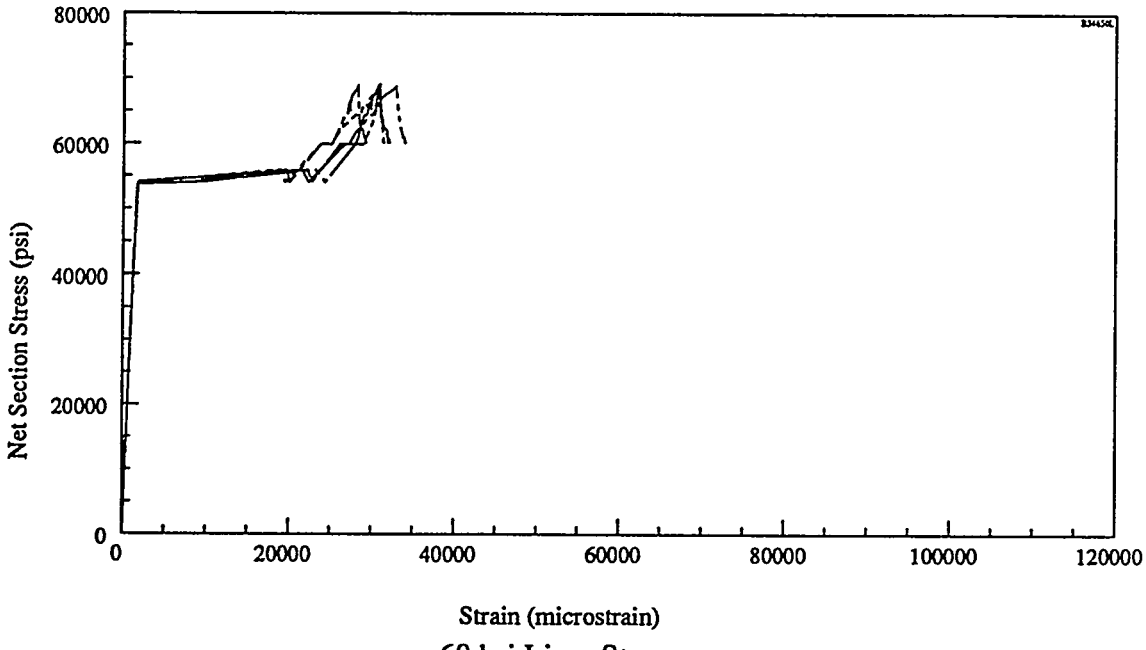

60 ksi Liner Stress

Lower Single Element Strains vs Load

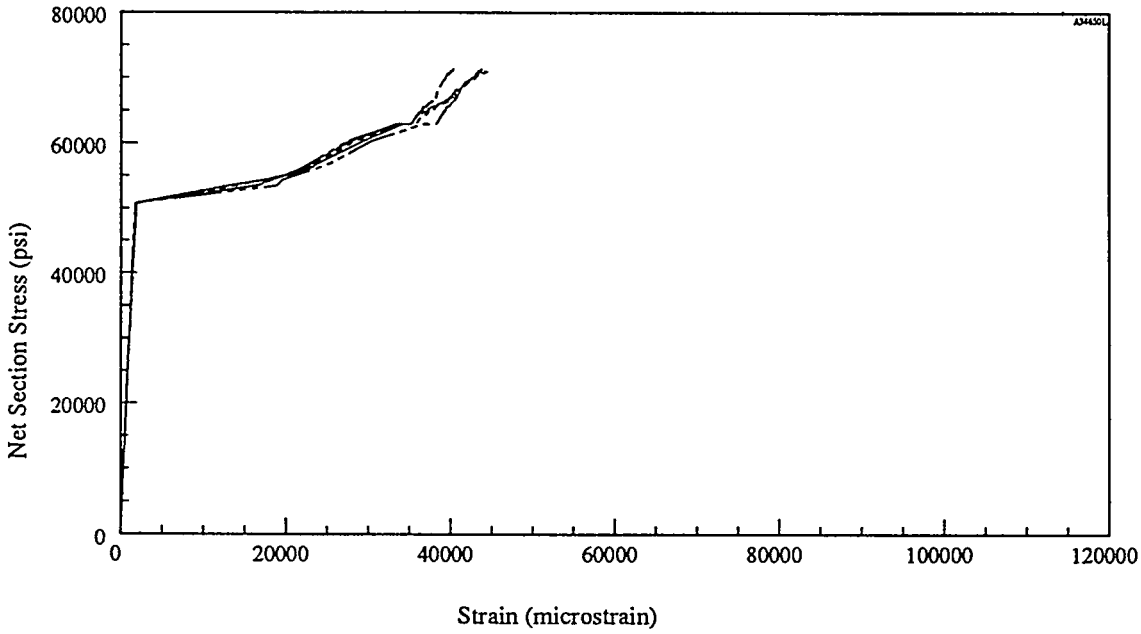

63 ksi Liner Stress

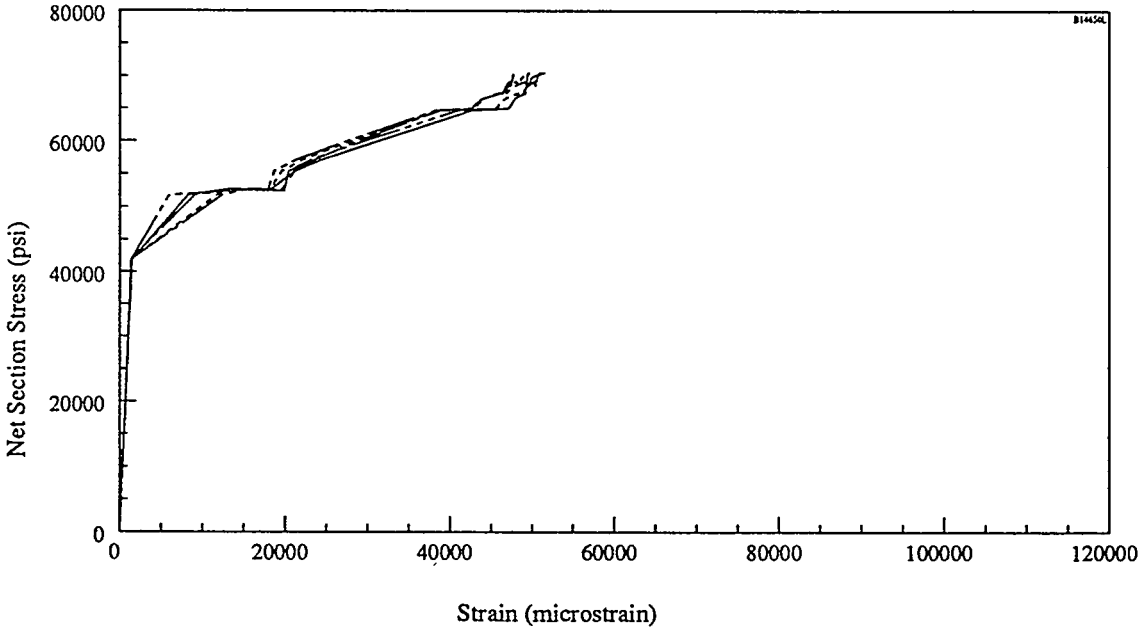

65 ksi Liner Stress

Lower Single Element Strains vs Load (cont.)

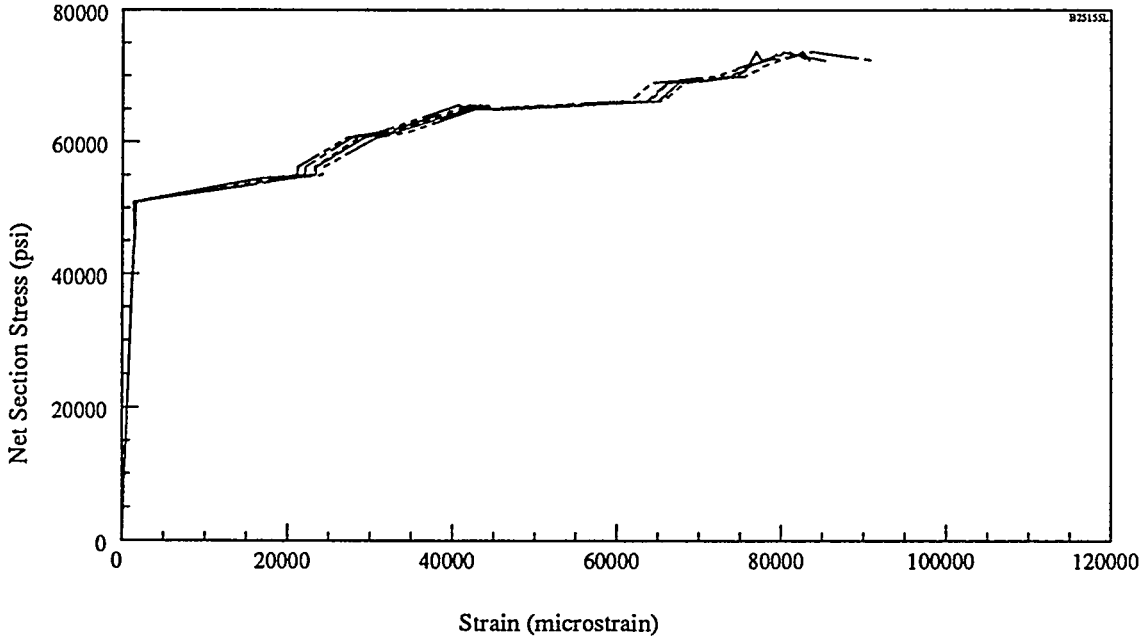

70 ksi Liner Stress

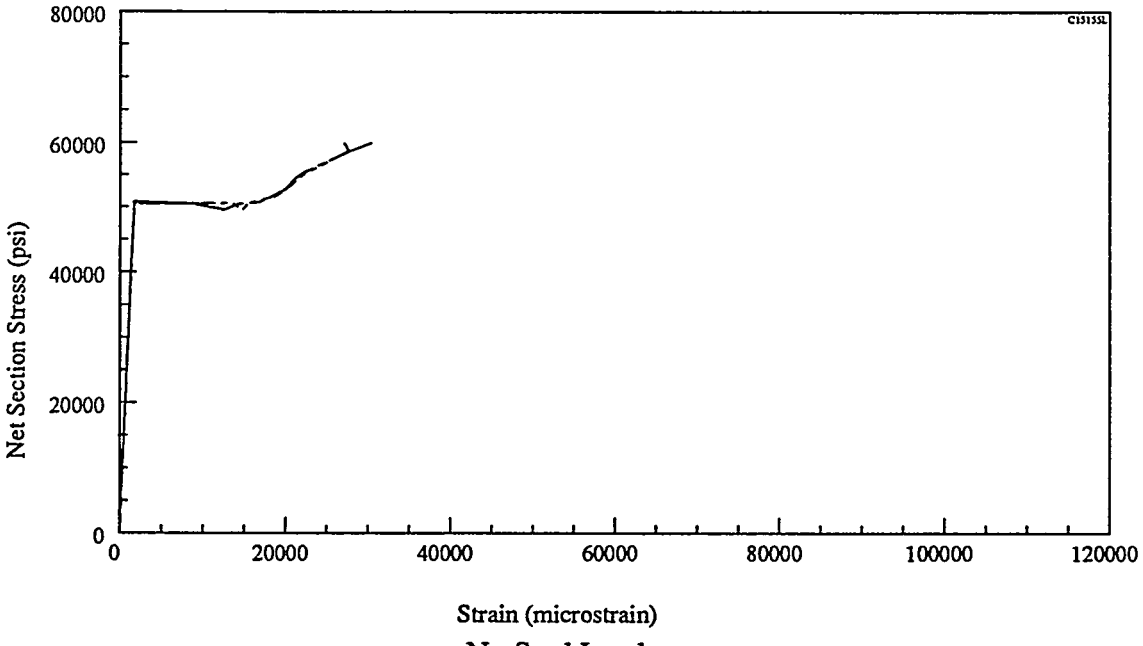

No Stud Load

Lower Single Element Strains vs Load (cont.)

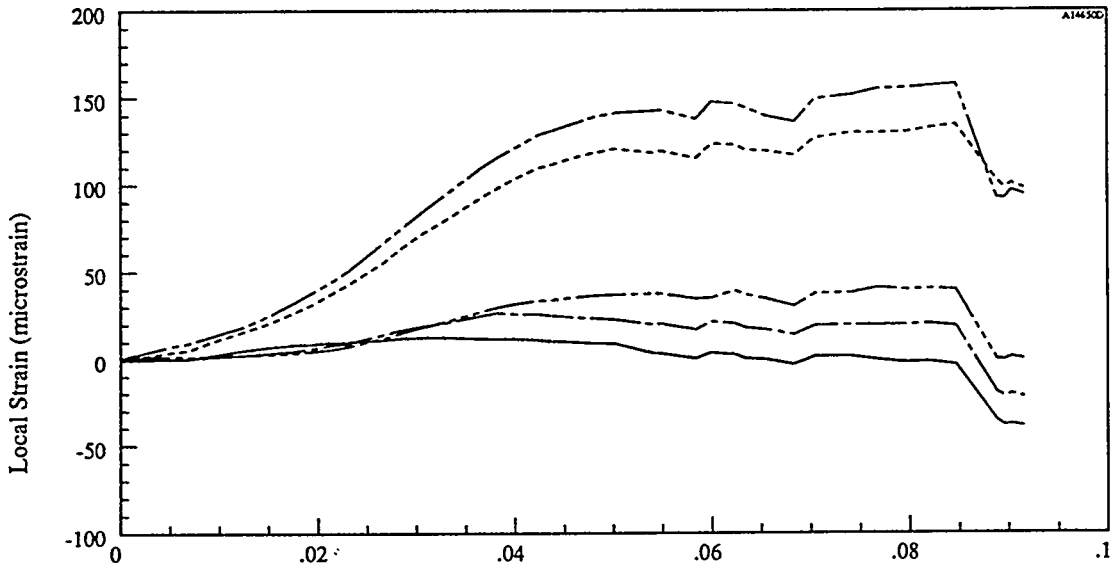

No Initial Liner Stress

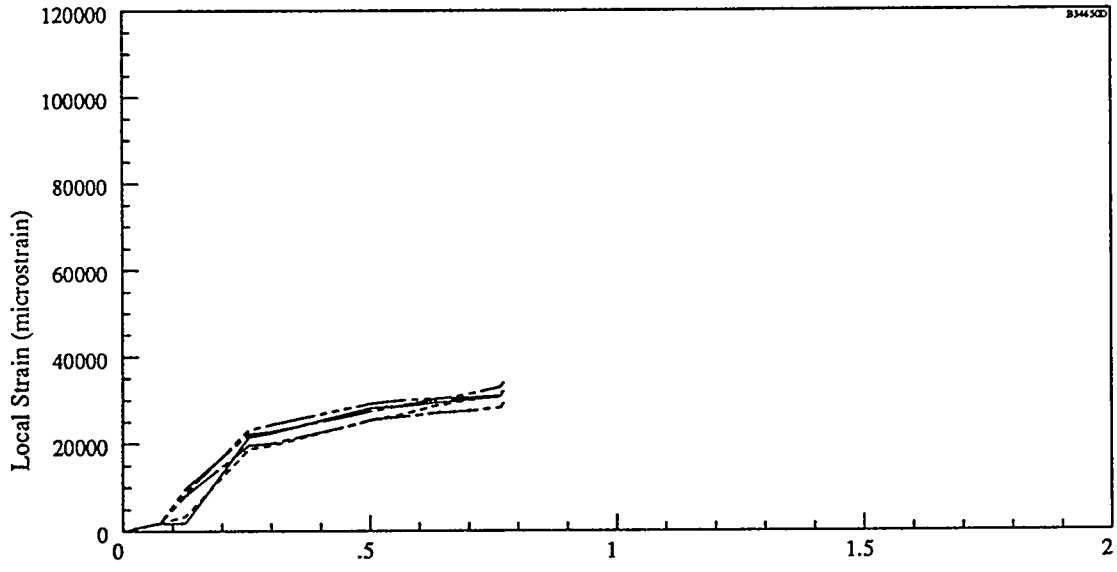

60 ksi Liner Stress

Lower Single Element Strains vs Displacement

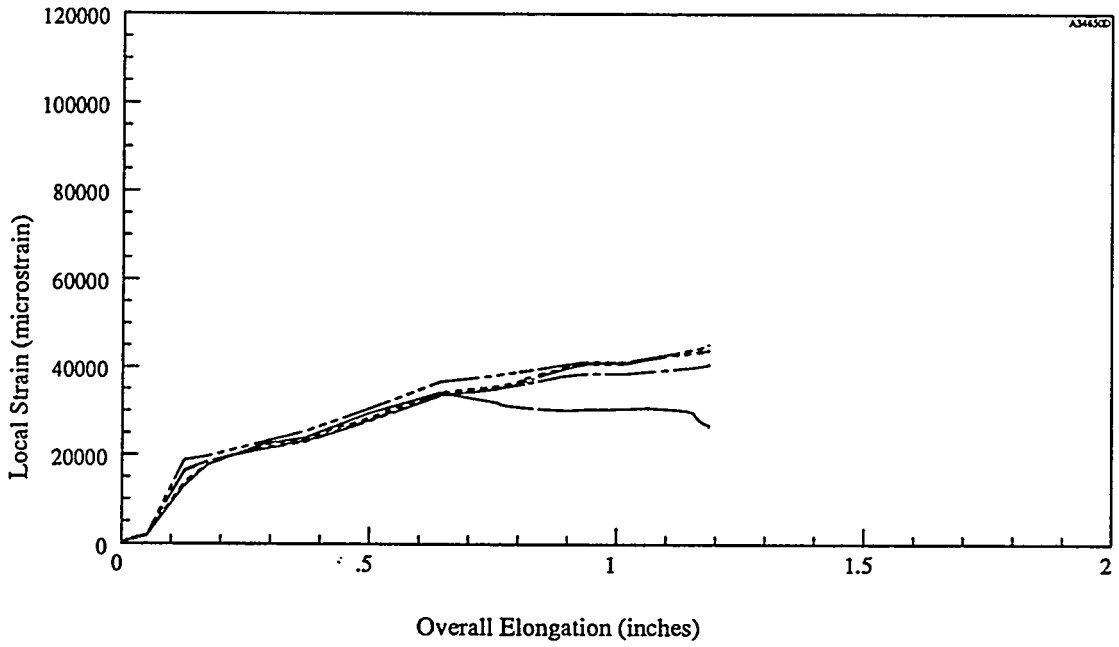

63 ksi Liner Stress

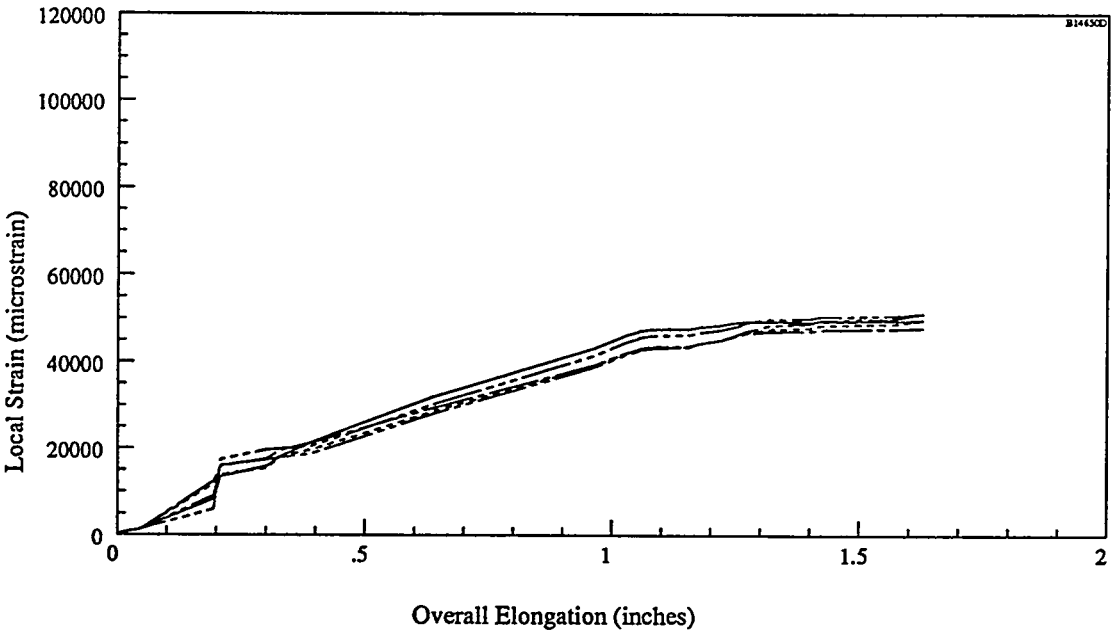

65 ksi Liner Stress

Lower Single Element Strains vs Displacement (cont.)

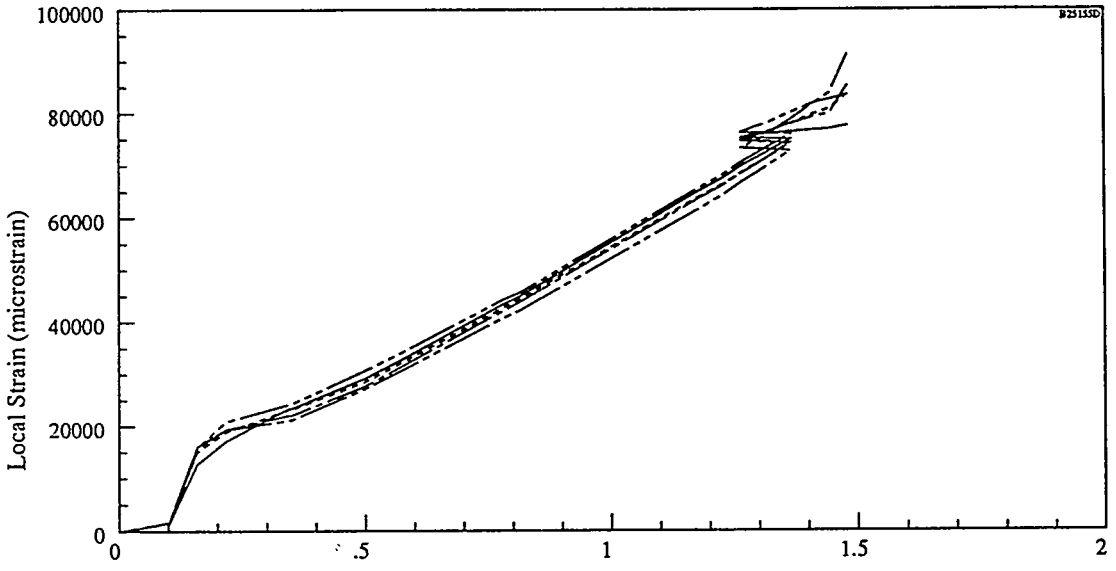

70 ksi Liner Stress

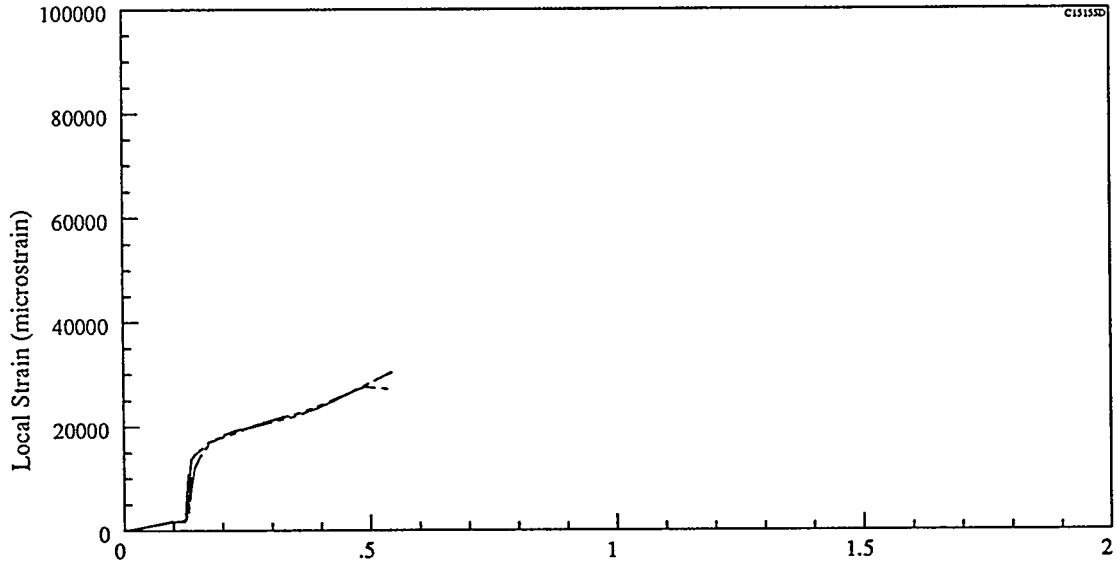

No Stud Load

Lower Single Element Strains vs Displacement (cont.)

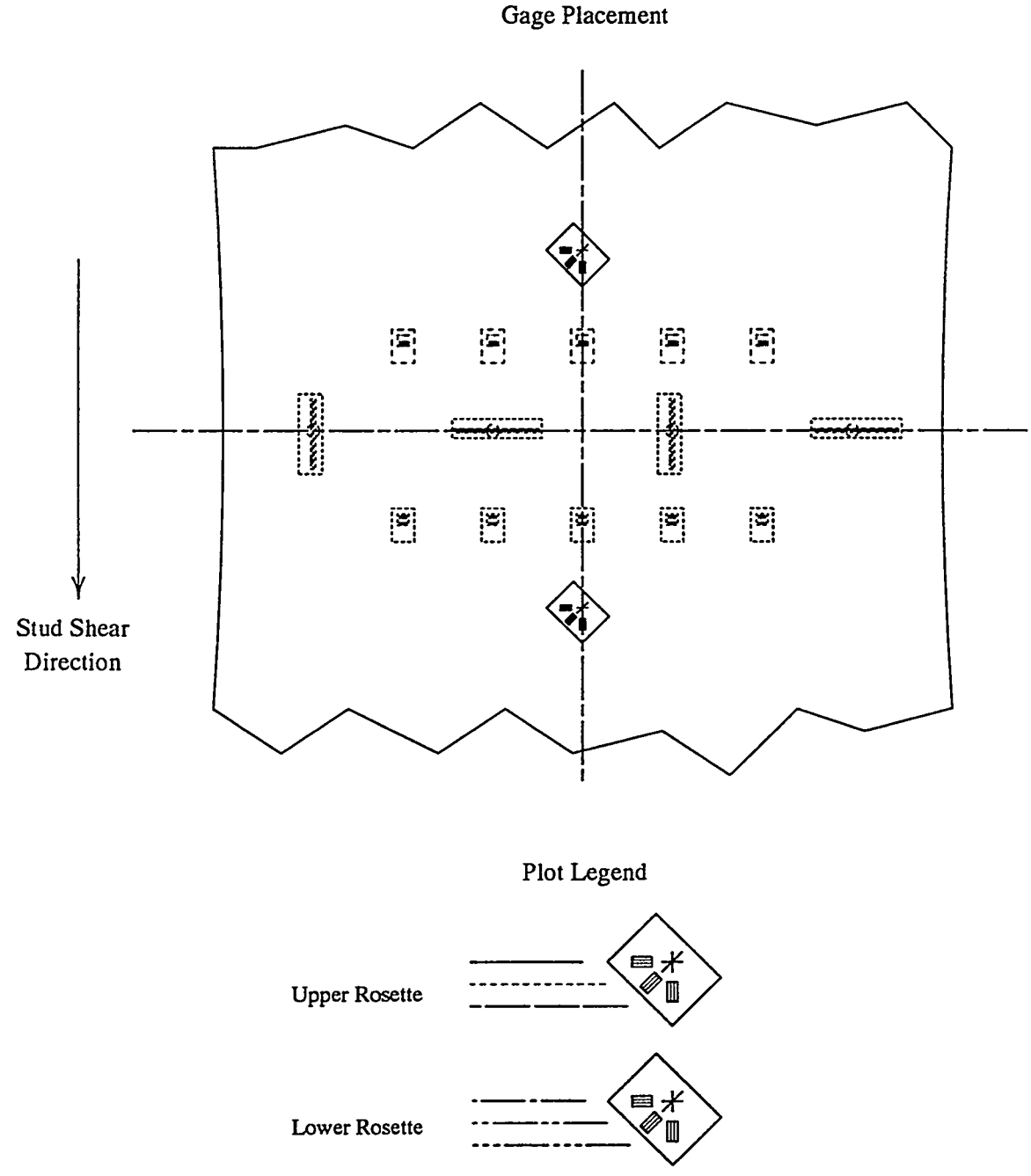

Three-Element Rosette Gages (all specimens)

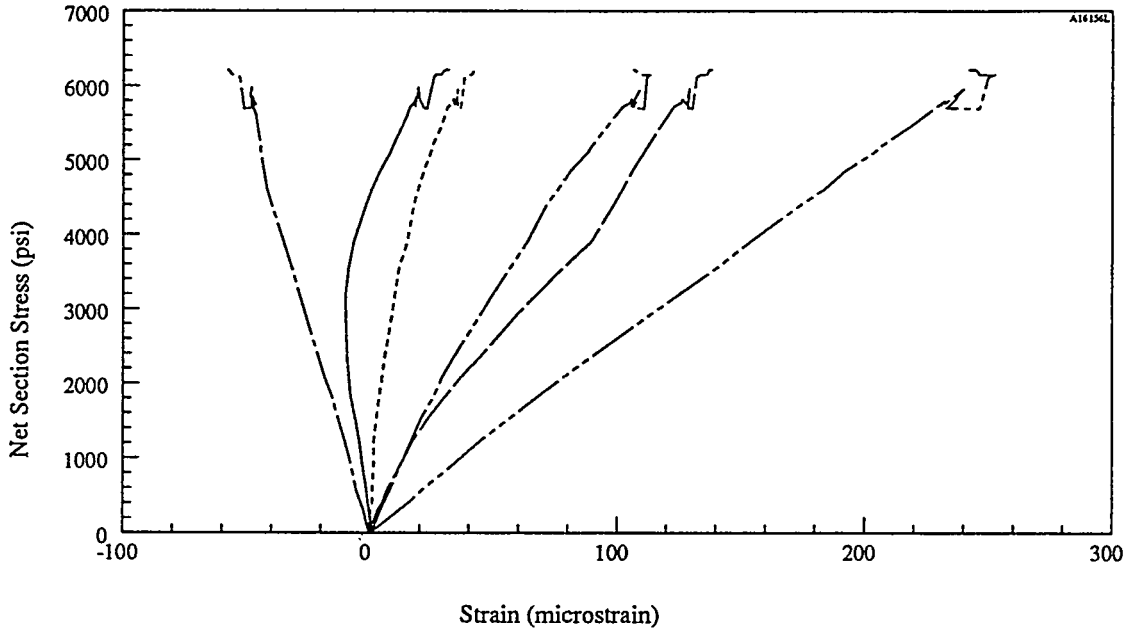

No Initial Liner Stress

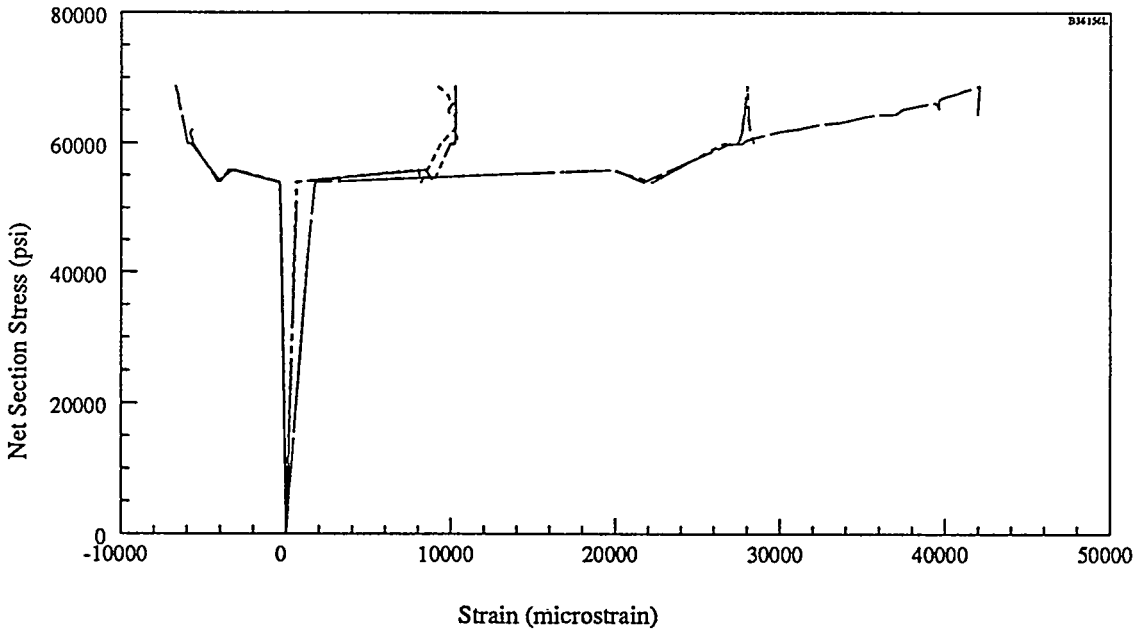

60 ksi Liner Stress

Rosette Strains vs Load

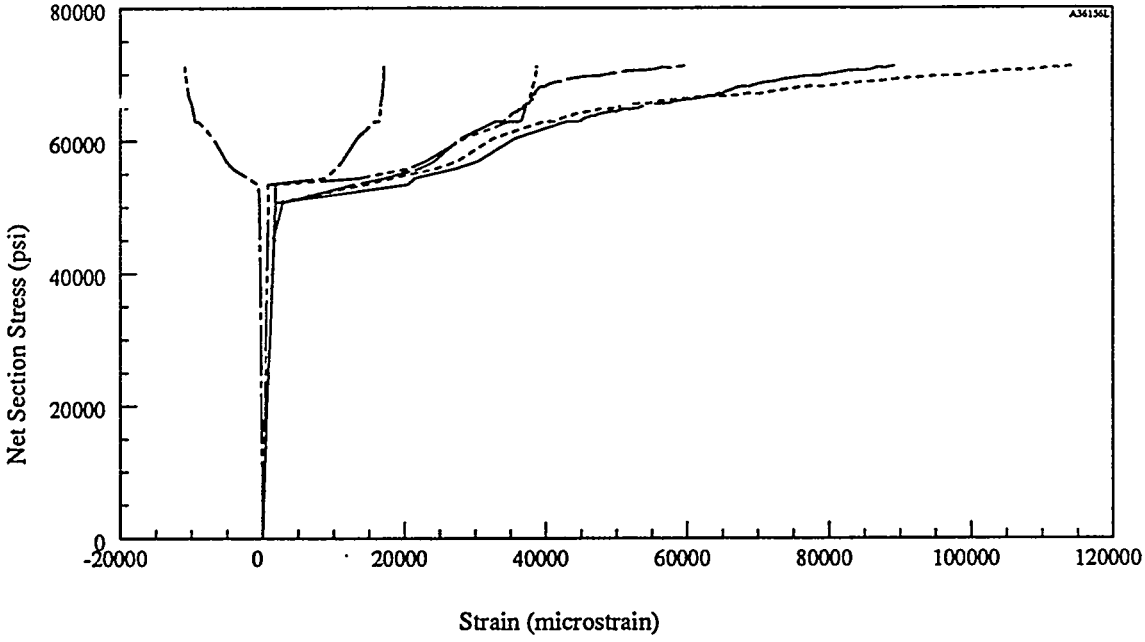

63 ksi Liner Stress

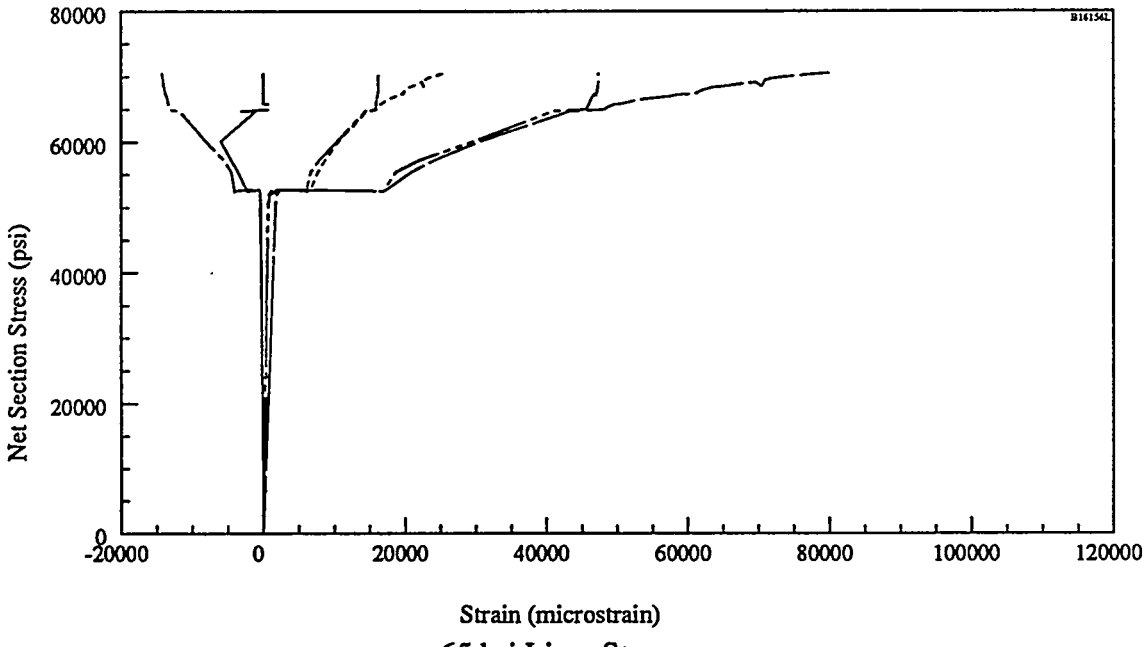

65 ksi Liner Stress

Rosette Strains vs Load (cont.)

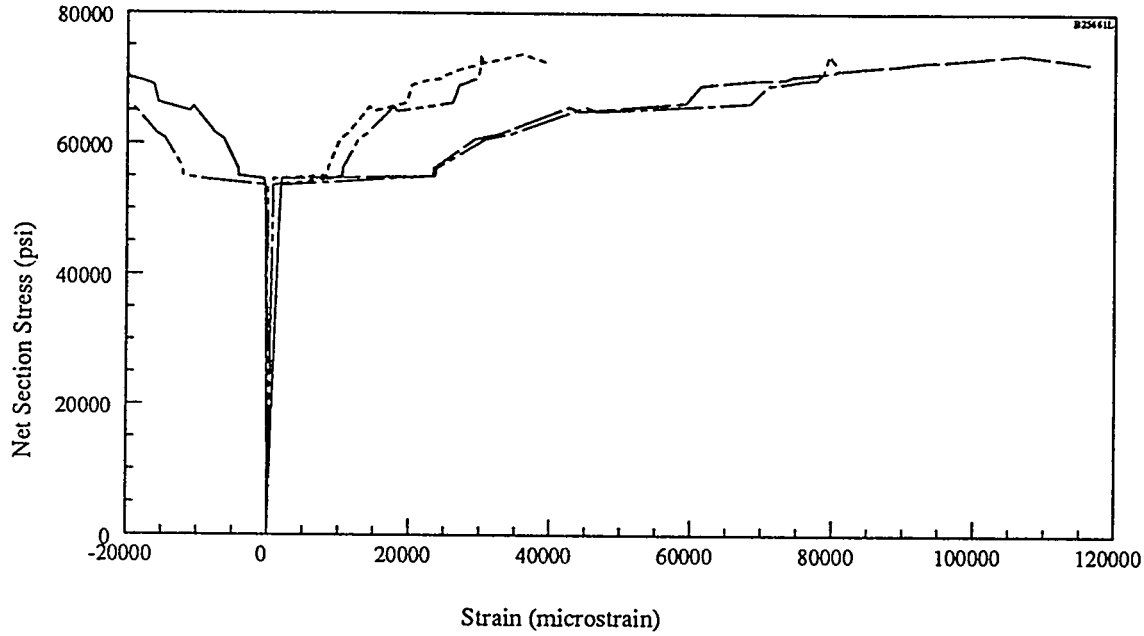

70 ksi Liner Stress

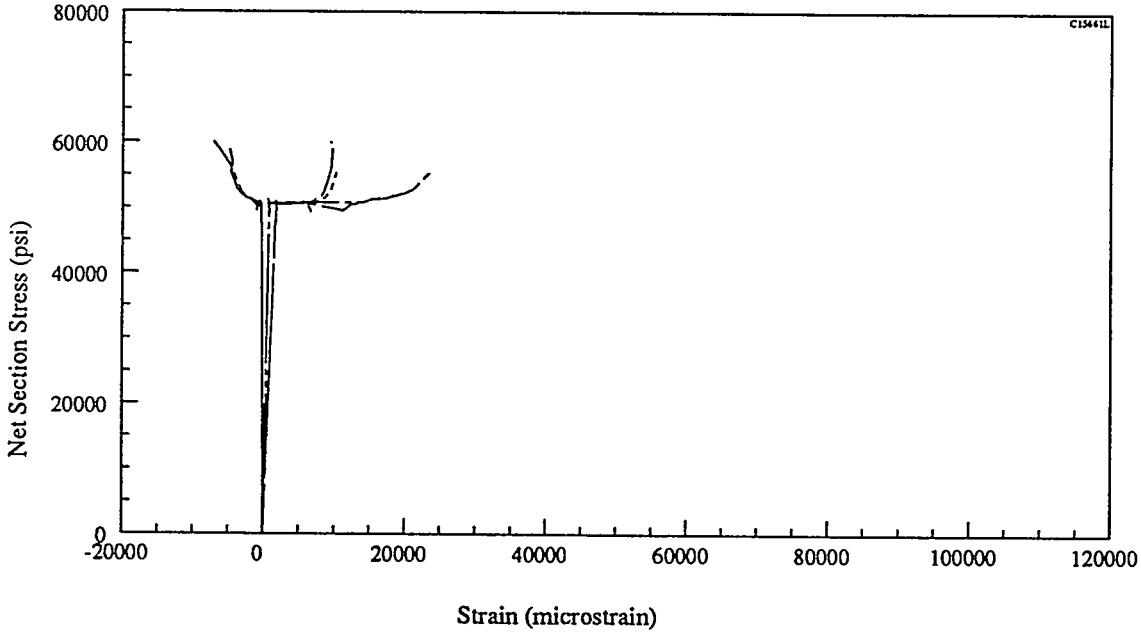

No Initial Liner Stress

Rosette Strains vs Load (cont.)

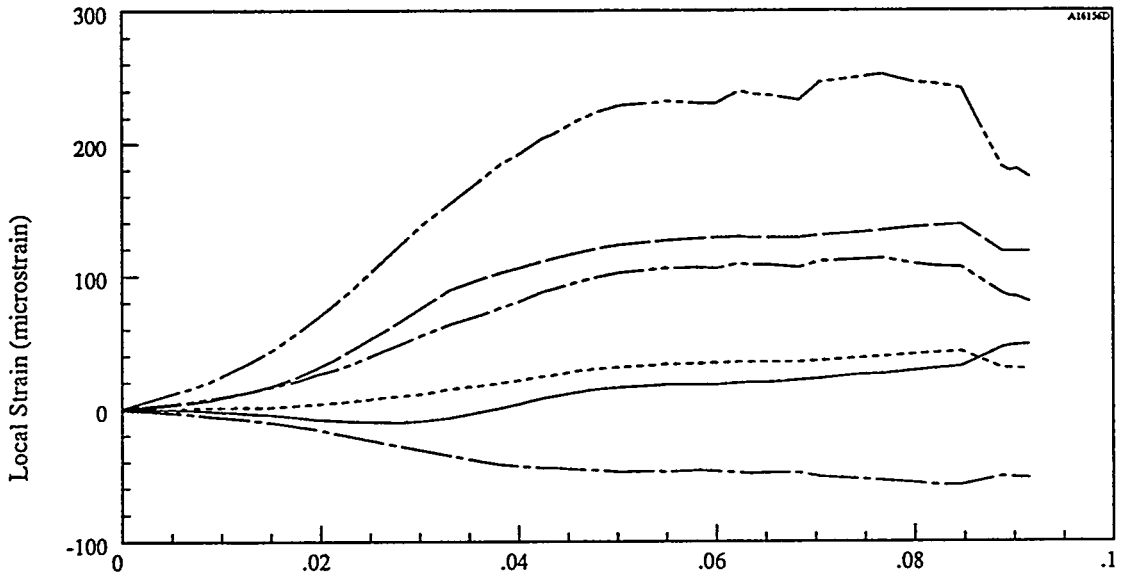

No Initial Liner Stress

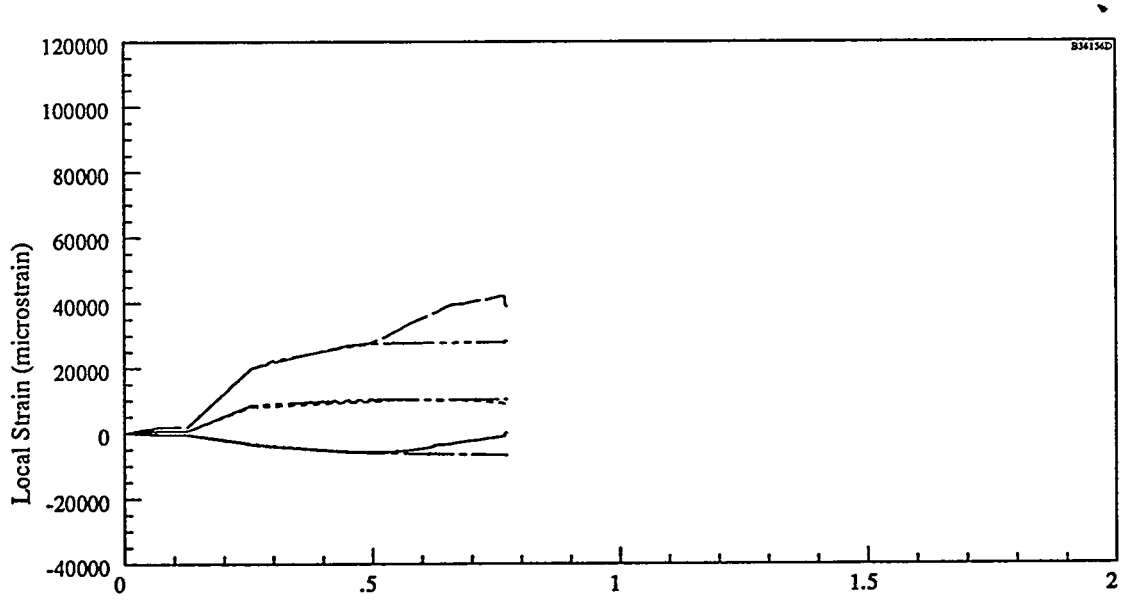

60 ksi Liner Stress

Rosette Strains vs Displacement

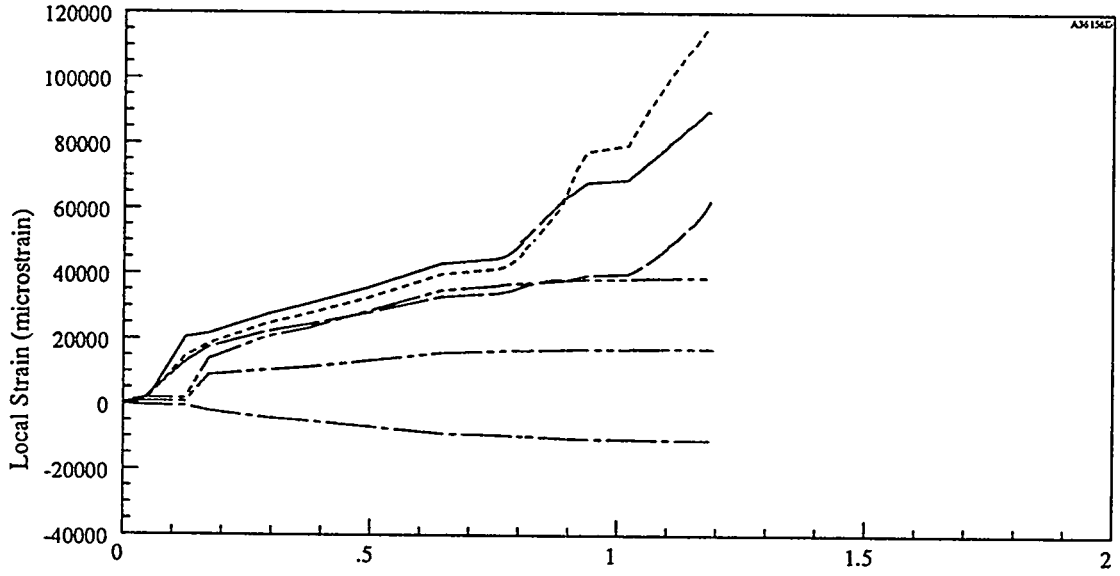

63 ksi Liner Stress

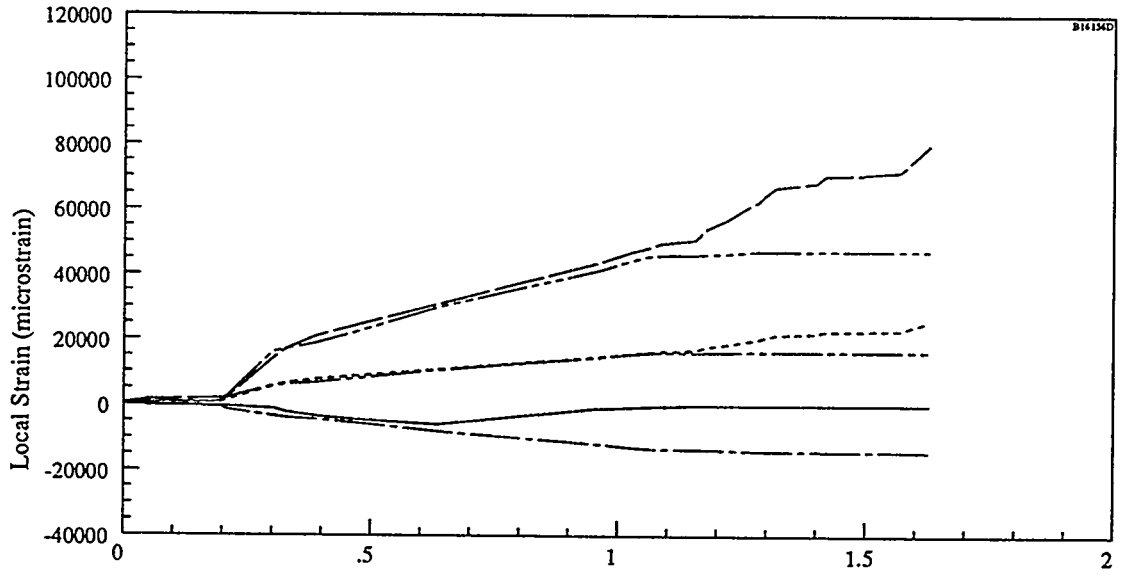

65 ksi Liner Stress

Rosette Strains ve Displacement (cont.)

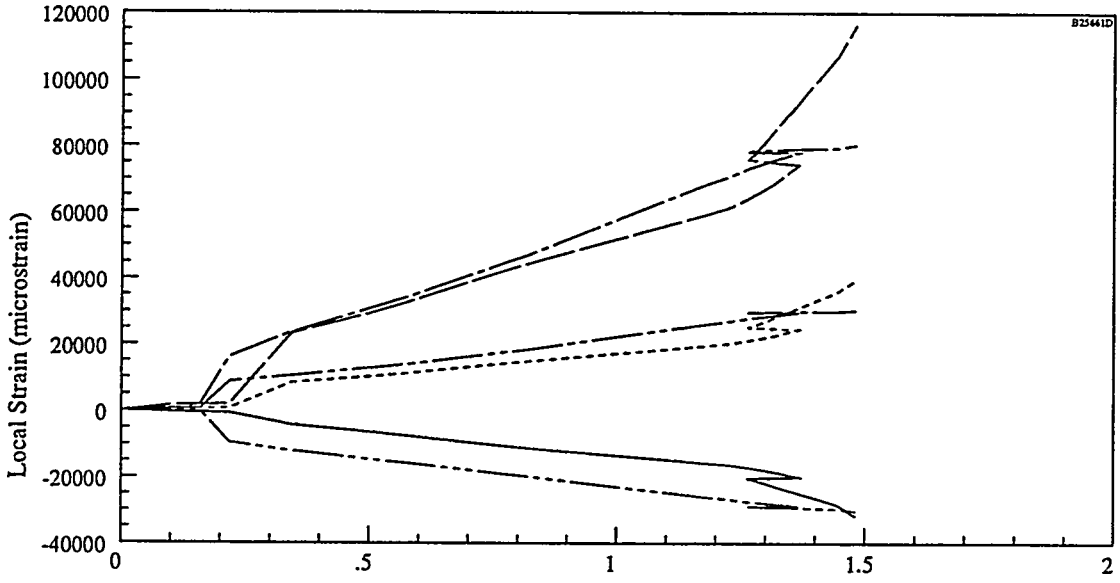

70 ksi Liner Stress

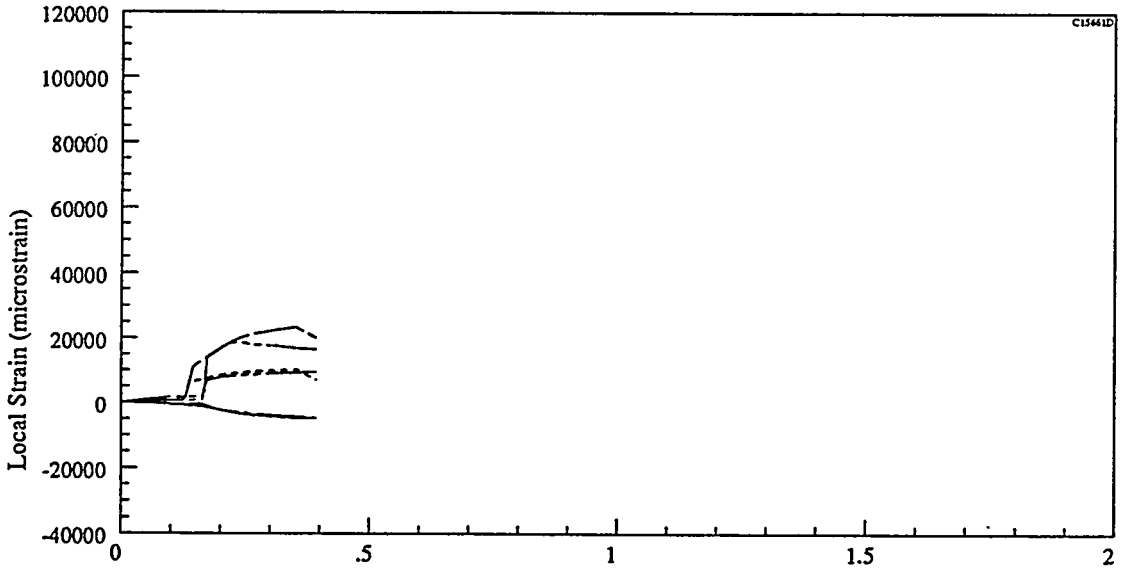

No Stud Load

Rosette Strains vs Displacement (cont.)

Weld and Thickness Transition Specimen (Phase 2A) Strain Gage Plots

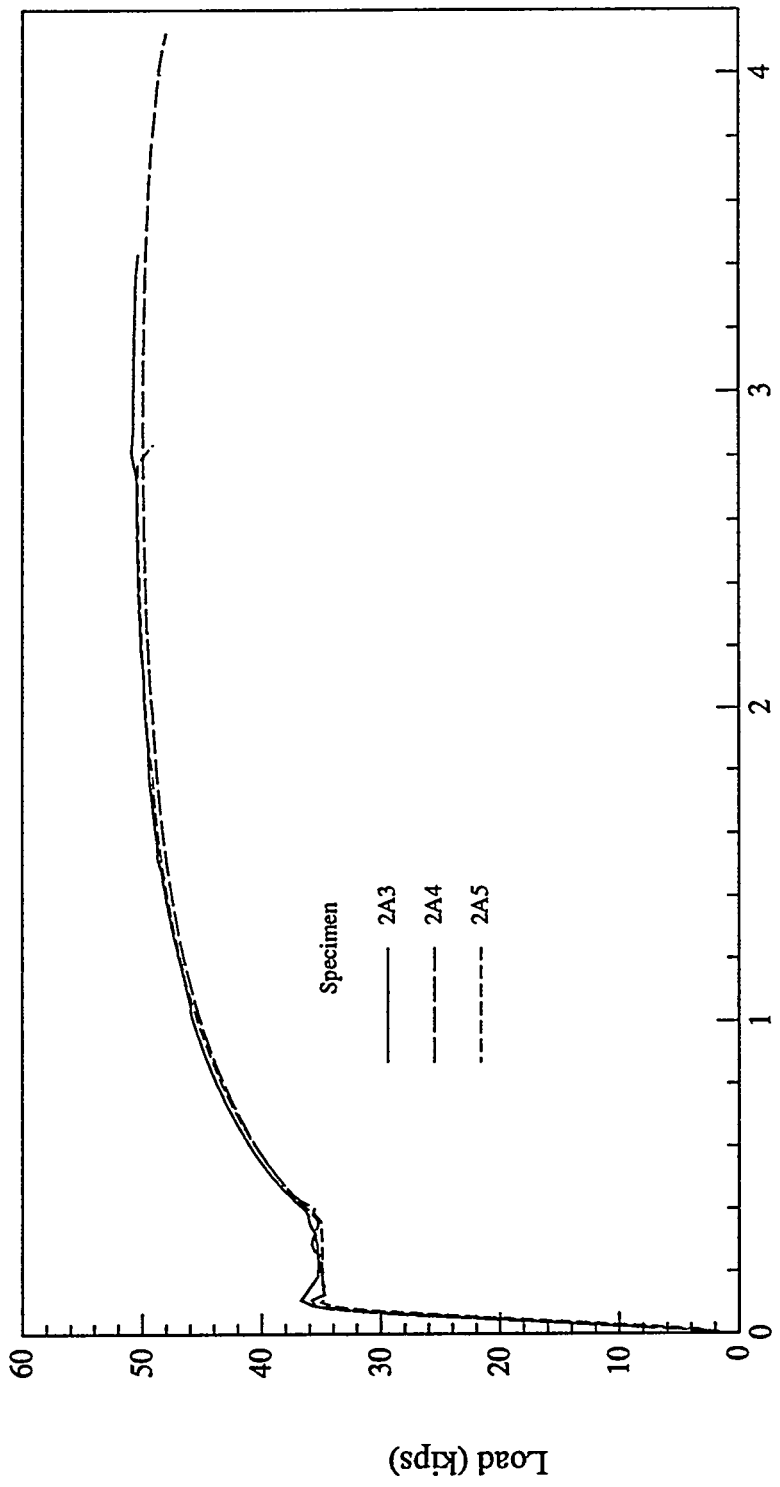

Overall Response of Phase 2A Specimens

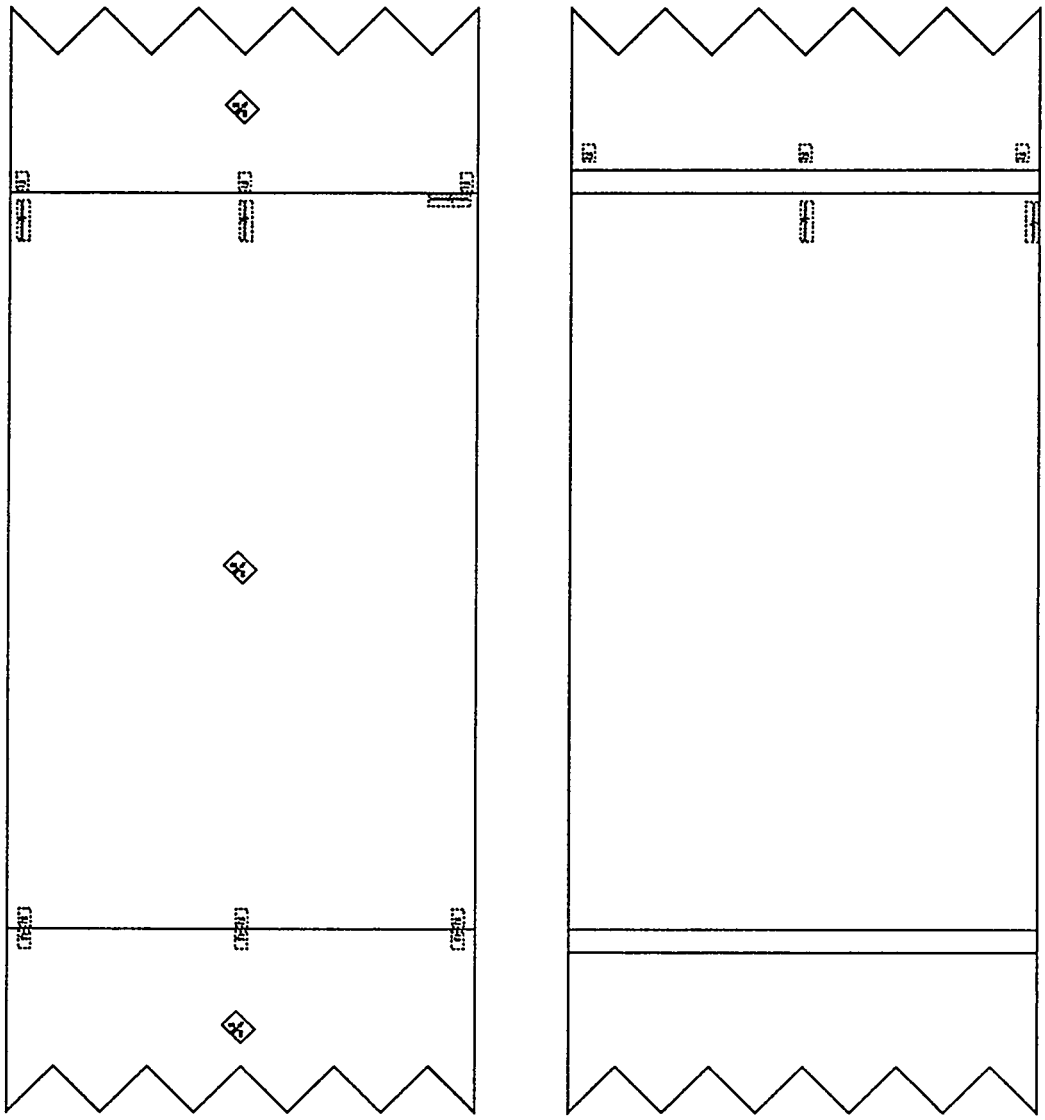

Insert Plate Rosette Gages

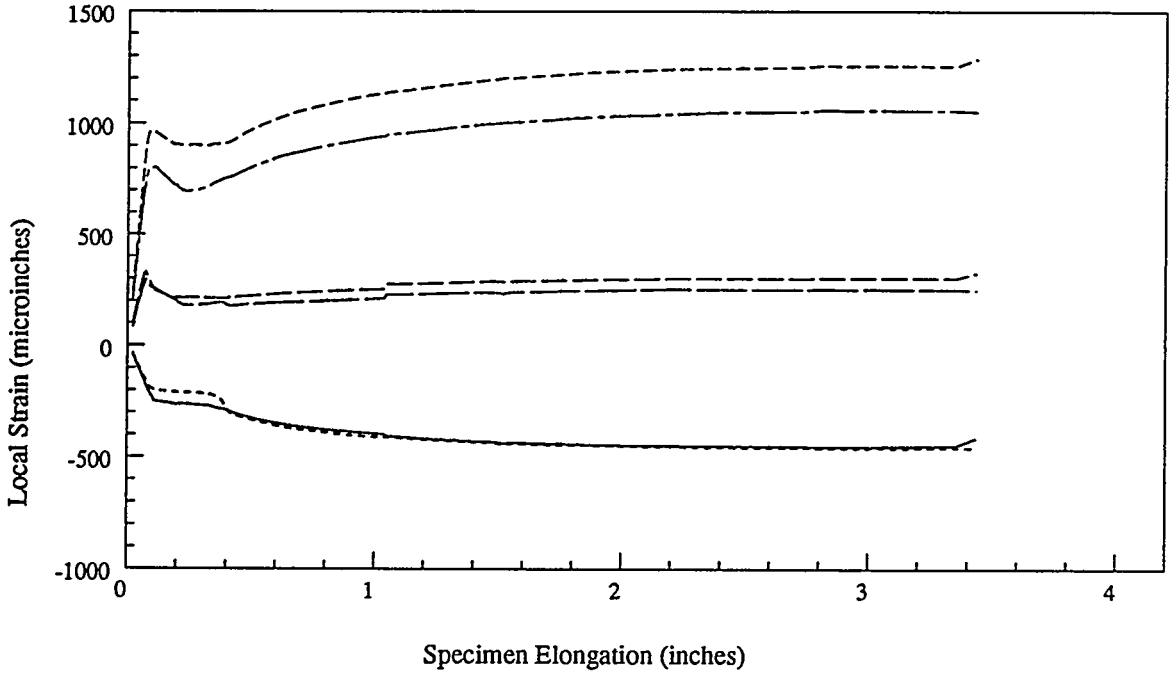

Insert Rosette Gage Response, Specimen 2A3

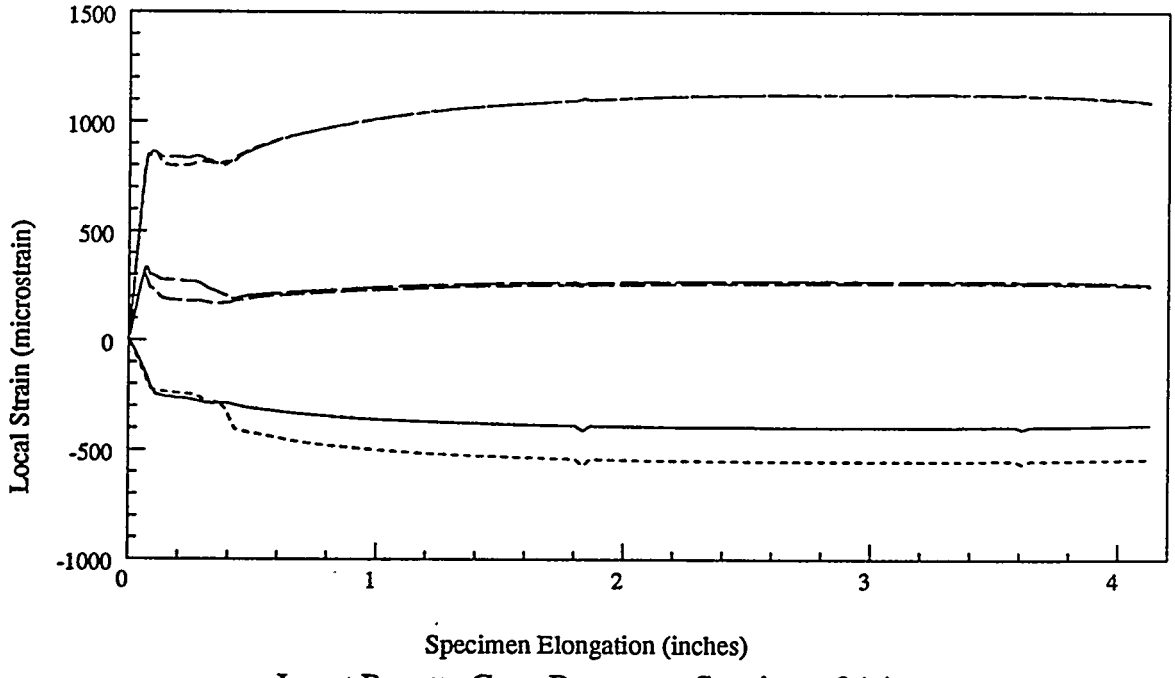

Insert Rosette Gage Response, Specimen 2A4

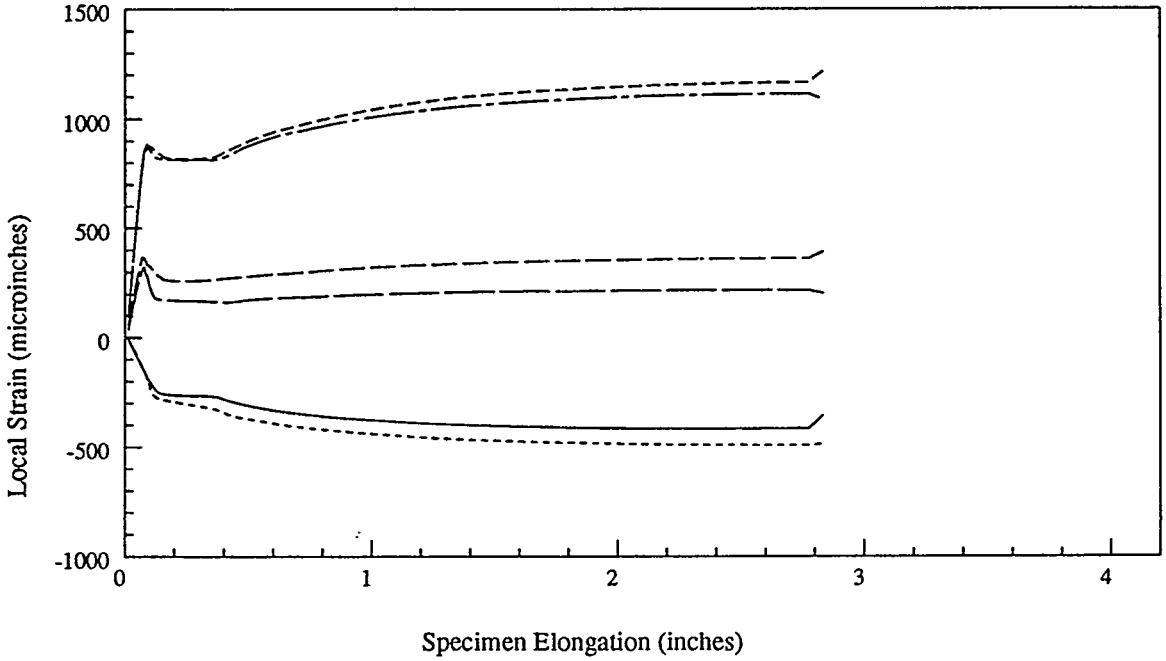

Insert Rosette Gage Response, Specimen 2A5

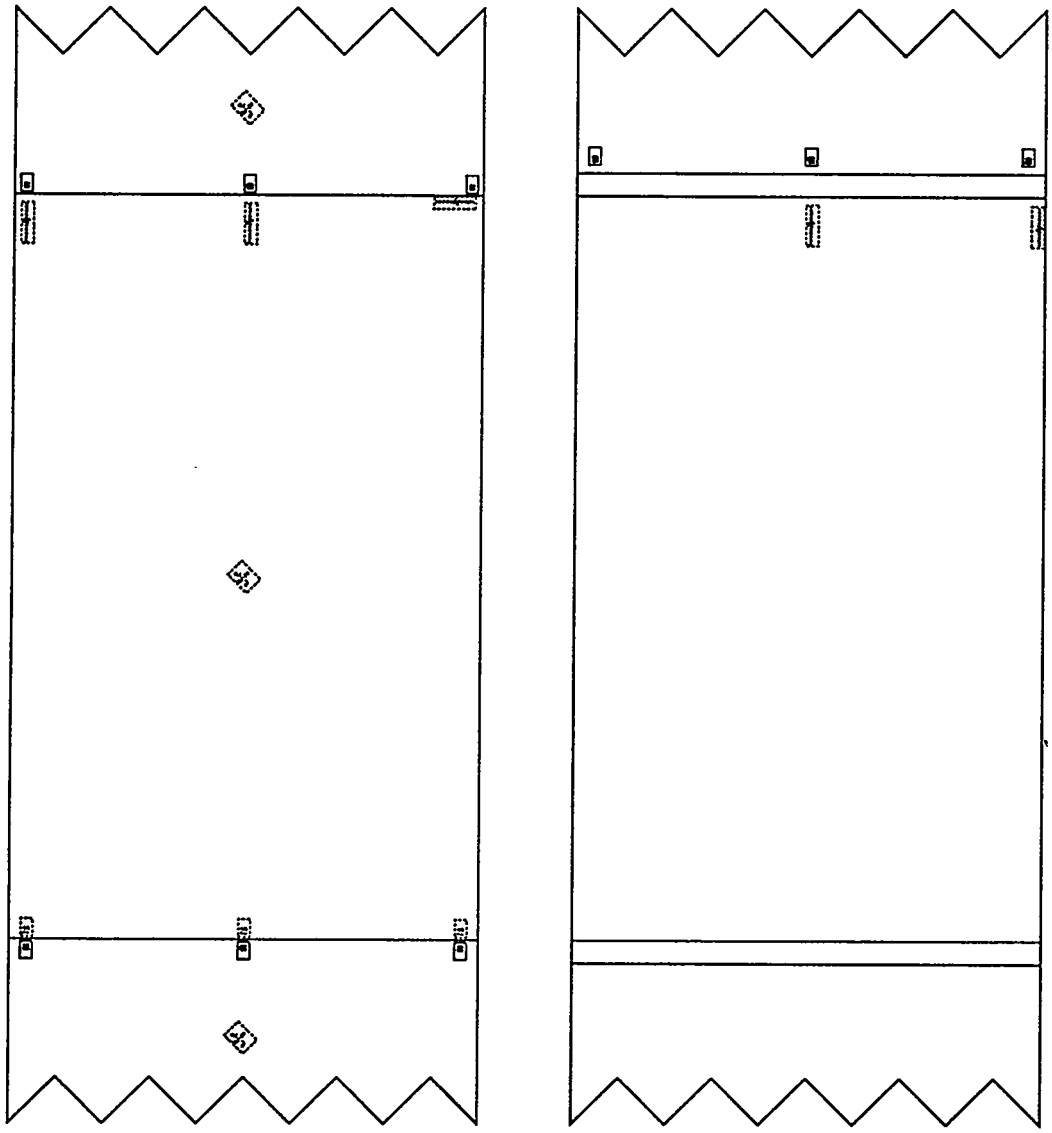

Insert Plate Single Gages

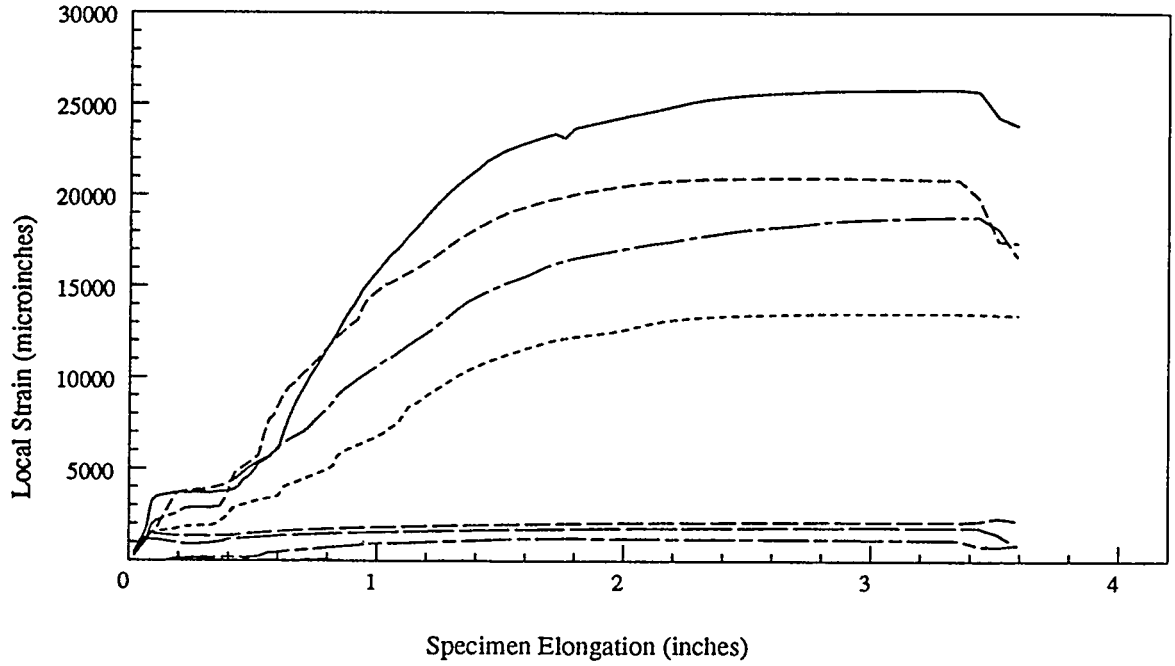

Insert Plate Single Gage Response, Specimen 2A3

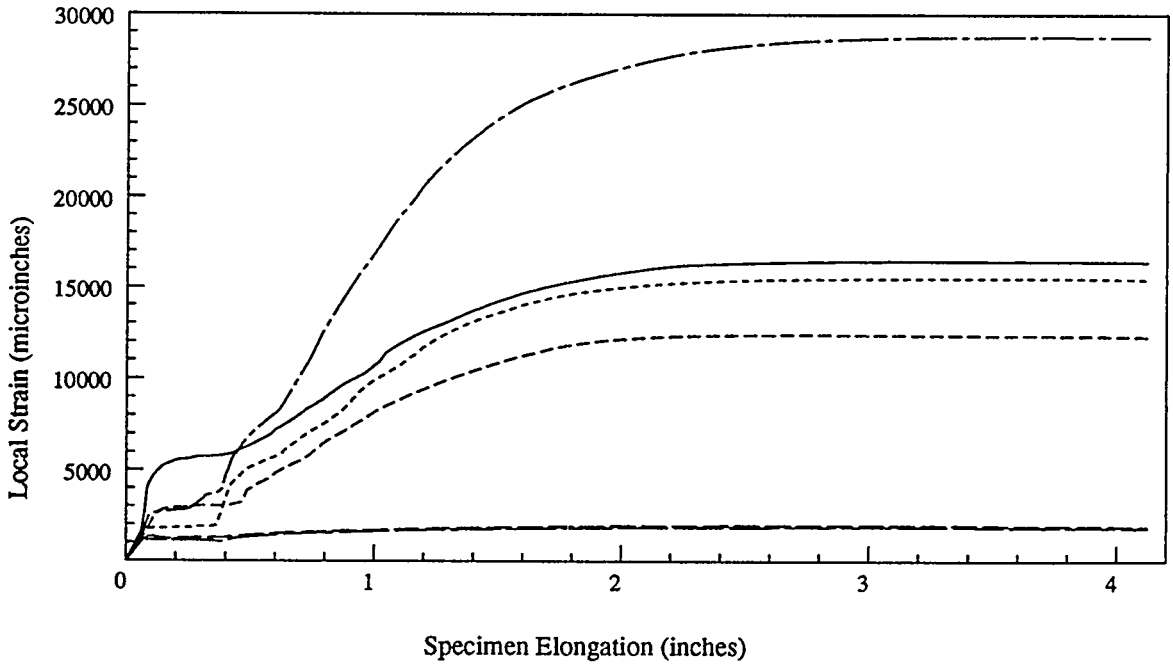

Insert Plate Single Gage Response, Specimen 2A4

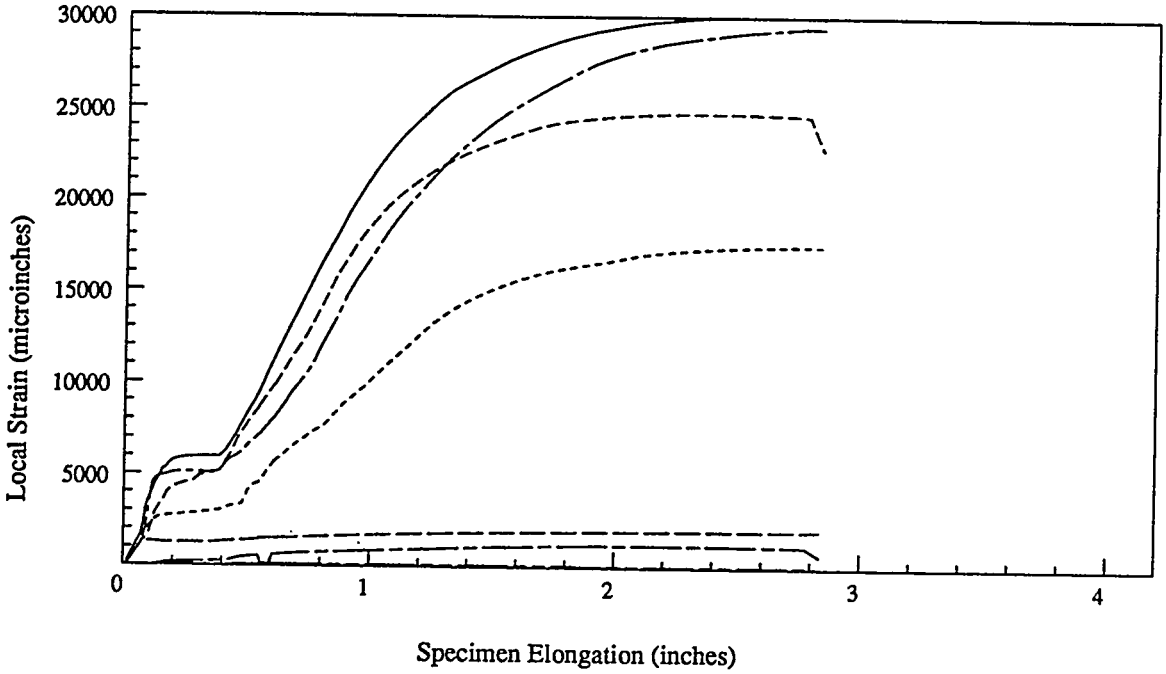

Insert Plate Single Gage Response, Specimen 2A5

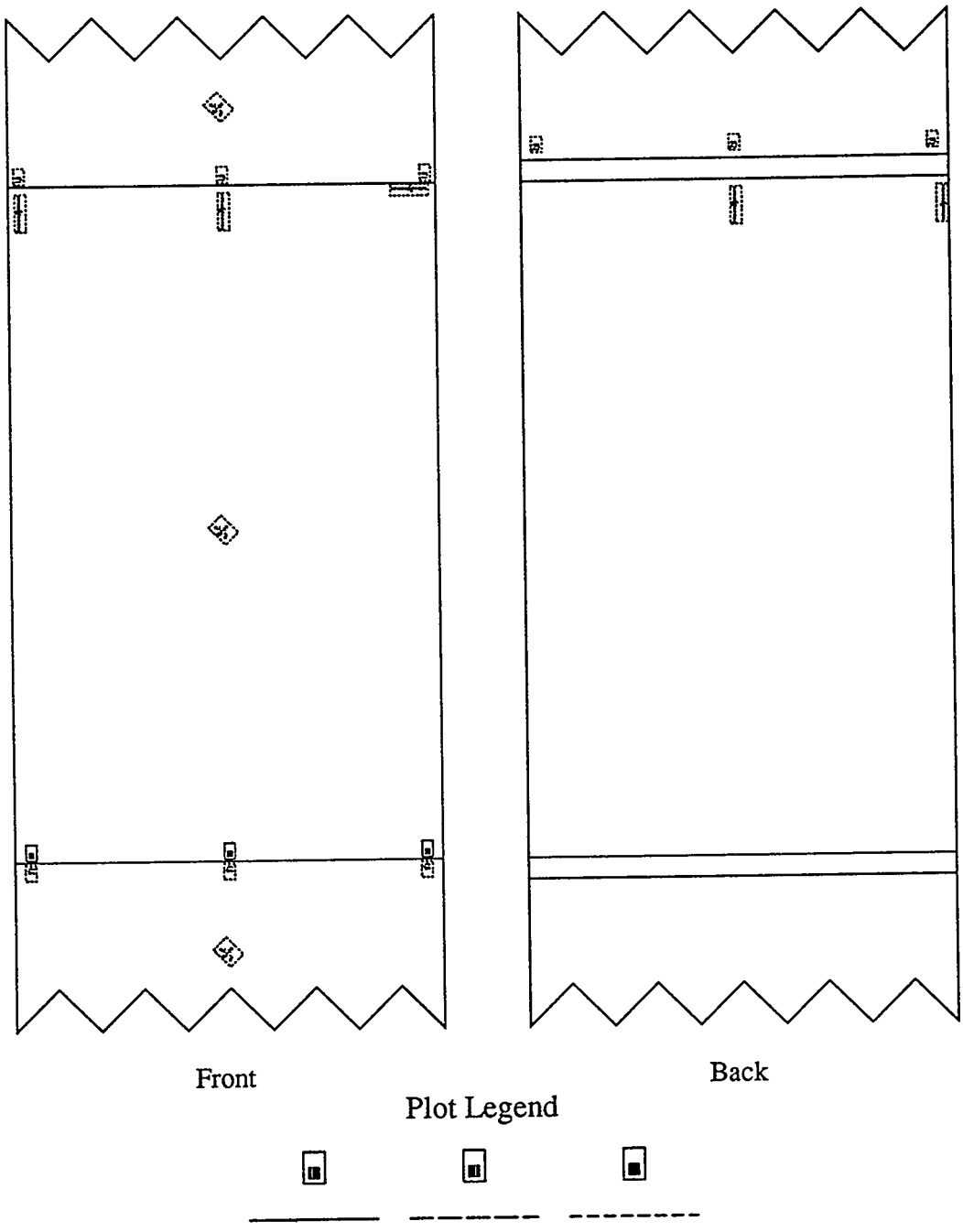

Liner Single-Element Gages

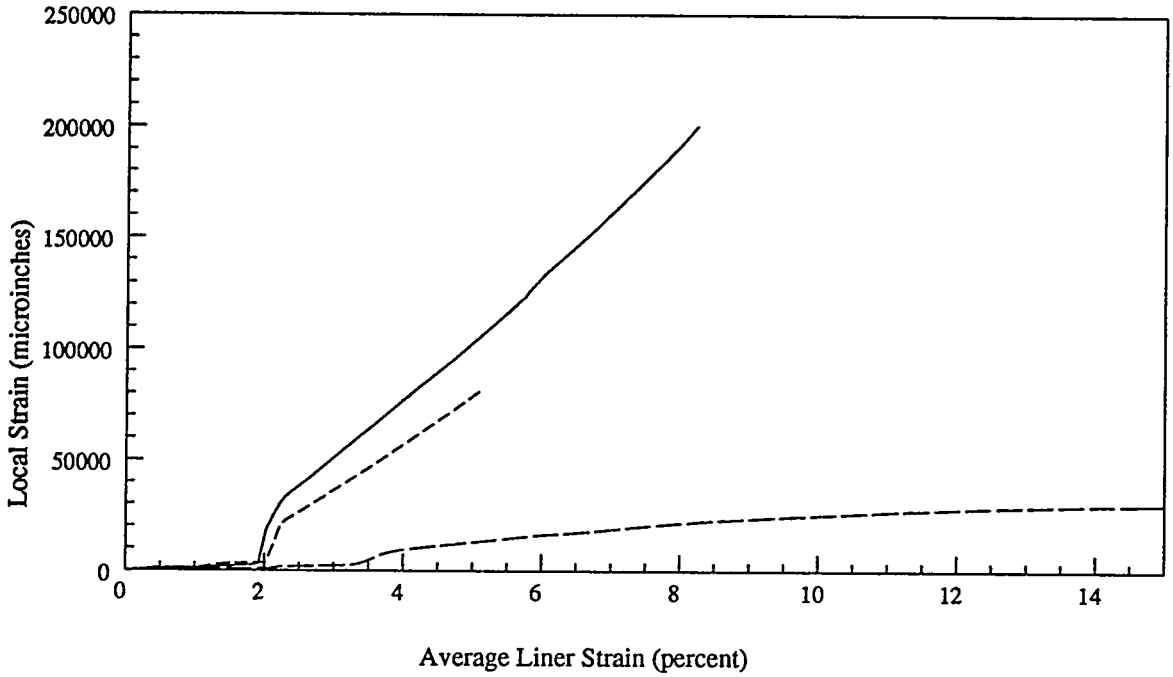

Liner Single Gage Response, Specimen 2A3

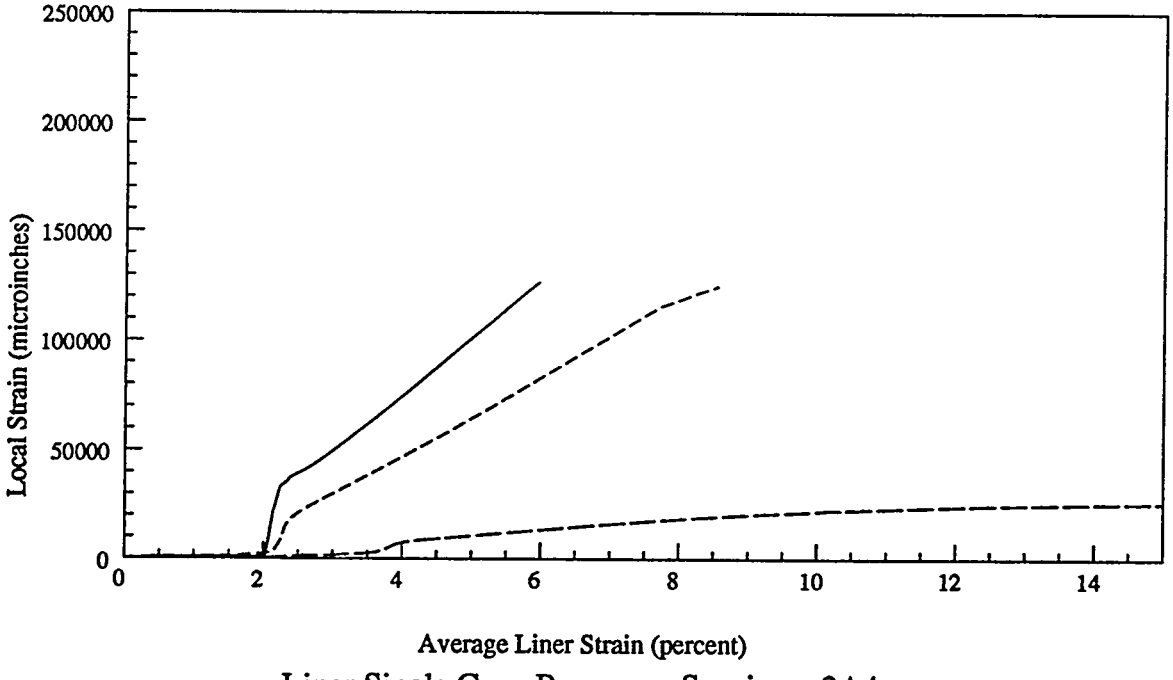

Liner Single Gage Response, Specimen 2A4

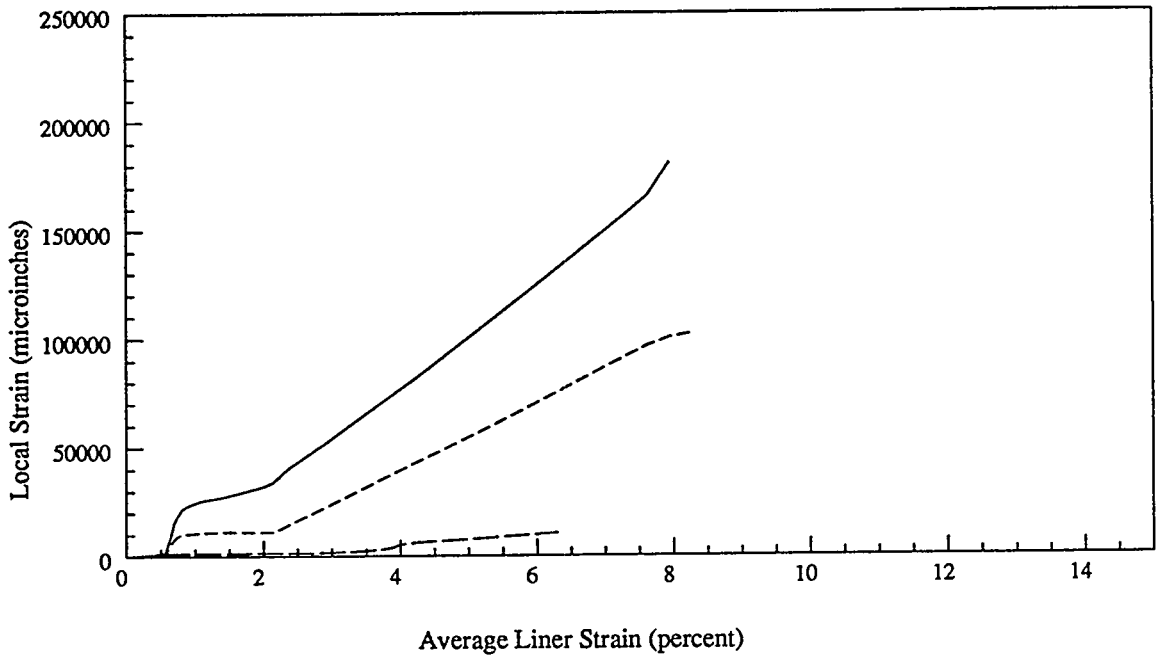

Liner Single Gage Response, Specimen 2A5

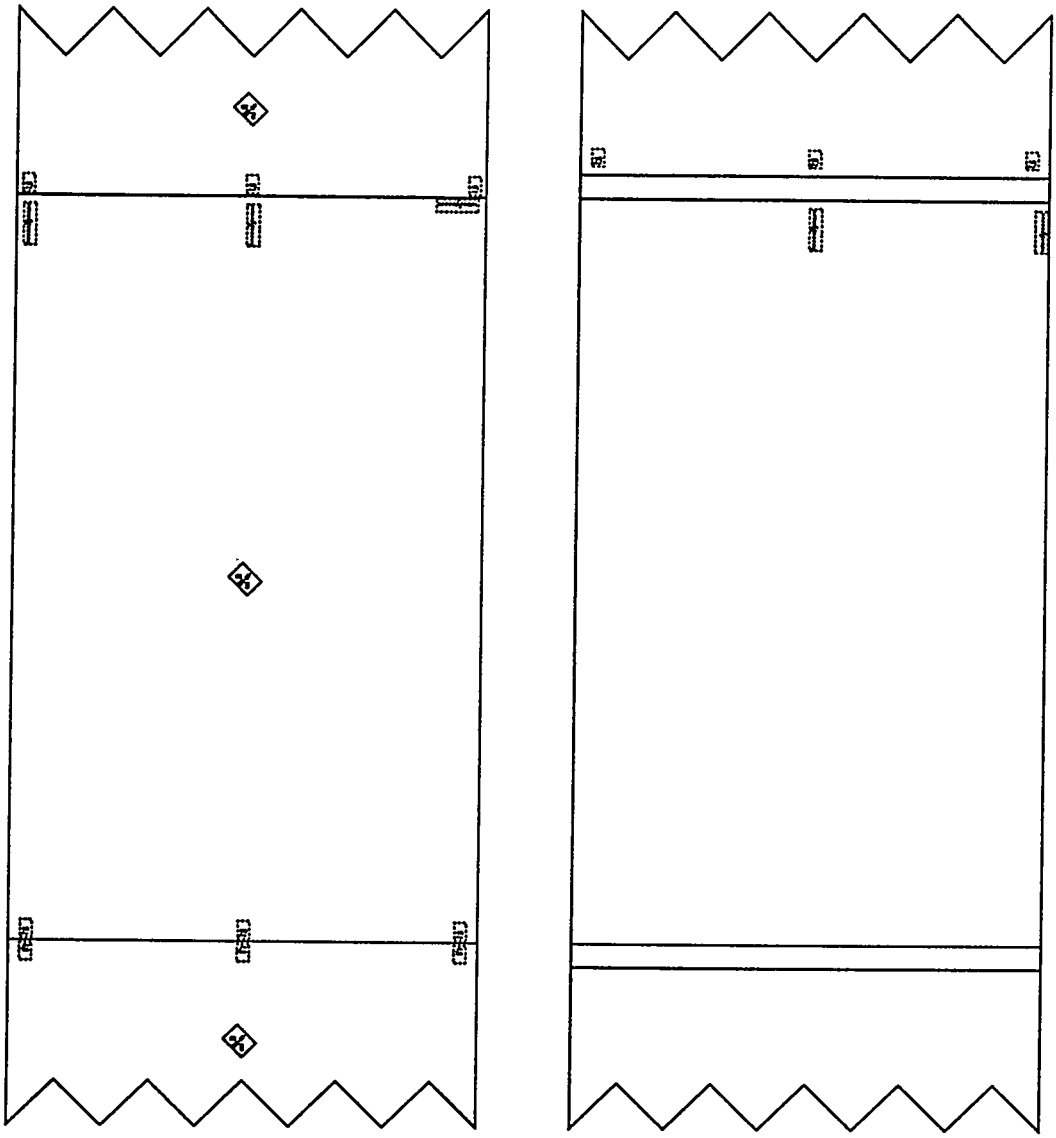

Liner Rosette Gages

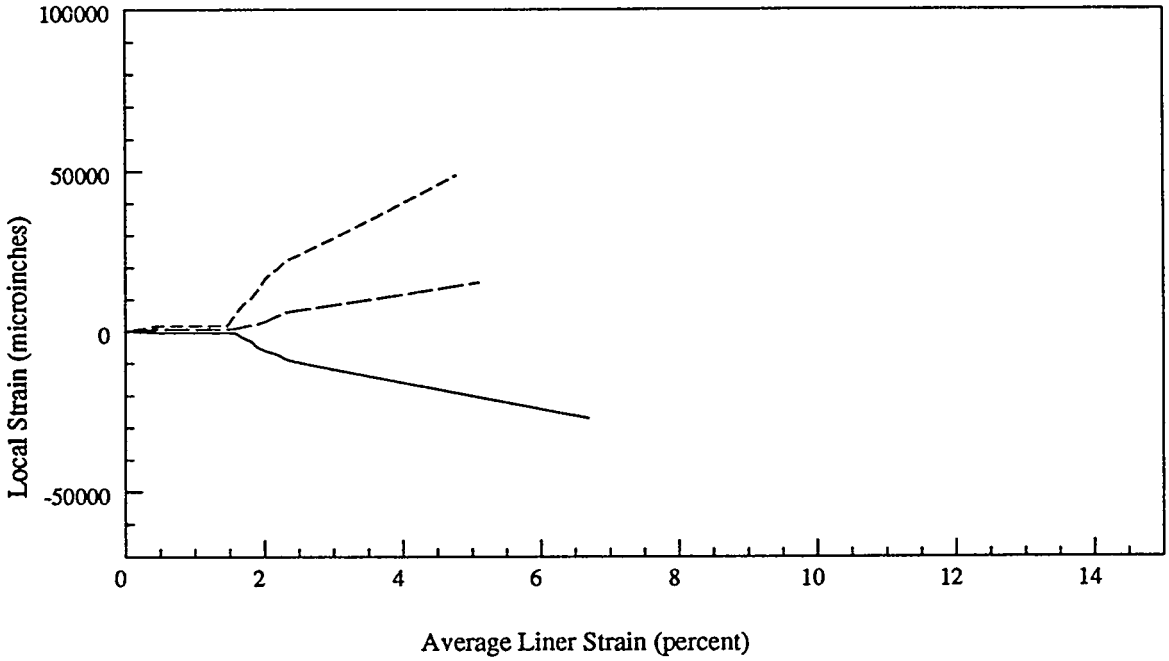

Liner Rosette Gage Response, Specimen 2A3

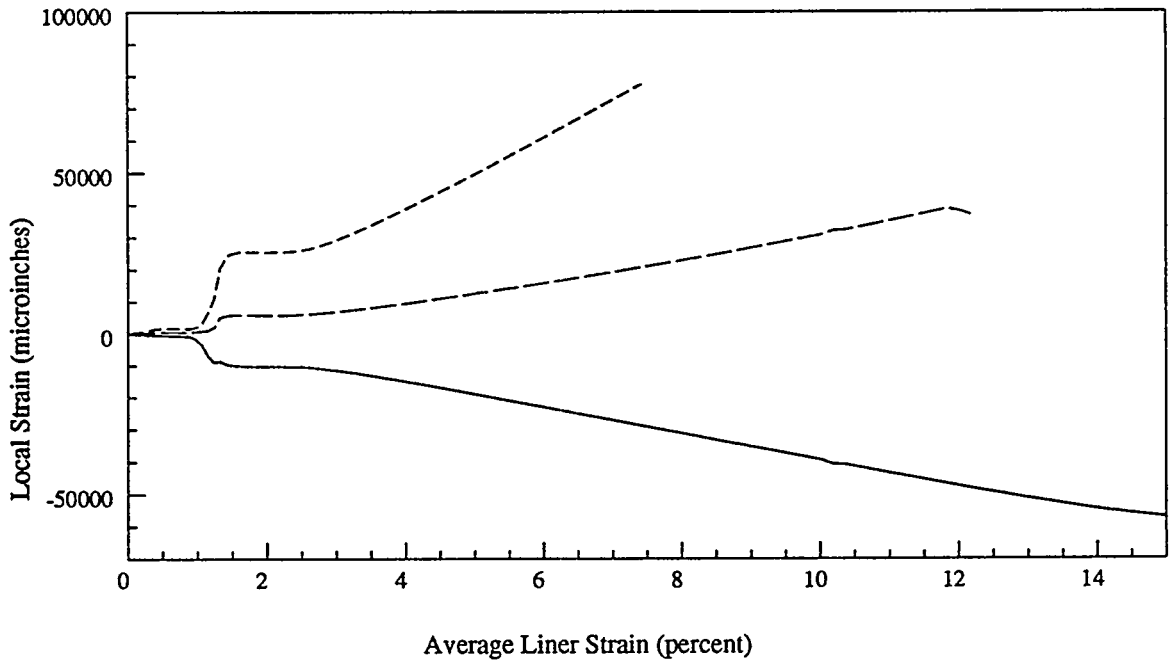

Liner Rosette Gage Response, Specimen 2A4

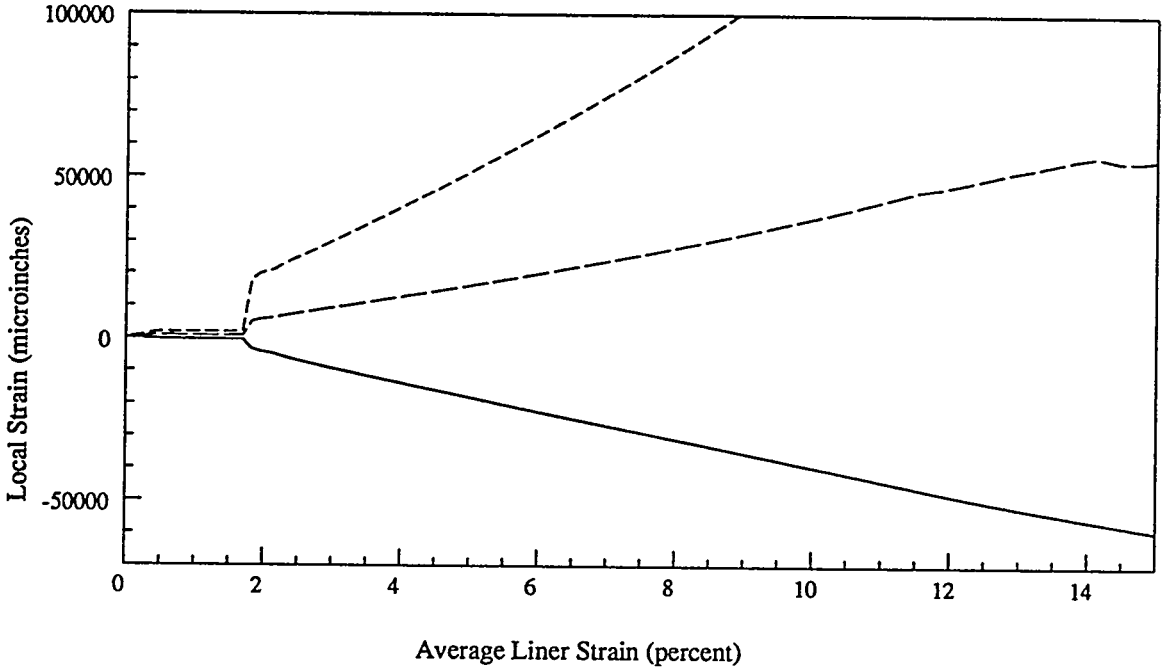

Liner Rosette Gage Response, Specimen 2A5

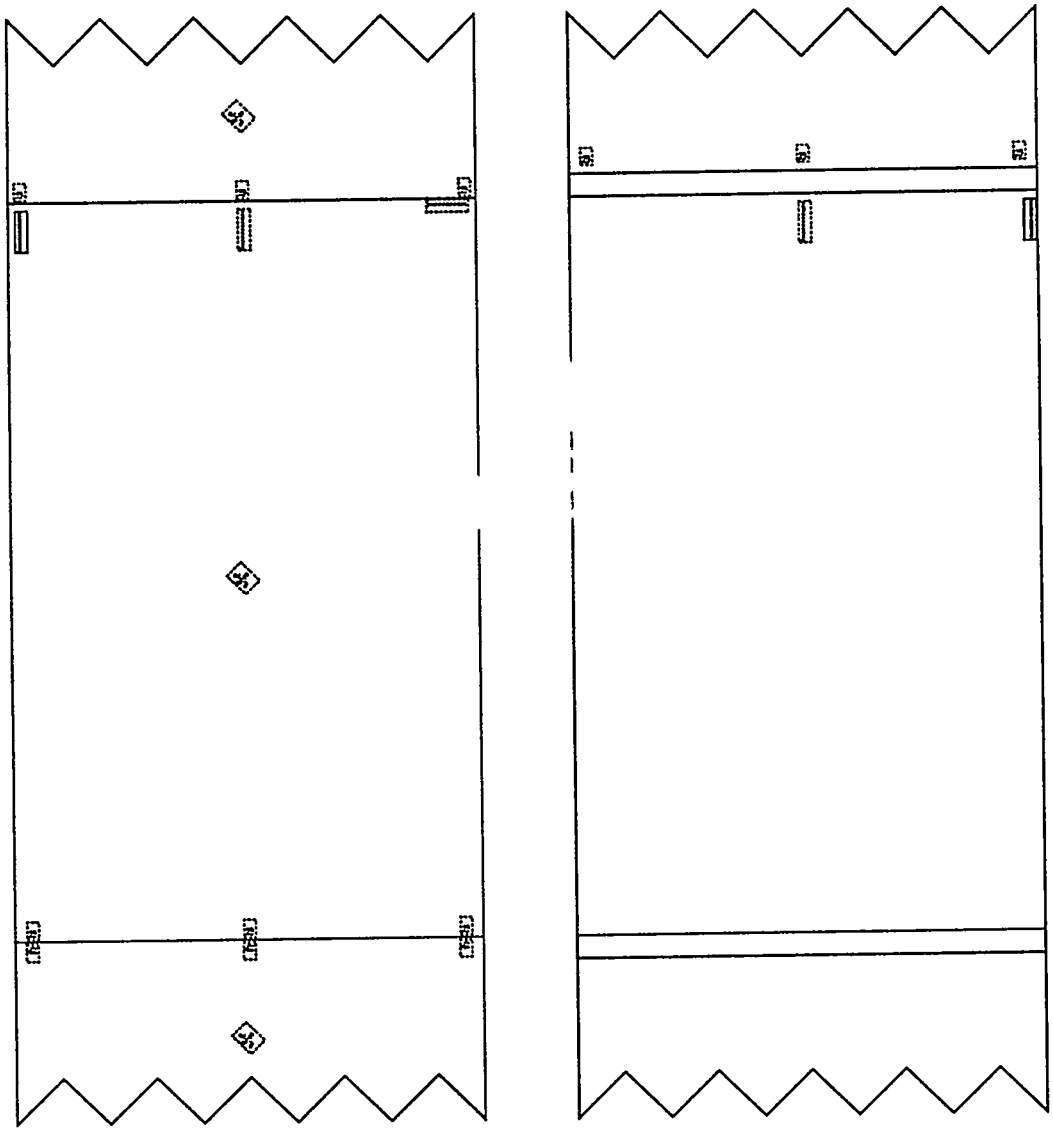

Plot Legend

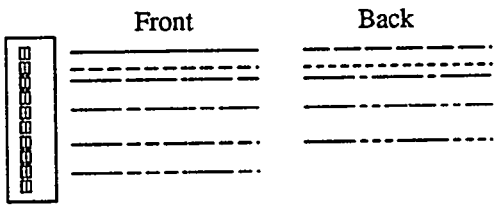

Liner Edge Strip Gages

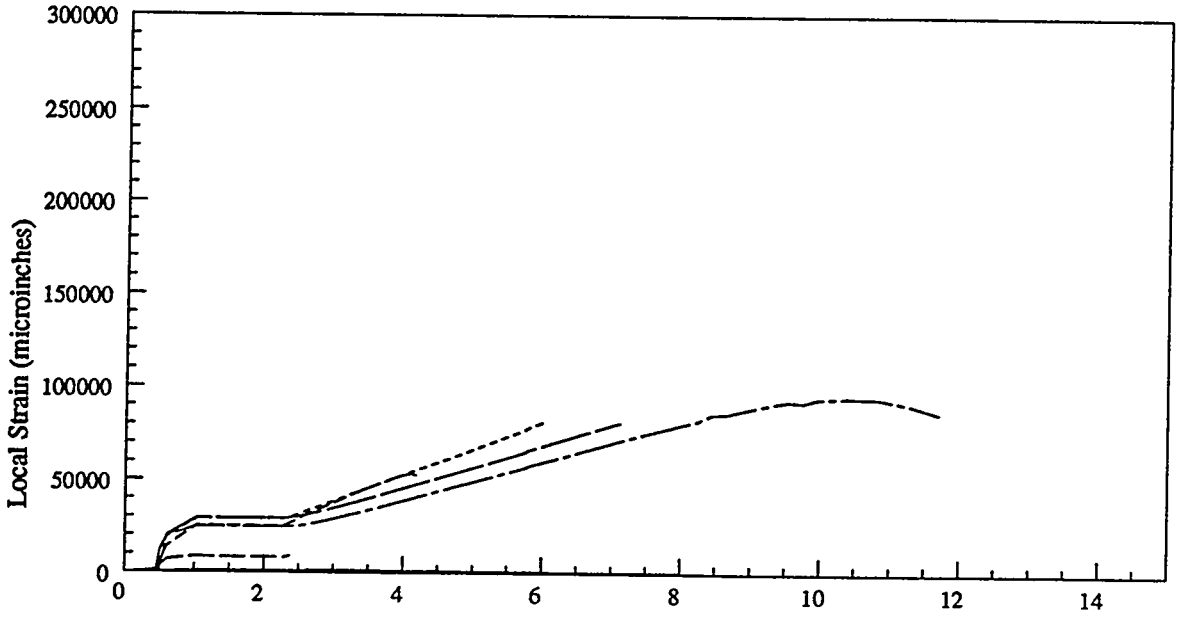

Liner Edge Strip Gage Response, Specimen 2A3

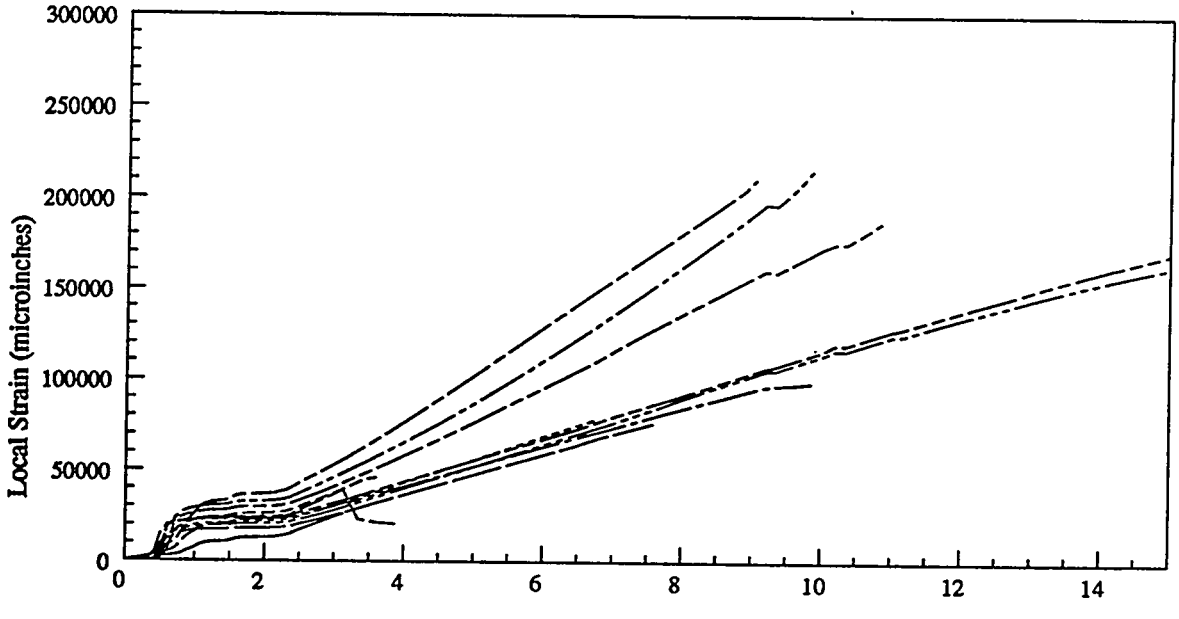

Liner Edge Strip Gage Response, Specimen 2A4

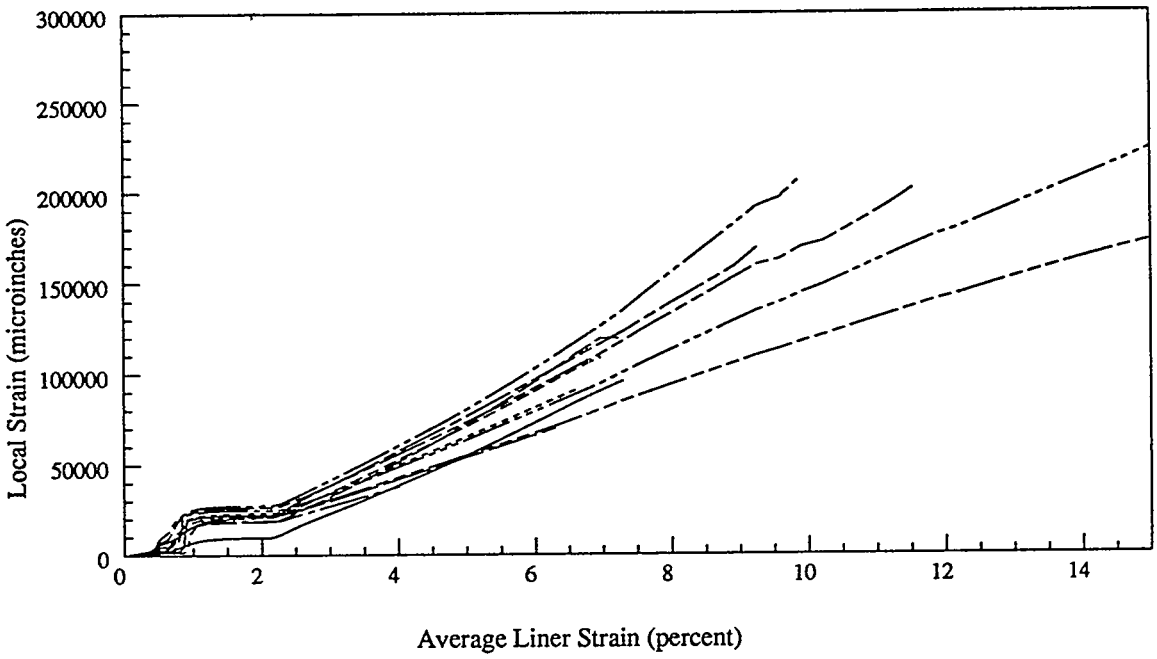

Liner Edge Strip Gage Response, Specimen 2A5

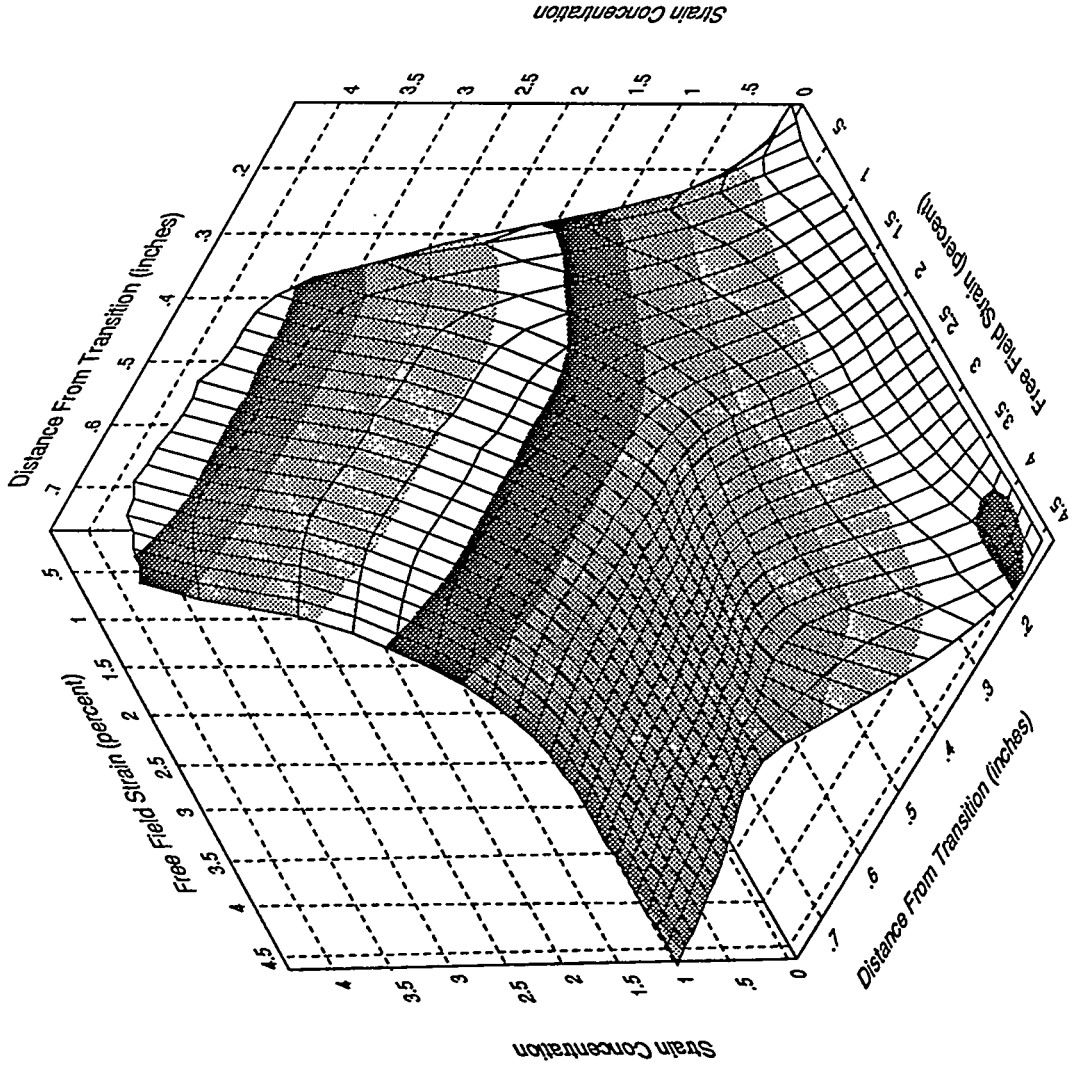

Front Edge Strip Gage, Specimen 2A3

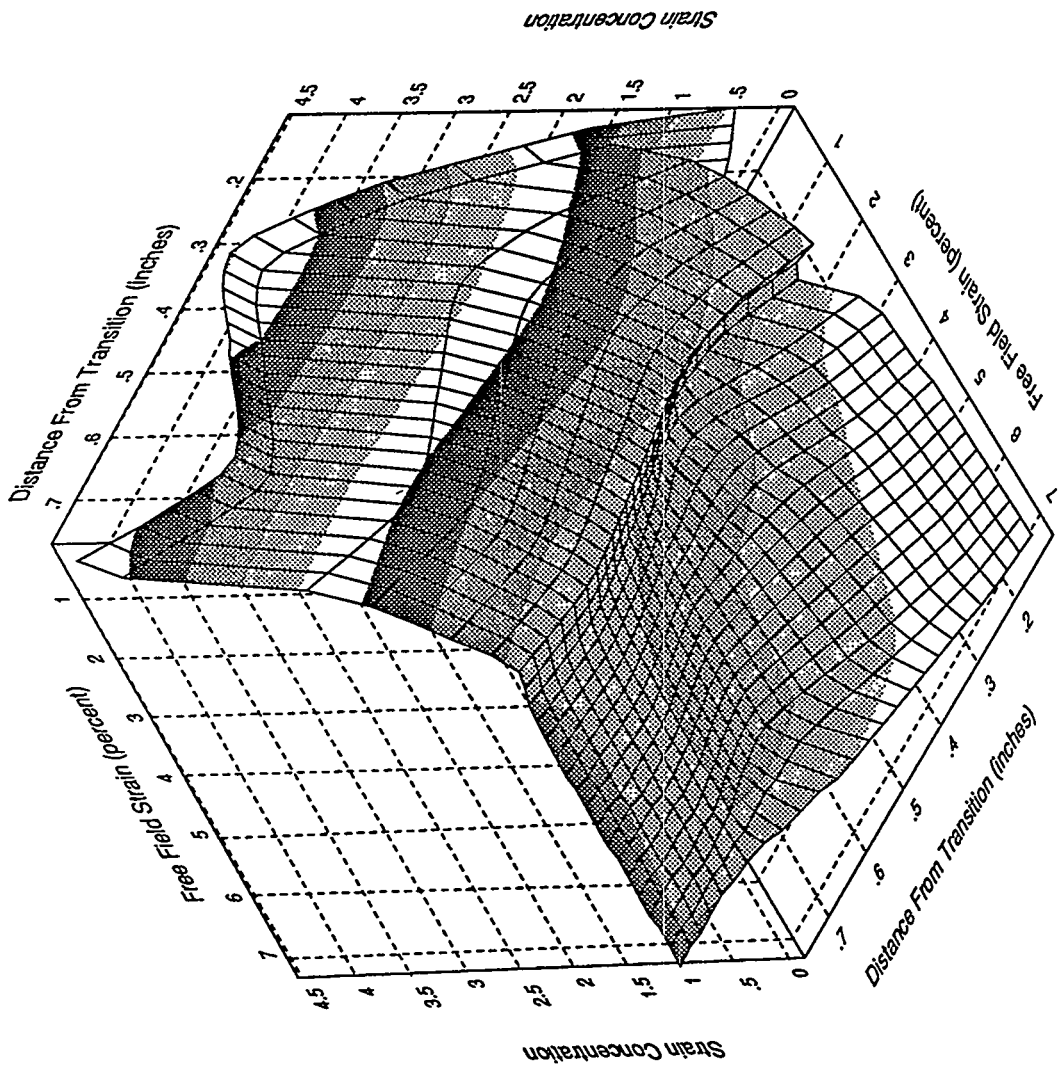

Front Edge Strip Gage, Specimen 2A4

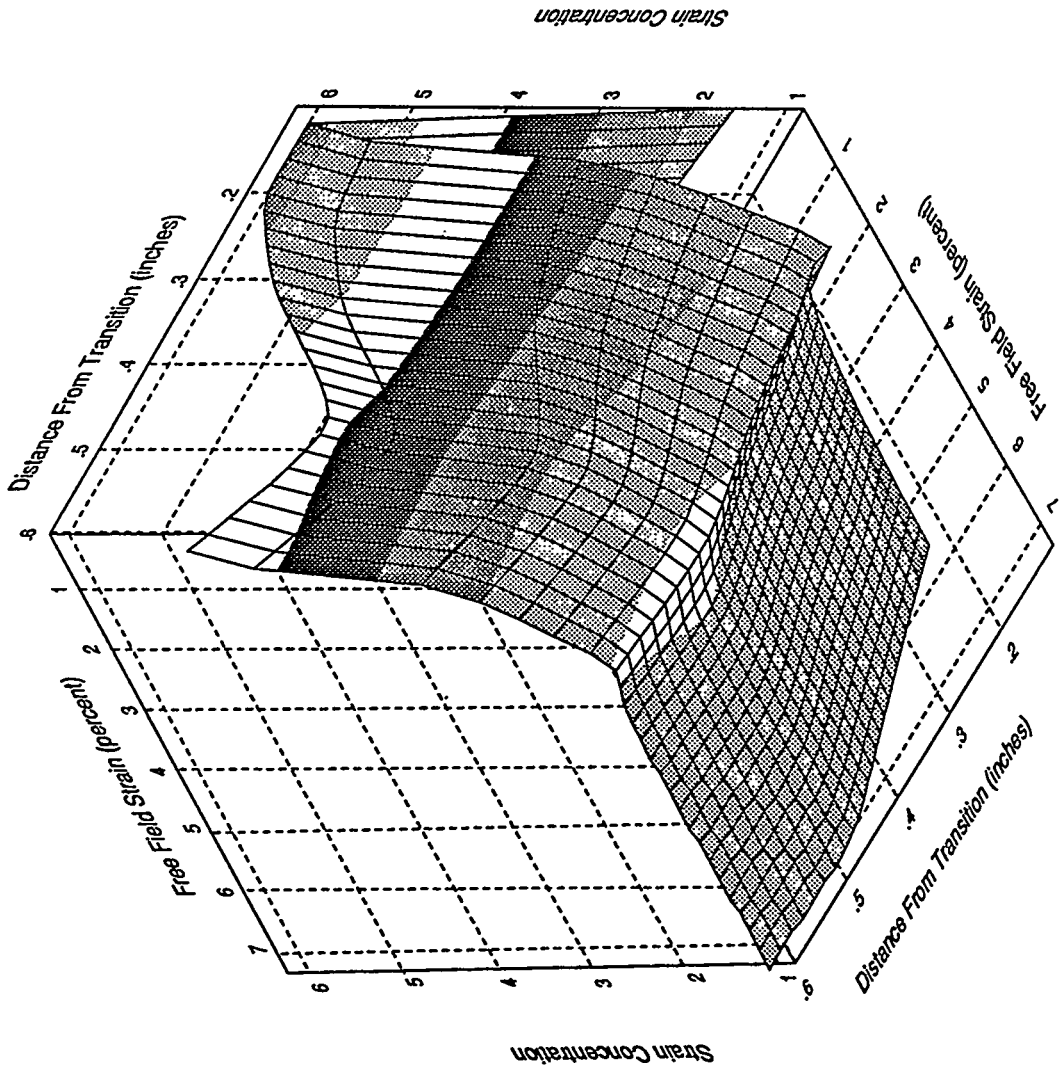

Back Edge Strip Gage, Specimen 2A4

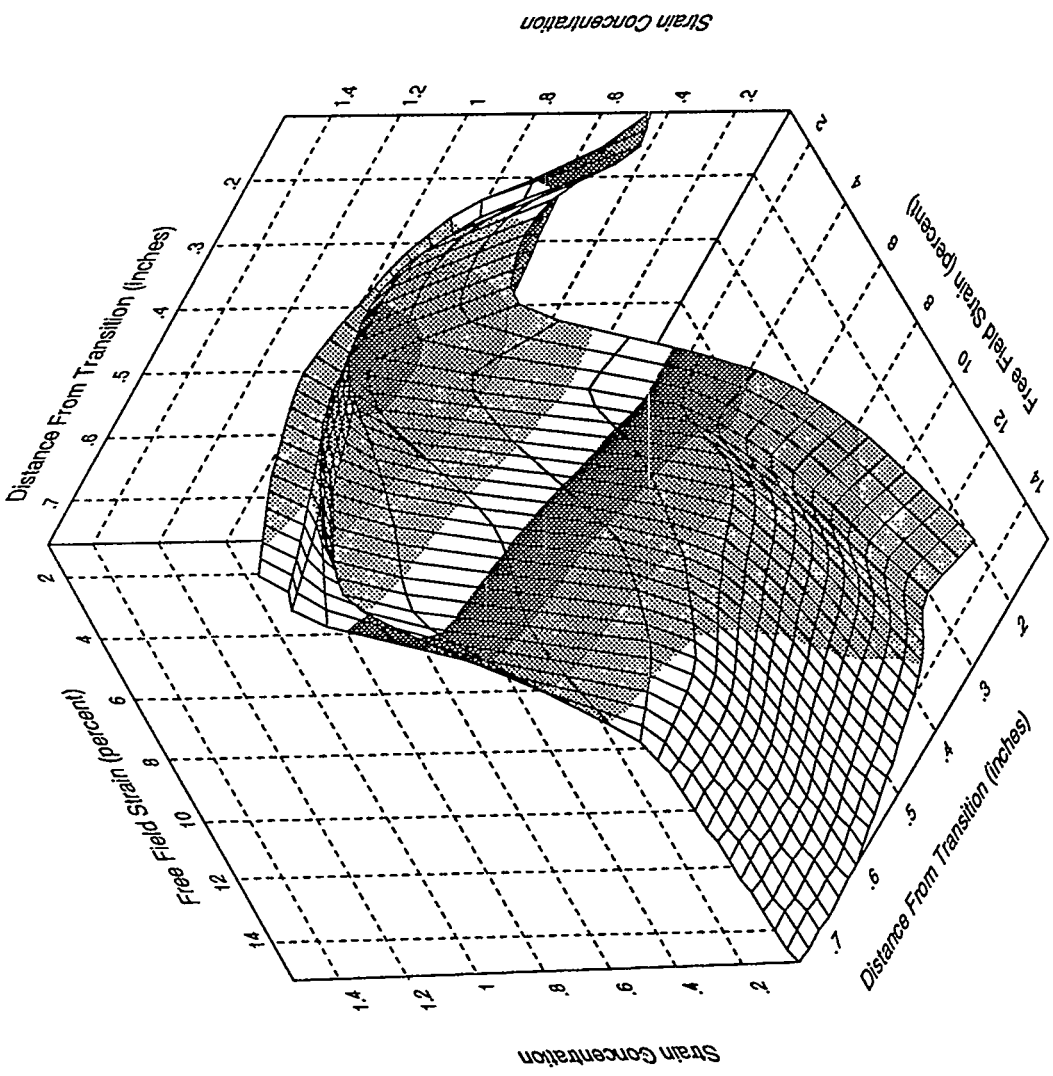

Front Edge Strip Gage, Specimen 2A5

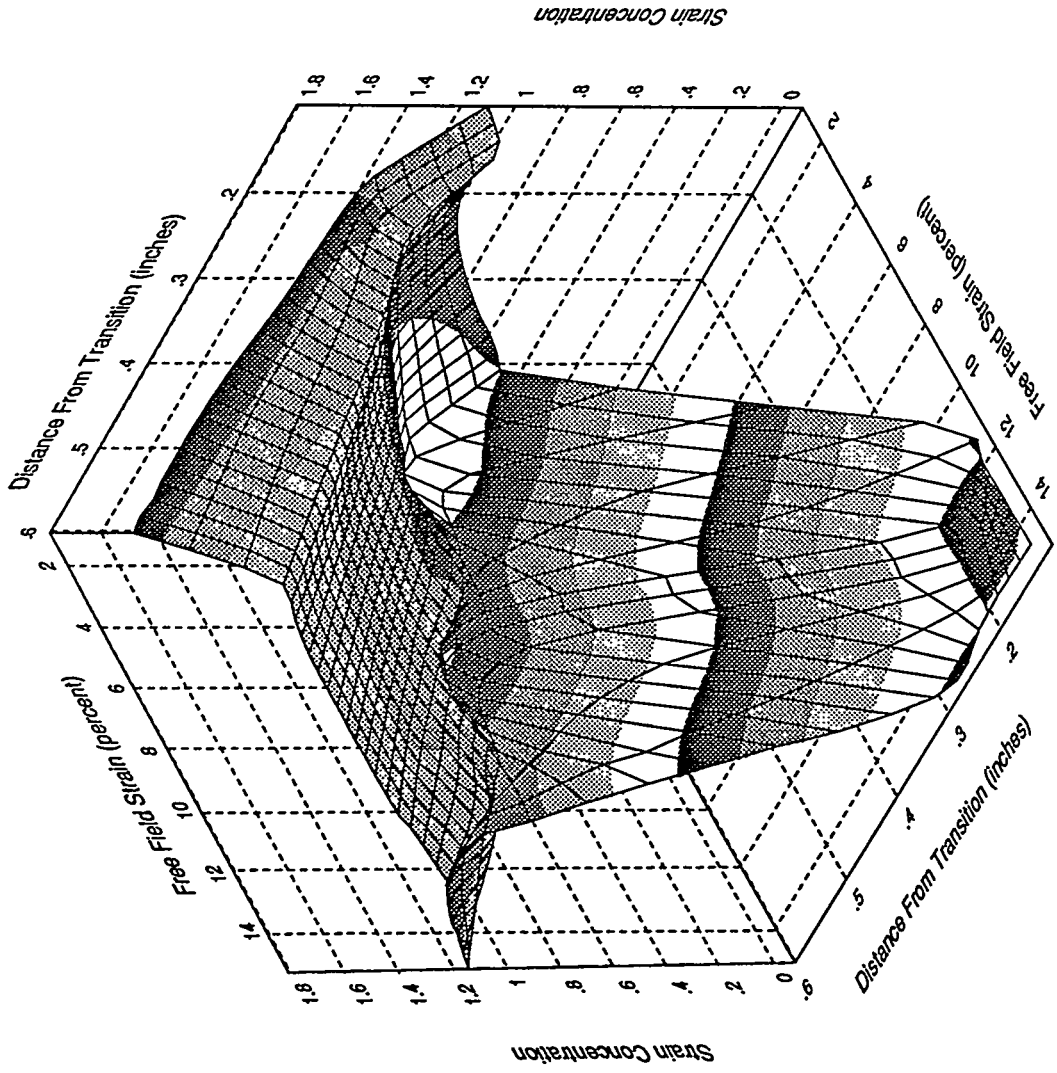

Back Edge Strip Gage, Specimen 2A5

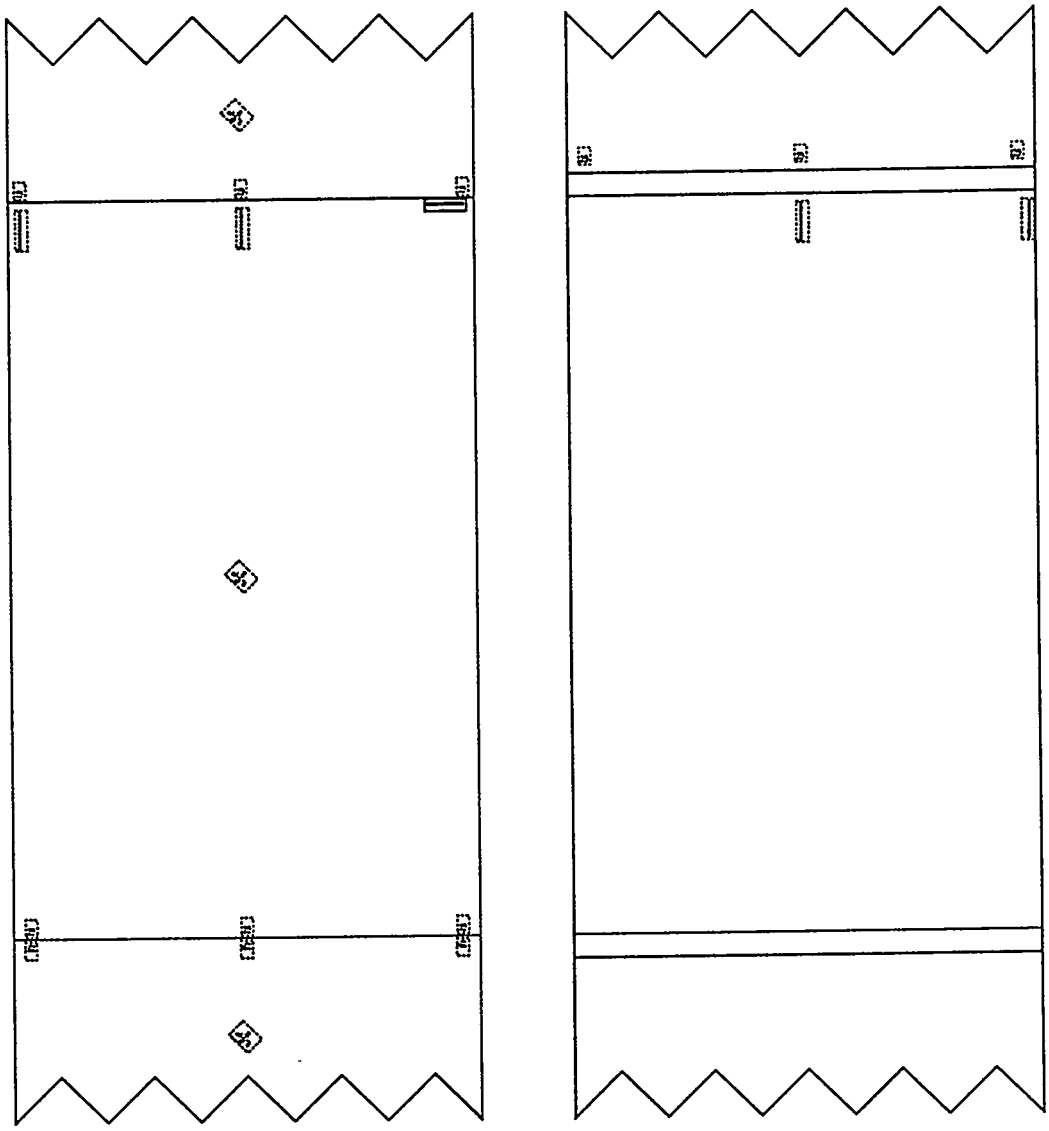

Liner Poisson Gages

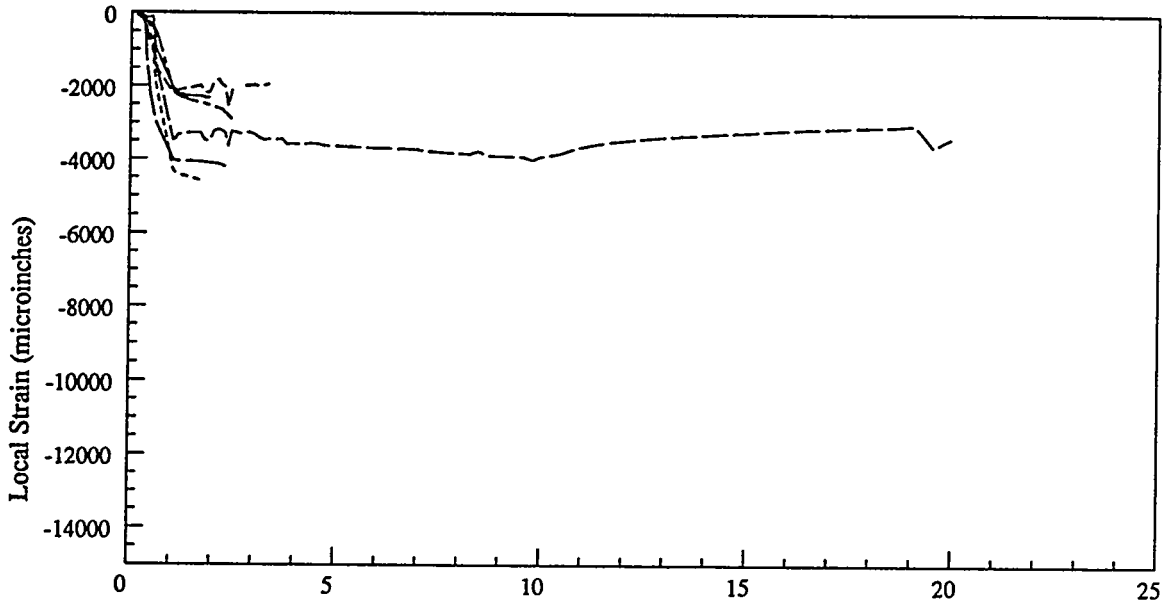

Poisson Strip Gage Response, Specimen 2A3

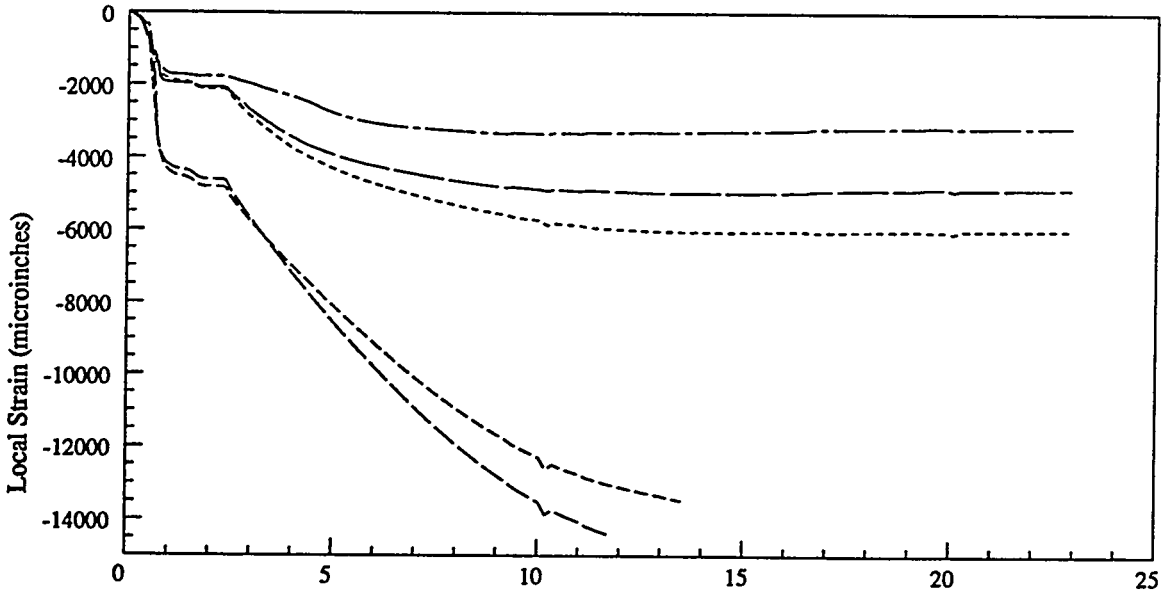

Poisson Strip Gage Response, Specimen 2A4

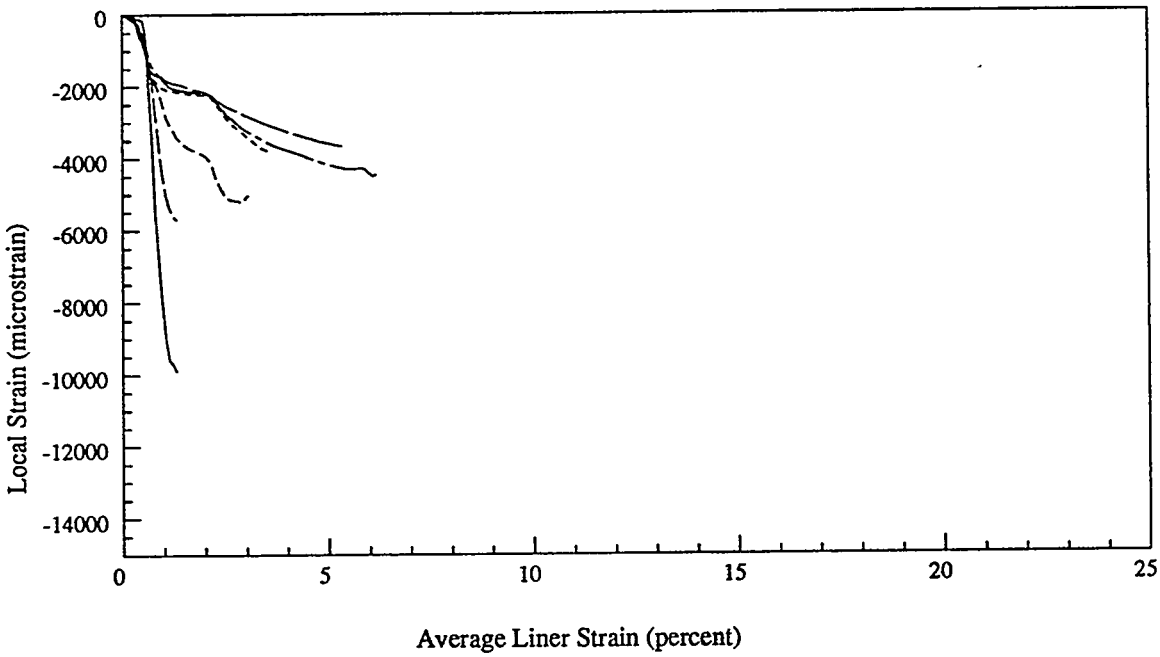

Poisson Strip Gage Response, Specimen 2A5

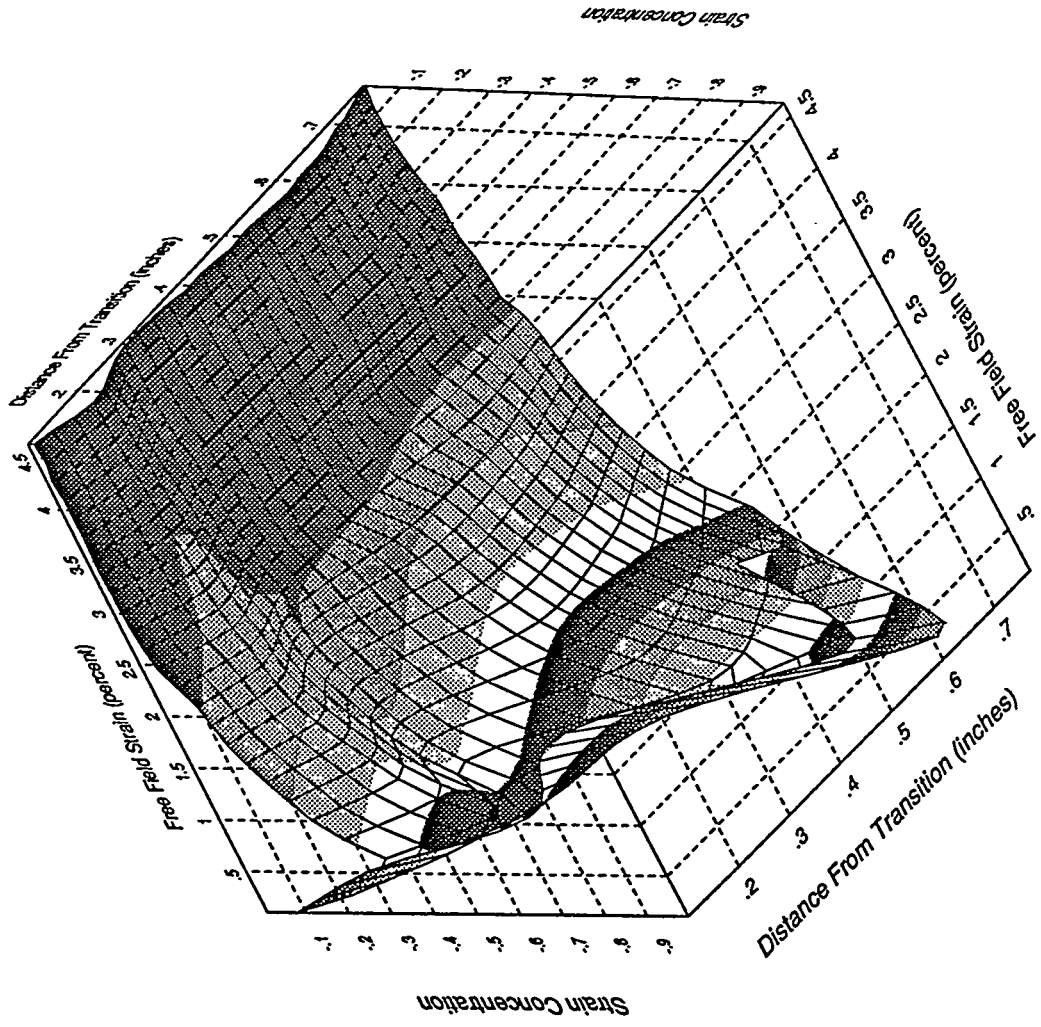

Poisson Strip Gage, Specimen 2A3

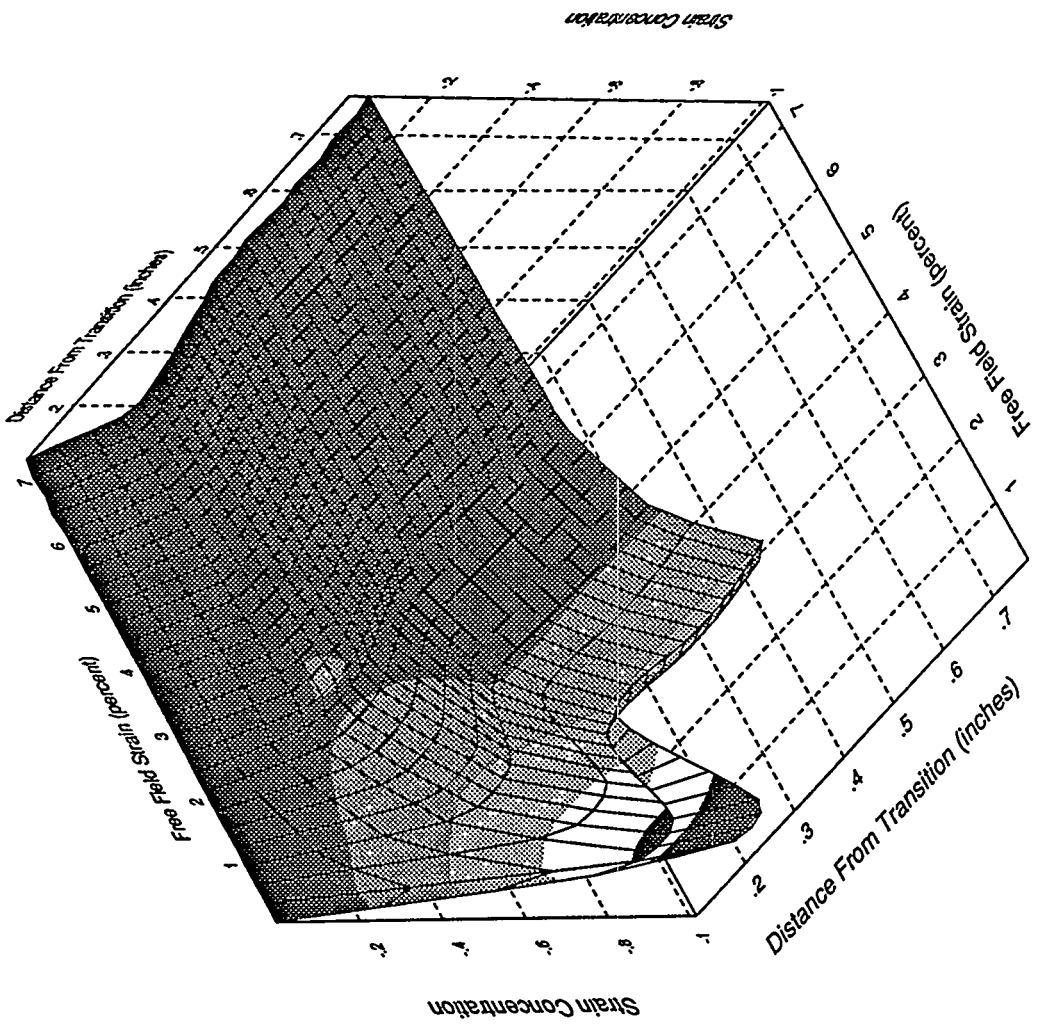

Poisson Strip Gage, Specimen 2A4

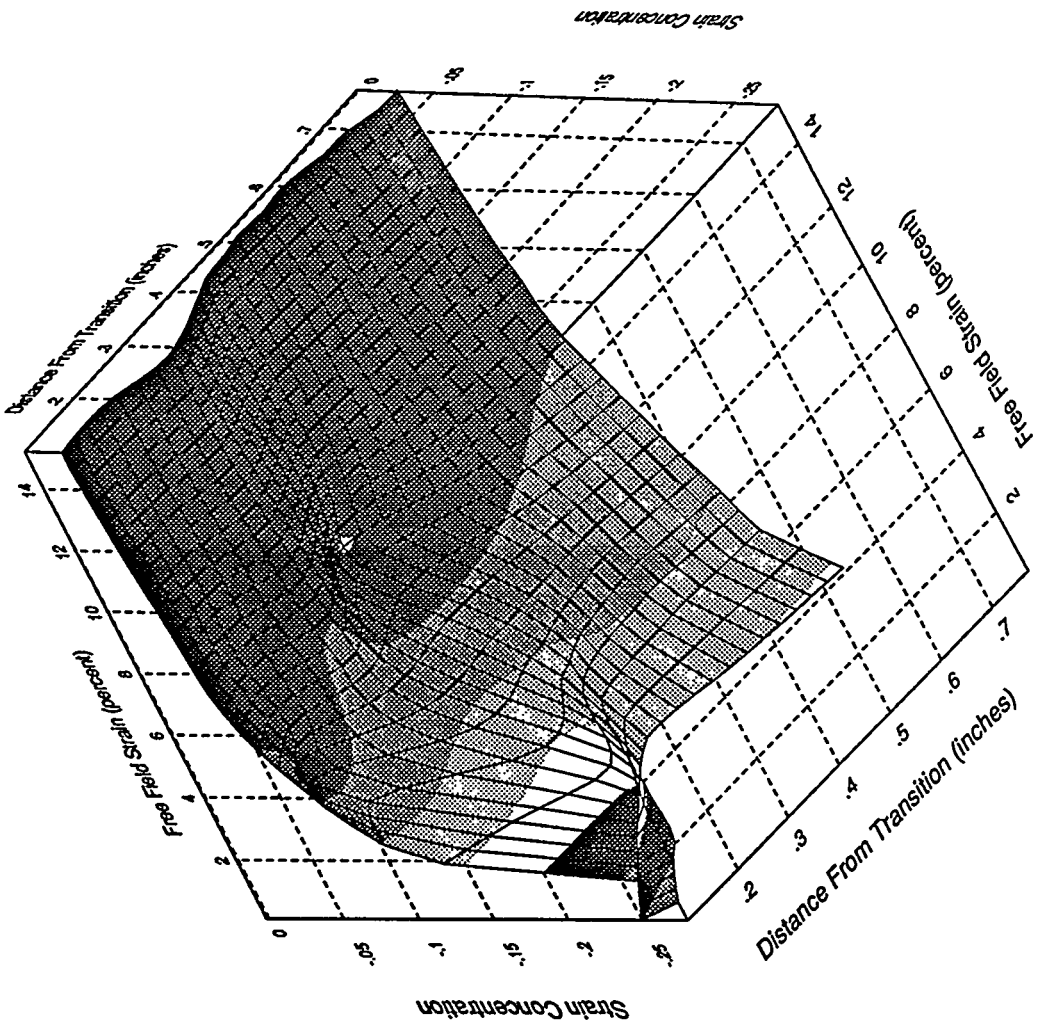

Poisson Strip Gage, Specimen 2A5

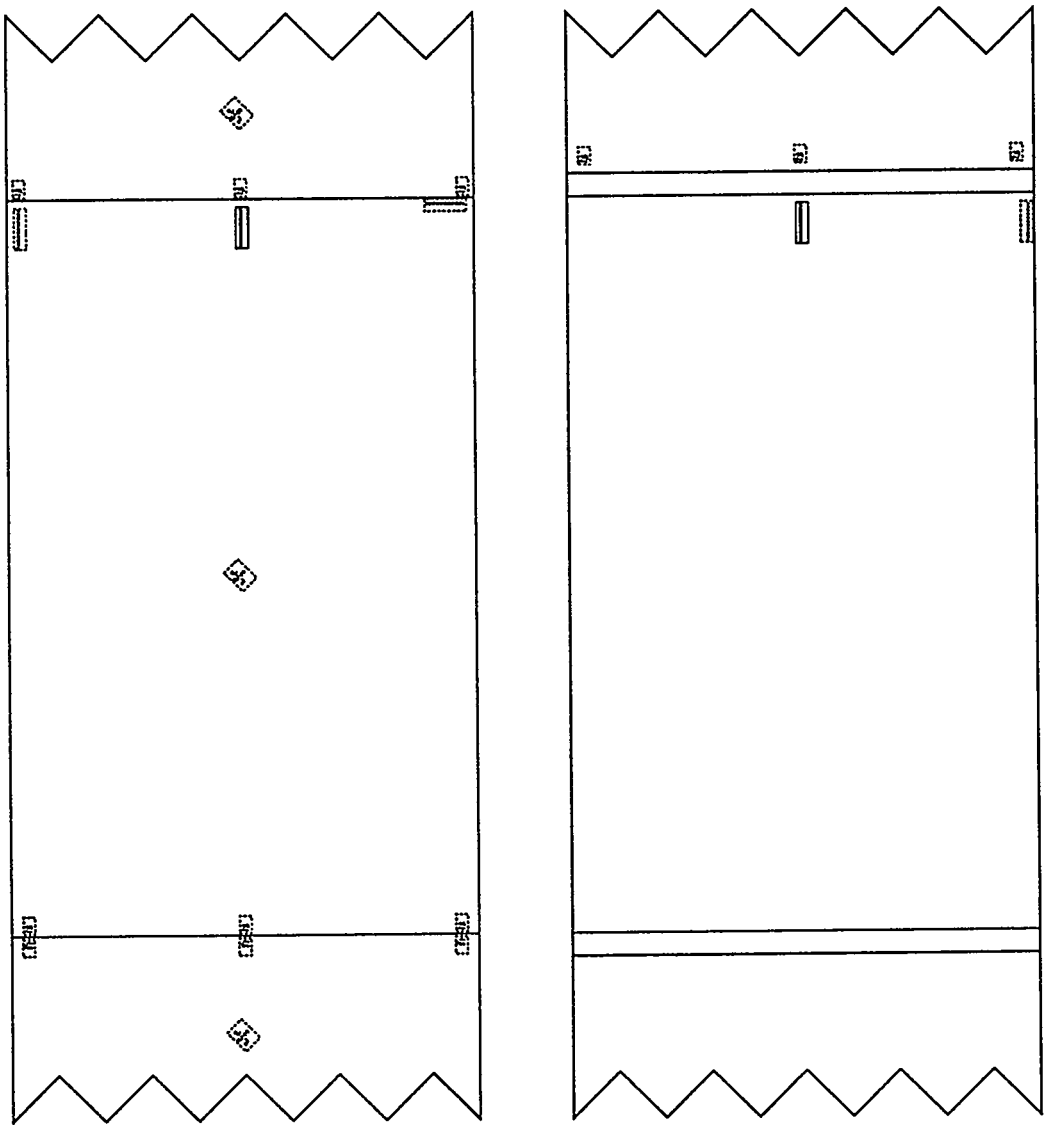

Front Back

Plot Legend

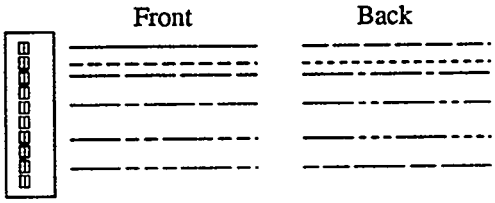

Liner Centerline Strip Gages

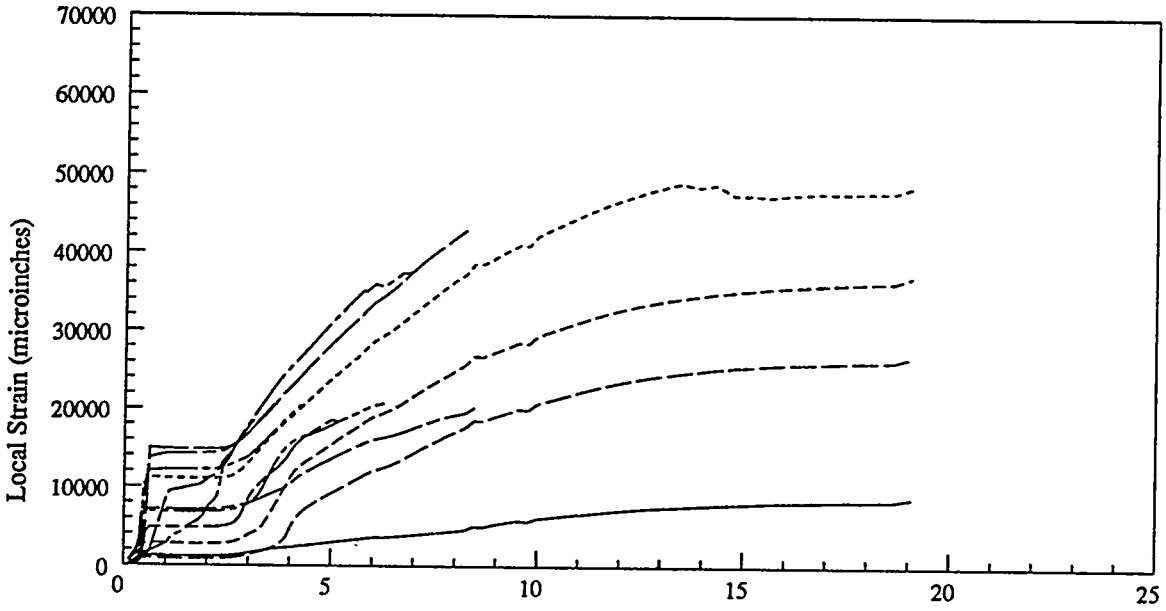

Centerline Strip Gage Response, Specimen 2A3

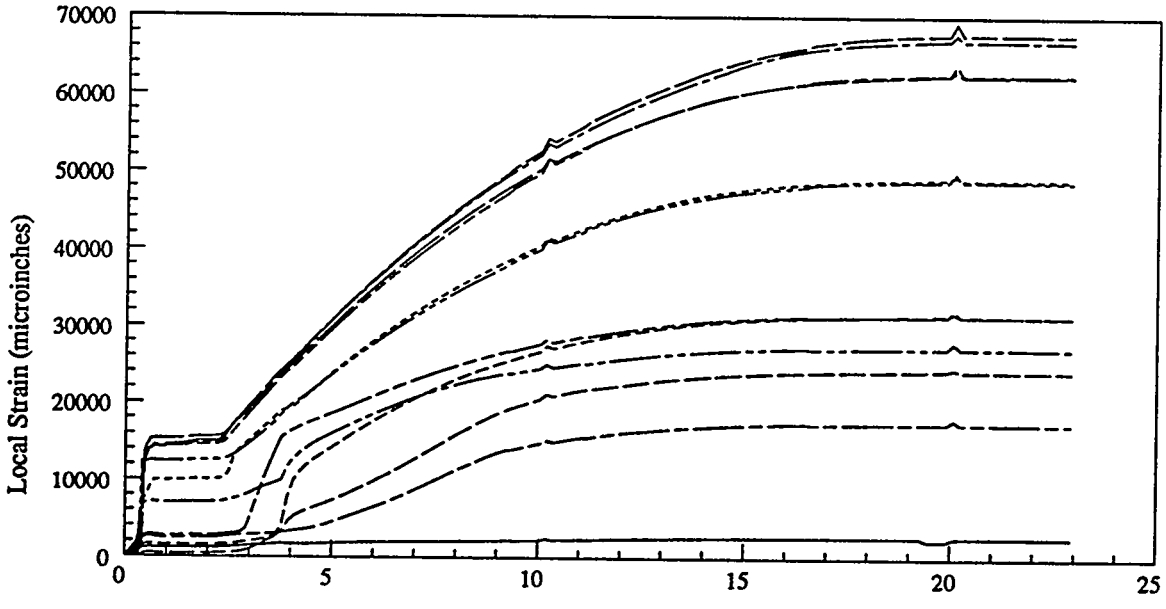

Centerline Strip Gage Response, Specimen 2A4

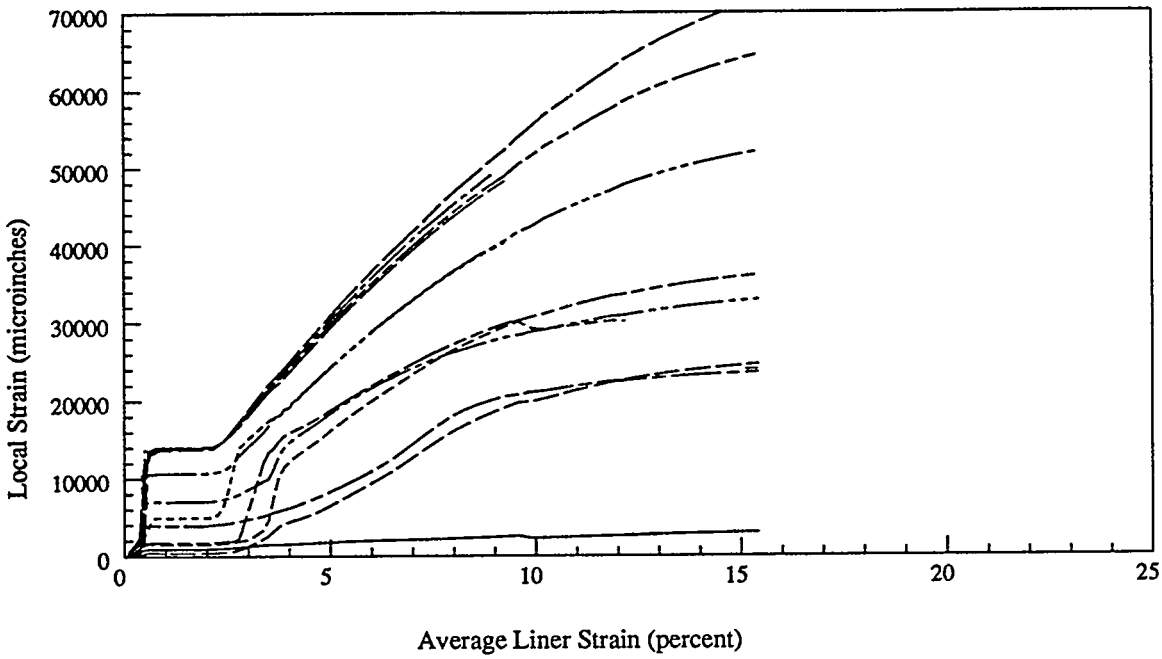

Centerline Strip Gage Response, Specimen 2A5

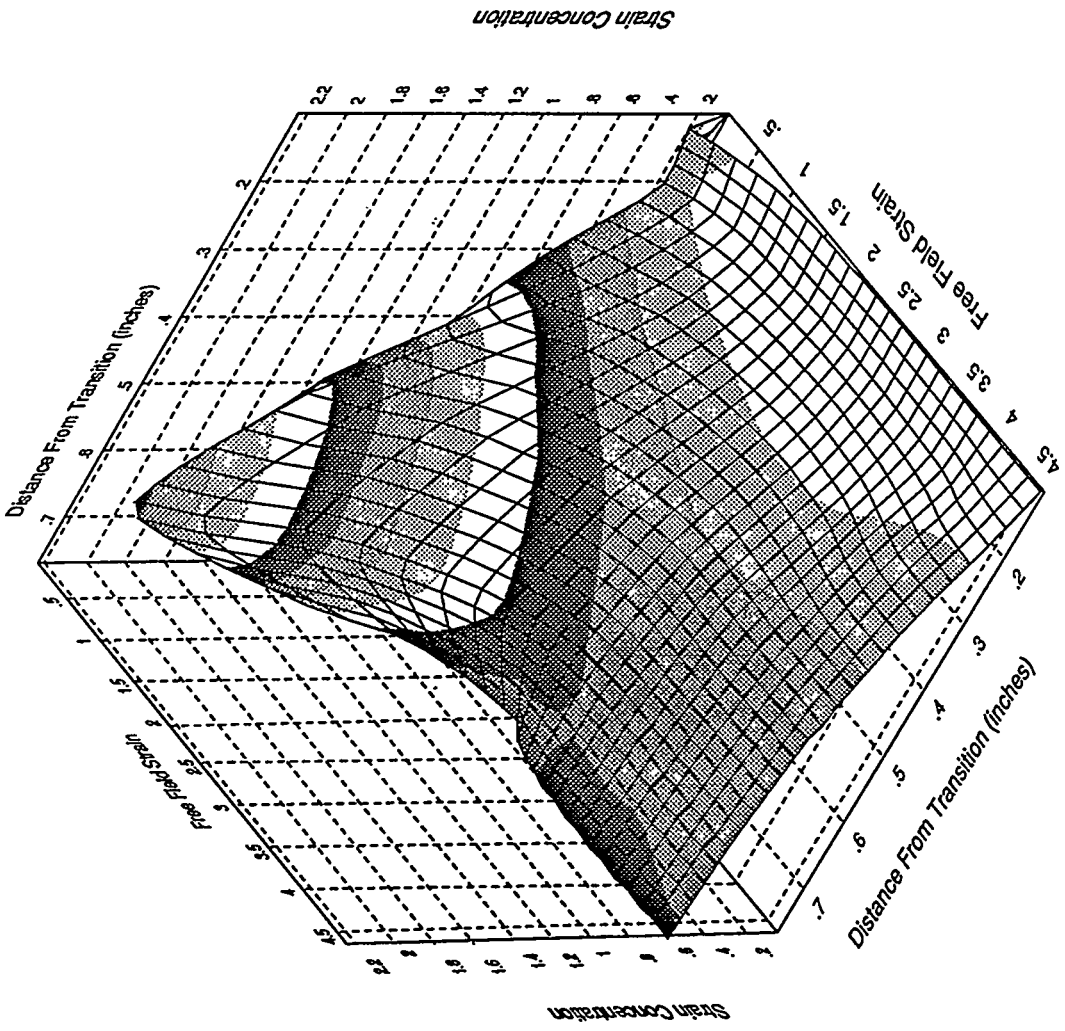

Front Centerline Strip Gage, Specimen 2A3

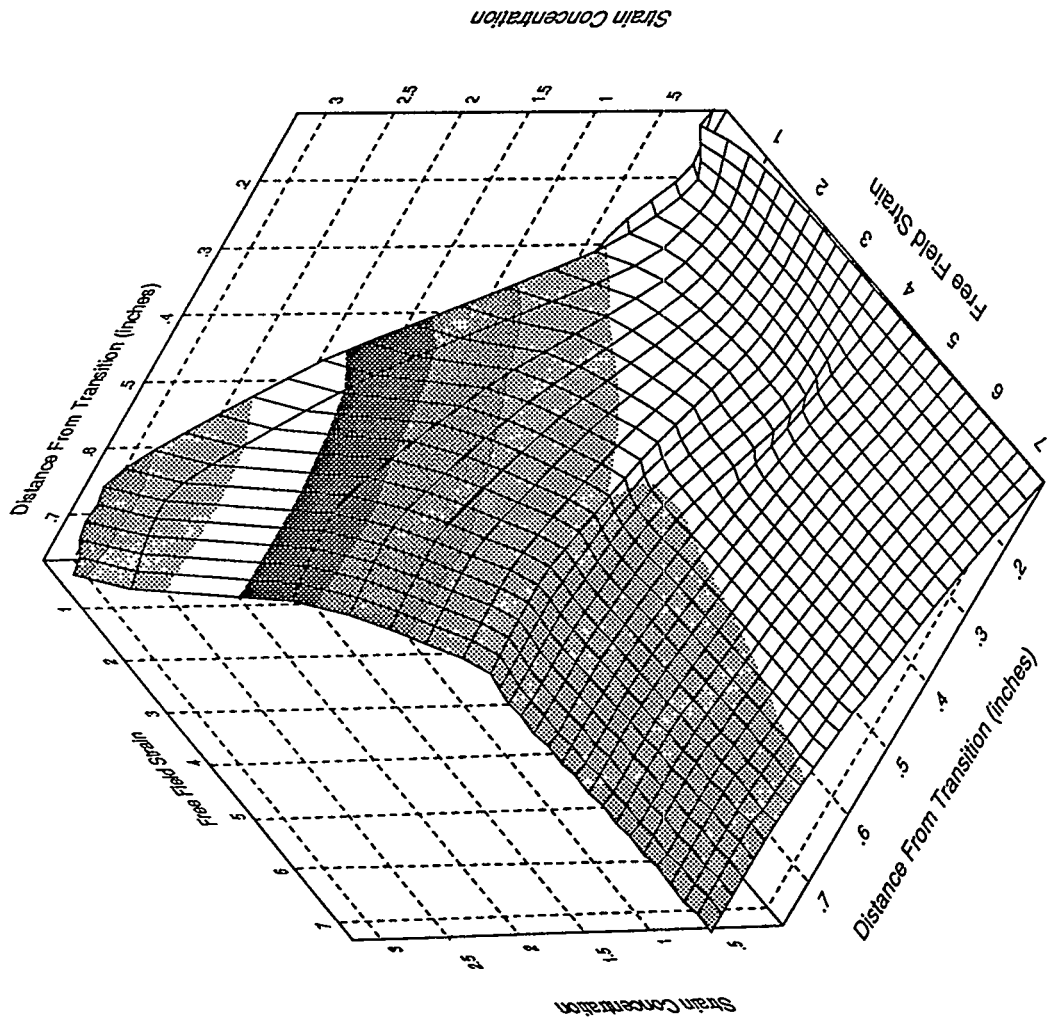

Front Centerline Strip Gage, Specimen 2A4

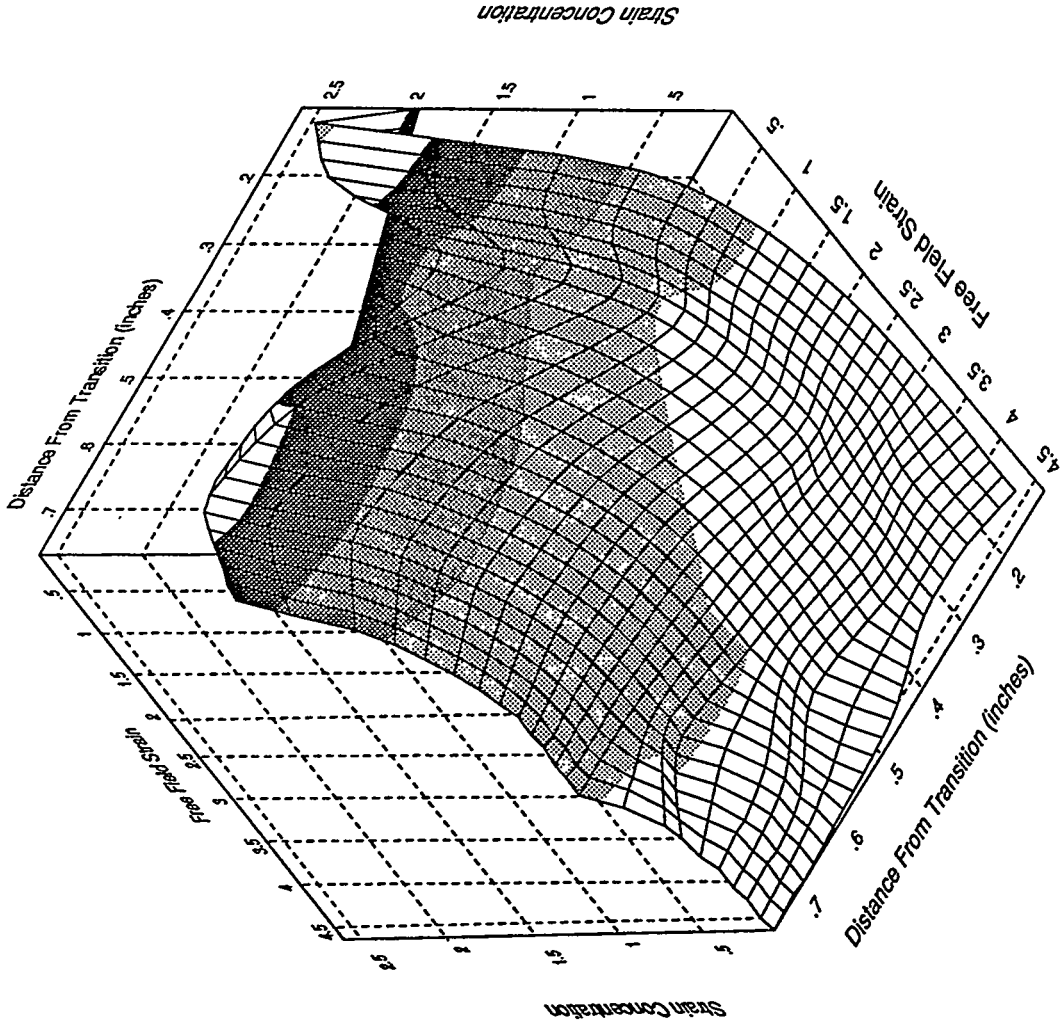

Back Centerline Strip Gage, Specimen 2A3

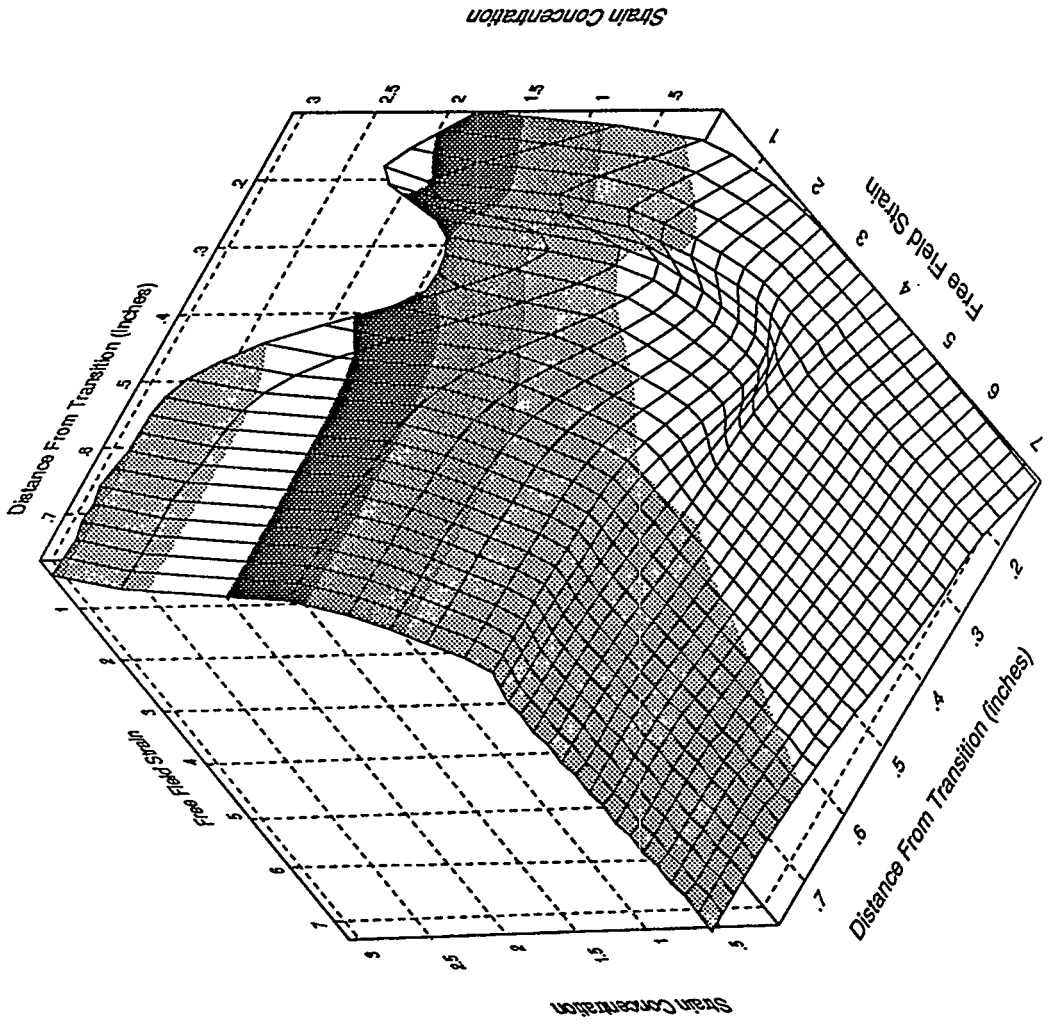

Back Centerline Strip Gage, Specimen 2A4

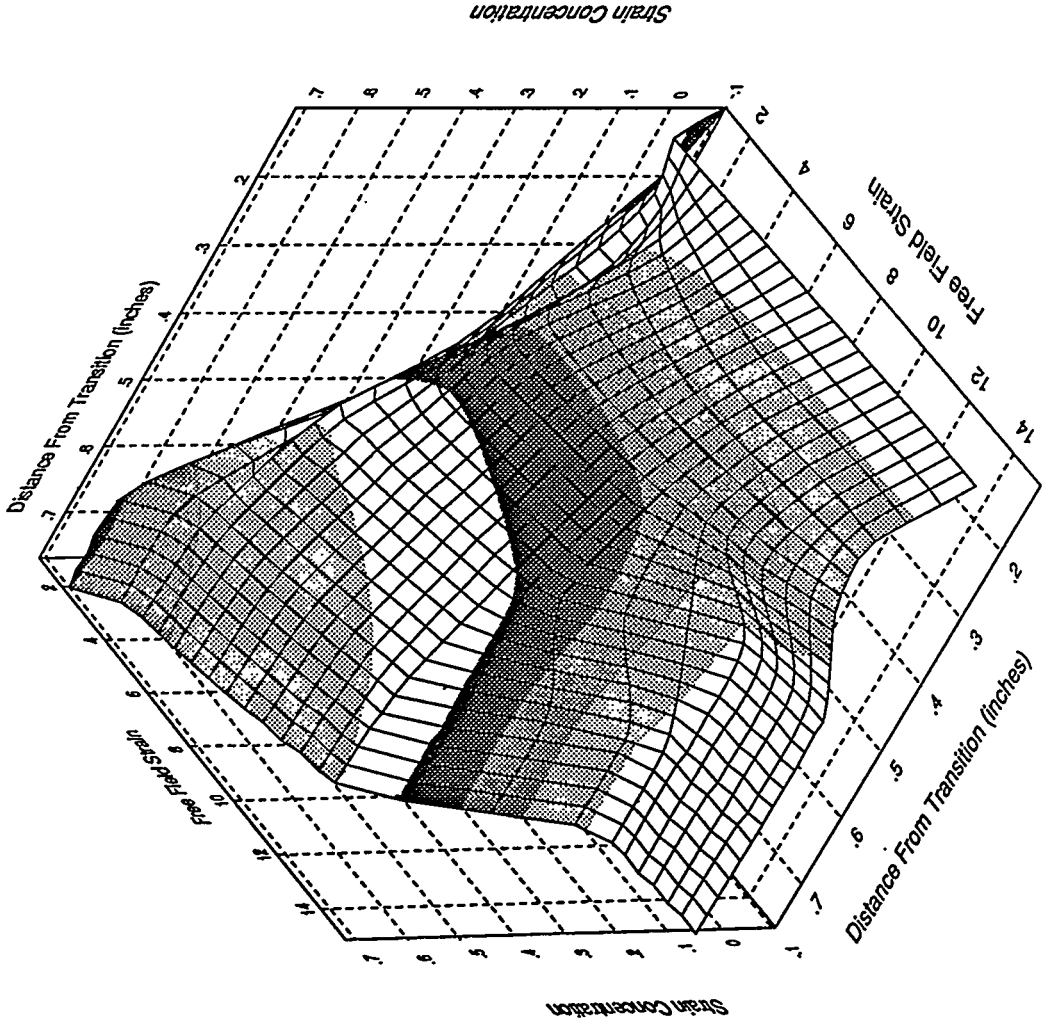

Front Centerline Strip Gage, Specimen 2A5

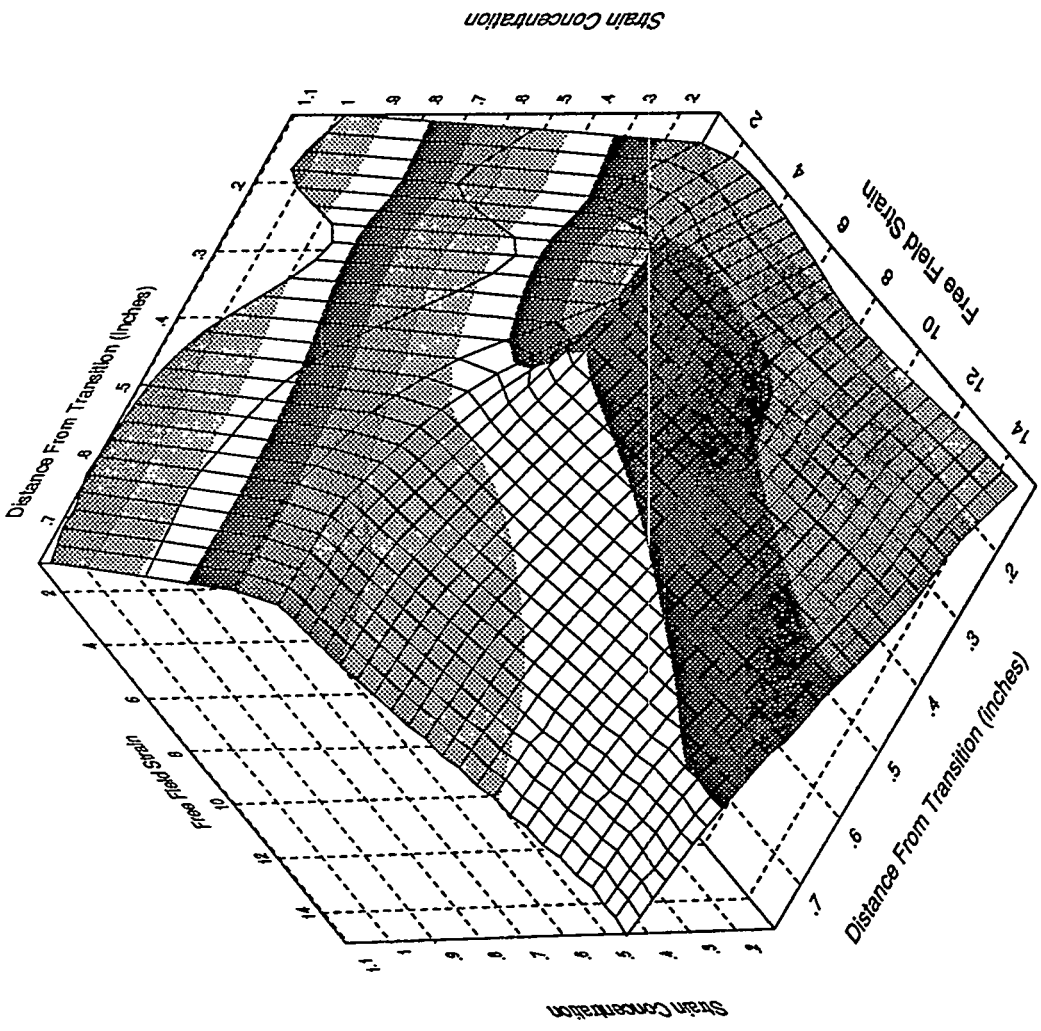

Back Centerline Strip Gage, Specimen 2A5

Full-Simulation Specimen (Phase 2B/2C) Strain Gage Plots

Phase 2B - No External Pressure

Phase 2C - External Pressure Applied

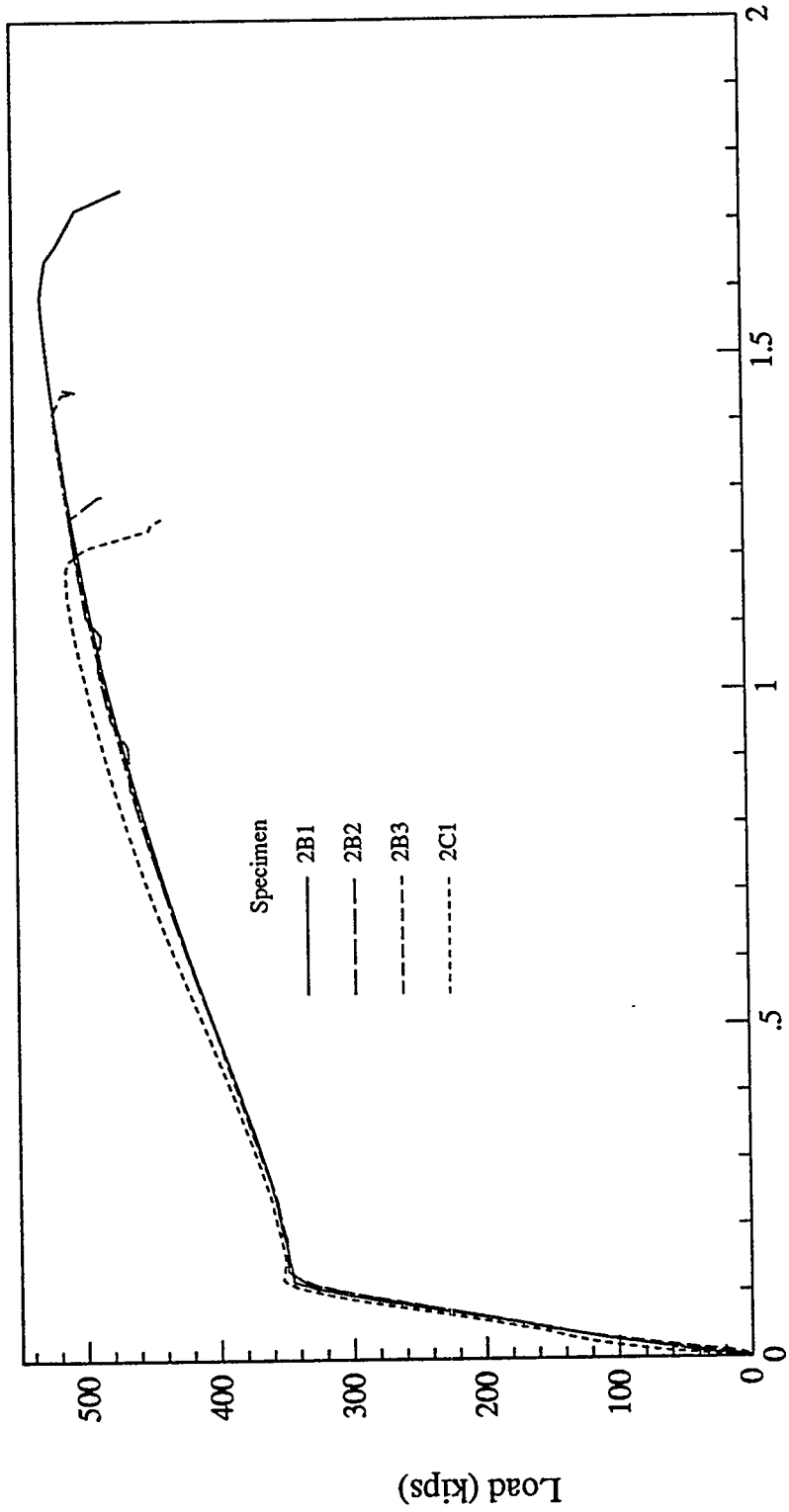

Overall Response of Phase 2B/C Specimens

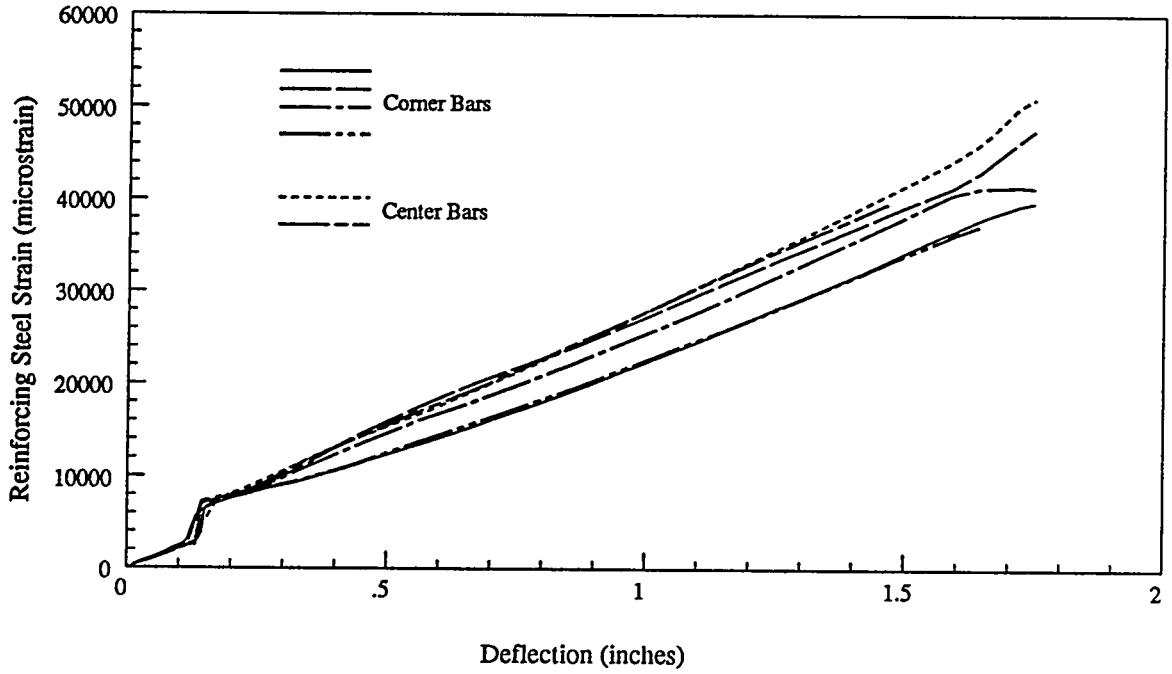

Response of Reinforcing Steel, Specimen 2B1

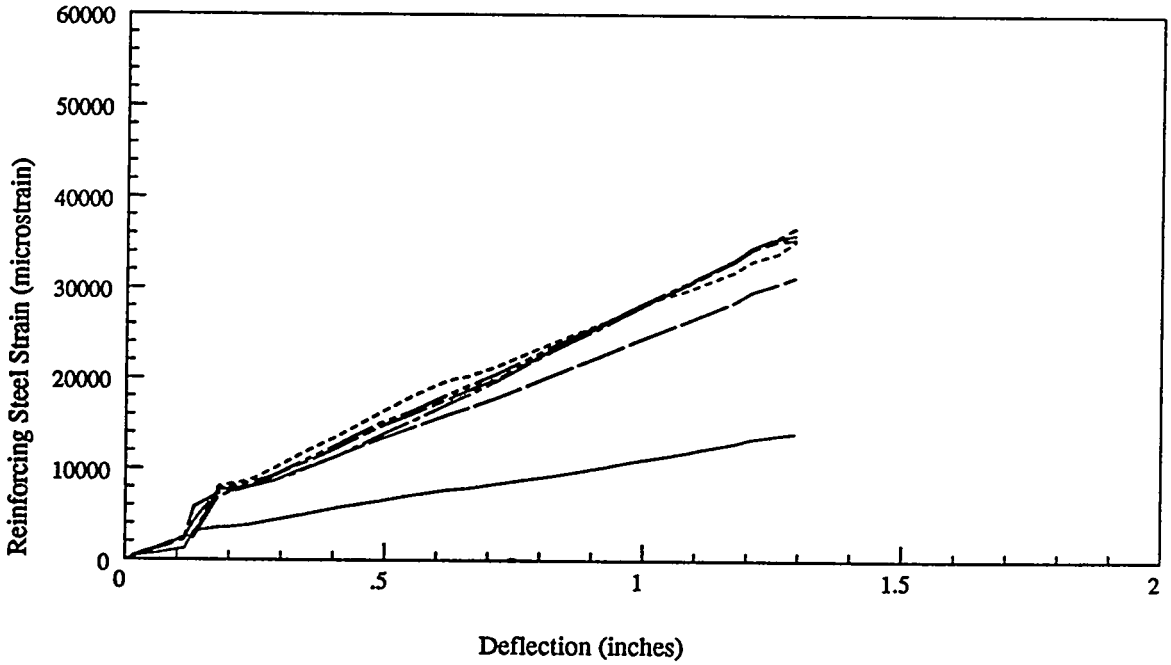

Response of Reinforcing Steel, Specimen 2B2

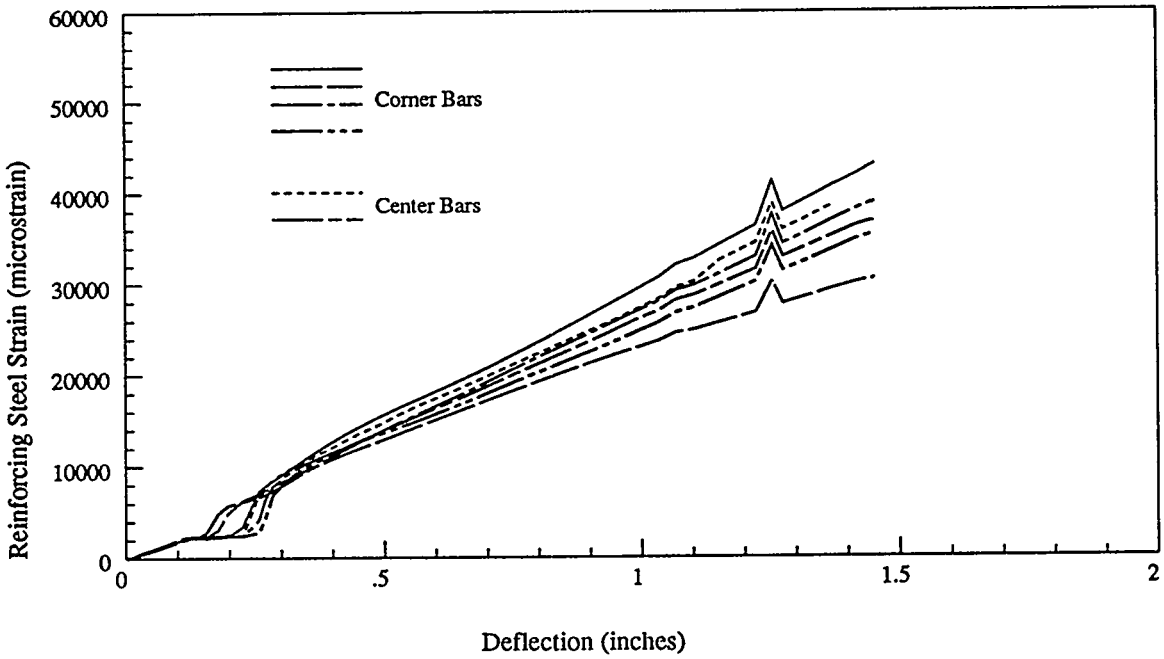

Response of Reinforcing Steel, Specimen 2B3

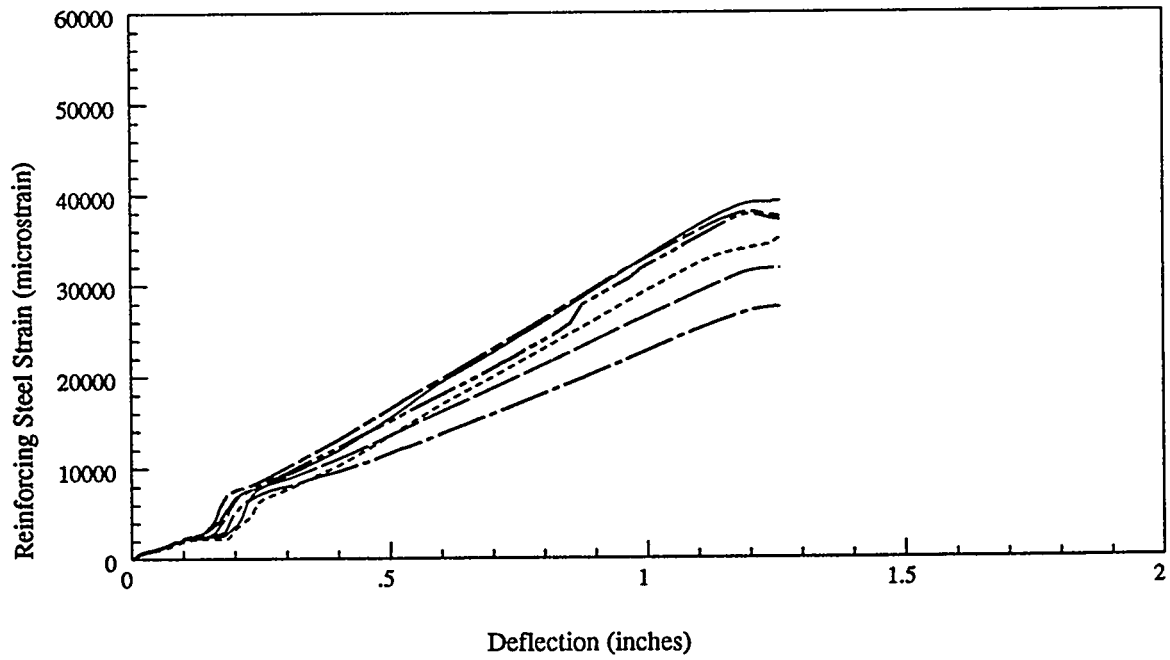

Response of Reinforcing Steel, Specimen 2C1

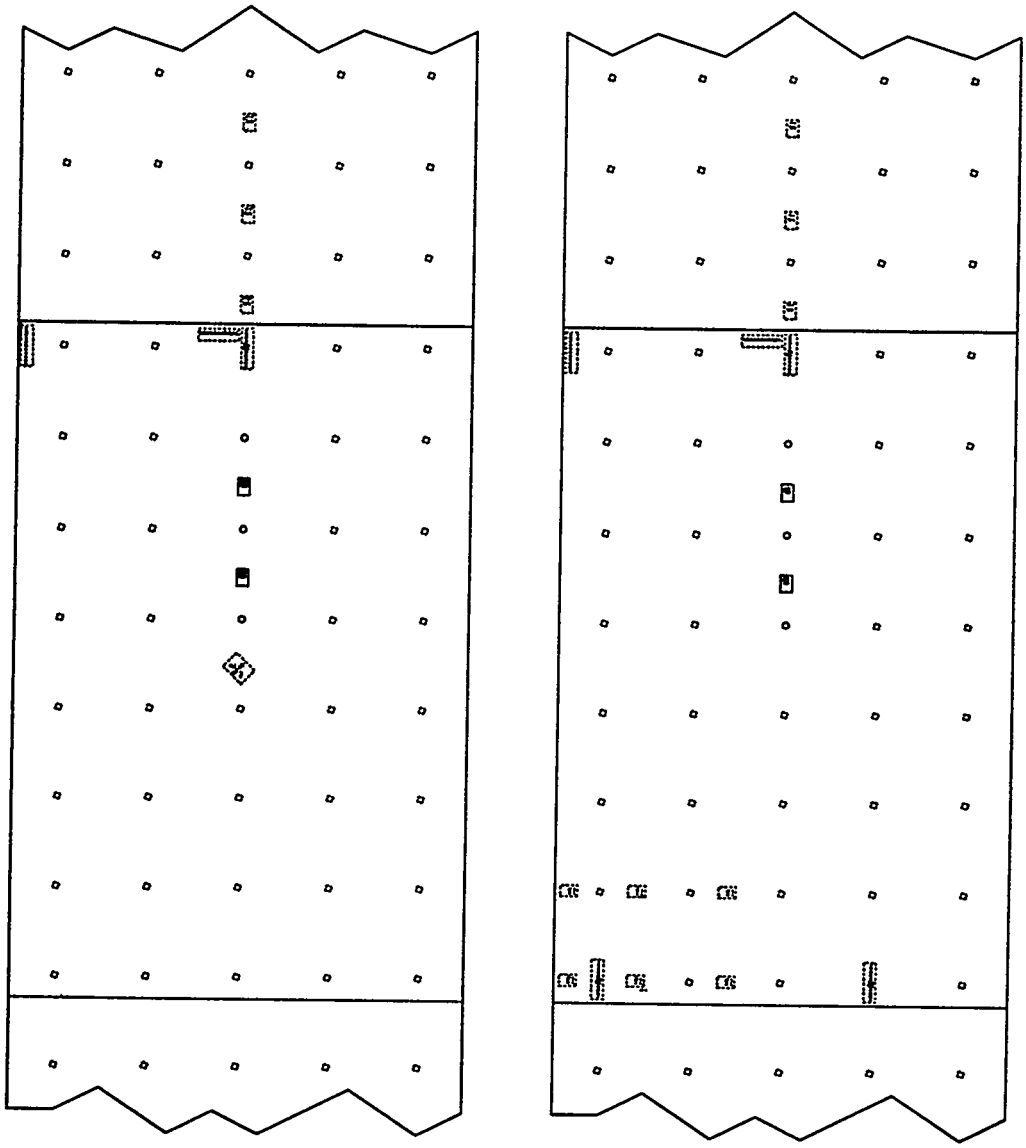

Liner Plate Single-Element Gages

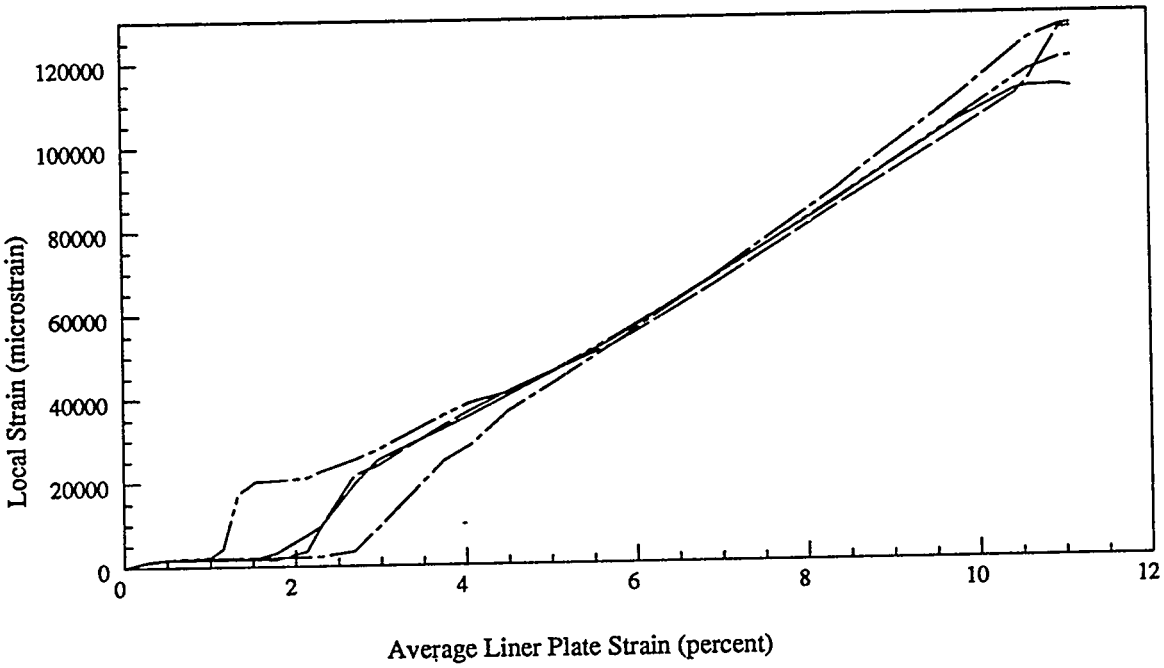

Liner Plate Single Gage Response, Specimen 2B1

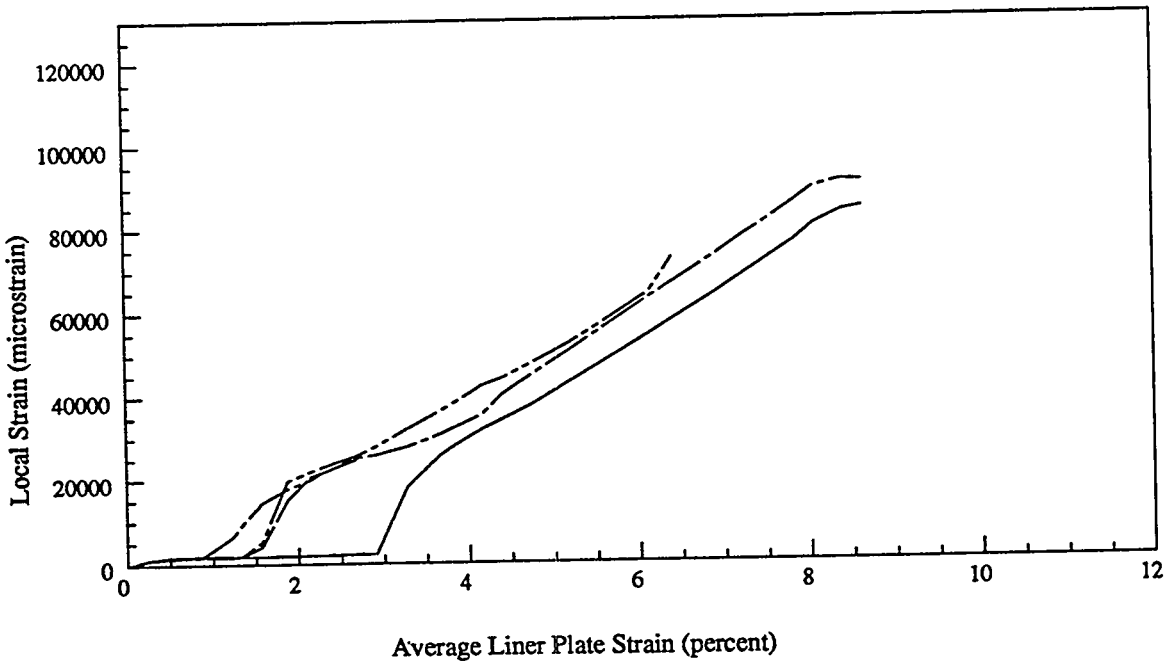

Liner Plate Single Gage Response, Specimen 2B2

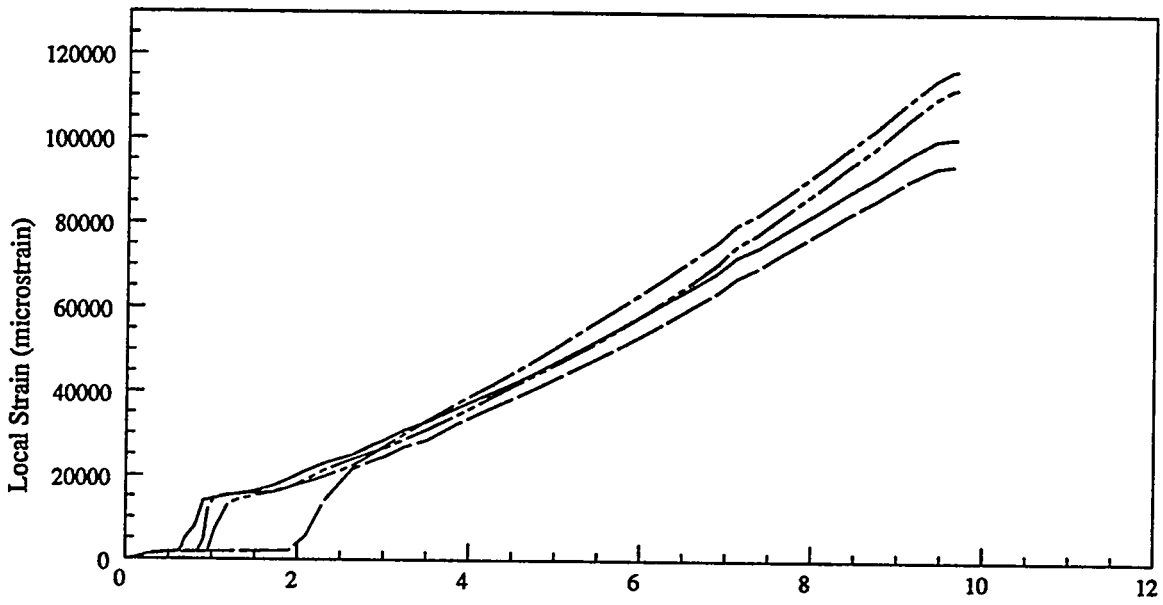

Liner Plate Single Gage Response, Specimen 2B3

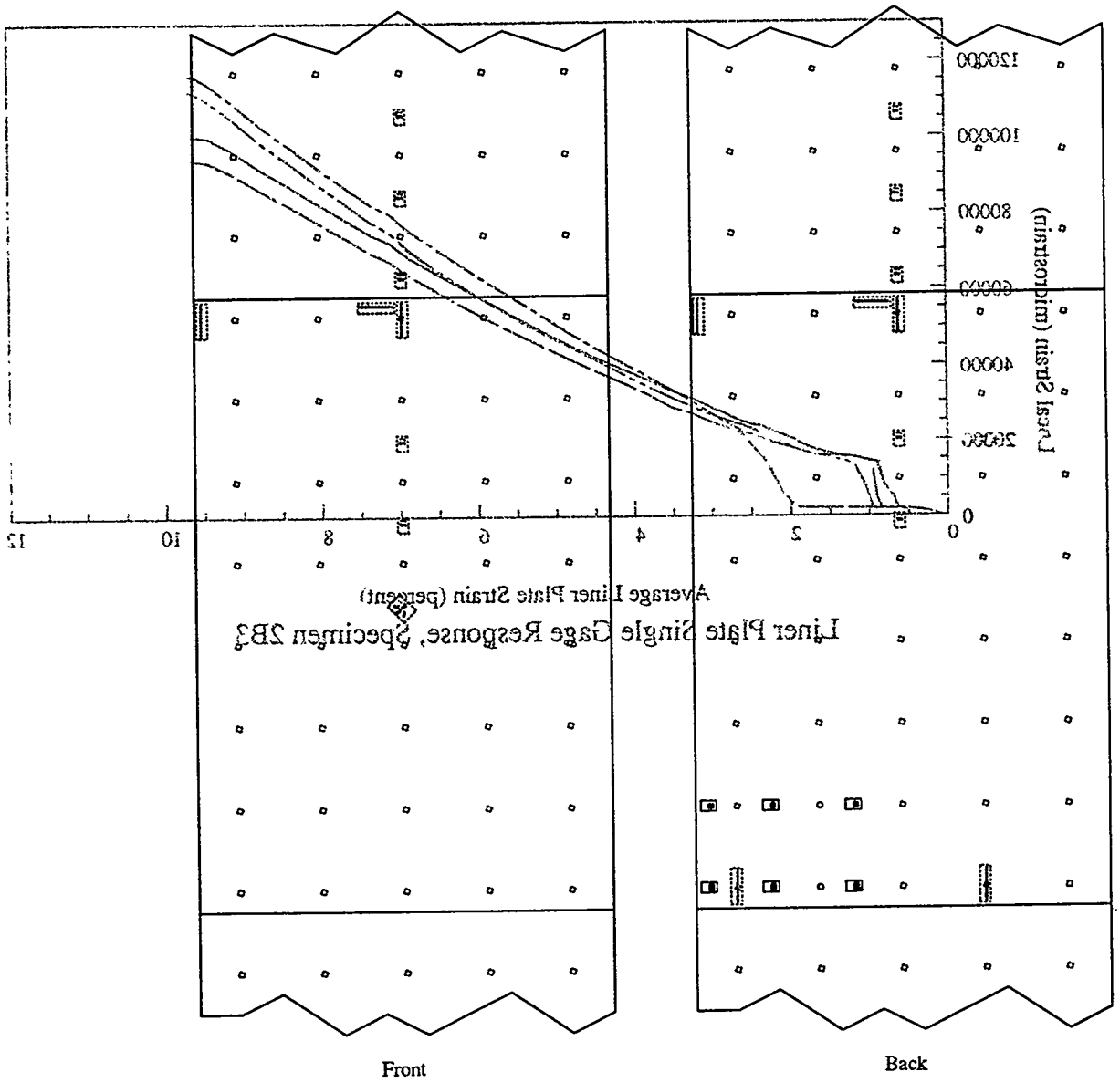
Front
Back
Plot Legend
Poisson Gages

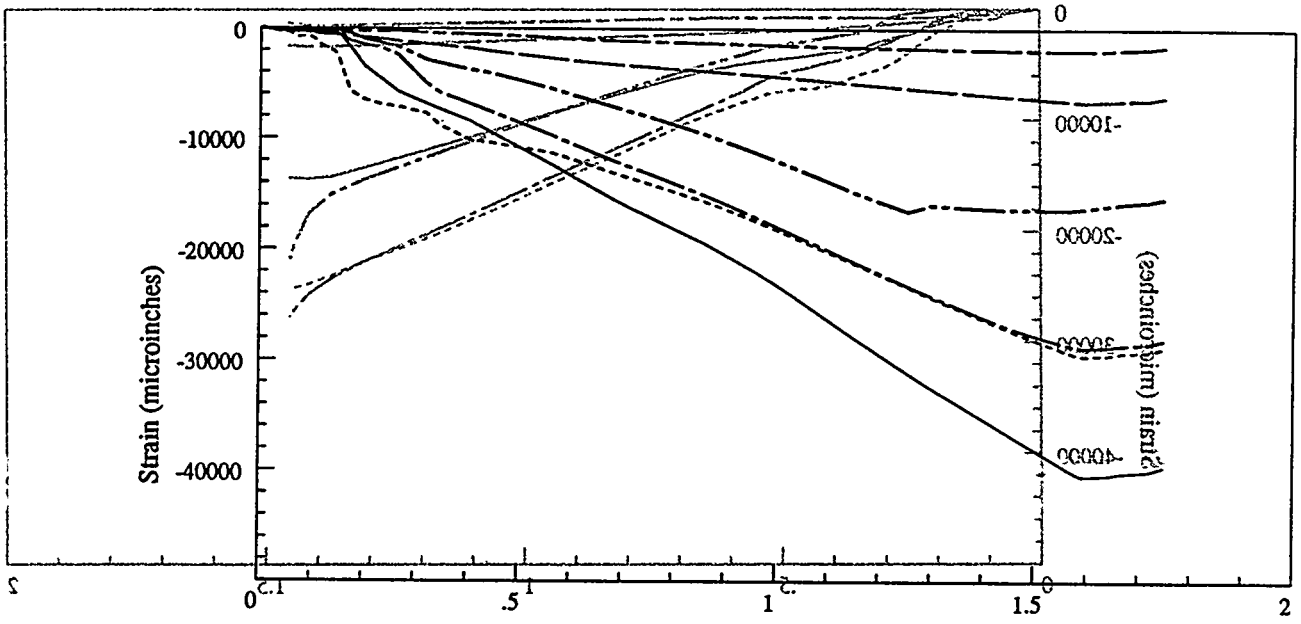

Single Element Poisson Gages, Specimen 2B1

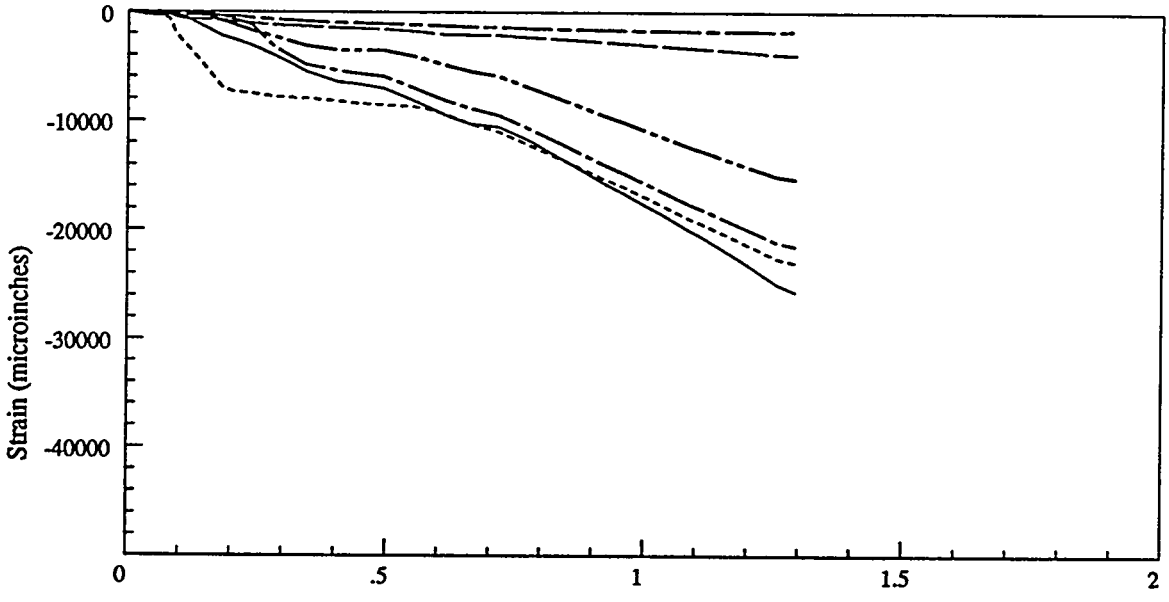

Single-Element Poisson Gages, Specimen 2B2

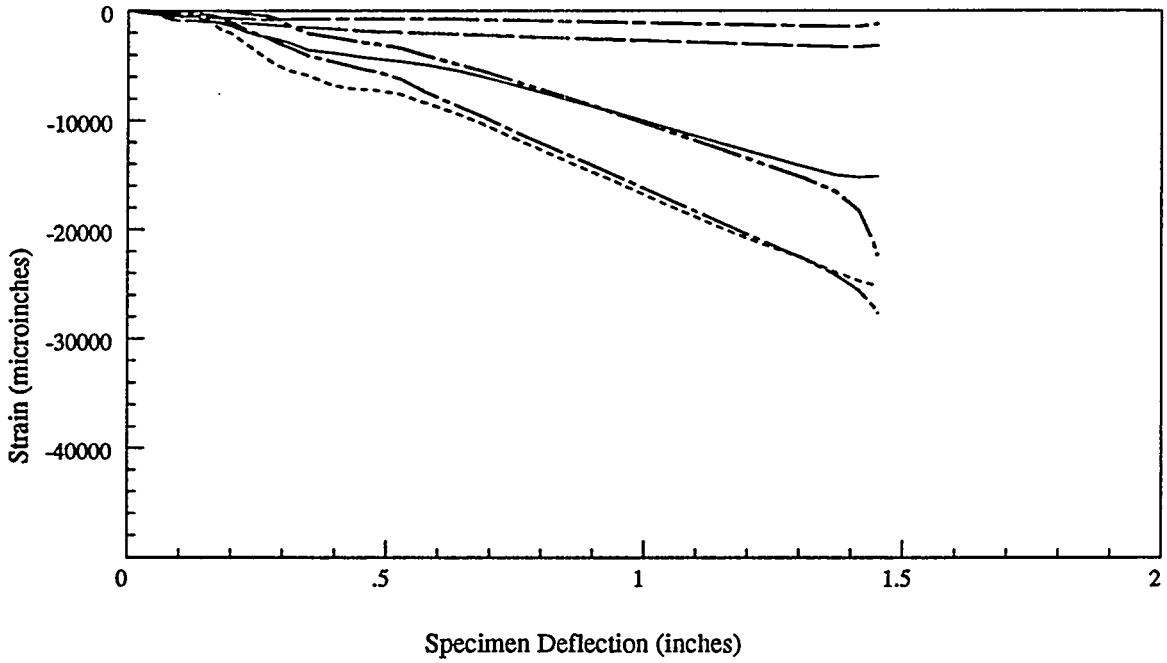

Single-Element Poisson Gages, Specimen 2B3

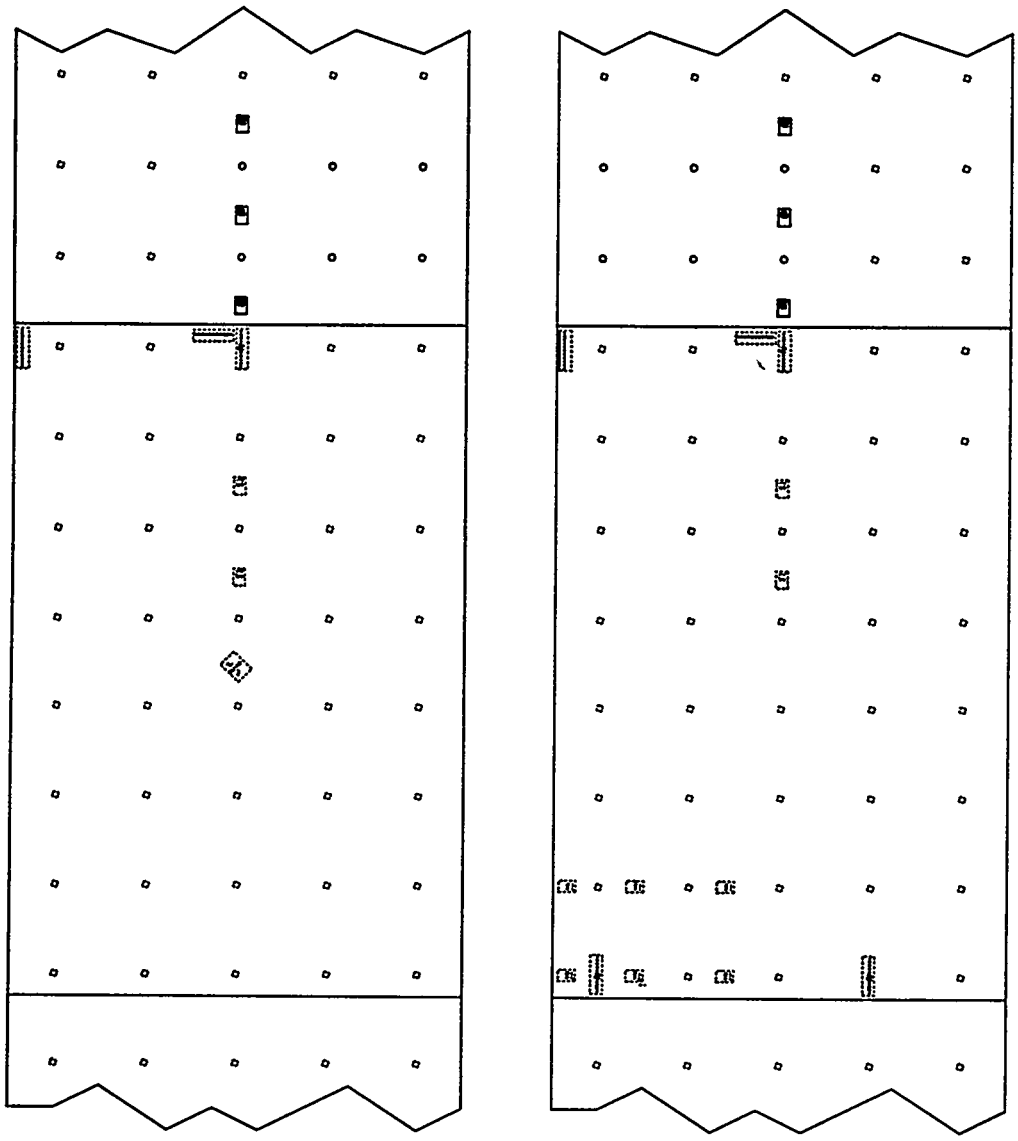

Insert Plate Gages

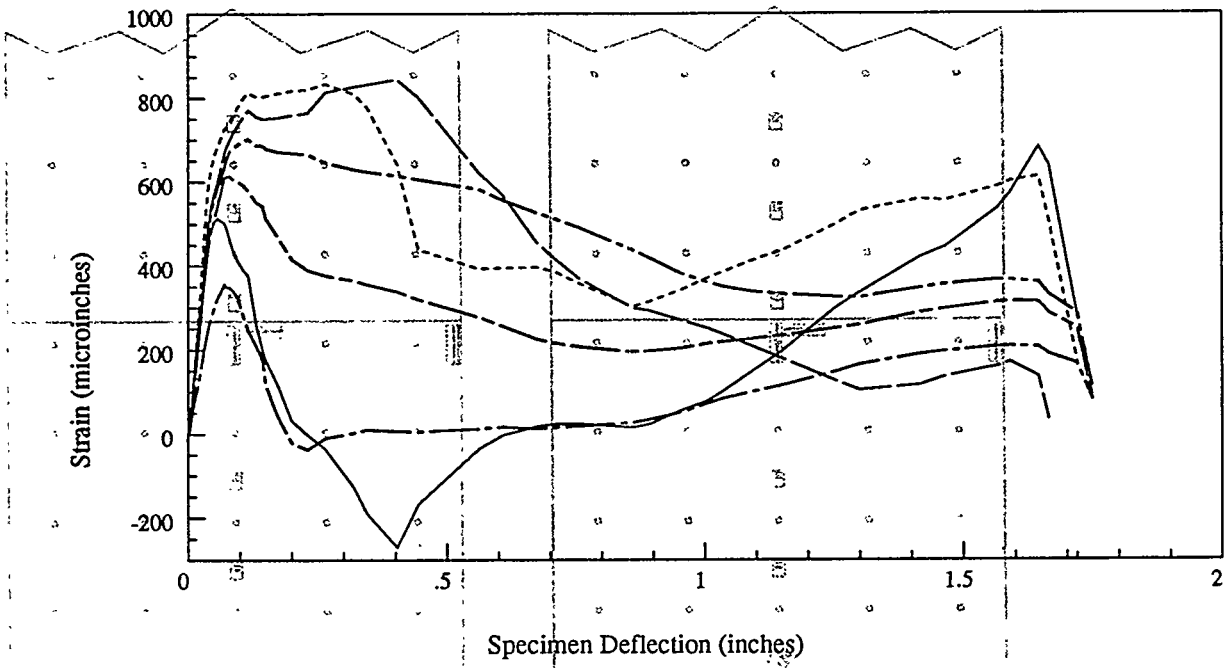

Response of Insert Plate, Specimen 2B1

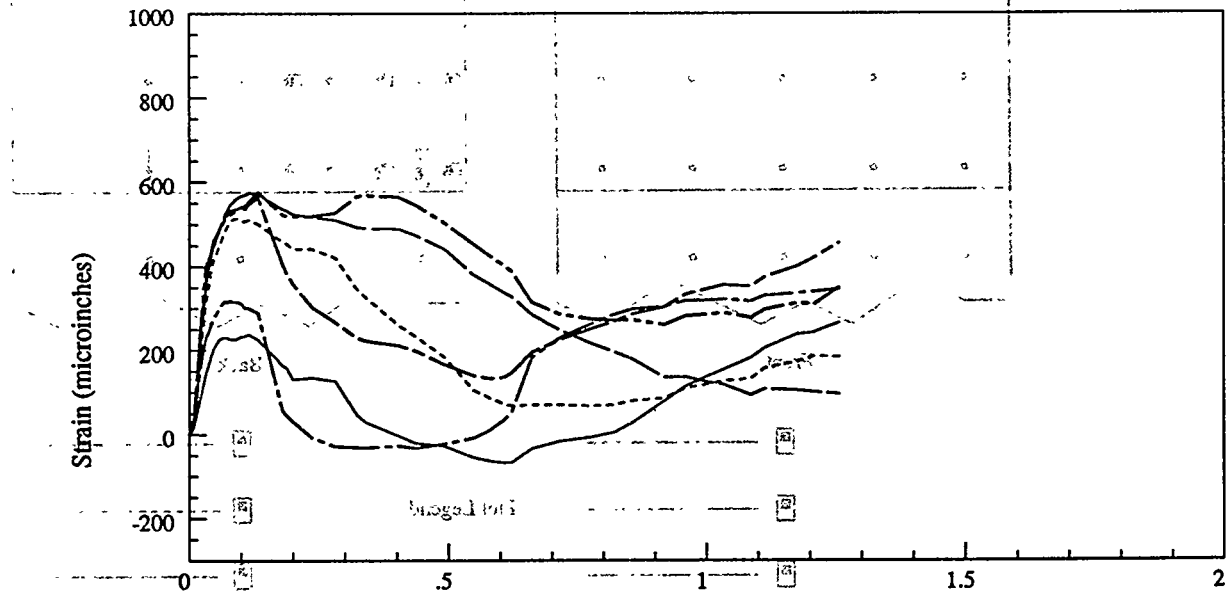

Response of Insert Plate, Specimen 2B2

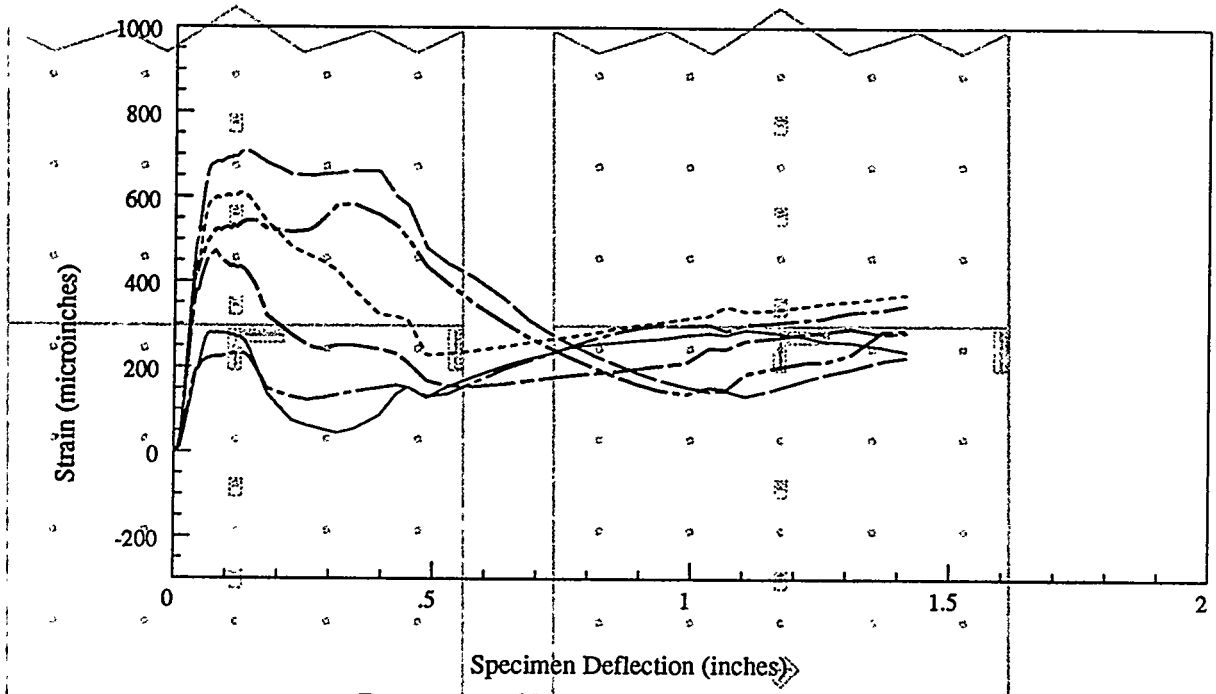

Response of Insert Plate, Specimen 2B3

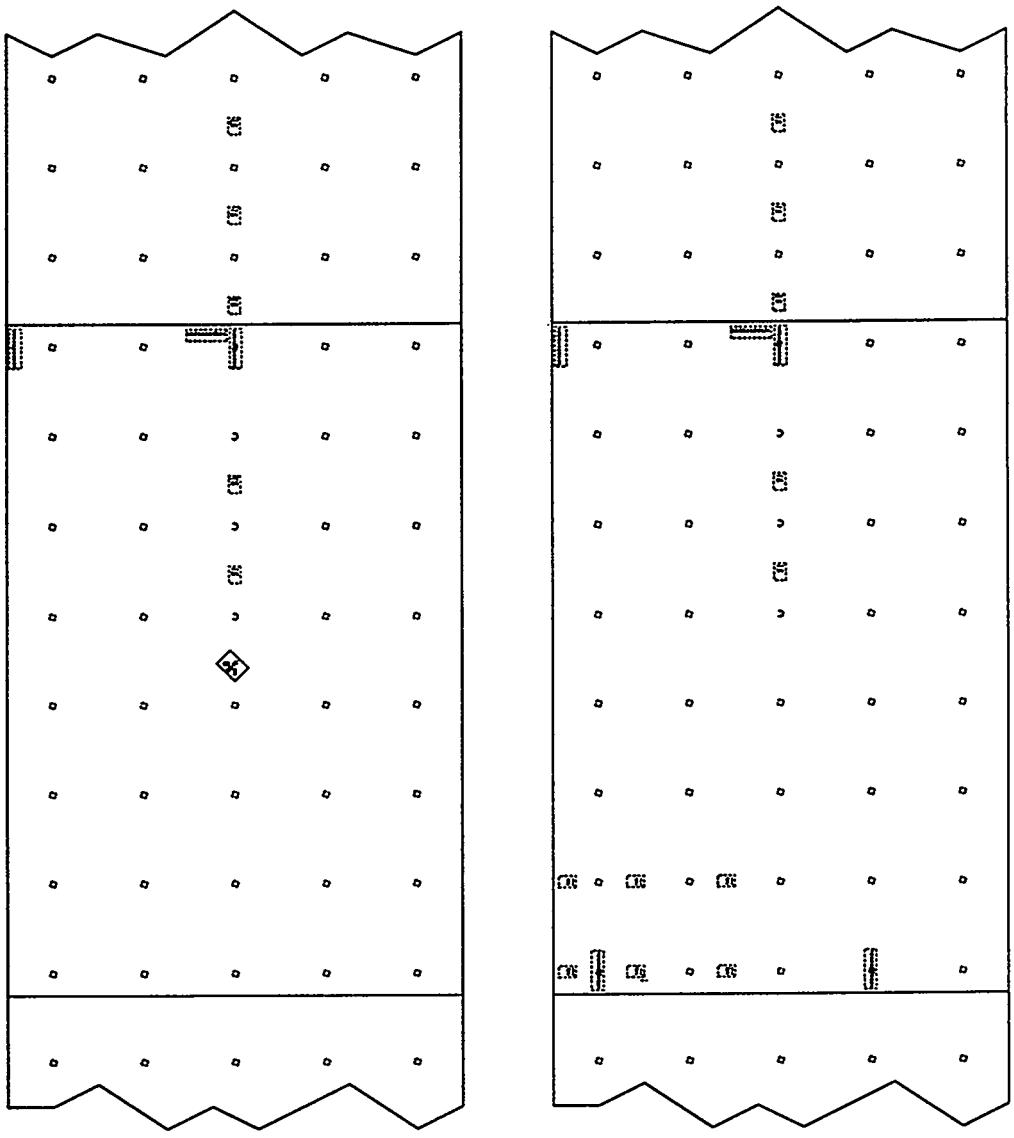

Rosette Gage

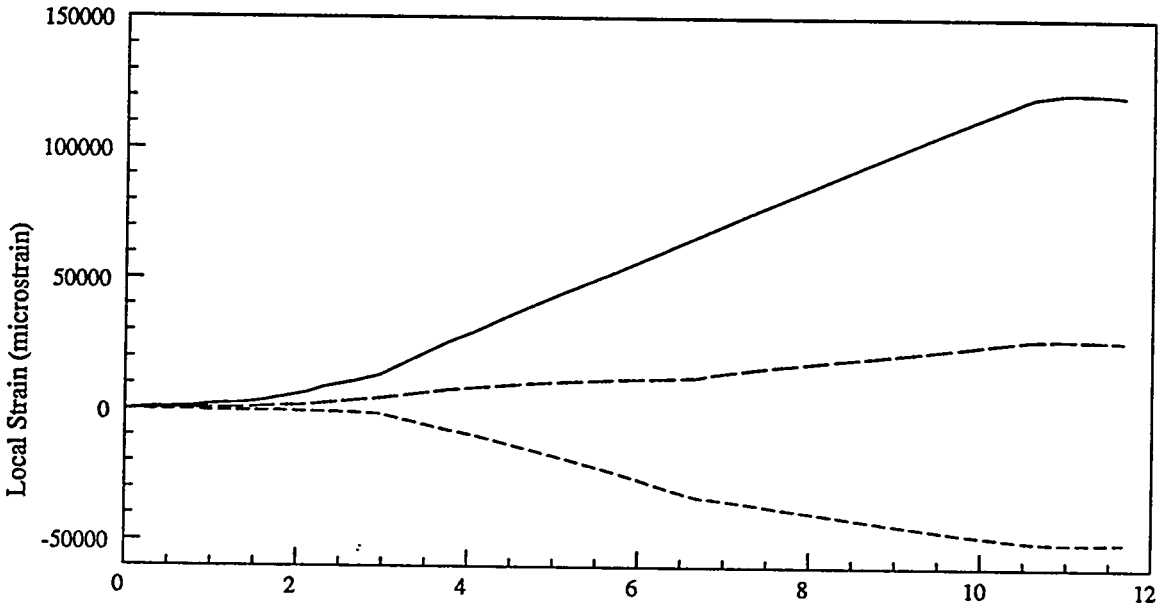

Rosette Gage Response, Specimen 2B1

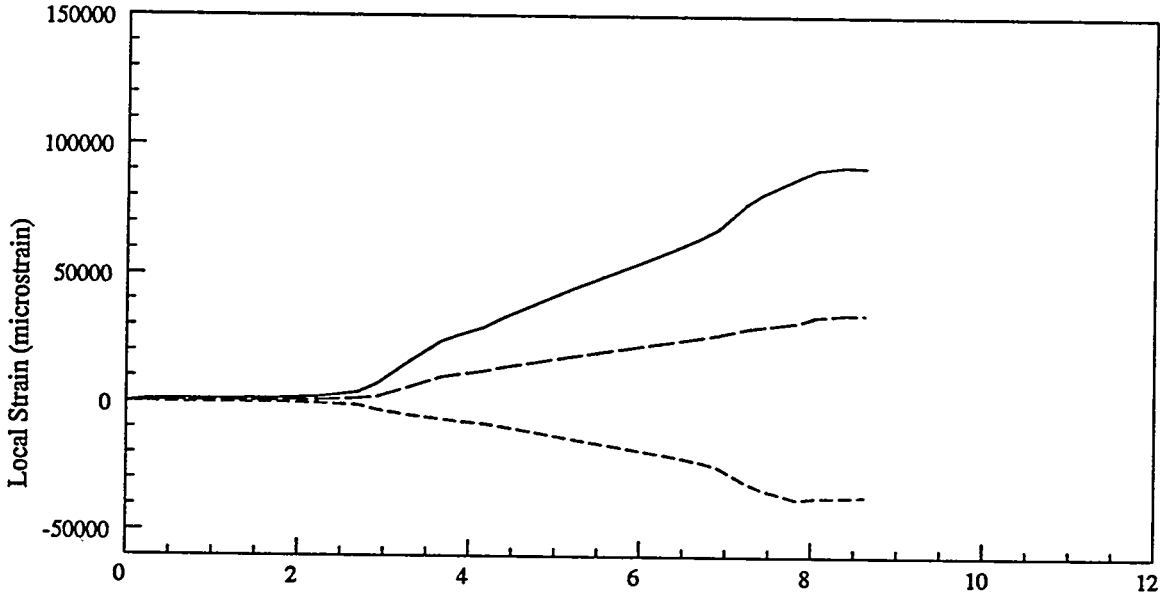

Rosette Gage Response, Specimen 2B2

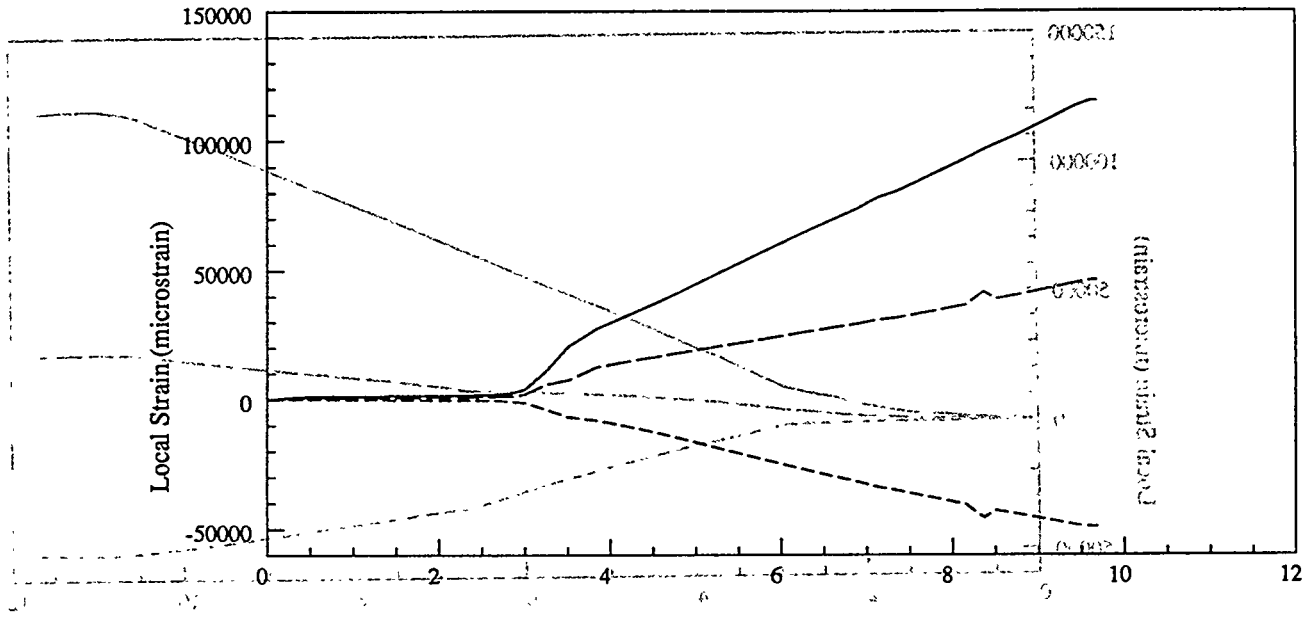

Rosette Gage Response, Specimen 2B3

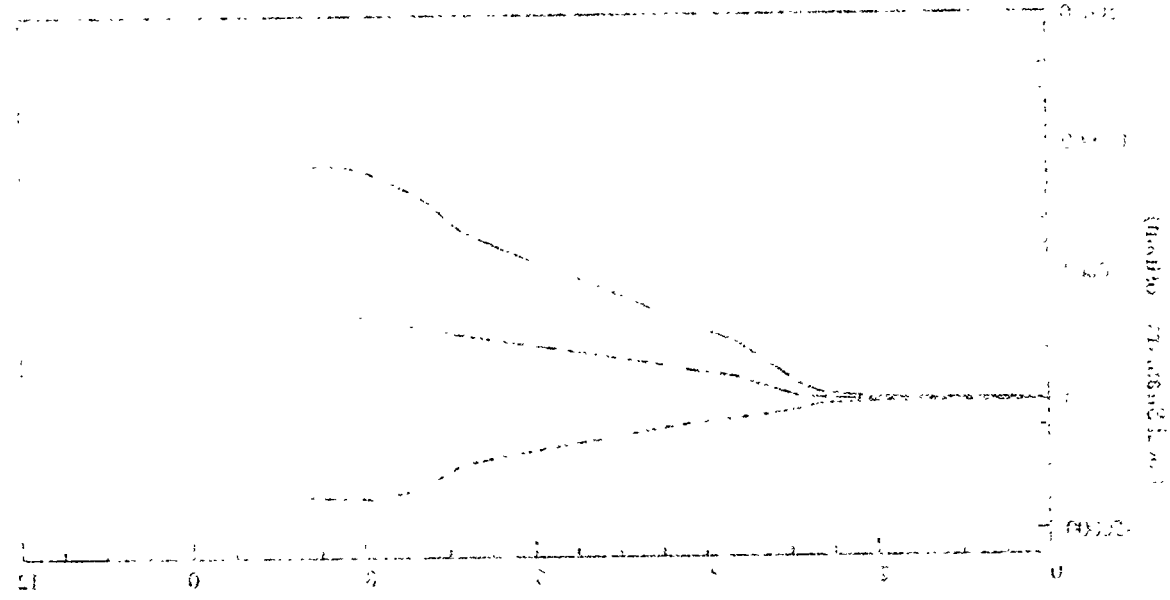

Lower Outboard Strip Gage, Specimen 2B1

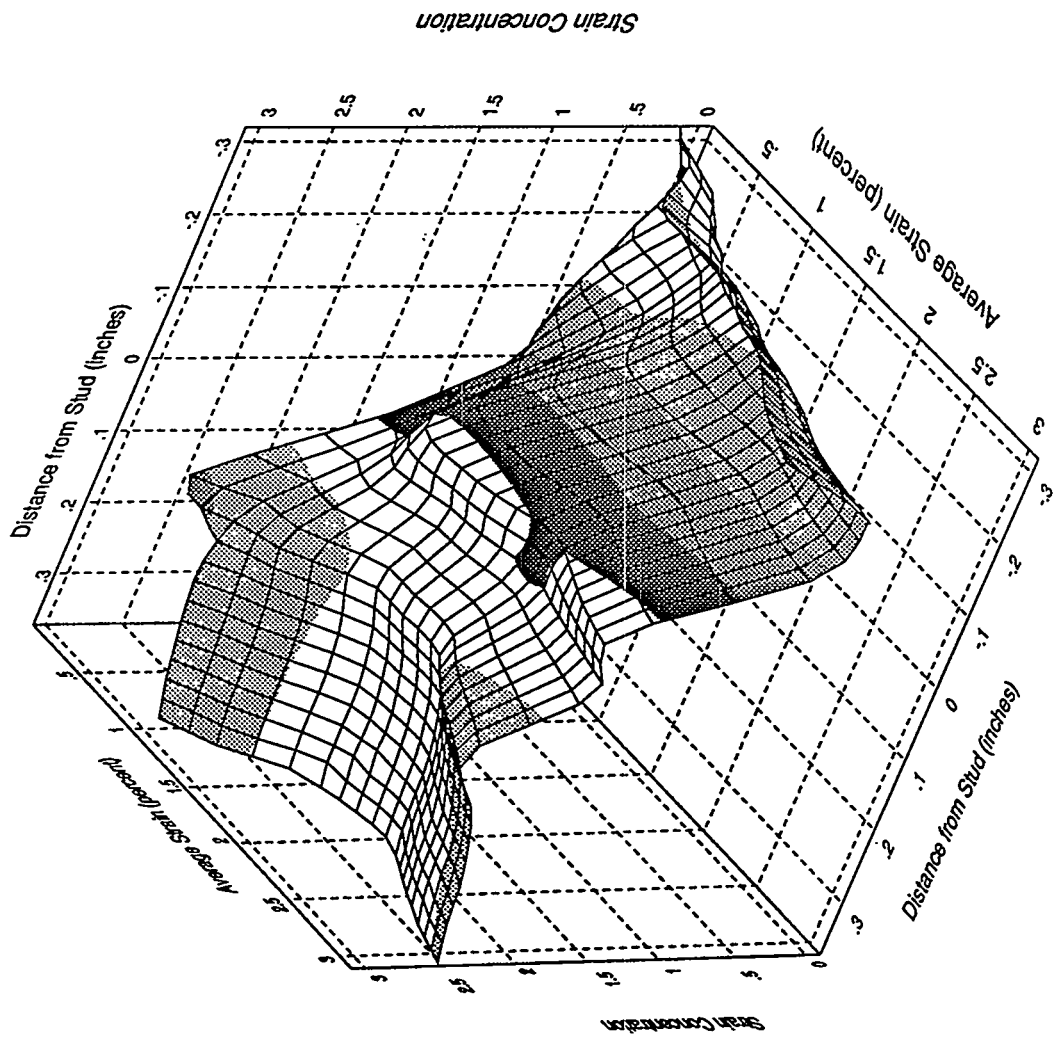

Lower Outboard Strip Gage, Specimen 2B2

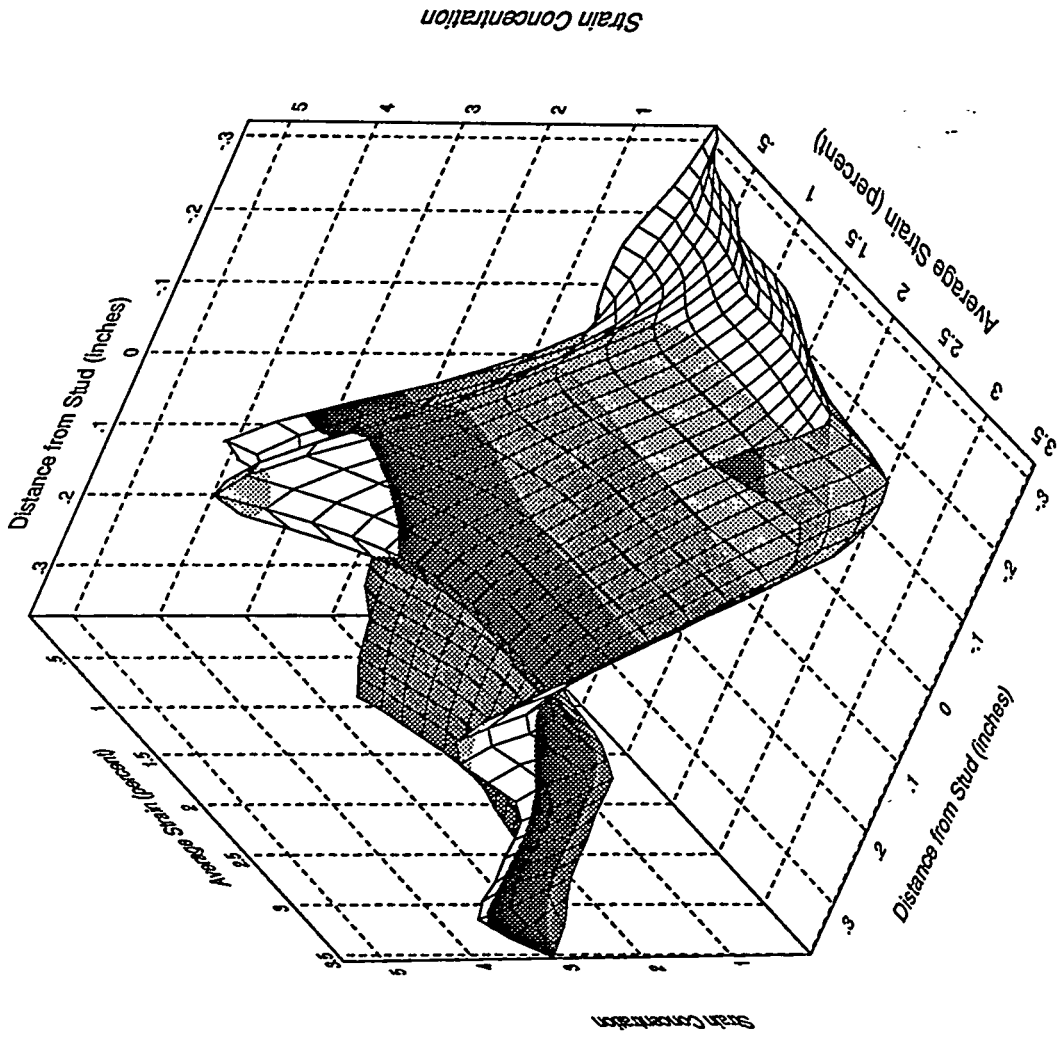

Lower Outboard Strip Gage, Specimen 2B3

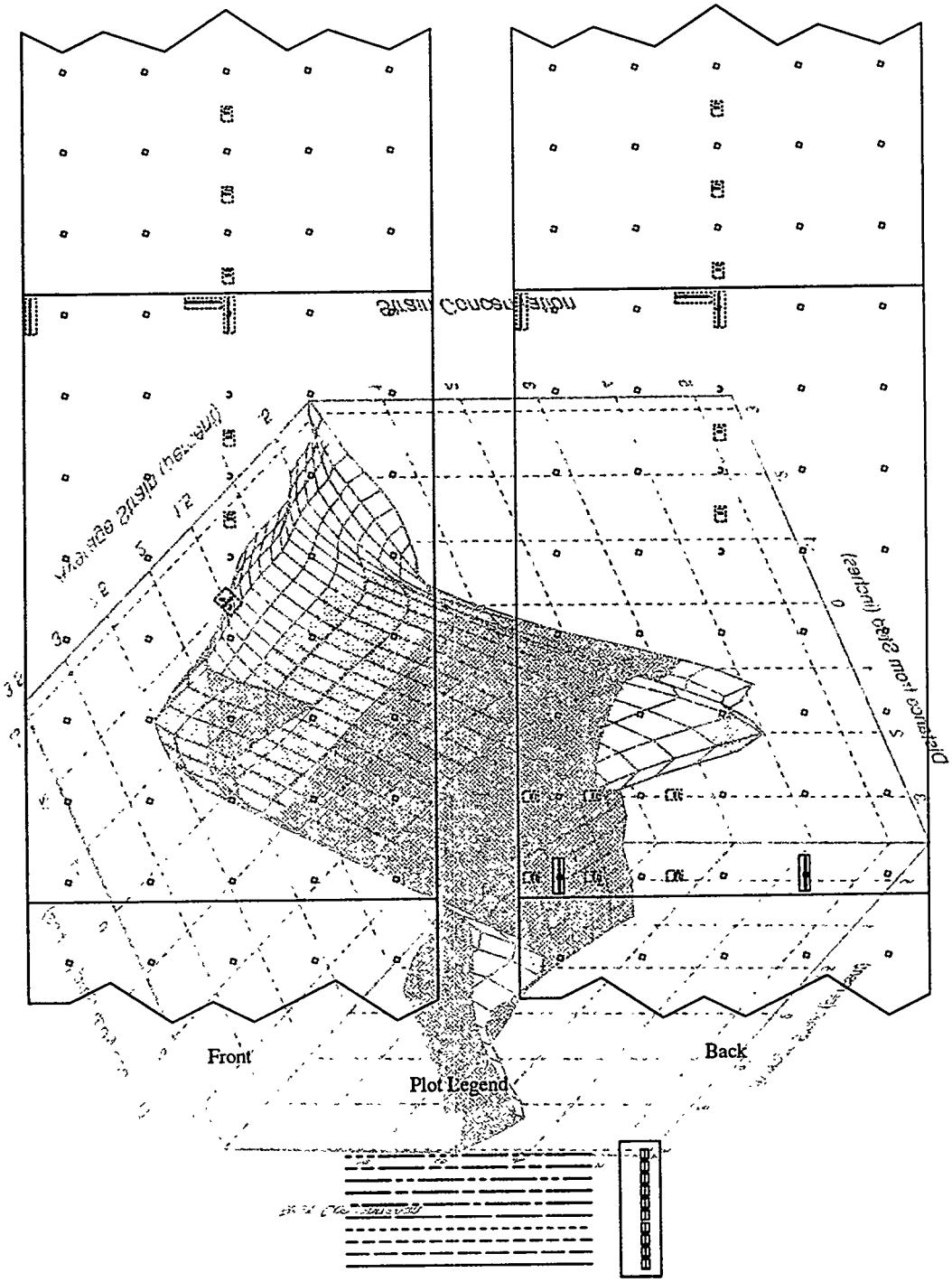

Lower Vertical Strip Gages

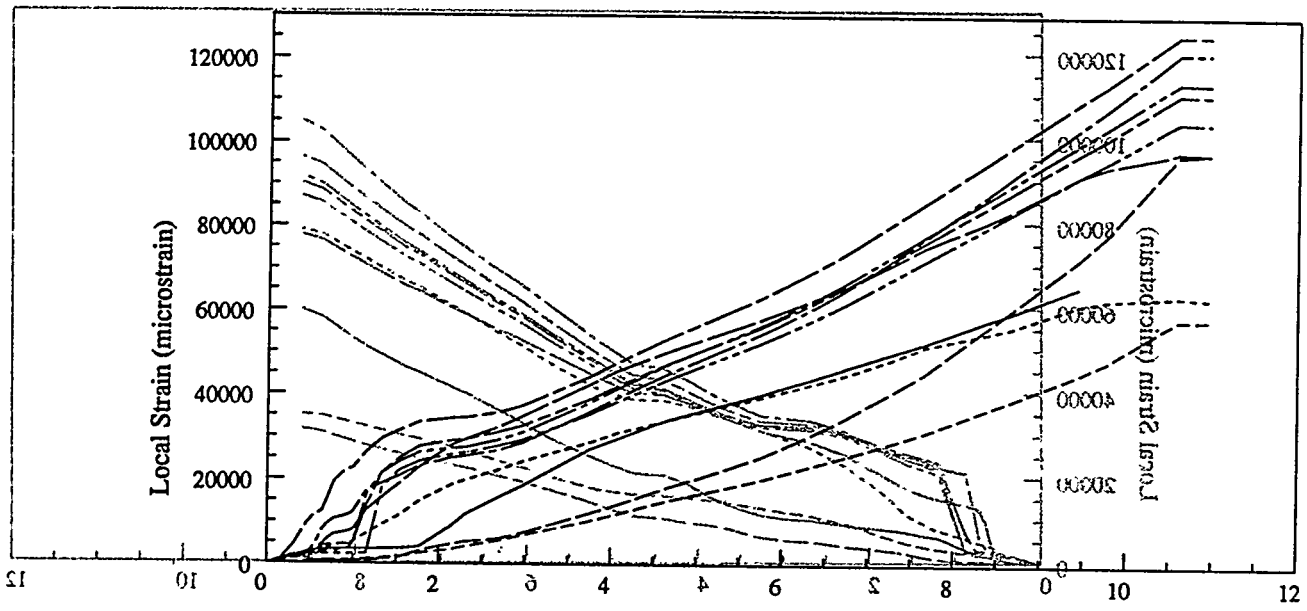

Vertical Lower Left Strip Gage Response, Specimen 2B1

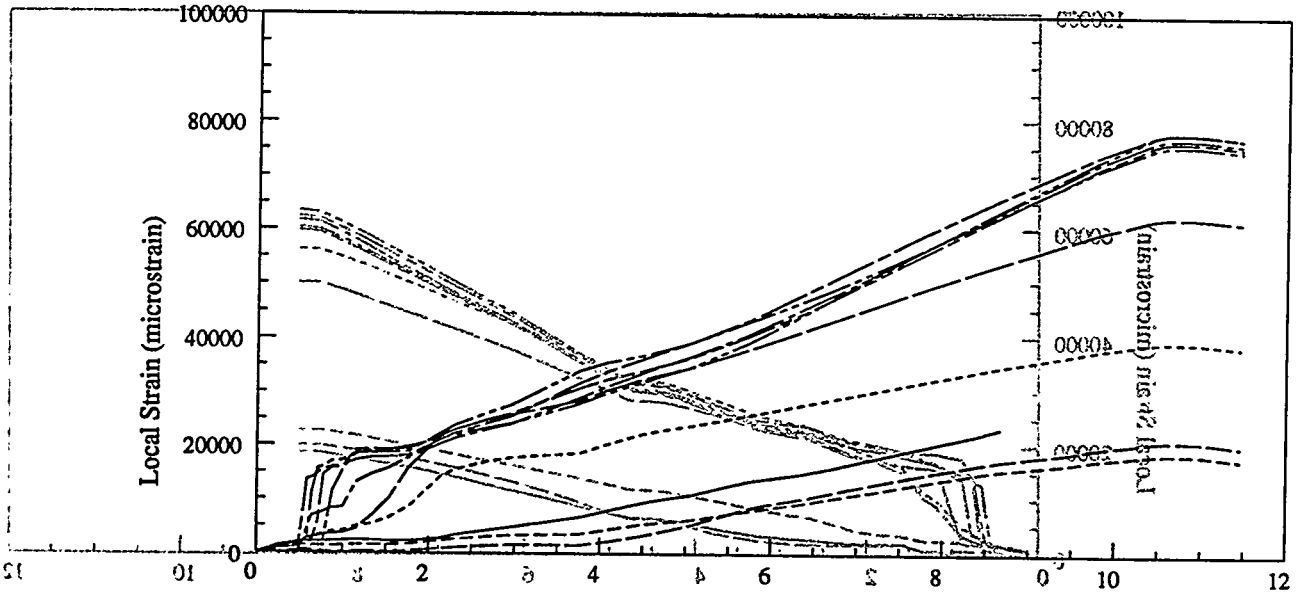

Vertical Lower Right Strip Gage Response, Specimen 2B1

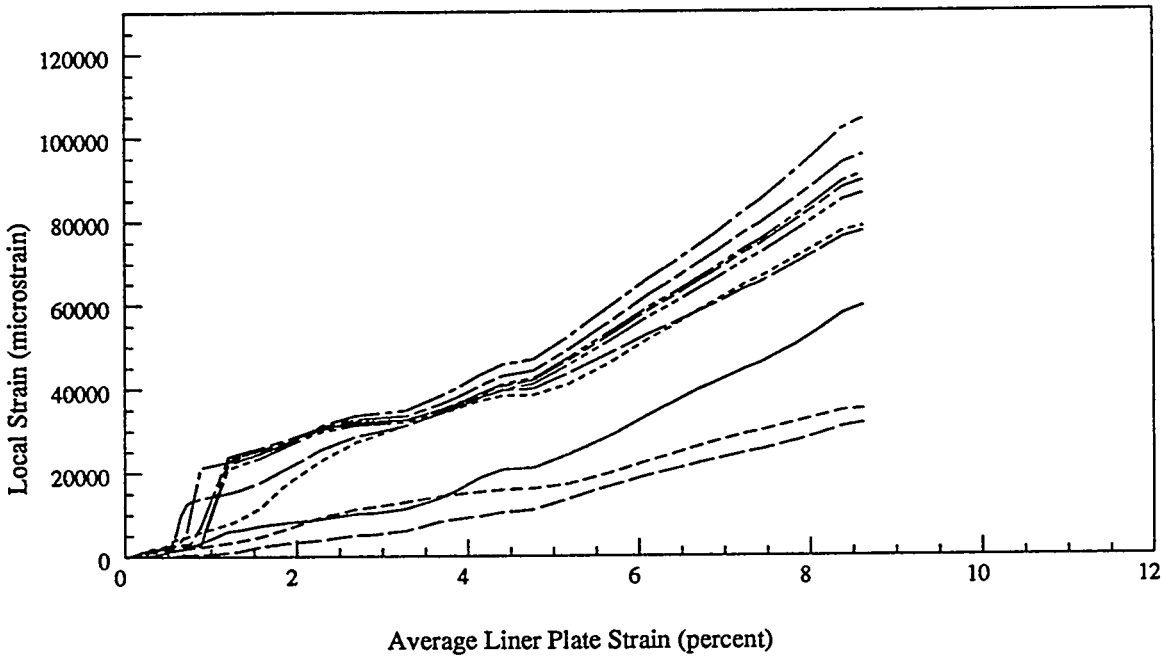

Vertical Lower Left Strip Gage Response, Specimen 2B2

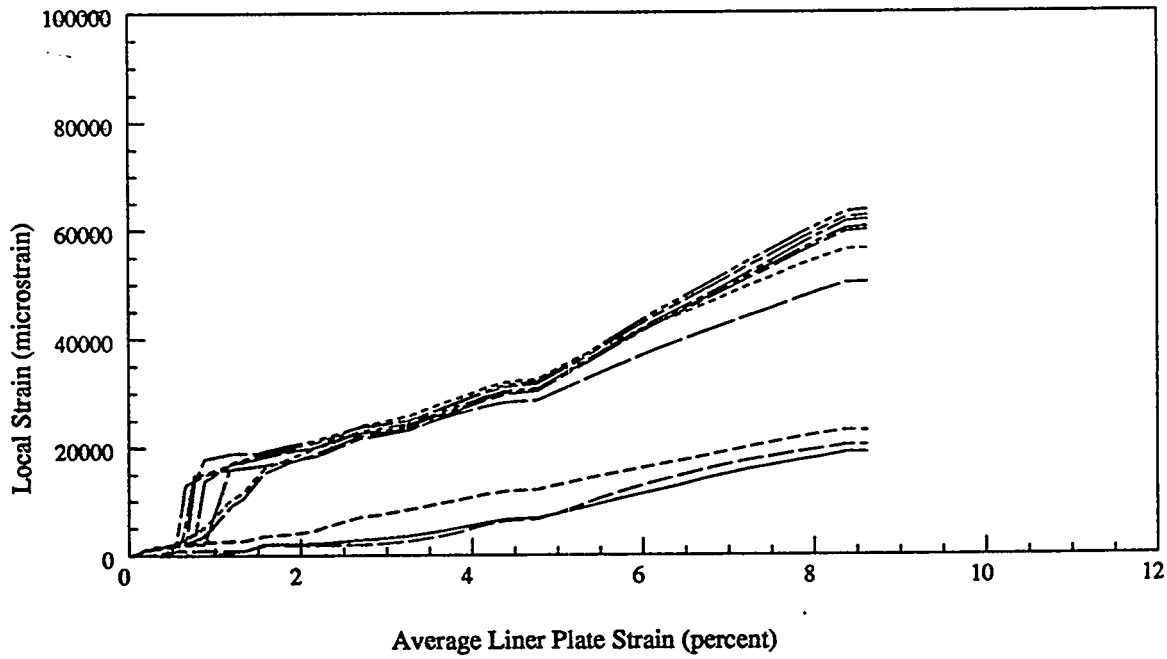

Vertical Lower Right Strip Gage Response, Specimen 2B2

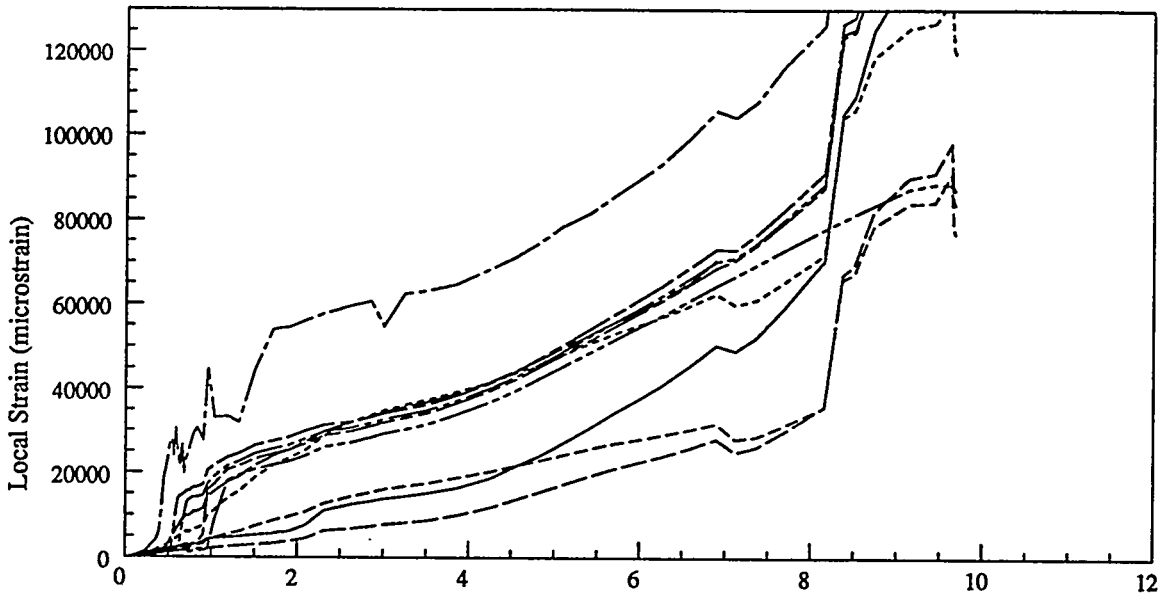

Vertical Lower Left Strip Gage Response, Specimen 2B3

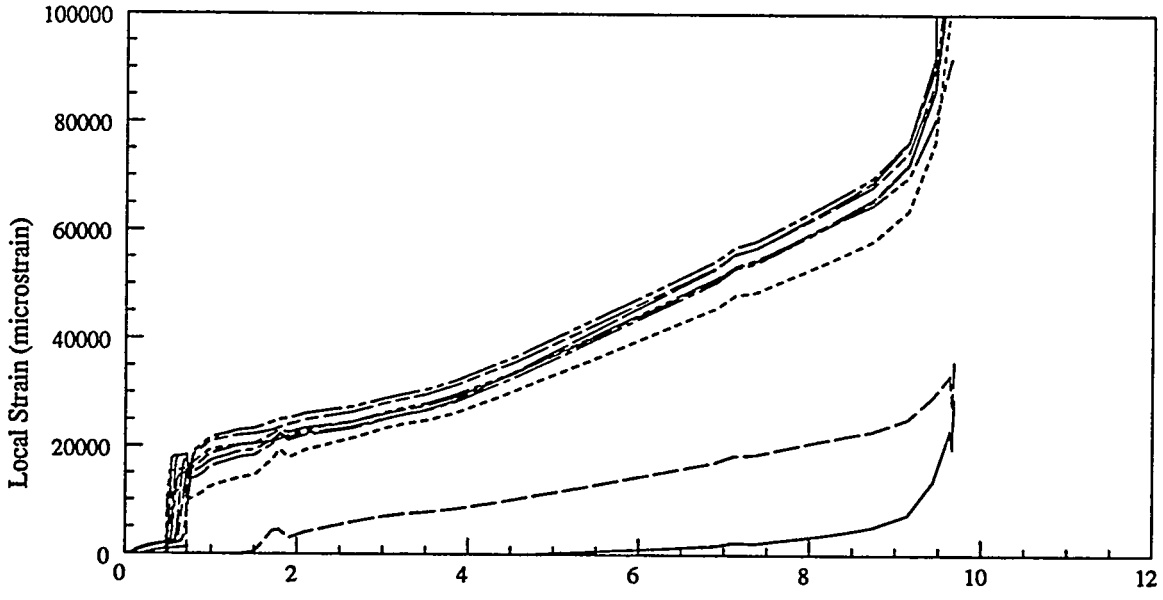

Vertical Lower Right Strip Gage Response, Specimen 2B3

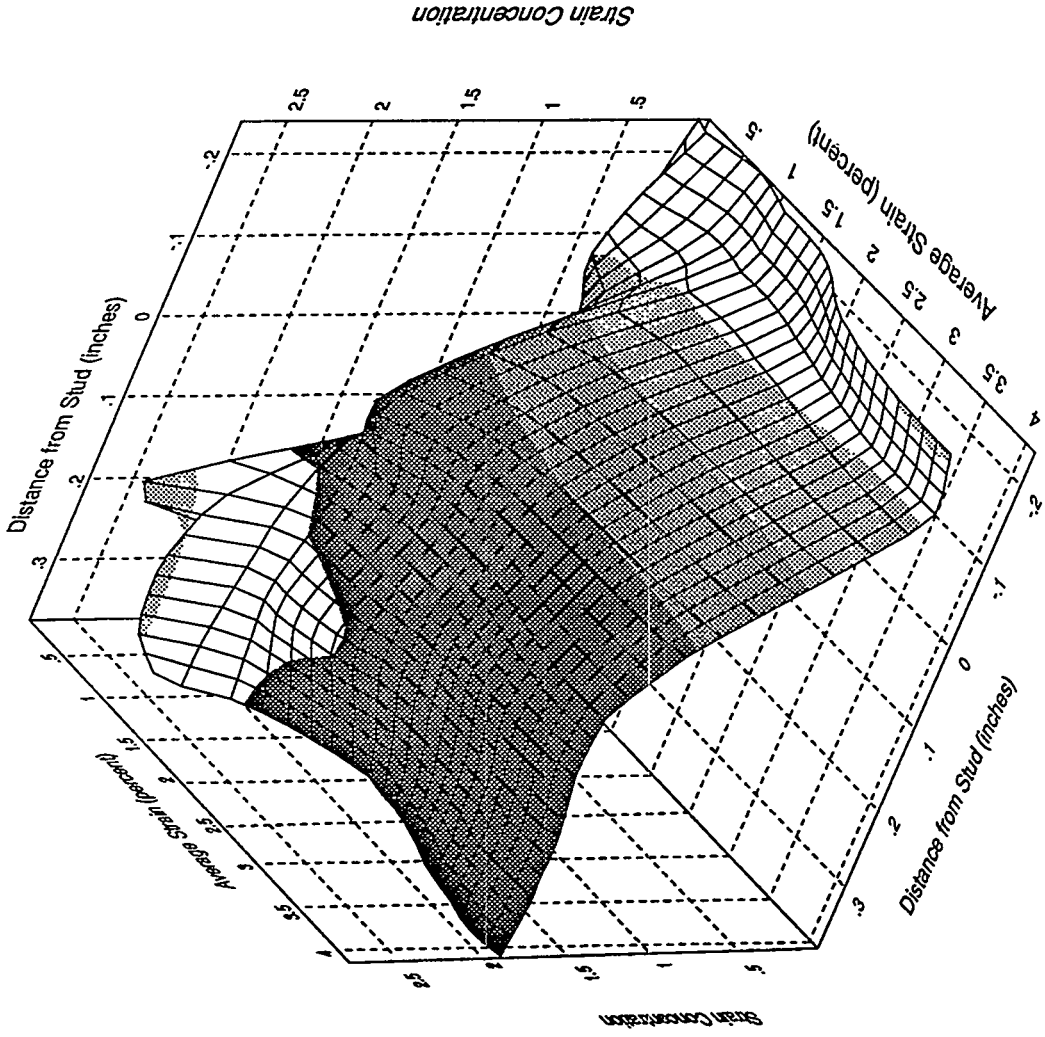

Lower Inboard Strip Gage, Specimen 2B1

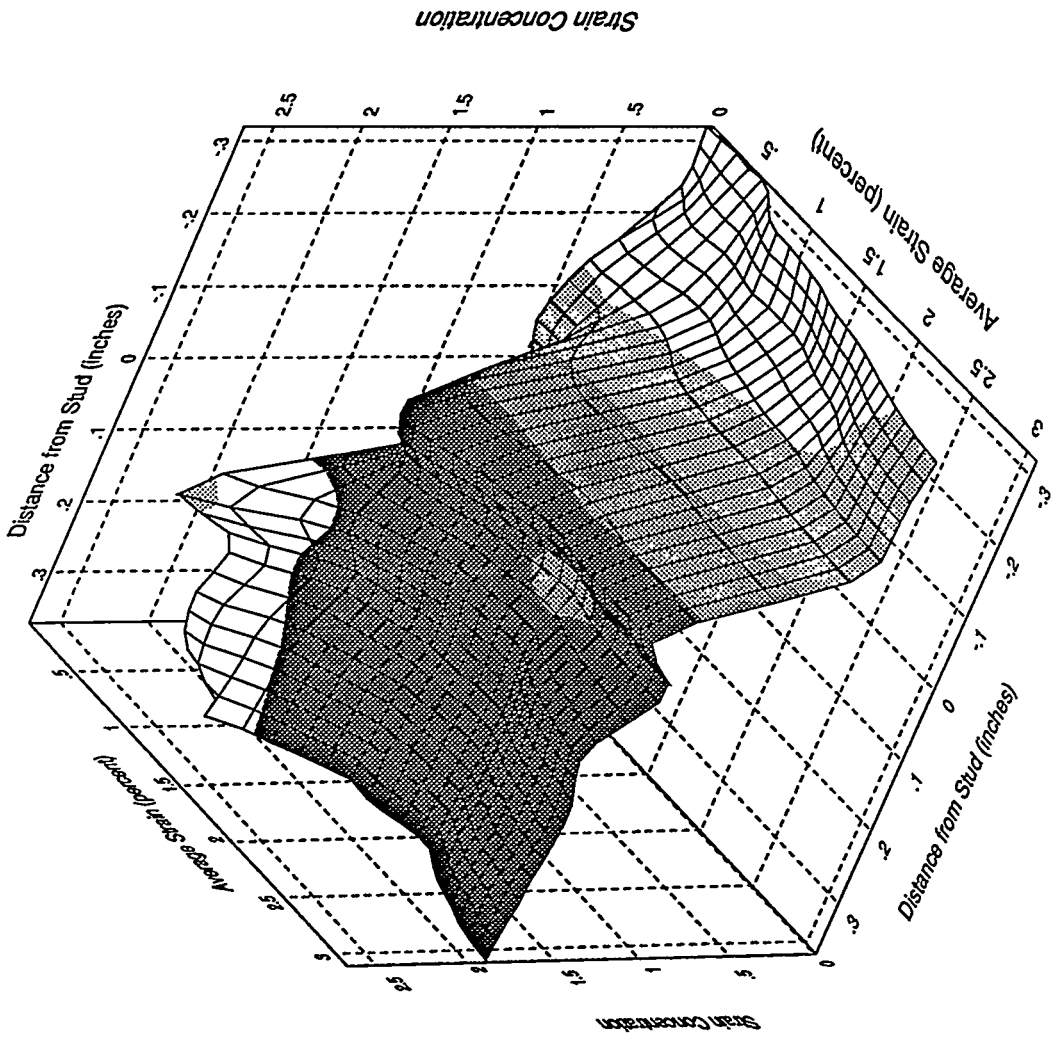

Lower Inboard Strip Gage, Specimen 2B2

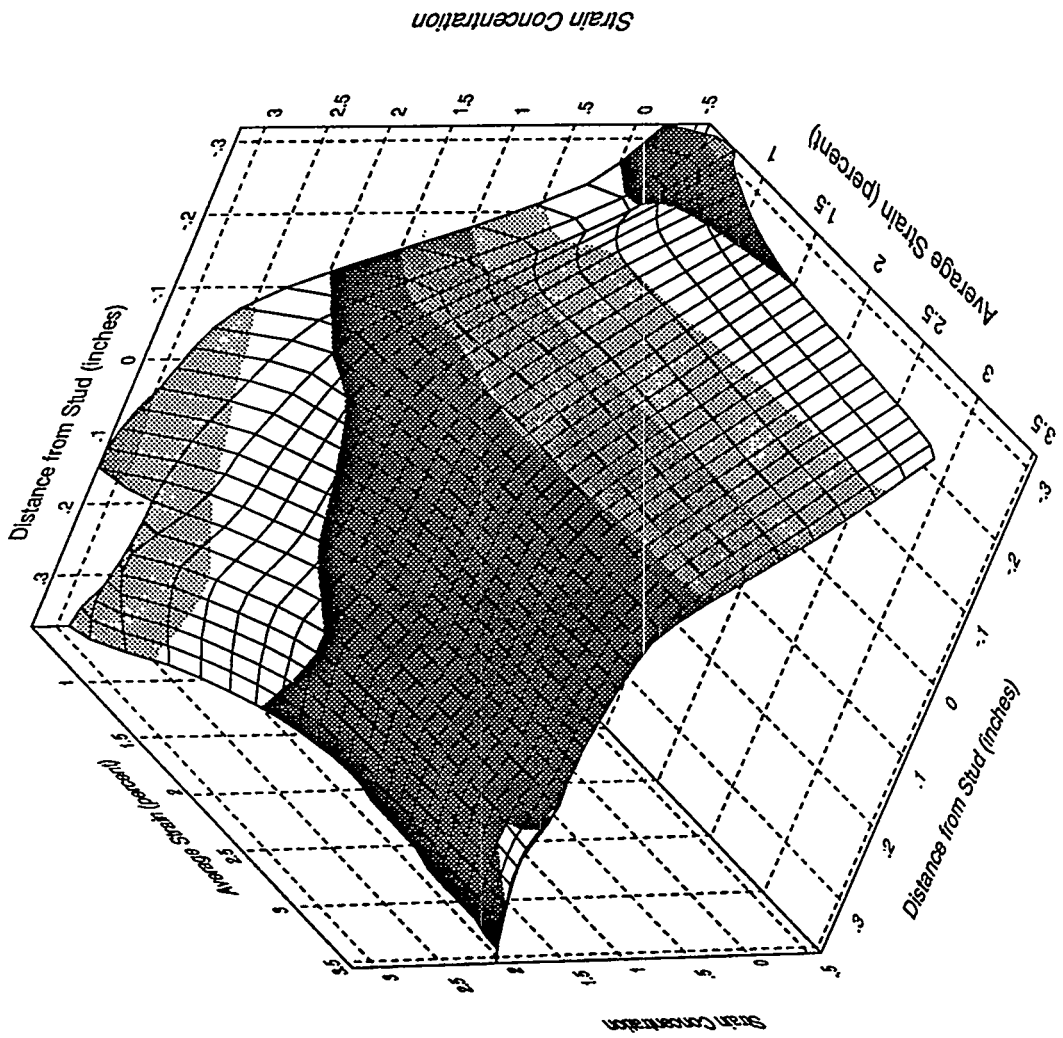

Lower Inboard Strip Gage, Specimen 2B3

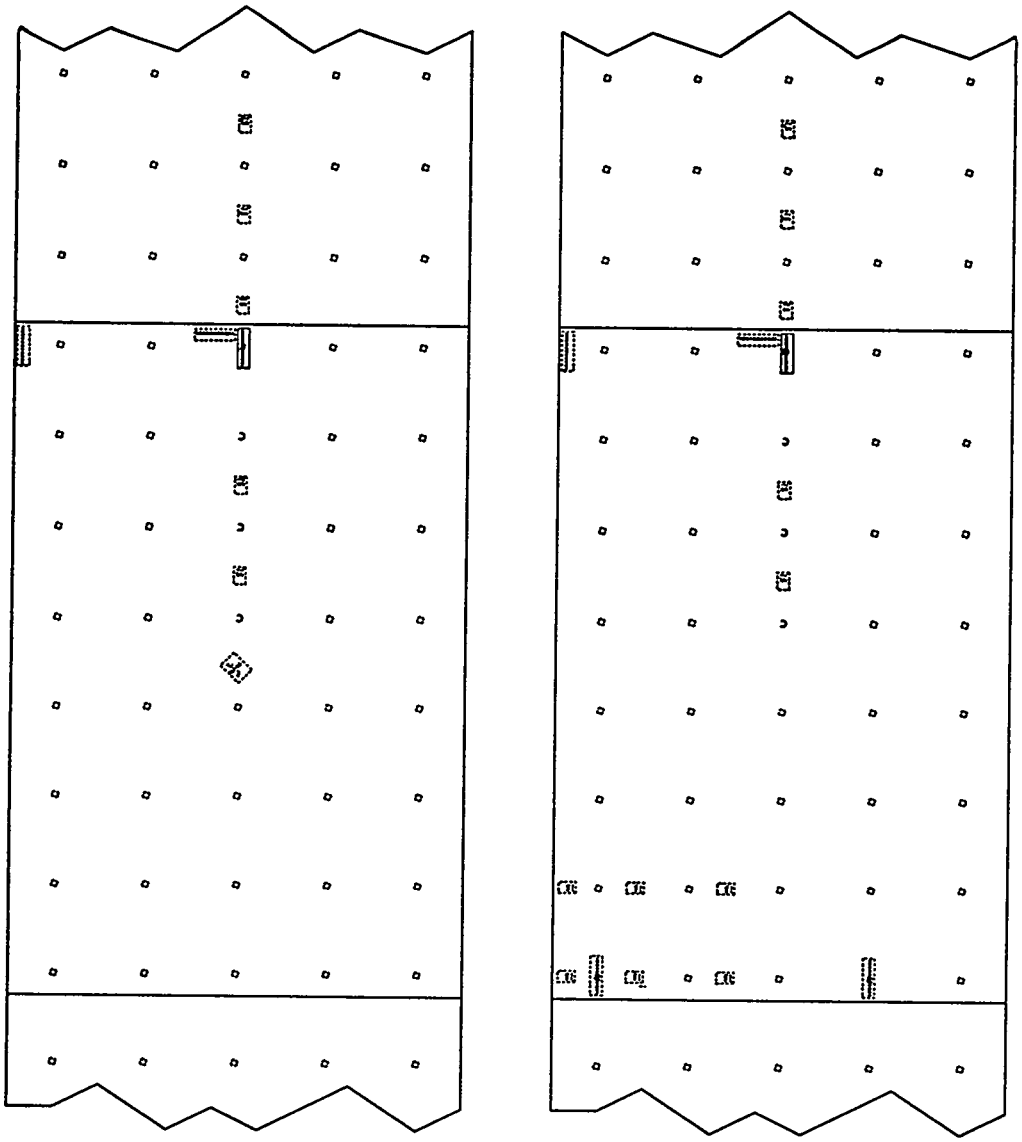

Centerline Vertical Strip Gages

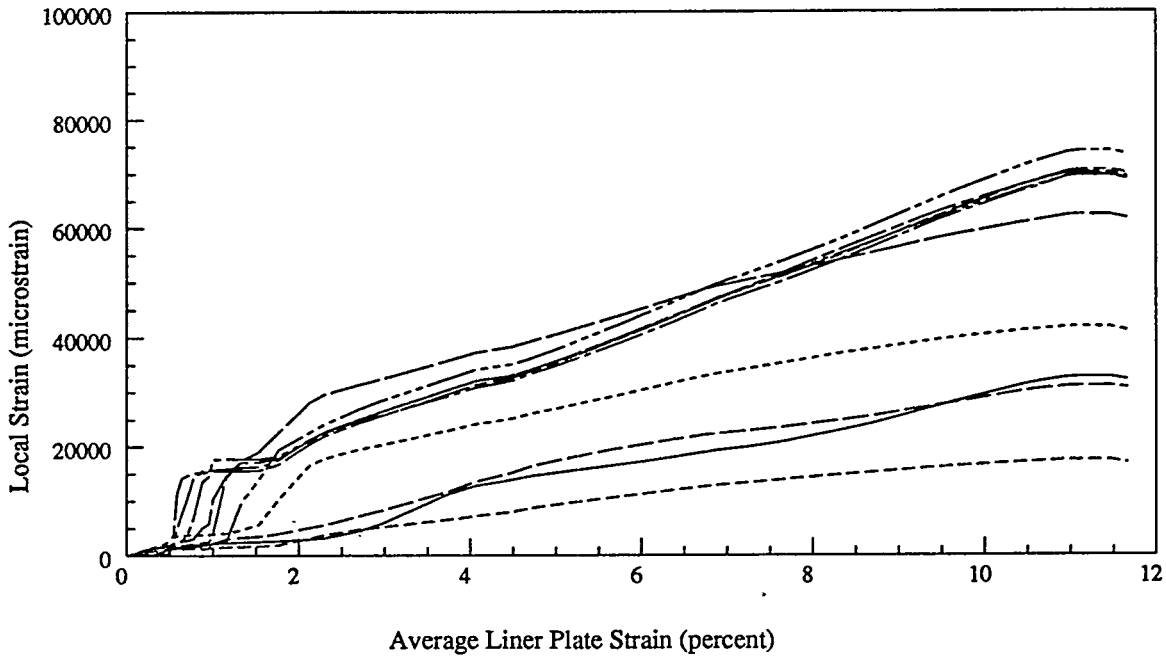

Vertical Strip Gage Response, Front Side,Specimen 2B1

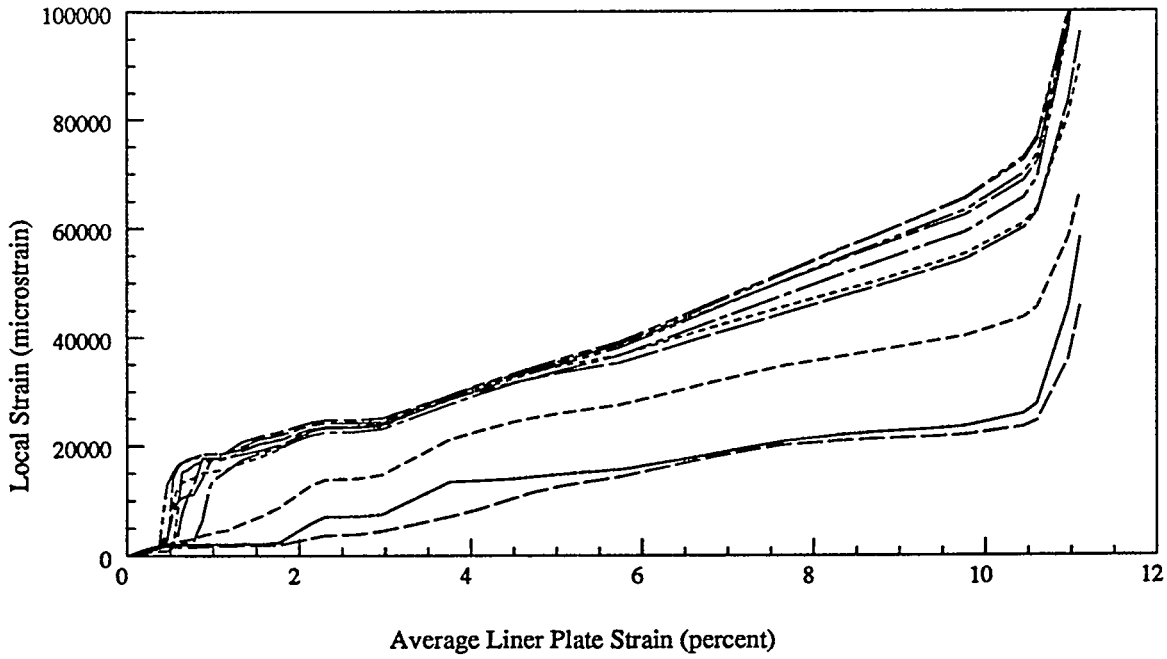

Vertical Strip Gage Response, Back Side, Specimen 2B1

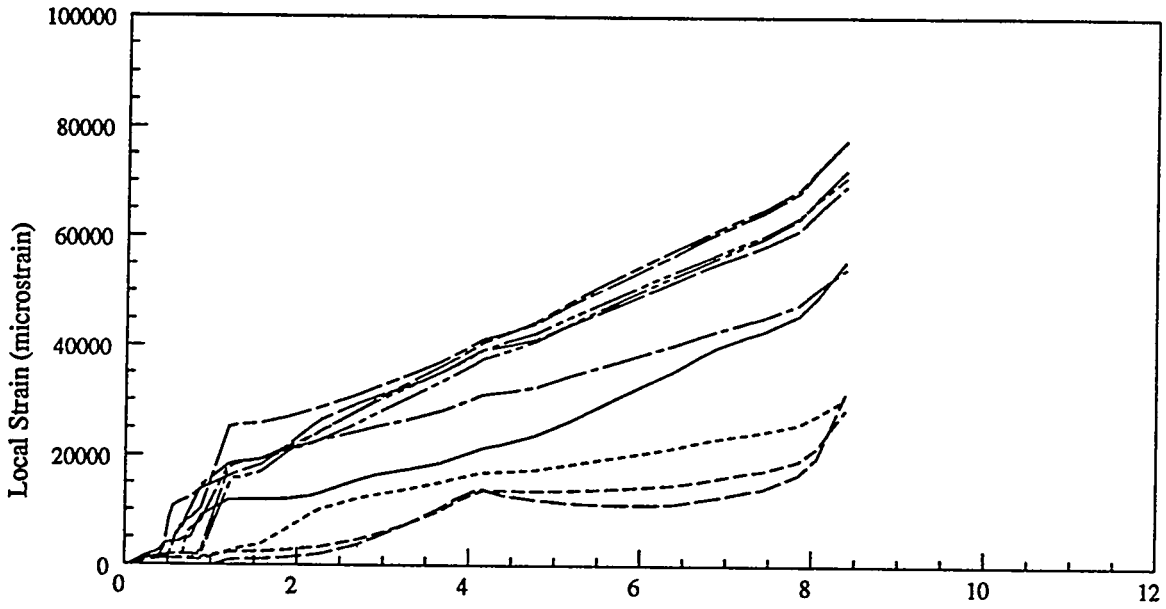

Vertical Strip Gage Response, Front Side, Specimen 2B2

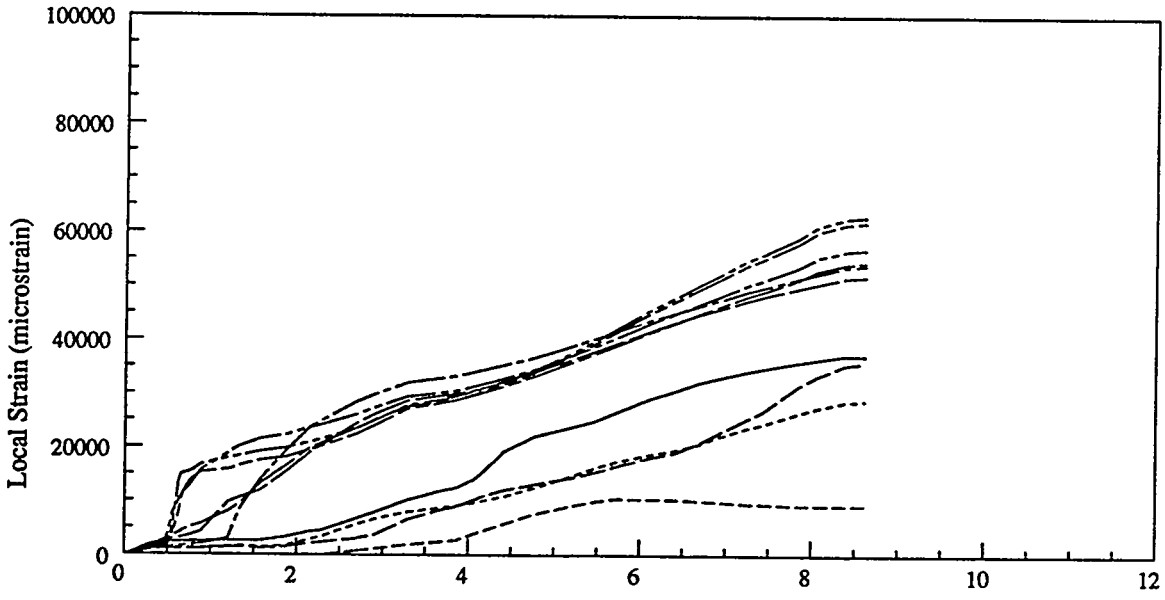

Vertical Strip Gage Response, Back Side, Specimen 2B2

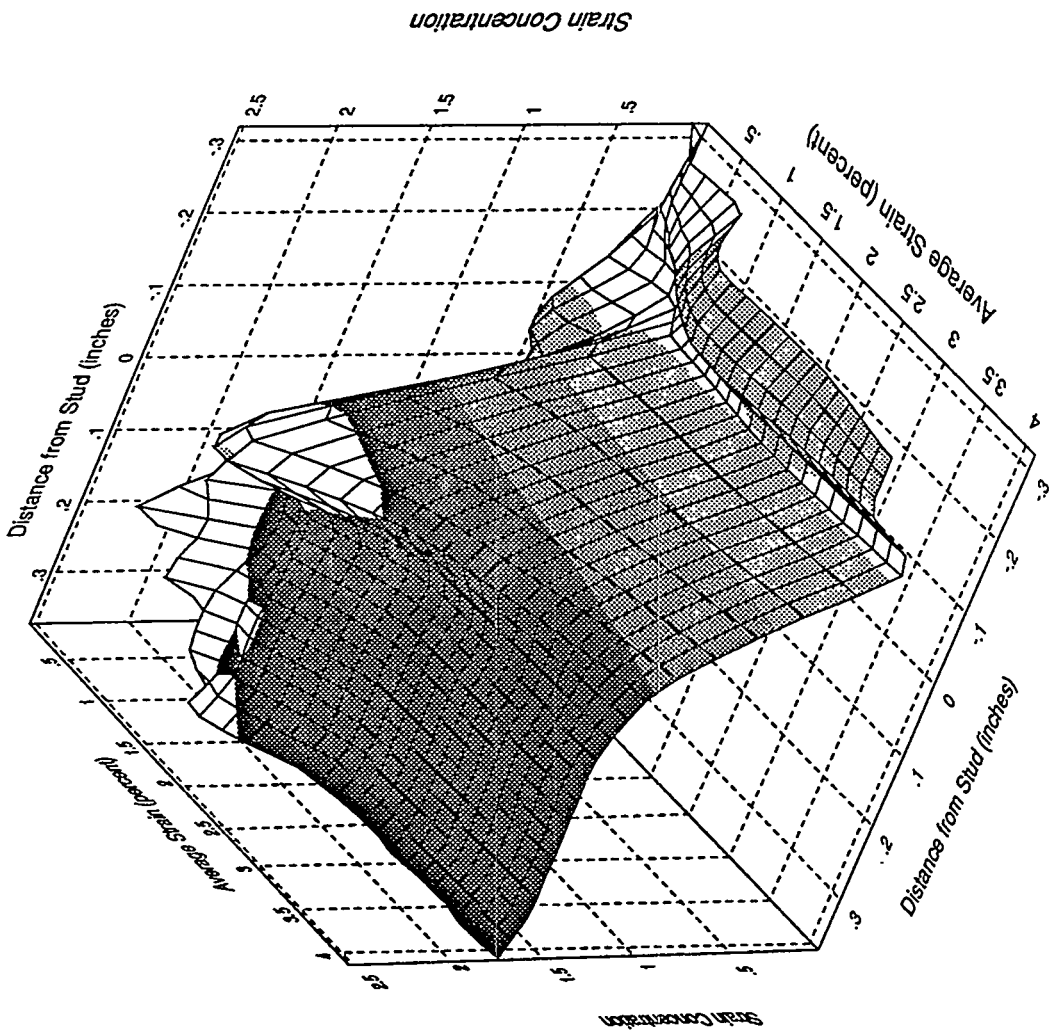

Front Centerline Strip Gage, Specimen 2B1

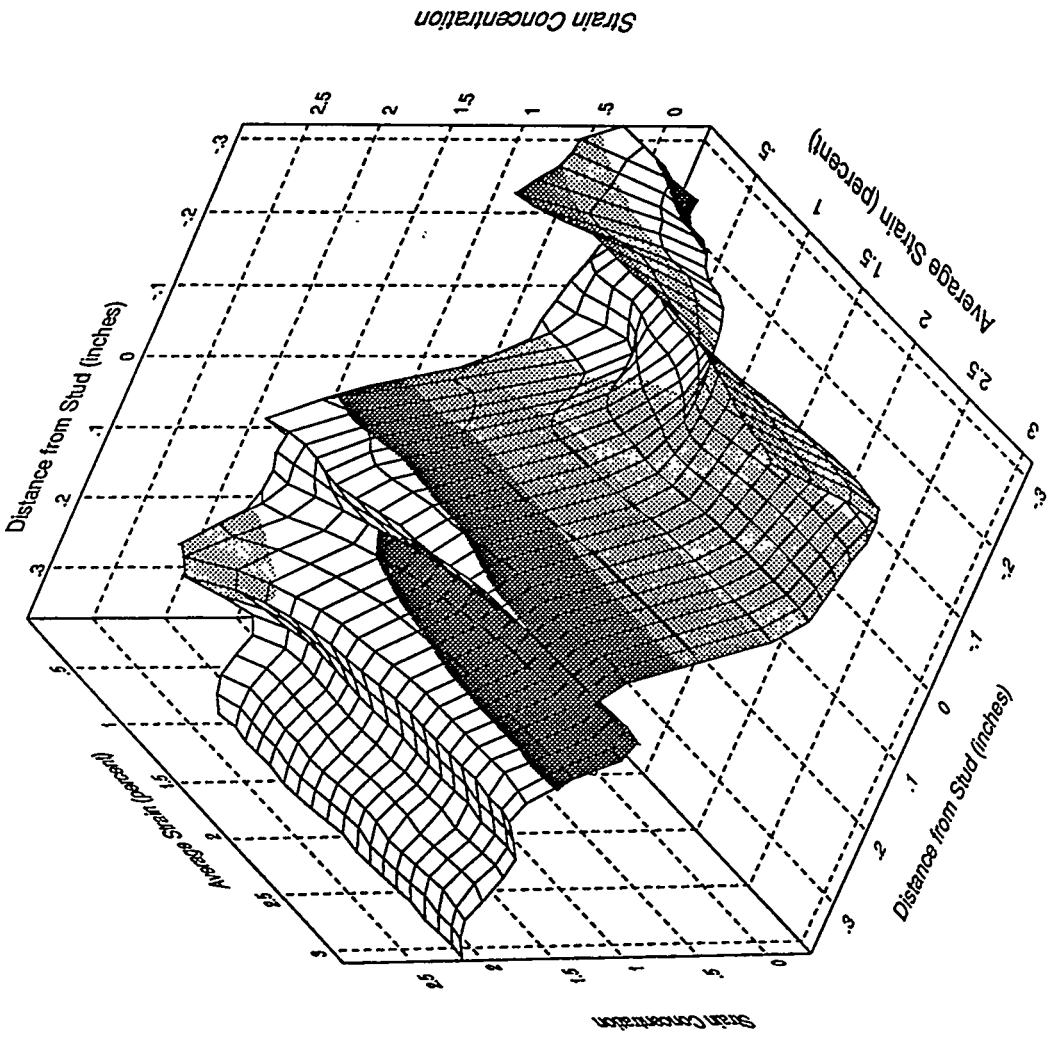

Front Centerline Strip Gage, Specimen 2B2

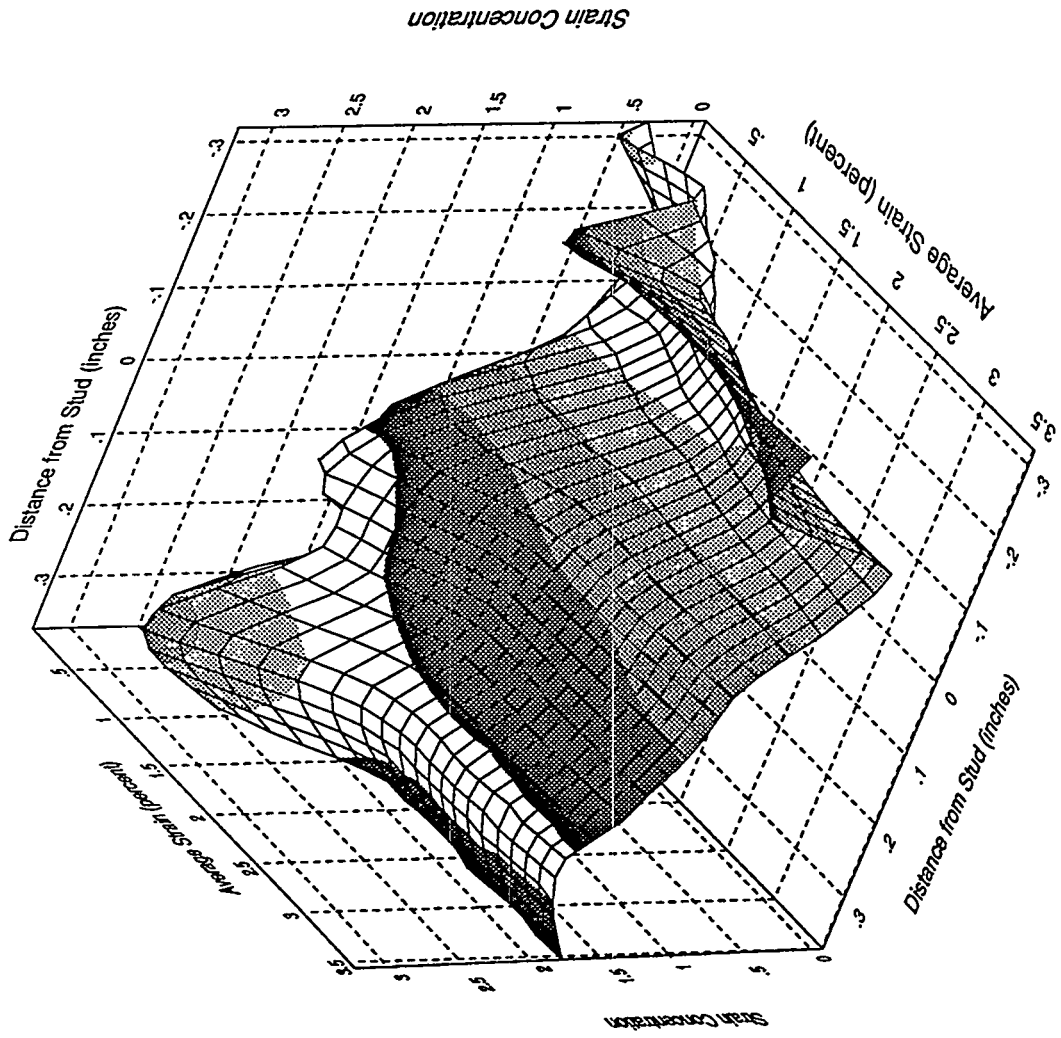

Front Centerline Strip Gage, Specimen 2B3

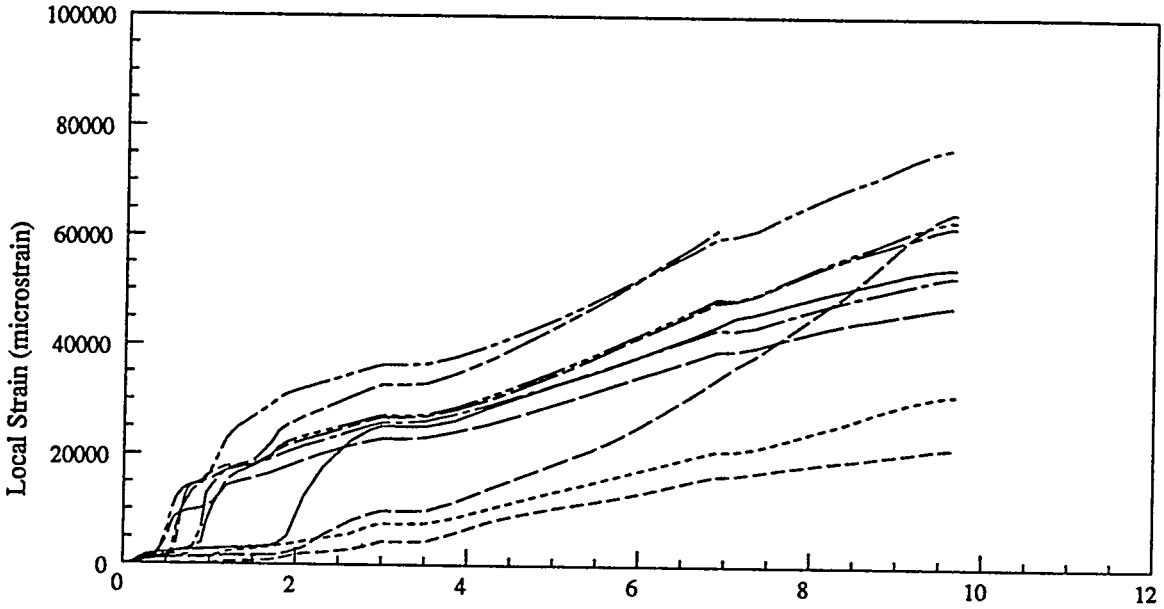

Vertical Strip Gage Response, Front Side,Specimen 2B3

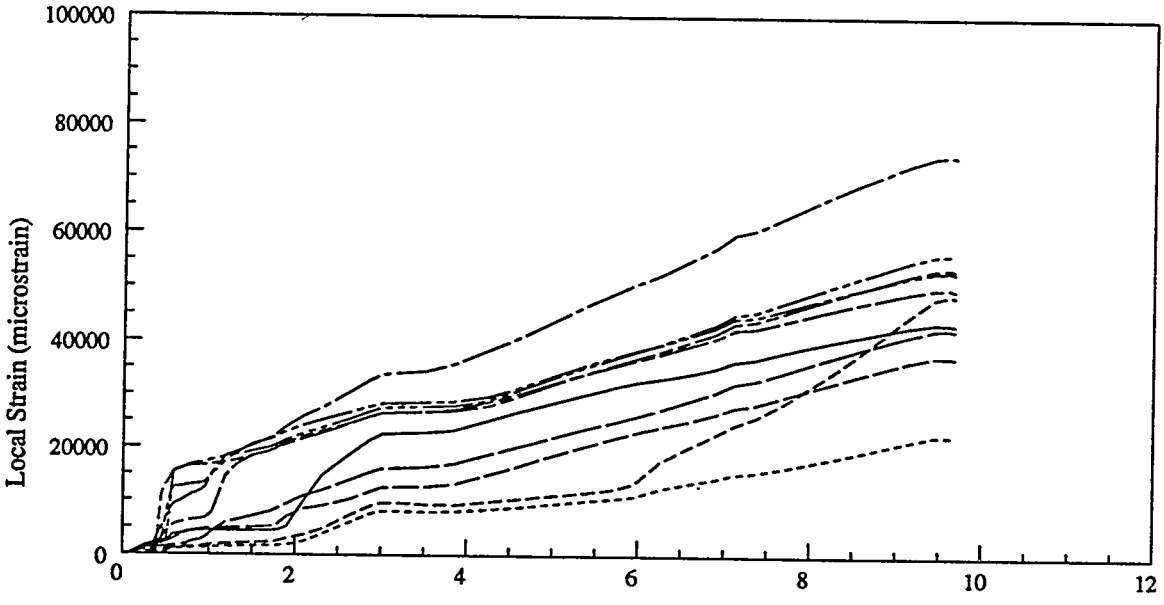

Vertical Strip Gage Response, Back Side, Specimen 2B3

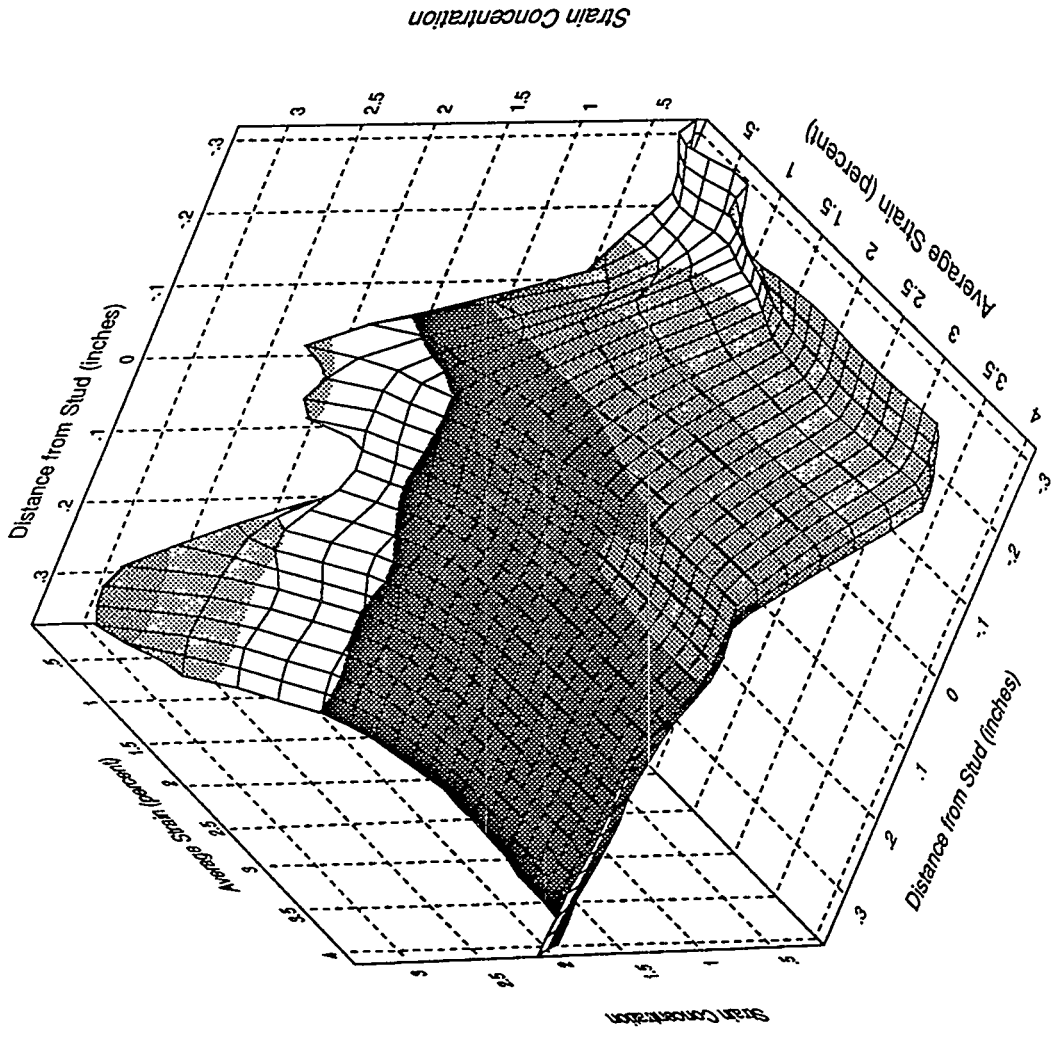

Back Centerline Strip Gage, Specimen 2B1

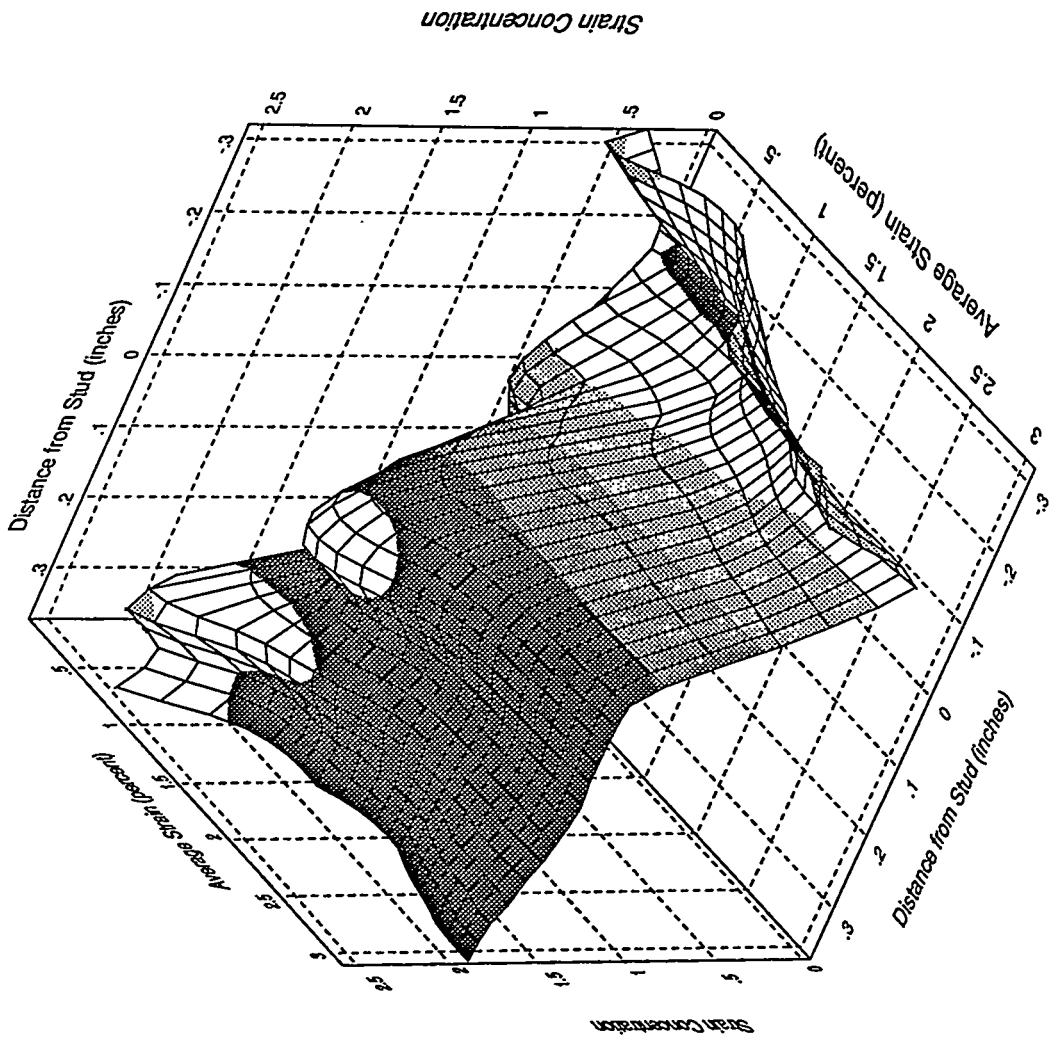

Back Centerline Strip Gage, Specimen 2B2

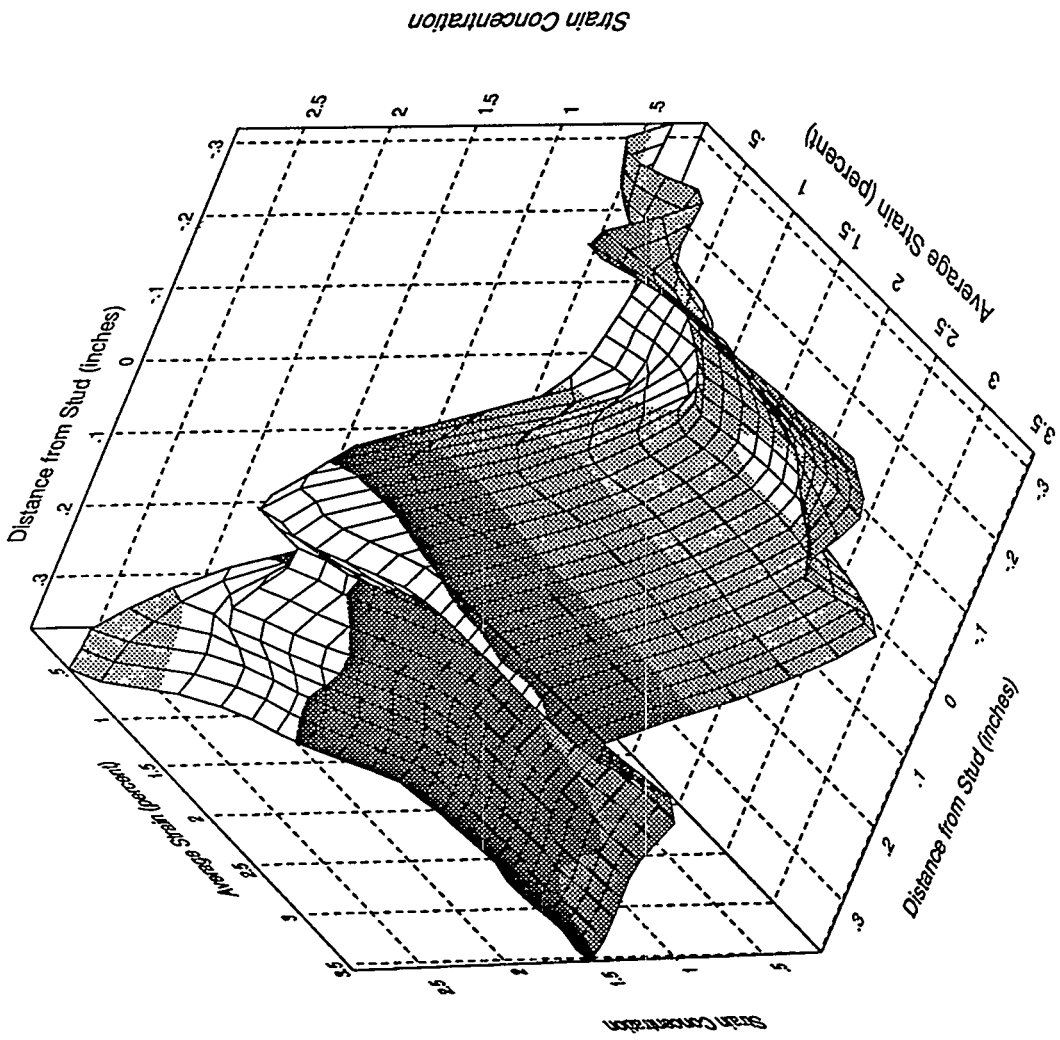

Back Centerline Strip Gage, Specimen 2B3

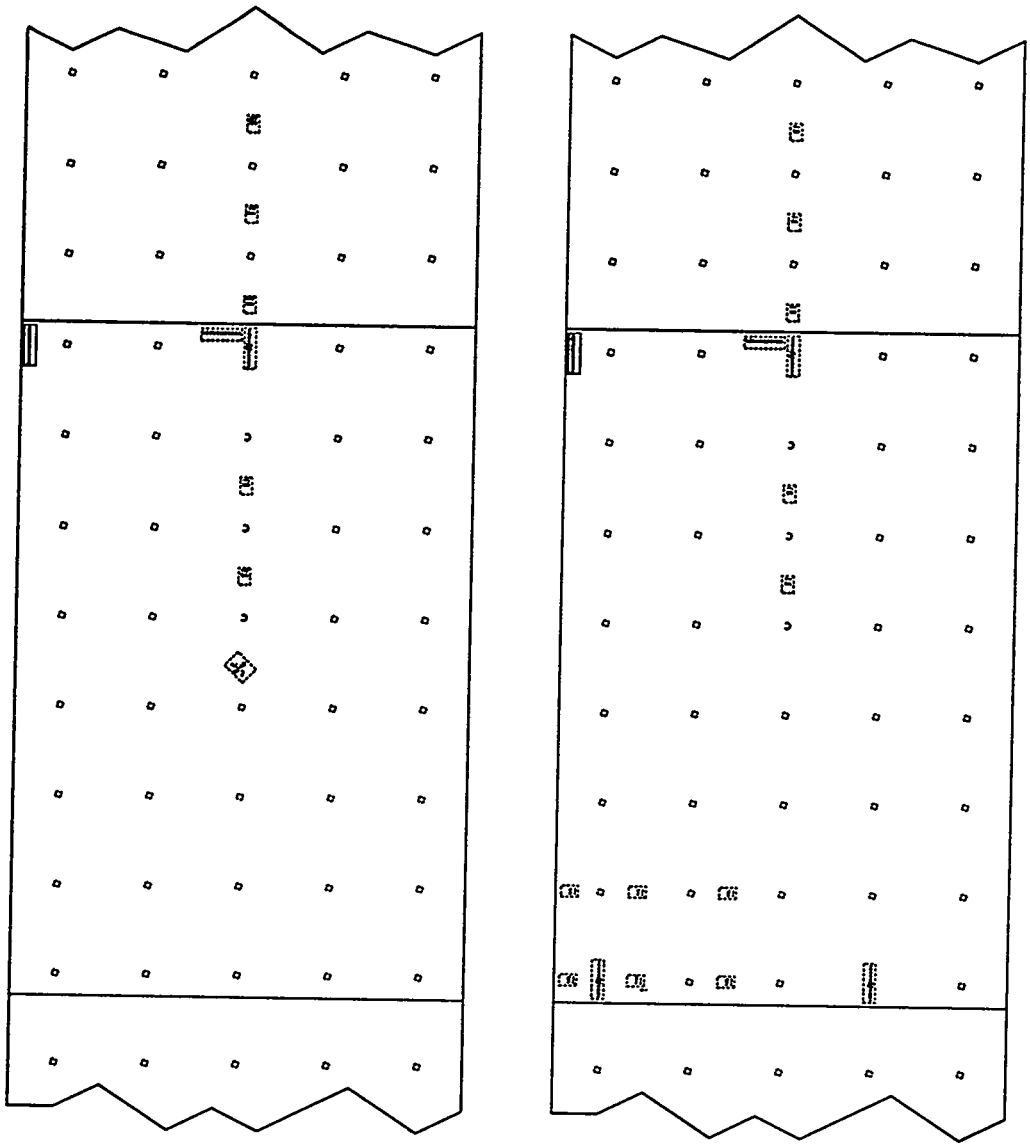

Edge Strip Gages

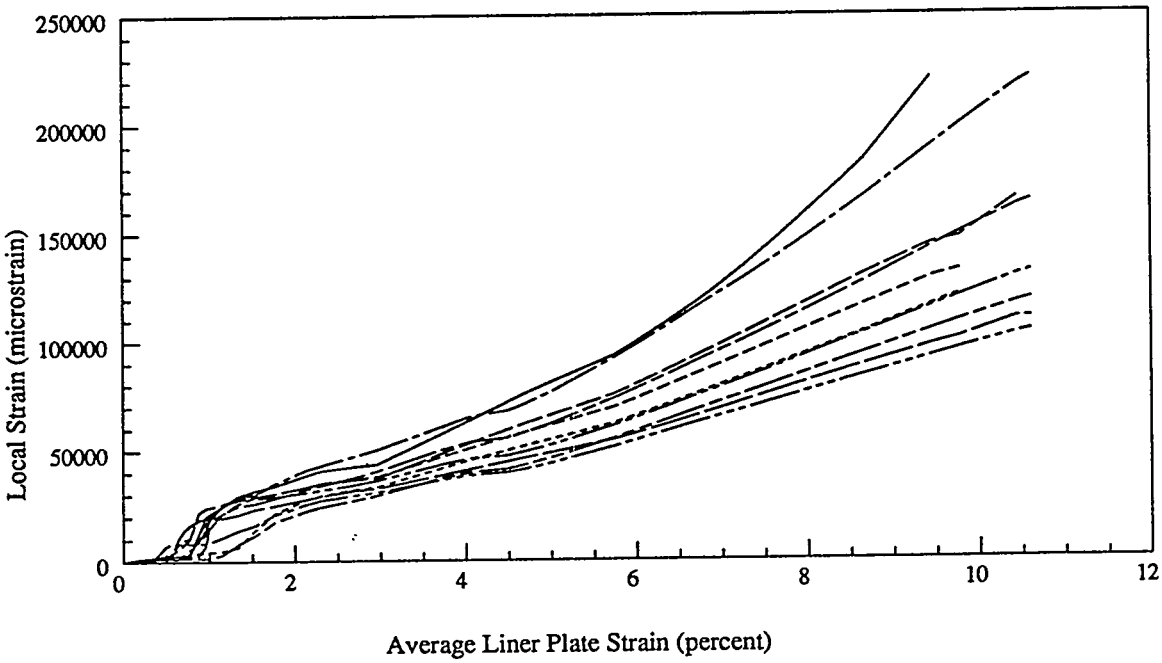

Edge Strip Gage Response, Specimen 2B1

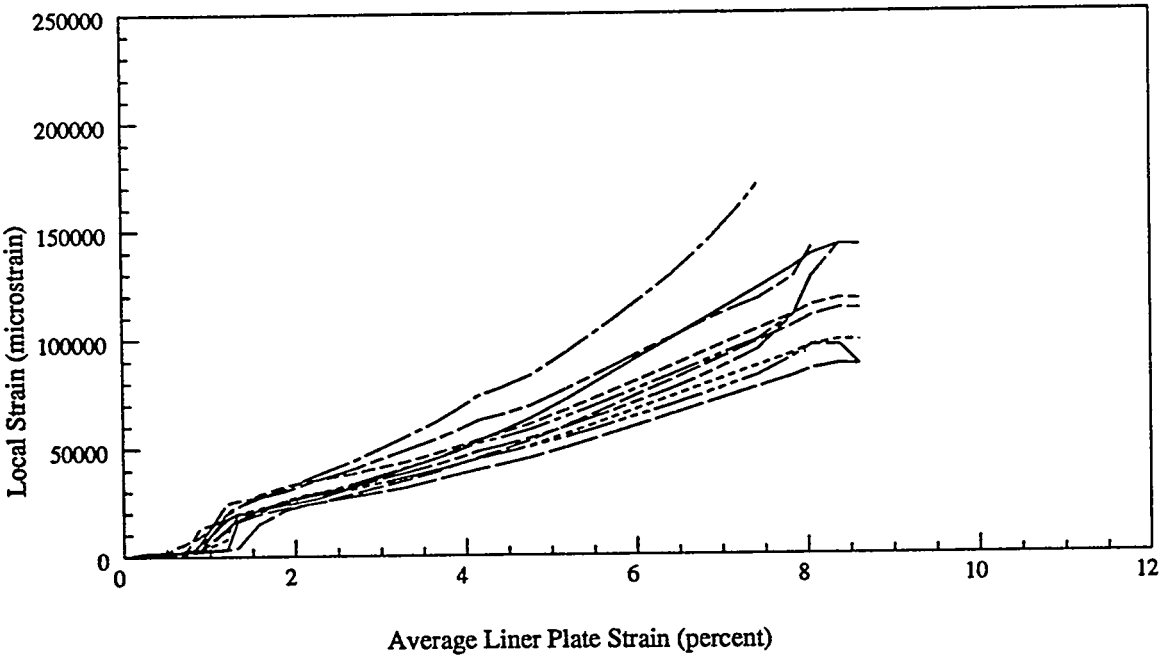

Edge Strip Gage Response, Specimen 2B2

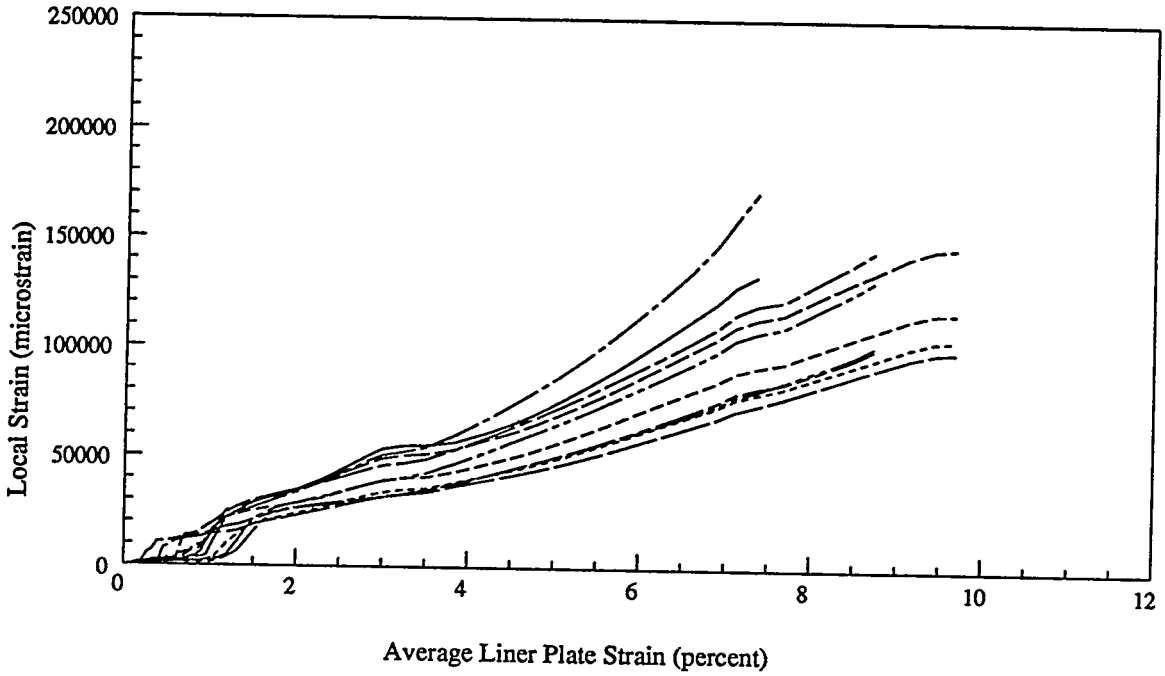

Edge Strip Gage Response, Specimen 2B3

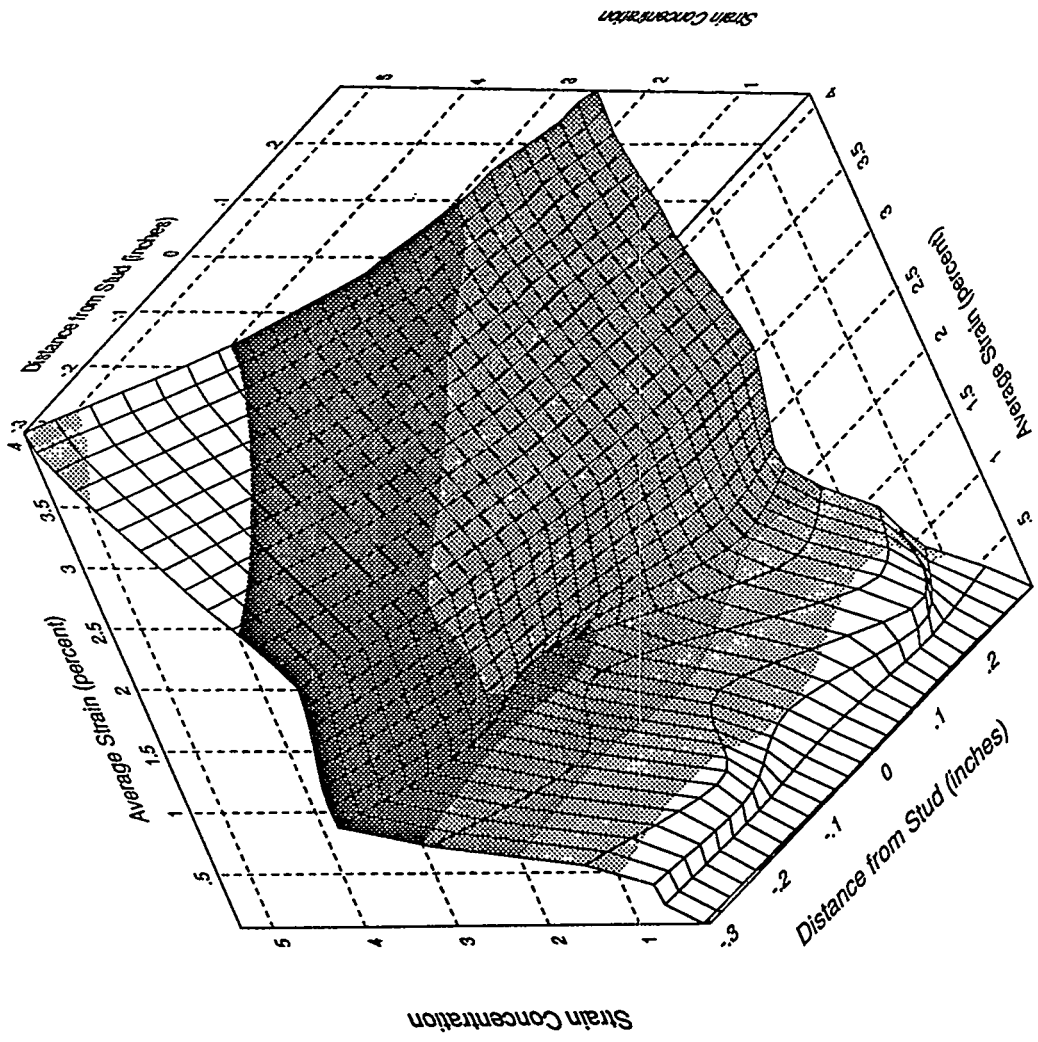

Front Edge Strip Gage, Specimen 2B1

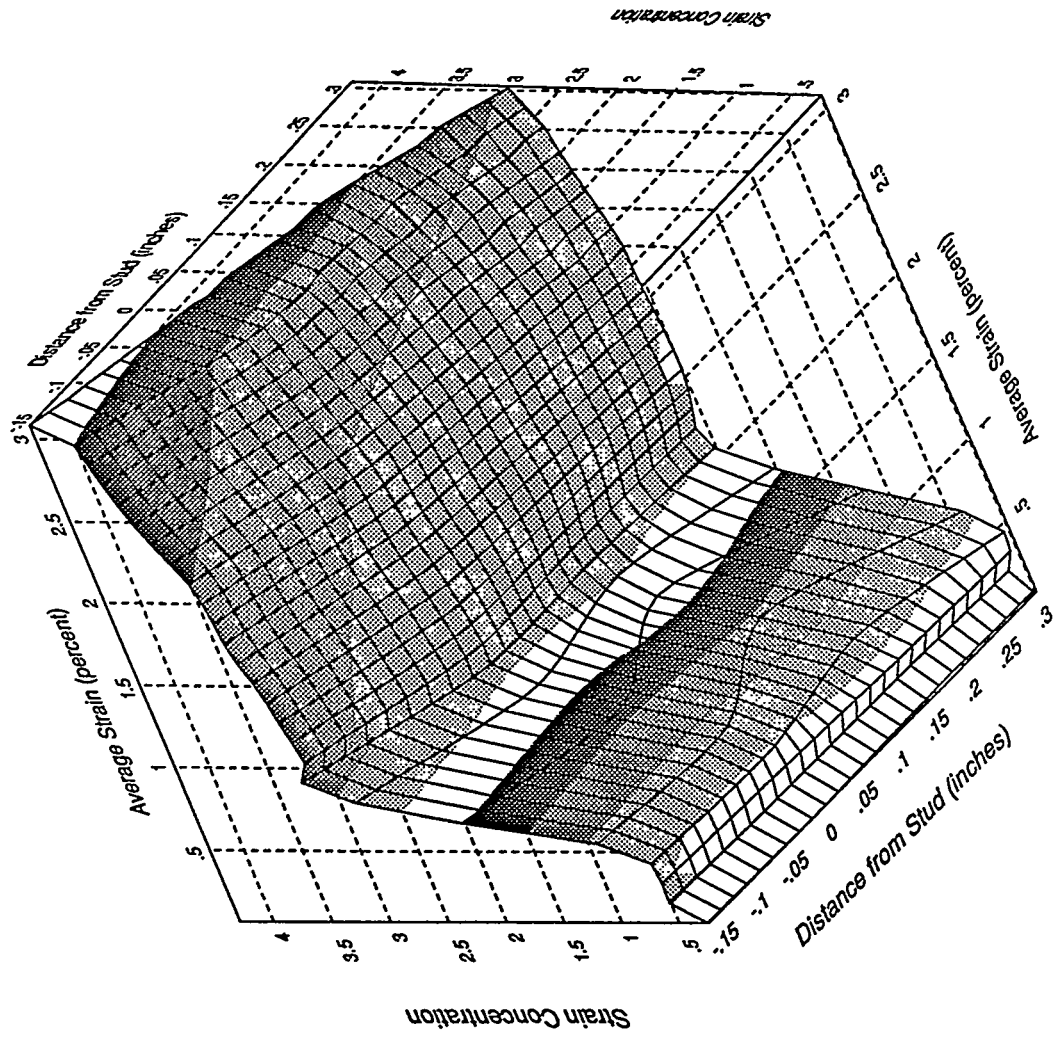

Front Edge Strip Gage, Specimen 2B2

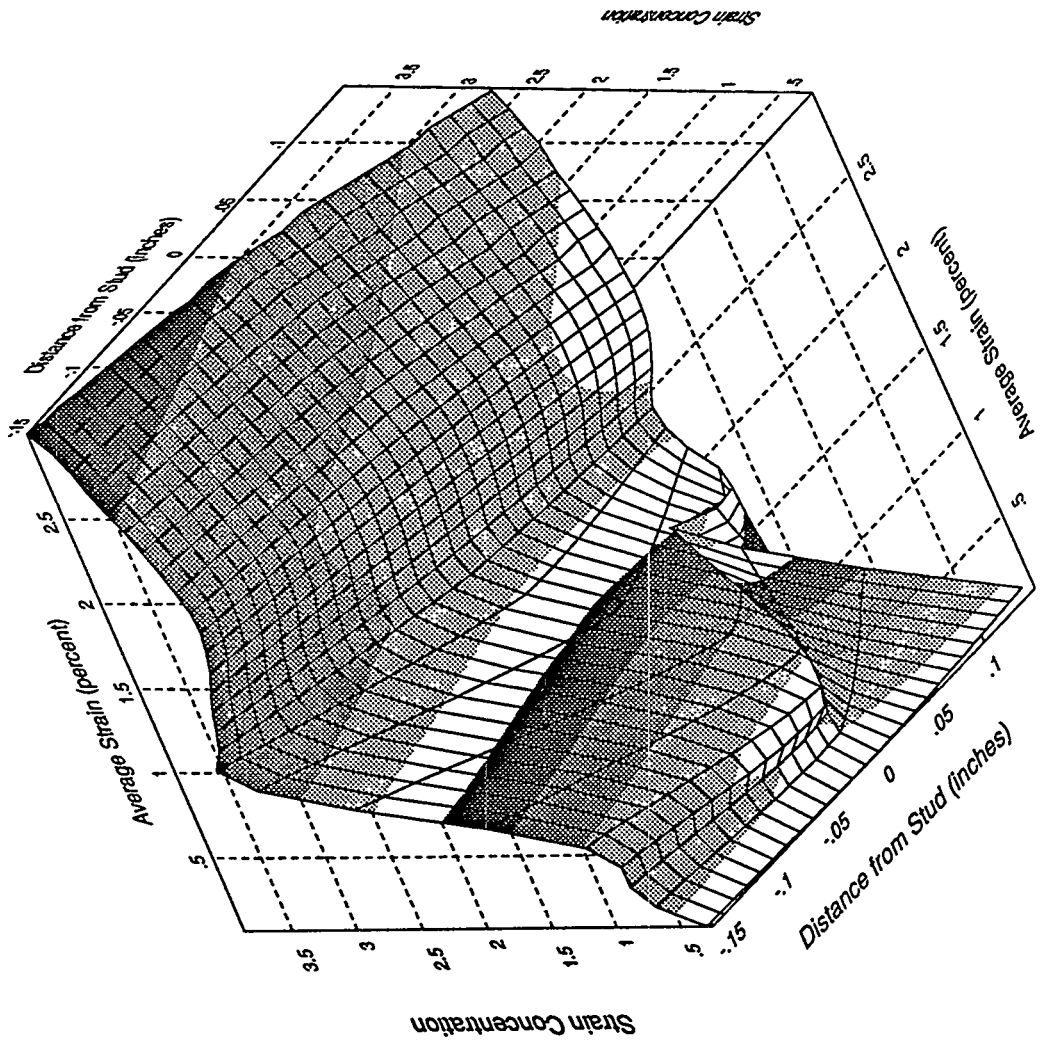

Front Edge Strip Gage, Specimen 2B3

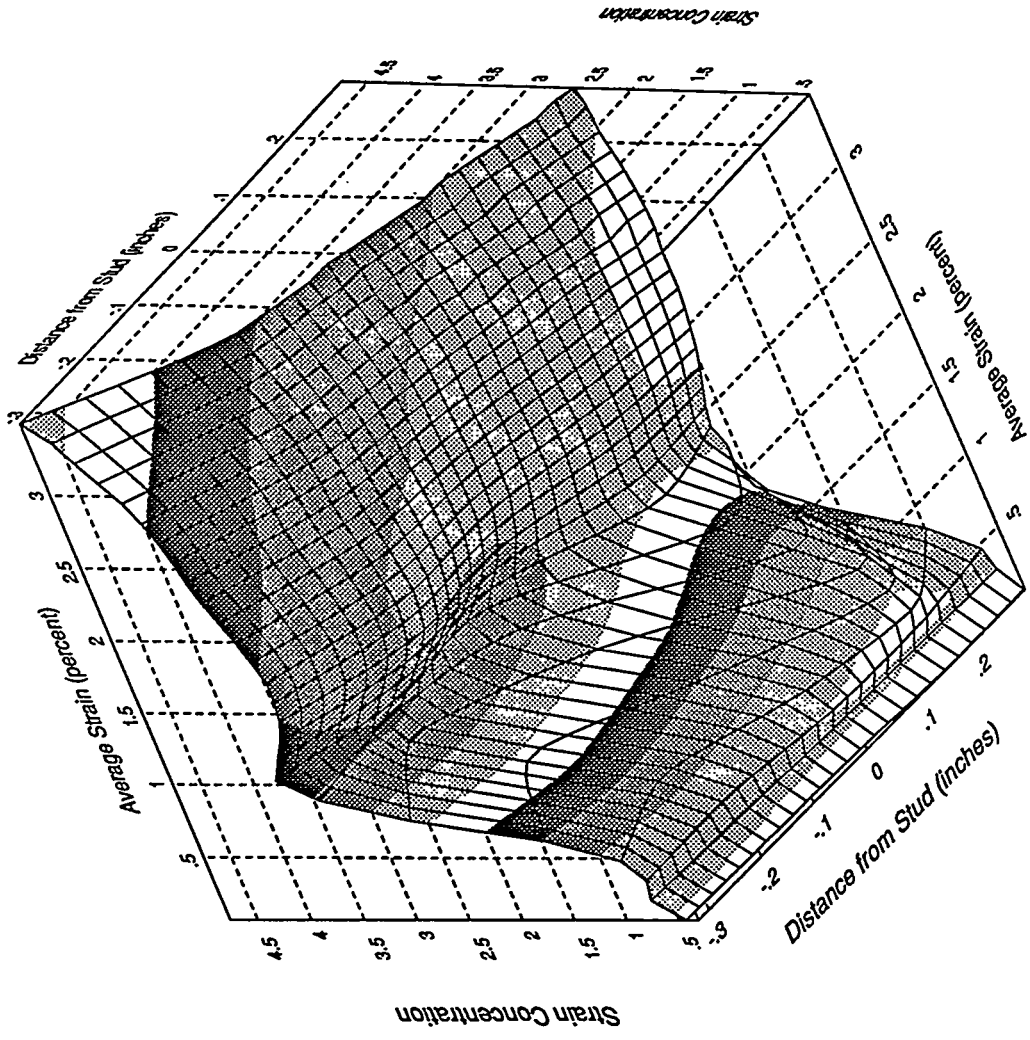

Back Edge Strip Gage, Specimen 2B1

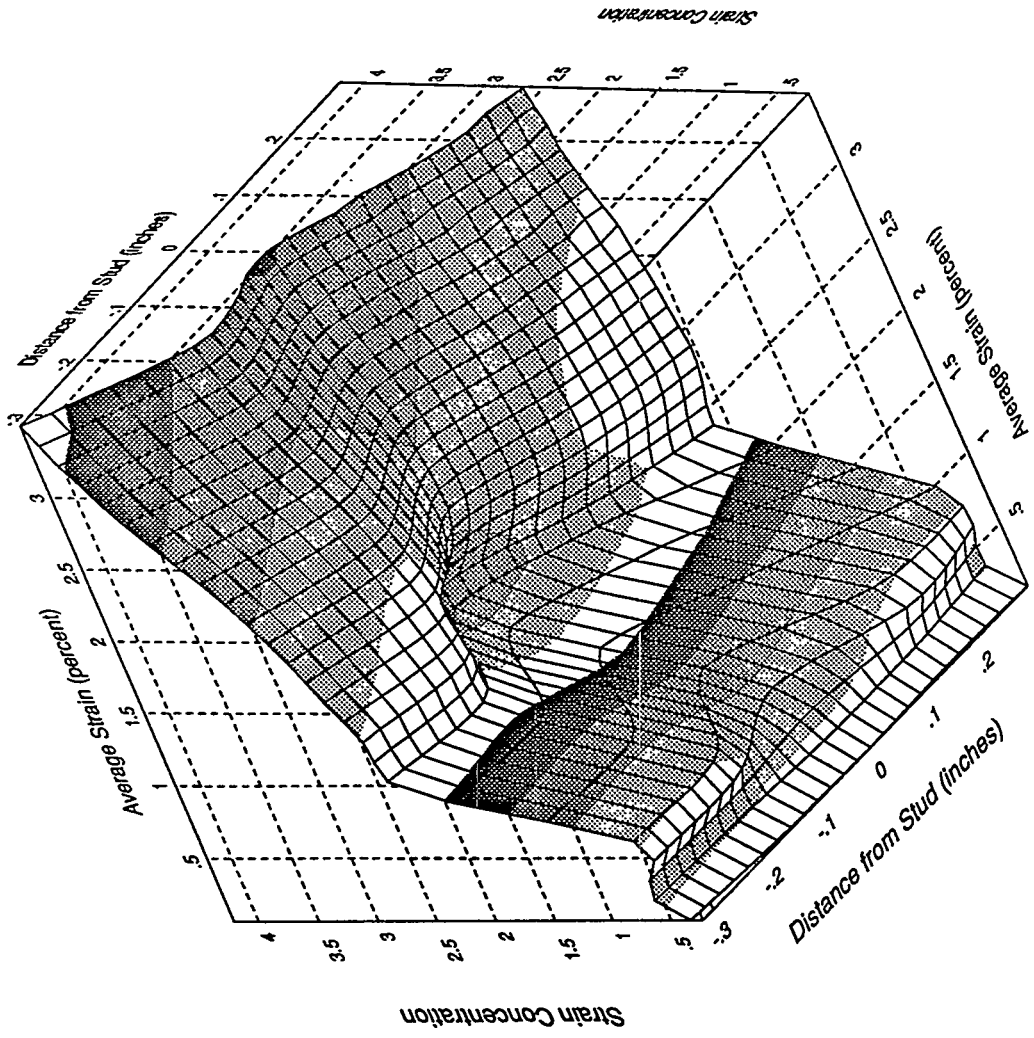

Back Edge Strip Gage, Specimen 2B2

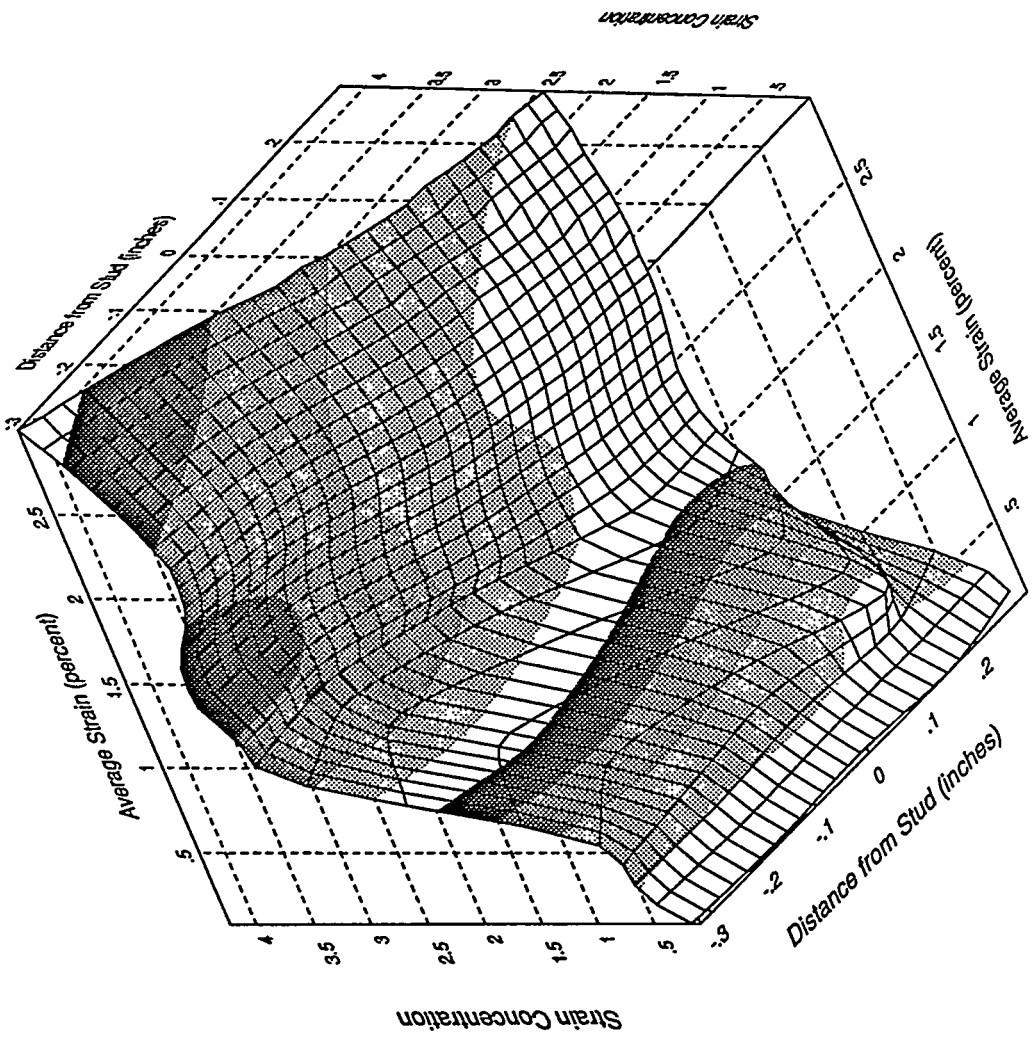

Back Edge Strip Gage, Specimen 2B3

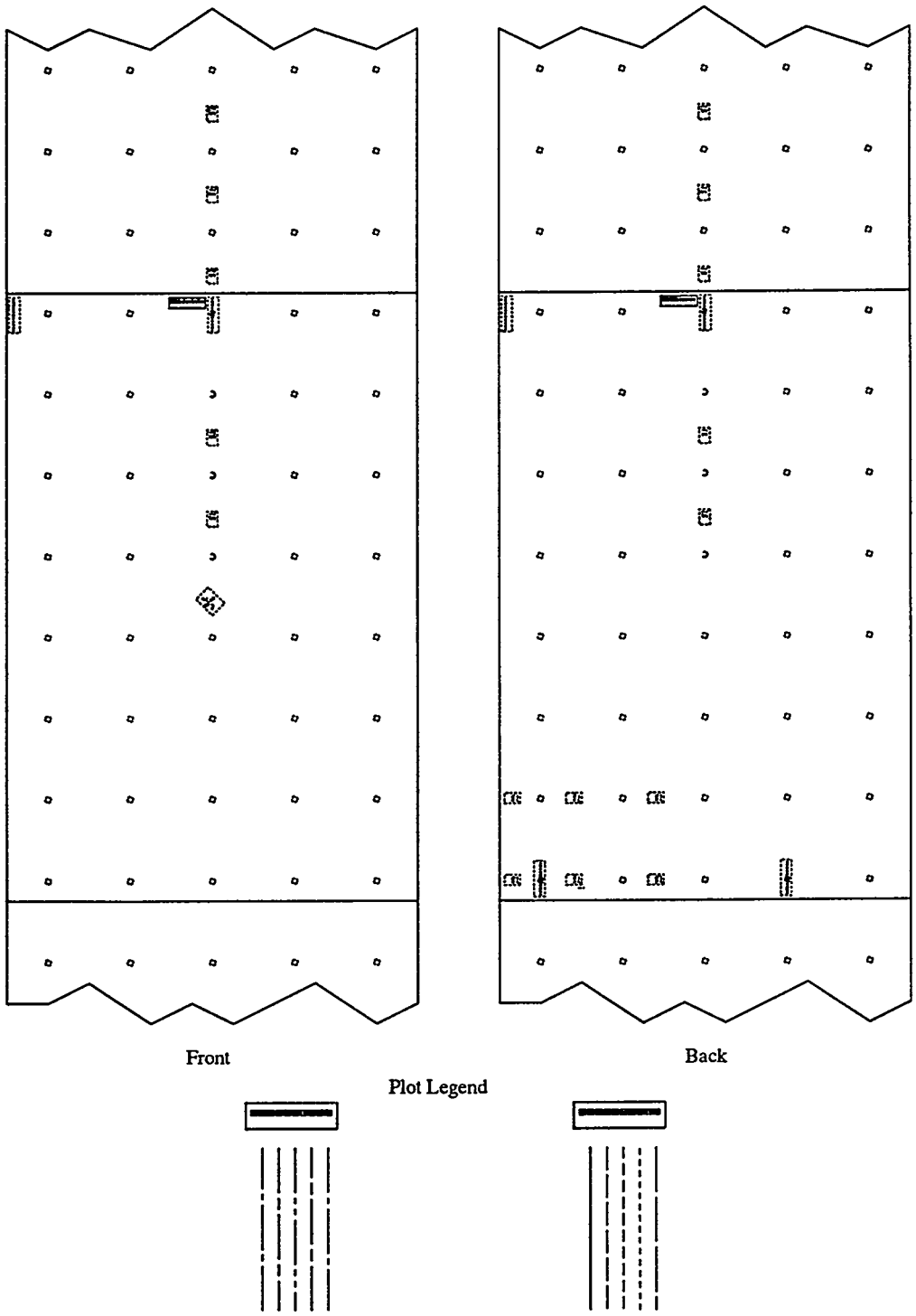

Poisson Strip Gages

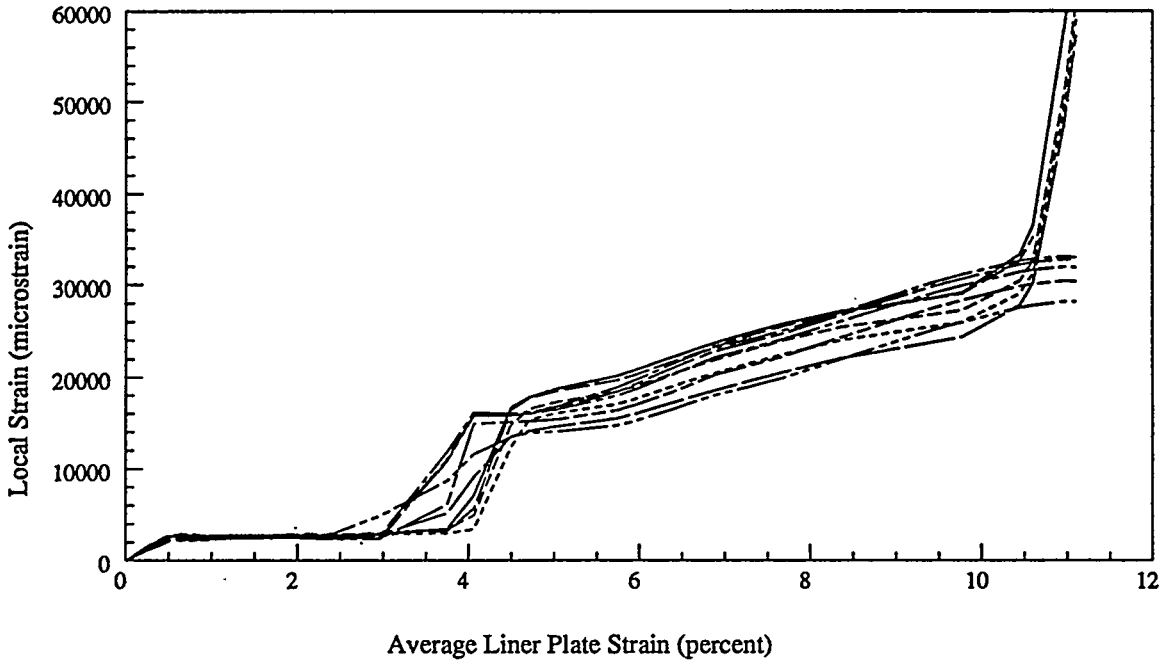

Poisson Strip Gage Response, Specimen 2B1

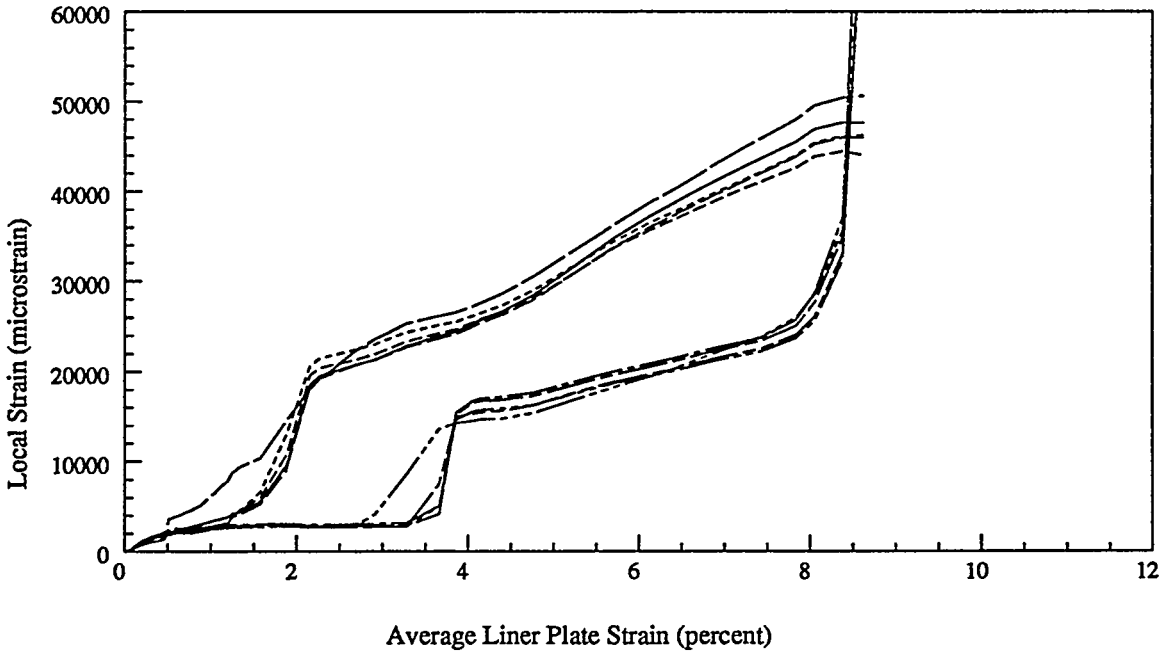

Poisson Strip Gage Response, Specimen 2B2

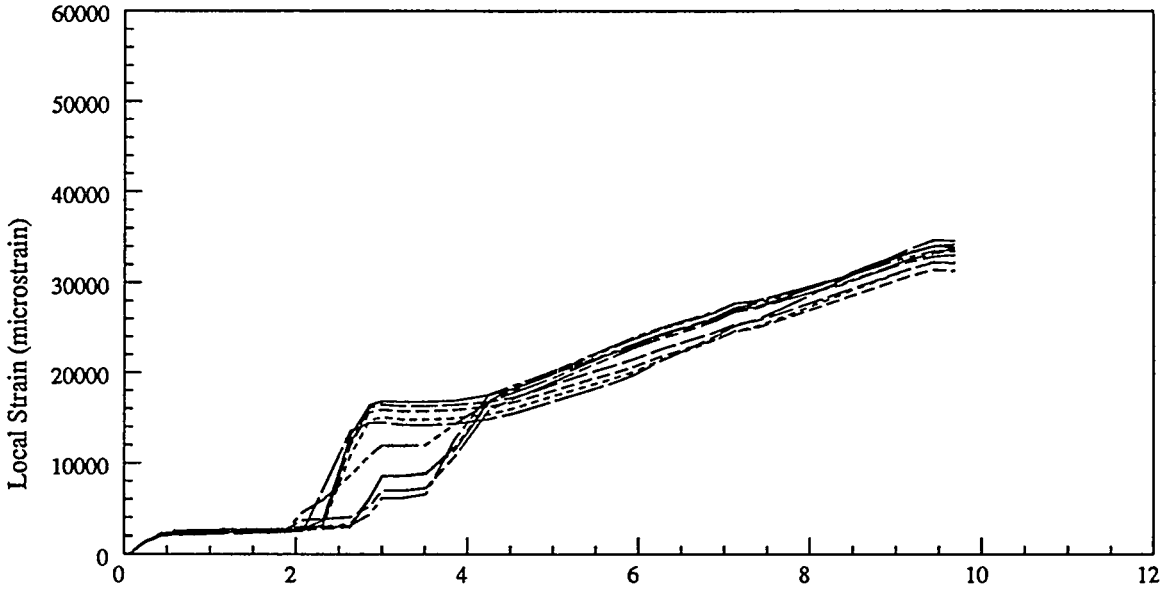

Poisson Strip Gage Response, Specimen 2B3

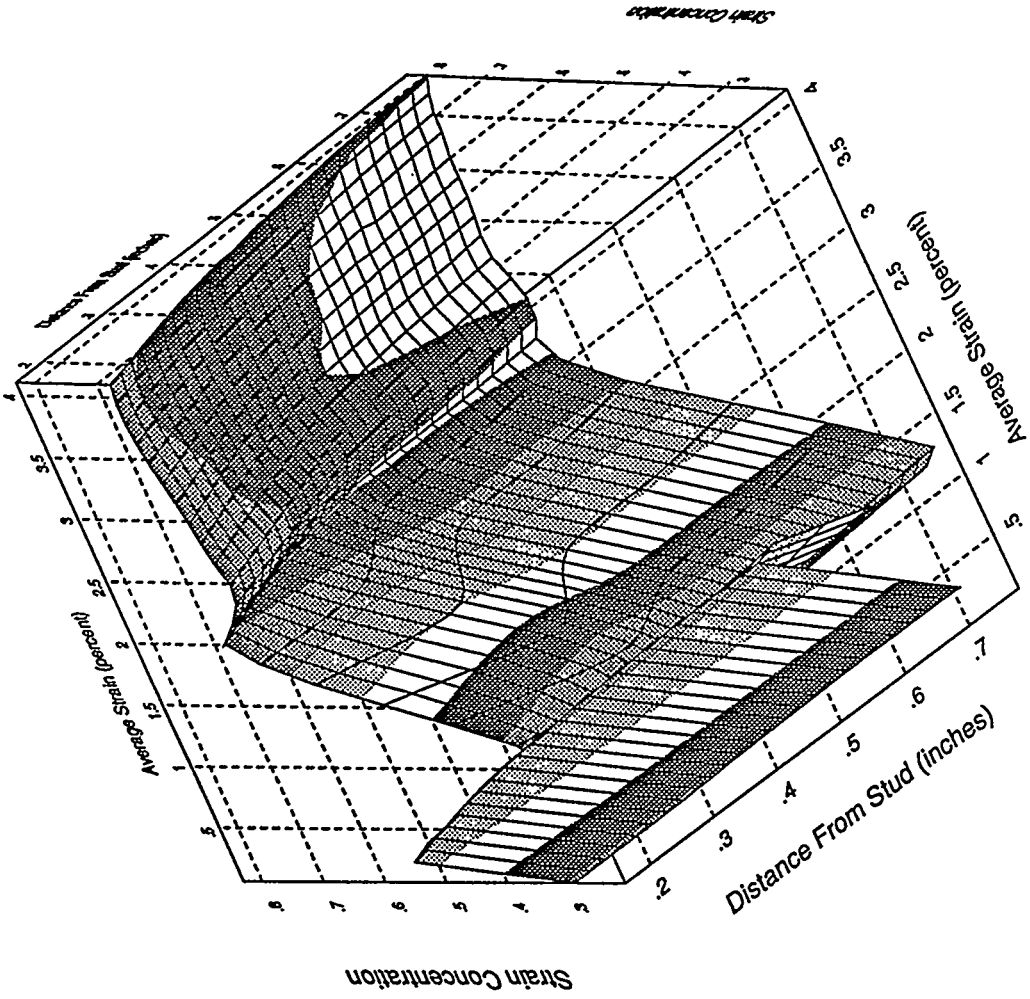

Front Transverse Strip Gage, Specimen 2B1

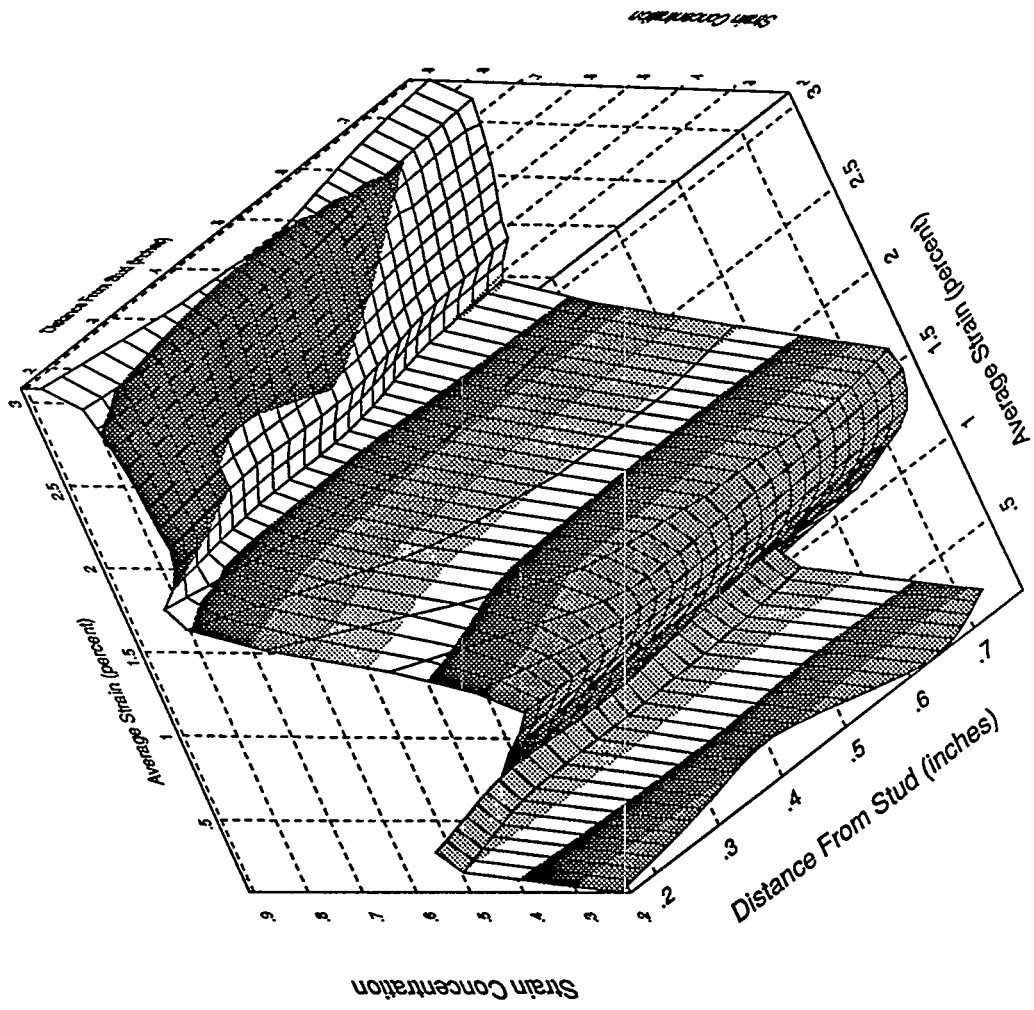

Front Transverse Strip Gage, Specimen 2B2

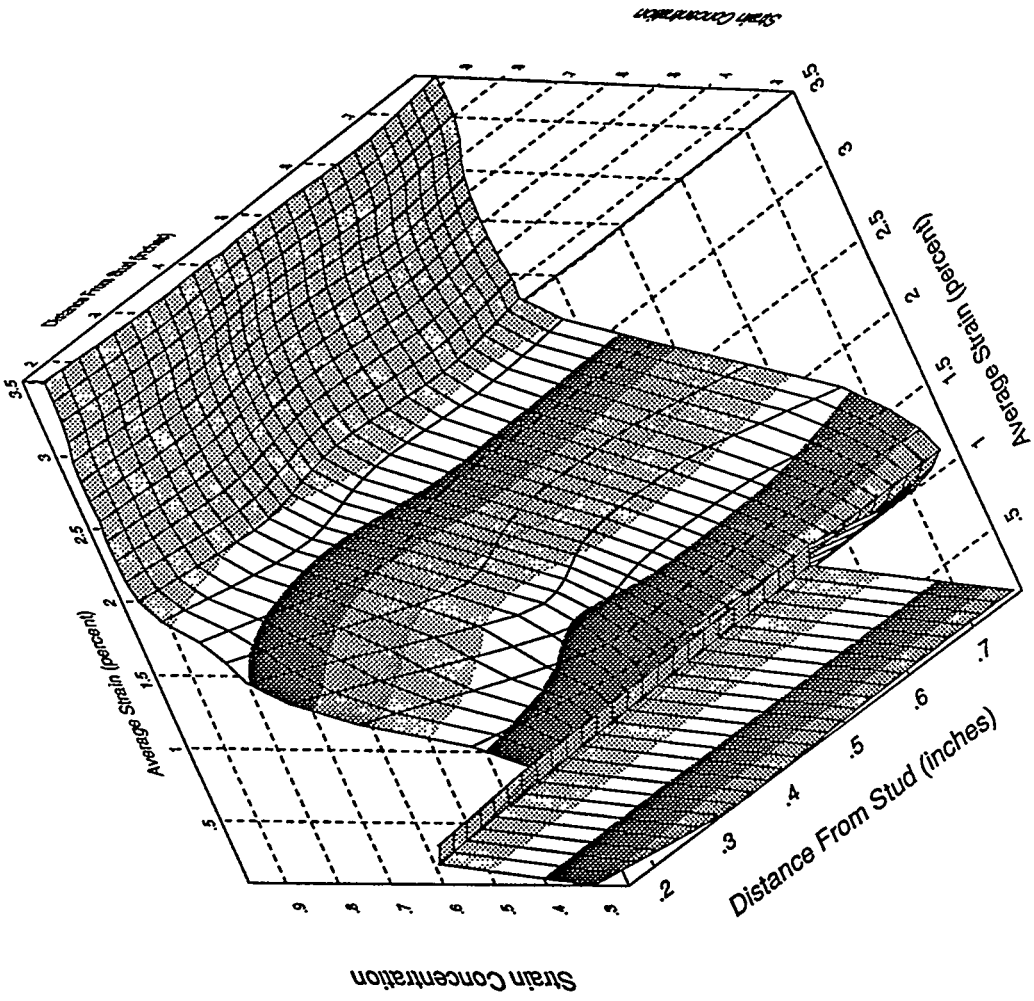

Front Transverse Strip Gage, Specimen 2B3

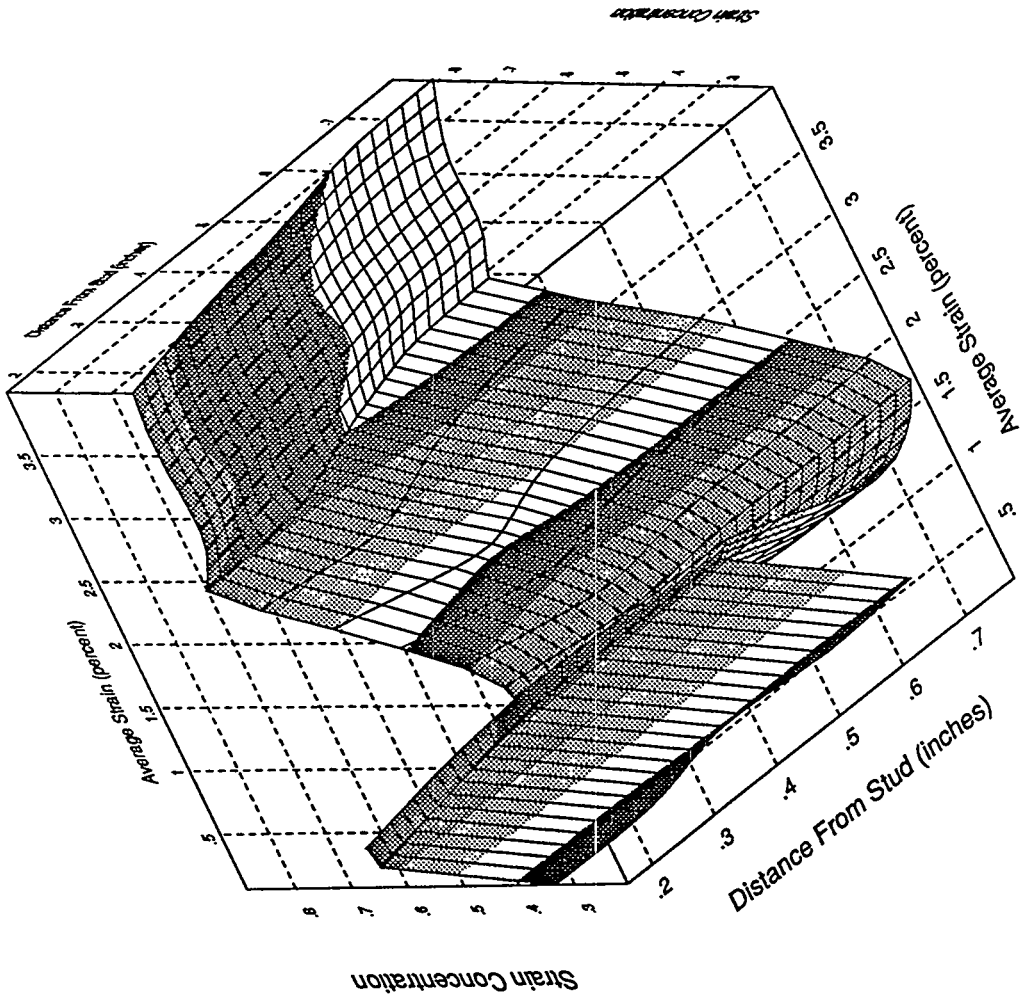

Back Transverse Strip Gage, Specimen 2B1

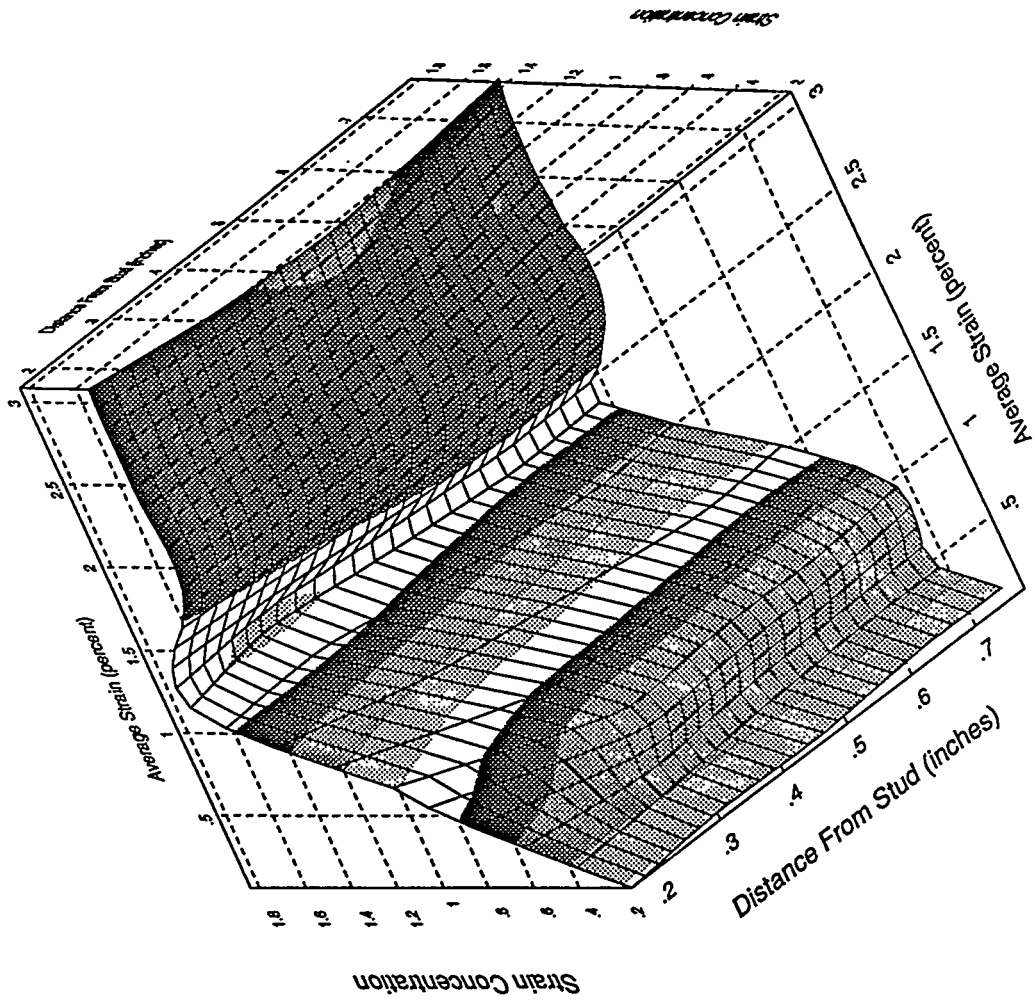

Back Transverse Strip Gage, Specimen 2B2

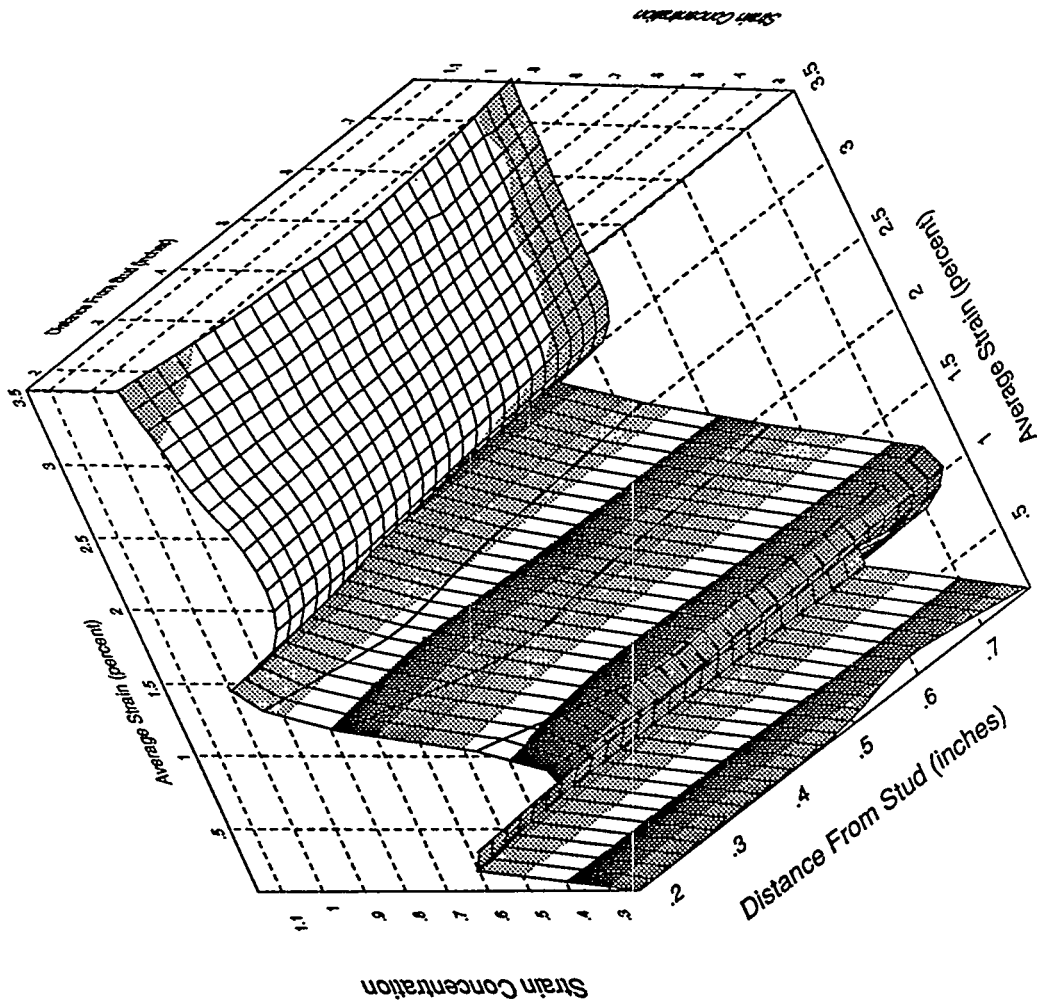

Back Transverse Strip Gage, Specimen 2B3

Appendix C
Summary of Reduced Photoelastic Data

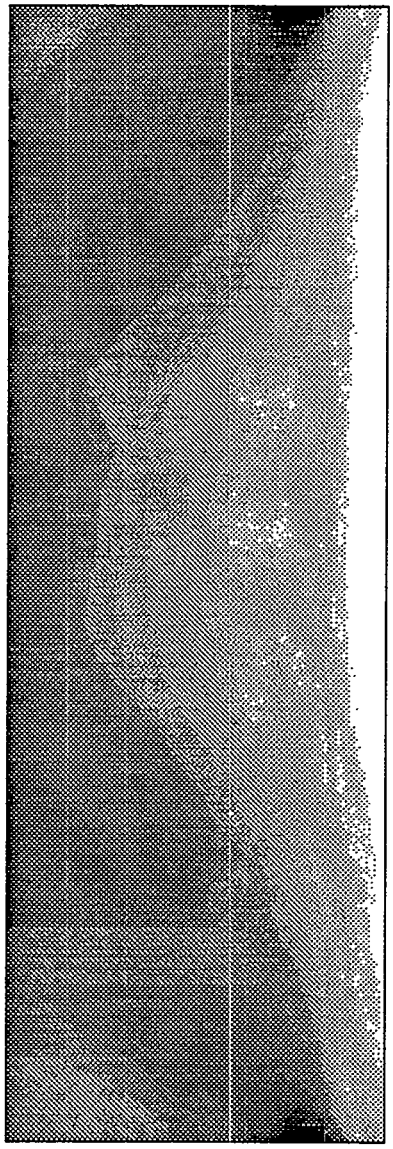

Weld/Thickness Transition Specimen at 49 kips/1.79" Elongation (weld at bottom)

Separately Controlled Loading Specimen Before Failure (Stud Load Only)

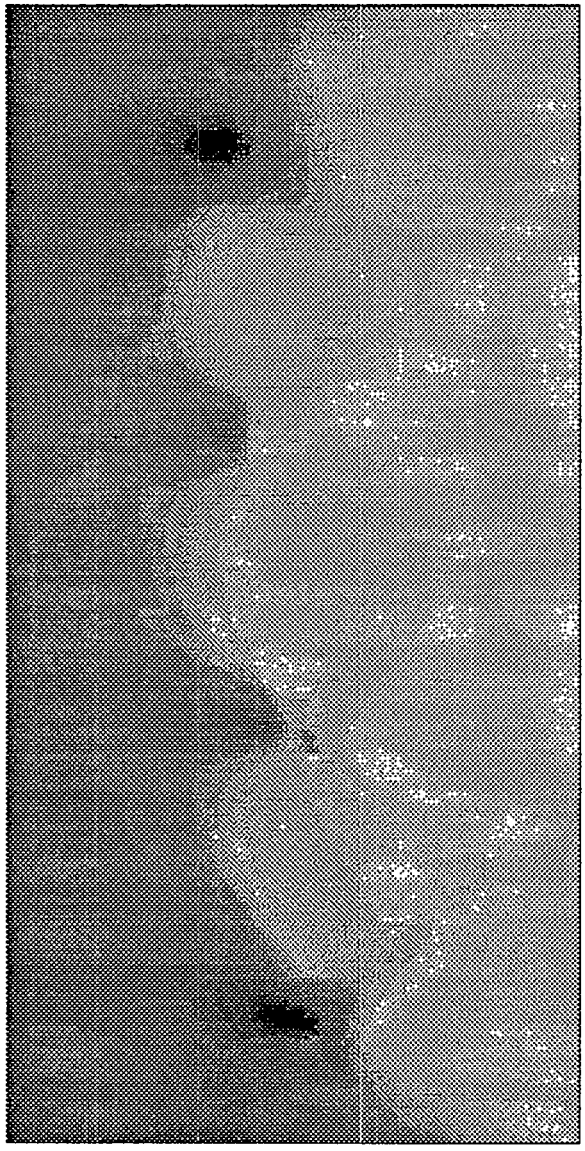

Separately Controlled Loading Specimen Before Failure (60 ksi Preload)

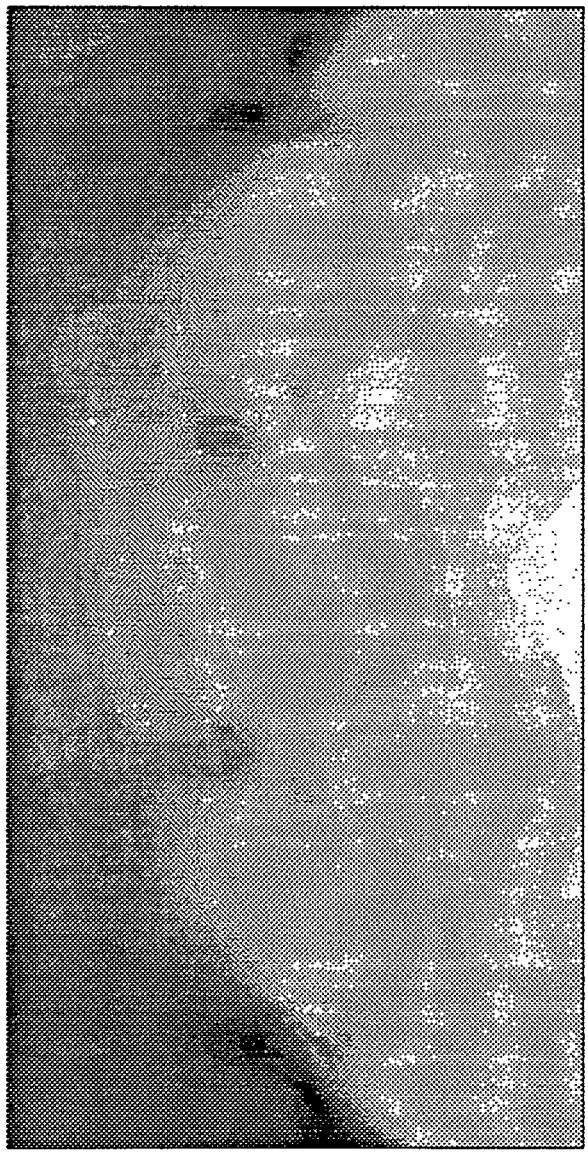

Separately Controlled Loading Specimen Before Failure (65 ksi Preload)

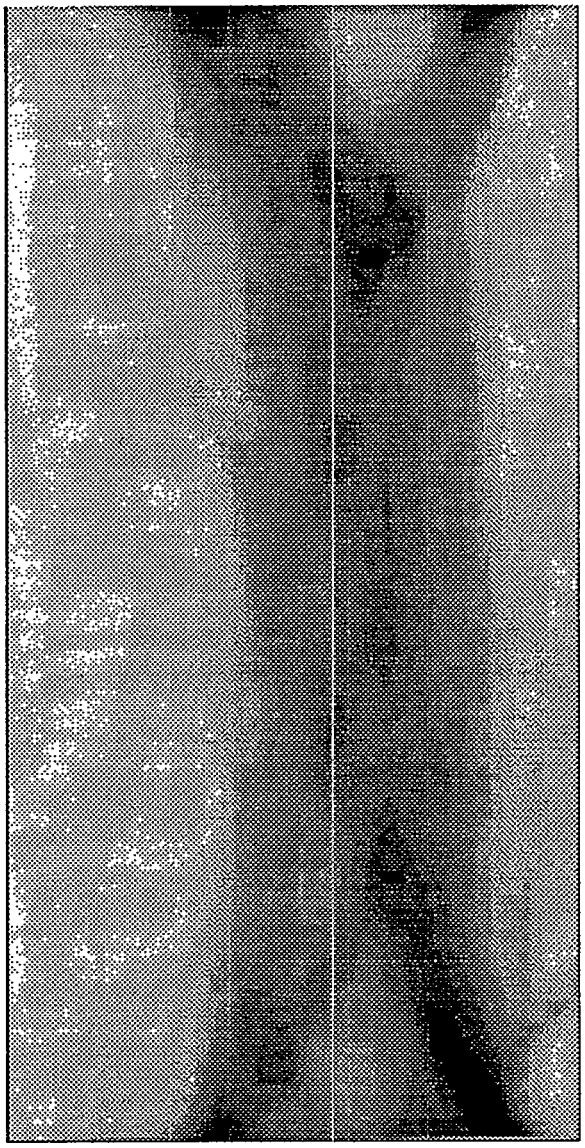

Separately Controlled Loading Specimen Before Failure (Liner Load Only)

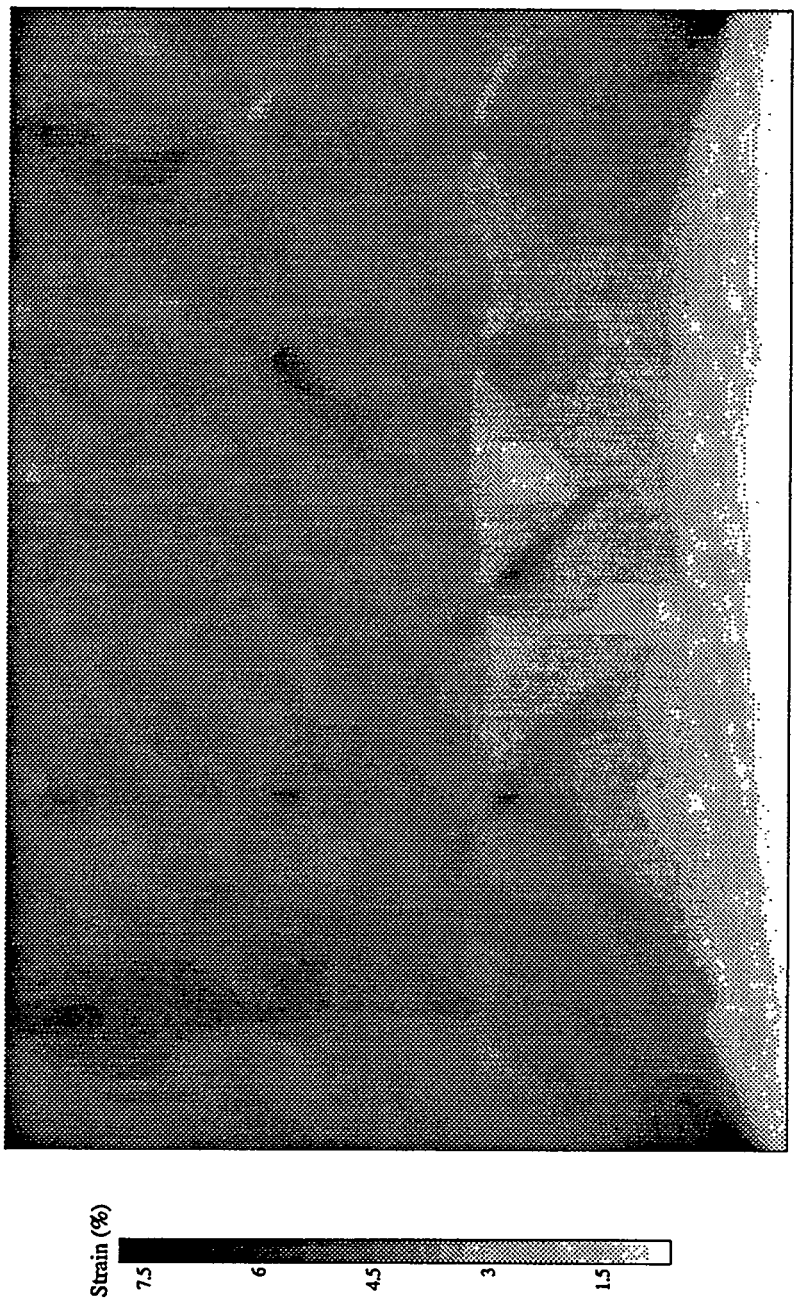

Full-Simulation Specimen at 1.79" Elongation

Richard N. White
School of Civil & Environmental
Engineering
Hollister Hall
Cornell University
Ithaca, NY 14853

M. Livolant
Commissariat a L'Energie Atomique
Centre d'Etudes Nucleaires de Saclay
F-91191 Gif-Sur-Yyette Cedex
France

P. Jamet
Commissariat a L'Energie Atomique
Centre d'Etudes Nucleaires de Saclay
F-91191 Gif-Sur-Yyette Cedex
France

A. Hoefler
Gesellschaft fuer Reaktorsicherheit
Schwertnergasse 1
D-5000 Koln 1
Germany

R. Krieg
Kernforschungszertrum Karlsruhe GmbH
Postfach 3640
D-7500 Karlsruhe
Germany

Dr. K. Kussmaul
Direktor der Staatlichen
Materialprufungsanstalt (MPA)
Universitat Stuttgart
D-70569 Stuttgart 80 (Vaihingen)
Germany

F. Schleifer
Gesellschaft fuer Reaktorsicherheit
Schwertnergasse 1
D-5000 Koln 1
Germany

H. Schulz
Gesellschaft fuer Reaktorsicherheit
Schwertnergasse 1
D-5000 Koln 1
Germany

Giuseppe Pino
ENEA-DISP
ACO-CIVME
Via Vitaliano Brancati, 48
Italy

Masashi Goto
Toshiba Corporation
Nuclear Plant Design & Engineering Department
Isogo Nuclear Engineering Center
8, Shinsugita-cho, Isogo-ku, Yokohama
Kanagawa 235, Japan

Katsuyoshi Imoto
Obayashi Corporation
Structural Engineering Department
Technical Research Institute
640, Shimokiyoto 4-chome, Kiyose-shi
Tokyo 204, Japan

Tadashi Kume
Hitachi, Ltd.
Nuclear Equipment 1st Design Section.
3-1-1, Saiwai-cho, Hitachi-shi
Ibaraki-ken 317, Japan

Dr. Takashi Kuroda
Shimizu Corporation
Nuclear Power Division
SEAVANS SOUTH
No. 2-3, Shibaura 1-chome, Minato-ku
Tokyo 105-07, Japan

Yasuyuki Murazumi
Taisei Corporation
1-25-1, Nishi Shinjuku, Shinjuku-ku
Tokyo 1 63-06, Japan

Masayuki Soejima
Senior Engineer
Mitsubishi Heavy Industries, Ltd.
Nuclear Containment Vessel Designing Section
1-1-1, Wadasaki-cho Hyogo-ku
Kobe 652, Japan

Dr. Toshikazu Takeda
Obayashi Corporation
Director & General Manager
Technical Research Institute
640, Shimokiyoto 4-chome, Kiyose-shi
Tokyo 204, Japan

Yoichiro Takeuchi
Deputy General Manager
Design Department
Nuclear Power Division
Shimizu Corporation
Mita 43, Mori Bldg. 13F,
No. 13-16, Mita 3-chome, Minato-ku,
Tokyo, 108, Japan

Dr. Hideo Ogasawara (2)
Director and General Manager
Systems Safety Department
Nuclear Power Engineering Corporation
Shuwa-Kamiyacho Building
3-13, 4-chome
Toranomon, Minato-ku
Tokyo 105, Japan

Dr. Kenji Takumi
Senior Advisor, Thermal & Nuclear
Power Plant Div.
Hitachi Plant Eng. & Const. Co., Ltd.
Imai-Mitsubshi Bldg. 5F
3-53-11 Minami-Otuska Toshima-Ku,
Tokoyo, 170 Japan

Haruji Tsubota
Kajima Corporation
Building Structural Engineering Department
Kajima Technical Research Institute
19-l Tobitakyu 2-Chome, Chofu-shi
Tokyo 182, Japan

Bertold W. Pfeifer
Bechtel Power Corporation
23rd Floor, Daewoo Center Building
541 5-ga, Namdaemoon-ro, Chung-ku
Seol, Korea

D. W. Phillips
Atomic Energy Authority
Safety and Reliability Directorate
Wigshaw Lane, Culcheth
Warrington WA3 4NE
United Kingdom

Peter Watson
HM Nuclear Installations Inspectorate BrC
St. Peter's House
Bootle, Merseyside L20 3LZ
United Kingdom

Internal SNL:
MS/0443 (1561) V. L. Bergman
MS/0443 (1561) J. R. Weatherby
MS/0736 (6400) N. R. Ortiz
MS/0744 (6403) W. A. vonRiesemann
MS/0744 (6403) J. L. Cherry
MS/0744 (6403) R. N. Eyers
MS/0744 (6403) M. F. Hessheimer
MS/0744 (6403) L. D. Lambert (10)
MS/0744 (6403) V. K. Luk
MS/0744 (6403) D. W. Pace
MS/0744 (6403) J. G. Pantuso
MS/0744 (6403) M. B. Parks
MS/0744 (6403) M. J. Rightley
MS/0949 (2111) B. L. Spletzer (5)
MS/0899 (13414) Technical Library (5)
MS/0619 (12615) Print Media
MS/9017 (8523) R. C. Christman
MS/9018 (8523-2) Central Technical Files

NRC FORM 335 (2-89) NRCM 1102, 3201, 3202

U.S. NUCLEAR REGULATORY COMMISSION

BIBLIOGRAPHIC DATA SHEET

(See instructions on the reverse)

1. REPORT NUMBER (Assigned by NRC, Add Vol., Supp., Rev., and Addendum Numbers, If any.)
NUREG/CR-6184
SAND92-1720

2. TITLE AND SUBTITLE
Separate Effects Testing and Analyses to Investigate Liner Tearing of the 1:16-Scale Reinforced Concrete Containment Building

3. DATE REPORT PUBLISHED
MONTH: May
YEAR: 1995

4. FIN OR GRANT NUMBER
A1817

5. AUTHOR(S)
B. L. Spletzer, L. D. Lambert, V. L. Bergman, J. R. Weatherby

6. TYPE OF REPORT
Technical

7. PERIOD COVERED *(Inclusive Dates)*

8. PERFORMING ORGANIZATION – NAME AND ADDRESS *(If NRC, provide Division, Office or Region, U.S. Nuclear Regulatory Commission, and mailing address; if contractor, provide name and mailing address.)*
Sandia National Laboratory
Albuquerque, NM 87185

9. SPONSORING ORGANIZATION – NAME AND ADDRESS *(If NRC, type "Same as above"; if contractor, provide NRC Division, Office or Region, U.S. Nuclear Regulatory Commission, and mailing address.)*
Division of Engineering Technology
Office of Nuclear Regulatory Research
U.S. Nuclear Regulatory Commission
Washington, DC 20555-0001

10. SUPPLEMENTARY NOTES

11. ABSTRACT *(200 words or less)*

The overpressurization of a 1:6-scale reinforced concrete containment building demonstrated that liner tearing is a plausible failure mode in such structures under severe accident conditions. A combined experimental and analytical program was developed to determine the important parameters that affect liner tearing and to develop reasonably simple analytical methods for predicting when tearing will occur. Three sets of test specimens were designed to allow individual control over and investigation of the mechanisms believed to be important in causing failure of the liner plate. The series of tests investigated the effect on liner tearing produced by the anchorage system, the loading conditions, and the transition in thickness from the liner to the insert plate. Before testing, the specimens were analyzed using two- and three-dimensional finite element models. Based on the analysis, the failure mode and corresponding load conditions were predicted for each specimen. Test data and post-test examination of test specimens show mixed agreement with the analytical predictions with regard to failure mode and specimen response for most tests. Many similarities were also observed between the response of the liner in the 1:6-scale reinforced concrete containment model and the response of the test specimens. This work illustrates the fact that the failure mechanism of a reinforced concrete containment building can be greatly influenced by details of liner and anchorage system design. Further, it significantly increases the understanding of containment building response under severe conditions.

12. KEY WORDS/DESCRIPTORS *(List words or phrases that will assist researchers in locating the report.)*
liner
tearing
containment
anchorage
separate effects
analysis

13. AVAILABILITY STATEMENT
Unlimited

14. SECURITY CLASSIFICATION
(This Page)
Unclassified
(This Report)
Unclassified

15. NUMBER OF PAGES

16. PRICE

NRC FORM 335 (2-89)

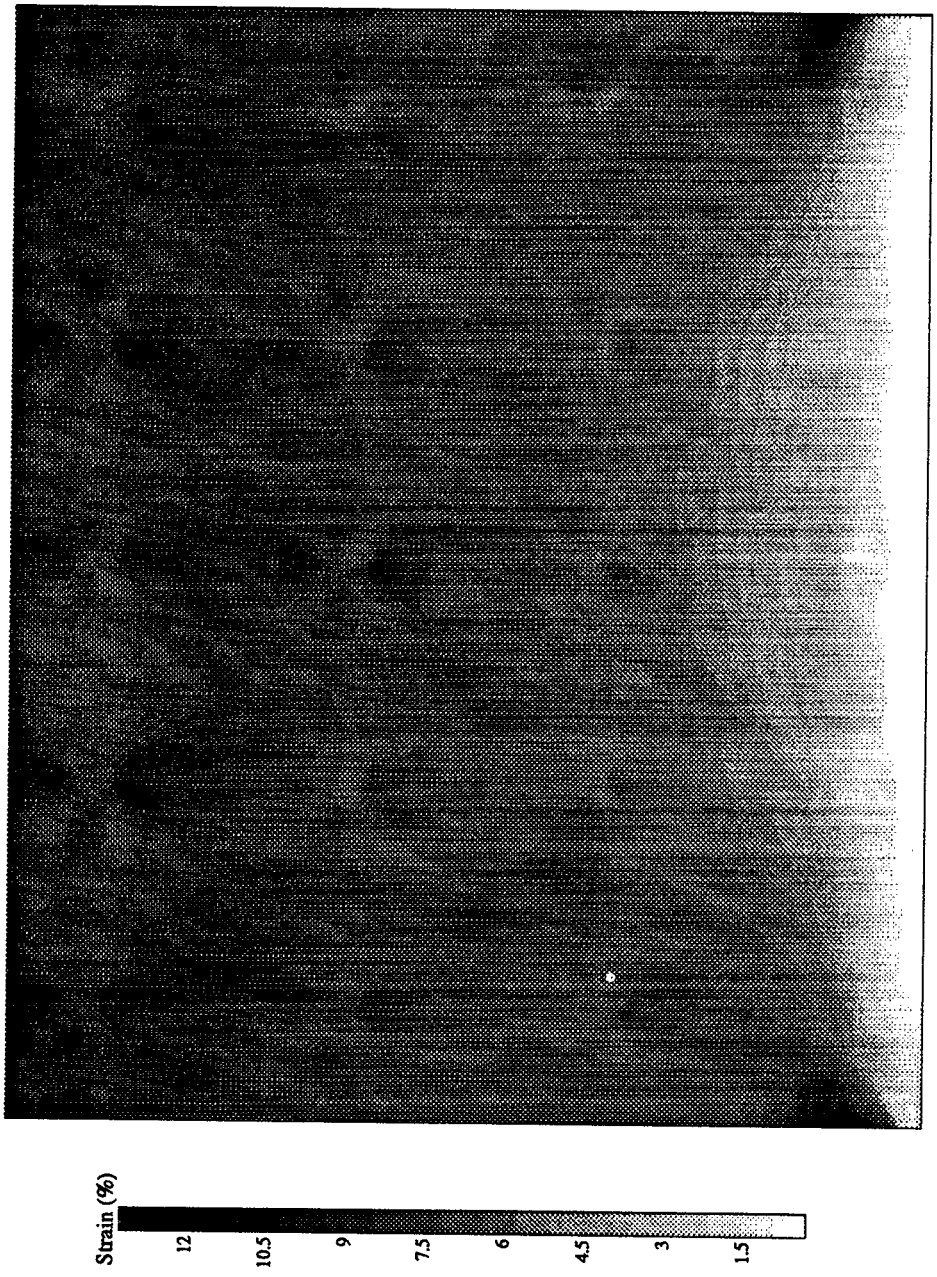

Full-Simulation Specimen Immediately Before Failure

Distribution:

James F. Costello (10)
U.S. Nuclear Regulatory Commission
RES/DE/SSEB
TWF-MS-L1
Washington, DC 20555-0001

Wallace E. Norris
U.S. Nuclear Regulatory Commission
RES/DE/SSEB/STS
TWF-MS-L1
Washington, D.C. 20555-0001

Hansraj G. Ashar
U.S. Nuclear Regulatory Commission
NRR/ESGB, OWFN 7H15
Washington, DC 20555-0001

Goutam Bagchi
U.S. Nuclear Regulatory Commission
NRR/ESGB, OWFN 7H15
Washington, DC 20555-0001

Herman L. Graves
U.S. Nuclear Regulatory Commission
RES/DE/SSEB/STS
TWF-MS-L1
Washington, DC 20555-0001

Thomas J. Ahl
Chicago Bridge & Iron
Technical Services Co.
800 Jorie Boulevard
Oak Brook, IL 60521

Bryan A. Erler
Sargent & Lundy Engineers
55 East Monroe Street
Chicago, IL 60603

Lyle D. Gerdes
ABB Combustion Engineering
Nuclear Power
Combustion Engineering, Inc.
P. O. Box 500
Windsor, CT 06095-0500

L. Greimann
Iowa State University
Dept. of Civil Engineering
420 Town Engineering Bldg.
Ames, IA 50011

Theodore E. Johnson
1435 Waters Edge Dr.
Augusta, GA 30901

J. M. Kennedy
Argonne National Laboratory
9700 South Cass Avenue
Argonne, IL 60439

R. F. Kulak
Argonne National Laboratory
9700 South Cass Avenue
Argonne, IL 60439

Richard S. Orr
Westinghouse Electric Corporation
NATD
MS 4-28
P. O. Box 355
Pittsburgh, PA 15230

Phillip Pfeiffer
Argonne National Laboratory
9700 South Cass Avenue
Argonne, IL 60439

Y. R. Rashid
ANATECH International Corp.
3344 N. Torrey Pines Court
LaJolla, CA 92037

Mete A. Sozen
Department of Civil Engineering
University of Illinois
Room 1245 Newmark Laboratory
205 N. Mathews Ave.
Urbana. IL 61801-2397

John D. Stevenson
Stevenson & Associates
9217 Midwest Ave.
Cleveland, OH 44125

H. T. Tang
Electrical Power Research Institute
3412 Hillview Avenue
Palo Alto, CA 94303

Harold Townsend
GE Nuclear Energy
ABWR Programs
175 Curtner Avenue
San Jose. CA 95125

Joseph J. Ucciferro
U E & C Nuclear Inc.,
% Philadelphia Electric
965 Chesterbrook Blvd.
MS 62C-3
Wayne, PA 19087